

UNIVERSIDAD DE CÓRDOBA

Programa de doctorado: QUÍMICA FINA

Título de la tesis: "MATERIALES PARA DESARROLLAR NUEVAS BATERÍAS DE ION-LITIO Y POST-LITIO" ("MATERIALS FOR DEVELOPING NEW LITHIUM ION BATTERIES AND POST LITHIUM ONES")

Director/Directores: RICARDO ALCÁNTARA ROMÁN Y GREGORIO ORTIZ JIMÉNEZ

Autor de la tesis: MARTA CABELLO BERMÚDEZ

Fecha de depósito tesis en el Idep:

TITULO: *MATERIALES PARA DESARROLLAR NUEVAS BATERÍAS DE ION-LITIO Y POST-LITIO*

AUTOR: *Marta Cabello Bermúdez*

© Edita: UCOPress. 2018
Campus de Rabanales
Ctra. Nacional IV, Km. 396 A
14071 Córdoba

<https://www.uco.es/ucopress/index.php/es/ucopress@uco.es>



UNIVERSIDAD DE CÓRDOBA

Tesis doctoral

**“MATERIALES PARA DESARROLLAR NUEVAS
BATERÍAS DE ION-LITIO Y POST-LITIO”**

Marta Cabello Bermúdez

DIRECTORES

Dr. D. Ricardo Alcántara Román

Catedrático de Universidad

Dr. D. Gregorio F. Ortiz Jiménez

Profesor Contratado Doctor

Departamento de Química Inorgánica e Ingeniería Química

UNIVERSIDAD DE CÓRDOBA

2018



TÍTULO DE LA TESIS: MATERIALES PARA DESARROLLAR NUEVAS BATERÍAS DE ION-LITIO Y POST-LITIO

DOCTORANDO/A: MARTA CABELLO BERMÚDEZ

INFORME RAZONADO DEL/DE LOS DIRECTORES DE LA TESIS

D. Ricardo Alcántara Román, Catedrático de Universidad, y D. Gregorio Ortiz Jiménez, Profesor Contratado Doctor, miembros del Departamento de Química Inorgánica e Ingeniería Química de la Universidad de Córdoba, informan que la Tesis Doctoral presentada por Marta Cabello Bermúdez, titulada

"MATERIALES PARA DESARROLLAR NUEVAS BATERÍAS DE ION-LITIO Y POST-LITIO"

se ha realizado dentro del Programa de Doctorado con Mención hacia la Excelencia de Química Fina, en el Departamento de Química Inorgánica e Ingeniería Química (Área de Química Inorgánica) de la Universidad de Córdoba, durante el desarrollo de los proyectos FQM7206 (excelencia de la Junta de Andalucía) y MAT2014-56470-R (Ministerio de Economía y Competitividad) y el contrato predoctoral (ayuda FPI con referencia BES-2015-071592) asociado a este último proyecto. La presente memoria reúne, a juicio de los directores, los requisitos exigidos, y ha dado lugar a más de tres artículos publicados en revistas científicas incluidas en el primer cuartil de la relación de revistas del ámbito de la especialidad, con índice de calidad relativo y en los cuales el doctorando es primer autor. Los directores de la Tesis informan además de la dedicación adecuada del doctorando, los conocimientos destacados en el campo objeto de su trabajo que ha adquirido, y su capacidad investigadora, incluyendo diseño y realización de experimentos, discusión de resultados y extracción de conclusiones. Así mismo, informan de la realización de una estancia de tres meses del doctorando en la School of Chemistry en Manchester (Reino Unido), y de la existencia de dos informes favorables de doctores extranjeros.

Por todo ello, se autoriza la presentación de la tesis doctoral.

Córdoba, 25 de Julio de 2018

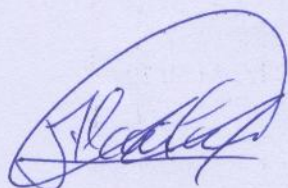
Firma de los directores

Fdo.: Ricardo Alcántara Román

Fdo.: Gregorio F. Ortiz Jiménez

D. Ricardo Alcántara Román, Catedrático de Universidad, y D. Gregorio F. Ortiz Jiménez, Profesor Contratado Doctor de Universidad, miembros del Departamento de Química Inorgánica e Ingeniería Química, INFORMAN: Que la Tesis Doctoral titulada **“MATERIALES PARA DESARROLLAR NUEVAS BATERÍAS DE ION-LITIO Y POST-LITIO”** presentada por Dña. Marta Cabello Bermúdez ha sido desarrollada en los laboratorios del Departamento de Química Inorgánica e Ingeniería Química de la Universidad de Córdoba durante el disfrute de un contrato predoctoral (ayuda FPI con referencia BES-2015-071592) del Ministerio de Economía y Competitividad asociado al proyecto nacional MAT2014-56470-R: “BATERIAS POST ION-LI: DEL SODIO AL ALUMINIO”, y que a su juicio reúne todos los requisitos exigidos a este tipo de trabajo.

Firmas:



Dr. D. Ricardo Alcántara Román



Dr. D. Gregorio F. Ortiz Jiménez

Mediante la defensa de esta memoria se pretende optar a la obtención de la mención de “Doctorado Internacional”, habida cuenta que el doctorando reúne los requisitos exigidos para tal mención:

1. Se cuenta con los informes favorables de dos doctores pertenecientes a instituciones de Enseñanza Superior, o instituto de investigación, de países europeos distintos al nuestro.
2. En el Tribunal, que ha de evaluar la Tesis, existe un miembro de un centro de Enseñanza Superior de un país europeo distinto al nuestro.
3. El doctorando ha realizado su estancia en el Manchester Electrochemistry Research Group (School of Chemistry, University of Manchester) en la ciudad de Manchester (Reino Unido). Esta estancia, de un trimestre de duración, se ha realizado gracias al contrato predoctoral (ayuda FPI con referencia BES-2015-071592) del Ministerio de Economía y Competitividad.
4. Parte de la redacción y defensa de la Memoria se realizará en la lengua oficial de un país europeo distinto al nuestro.

**“MATERIALES PARA
DESARROLLAR NUEVAS
BATERÍAS DE ION-LITIO Y POST-
LITIO”**

Memoria presentada por **MARTA CABELLO BERMÚDEZ** para optar al
grado de **DOCTORA** por la **UNIVERSIDAD DE CÓRDOBA**

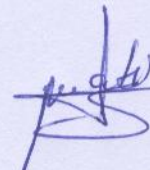


Fdo.: Marta Cabello Bermúdez

Dirigido por:



Dr. D. Ricardo Alcántara Román



Dr. D. Gregorio F. Ortiz Jiménez

INFORME DE LOS ARTÍCULOS PUBLICADOS SEGÚN EL JOURNAL CITATION REPORT

Los artículos que se exponen en la presente memoria han sido publicados en revistas cuyos factores de impacto están recogidos en la siguiente tabla, y según el Journal Citation Report del Web of Science teniendo en cuenta el año de publicación:

Journal	Year of publication	Impact factor	Category	Rank	Quartile
<i>Journal of The Electrochemical Society</i>	2017	3.662	Materials Science, Coatings & Films	2/19	Q1
			Electrochemistry	10/28	Q2
	2016	3.259	Materials Science, Coatings & Films	2/19	Q1
			Electrochemistry	9/29	Q2
<i>Electrochimica Acta</i>	2017	5.116	Electrochemistry	5/28	Q1
<i>Electrochemistry Communications</i>	2016	4.396	Electrochemistry	5/29	Q1
	2015	4.569	Electrochemistry	5/27	Q1
<i>Journal of Power Sources</i>	2017	6.945	Chemistry, Physical	26/146	Q1
			Electrochemistry	3/28	Q1
			Energy & fuels	9/97	Q1
			Materials science, multidisciplinary	34/285	Q1
	2016	6.395	Chemistry, Physical	22/146	Q1
			Electrochemistry	2/29	Q1
			Energy & fuels	8/92	Q1
			Materials science, multidisciplinary	31/275	Q1
<i>Scientific Reports</i>	2016	4.259	Multidisciplinary sciences	10/64	Q1
<i>Journal of Alloys and Compounds</i>	2015	3.014	Chemistry, Physical	52/144	Q2
			Materials science, multidisciplinary	58/271	Q1
			Metallurgy & Metallurgical Engineering	4/73	Q1
<i>CrystEngComm</i>	2015	3.849	Chemistry, Multidisciplinary	38/163	Q1
			Crystallography	5/26	Q1
<i>RSC Advances</i>	2016	3.108	Chemistry, Multidisciplinary	59/166	Q2

AGRADECIMIENTOS

Me gustaría mostrar mi agradecimiento a aquellas personas e instituciones que han contribuido a que la realización de esta tesis doctoral sea posible.

En primer lugar, me gustaría dar las gracias a mis directores de tesis, Dr. Ricardo Alcántara Román y Dr. Gregorio Ortiz Jiménez, por la oportunidad de realizar esta tesis. Gracias por guiarme y ayudarme durante toda la etapa de investigación y por vuestro constante apoyo y ayuda durante la recta final de la redacción de esta tesis. Habéis aportado mucho a mi formación.

Al programa de doctorado “ Química Fina”, al grupo PAI FQM288 y al departamento de Química Inorgánica e Ingeniería Química de la Universidad de Córdoba, por aceptarme como estudiante de postgrado y permitir así desarrollar mi labor investigadora.

También agradezco a las instituciones que han financiado este trabajo: Junta de Andalucía (proyecto de Excelencia FQM7206) y Ministerio de Economía y Competitividad (proyecto MAT2014-56470-R con la ayuda predoctoral asociada BES-2015-071592).

Al Servicio Central de Apoyo a la Investigación (SCAI) de la Universidad de Córdoba.

Al Prof. Robert Dryfe, de la Universidad de Manchester (Reino Unido), por permitir la realización de mi estancia predoctoral en su grupo de investigación. También agradezco al resto de compañeros de este laboratorio mancomuniano, por hacer más amena y productiva mi estancia en la ciudad, y por proporcionar ese gran ambiente de trabajo.

Al Dr. José Luis Tirado Coello, para mí ha sido un tercer director de tesis. Gracias por aceptarme en tu grupo de investigación y por el apoyo recibido. También agradezco la ayuda y ánimo transmitidos por el Dr. Pedro Lavela Cabello y Dr. Carlos Pérez Vicente.

A los compañeros y ex compañeros del grupo de investigación, al Dr. Daniel Cíntora, a la Dra. Mayca Zafra, a Saúl Rubio y a David Tirado. También a María del Carmen Mohedano.

Al Dr. Rafael Klee, por todas las historias vividas dentro y fuera del “lab” que a ambos nos hicieron más amena nuestra etapa como doctorandos (nuestros “holaaaa”, el “*trambóliko*” y todos los memes que nos recordaban el uno al otro).

A los veteranos del laboratorio, la Dra. María José Aragón y el Dr. Francisco Nacimiento, por el fantástico ambiente de trabajo durante estos años y por los momentos vividos. Compis, gracias por aguantarme en ciertos momentos, por escuchar mis “historias”, por los consejos recibidos, por todas las risas, por apagar la “mecha corta”, etc. En cuanto a lo profesional, he aprendido muchísimo de vosotros. ¡Gracias amigos!

También a las personas que han formado parte de mi aventura por tierras cordobesas a lo largo de estos cinco años. Espero que sigan presentes de un modo u otro en mis próximas aventuras.

Finalmente, mi mayor agradecimiento es para mi familia (Peluso, tú también), en especial a mi madre. Tú me diste el “empujón” necesario para venir a Córdoba y gracias a ti siempre he llegado a finalizar todo lo que me he propuesto. Porque tú también eres una “doctora en cómo se hace el doctorado” al haberme escuchado tantas veces hablar del tema, de los artículos, de las clases, de los congresos, de la estancia... Desde el principio “no tengo artículos” a la recta final “la silla está rota, esta mesa no sirve pa’ estudiar” siempre he tenido tu apoyo y cariño. GRACIAS.

A Custodia y Máximo

“Todo esfuerzo tiene su recompensa”

ÍNDICE

Capítulo 1. Introducción

1.1	La problemática energética.....	1
1.2	Celda galvánica.....	3
1.3	Fundamentos de las baterías	4
1.4	Baterías de ion litio.	9
1.5	Baterías de ion sodio.....	11
1.6	Baterías de magnesio y de ion magnesio.....	13
1.7	Baterías híbridas Mg-X (X=Li o Na).....	15
1.8	Baterías de ion calcio	16
1.9	Baterías de ion aluminio.....	18
1.10	Baterías acuosas	19
1.11	Objetivos y plan de trabajo.....	22
	Bibliografía.....	25

Capítulo 2. Materiales nanoestructurados para baterías de ion litio..... 31

2.1	Self-assembled $\text{Li}_4\text{Ti}_5\text{O}_{12}$ / TiO_2 / Li_3PO_4 for integrated Li-ion microbatteries.....	33
	2.1.1 <i>Introduction</i>	
	2.1.2 <i>Experimental</i>	
	2.1.3 <i>Results and discussion</i>	
	2.1.4 <i>Conclusions</i>	
	2.1.5 <i>References</i>	
2.2	Exploring a Li-ion battery using surface modified titania nanotubes versus high voltage cathode nanowires.....	47
	2.2.1 <i>Introduction</i>	
	2.2.2 <i>Experimental</i>	
	2.2.3 <i>Results and discussion</i>	
	2.2.4 <i>Conclusions</i>	

2.2.5	<i>References</i>	
2.2.6	<i>Supplementary information</i>	
2.3	Enhancing the energy density of safer Li-ion batteries by combining high-voltage lithium cobalt fluorophosphate cathodes and nanostructured titania anodes.....	73
2.3.1	<i>Introduction</i>	
2.3.2	<i>Experimental</i>	
2.3.3	<i>Results and discussion</i>	
2.3.4	<i>Conclusions</i>	
2.3.5	<i>References</i>	
2.3.6	<i>Supplementary information</i>	
Capítulo 3. Baterías post-litio: ánodos para baterías de ion sodio		91
3.1	Self-organized sodium titanate/titania nanoforest for the negative electrode of sodium-ion microbatteries.....	93
3.1.1	<i>Introduction</i>	
3.1.2	<i>Experimental</i>	
3.1.3	<i>Results and discussion</i>	
3.1.4	<i>Conclusions</i>	
3.1.5	<i>References</i>	
3.1.6	<i>Supplementary information</i>	
3.2	Treasure Na-ion anode from trash coke by adept electrolyte selection.....	121
3.2.1	<i>Introduction</i>	
3.2.2	<i>Experimental</i>	
3.2.3	<i>Results and discussion</i>	
3.2.4	<i>Conclusions</i>	
3.2.5	<i>References</i>	
3.2.6	<i>Supplementary information</i>	

3.3	On the reliability of sodium co-intercalation in expanded graphite prepared by different methods as anodes for sodium-ion batteries.....	151
3.3.1	<i>Introduction</i>	
3.3.2	<i>Experimental</i>	
3.3.3	<i>Results and discussion</i>	
3.3.4	<i>Conclusions</i>	
3.3.5	<i>References</i>	
3.3.6	<i>Supplementary information</i>	

Capítulo 4. Baterías post-litio: materiales para baterías de iones multivalentes..... 185

4.1	Electrochemical and chemical insertion/deinsertion of magnesium in spinel-type MgMn_2O_4 and $\lambda\text{-MnO}_2$ for both aqueous and non-aqueous magnesium-ion batteries.....	187
4.1.1	<i>Introduction</i>	
4.1.2	<i>Experimental</i>	
4.1.3	<i>Results and discussion</i>	
4.1.4	<i>Conclusions</i>	
4.1.5	<i>References</i>	
4.1.6	<i>Supplementary information</i>	
4.2	Nanobelts of beta-sodium vanadate as electrode for magnesium and dual magnesium-sodium batteries.....	213
4.2.1	<i>Introduction</i>	
4.2.2	<i>Experimental</i>	
4.2.3	<i>Results and discussion</i>	
4.2.4	<i>Conclusions</i>	
4.2.5	<i>References</i>	
4.2.6	<i>Supplementary information</i>	
4.3	$\text{Na}_3\text{V}_2(\text{PO}_4)_3$ as electrode material for rechargeable magnesium batteries: a case of sodium-magnesium hybrid battery.....	251

4.3.1	<i>Introduction</i>	
4.3.2	<i>Experimental</i>	
4.3.3	<i>Results and discussion</i>	
4.3.4	<i>Conclusions</i>	
4.3.5	<i>References</i>	
4.4	Advancing towards a veritable calcium-ion battery: CaCo_2O_4 positive electrode material.....	269
4.4.1	<i>Introduction</i>	
4.4.2	<i>Experimental</i>	
4.4.3	<i>Results and discussion</i>	
4.4.4	<i>Conclusions</i>	
4.4.5	<i>References</i>	
4.5	Reversible intercalation of aluminium into vanadium pentoxide xerogel for aqueous rechargeable batteries.....	283
4.5.1	<i>Introduction</i>	
4.5.2	<i>Experimental</i>	
4.5.3	<i>Results and discussion</i>	
4.5.4	<i>Conclusions</i>	
4.5.5	<i>References</i>	
4.5.6	<i>Supplementary information</i>	
4.6	NASICON-type $\text{Na}_3\text{V}_2(\text{PO}_4)_3$ as a new positive electrode material for rechargeable aluminium battery.....	305
4.6.1	<i>Introduction</i>	
4.6.2	<i>Experimental</i>	
4.6.3	<i>Results and discussion</i>	
4.6.4	<i>Conclusions</i>	
4.6.5	<i>References</i>	
Capítulo 5. Resumen y conclusiones finales.....		327
5.1	Resumen.....	329

5.2	Summary.....	337
5.3	Conclusiones finales.....	344
5.4	Final conclusions.....	348
Anexo I. Otras aportaciones científicas.....		353
Anexo II. Técnicas.....		361

CAPÍTULO 1

Introducción

1.1 La problemática energética

La demanda mundial de energía es cada vez mayor (Figura 1). Actualmente es necesario explotar nuevas fuentes de energía, de una manera más ecoeficiente, y además con suficiente potencia ininterrumpida como para hacer frente a la demanda de la sociedad en el siglo XXI.

Durante el siglo XX, la energía que se utilizó fue principalmente de procedencia no renovable (carbón, petróleo, gas natural y uranio). Sin embargo, en el siglo XXI parece muy conveniente realizar una transición progresiva hacia fuentes de energía renovables (Figura 1). Los factores principales que propician el incremento en el uso de las energías renovables son el aumento neto de la demanda de energía mundial, el agotamiento de los recursos no renovables y la protección del medio ambiente.

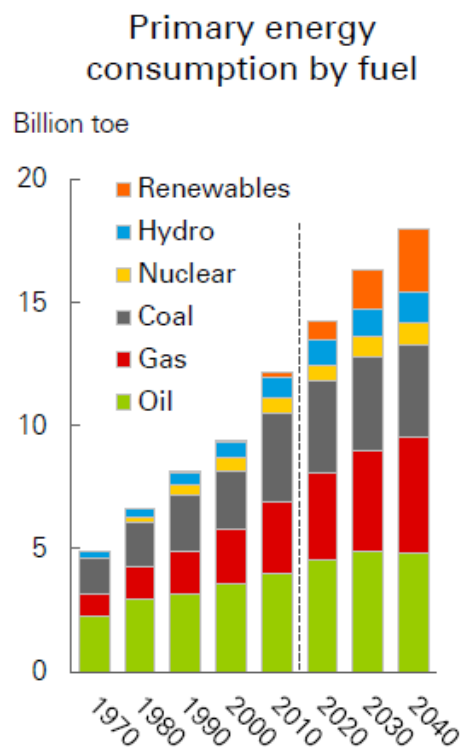


Figura 1. Consumo mundial de energía en millardos (billones en inglés) de toneladas equivalentes de petróleo (toe) por año. 1toe=11630 kW h [1].

Según el BP Energy Outlook en su edición 2018 [1], la demanda global de energía aumentará un 35% de aquí hasta el año 2040. El 14% de la energía consumida

en 2040 será de procedencia renovable, el 74% corresponderá a la energía ofrecida por los combustibles fósiles, mientras que la hidroeléctrica y nuclear representará el 12% restante.

Las fuentes de energía renovables serían hipotéticamente ilimitadas, pero tampoco están exentas de problemas. Por ejemplo, hay que considerar la emisión de contaminantes al medio ambiente durante los procesos de fabricación y transporte de piezas como turbinas, paneles solares, calderas de las plantas de biomasa y aspas de aerogeneradores, entre otros. Además, algunas de estas fuentes de energía presentan como inconveniente una naturaleza geográficamente difusa, como es el caso de los yacimientos geotérmicos localizados sólo en zonas concretas de la corteza terrestre; y el de las regiones dónde la presencia de vientos es mayor. Otras, como la solar, muestran discontinuidad temporal. Para solucionar esta discontinuidad, es necesario algún sistema que permita almacenar la energía sobrante producida en momentos de mayor producción para posteriormente recuperarla.

Una alternativa muy recomendable para el almacenamiento de la energía, sea ésta de origen renovable o convencional, son las baterías o acumuladores eléctricos. Las baterías son un sistema eficaz de almacenamiento energético en cuanto a densidad energética, potencia, capacidad, tiempos relativamente cortos de fabricación y posibilidad de diseños de varias formas y tamaños según las distintas aplicaciones a las que se destinen. Por supuesto, las baterías no sólo se limitan al almacenamiento de las energías renovables, sino que también son muy recomendables para dispositivos electrónicos portátiles de comunicación y/o de entretenimiento.

En las últimas décadas, destacan las baterías de ion litio, que empezaron a comercializarse a finales del siglo XX, y que hoy en día ocupan una buena parte del mercado mundial de baterías aunque su fabricación está dominada por países asiáticos. Pese a su éxito, el uso de baterías de ion litio presenta algunos inconvenientes como son la limitada abundancia natural del litio, el precio de este elemento y el elevado tiempo de carga de estas baterías. Así, para dar solución a estos inconvenientes, se presenta como alternativa el desarrollo de las baterías “post-litio”. Son sistemas electroquímicos basados en elementos como el sodio, el magnesio, el calcio y el aluminio; y presentan ventajas tales como la abundancia natural de los elementos y el carácter multivalente

(+2 ó +3) de algunos de ellos, lo cual podría suponer un aumento en la densidad energética de la batería.

1.2 Celda galvánica

Una celda galvánica es un dispositivo capaz de transformar reversiblemente la energía química en energía eléctrica a través de una reacción redox. Dicha celda consta de cuatro partes principales:

- Electrodo negativo: es el electrodo donde se produce la oxidación durante la descarga y la reducción durante la carga.
- Electrodo positivo: es el electrodo donde se produce la reducción durante la descarga y la oxidación durante la carga.
- Electrolito: es el medio conductor de iones, formado habitualmente por un disolvente en cuyo seno se encuentra disuelta una sal. Debido al campo eléctrico existente entre los dos electrodos, los cationes del electrolito tienden a desplazarse hacia el cátodo y los aniones hacia el ánodo.
- Conductor externo de electrones: un cable metálico que conecta los dos electrodos y por el que circulan los electrones.

El esquema idealizado de una celda electroquímica se muestra en la Figura 2.

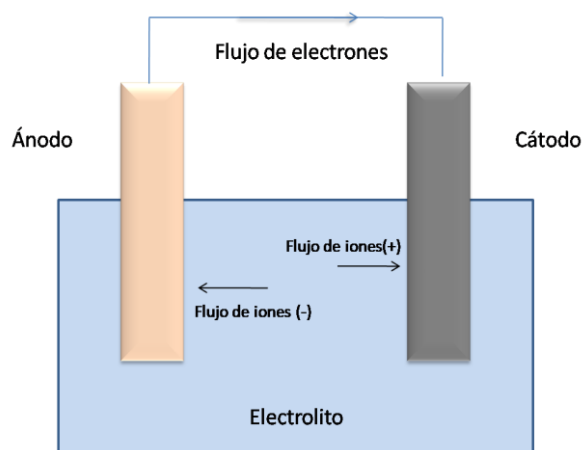


Figura 2. Esquema de celda galvánica.

Clásicamente, las celdas pueden conectarse en serie o en paralelo, y de este modo se obtiene una batería. Sin embargo, hoy en día se llama batería a la celda recargable, aunque esté formada por una única celda galvánica. Y se usa popularmente la palabra “pila” para nombrar a la celda no recargable.

Durante la descarga de la celda galvánica, el ánodo se oxida espontáneamente cediendo electrones al circuito externo, generando así una fuerza electromotriz. Por su parte, durante la descarga, el cátodo recibe estos electrones a través del circuito para reducirse. Esta transferencia de carga eléctrica a través del circuito eléctrico se ve compensada por la cesión de carga positiva (por ejemplo, en forma de Li^+) desde el ánodo hacia el cátodo a través del electrolito. Así pues, el electrolito debe ser un medio que favorezca la conductividad iónica y que impida la conductividad electrónica.

A veces las baterías se clasifican en primarias y secundarias. Las baterías primarias serían no recargables, y cuando son conectadas liberan la energía eléctrica almacenada. Por otra parte, las baterías secundarias sí son recargables debido a que las reacciones químicas son reversibles en cierto grado, esto quiere decir que con ayuda de una fuente externa de electricidad, la energía liberada puede ser restituida [2]. Algunos ejemplos de baterías recargables son las baterías de plomo-ácido, de níquel-cadmio, de ion litio y los sistemas post ion litio.

1.3 Fundamentos de las baterías

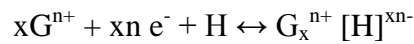
En este apartado, se realiza un breve resumen introductorio de algunos aspectos básicos a tener en cuenta para la mejor comprensión de las baterías que se estudian en esta tesis doctoral.

1.3.1 Tipos de reacciones en los materiales de electrodo

Las reacciones que suceden en los electrodos de las baterías, principalmente de litio, las podemos clasificar en cuatro tipos.

- **Reacciones de inserción:** moléculas e iones (G^{n+}) se introducen en una red de un sólido anfitrión (H). Si no hay cambio estructural en los materiales electródicos durante el proceso electroquímico, la reacción es topotáctica, y

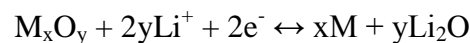
estos electrodos pueden ser cargados y descargados varias veces sin perder su estabilidad mecánica. La reacción simplificada es:



- **Reacciones de intercalación:** su fundamento es el mismo que para las reacciones de inserción con la salvedad de que el término intercalación se aplica cuando la inserción se produce en compuestos laminares. Algunos ejemplos son: i) la reacción del litio con TiS_2 para formar $LiTiS_2$ [3] en la que se produce una retención de litio en la estructura de manera muy rápida; ii) reacción con grafito para formar LiC_6 [4].

El grafito es un material ligero y que presenta una capacidad teórica de 372 mA h g^{-1} , debida a la intercalación de un litio por cada seis átomos de carbono (LiC_6). Además, el proceso de intercalación en el grafito se desarrolla a valores de voltaje cercanos a 0 V respecto al potencial del par Li^+/Li , conllevando problemas de seguridad, ya que pequeñas cantidades de litio metal pueden depositarse sobre la superficie del carbono mediante electrodeposición.

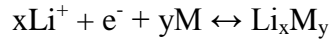
- **Reacciones de conversión:** el litio puede reaccionar con óxidos de metales de transición a través del proceso de conversión, desplazando al metal de su unión con el oxígeno, y la reacción simplificada es:



donde M es el metal (Co, Cu, Ni, etc.) [5,6,7]. En estas reacciones, el óxido de metal de transición se reduce y se forman nanopartículas del metal M que están embebidas en una matriz de Li_2O . Durante la carga, se vuelve a formar el óxido de metal de transición conservando el carácter nanométrico de las partículas formadas en la descarga. Debido a la naturaleza nanométrica, estos materiales proporcionan altas capacidades (Tarascon y colaboradores encontraron capacidades reversibles para el CoO de hasta 700 mA h g^{-1} [5]) para almacenar litio durante un gran número de ciclos.

- **Formación de aleaciones o compuestos intermetálicos:** entre los materiales que presentan una capacidad mayor que el grafito encontramos las aleaciones de litio que se han propuesto desde 1971 por Dey [8]. En las reacciones de aleación

se forma un compuesto intermetálico al reaccionar el litio con un elemento matriz que puede ser Si, Sn, Al, etc. Se trata de una reacción reversible que transcurre por debajo de 1 V y que puede simplificarse como:



Estos compuestos intermetálicos pueden almacenar y liberar grandes cantidades de litio, proporcionando valores de capacidad teórica superiores al grafito (994 mA h g⁻¹ para el caso del estaño). Algunos ejemplos de compuestos intermetálicos son: LiAl, Li₂Si, Li₄Si y Li₂₂Sn₅ [2,9,10]. En este tipo de reacciones de aleación, el principal problema es la variación de volumen durante la descarga y carga que hace que las partículas del material sufran una aglomeración y estrés que llegan a deteriorar su funcionamiento. Para evitar estos inconvenientes se han diseñado nuevas formas de preparación de estos materiales: i) con diferente morfología [11], ii) con tamaño de partícula nanométrico, o iii) formando aleaciones como FeSn₂ [12].

1.3.2 Voltaje

El voltaje teórico de la celda medido en condiciones estándar (E°_{Celda}) puede determinarse usando los valores de potenciales de reducción estándar de los electrodos implicados según la siguiente ecuación:

$$E^{\circ}_{\text{Celda}} = E^{\circ}_{\text{Cátodo}} - E^{\circ}_{\text{Ánodo}}$$

El electrodo, generalmente un conductor electrónico (M), se pone en contacto con un electrolito que contiene sus iones (M⁺), constituyendo un par redox. El ion debe realizar un trabajo para migrar desde la disolución del electrolito hasta la superficie del sólido pero, para ello, debe llegar a la interfase electrodo/electrolito y atravesarla. Conforme los iones van acumulándose en la superficie del metal, se ralentiza su avance debido a la generación de un campo eléctrico. Por lo tanto, el voltaje de la celda dependerá de la combinación de los materiales activos utilizados y de la energía necesaria para superar la barrera de activación de la reacción.

1.3.3 Relación entre la energía libre y el voltaje

El máximo de energía libre que teóricamente se puede liberar de una celda electroquímica viene dado por la siguiente ecuación [13]:

$$\Delta G = -nFE$$

donde E es la diferencia de potencial entre electrodos, n es el número de electrones que se transfieren en la reacción redox y F es la constante de Faraday. El proceso es espontáneo si $\Delta G < 0$. Cuando el potencial redox es cero, el sistema está en equilibrio termodinámico. Aunque en la práctica, hay varios mecanismos de resistencia (transferencia de carga, resistencia óhmica, entre otros.) que reducen el voltaje práctico de operación de la batería respecto al voltaje teórico.

1.3.4 Capacidad y densidad de energía

El término capacidad hace referencia al total de carga (número de electrones) que puede almacenar un material. Puede medirse en culombios (C) o amperios-hora (A h). Siguiendo las leyes de Faraday, un equivalente gramo de material de electrodo puede suministrar 96485 C ó 26,8 A h.

En el campo de las baterías, los valores de capacidad suelen normalizarse en términos gravimétricos ($A h kg^{-1}$), volumétricos ($A h L^{-1}$) o por unidad de área ($A h m^{-2}$). Se utiliza el primero cuando las aplicaciones de las baterías sean para dispositivos que requieran movilidad y autonomía, mientras que para aquellas aplicaciones relacionadas con el almacenamiento de energía a gran escala se emplea el segundo. Para el caso de las microbaterías es muy útil el empleo de las unidades normalizadas por área. La densidad energética de la celda se define como la energía liberada por la celda electroquímica. Se calcula como el producto de la capacidad específica por el voltaje promedio de operación y se expresa en $W h kg^{-1}$ o $W h L^{-1}$.

En algunas baterías puede haber situaciones en las que el almacenamiento de energía, al menos en parte, puede ser pseudocapacitivo o capacitivo, en vez de faradaico. Hay un número creciente de nuevos materiales de electrodo (óxidos de metales de transición, hidróxidos, sulfuros, carburos, nitruros, polímeros conductores, etc.) que muestran características electroquímicas que no son ni puramente capacitivas

ni puramente faradaicas [14]. Un aspecto crítico para poder proporcionar una comprensión de los mecanismos de almacenamiento de carga que están operando es la capacidad de descomponer la corriente total en contribuciones de pseudocapacitancia faradaica o capacitancia asociada a la doble capa [14].

1.3.5 Criterios para seleccionar el ion activo

En las baterías de ion litio, los iones litio se desplazan de un electrodo a otro. Pero, además de con litio, este tipo de baterías puede funcionar con otros iones de elementos metálicos. Las características principales que debe reunir una batería de ion metal son:

- El potencial del compuesto que contiene al ion debe ser cercano al par redox del mismo en estado metal para, así, obtener voltajes elevados.
- Para lograr cargas y descargas rápidas, el coeficiente de difusión de los iones en ambos electrodos debe presentar valores lo más altos posible. Por ejemplo, Takami y colaboradores obtuvieron valores de $10^{-6.4} \text{ cm}^2 \text{ s}^{-1}$ para el caso de la intercalación de litio en fibras de carbono [15].
- Para obtener una capacidad gravimétrica elevada, el peso equivalente del material activo de ambos electrodos debe ser bajo.
- Los iones deben tener un tamaño pequeño para que puedan ocupar las vacantes libres presentes en el sólido anfitrión y puedan difundirse a través de él con facilidad. El litio presenta un radio iónico de 0,76 Å. Para el sodio y el magnesio el radio iónico es de 1,02 y 0,72 Å respectivamente.
- Para propiciar esta acomodación de los iones, los materiales que actúan como redes anfitrionas deben reunir características tales como: estabilidad termodinámica y cinética, carácter conductor mixto iónico/electrónico que permita la conductividad de los electrones recibidos del circuito externo, y un sistema de posiciones de red vacantes que compartan caras poliédricas [2].
- Ambos materiales electródicos deben presentar un proceso fácil de obtención (para controlar el coste económico) y no ser tóxicos (para prevenir el impacto ambiental).

1.4 Baterías de ion litio

Actualmente las baterías más comúnmente empleadas en tecnología electrónica portátil son las de ion litio. De entre todas las baterías recargables actuales, las baterías de ion litio son las que ofrecen unos valores más altos en cuanto a densidad energética (Figura 3) y voltaje de operación.

Las baterías que emplean un ánodo de litio metal presentan alta densidad energética por masa (hasta 230 W h kg^{-1}), pero el uso de este elemento alcalino presenta efectos adversos como son una disminución acusada de la capacidad en el ciclado y la aparición de dendritas en el metal debido a la mala reconstrucción de la superficie del litio durante la carga. Estas dendritas crecen hacia el electrodo positivo, pudiendo llegar a perforar el separador y provocando el cortocircuito de la celda [16,17].

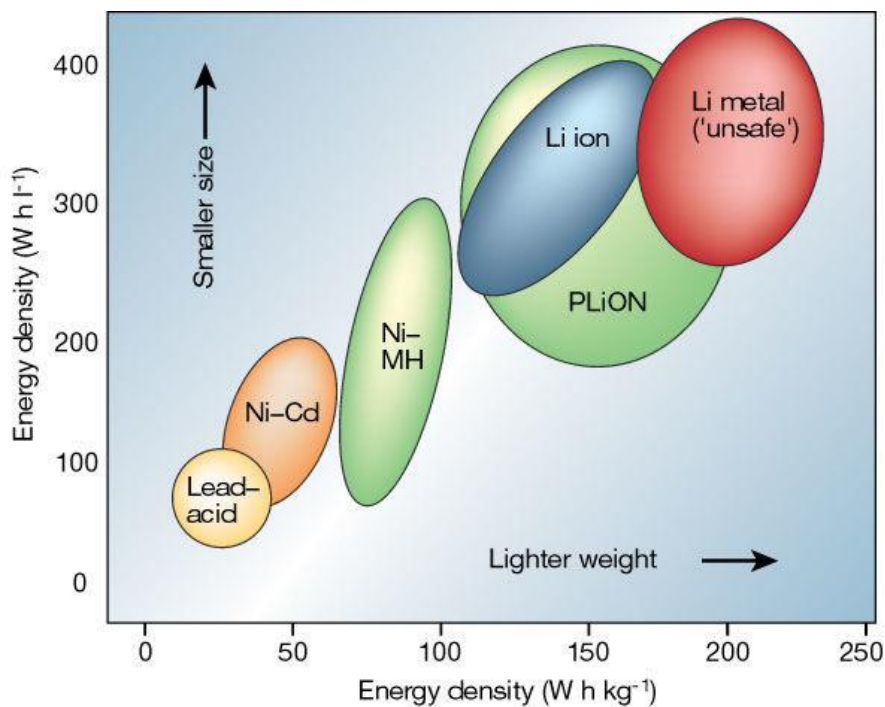


Figura 3. Densidades energéticas específicas gravimétricas y volumétricas de las distintas tecnologías de almacenamiento electroquímico [18].

El concepto de batería ion litio inicialmente se basa en la sustitución de este ánodo de litio metal por un material que reacciona reversiblemente con el litio

ligeramente por encima de 0 V frente al par redox Li^+/Li [10]. La existencia de dos electrodos de intercalación permite el movimiento de los iones litio entre ambos polos de la celda durante la carga y la descarga, siguiendo un movimiento que algunos han visto análogo al de una mecedora. A la misma vez, los electrones circulan por el circuito externo de la celda. El principio de transferencia de iones parece que fue propuesto por primera vez por Armand [19] y demostrado experimentalmente por Lazzari y Scrosati [20]. Así, a estas baterías se les denomina ion litio, batería mecedora o *rocking chair*.

En 1990, en los laboratorios de Sony desarrollan la primera batería ion litio, en la cual se emplea electrodo de carbono como material anódico y LiCoO_2 como material catódico [21].

En realidad, las baterías ion litio permitirían el uso de una amplia gama de materiales de electrodo negativos (C, Sn, Si, etc.) y positivos (LiCoO_2 , LiMn_2O_4 , LiFePO_4) [22,23]. Pero muchos de estos posibles sistemas no se han llegado a comercializar con éxito.

Como puede observarse en la Figura 4, ha habido un gran progreso en el desarrollo de materiales electródicos tanto negativos como positivos para baterías recargables de litio.

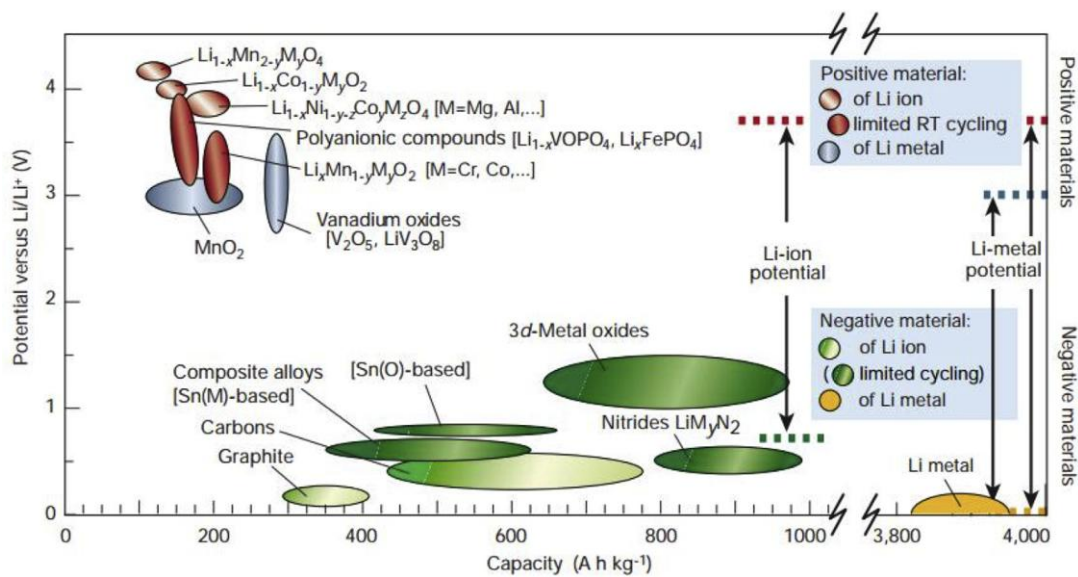


Figura 4. Materiales de electrodo para baterías recargables de litio clasificados por su potencial de reacción y capacidad [18].

1.5 Baterías de ion sodio

La demanda de litio es cada vez mayor para su aplicación en dispositivos portátiles, lo cual supondrá un incremento acelerado del precio de litio. Además, la distribución de recursos de litio no es uniforme ya que está concentrado mayormente en las regiones sudamericanas [24,25]. Si tenemos en cuenta la producción estimada de vehículos eléctricos, ordenadores, cámaras digitales y teléfonos inteligentes, sobre el año 2025, las reservas de litio se agotarían [26] por lo que es necesario encontrar una alternativa.

Como alternativa a la batería de ion litio, se ha propuesto el desarrollo de baterías que sustituyen los compuestos de litio por sodio. El sodio es uno de los elementos más abundantes en la corteza terrestre, a diferencia de las 20 ppm de litio presentes en la corteza (Figura 5). Los recursos de sodio que pueden encontrarse en los océanos cuentan con una distribución mucho más amplia que para el caso del litio. Por todo esto, el sodio se presenta como una alternativa muy conveniente a las baterías de ion litio [27].

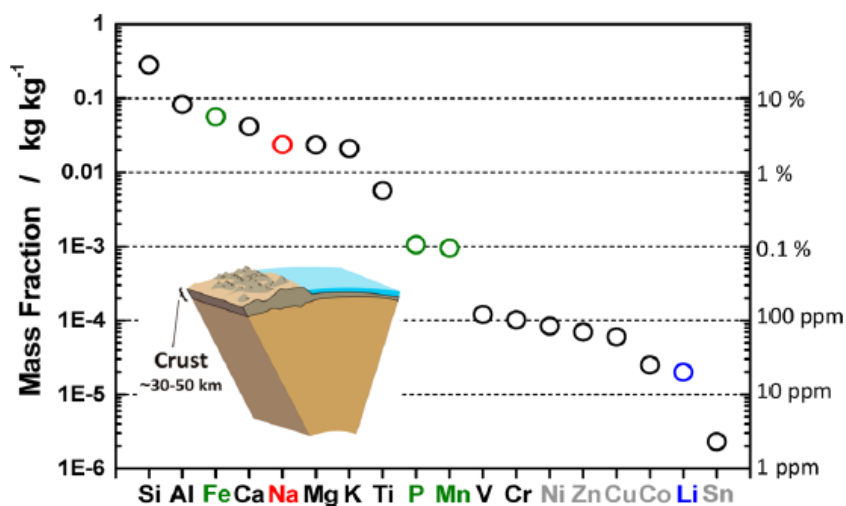


Figura 5. Abundancia de los elementos en la corteza terrestre [25].

Algunas baterías de ion sodio fueron inicialmente investigadas a la par que las de ion litio en la década de 1980. Sin embargo, los resultados con litio eran más prometedores, lo que supuso temporalmente el abandono de su estudio. En la

actualidad, el interés en la investigación sobre baterías de ion sodio ha ido en aumento debido al descubrimiento de nuevos materiales catódicos y anódicos, que han minimizado la diferencia en términos de rendimiento con respecto a las baterías de ion litio [28].

Los principios electroquímicos son análogos en ambos tipos de baterías, aunque existen diferencias entre ambos elementos. Los iones sodio tienen mayor radio iónico que los iones litio, el sodio tiene un peso atómico mayor ($22,99 \text{ g mol}^{-1}$ frente a $6,96 \text{ g mol}^{-1}$ del litio), y el sodio también posee un menor potencial de reducción frente al hidrógeno ($-2,71 \text{ V}$) que el litio ($-3,04 \text{ V}$) (Tabla 1).

Como materiales de electrodo positivo se emplean óxidos laminares (NaCoO_2), olivinos (NaFePO_4) y materiales con estructura NASICON (Natrium superionic conductor, $\text{A}_x\text{M}_y(\text{PO}_4)_3$) [29]. Los materiales electródicos negativos abarcan materiales carbonosos, óxidos de metales de transición [11,30], compuestos basados en titanio como titanatos, etc. [24,31,32]. Se muestra una comparación de la capacidad de estos materiales y su voltaje medio en la Figura 6.

Tabla 1. Comparación de las propiedades de elementos metálicos electroactivos para baterías.

	Litio	Sodio	Magnesio	Calcio	Aluminio
Peso atómico (g mol^{-1})	6,96	22,99	24,31	40,03	26,98
Valencia	1	1	2	2	3
Capacidad gravimétrica (A h kg^{-1})	3862	1166	2205	1340	2981
Capacidad volumétrica (A h L^{-1})	2062	1128	3833	2081	8056
Potencial (V)*	-3,04	-2,71	-2,36	-2,87	-1,66
Abundancia en la corteza terrestre (ppm) [33]	20	23000	29000	50000	82000
Precio (USD kg^{-1}) [34]	19,2	3,1	2,2	2,4	1,9

* Referido al potencial estándar de hidrógeno

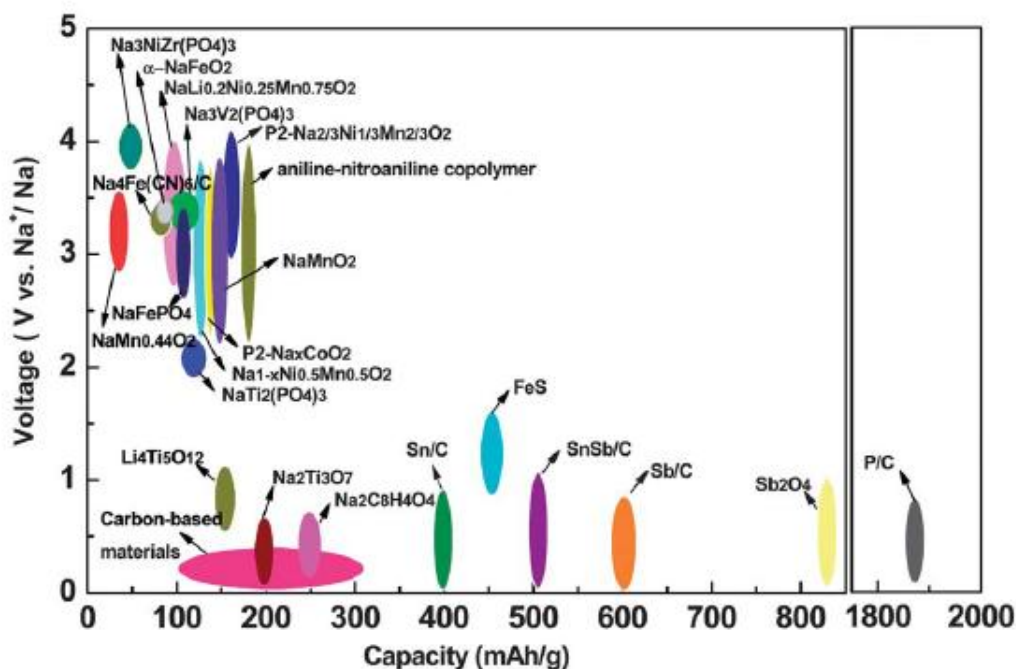


Figura 6. Relación voltaje-capacidad de los materiales electroquímicos empleados en baterías de ion sodio [32].

1.6 Baterías de magnesio y de ion magnesio

El carácter divalente del magnesio ofrece la ventaja de insertar dos electrones por ion en el material de electrodo. Esto permitiría el desarrollo de baterías con una alta densidad energética, las cuales pueden llegar a ser competitivas frente a los sistemas que emplean iones monovalentes [35,36].

La competitividad del magnesio radica en aspectos como su bajo coste y seguridad en la batería al no producirse formación de dendritas. En términos de capacidad volumétrica, puede ofrecer hasta 3833 A h L^{-1} frente a los 2062 A h L^{-1} del litio y 1128 A h L^{-1} del sodio, mientras que en términos de capacidad gravimétrica puede proporcionar 2205 A h kg^{-1} (3862 A h kg^{-1} presenta el litio y 1166 A h kg^{-1} el sodio) (Tabla 1). Las baterías de magnesio presentan un potencial normal de reducción frente al hidrógeno de $-2,36 \text{ V}$, el más bajo con respecto al resto de metales relativamente estables al aire.

Cuando se utiliza magnesio metal como electrodo negativo, es aún muy necesario optimizar el material que actúa como electrodo positivo y el electrolito. Los

electrolitos adecuados son aquellos que permiten una electrodeposición/disolución reversible del ion. Así, el magnesio metal no puede utilizarse eficazmente como ánodo en presencia de disolventes carbonatados (carbonato de etileno, carbonato de propileno, etc.) debido a que la electrodeposición no ocurre. Este hecho se debe a que el electrolito reacciona con el magnesio formando una capa aislante sobre él (Figura 7). Esta capa bloquea la difusión de los iones magnesio, impidiendo por tanto una reacción reversible en la batería [37]. Este problema puede solventarse con el uso de compuestos de *Grignard* en el electrolito [38], pero estos compuestos no suelen ser muy estables en el rango de voltaje en el que opera el electrodo positivo.

Por otra parte, se puede utilizar magnesio metal como ánodo en baterías en las que se emplean electrolitos híbridos que contienen Mg^{2+} con otros iones como Li^+ o Na^+ (que se describen en el capítulo 1.5.).

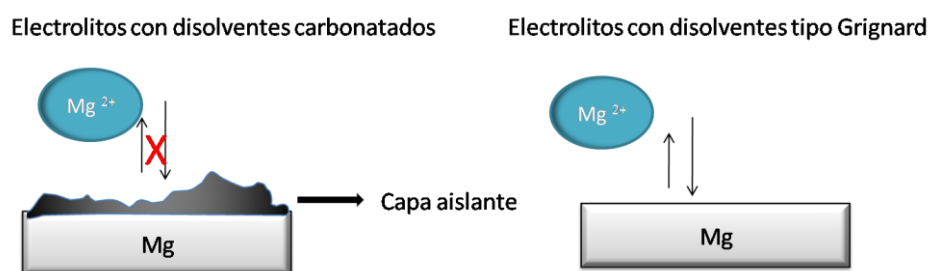


Figura 7. Capa formada por la interacción magnesio-electrolito en disolventes convencionales.

Es posible desarrollar sistemas de magnesio de alto voltaje sustituyendo el magnesio metal por un ánodo de inserción. Esto se conoce como batería de ion magnesio. Algunos compuestos utilizados como ánodo son Sn o Bi, entre otros [39,40]. Debido a la carga divalente (+2) del magnesio, se producen fuertes interacciones con otros iones presentes en la estructura del cátodo, impidiendo la inserción del ion Mg^{2+} , por lo que se hace difícil encontrar un material adecuado que actúe como cátodo. Así, entre los materiales propuestos encontramos $MgMn_2O_4$ [41], MnO_2 , $MgCO_2O_4$, V_2O_5 y Mo_6S_8 [42,43].

1.7 Baterías híbridas Mg-X (X=Li o Na)

Para evitar la difusión lenta de los iones magnesio en el material de electrodo, poder ampliar la selección de cátodos y por otras ventajas, muy recientemente surgen como alternativa las baterías híbridas que usan Mg metal como electrodo. Por lo general, el diseño híbrido combina un ánodo de magnesio metal y un cátodo de intercalación de litio o de sodio, o incluso de intercalación de dos iones (litio, sodio o magnesio). El electrolito contiene ambas especies Mg^{2+} y Li^+ , o Mg^{2+} y Na^+ . El esquema de una batería híbrida se muestra en la Figura 8.

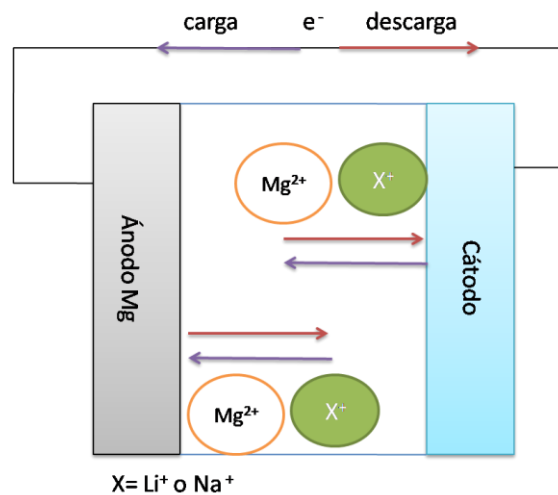


Figura 8. Esquema de una batería híbrida.

Según la región de intercalación e interacción, los prototipos de baterías híbridas pueden clasificarse de la siguiente manera [44]:

- 1) Dos iones (A y B) que se intercalan separadamente en dos electrodos distintos.
 - a) Compuesto de intercalación (A) // Electrolito (A+B) // Metal (B) o Compuesto de intercalación (B)
- 2) Dos iones que se intercalan simultáneamente en al menos uno de los dos electrodos.
 - a) Compuesto de intercalación (A+B) // Electrolito (A+B) // Metal (B) o Compuesto de intercalación (B)

- b) Compuesto de intercalación (A+B) // Electrolito (A+B) // Aleación (A+B)
o Compuesto de intercalación (A+B)
 - c) Compuesto de intercalación (A+B) // Electrolito (B) // Metal (B) o
Compuesto de intercalación (B)
- 3) Dos iones (A y B) que interactúan en el electrolito pero sólo uno de ellos (A) se intercala en los dos electrodos.
- a) Compuesto de intercalación (A) // Electrolito (A+B) // Metal (A) o
Compuesto de intercalación (A)

Las ventajas de estas baterías residen en una mejor seguridad del dispositivo, posibilidad de ciclarlas a cinética rápida y una alta reversibilidad. En las híbridas de Mg-Li, los cátodos empleados son TiO_2 [45], $\text{Li}_4\text{Ti}_5\text{O}_{12}$ [46], TiS_2 [47], LiFePO_4 [48], y más recientemente VS_2 [49].

Una de las primeras baterías híbridas Mg-Na fue propuesta por Walter y colaboradores utilizando FeS_2 como cátodo y magnesio metal como ánodo. Esta batería híbrida ofrece valores de densidad energética de hasta 215 W h kg^{-1} a un voltaje promedio de $1,0 \text{ V}$ [50]. Por otra parte, Li y colaboradores propusieron la batería Mg-Na empleando $\text{Na}_3\text{V}_2(\text{PO}_4)_3$ como cátodo y magnesio metal como ánodo. En este sistema, se consiguen valores de 150 W h kg^{-1} de densidad de energía a un voltaje promedio de $2,6 \text{ V}$ [51].

Es todo un reto encontrar electrolitos duales que presenten una compatibilidad química y electroquímica con los electrodos, que permitan una deposición/disolución reversible del metal y que muestren estabilidad frente a los colectores de corriente (evitando la corrosión de los mismos).

1.8 Baterías de ion calcio

El calcio, al igual que ocurre con el magnesio y con el sodio, presenta mayor abundancia natural y menor coste en comparación con el litio (Tabla 1). Además, su potencial de reducción frente al hidrógeno es de $-2,78 \text{ V}$, unos $0,5 \text{ V}$ mayor que el

ofrecido por las baterías de magnesio y muy parecido al del litio, haciéndolo atractivo para el desarrollo de baterías con alto potencial y densidad de energía.

Estas baterías no han atraído gran atención debido a que la difusión de los iones calcio en el material de electrodo es muy lenta (aunque la cinética que presenta el Ca^{2+} es más rápida que la de Mg^{2+} debido a su carácter menos polarizante). Otro factor a tener en cuenta es la extrema reactividad del calcio, cualquier traza de oxígeno o agua en la celda puede provocar una reacción irreversible inmediata.

En la actualidad, no se ha encontrado ningún electrolito suficientemente satisfactorio que permita una deposición/disolución reversible del calcio a temperatura ambiente, debido a que la descomposición del disolvente ocurre en la superficie del calcio, formando una capa superficial que tiende a ser iónica y electrónicamente aislante. Sin embargo, se ha encontrado que el calcio metal es estable en disoluciones que emplean acetonitrilo como disolvente, mientras que si se emplean disoluciones carbonatadas, se corroe [52]. Para conseguir mejorar el ciclado de las baterías de calcio se ha propuesto emplear electrolitos orgánicos como $\text{Ca}(\text{BF}_4)_2$ en EC:PC o $\text{Ca}(\text{TFSI})_2$ en EC:PC, aplicando temperaturas moderadas (entre 75 y 100°C) [53]. Muy recientemente, Bruce y colaboradores han conseguido la deposición y posterior disolución de calcio a temperatura ambiente empleando como electrolito $\text{Ca}(\text{BH}_4)_2$ en tetrahidrofurano (THF) [54] aunque, debido a la reacción del calcio depositado con el electrolito, se forman subproductos como CaH_2 que pueden afectar al calcio metal.

Podemos confirmar que existe cierto interés en la búsqueda de compuestos de intercalación como electrodo positivo y negativo para desarrollar una batería de ion calcio. Así, algunos autores han estudiado la inserción del calcio en V_2O_5 [55] y en $\text{K}_2\text{BaFe}(\text{CN})_6$ [56] empleando grafito como ánodo. Ingram y colaboradores desarrollaron una batería de ion calcio basada en un cátodo de $\text{MnFe}(\text{CN})_6$ y un ánodo de Sn-Ca [57]. Las baterías que utilizan hexacianoferratos como electrodo positivo, exhiben capacidades comprendidas entre 80 y 120 mA h g⁻¹. Más recientemente, se ha estudiado el empleo de materiales con estructura perovskita CaMO_3 (M= Mo, Cr, Mn, Fe, Co, Ni) [58], siendo CaMoO_3 el cátodo más prometedor ya que posee buena conductividad electrónica, ofrece un voltaje medio de operación de 2,5 V y su estructura cristalina se ve poco afectada durante el ciclado.

1.9 Baterías de ion aluminio

El aluminio es el elemento metálico más abundante en la corteza terrestre (Tabla 1), lo cual podría implicar un menor coste de las baterías que lo emplean. En 1988, Griford y colaboradores describieron una batería recargable de aluminio [59] en la cual grafito y aluminio actuaban como electrodo positivo y negativo respectivamente, y el electrolito empleado consistía en un líquido iónico en medio ácido. Este batería pionera alcanzaba los 64 W h kg^{-1} de densidad de energía a un voltaje medio de operación de 1,7 V. Entre 1992 y 1995, se desarrollaron las baterías primarias de aluminio tales como Al-AgO [60], Al-S [61], y Al-Ni [62], con densidades de energía comprendidas entre los 82 y 140 W h kg^{-1} . Estos sistemas empleaban soluciones alcalinas como electrolitos y no podían ser recargados ya que la disolución del aluminio ocurre a un potencial más negativo que la evolución de hidrógeno.

Hay tres factores que han propiciado de nuevo el interés hacia la investigación de las baterías de aluminio [34]:

- El aluminio puede intercambiar 3 electrones por catión, por lo que la inserción de un catión Al^{3+} sería equivalente a la inserción de tres cationes Li^+ (en cátodos de intercalación convencionales).
- La inercia del material y su fácil manejo en el ambiente puede ofrecer mejoras en la seguridad de dichas baterías.
- Presenta la capacidad volumétrica más alta (8056 A h L^{-1}) con respecto al resto de metales. La capacidad gravimétrica también es más alta (2981 A h kg^{-1}), a excepción del litio (Tabla 1).

En la literatura podemos encontrar diferentes materiales propuestos como material de electrodo para las baterías de aluminio. Estos son: óxidos de vanadio (VO_2 y V_2O_5) [63,64], sulfuro de molibdeno (Mo_6S_8) [65], grafito [66], etc. Estos óxidos de vanadio estudiados son en forma de partículas con tamaño nanométrico y reaccionan reversiblemente con el aluminio formando compuestos como $\text{Al}_x\text{V}_2\text{O}_5$, proporcionando capacidades de hasta 150 mA h g^{-1} . Cuando se emplea Mo_6S_8 , el proceso de inserción de aluminio consta de dos etapas en función de los sitios que ocupan los cationes Al^{3+} durante la inserción. Esta batería presenta una capacidad reversible de 120 mA h g^{-1}

durante 30 ciclos. Por otra parte, el grafito presenta la particularidad de intercalar y desintercalar los iones cloroaluminato (AlCl_4^-), proporcionando capacidades de 110 mA h g^{-1} durante 6000 ciclos y manteniendo estable su estructura a lo largo del ciclado. Además, los grafitos se posicionan como ánodos prometedores en este tipo de baterías al ser económicamente baratos.

Un factor a tener en cuenta en la electroquímica de estas baterías es la redistribución de carga durante la inserción de un catión multivalente. Cuando un catión se inserta en la estructura de un compuesto, debe haber una reducción de este compuesto para mantener la neutralidad global de carga. Para el caso del Al^{3+} , la redistribución de carga se hace más compleja si la comparamos con la inserción de iones monovalentes [67].

Por otra parte, el papel del electrolito es crítico. Los electrolitos acuosos están relacionados con altas tasas de corrosión, formación de óxidos y evolución de hidrógeno en el ánodo (aluminio), conllevando una baja eficiencia anódica. Hasta ahora, la deposición/disolución reversible del aluminio solo ocurre cuando se utilizan líquidos iónicos como electrolitos compuestos por AlCl_3 y otras sales como cloruro de 1-etil-3-metilimidazolio ([EMIm]Cl), cloruro de 1-butil-3-metilimidazolio ([BMIm]Cl) y cloruro de 1-butilpiridinio. Debido a la capacidad de producir corrosión de los líquidos iónicos y las reacciones secundarias, existen dudas sobre la validez de algunas de las reacciones de intercalación reportadas.

1.10 Baterías acuosas

Las baterías que emplean electrolitos acuosos se presentan como buenos candidatos para sistemas que requieran el almacenamiento de grandes cantidades de energía a largo plazo. En ellos se persigue un coste de instalación bajo, un tiempo de vida útil largo y una alta eficiencia energética; así, pueden pasar de producir en el rango de los kW h a los MW h.

Las baterías acuosas presentan más seguridad, por el hecho de que no usan disolventes orgánicos inflamables, y bajo coste, pero hay un inconveniente principal. Éste radica en la electrolisis del agua que ocurre a unos 1,23 V frente al electrodo normal de hidrógeno, provocando una evolución de gas H_2 y O_2 . Otro factor a tener en

cuenta es el pH de la disolución, el cual influye al potencial al que ocurre esta evolución de gases y puede afectar a los materiales de electrodo. Por tanto, los materiales electródicos más adecuados son aquellos que tienen su potencial de reducción dentro del rango de potencial en el que es estable el disolvente empleado, tal y como se muestra en la Figura 9.

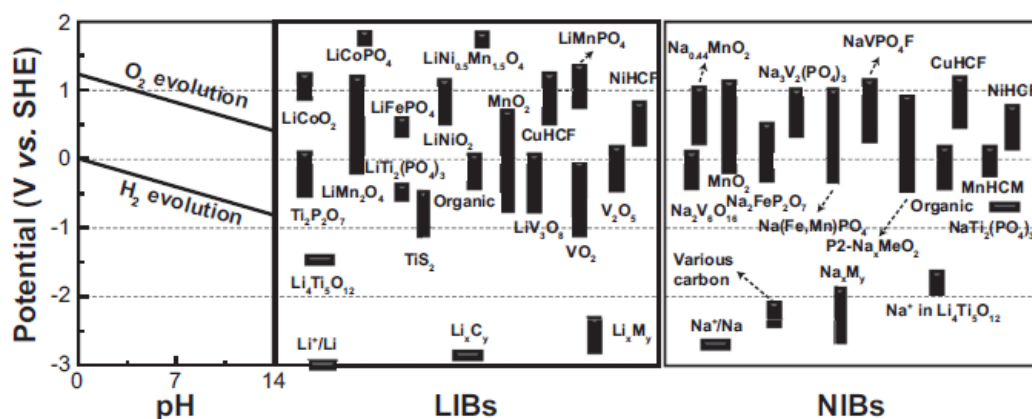


Figura 9. Estabilidad electroquímica del agua y potenciales redox en baterías acuosas de litio (centro) y acuosas de sodio (derecha) [68].

En la literatura podemos encontrar algunos ejemplos de baterías “*rocking chairs*” acuosas. Por ejemplo, $LiTi_2(PO_4)_3$ como ánodo, $LiMn_2O_4$ como cátodo y Li_2SO_4 en agua como electrolito. Con electrolito formado por Na_2SO_4 en agua destacan λ - MnO_2/C y $Na_3V_2(PO_4)_3/NaTi_2(PO_4)_3$ [69]. El óxido de manganeso es considerado un buen material anfitrión para acomodar iones multivalentes. Cui y colaboradores estudiaron hexacianoferrato de níquel nanométrico como posible candidato para la inserción de divalentes tales como Mg^{2+} , Ca^{2+} , Sr^{2+} y Ba^{2+} [70]. Liu y colaboradores consiguieron la inserción de Al^{3+} en anatasa con tamaño de partícula nanométrico [71].

Cuando se utilizan electrolitos no acuosos, se forma una interfase electrodo/electrolito debido a la descomposición de éste durante el proceso de carga inicial. Esta interfase permite la conductividad iónica. En el caso de los electrolitos acuosos, la interfase no se forma, ya que no puede depositarse en estado sólido ningún producto resultante de la descomposición del agua.

Recientes avances muestran que se puede ampliar la ventana segura de potencial de la batería hasta 3-4 V cuando se emplean electrolitos de tipo “agua-en-sal” (*water-in-salt*) [72,73]. Estos, permiten manipular la descomposición del electrolito para crear la interfase electrodo/electrolito. Suo y colaboradores muy recientemente han propuesto un electrolito *water-in-salt* basado en trifluorometanosulfonimida de litio (LiTFSI) con concentración 20 M en agua [72], al trabajar con una concentración tan alta, se producen cambios en el núcleo de solvatación del litio al no haber suficiente agua para neutralizar las cargas de Li^+ , suprimiendo por tanto la evolución de hidrógeno y la oxidación del electrodo.

1.11 Objetivos y plan de trabajo

Teniendo en cuenta el estado actual de la investigación científica que se ha resumido en la introducción, los **principales objetivos** de las investigaciones realizadas en esta tesis doctoral han sido los siguientes:

1. Sintetizar óxidos de metales de transición con tamaños de partículas en el rango micro- y nano-métrico que sean útiles para su potencial empleo como electrodo en baterías recargables de litio.
2. Seleccionar los mejores materiales preparados para su utilización en baterías de ion litio, en base a sus propiedades.
3. Evaluar la viabilidad de nuevos materiales de electrodo para baterías recargables post-litio de los siguientes tipos:
 - a. Materiales para baterías de ion sodio
 - b. Materiales para baterías de ion magnesio
 - c. Materiales para baterías de ion calcio
 - d. Materiales para baterías de ion aluminio
4. Preparar disoluciones electrolíticas para usarlas en baterías recargables post-litio.
5. Construir nuevas celdas electroquímicas que permitan el estudio de baterías post-litio, incluyendo electrodo de trabajo, electrodo de referencia y contraelectrodo.
6. Estudiar los mecanismos de las reacciones, electroquímicas y de inserción, implicadas en las baterías de ion litio y post-litio. Analizar las posibles causas del fallo de las baterías y proponer cómo podrían solucionarse.

Para conseguir estos objetivos se ha llevado a cabo el **plan de trabajo**, que se expone a continuación, y cuyos resultados han dado lugar a las diferentes publicaciones que se desarrollan en la presente memoria.

1. Síntesis de compuestos del tipo MO_x , donde M representa uno o varios elementos metálicos. Preparación de electrodos con nanotubos de dióxido de titanio auto-organizados a través de anodización. Electrodeposición de películas finas formando “*composites*” con propiedades únicas, como $Li_4Ti_5O_{12}$. También se ha empleado el método sol-gel para la síntesis de $LiNi_{0.5}Mn_{1.5}O_4$ y Li_2CoPO_4F .
2. Construcción de celdas electroquímicas: celdas recargables de litio. Celdas de dos y tres electrodos fabricadas en caja de guantes con atmósfera de Ar. Celdas de tres electrodos tipo “*flooded-cell*”.

Los puntos 1 y 2 se desarrollan a lo largo del capítulo 2 de la presente memoria.

3. Preparación de nanotubos de dióxido de titanio auto-organizados a través de anodización. Electrodeposición de películas finas formando *composites* con propiedades únicas como $Na_2Ti_6O_{13}$. Síntesis de materiales carbonosos avanzados.
4. Construcción de celdas electroquímicas recargables de sodio, de dos y tres electrodos, fabricadas en caja de guantes con atmósfera de Ar. También celdas de sodio de tres electrodos tipo *flooded-cell*.

Los puntos 3 y 4 se desarrollan a lo largo del capítulo 3 de la presente memoria.

5. Síntesis por método sol-gel, o método del precursor o por vía hidrotermal de $CaCo_2O_4$, $MgMn_2O_4$, $Na_3V_2(PO_4)_3$ y NaV_6O_{15} .
6. Construcción de celdas electroquímicas para iones multivalentes (magnesio, calcio y aluminio). Celdas con electrolito no acuoso de dos y tres electrodos fabricadas en caja de guantes con atmósfera de Ar, y también celdas de tres electrodos tipo *flooded-cell*.

Los puntos 5 y 6 se desarrollan a lo largo del capítulo 4 de la presente memoria.

Se han llevado a cabo ensayos electroquímicos de los materiales de electrodo y su caracterización físico-química antes y después del ciclado en la batería. Esto se aborda en los capítulos 2, 3 y 4.

Para la caracterización de los materiales sintetizados, y de los electrodos recuperados de las celdas, se han empleado como técnicas principales difracción de rayos-X, microscopía electrónica de barrido y de transmisión, espectroscopia fotoelectrónica de rayos-X, y espectrometría de dispersión de energía de rayos-X. Otras técnicas empleadas han sido espectroscopia Raman, espectroscopia infrarroja con transformada de Fourier, resonancia paramagnética electrónica, resonancia magnética nuclear, análisis termogravimétrico, análisis térmico diferencial y adsorción física de nitrógeno.

Los ensayos electroquímicos realizados incluyen técnicas galvanostáticas, potencioestáticas, voltametría cíclica y espectroscopia de impedancia compleja.

Bibliografía

1. BP Energy Outlook, (2018). www.bp.com/en/global/corporate/media/reports-and-publications.html (último acceso 13 Junio 2018).
2. P. Lavela, J. L. Tirado, Baterías avanzadas, Servicio de publicaciones de la Universidad de Córdoba, 1999.
3. M.S. Whittingham, *Science* 192 (1976) 1126.
4. K. R. Kganyago, P. E. Ngoepe, *Phys. Rev. B* 68 (2003) 205111.
5. P. Poizot, S. Laruelle, S. Grugeon, L. Dupont, J. M. Tarascon, *Nature* 407 (2000) 496.
6. S. Grugeon, S. Laruelle, R. Herrera-Urbina, L. Dupont, P. Poizot, J. M. Tarascon, *J. Electrochem. Soc.* 148 (2001) A285.
7. S. Grugeon, S. Laruelle, L. Dupont, J. M. Tarascon, *Solid State Sciences* 6 (2003) 895.
8. A.N. Dey, *J. Electrochem. Soc.* 118 (1971) 1547.
9. R. Huggins, *Energy storage*, Springer, 2010.
10. M. Winter, J. O. Besenhard, M. E. Spahr, P. Novák, *Adv. Mater.* 10 (1998) 725.
11. G. F. Ortiz, I. Hanzu, P. Lavela, P. Knauth, J. L. Tirado, T. Djenizian, *Chem. Mater.* 22 (2010) 1926.
12. U. Nwokeke, R. Alcantara, Ricardo, J. L. Tirado, R. Stoyanova, M. Yoncheva, E. , *Chem. Mater.* 22 (7) (2010) 2268.
13. J. A. Bard, L. R. Faulkner, *Electrochemical Methods: Fundamentals and applications*, 2nd Edition, Wiley, 2001.
14. Y. Gogotsi, R. M. Penner, *ACS Nano* 12 (3) (2018) 2081.
15. N. Takami, A. Satoh, M. Hara, T. Ohsaki, *J. Electrochem. Soc.* 142 (2) (1995) 371.

16. D. Aurbach, E. Zinigrad, Y. Cohen, H. Teller, *Solid State Ionics* 148 (2002) 405.
17. K. Yan, H-W. Lee, T. Gao, G. Zheng, H. Yao, H. Wang, Z. Lu, Y. Zhou, Z. Liang, Z. Liu, S. Chu, Y. Cui, *Nano Lett.* 14 (2014) 6016.
18. J. M. Tarascon, M. Armand, *Nature* 414 (2001) 359.
19. M. Armand, *Materials for Advanced Batteries*, Springer, 1980.
20. M. Lazzari, B. Scrosati, *J. Electrochem. Soc.* 127 (1980) 773.
21. T. Nagaura, K. Tazawa, *Prog. Batt. Col. Cells.* 9 (1990) 20.
22. V. Palomares, P. Serras, I. Villaluenga, K. B. Hueso, J. Carretero-González, T. Rojo, *Energy Environ. Sci.* 5 (3) (2012) 5884.
23. M. V. Reddy, G. V. Subba Rao, B. V. R. Chowdari, *Chem. Rev.* 113 (2013) 5364.
24. E. De la Llave, V. Borgel, K. J. Park, J-Y. Hwang, Y-K. Sun, P. Hartmann, F. Chesneau, D. Aurbach, *ACS Appl. Mater. Interfaces* 8 (2016) 1867.
25. N. Yabuuchi, K. Kubota, M. Dahbi, S. Komaba, *Chem. Rev.* 114 (23) (2014) 11636.
26. T. C. Wanger, *Conservation Letters* 4 (2011) 202.
27. J-Y. Hwang, S-T. M. Myung, Y-K. Sun, *Chem. Soc. Rev.* 46 (2017) 3529.
28. V. Palomares, M. Casas-Cabañas, E. Castillo-Martínez, M. H. Han, T. Rojo, *Energy Environ. Sci.* 6 (8) (2013) 2312.
29. Y. Fang, J. Zhang, L. Xiao, X. Ai, Y. Cao, H. Yang, *Adv. Sci.* 4 (2017) 1600392.
30. J. R. González, R. Alcántara, F. Nacimiento, G. F. Ortiz, J. L. Tirado, E. Zhecheva, R. Stoyanova, *J. Phys. Chem. C* 116 (2012) 20182.
31. P. K. Nayak, L. Yang, W. Brehm, P. Adelhelm, *Angew. Chem. Int. Ed.* 57 (2018) 102.

32. H. Pan, Y-S. Hu, L. Chen, *Energy Environ. Sci.* 6 (2013) 2338.
33. D. R. Lide, *Handbook of Chemistry and Physics*, 85th Edition, CRC press, 2005.
34. S. K. Das, S. Mahapatra, H. Lahan, *J. Mater. Chem. A.* 5 (2017) 6347.
35. A. Luntz, *J. Phys. Chem. Lett.* 6 (2015) 300.
36. M. Armand, J. M. Tarascon, *Nature* 451 (2008) 652.
37. R. Mohtadi, F. Mizuno, *Beilstein J. Nanotechnol.* 5 (2014) 1291.
38. S. Yagi, A. Tanaka, Y. Ichikawa, T. Ichitsubo, E. Matsubara, *J. Electrochem. Soc.* 160 (2013) C83.
39. N. Singh, T. Arthur, C. Ling, M. Matsui, F. Mizuno, *Chem. Commun.* 49 (2013) 149.
40. P. Novák, R. Imhof, O. Hass, *Electrochim. Acta* 45 (1999) 351.
41. C. Ling, F. Mizuno, *Chem. Mater.* 25 (2013) 3062.
42. M. M. Huie, D. C. Bock, E. S. Takeuchi, A. C. Marschilok, K. J. Takeuchi, *Coord. Chem. Rev* 287 (2015) 15.
43. J. Muldoon, C. B. Bucur, T. Gregory, *Chem. Rev.* 114 (2014) 11683.
44. H. R. Yao, Y. You, Y. X. Yin, L. J. Wan, Y. G. Guo, *Phys. Chem. Chem. Phys.* 18 (2016) 9326.
45. S. Su, Y. Nuli, Z. Huang, Q. Miao, J. Yang, J. Wang, *ACS Appl. Mater. Interfaces* 8 (2016) 7111.
46. J. Bitenc, M. Firm, A. R. Vitanova, R. Dominko, *Electrochem. Commun.* 76 (2017) 29.
47. H. D. Yoo, Y. Liang, Y. Li, Y. Yao, *ACS Appl. Mater. Interfaces* 7 (2015) 7001.
48. Y. Cheng, D. Choi, K. S. Han, K. T. Mueller, J-G. Zhang, V. L. Sprenkle, J. Liu, G. Li, *Chem. Commun.* 52 (2016) 5379.

49. R. Sun, C. Pei, J. Sheng, D. Wang, L. Wu, S. Liu, Q. An, L. Mai, *Energy Storage Materials* 12 (2018) 61.
50. M. Walter, K. V. Kravchyk, M. Ibañez, M. V. Kovalenko, *Chem. Mater.* 27 (2015) 7452.
51. Y. Li, Q. An, Y. Cheng, Y. Liang, Y. Ren, C-J. Sun, H. Dong, Z. Tang, G. Li, Y. Yao, *Nano Energy* 34 (2017) 188.
52. M. Hayashi, H. Arai, H. Ohtsuka, Y. Sakurai, *J. Power Sources* 119-121 (2003) 617.
53. A. Ponrouch, C. Frontera, F. Bardé, M. R. Palacín, *Nature Materials* 15 (2015) 169.
54. D. Wang, X. Gao, Y. Chen, L. Jin, C. Kuss, P. G. Bruce, *Nature Materials* 17 (2018) 16.
55. M. Bervas, L. C. Klein, G. G. Amatucci, *Solid State Ionics* 176 (2005) 2735.
56. P. Padigi, D. Evans, R. Solanki, *J. Power Sources* 273 (2015) 460.
57. A. L. Lipson, B. Pan, S. H. Lapidus, C. Liao, J. T. Vaughey, B. J. Ingram, *Chem. Mater.* 27 (24) (2015) 8442.
58. M. E. Dompablo, C. Krich, J. Nava-Avendaño, M.R. Palacín, F. Bardé, *Phys. Chem. Chem. Phys.* 18 (2016) 19966.
59. P. R. Gifford, J. B. Palmisano, *J. Electrochem. Soc.* 135 (1988) 650.
60. K. J. Gregg, M. J. Niksa, *Proceedings of the 1992 Symposium on Autonomous Underwater Vehicle Technology*, Washington, DC., 1992, p.181.
61. S. Licht, D. Peramunage, *J. Electrochem. Soc.* 140 (1993) L4.
62. S. Licht, N. Myung, *J. Electrochem. Soc.* 142 (1995) L179.
63. W. Wang, B. Jiang, W. Xiong, H. Sun, Z. Lin, L. Hu, J. Tu, J. Hou, H. Zhu, S. Jiao, *Sci. Rep.* 3 (2013) 3383.

64. M. Chiku, H. Takeda, S. Matsumura, E. Higuchi, H. Inoue, *ACS Appl. Mater. Interfaces* 7 (44) (2015) 24385.
65. B. Lee, H. R. Lee, T.Yim, J. H. Kim, G. J. Lee, K. Y. Chung, B. W. Cho, S. H. Oh, *J. Electrochem. Soc.* 163 (6) (2016) A1070.
66. D-Y.Wang, C-Y. Wei, M-C. Lin, H-L. Chou, H-A. Chen, M. Gong, Y. Wu, C. Yuan, M. Angell, Y-J. Hsieh, Y-H. Chen, C-Y. Wen, C-W. Chen, B-J. Hwang, C-C. Chen, H. Dai, *Nat. Commun.* 8 (2017) 14283.
67. W. Kaveevivitchai, A.Huq, S. Wang, M. J. Park, A.Manthiram, *Small* 13 (34) (2017) 1701296.
68. H. Kim, J. Hong, K-Y. Park, H. Kim, S-W. Kim, K. Kang, *Chem. Rev.* 114 (2014) 11788.
69. J. O. Gil-Posada, A. J. R. Rennie, S. Perez-Villar, V. L. Martins, J. Marinaccio, A. Barnes, C. F. Glover, D. A.Worsley, P. J. Hall, *Renew. Sustain. Energy Rev.* 68 (2017) 1174.
70. R.Y. Wang, C. D. Wessells, R. A. Huggins, Y. Cui, *Nano Lett.* 13 (2013) 5748.
71. J. Liu, C. Xu, Z. Chen, S. Ni, Z-X.Shen, *Green Energy and Environment* 3 (2018)20.
72. L. Suo, O. Borodin, T. Gao, M. Olguin, J. Ho, X. Fan, C. Luo, C. Wang, K. Xu, *Science* 350 (6263) (2015) 938.
73. W. Sun, L. Suo, F. Wang, N. Eidson, C. Yang, F. Han, Z. Ma, T. Gao, M. Zhu, C. Wang, *Electrochem. Comm.* 82 (2017) 71.

CAPÍTULO 2

**Materiales nanoestructurados para
baterías de ion litio**

2.1 Self-assembled $\text{Li}_4\text{Ti}_5\text{O}_{12}$ / TiO_2 / Li_3PO_4 for integrated Li-ion microbatteries

Marta Cabello, Gregorio F. Ortiz, María C. López, Pedro Lavela, Ricardo Alcántara,
José L. Tirado.

Laboratorio de Química Inorgánica. Universidad de Córdoba. Edificio C3, Campus de Rabanales. Spain

Abstract

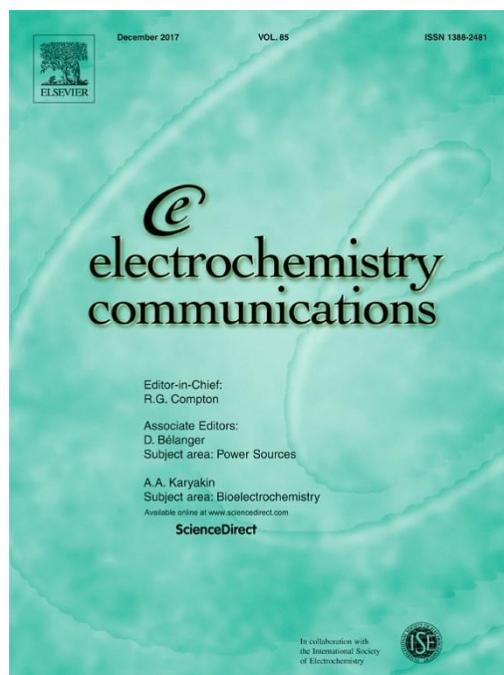
This work aims to maximize the number of active sites for energy storage per geometric area, by approaching the investigation to 3D design for microelectrode arrays. Self-organized $\text{Li}_4\text{Ti}_5\text{O}_{12}$ / TiO_2 / Li_3PO_4 composite nanoforest layer (LTL) is obtained from a layer of self organized TiO_2 / Li_3PO_4 nanotubes. The electrochemical response of this thin film electrode prepared at 700 °C exhibited lithium insertion and de-insertion at 1.55 and 1.57 V respectively, which is the typical potential found for lithium titanates. The effects of lithium phosphate on lithium titanate are explored for the first time. By cycling between 2.7 and 0.70 V the LTL / LiFePO_4 full cell delivered 145 mA h g⁻¹ at an average potential of 1.85 V leading to an energy density of 260 W h kg⁻¹ at C/2. Raman spectroscopy revealed that the γ - Li_3PO_4 / lithium titanate structure is preserved after prolonged cycling. This means that Li_3PO_4 plays an important role for enhancing the electronic conductivity and lithium ion diffusion.

Keywords

Lithium phosphate, lithium titanate, three-dimensional electrode, Li-ion microbattery



ELSEVIER



Electrochemistry Communications 56 (2015) 61-64

2.1.1 Introduction

The novel three-dimensional (3D) microbatteries are considered as the most suitable batteries for advanced small-scale devices such as microelectromechanical systems (MEMS) due to their remarkable advantages. These include large surface area, short Li^+ diffusion paths and densely packed active materials as compared to conventional two-dimensional (2D) thin-film batteries [1-4].

During the last decade, the 3D electrode concept has been applied to $\text{Li}_4\text{Ti}_5\text{O}_{12}$. The spinel-type $\text{Li}_4\text{Ti}_5\text{O}_{12}$ is one of the most promising negative electrode for Li-ion batteries. It delivers capacities close to the theoretical value (168 mA h g^{-1}) alongside with great cycling performance and high safety, because of unit cell volume changes less than 1 % upon electrode cycling [5]. Nonetheless, the electronic conductivity of $\text{Li}_4\text{Ti}_5\text{O}_{12}$ is still very low ($\sim 10^{-13} \text{ S cm}^{-1}$) which results in a significant loss of the initial capacity and poor rate capability [6-8]. Sorensen et al. [6] reported a pioneering work of three-dimensionally ordered macroporous (3DOM) $\text{Li}_4\text{Ti}_5\text{O}_{12}$ synthesized by using colloidal crystal templates and metal organic aqueous precursors. Also, Woo et al. [9] prepared 3DOM- $\text{Li}_4\text{Ti}_5\text{O}_{12}$ membranes being able to deliver a capacity value of 160 mA h g^{-1} at 0.1 C rate. The enhanced rate capability was attributed to the interconnected network of nanometer-scale walls providing short Li diffusion paths and a satisfactory contact with the electrolyte. Recently, nanocrystalline dual $\text{Li}_4\text{Ti}_5\text{O}_{12}$ - TiO_2 phases have been reported to perform excellently because of the benefits of a large interphase and small particle size. This morphology promotes a short Li^+ diffusion distance and high electrode reactivity [10-14].

In order to build a full microbattery, a procedure to dispose a thin layer of a solid electrolyte must be taken into account. The role of electrolytic Li_3PO_4 deposits on $\text{Li}_4\text{Ti}_5\text{O}_{12} / \text{TiO}_2$ thin film electrodes has not been studied so far. Li_3PO_4 is known to be a fast lithium solid conductor [15]. Also, Li_3PO_4 surface coating has been studied in several high voltage cathodes such as $\text{Li}_2\text{CoPO}_4\text{F}$ [16], $\text{LiNi}_{0.5}\text{Mn}_{1.5}\text{O}_4$ [17,18], LiMn_2O_4 [19] or LiCoO_2 [20]. Very recently, our group reported a Li-ion battery concept based on $\text{TiO}_2 / \text{Li}_3\text{PO}_4 / \text{LiFePO}_4$ with improved Li^+ diffusion [21]. This cell performed capacity values of 110 mA h g^{-1} at 5C as compared to 70 mA h g^{-1} at C/10, exhibited by a $\text{TiO}_2 / \text{LiFePO}_4$ cell [22].

Our scientific strategy is to go further in the design of Li-ion microbatteries with high energy and power densities. For accomplishing this task, a self-organized $\text{Li}_4\text{Ti}_5\text{O}_{12}$ / TiO_2 / Li_3PO_4 (LTL) nanoforest composite layer was synthesized by a versatile, simple and cheap electrochemical fabrication route. The direct growth of the active material onto the current collector provides good mechanical stability and ensures the electrical contact. It makes unnecessary the use of polymer binders and carbon additives. The stabilization effect exerted by Li_3PO_4 thin layer at the electrode/electrolyte interface will be studied in full Li-ion microbatteries using LiFePO_4 as a cathode.

2.1.2 Experimental

The synthesis of a LTL nanoforest composite layer is carried out in three steps. In a first step, the self organized titania nanotubes (nt- TiO_2) layer was fabricated by an anodization process at 60 V for 2 h, as described elsewhere [23-26]. Then, the working electrode (nt- TiO_2) is assembled in an electrochemical cell where the reference electrode is Ag/AgCl and a Pt wire is used as a counter electrode. The electrolyte was an aqueous solution containing 0.5M LiNO_3 and 0.02 M $\text{NH}_4\text{H}_2\text{PO}_4$. In this cell, lithium ions are electrochemically inserted into nt- TiO_2 and Li_3PO_4 is electrolytically deposited under a constant current of $-37.5 \text{ mA}\cdot\text{cm}^{-2}$ during 20 minutes [21,27]. Eventually, the as-prepared electrodes were further annealed at 700 °C for 2 h in air.

The crystalline structure of the as-deposited and annealed thin films was analyzed by X-ray diffraction (XRD) in a D5000 Siemens diffractometer (CuK α radiation). The morphology and chemical composition of the material was examined in a JEOL SM6300 Scanning Electron Microscopy (SEM) instrument equipped with Energy-Dispersive X-ray Spectroscopy (EDS) microanalysis and in a Philips CM10 Transmission Electron Microscopy (TEM) instrument. Raman spectra were recorded in a Renishaw Raman instrument (InVia Raman Microscope) furnished with a Leica microscope. The spectra were acquired between 100 and 1200 cm^{-1} by using a green laser light excitation source (532 nm).

Li cells were assembled into an argon-filled glove box. The auxiliary electrode was a 9 mm of diameter lithium disk. The electrolyte solution was 1 M LiPF_6

(EC:DEC) embedded in Whatman glass fiber disks. The full cells were assembled in 3 electrodes cells consisting of LiFePO_4 as positive, LTL as negative and metallic lithium as reference electrode. The electrochemical behavior of the electrode material was studied in a VMP-type apparatus (Biologic Science Instruments). Neither binder nor conductive additives were needed.

2.1.3 Results and discussion

2.1.3.1 Structure and morphology

X-ray diffraction patterns (XRD) were scanned to determine the crystalline phase existing in the prepared electrodes (Fig. 1A and B). As can be seen, crystalline $\beta\text{-Li}_3\text{PO}_4$ (JCPDS # 25-1030) was successfully deposited onto amorphous nt- TiO_2 while the Ti-substrate is preserved. After annealing at 700°C , the observed reflections are ascribed to rutile (JCPDS # 21-1276), $\gamma\text{-Li}_3\text{PO}_4$ (JCPDS # 15-0760) and spinel-type $\text{Li}_4\text{Ti}_5\text{O}_{12}$ (JCPDS # 49-0207). The phase $\text{Li}_4\text{Ti}_5\text{O}_{12}$ can be formed by crystallization of amorphous Li_xTiO_2 which is formed by intercalation of lithium into amorphous nt- TiO_2 in aqueous solution. These results show that a triple-phase microelectrode $\text{Li}_4\text{Ti}_5\text{O}_{12}/\text{TiO}_2/\gamma\text{-Li}_3\text{PO}_4$ has been obtained.

Anodization of titanium drives to the occurrence of a thin film of self-organized titania nanotubes with about $8\ \mu\text{m}$ of tube length and about $55\ \text{nm}$ of tube diameter [21,26]. We also found that a thin film of Li_3PO_4 can be deposited onto nt- TiO_2 without affecting the overall thickness of the nt- TiO_2 thin film [21]. The SEM image (Fig. 1C) reveals that the triple-phase microelectrode consists of self-organized crowded nanoforests with thickness of $8\ \mu\text{m}$. TEM image shows a detailed inspection of the elongated particles forming the nanoforest (Fig. 1D). The self-organized nanotubes of amorphous TiO_2 are transformed into one-dimensional aggregates of the triple-phase microelectrode which are randomly distributed in the nanotree.

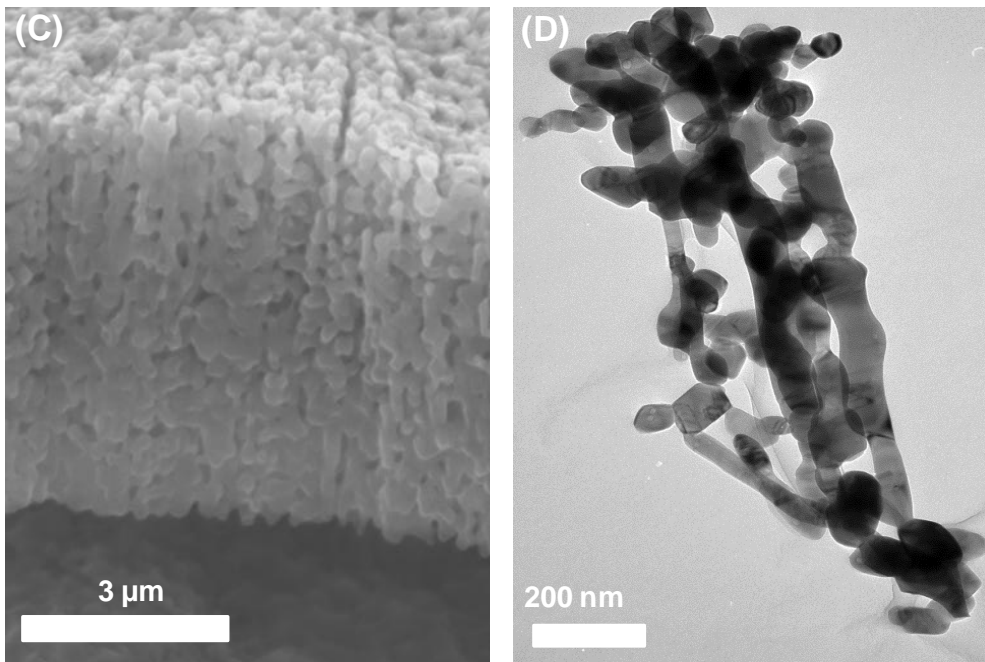
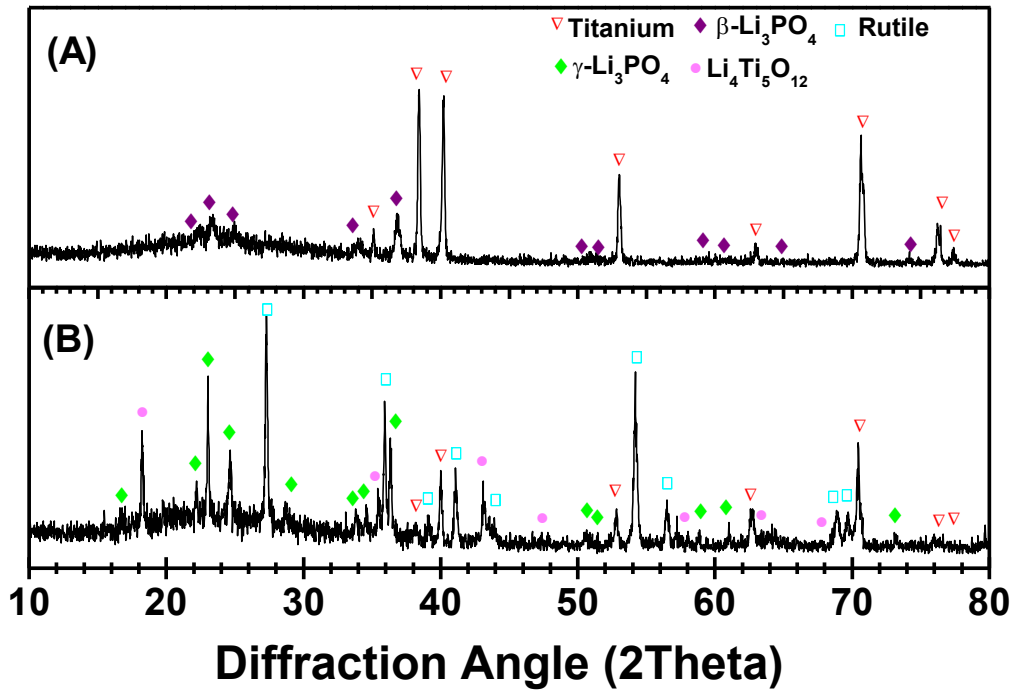


Fig.1. (A) XRD patterns for the as-prepared electrode and (B) after its annealing at 700°C. (C) Representative SEM and (D) TEM images of LTL at 700 °C.

2.1.3.2 Electrochemical behaviour in lithium half cells

The electrochemical behavior of the triple-phase microelectrode $\text{Li}_4\text{Ti}_5\text{O}_{12}/\text{TiO}_2/\gamma\text{-Li}_3\text{PO}_4$ versus lithium is shown in Fig. 2. A flat discharge plateau appears at about 1.55 V (Fig. 2A) [28,29], corresponding to the typical two-phase transition of $\text{Li}_4\text{Ti}_5\text{O}_{12}$ to $\text{Li}_7\text{Ti}_5\text{O}_{12}$ [12,30,31]. On charging, the reverse reaction at 1.57 V takes places. Electrochemical features ascribable to other phases than $\text{Li}_4\text{Ti}_5\text{O}_{12}$ could not be observed. Although rutile was confirmed by XRD, this phase seems to be electrochemically inactive [32]. The first discharge capacity value is $88 \mu\text{A h cm}^{-2}$, exhibiting an efficiency from the first to the second cycle of 83 %. The polarization between charge and discharge is about 0.02 V. This polarization value is slightly lower than the value (0.04 V) reported by Lu et al. [10]. The triple-phase microelectrode exhibits good cycling behavior (Fig. 2B). The role of rutile and Li_3PO_4 seems to be an improvement of the cycling stability, Li^+ diffusion and enhancement of the electrode reactivity.

Figure 2C gives the cyclic voltammogram recorded at various scan rates (5 – 100 mV s^{-1}) of the LTL nanoforest electrode annealed at 700°C . There is one pair of redox peaks around 1.5 and 1.7 V in each curve, which is characteristic of $\text{Li}_4\text{Ti}_5\text{O}_{12}$, and no other redox peaks are detected. This means that in LTL electrodes only $\text{Li}_4\text{Ti}_5\text{O}_{12}$ is electroactive. Thus the results observed from the galvanostatic experiments in Fig. 2A-B, are confirmed. The smallest difference between the cathodic and anodic peak potentials is observed for a scan rate of 5 mV s^{-1} . Moreover, the current peaks of cathodic and anodic traces are symmetric and have similar intensity values, indicating excellent reversibility. The areal capacity at 5 mV s^{-1} is quite close to that obtained under galvanostatic regime ($\sim 70 \mu\text{A h cm}^{-2}$). On increasing scan rate, the capacity decreases, but is preserved basically constant during 10 cycles, even when cycling at 100 mV s^{-1} (Fig. 2D).

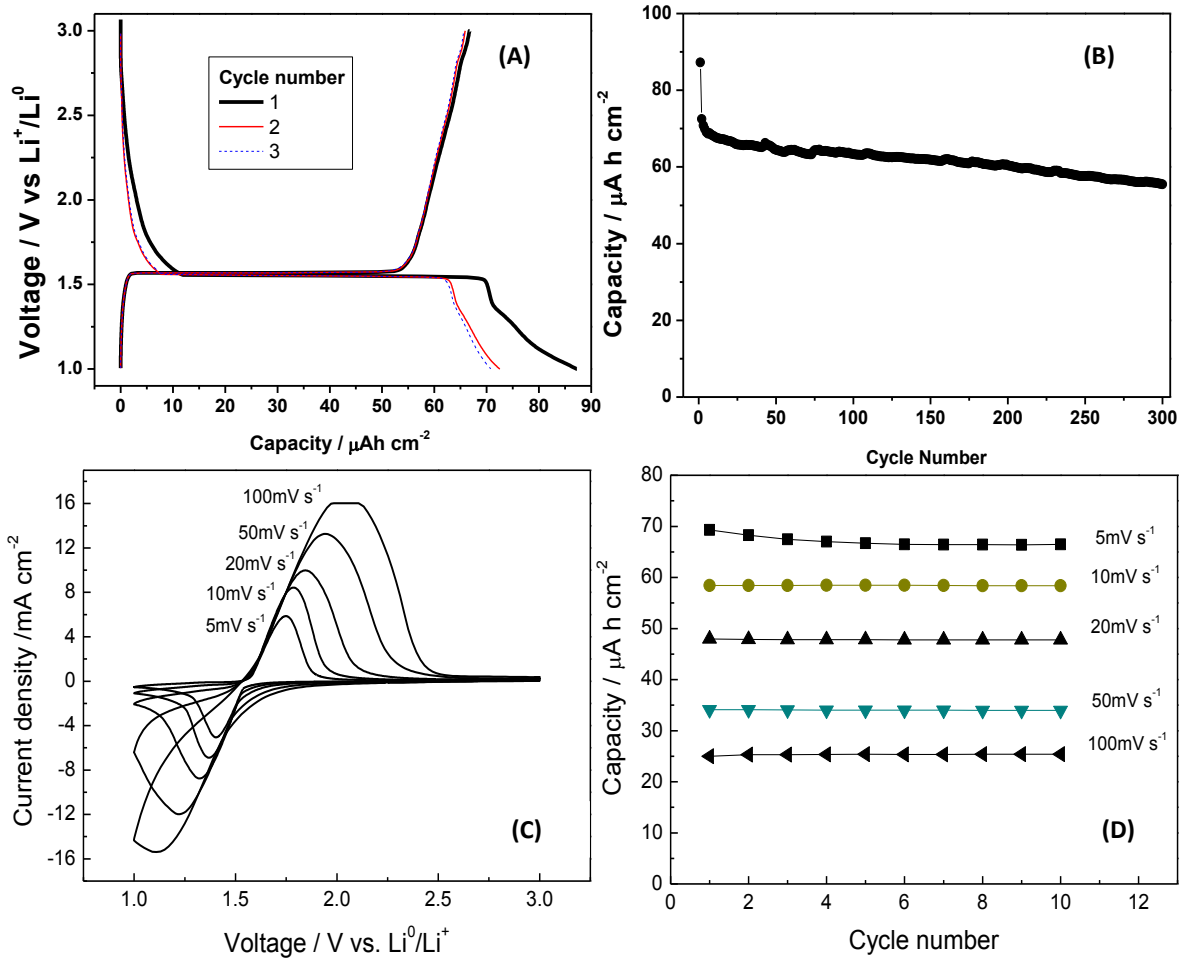


Fig.2. (A) Galvanostatic discharge/charge curves of triple-phase microelectrode in lithium cell and (B) capacity retention on cycling. The voltage window is 1.0 – 3.0 V and the current density is $50 \mu\text{A cm}^{-2}$. (C) Cyclic voltammograms of LTL electrode prepared at 700°C and (D) capacity retention at different scan rates.

2.1.3.3 Electrochemical behaviour in lithium-ion full cell

Figure 3 shows the galvanostatic cycling of the lithium-ion cell using $\text{Li}_4\text{Ti}_5\text{O}_{12}/\text{TiO}_2/\gamma\text{-Li}_3\text{PO}_4$ as negative electrode and LiFePO_4 as positive electrode. The capacity after the first charge is about 185 mA h g^{-1} , which matches well with its theoretical capacity. During charge, a plateau at about 1.9 V, ascribable to lithium transfer from LiFePO_4 to LTL, is observed. The corresponding discharge plateau, ascribable to the reverse reaction, appears at ca. 1.8 V. A reversible capacity of about 140 mA h g^{-1} is recorded after the first cycle at C/2. Then, the resulting energy density

value is about 260 W h Kg⁻¹. It is quite similar to those previously described [33-36]. Alternatively, the cell was subjected to cycling at several current rates from C (102 mA h g⁻¹), 2C (80 mA h g⁻¹), and 5C (45 mA h g⁻¹) (Fig. 3B). Further, cycling at C and C/2 showed an acceptable capacity recovery after 60 cycles (~ 140 mA h g⁻¹). The utility of rutile (TiO₂) is to improve the kinetics of Li₄Ti₅O₁₂ toward fast lithium insertion/extraction as previously studied by Wang et al. [13]. Additionally, the stabilization effect exerted by the Li₃PO₄ thin layer at the electrode/electrolyte interface is high, as in the case of TiO₂/Li₃PO₄ [21]. Both, rutile and lithium phosphate seem to play an important role for enhancing the electrochemical behavior in full cell, particularly when cycling at high rates. These results are encouraging and evidence the reliability of triple-phase microelectrode thin films, as candidates for anodes in lithium-ion microbatteries.

Raman spectroscopy revealed that γ -Li₃PO₄ is still remaining in the triple-phase microelectrode electrode after prolonged cycling as revealed by the small peaks located at 952 and 1025 cm⁻¹ attributed to the A_g and B_{2g} modes of the internal vibrations of PO₄ tetrahedron in γ -Li₃PO₄, respectively [37] (Fig. 4). Also, lithium titanate structure is preserved after prolonged cycling since a broadened band at 340 cm⁻¹ can be assigned to the F_{2g}. Also, a shoulder at ca. 673 cm⁻¹ and a peak at ca. 745 cm⁻¹ correspond to the A_{1g} modes of Li₄Ti₅O₁₂ [38]. This means that Li₃PO₄ is preserved upon cycling and plays an important role for enhancing the electronic conductivity and lithium ion diffusion.

2.1.4 Conclusions

We have explored the synthesis of nanoarchitected anode materials by a versatile fabrication route based on electrochemical procedures. The self-organized Li₄Ti₅O₁₂ /TiO₂ / Li₃PO₄ nanoforest remains firmly attached to the Ti current collector provide a rather facile electronic transfer pathway. Thus, a maximum energy density of about 260 W h kg⁻¹ at C/2 was reached. Lithium phosphate is preserved upon cycling allowing fast lithium ion mobility and playing an important role in the full cell.

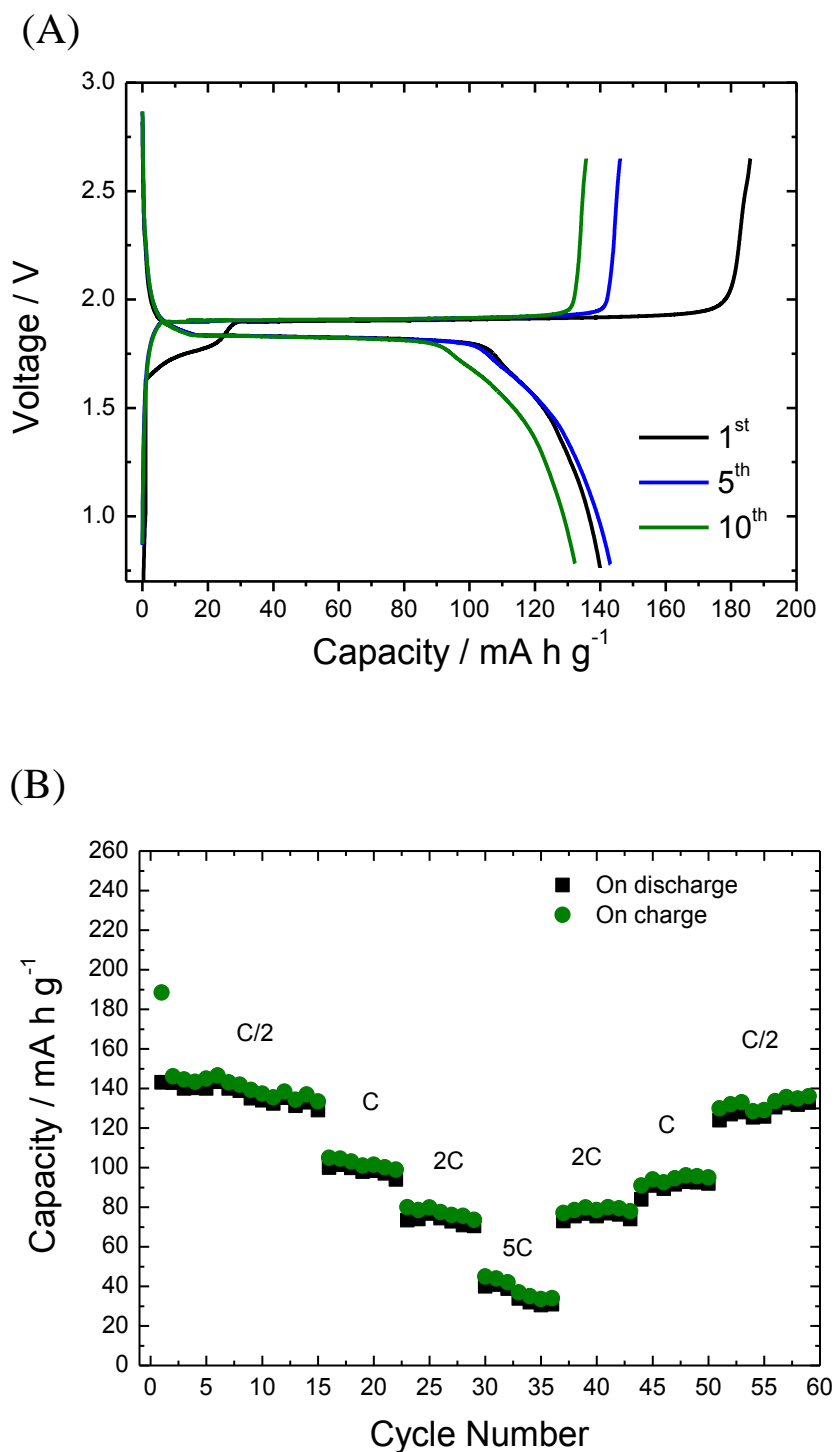


Fig.3. Galvanostatic cycling of the full Li-ion cell made by using $\text{Li}_4\text{Ti}_5\text{O}_{12} / \text{TiO}_2 / \text{Li}_3\text{PO}_4$ as negative electrode and LiFePO_4 as positive electrode. (A) Selected charge and discharge curves recorded at C/2 between 2.7 – 0.75 V. (B) Plot of capacity versus number of cycles recorded at several rates (C/2, C, C and 5C). The gravimetric capacity is referred to the mass of LiFePO_4 active material.

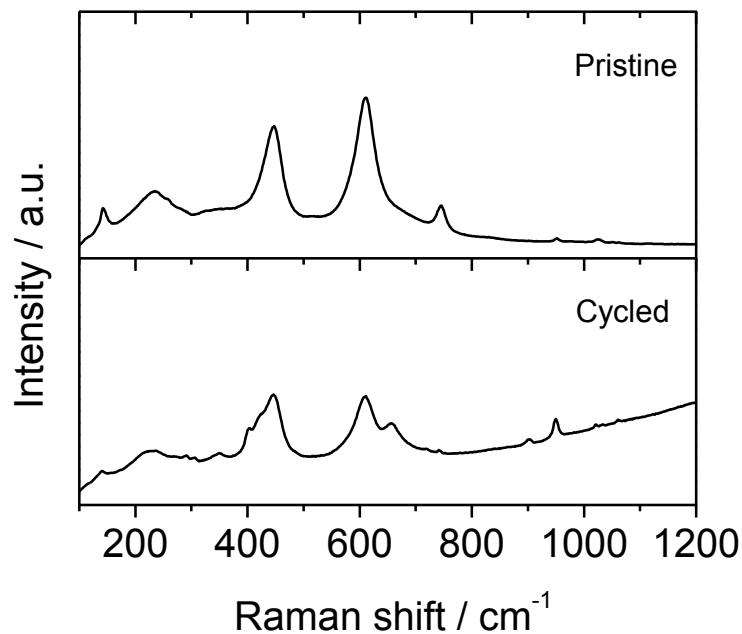


Fig.4. Raman spectra recorded for pristine and a cycled triple-phase micro electrode after 84 cycles.

Acknowledgements

The authors are grateful to MEC for project n° MAT2011- 22753 and “Ramón y Cajal” contract. Also, the authors are indebted to Junta de Andalucía for financial support (FQM288, FQM-7206 and FQM-6017).

2.1.5 References

1. J. W. Long, B. Dunn, D. R. Rolison, H. S. White, *Chem. Rev.* 104 (2004) 4463.
2. B. Kang, G. Ceder, *Nature* 458 (2009) 190.
3. H. Ji, L. Zhang, M. T. Pettes, H. Li, S. Chen, L. Shi, R. Piner, R. S. Ruoff, *Nano Lett.* 12 (2012) 2446.
4. B. L. Ellis, P. Knauth, T. Djenizian, *Adv. Mater.* 26 (2014) 3368.

5. T. Ohzuku, A. Ueda, N. Yamamoto, *J. Electrochem. Soc.* 142 (1995) 1431.
6. E. M. Sorensen, S. J. Barry, H. K. Jung, J. M. Rondinelli, J. T. Vaughey, K. R. Poeppelmeier, *Chem. Mater.* 18 (2006) 482.
7. W. J. H. Borghols, M. Wagemaker, U. Lafont, E. M. Kelder, F. M. Mulder, *J. Am. Chem. Soc.* 131 (2009) 17786.
8. L. Zhao, Y. S. Hu, H. Li, Z. X. Wang, L. Q. Chen, *Adv. Mater.* 23 (2011) 1385.
9. S. W. Woo, K. Dokko, K. Kanamura, *Electrochim. Acta* 53 (2007) 79.
10. H. W. Lu, W. Zeng, Y. S. Li, Z. W. Fu, *J. Power Sources* 164 (2007) 874.
11. J. Wang, H. Zhao, Q. Yang, C. Wang, P. Lv, Q. Xia, *J. Power Sources* 222 (2013) 196.
12. X. P. Li, J. Mao, *Ceram. Int.* 40 (2014) 13553.
13. Y. Q. Wang, L. Gu, Y. G. Guo, H. Li, X. Q. He, S. Tsukimoto, Y. Ikuhara, L. J. Wan, *J. Am. Chem. Soc.* 134 (2012) 7874.
14. T. Yiping, T. Xiaoxu, H. Guangya, Z. Guoqu, *Electrochim. Acta* 117 (2014) 172.
15. S. Q. Zhang, S. Xie, C. H. Chen, *Mater. Sci. Eng. B* 121 (2005) 160.
16. X. Wu, S. Wang, X. Lin, G. Zhong, Z. Gong, Y. Yang, *J. Mater. Chem A* 2 (2014) 1006.
17. H. Konishi, K. Suzuki, S. Taminato, K. Kim, Y. Zheng, S. Kim, J. Lim, M. Hirayama, J. Y. Son, Y. Cui, R. Kanno, *J. Power Sources* 269 (2014) 293.
18. J. Chong, S. Xun, X. Song, G. Liu, V. S. Battaglia, *Nano Energy* 2 (2013) 283.
19. X. Li, R. Yang, B. Cheng, Q. Hao, H. Xu, J. Yang, Y. Qian, *Mater. Lett.* 66 (2012) 168.
20. K. Sun, S. J. Dillon, *Electrochem. Commun.* 13 (2011) 200.
21. M. C. López, G. F. Ortiz, J. R. González, R. Alcántara, J. L. Tirado, *ACS Appl. Mater. Interfaces* 6 (2014) 5669.

22. P. P. Prosini, C. Cento, A. Pozio, J. Solid State Electrochem. 18 (2014) 795.
23. J. M. Macák, H. Tsuchiya, P. Schmuki, Angew. Chem., Int. Ed. 44 (2005) 2100.
24. G. K. Mor, K. Shankar, M. Paulose, O. K. Varghese, C. A. Grimes, Nano Lett. 6 (2006) 215.
25. G. F. Ortiz, I. Hanzu, T. Djenizian, P. Lavela, J. L. Tirado, P. Knauth, Chem. Mater. 21 (2009) 63.
26. J. R. González, R. Alcántara, F. Nacimiento, G. F. Ortiz, J. L. Tirado, E. Zhecheva, R. Stoyanova, J. Phys. Chem. C 116 (2012) 20182.
27. H. C. Liu, S. K. Yen, J. Power Sources 159 (2006) 245.
28. K. Zaghib, M. Simoneau, M. Armand, M. Gauthier, J. Power Sources 81 (1999) 300.
29. K. Nakahara, R. Nakajima, T. Matsushima, H. Majima, J. Power Sources 117 (2003) 131.
30. A. S. Prakash, P. Manikandan, K. Ramesha, M. Sathiya, J. M. Tarascon, A. K. Shukla, Chem. Mater. 22 (2010) 2857.
31. G. N. Zhu, Y. G. Wang, Y. Y. Xia, Energy Environ. Sci. 5 (2012) 6652.
32. B. Han, S. J. Kim, B. M. Hwang, S. B. Kim, K. W. Park, J. Power Sources 222 (2013) 225.
33. H. G. Jung, M. W. Jang, J. Hassoun, Y. K. Sun, B. Scrosati, Nat. Commun. 2 (2011) 516.
34. A. Swiderska-Mocek, Electrochim. Acta 139 (2014) 337.
35. J. W. Kim, D. H. Kim, D. Y. Oh, H. Lee, J. H. Kim, J. H. Lee, Y. S. Jung, J. Power Sources 274 (2015) 1254.
36. J. Hassoun, F. Bonaccorso, M. Agostini, M. Angelucci, M. G. Betti, R. Cingolani, M. Gemmi, C. Mariani, S. Panero, V. Pellegrini, B. Scrosati, Nano Lett. 14 (2014) 4901.

37. B. N. Mavrin, V. V. Asonov, V. V. Fomichev, A. K. Ivanov-Shits, V. V. Kireev, J. Exp. Theor. Phys. 96 (2003) 53.
38. W. Liu, Q. Wang, C. Cao, X. Han, J. Zhang, X. Xie, B. Xia, J. Alloys Compd. 621 (2015) 162.

2.2 Exploring a Li-ion battery using surface modified titania nanotubes versus high voltage cathode nanowires

Gregorio F. Ortiz ^a, Marta Cabello ^a, María C. López ^a, José L. Tirado ^a, Matthew J. McDonald ^b, Yong Yang ^b.

^a Laboratorio de Química Inorgánica. Universidad de Córdoba. Edificio C3, Campus de Rabanales. Spain

^b State Key Laboratory of Physical Chemistry of Solid Surfaces, Department of Chemistry, College of Chemistry and Chemical Engineering, Xiamen University. China.

Abstract

Novel battery architectures with improved safety, power and energy density are currently being demanded for battery miniaturization. We present a rechargeable full cell fabricated with self-organized titania nanotubes (nt-TiO₂) and self-organized LiNi_{0.5}Mn_{1.5}O₄ nanowires (LNMO). The effects of the Li₃PO₄-coated nt-TiO₂ on the electrochemical performance of the full cell are studied. A complete (de)-intercalation of lithium into both electrodes is observed, and cells avoid the use of metallic lithium while displaying improved safety and restrained lowering of the overall cell voltage. The surface modified electrodes exhibit better rate capability and cycling performance compared to non-treated electrodes. The nt-TiO₂,Li₃PO₄/ED:DEC LiPF₆/LiNi_{0.5}Mn_{1.5}O₄ cell could be cycled at 5 C rate, with associated capacity of 125 mA h g⁻¹, energy density of 325 W h kg⁻¹ and power density of 637 μW cm⁻² μm⁻¹. These results give evidence to the compatibility between both nanostructured electrodes particularly when lithium phosphate exerts a stabilization effect at the electrode/electrolyte interface, facilitating improved mass transfer and Li-diffusion at high rates.

Keywords

Nanostructures; binderless electrode; lithium-ion microbattery; self-organized titania nanotubes; lithium nickel manganese oxide nanowires



ELSEVIER



Journal of Power Sources 303 (2016) 194-202

2.2.1 Introduction

Lithium-ion batteries are attracting widespread attention due to their demonstrated importance to consumer and computer electronics and high potential for use in electromobility applications such as electric vehicles. However, battery development faces the challenge of keeping up with advances in microelectronics, necessitating the fabrication of thin-film batteries with small scale anodes and cathodes. The development of thin film batteries as compact power sources with efficient performance is desirable for future application in electronic portable devices. On the anode side of development, self-organized titania nanotubes (nt-TiO₂) with an anatase structure are being positioned as an excellent candidate material because the average potential of reaction vs. Li⁺/Li⁰ is around 1.7-1.9 V, which provides cells with enhanced safety properties as compared to carbon based electrodes. Moreover, TiO₂ has good capacity retention on cycling, a low self-discharge, is chemically stable, economically competitive, nontoxic, and environmentally friendly. The nt-TiO₂ layers can be easily prepared by a simple anodization process and their electrochemical performance compares very favorably with conventional TiO₂ compact layers. In particular, five times larger area capacity values can be obtained using a layer of self-organized titania nanotubes with a thickness of around 1 μm vs. compact layers [1]. Also, mesoscopic structured TiO₂ with nanoporous nature and large surface area showed enhanced electrochemical properties [2]. For the cathode, lithium insertion compounds such as LiMn_{1.5}Ni_{0.5}O₄ or LiFePO₄ among others are suitable options, particularly because they display clear voltage plateaus and avoid the presence of expensive and toxic cobalt in their stoichiometry. The latter is used as a positive electrode in lithium-ion batteries due to its relatively high theoretical energy density (170 mA h g⁻¹), stable voltage (3.5 V vs. Li⁺/Li) and excellent thermal/chemical stability [3,4]. However, one of the most thoroughly studied high-voltage spinel-based cathodes is the 4.7 V spinel-type LiMn_{1.5}Ni_{0.5}O₄ material [5-7].

It is well known that the electrochemical properties of spinel LiNi_{0.5}Mn_{1.5}O₄ mainly depend on factors such as oxygen deficiency, Ni/Mn ordering, the amount of Mn³⁺, the presence of the rock salt phase and so on [8-10]. These factors are correlated with each other in the literature and corroborated here. From previous studies, two important points can be understood. First, considering the family of LiMn₂O₄-based

spinel, the $\text{LiNi}_{0.5}\text{Mn}_{1.5}\text{O}_4$ cathode is capable of exchanging one electron per formula unit, i.e. storing the largest amount of energy compared with pristine LiMn_2O_4 [11-17]. Second, several strategies can be used to improve the electrochemical performance (energy density and power) of $\text{LiNi}_{0.5}\text{Mn}_{1.5}\text{O}_4$ in advanced batteries. However, the use of $\text{LiNi}_{0.5}\text{Mn}_{1.5}\text{O}_4$ nanowires (nw-LNMO) is a different approach than normal, which significantly changes procedures compared to using the same materials in the bulk. The electrochemical properties of the spinel grown as self organized nanowires are studied here for first time versus lithium in a half cell and in full cells vs. nt- TiO_2 .

As compared with planar thin-film configurations, the development of 3D micro-batteries allowed an increase in capacity per footprint area, which is particularly relevant for those applications requiring small and lightweight energy sources with prolonged usage. Also, 3D batteries achieve high-power density without sacrificing energy density [18]. Thus, using cheap and light micro-fabricated materials is necessary for enabling on-board power delivery in microscale devices such as microelectromechanical systems (MEMS) or other small autonomous devices [19,20]. Up to now, most studies have been focused on the nano-design of negative electrodes (e.g. TiO_2), but relatively few studies for designing the nano-architectures of positive electrodes can be found in literature. These battery designs are expected to offer noticeable improvements in power while maintaining a comparable energy density. Several configurations have been recently proposed for 3D Li-ion microbatteries to meet the required energy and power densities of their expected applications [19]. In addition, the electrochemical route of fabrication has been envisaged as a very promising technology, being a versatile and inexpensive route to getting deposition/anodization of electrodes in the form of nanotubes, nanorods, nanowires or nanoforests and offering the possibility of layering electrolyte onto nanostructured current collectors or of using templates [1, 21-25]. Moreover, this 3D battery approach can deliver variable power according to the battery volume.

The aim of this work is to optimize the performance of a Li-ion battery through nanostructuring of the cathode and anode that could be used for microbattery applications. In addition, the effect of lithium phosphate-coated anode on the electrochemical performance of a nt- $\text{TiO}_2/\text{LiNi}_{0.5}\text{Mn}_{1.5}\text{O}_4$ full cell was studied and compared to uncoated electrodes. Although, the use of micro-batteries based on liquid

electrode is not compatible with the integrated circuit technology, different authors have examined miniaturized Li-ion batteries using conventional electrolyte solutions in organic liquids to evaluate the performance of combined 3-D electrodes in full cells [18,26]. This approach is followed here. The nanoarchitected battery explored here is electrochemically robust and compares very favorably with other results reported in the literature.

2.2.2 Experimental

The growth of nt-TiO₂ was carried out by an anodization process in a cell that consists of Ti foil (0.127 mm thick, 99.7 % purity) and Pt wire as a working electrode and counter electrode, respectively. A 0.3 wt % solution of NH₄F in ethylenglycol (EG)/water (92:8 vol) mixture was used as electrolyte [21]. The experiments consisted of applying a constant voltage of 60 V during 120 min using a voltage source (Agilent B2912A). The deposition of electrolytic Li₃PO₄ was performed on nt-TiO₂ samples obtained at room temperature (RT), which were then calcined at 500 °C (referred to as anodized-deposited-calcined, ADC) to induce the formation of γ -Li₃PO₄ [25]. Electrolytic Li₃PO₄ films were deposited by an electrochemical procedure consisting of proton reduction with a subsequent local increase of pH in the vicinity of the substrate surface, hydrogen phosphate dissociation and Li₃PO₄ deposition on the surface of the cathode. The alternate fabrication process of electrodeposition of β -Li₃PO₄ on crystalline nt-TiO₂ was also performed (referred to as anodized-calcined-deposited, ACD). The mass of the titania nanotubes obtained at 60 V for 2 h is 0.935 mg cm⁻² [21].

To ensure success in fabricating the LiNi_{0.5}Mn_{1.5}O₄ nanowires (LNMO) with this exact composition, a sol gel route was first used to get an optimized mixture of reagents before attempting to utilize the porous membrane-based method. For the former method, reagent grade LiNO₃, Ni(NO₃)₂·4H₂O and Mn(NO₃)₂·6H₂O in three different molar ratios were used: (i) 1.05:0.5:1.5, (ii) 1.10:0.5:1.5 and (iii) 1.15:0.5:1.5. The reagents were dissolved together in distilled water and left overnight in a beaker at 110 °C until dry. The optimal solution was determined to be (iii). To prepare the LNMO using the second method, a porous alumina membrane with pores 200 nm in diameter (ANODISC from Fisher Scientific) was used, following a similar procedure to that of

Nishizawa et al [22]. The porous alumina-membrane was then placed in a homemade cell and was filled with an optimum amount of an aqueous solution composed of 1.15 M LiNO₃, 0.5 M Ni(NO₃)₂, and 1.5 M Mn(NO₃)₂, then left for gravity to act on. This solution was applied to fill the pores of the alumina membrane, with an excess of solution at the membrane surface avoided by wiping using a laboratory tissue. Next, the membrane was heated at 500 °C for 5 h in air, resulting in the formation of LNMO inside the alumina membrane. In order to dissolve the alumina, an optimal treatment was devised, involving a repeated (20 times) washing/dissolving using 10 mL of 2 M NaOH in each wash step. Once the alumina template was dissolved, further cleaning with deionized water was performed. Finally, the resulting tubular arrays of lithium nickel manganese oxide were further heated at 800°C for 1 h.

SEM, HRTEM and SAED images were collected with JEOL JSM 6300, JEOL JEM (1400 and 2010) and Tecnai F-20 devices, respectively. Phase formation was studied by powder X-ray diffraction (XRD) on a Siemens D5000 diffractometer with Cu K α radiation operating at 40 kV and 30 mA. Inductively coupled plasma mass spectrometry (ICP-MS, Philips PU 70000) was employed to accurately determine the Mn to Ni ratio of the LNMO active material. X-ray photoelectron spectroscopy (XPS) measurements were performed on a SPECS Phoebos 150MCD instrument using a Mg K α source (1253.6 eV) and a chamber pressure of 4×10^{-9} mbar. The C1s peak at 284.9 eV of adventitious carbon was used as a reference.

Lithium cells were used to study LiNi_{0.5}Mn_{1.5}O₄ cathode and Li₃PO₄-coated anodes. The Swagelok cells were fabricated using 1 M LiPF₆ in EC:DEC (50:50 wt. %) inside an Ar-filled glovebox. A VMP (Bio-Logic Sciences) apparatus was used to perform the galvanostatic experiments at different rates (C/2 – 10 C). The C/h value corresponds to a full charge/discharge of the theoretical capacity in ‘h’ hours. Several rocking chair batteries were tested in three electrodes configuration: (i) nt-TiO₂/EC:DEC LiPF₆/LiNi_{0.5}Mn_{1.5}O₄, labeled as ‘RC1’, (ii) nt-TiO₂,Li₃PO₄/ED:DEC LiPF₆/LiNi_{0.5}Mn_{1.5}O₄ labeled as ‘RC2’. The specific capacity for the full battery was calculated using the mass of the cathode, as commonly found in the literature [26]. Brutti et al. [31] emphasized that the cathode mass has a much larger impact on the total mass of the cell and on the specific energy. The calculation of the energy density of the battery only considered the specific capacity and the working potential ($E_{\text{cathode}} - E_{\text{anode}}$)

of the full battery, without further consideration of the mass of the active materials, electrolyte and packing materials.

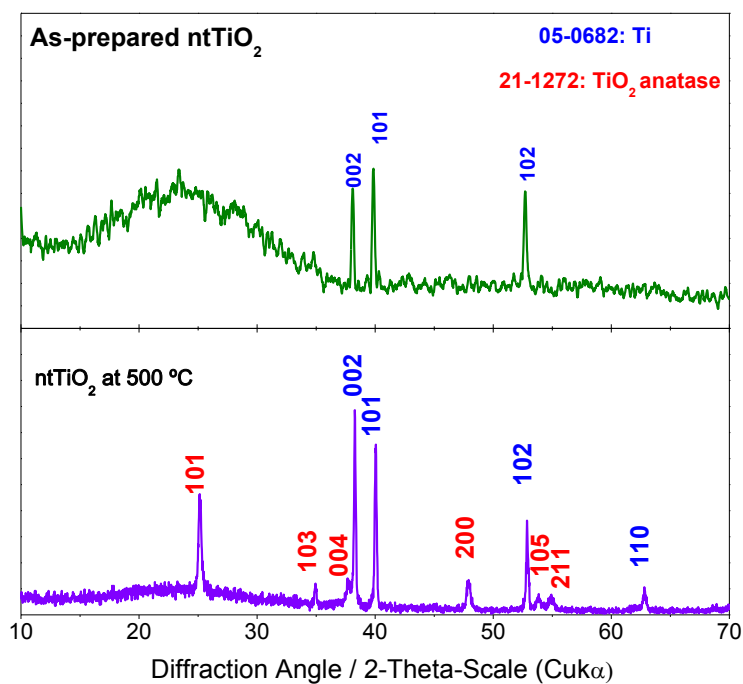
2.2.3 Results and discussion

2.2.3.1 Chemical characterization

Figure 1A shows the XRD patterns of self-organized titania nanotubes obtained by anodization of Ti foil at 60 V for 2 h at room temperature, and after annealing at 500 °C. An amorphous character is evidenced by the XRD data from the as-prepared nt-TiO₂. The degree of amorphization has been previously discussed on the basis of the observation of a hump between ca. 15 and 35°-2θ that has been ascribed to amorphous titania [21]. A conversion of the nt-TiO₂ layer to an anatase structure (JCPDS file no. 21-1272, space group *I4₁/amd*) takes place after thermal treatment. The electrochemical results of such a nanotube layer have been thoroughly considered in the literature, with the anatase phase being more interesting because of the presence of a well-defined flat plateau at 1.75 V during discharge and 1.9 V during charge [1,21,27].

The XRD patterns of ADC and ACD samples did not show any clear proof of the presence of lithium phosphate, which was probably due to the low time (1 min) and low current density (- 3.75 mA cm⁻²) of deposition [25]. Lithium phosphate could easily form very small particles that are not detected by XRD. Figure 2A shows HRTEM imagery of the ACD sample, with areas having visible lattice fringes measured and labeled according to their particular crystal structures. It can be seen that anatase TiO₂ and β-Li₃PO₄ along with ambiguous (either anatase or Li₄Ti₅O₁₂) regions are located throughout the examined area, marked as “1”, “2” and “3”, respectively. The SAED data in Figure 2B matches these d-spacings and confirms the presence of these materials, in addition to revealing that a relatively small amount of Li₄Ti₅O₁₂ (space group *Fd-3m*) [28] coexists with the other compounds. The latter is labeled as “4” for clarity.

(A)



(B)

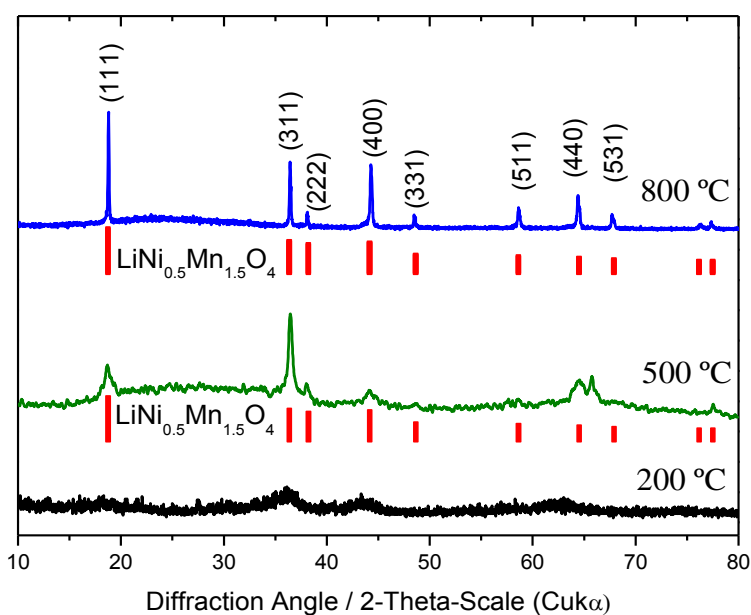


Fig.1. XRD patterns of: (A) nt-TiO₂ fabricated from Ti foil, anodized at 60 V for 120 min and calcined at 500°C, and (B) nw-LiNi_{0.5}Mn_{1.5}O₄ using porous alumina membrane as a template.

Figure 2C shows TEM imagery of the ADC sample, with regions of visible lattice fringes measured and labeled to identify their respective crystal structures. Here, anatase TiO_2 is again present, however, in contrast to the ACD sample the observed form of lithium phosphate is $\gamma\text{-Li}_3\text{PO}_4$, as expected after calcination at $500\text{ }^\circ\text{C}$. In addition, fringes corresponding to $\text{Li}_4\text{Ti}_5\text{O}_{12}$ are also visible. The anatase TiO_2 , $\gamma\text{-Li}_3\text{PO}_4$ and $\text{Li}_4\text{Ti}_5\text{O}_{12}$ regions are labeled “1”, “2” and “3” respectively to avoid confusion. Figure 2D gives the SAED data collected from the same sample, with labels matching the TEM imagery. While the precise value of the spacing of the $\text{Li}_4\text{Ti}_5\text{O}_{12}$ fringes measured in Figure 2C was not found as a diffraction peak in the SAED image, possibly due to image resolution and intensity limitations and the fact that the areas of $\text{Li}_4\text{Ti}_5\text{O}_{12}$ were relatively miniscule, another $\text{Li}_4\text{Ti}_5\text{O}_{12}$ diffraction peak was discovered and labeled accordingly.

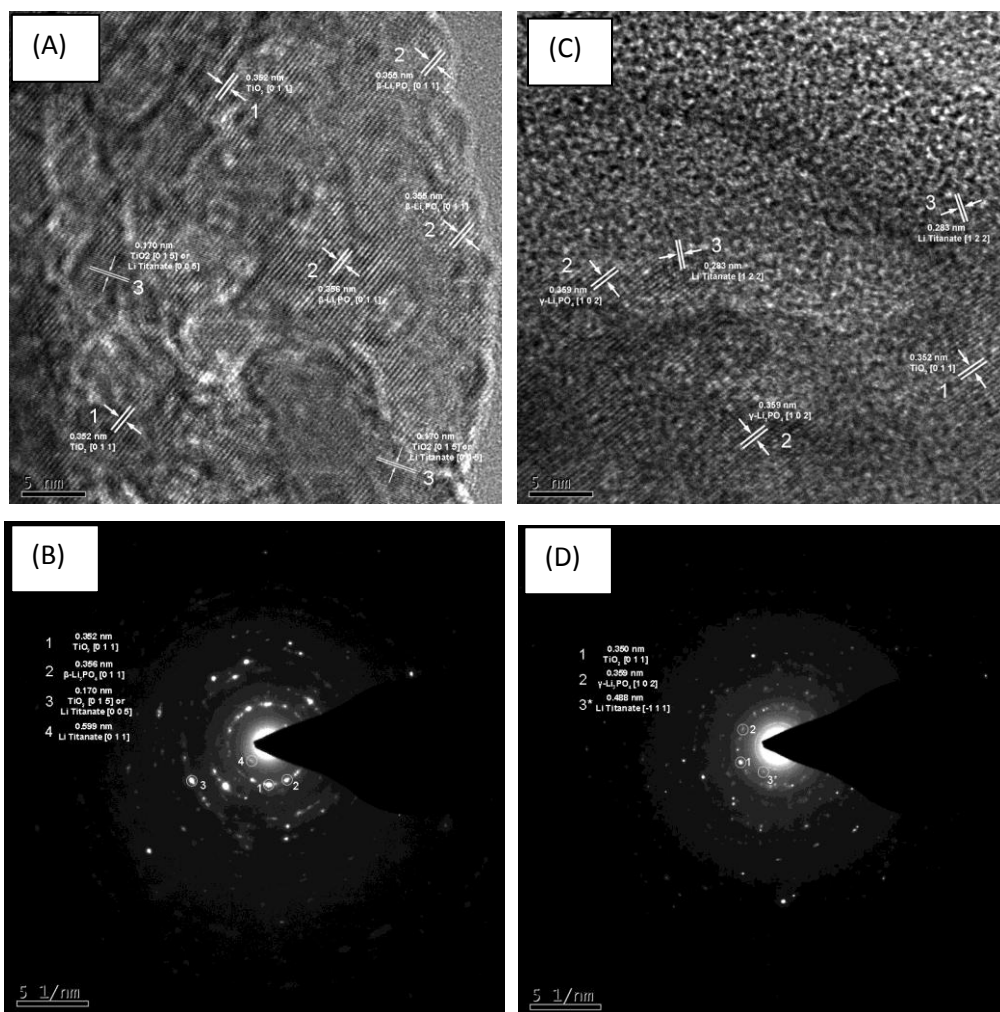


Fig.2. HRTEM and SAED of: (A and B) ACD, and (C and D) ADC electrodes, respectively.

$\text{LiNi}_{0.5}\text{Mn}_{1.5}\text{O}_4$ powder synthesized at 800 °C by using the lithium excess method (5, 10 and 15 %) gave X-ray diffraction patterns perfectly assignable to spinel $\text{LiNi}_{0.5}\text{Mn}_{1.5}\text{O}_4$ (not shown). These powder samples were preliminarily tested in Li-cells to find the best electrode material with a negligible 4 V region, as a first step in fabricating LNMO nanowires with an optimized potential. The XRD patterns of the porous membrane-based materials recorded after calcining at 800 °C unequivocally exhibit peaks of spinel-type $\text{LiNi}_{0.5}\text{Mn}_{1.5}\text{O}_4$ compounds (PDF file no. 32-0581), as shown in Figure 1B. At 200 °C the compound was amorphous and at 500 °C the patterns show spinel-type $\text{LiNi}_{0.5}\text{Mn}_{1.5}\text{O}_4$ peaks, but the data still exhibits evidence of unreacted Mn_2O_3 impurities (PDF file no. 41-1442), with reflections at 32.9° and 65.5° (2-theta). The $\text{LiNi}_{0.5}\text{Mn}_{1.5}\text{O}_4$ structure has been previously separated into “ordered” and “disordered” phases. The former, with space group $P4332$, has Mn and Ni atoms placed in two types of pseudo-octahedral 12d and 4b sites, respectively, Li ions located in the tetrahedral 8c sites, and oxide ions distributed in a distorted cubic close packing, occupying 8c and 24e sites [6, 30]. In the “disordered” phase, with space group $Fd-3m$, only one set of octahedral sites is occupied (16c) where both Ni^{2+} and Mn^{4+} cations are randomly distributed, which is similar to the $\text{Mn}^{3+}/\text{Mn}^{4+}$ in the LiMn_2O_4 spinel. This latter description seems to fit the best for the samples examined here [30].

The texture and morphology of the films were investigated using SEM and TEM. As can be seen in the SEM imagery (Figure 3A, C), nt- TiO_2 film formation is related to the intrinsic characteristics of the potentiodynamic technique. A nanotubular array of TiO_2 was grown on Ti foil through a controlled anodization process, leading to a nanotube length of about 8 – 8.5 μm , an inner diameter of about 60 – 80 nm and a wall thickness of 25 – 30 nm as deduced from TEM (Figure 3C). Typical SEM images of the LNMO spinel are shown in Figs. 3B and 3D, respectively. The successful formation of $\text{LiNi}_{0.5}\text{Mn}_{1.5}\text{O}_4$ nanowires is clearly shown. The diameter and the length of the nanowires agreed with the diameter of the pores (~ 220 nm) and the thickness (65 μm) present in the membrane template. The observed tubular formation can be considered a result of the vertical preferential penetration of the liquid precursor of lithium-nickel-manganese-nitrate on the pore wall of the template membrane, probably assisted by the extended contact time (60 h). The high adsorb-ability of the alumina surface would be favorable for this process. The amount of synthesized oxide oscillated between 2.8 - 3.0 mg per 3.98 cm^2 of alumina membrane. Typical TEM images clearly

reveal that the LNMO nanowires are formed by numerous crystal grains but with an arbitrary stacking arrangement within the wall created by the alumina pore membrane. Some voids are also observable along the wires, as seen in Figure 3D. The selected area in Figure 3B was also characterized by energy dispersive spectroscopy (EDS), indicating the presence of Ni and Mn with a 1.22 and 3.59 atomic percentage in the sample respectively (Mn/Ni ratio of 2.9). The ICP analysis showed the presence of Mn and Ni in a ratio of about 2.97, very close to the theoretical value of 3 in $\text{LiNi}_{0.5}\text{Mn}_{1.5}\text{O}_4$. This data could be indicative of a slight deficiency of Mn^{3+} in the structure, which was not detected in the X-ray diffraction patterns. A detailed HRTEM image indicated the presence of small particles along the nanowires, as deduced from the observation of different lattice fringes which are typical of spinel type compounds (e.g. 111 and 220). Moreover, the parallel self-organization of a few LNMO nanowires can be observed in Figure 4.

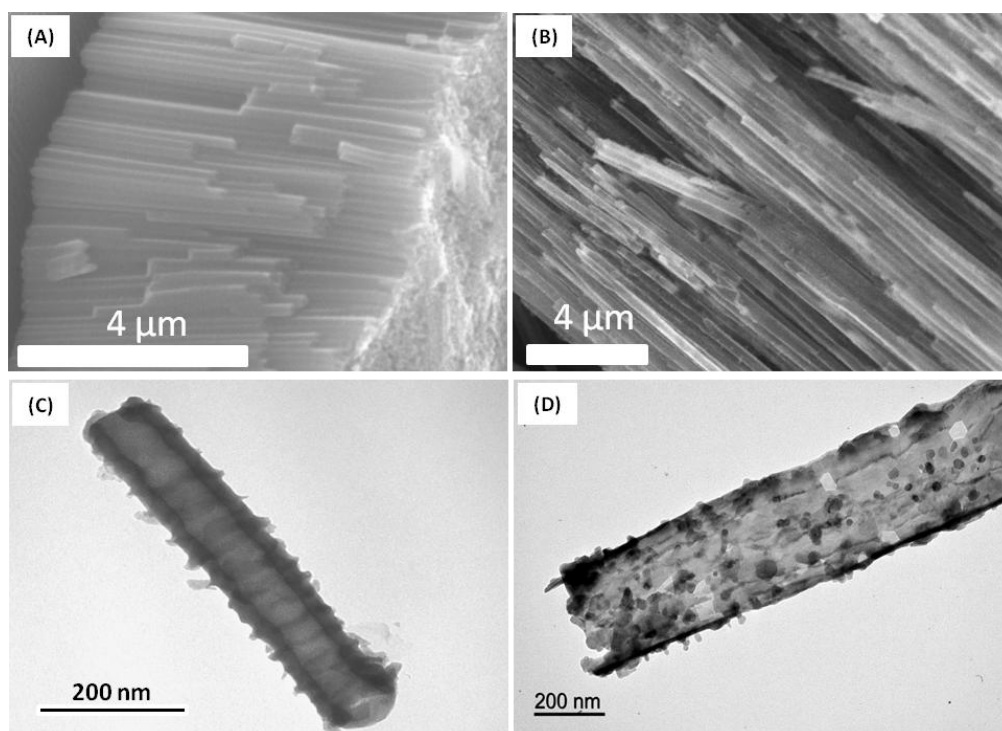


Fig.3. Cross-sectional SEM view of: (A) nt-TiO_2 obtained using 60 V for 2 h, (B) $\text{LiNi}_{0.5}\text{Mn}_{1.5}\text{O}_4$ nanowires grown on alumina templates. (C) and (D) are their corresponding TEM images, respectively.

The oxidation state of the different elements present in the $\text{LiNi}_{0.5}\text{Mn}_{1.5}\text{O}_4$ nanowires was analyzed by XPS (Figure 5). The Mn $2p_{3/2}$ XPS binding energies of Mn^{3+} and Mn^{4+} are 641.9 and 643.2 eV, respectively [32,33]. The LNMO sample gave the Mn $2p_{3/2}$ peak at 643.5 eV which was ascribable to Mn^{4+} (Figure 5). The Ni $2p_{3/2}$ XPS binding energy presents a profile with a peak at 854 eV that can be assigned to Ni^{2+} [34]. The O 1s spectrum displayed a complex profile with a major component centered at 529.6 eV that can be assigned to Mn-O, Ni-O, and Li-O bonds. The components at higher binding energies are of lower intensity and are typically associated with OH^- or O_2^- or are due to water chemi- and/or physi-sorbed onto the surface [35].

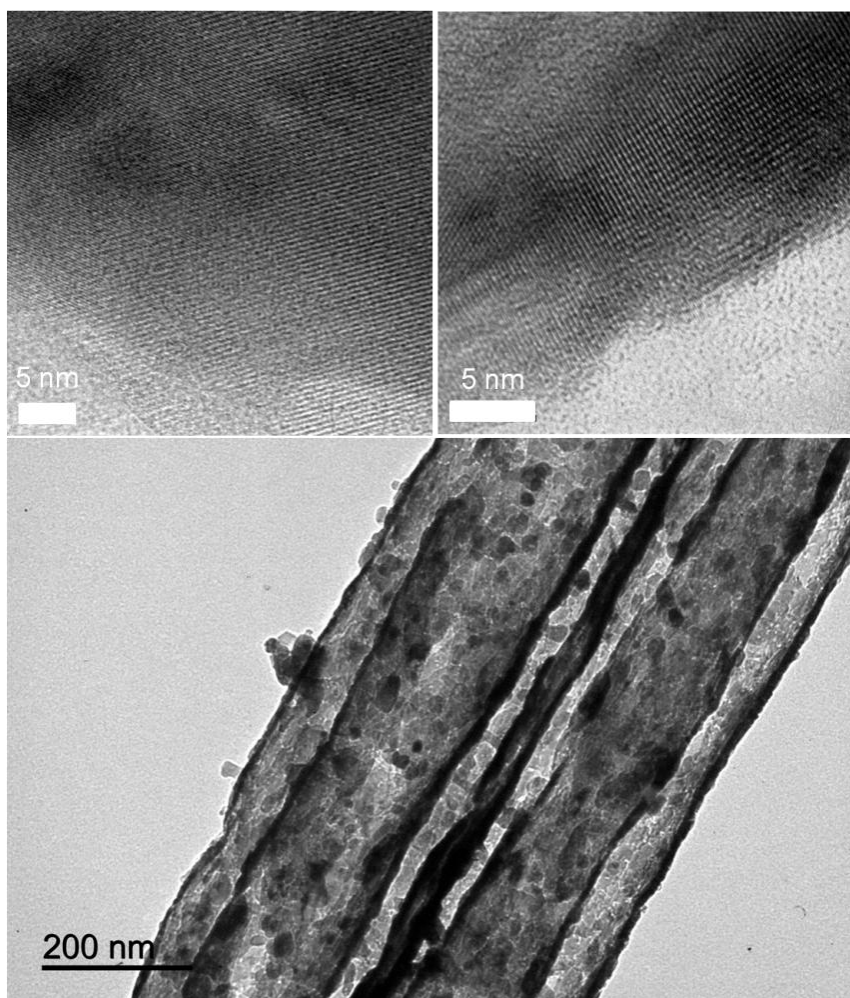


Fig.4. HRTEM images of the self-organized $\text{LiNi}_{0.5}\text{Mn}_{1.5}\text{O}_4$ nanowires. The top left image shows the inner part of a nanowire and the top right shows the wall area of a wire.

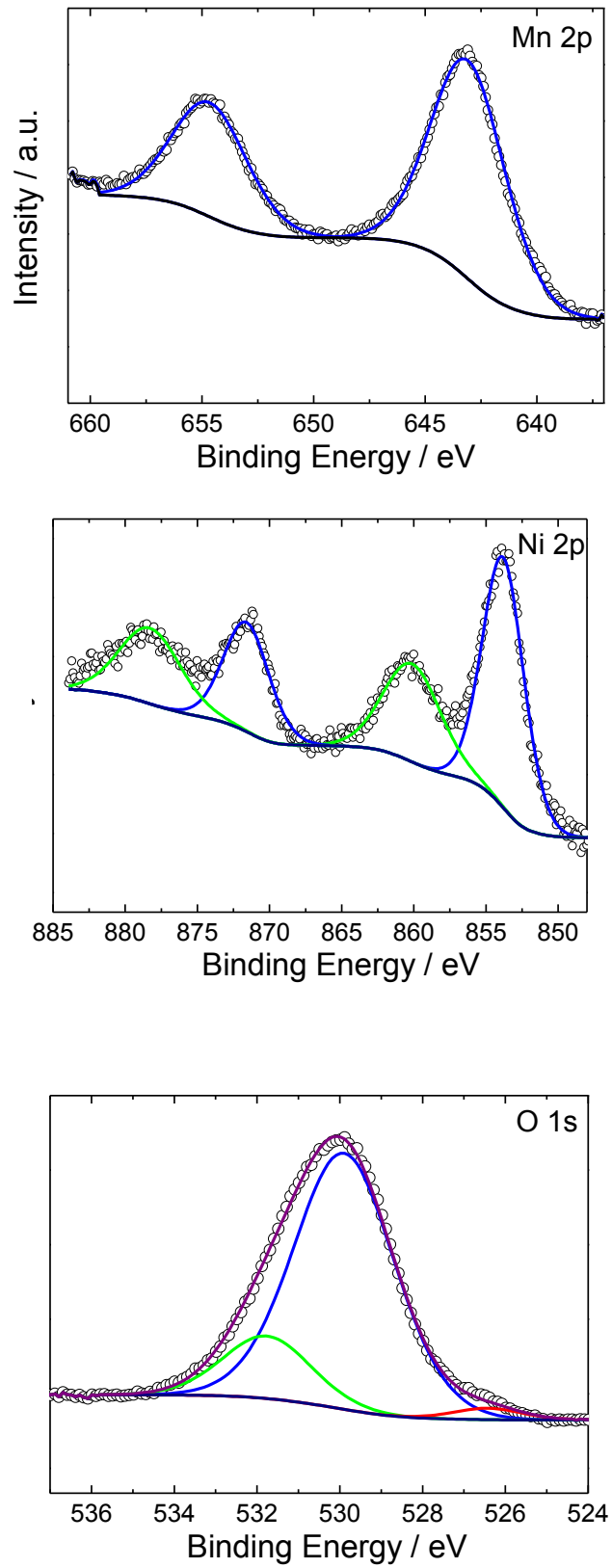


Fig.5. Selected Ni2p, Mn2p and O1s zones corresponding to the XPS spectra of $\text{LiNi}_{0.5}\text{Mn}_{1.5}\text{O}_4$ nanowires.

2.2.3.2 Li half cells

Regarding the effects of lithium phosphate on the nt-TiO₂ anode, a previous study suggested that γ -Li₃PO₄ and β -Li₃PO₄ produced a performance improvement in terms of higher capacity and better capability versus unmodified nt-TiO₂ [25]. In fact, surface deterioration at the mouths of the nanotubes leads to poor capacity retention on prolonged cycling of bare nt-TiO₂ (Figure S1). Our new results using 2% of FEC as additive in the electrolyte confirmed the conclusions of this previous work [25], as the capacity of anatase nt-TiO₂ (labeled ‘AC’) faded below 220 $\mu\text{A h cm}^{-2}$ with 81 % of capacity retention after 80 cycles. Meanwhile, the ADC and ACD samples retained 300 and 255 $\mu\text{A h cm}^{-2}$ with 95 % and 94 % of capacity retention over 90 cycles, respectively (Figure S1). To better understand this improvement, attention should be drawn to the small Li₄Ti₅O₁₂ domains that are formed on the TiO₂/Li₃PO₄ interface, as confirmed by HRTEM and SAED (Figure 2). Indeed, the Li₄Ti₅O₁₂ phase can be formed by the intercalation of lithium into nt-TiO₂ at room temperature during the electrodeposition of Li₃PO₄ in both ACD and ADC samples (Figure 2). At the preparation temperature used in this work (500 °C), the crystallinity of the Li₄Ti₅O₁₂ phase was so low that it could not be observed by XRD. However, in previous studies it was shown that further calcining at 700 °C allowed the formation of larger Li₄Ti₅O₁₂ particles that exhibited clear X-ray reflections [24]. These temperatures are low enough to avoid decomposing Li₄Ti₅O₁₂ into the ramsdellite-type phase Li₂Ti₃O₇ and the cubic Li₂TiO₃ (γ -Li₂TiO₃) [28]. Thus, for the full cell we selected the nt-TiO₂ anode to serve as a reference and the ADC anode as the experimental focus, both versus a LNMO cathode. The presence of traces of the Li₄Ti₅O₁₂ phase at the interface between Li₃PO₄ and TiO₂ gives additional understanding of the structure of these composites as compared with previous reports [24]. However, the minute amounts of the Li₄Ti₅O₁₂ spinel phase does not have a significant effect on the voltage/capacity curves but may facilitate fast ionic transport at the interface, and enhanced rate performance of the full Li-ion battery, as shown below.

Regarding the LiMn_{1.5}Ni_{0.5}O₄ cathode, Figure 6A shows typical galvanostatic charge–discharge profiles. The first charge capacity is 167.4 mA h g⁻¹ which is higher than the theoretical capacity value (146.7 mA h g⁻¹) that corresponds to the extraction of one Li per formula unit. This discrepancy is due to irreversible reactions with the

electrolyte. In fact, an efficiency of 94 % from the first to the second cycle is observed. The derivative curves can help to observe and identify all the processes occurring in the cell (Figure 6 B). Thus, during charging, electrochemical activity in the 3.85 – 4.25 V and 4.5 – 4.95 V ranges can be observed. The former is related to the $\text{Mn}^{3+}/\text{Mn}^{4+}$ redox couple that is negligible [36,37]. Moreover, our $\text{LiMn}_{1.5}\text{Ni}_{0.5}\text{O}_4$ nanowires show two well defined plateaus at 4.7 V and 4.76 V during charge and 4.71 and 4.66 V during discharge, respectively. These are undoubtedly attributable to the $\text{Ni}^{2+}/\text{Ni}^{4+}$ redox couple [38-40]. The total capacity in the first charge can be split into the capacity obtained from the high voltage plateau (~ 4.7 V) and a much less substantial contribution from the low voltage (~ 4 V) plateau, with $Q_{4.7\text{V}} = 125.6 \text{ mA h g}^{-1}$ and $Q_{4\text{V}} = 20 \text{ mA h g}^{-1}$. A capacity of 128 mA h g^{-1} (on discharge) is obtained after 30 cycles. Therefore, the capacity retention upon cycling is about 99 % (Figure 6 C) entailing that fast Li-ion diffusion into the nanowires is ongoing.

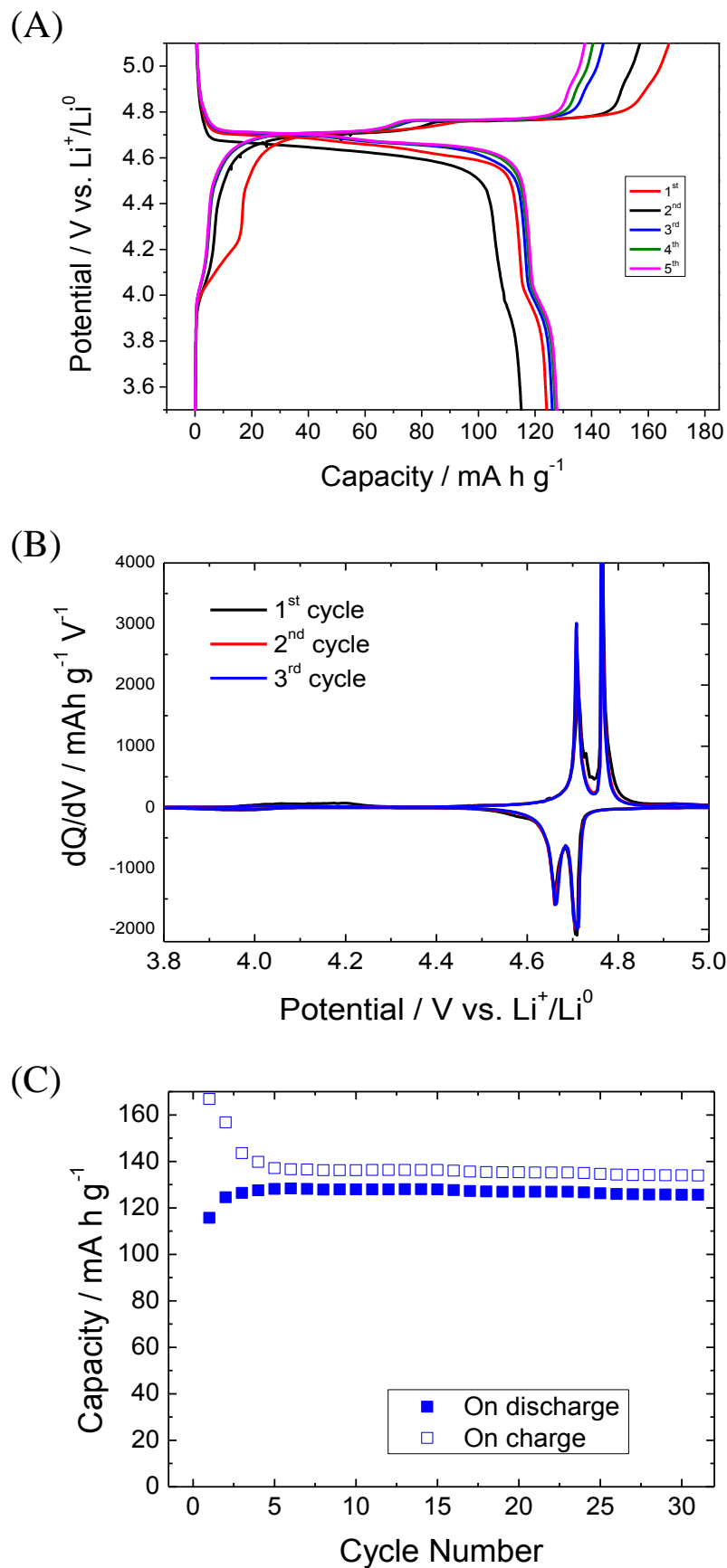
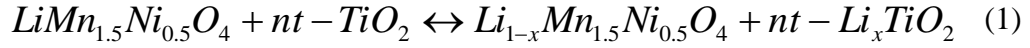


Fig.6. Electrochemical properties of $\text{LiNi}_{0.5}\text{Mn}_{1.5}\text{O}_4$ nanowires in a lithium half cell: (A) Galvanostatic discharge/charge curves (B) its respective dQ/dV curves and (C) the respective cycling performances.

2.2.3.3 Li-ion cells

The main overall reaction that takes place in the full cells can be summarized as follows:



The theoretical capacity delivered by anatase is around 167 mA h g⁻¹ (for x = 0.5) and that of LiNi_{0.5}Mn_{1.5}O₄ is 146.7 mA h g⁻¹ (x = 1.0). As expected from their individual voltages, the combination of nt-TiO₂ with LiNi_{0.5}Mn_{1.5}O₄ gives rise to a battery operating in the 2.6 – 3.0 V range. For the sake of clarity, the nt-TiO₂ / LiNi_{0.5}Mn_{1.5}O₄ cell fabricated without using surface coating treatments (labeled as RC1) is plotted (Figure 7A). The effects of lithium phosphate have been studied in the full cell (labeled as RC2) and their electrochemical performance is shown in Figure 7B. The voltage profile during charge denoted the lithium transfer from LiNi_{0.5}Mn_{1.5}O₄ to nt-TiO₂ and during discharge the transfer of lithium back from nt-TiO₂ to LiNi_{0.5}Mn_{1.5}O₄. The capacity of the full cell in the upper plot (E_C-E_A vs. capacity) is calculated using the mass of the cathode (Figure 7). For a better comparison, the voltage profiles of the cathode (E_C vs. capacity) and the anode (E_A vs. capacity) are also represented in the middle and bottom plots, respectively. All the galvanostatic profiles are similar for the two full cells, but there are some differences in terms of polarization, capacity and efficiency values when cycled at a 1 C rate. Then, the nt-TiO₂ / LiNi_{0.5}Mn_{1.5}O₄ cell (RC1) shows a polarization of 0.2 V, a capacity value of 110 mA h g⁻¹ and a first cycle efficiency of 96%. The nt-TiO₂,Li₃PO₄/ED:DEC LiPF₆/LiNi_{0.5}Mn_{1.5}O₄ cell (RC2) shows a polarization of 0.17 V, a capacity of 125 mA h g⁻¹ and a first cycle efficiency of 99%. In addition, the 4 V zone is minimized when lithium phosphate is present in the electrode/electrolyte interphase. More outstanding results are found when using a lithium phosphate coating because the reversible capacity (125 mA h g⁻¹) is close to the theoretical maximum value.

The reversible capacity observed for the cathode is consistent with the above results and that observed for the anode is consistent with previous studies [41]. However, under fast rates (5 C) an improved capability for nt-TiO₂,Li₃PO₄/ED:DEC LiPF₆/LiNi_{0.5}Mn_{1.5}O₄ (RC2) can be observed as compared to nt-TiO₂/EC:DEC LiPF₆/LiNi_{0.5}Mn_{1.5}O₄ (RC1) in Figure 8A. To assess these findings, several rates were used

(Figure 8B). When using a constant rate of 5 C, the RC2 cell exhibited a first discharge capacity of 125 mA h g^{-1} and could retain around 110 mA h g^{-1} over 100 cycles. Although the RC1 cell exhibited a similar first reversible capacity (125 mA h g^{-1}), the rate capability was poorer as capacity fell below 90 mA h g^{-1} after just 60 cycles (Fig. 8A). In order to confirm the good capability of the RC2 sample, the designed nano-architected battery was cycled at 5 C, 2C, C, and C/2 rates and delivered 125, 120, 120 and 125 mA h g^{-1} of capacity, respectively (Figure 8B). In this way, a careful design of the nt-TiO_2 , $\text{Li}_3\text{PO}_4/\text{ED}:\text{DEC LiPF}_6/\text{LiNi}_{0.5}\text{Mn}_{1.5}\text{O}_4$ architecture enabled an electrochemically robust full cell operating at 2.6 – 3.0 V.

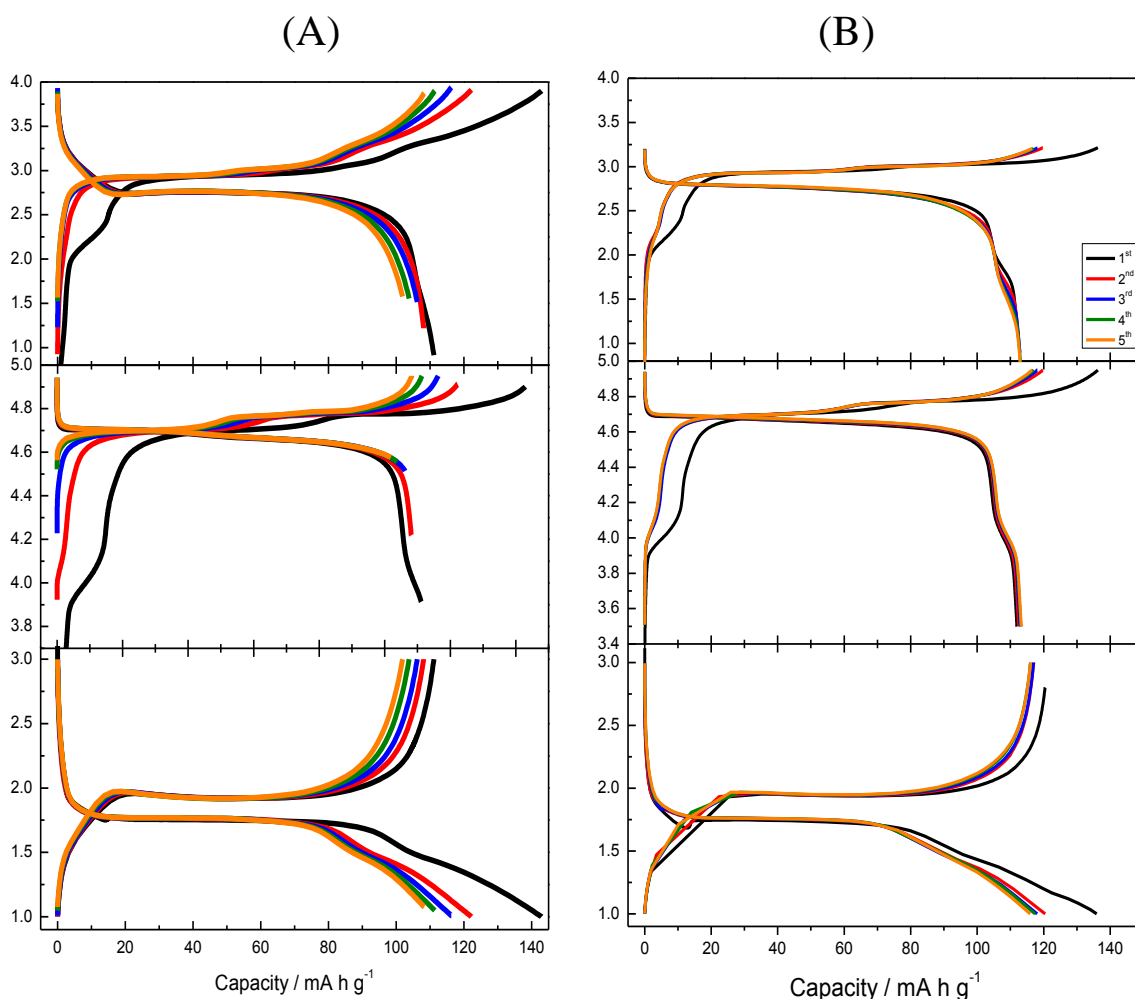


Fig.7. Galvanostatic charge/discharge cycles of: (A) $\text{nt-TiO}_2/\text{EC}:\text{DEC LiPF}_6/\text{LiNi}_{0.5}\text{Mn}_{1.5}\text{O}_4$ and (B) $\text{nt-TiO}_2,\text{Li}_3\text{PO}_4/\text{ED}:\text{DEC LiPF}_6/\text{LiNi}_{0.5}\text{Mn}_{1.5}\text{O}_4$ cells. For a better comparison, the voltage profiles of the cathode (E_C vs. capacity) and the anode (E_A vs. capacity) are also represented in the middle and bottom plots, respectively. The capacity of the full cell in the upper plot ($E_C - E_A$ vs. capacity) is calculated using the mass of cathode.

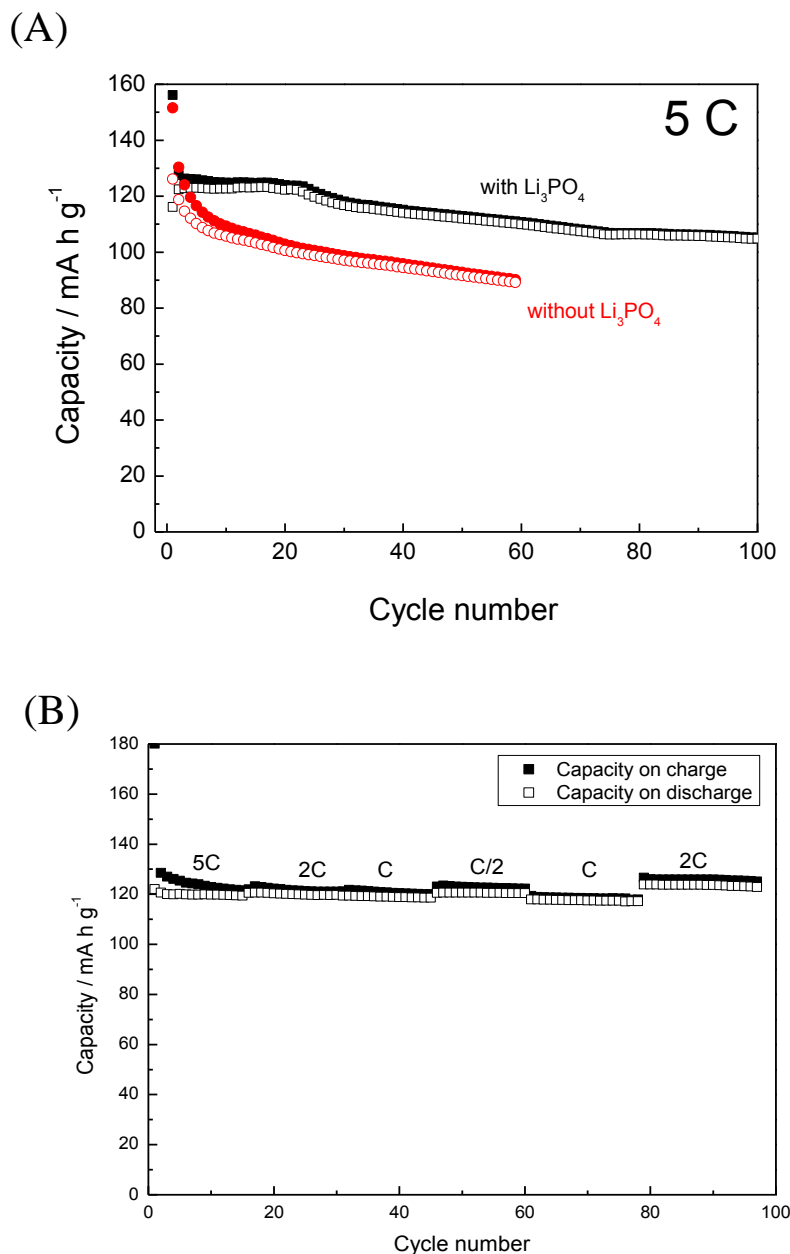


Fig.8. (A) Comparison of the capacity retention of nt-TiO₂/EC:DEC LiPF₆/LiNi_{0.5}Mn_{1.5}O₄ (RC1) and nt-TiO₂/Li₃PO₄/ED:DEC LiPF₆/LiNi_{0.5}Mn_{1.5}O₄ (RC2) full cells at a 5 C rate. (B) Rate capability data from a nt-TiO₂ / γ -Li₃PO₄ / LiNi_{0.5}Mn_{1.5}O₄ (RC2) cell, using variable rates from 10 C to C/2.

Using this chemistry and the associated nano-architected configuration, we have demonstrated a combination of active materials that provides a gravimetric energy density of 325 W h kg⁻¹ during discharge at 2.6 V and referred to the mass of the cathode, and 127 μ W h cm⁻² μ m⁻¹ (or 637 μ W cm⁻² μ m⁻¹) at 5 C rate, which are compatible with potential 3D microbatteries. These results compare well with different

reports in the literature. Brutti et al. reported an energy density of about 150 W h kg^{-1} using a C/3 rate for nano-TiO₂/ LiNi_{0.5}Mn_{1.5}O₄-ZnO [31]. A recent paper by Djenizian's group reported an energy density of 168 W h kg^{-1} referred to the mass of the anode (or $60 \mu\text{Wh cm}^{-2} \mu\text{m}^{-1}$) at a C/10 rate for a cell with self-supported nt-TiO₂ as anode, a polymer thin film as electrolyte, and a layer of LiNi_{0.5}Mn_{1.5}O₄ as cathode [42]. Jung et al. [26] studied the Li₄Ti₅O₁₂ /Li[Ni_{0.45}Co_{0.1}Mn_{1.45}]O₄ cell and reported an excellent energy density of 225 W h kg^{-1} referred to the mass of the cathode. Using other chemistries, MCMB—MoO_yS_z provided $2.3 \mu\text{W h cm}^{-2} \mu\text{m}^{-1}$ at high rate [43] and NiSn—LMO $15 \mu\text{W h cm}^{-2} \mu\text{m}^{-1}$ at 1.5C rate [18]. It should be highlighted that in these studies carbon-coated LNMO and LTO with conductive additives and binders were used, while here we are fabricating binder-free electrode battery materials with very favorable power and energy densities.

Besides the reduced expected contribution of the minute amounts of Li₄Ti₅O₁₂ to surface protection, the results reported here evidence that lithium phosphate exerts a stabilization effect at the anode/electrolyte interface, facilitating an improved mass transfer and Li-diffusion at high rates. Phosphates have also been reported as an effective protection of cathodes. Xiao et al. [44] used an electroactive FePO₄ coating that showed advantages associated to the electron/ion diffusion on the surface. Our results are closer to those of Chong et al. [45], who used ion-conducting Li₄P₂O₇ coating on LNMO, leading to the formation of an artificial SEI layer between the electrolyte and LNMO. Here the protection of TiO₂ electrodes also involves the generation of an ion conductive layer that avoids contact with the electrolyte solution.

2.2.4 Conclusions

The development of LiNi_{0.5}Mn_{1.5}O₄ nanowire cathodes and their combination with pristine and surface-modified nano-architected nt-TiO₂ anodes in Li-ion test cells was presented as a promising possibility for a future application in three-dimensional microbatteries. The intercalation reactions avoid the use of metallic lithium, enhance safety, and preserve a high voltage cell operation. Two major research approaches have been pursued for the improvement of battery performance at the nanoscale in this work: the use of electrochemical and template-based procedures, and the preparation of

nanostructured electrodes. The combined approach showed here results in an increased available surface area and active material loading for the same device footprint, which enhances energy and power densities as compared to traditional 2D thin-film batteries. The use of Li_3PO_4 -coated anode resulted in a superior electrochemical performance. There was a flat voltage profile centered at about 2.6 - 3 V with a hysteresis of 0.17 V between charge and discharge during prolonged cycling, clear evidence of a high reversibility and fast kinetics. The maximum energy and power densities of the microbattery cells cycled at a 5 C rate was 325 mW h g^{-1} and $637 \mu\text{W cm}^{-2} \mu\text{m}^{-1}$. The scalability of the synthesis and fabrication of the battery is promising, and fabrication could be easily implemented in an industrial setting. The results of the combination of the material, fabrication method and nano-architecture chosen suggest many potentially fruitful applications to microdevices.

Acknowledgements

The authors are grateful to MEC (MAT2011-22753) and Junta de Andalucía for financial support (FQM-7206). G. F. Ortiz is indebted to the “Ramón y Cajal” program (RYC-2010-05596) and to *MESC* for a scholarship at Xiamen University. Y. Yang acknowledges funding from the National Natural Science Foundation of China (Grant No. 21233004).

2.2.5 References

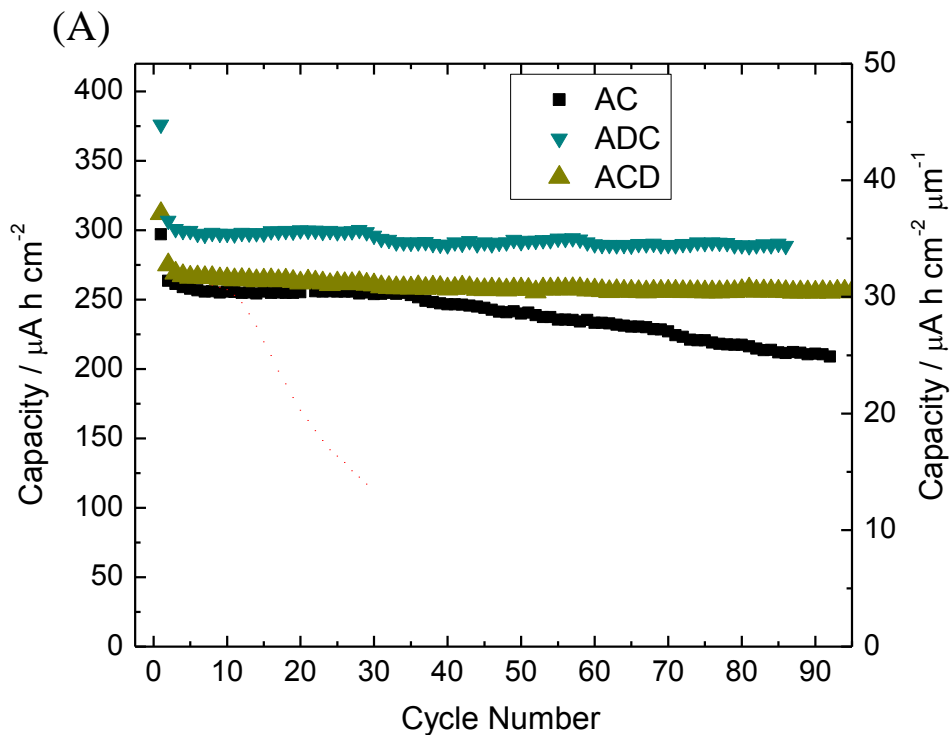
1. G. F. Ortiz, I. Hanzu, T. Djenizian, P. Lavela, J. L. Tirado, P. Knauth, *Chem. Mater.* 21 (2009) 63.
2. Z. Hong, M. Wei, T. Lan, G. Cao, *Nano Energy* 1 (2012) 466.
3. A. K. Padhi, K. S. Nanjundaswamy, J. B. Goodenough, *J. Electrochem. Soc.* 144 (1997) 1188.
4. B. León, C. P. Vicente, J. L. Tirado, P. Biensan, C. Tessier, *J. Electrochem. Soc.* 155 (2008) A211.

5. T. A. Arunkumar, A. Manthiram, *Electrochem. Solid-State Lett.* 8 (2005) A403.
6. J. H. Kim, S. T. Myung, C. S. Yoon, S. G. Kang, Y. K. Sun, *Chem. Mater.* 16 (2004) 906.
7. Y. Talyosef, B. Markovsky, R. Lavi, G. Salitra, D. Aurbach, D. Kovacheva, M. Gorova, E. Zhecheva, R. Stoyanova, *J. Electrochem. Soc.* 154 (2007) A682.
8. M. Mohamedi, M. Makino, K. Dokko, T. Itoh, I. Uchida, *Electrochim. Acta* 48 (2002) 79.
9. L. Wang, H. Li, X. Huang, E. Baudrin, *Solid State Ionics* 193 (2011) 32.
10. J. Xiao, X. Chen, P. V. Sushko, M. L. Sushko, L. Kovarik, J. J. Feng, Z. Q. Deng, J. M. Zheng, G. L. Graff, Z. M. Nie, D. W. Choi, J. Liu, J. G. Zhang, M. S. Whittingham, *Adv. Mater.* 24 (2012) 2109.
11. Q. Zhong, A. Bonakdarpour, M. Zhang, Y. Gao, J. R. Dahn, *J. Electrochem. Soc.* 144 (1997) 205.
12. T. Ohzuku, S. Takeda, M. Iwanaga, *J. Power Sources* 81 (1999) 90.
13. M. G. Lazarraga, L. Pascual, H. Gadjov, K. Petrov, J. M. Amarilla, R. M. Rojas, M. A. Martín-Luengo, J. M. Rojo, *J. Mater. Chem.* 14 (2004) 1640.
14. R. Alcántara, M. Jaraba, P. Lavela and J. L. Tirado, *J. Electrochem. Soc.* 151 (2004) A53.
15. K. M. Shaju, P. G. Bruce, *Dalton Trans.* 40 (2008) 5471.
16. S. Patoux, L. Sannier, H. Lignier, Y. Reynier, C. Bourbon, S. Jouanneau, F. Le Cras, S. Martinet, *Electrochim. Acta* 53 (2008) 4137.
17. R. Santhanam, B. Rambabu, *J. Power Sources* 195 (2010) 5442.
18. J. H. Pikul, H. G. Zhang, J. Cho, P. V. Braun, W. P. King, *Nat. Commun.* 4 (2013) 1732.
19. J. W. Long, B. Dunn, D. R. Rolison, H. S. White, *Chem. Rev.* 104 (2004) 4463.
20. I. Exnar, L. Kavan, S.Y. Huang and M. Grätzel, *J. Power Sources* 68 (1997) 720.

21. J. R. González, R. Alcántara, F. Nacimiento, G. F. Ortiz, J. L. Tirado, E. Zhecheva, R. Stoyanova, *J. Phys. Chem. C*. 116 (2012) 20182.
22. M. Nishizawa, K. Mukai, S. Kuwabata, C. R. Martin, H. J. Yoneyama, *J. Electrochem. Soc.* 144 (1997) 1923.
23. B. L. Ellis, P. Knauth, T. Djenizian, *Adv. Mater.* 26 (2014) 3368.
24. M. Cabello, G. F. Ortiz, M. C. López, P. Lavela, R. Alcántara, J. L. Tirado, *Electrochem. Commun.* 56 (2015) 61.
25. M. C. López, G. F. Ortiz, J. R. González, R. Alcántara, J. L. Tirado, *ACS Appl. Mater. Interfaces* 6 (2014) 5669.
26. H. G. Jung, M. W. Jang, J. Hassoun, Y. K. Sun, B. Scrosati, *Nat. Commun.* 2 (2011) 516.
27. J. R. González, R. Alcántara, G. F. Ortiz, F. Nacimiento, J. L. Tirado, *J. Electrochem. Soc.* 160 (2013) A1390.
28. A. Laumann, H. Boysen, M. Bremholm, K. T. Fehr, M. Hoelzel, M. Holzappel, *Chem. Mater.* 23 (2011) 2753.
29. K. Ariyoshi, Y. Iwakoshi, N. Nakayama, T. Ohzuku, *J. Electrochem. Soc.* 151 (2004) A296.
30. U. Lafont, A. Anastasopol, E. Garcia-Tamayo and E. Kelder, *Thin Solid Films* 520 (2012) 3464.
31. S. Brutti, V. Gentili, P. Reale, L. Carbone, S. Panero, *J. Power Sources* 196 (2011) 9792.
32. B. N. Ivanov-Emin, N. A. Nevskaya, B. E. Zaitsev, T. M. Ivanova, *Zh. Neorg. Khimii* 27 (1982) 3101.
33. Y. Umezawa, C. N. Reilley, *Anal. Chem.* 50 (1978) 1290.
34. K. Amine, H. Tukamoto, H. Yasuda, Y. Fujita, *J. Power Sources* 68 (1997) 604.

35. T. Choudhury, S. O. Saied, J. L. Sullivan, A. M. Abbot, *J. Phys. D: Appl. Phys.* 22 (1989) 1185.
36. T. Y. Yang, N. Q. Zhang, Y. Lang, K. Sun, *Electrochim. Acta* 56 (2011) 4058.
37. J. H. Cho, J. H. Park, M. H. Lee, H. K. Song, S. Y. Lee, *Energy Environ. Sci.* 5 (2012) 7124.
38. K. Ariyoshi, Y. Iwakoshi, N. Nakayama, T. Ohzuku, *J. Electrochem. Soc.* 151 (2004) A296.
39. M. Kunduraci, G. G. Amatucci, *J. Power Sources* 165 (2007) 359.
40. M. Aklalouch, R. M. Rojas, J. M. Rojo, I. Saadoune, J. M. Amarilla, *Electrochim. Acta* 54 (2009) 7542.
41. R. Menéndez, P. Álvarez, C. Botas, F. Nacimiento, R. Alcántara, J. L. Tirado, G. F. Ortiz, *J. Power Sources* 248 (2014) 886.
42. N. Plylahan, M. Letiche, M. K. S. Barr, T. Djenizian, *Electrochem. Comm.* 43 (2014) 121.
43. M. Nathan, D. Golodnitsky, V. Yufit, E. Strauss, T. Ripenbein, I. Shechtman, S. Menkin, E. Peled, *J. Microelectromechanical Syst.* 14 (2005) 879.
44. B. Xiao, J. Liu, Q. Sun, B. Wang, M. N. Banis, D. Zhao, Z. Wang, R. Li, X. Cui, T. K. Sham, X. Sun, *Adv. Sci.* 2 (2015) 1500022.
45. J. Chong, S. Xun, X. Song, G. Liu, V. S. Battaglia, *Nano Energy*, 2 (2013) 283.

2.2.6 Supplementary information



(B)

(C)

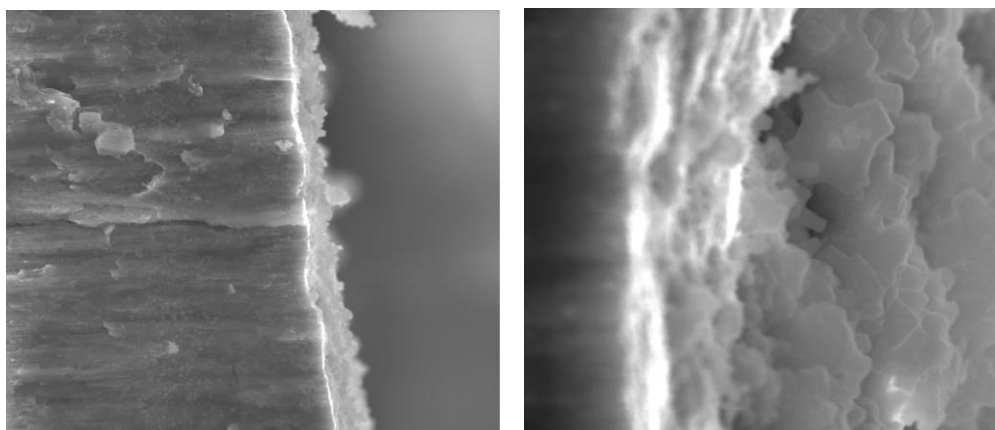


Fig.S1. (A) Capacity retention of ‘AC’ (anatase nt-TiO₂), ‘ACD’ (nt-TiO₂/β-Li₃PO₄) and ‘ADC’ (nt-TiO₂ / γ-Li₃PO₄) electrodes using 2% FEC in 1 M LiPF₆ (EC: DMC, 1:1, v: v) electrolyte. (B and C) Images of surface deterioration in used bare anatase nt-TiO₂ electrodes.

2.3 Enhancing the energy density of safer Li-ion batteries by combining high-voltage lithium cobalt fluorophosphate cathodes and nanostructured titania anodes

Gregorio F. Ortiz ^a, María C. López ^a, Yixiao Li ^b, Matthew J. McDonald ^b, Marta Cabello ^a, José L. Tirado ^a, Yong Yang ^b.

^a Laboratorio de Química Inorgánica. Universidad de Córdoba. Edificio C3, Campus de Rabanales. Spain

^b State Key Laboratory of Physical Chemistry of Solid Surfaces, Department of Chemistry, College of Chemistry and Chemical Engineering, Xiamen University. China.

Abstract

Recently, Li-ion batteries have been heavily scrutinized because of the apparent incompatibility between safety and high energy density. This work report a high voltage full battery made with TiO₂/Li₃PO₄/Li₂CoPO₄F. The Li₂CoPO₄F cathode and TiO₂ anode materials are synthesized by a sol-gel and anodization methods, respectively. X-ray diffraction (XRD) analysis confirmed that Li₂CoPO₄F is well-crystallized in orthorhombic crystal structure with *Pnma* space group. The Li₃PO₄-coated anode was successfully deposited as shown by the (011) lattice fringes of anatase TiO₂ and (200) of γ -Li₃PO₄, as detected by HRTEM. The charge profile of Li₂CoPO₄F versus lithium shows a plateau at 5.0 V, revealing its importance as potentially high-voltage cathode and could perfectly fit with the plateau of anatase anode (1.8–1.9 V). The full cell made with TiO₂/Li₃PO₄/Li₂CoPO₄F delivered an initial reversible capacity of 150 mA h g⁻¹ at C rate with good cyclic performance at an average potential of 3.1–3.2 V. Thus, the full cell provides an energy density of 472 W h kg⁻¹. This full battery behaves better than TiO₂/Li₂CoPO₄F. The introduction of Li₃PO₄ as buffer layer is expected to help the cyclability of the electrodes as it allows a rapid Li-ion transport.



Scientific Reports 6 (2016) 20656-20663

2.3.1 Introduction

Li-ion technology is now mature enough to meet the exacting demands of portable electronic devices and even electric vehicles. However, recently Li-ion batteries (LIBs) have come under heavy scrutiny because of an apparent incompatibility between safety and high energy density. The capabilities of LIBs are governed by the chemistry of the cathode, which almost exclusively utilizes transition metal insertion/intercalation reactions. The cathode material is not only the most expensive part of the battery but also the primary limitation on the electrochemical performance. It is thus desirable to find high voltage cathode materials with high capacity ($xLi \gg 1$) and good electrolyte stability. $LiNi_{0.5}Mn_{1.5}O_4$ spinel, $LiCoPO_4$ olivine, $LiNiVO_4$ inverse spinel and Li_2CoPO_4F fluorophosphates are currently considered to be the most promising 5-V cathode voltage materials available [1-6]. On the other side of the battery, there are a large number of possibilities for anodes to be combined with cathodes, but some of the most outstanding anodes with respect to safety performance are $Li_4Ti_5O_{12}$ and TiO_2 , which can replace carbonaceous materials [7-10]. The TiO_2 electrodes vs. Li_2CoPO_4F can be considered safer than other Li-ion systems based on carbon anodes, due to the higher working voltage of the anode that avoids lithium electrodeposition, which is well known to jeopardize safety, while energy density is preserved or even improved by the use of the high-voltage cathode.

Up until now, one of the more impressive LIB electrochemical performances has been seen in the $Li_4Ti_5O_{12}/Li_2CoPO_4F$, primarily because it exhibits a voltage plateau at about 3.4 V which is higher than that of a $Li_4Ti_5O_{12}/LiFePO_4$ full cell at ~1.9 V [11,12]. However, an unresolved problem with the former system is that capacity decays abruptly in the first few cycles, and as of yet no improvement in cycling performance has been achieved. As far as we know, there are no reports in the literature dealing with TiO_2/Li_2CoPO_4F that can reach theoretical energy densities above 450 W h kg^{-1} , performance close to the demands of modern applications.

In order to improve the cyclability of high voltage LIBs, the effects of a surface treatment of lithium phosphate on a full cell made with Li_2CoPO_4F as cathode and TiO_2 as anode were studied. This report shows how the electrochemical performance of this material compared very favorably with Li_3PO_4 -free electrodes. The introduction of

an inactive matrix such as Li_3PO_4 for use as a buffer layer is expected to help the cyclability of the electrodes by allowing a rapid transportation of Li ions [13,14].

2.3.2 Experimental

The $\text{Li}_2\text{CoPO}_4\text{F}/\text{C}$ nanocomposite was synthesized by the sol-gel (SG) method as previously reported [11,15]. The self-organized titania nanotube (nt- TiO_2) layer was fabricated by an anodization process using Ti foils at 60 V for 2 h, with a freshly prepared mixture of EG/water (92:8 vol.) containing 0.3 wt. % NH_4F as an electrolyte solution. The deposition of electrolytic Li_3PO_4 was performed on nt- TiO_2 as either amorphous material (labeled as AD) or, after calcination, as an anatase material (labeled as ADC), using a current density of -3.75 mA cm^{-2} for 1 min. Electrolytic Li_3PO_4 films were deposited by an electrochemical procedure consisting of proton reduction with a subsequent local increase of pH in the vicinity of the substrate surface, hydrogen phosphate dissociation and Li_3PO_4 deposition on the surface of the cathode [13]. Optional thermal annealing at 500°C was performed. The thickness and active mass of the anode was $8 \mu\text{m}$ and 0.935 mg cm^{-2} respectively [13].

HRTEM and SAED images were collected with a Tecnai F-20 device operating at 200 kV. The X-ray diffraction (XRD) patterns were recorded with a Siemens D5000 instrument utilizing $\text{Cu K}\alpha$ radiation. The X-ray photoelectron spectroscopy (XPS) measurements were performed with a SPECS Phobios 150MCD instrument using a $\text{Mg K}\alpha$ source (1253.6 eV) and a chamber pressure of 4×10^{-9} mbar.

Electrochemical characterization and cycling properties (discharge-charge) were performed using a three electrode configuration with a Biologic-VMP instrument. The full cells were assembled in a glovebox under an Ar atmosphere. A 9 mm diameter lithium disk was used as reference electrode, with Li_3PO_4 -nt TiO_2 -based films and $\text{Li}_2\text{CoPO}_4\text{F}$ used as counter and working electrodes. The electrolyte solution was 1 M LiPF_6 (EC:DEC) embedded in Whatman glass fiber disks. The full cell was cycled at 1C, 2 C and 5 C rates ($C=0.3 \text{ mA cm}^{-2}$). The activation of the positive electrode ($\text{Li}_2\text{CoPO}_4\text{F}$) offers the possibility of achieving a remarkable reversible capacity for the full cell. In the present study, the activation step of the $\text{Li}_2\text{CoPO}_4\text{F}$ consisted of two

successive cycles of galvanostatic charging to 5.4 V, followed by discharging to 3.0 V, at a 100 mA g⁻¹ current density and using metallic Li as a counter electrode. When designing the full battery, it is quite important to obtain an optimal balance of cathode and anode both in terms of weight and electrochemical properties. The calculation of the energy density of the battery only considered the specific capacity and the working potential ($E_{\text{cathode}} - E_{\text{anode}}$) of the full battery, without further consideration of the mass of the active materials, electrolyte and packing materials.

2.3.3 Results and discussion

Figure 1A shows a schematic view of the Li₂CoPO₄F structure. It is formed by chains of CoO₄F₂ octahedra sharing their edges and interconnected with PO₄ tetrahedral oxo-anions by corner sharing. The solid possesses an orthorhombic unit cell with *Pnma* space group, where there are 3 types of Li; Li1 in 8d sites and Li2 and Li3 in two sets of 4c sites. The Co is in 4a and 4b sites, the P in two sets of 4c sites, the F in two sets of 4c sites, and the O in four sets of 4c and two sets of 8d sites [6]. The cross linked structure forms an opened 3D framework, permitting Li ions to be inserted and extracted from multiple directions [15-17]. The XRD pattern of the synthesized Li₂CoPO₄F sample shown in Figure 1B shows diffraction peaks indexed in agreement with the literature values, with $a=10.452 \text{ \AA}$, $b=6.3911 \text{ \AA}$, and $c=10.874 \text{ \AA}$ [6-17]. A LiCoPO₄ impurity phase was detected (marked with symbol * in Figure 1B), which could have been due to the relatively low heat treatment temperature [11-15]. The XPS signal of the Co2p, split into the 2p_{3/2} and 2p_{1/2} multiplet separated by 15.7 eV, is formed by a double peak at 781.7 eV and 786.2 eV (Fig. 1C), assigned to the Co²⁺ in Li₂CoPO₄F in very good agreement with the observation reported in ref 15.

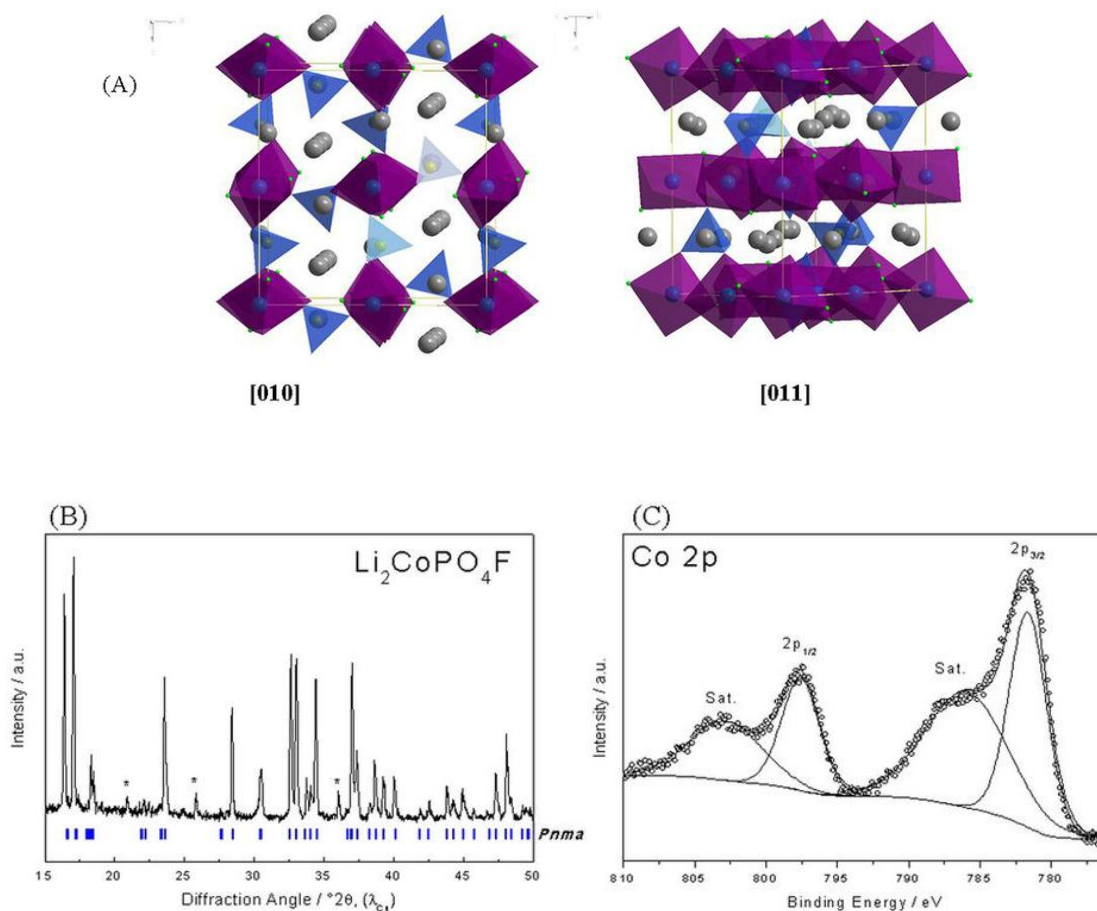


Fig. 1.(A) Schematic view of the crystal structure of $\text{Li}_2\text{CoPO}_4\text{F}$ along the [010] and [011] directions. (B) XRD pattern, and (C) XPS of the Co2p area from a $\text{Li}_2\text{CoPO}_4\text{F}$ sample.

The Li_3PO_4 -coated TiO_2 anode was prepared at room temperature, with some material also annealed at 500°C in air for 2 h. The XRD patterns of the materials exhibit different features (Figure 2). While for the as-prepared specimen, only Ti reflections (JCPDS file 05–0682 and space group $P6_3/mmc$) can be observed, the annealed sample shows very intense peaks of anatase (JCPDS 21-1272 and space group $I4_1/amd$). In both cases the presence of Li_3PO_4 could not be detected by XRD, due to the low crystallinity and small amounts of solid controlled by the conditions of the electrolytic deposition. Since the Li_3PO_4 is on the surface of TiO_2 nanotubes further experiments allowed us to detect the (110), (101), (210) and (002) reflections of β - Li_3PO_4 (JCPDS 25–1030) phase for large time (20 min) and high current density (75 mA cm^{-2}) during electrolytic deposition [13]. Previous experiments conducted to synthesize thick layers of lithium phosphate covering the complete surface of titania nanotubes [13]. So, this over $20 \mu\text{m}$

thick layer would passivate the active electrode and cannot be beneficial for such cycling purposes as electrodes in batteries. For this reason, we scaled down the fabrication of Li_3PO_4 layer to the nanometric size, observing that the best ratio of Li_3PO_4 to TiO_2 is $9.03 \cdot 10^{-3}$ g Li_3PO_4 /g TiO_2 . By using optimal current densities and deposition times of ca. -3.75 mA cm^{-2} and 1 min a finely dispersed layer of Li_3PO_4 can fill the titania nanotubes (Figure S1). Under these conditions no diffraction peaks either of β - Li_3PO_4 or γ - Li_3PO_4 were detected in the X-ray diffraction patterns which were recorded from 10 – 80° (2θ) with 0.02° of step size each 2 seconds as discussed above. Having a detailed inspection with HRTEM and SAED, the formation of β - Li_3PO_4 (at room temperature) or γ - Li_3PO_4 (when annealing) on titania nanotubes was unveiled as discussed below.

The lithium phosphate seems to play an important role enhancing the electrochemical response, both in Li half cells and in full Li-ion batteries, and deserves to be studied in more detail [13,17-19]. The β - Li_3PO_4 has a basic wurtzite structure where one position of the tetrahedral sites, T^+ or T^- , is fully occupied, along with cation ordering (Figure 2C). It has twice the value of the unit cell along the axis when the phase transition from β - to γ - Li_3PO_4 (Figure 2D) occurs. The γ -phase also consists of hexagonal close-packed oxide layers, but these are more distorted in comparison with the β -structure. Moreover, the cations are distributed over both sets of T^+ and T^- sites, leading LiO_4 tetrahedra to share some of their edges, while only corner-sharing is present in the β -structure [20-22].

In order to examine the formation of phosphate phases on titania nanotubes and discover whether or not an additional phase is formed at the interface, HRTEM and SAED measurements were performed. The HRTEM image of the “AD” sample (which was not calcined) is shown in Figure 3A, which shows areas having visible lattice fringes measured and labeled according to their particular crystal structures. It can be seen that β - Li_3PO_4 was successfully formed, with the image containing a small region of ordered crystalline structure with a (110) interplanar spacing of 0.399 nm [23]. Here, amorphous TiO_2 was not detected, but fringes corresponding to the (222) reflection of $\text{Li}_4\text{Ti}_5\text{O}_{12}$ with an interplanar spacing of 0.245 nm were found [24]. This image was taken at the tip of the nanotube and we can observe that lithium titanate appeared at both sides of the region of lithium phosphate, which could explain the lack of TiO_2 detection.

The SAED data in Figure 3B matches these d-spacings and confirms the presence of these materials. Figure 3C shows HRTEM imagery of the ADC sample (which was calcined), with regions of visible lattice fringes measured and labeled to identify their respective crystal structures. Here, a small region showing an ordered crystalline structure with a (011) interplanar spacing of 0.352 nm was detected, corresponding to anatase TiO₂ [25]. However, the observed form of lithium phosphate was γ -Li₃PO₄ as deduced from the (200) reflection (d_{200} =0.247 nm), as expected after thermal annealing at 500°C [26]. In addition, fringes corresponding to lithium titanate are also visible (d_{113} =0.255 nm) [24]. The anatase TiO₂, γ -Li₃PO₄ and Li₄Ti₅O₁₂ regions are labeled “1”, “2” and “3” respectively to avoid confusion. The SAED data in Figure 3D shows fine diffraction points corresponding to these three phases. The presence of small amounts of the Li₄Ti₅O₁₂ phase at the interface between Li₃PO₄ and TiO₂ gives an additional understanding of the structure of these composites.

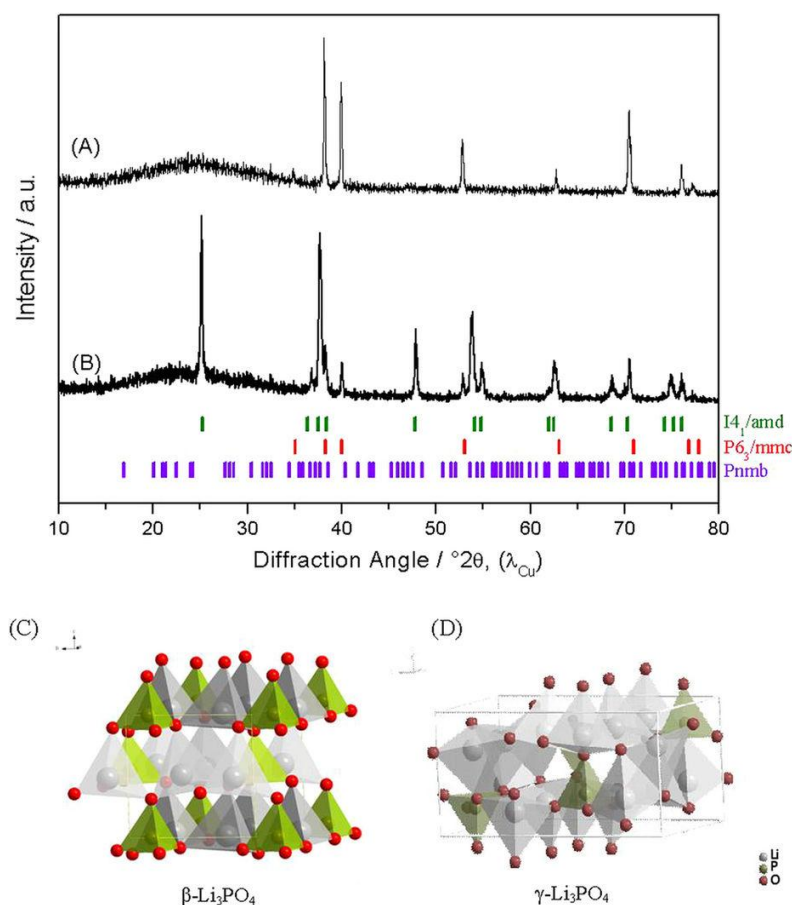


Fig.2. XRD patterns of Li₃PO₄-coated TiO₂ anode (A) as-prepared and (B) after thermal annealing at 500°C in air for 2 h. (C,D) show representations of the crystal structure of β -Li₃PO₄ and γ -Li₃PO₄, respectively.

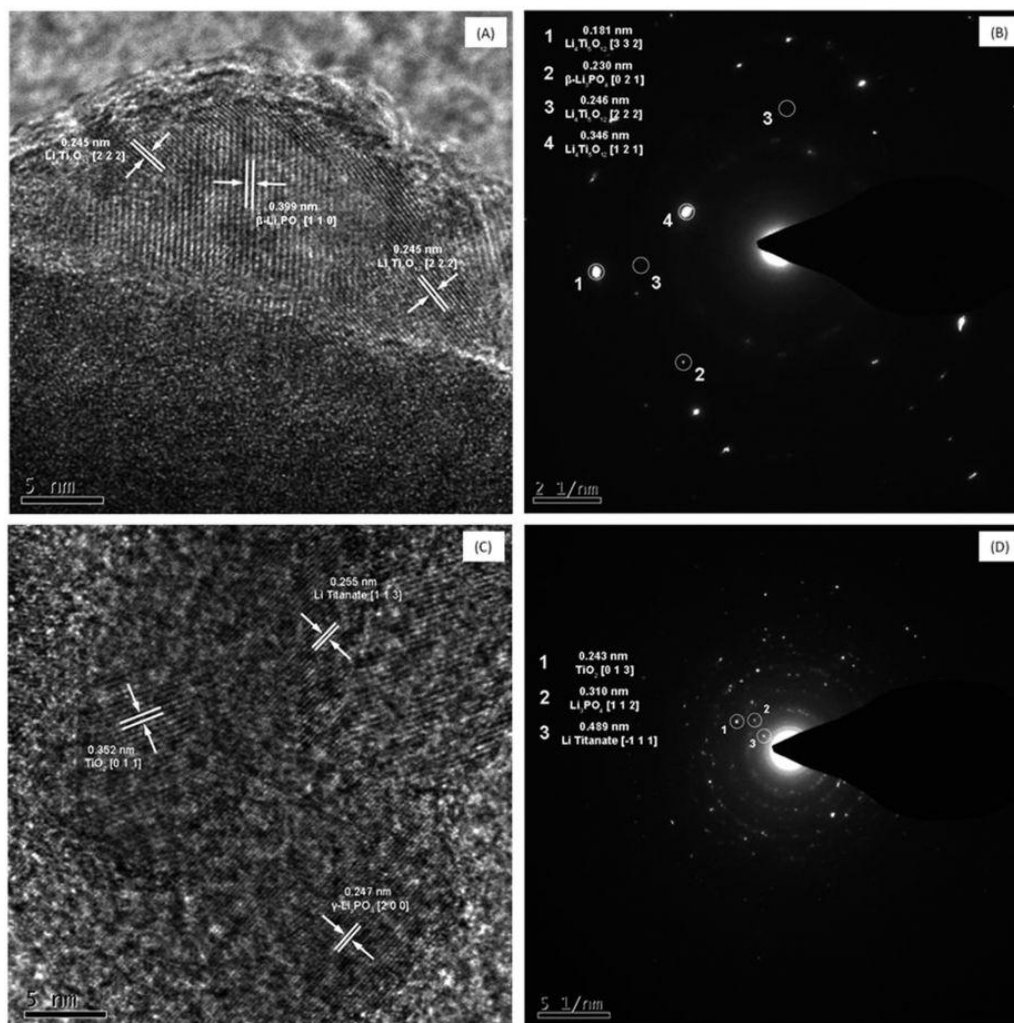


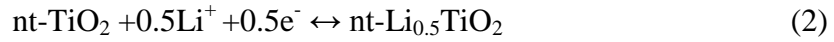
Fig.3. HRTEM and SAED imagery of (A,B) AD and (C,D) ADC samples, respectively.

The cathode half-cell reaction can be written as:



The theoretical capacity of $\text{Li}_2\text{CoPO}_4\text{F}$ is 287 mA h g^{-1} for $x=2$. However, recent studies have indicated that $\text{Li}_2\text{CoPO}_4\text{F}$ can reach a maximum reversible capacity of 150 mA h g^{-1} , with an outstanding high-voltage operation of $\sim 5 \text{ V vs. Li}^+/\text{Li}$ [11,15,27-30]. Because of the high inefficiency from the first to the second cycle observable in $\text{Li}_2\text{CoPO}_4\text{F}$, these electrodes were subjected to activation cycles before being used in the complete lithium-ion cell (Fig. S2.). The first-cycle irreversible capacity due to electrolyte decomposition was then avoided in the full cells [11,15]. Anatase is well known in the literature to exhibit a high reversibility in the first cycle and to operate at a

safe average potential of 1.8–1.9 V vs. Li⁺/Li. The theoretical capacity delivered by anatase is around 167 mA h g⁻¹ according to the following reaction:



Taking into account their individual voltages, the combination of nt-TiO₂ with Li₂CoPO₄F could give rise to a battery operating in the 3.1–3.2 V range. While considering the expected capacity of each electrode, the main overall reaction that may take place in the full cells can be summarized as follows:



Capacity balance was carried out by assuming 140 mA h g⁻¹ reversible capacity of the cathode after activation and 160 mA h g⁻¹ of the anode (Figure 4), the resulting cathode mass to anode mass was: m+/m-=1.14.

Figure 4A and B compare the reversible voltage profile versus Li of the TiO₂ with and without Li₃PO₄ (bottom) and of the Li₂CoPO₄F cathode (middle). The anode operates reversibly with continuous, plateaued charge-discharge curves with a reversible capacity of 150 mA h g⁻¹ at an average voltage value of about 1.8–1.9 V, while the Li₂CoPO₄F cathode cycles with a reversible capacity of 148 mA h g⁻¹ at a voltage value of 5 V vs. Li with a flat plateau, typical of the two phase reaction of lithium-cobalt fluorophosphates [19].

The upper plots of Figure 4A and B show the trend of the full-cell voltage profile, demonstrating very stable behavior. The cell operates with an average voltage of around 3.1–3.2 V, while the voltage profile is the combination of the flat voltage of the Li₂CoPO₄F cathode (Figure 4 middle plots) and the flat voltage of the TiO₂ (Figure 4B bottom plot) or TiO₂/γ-Li₃PO₄ anodes (Figure 4A bottom plot). The reversible capacity of the full battery measured at a state of discharge is about 150 mA h g⁻¹, reaching about 99% of the maximum reversible capacity. The achieved energy density is 472 W h kg⁻¹, an enhanced value as compared to the majority of published batteries [31-36].

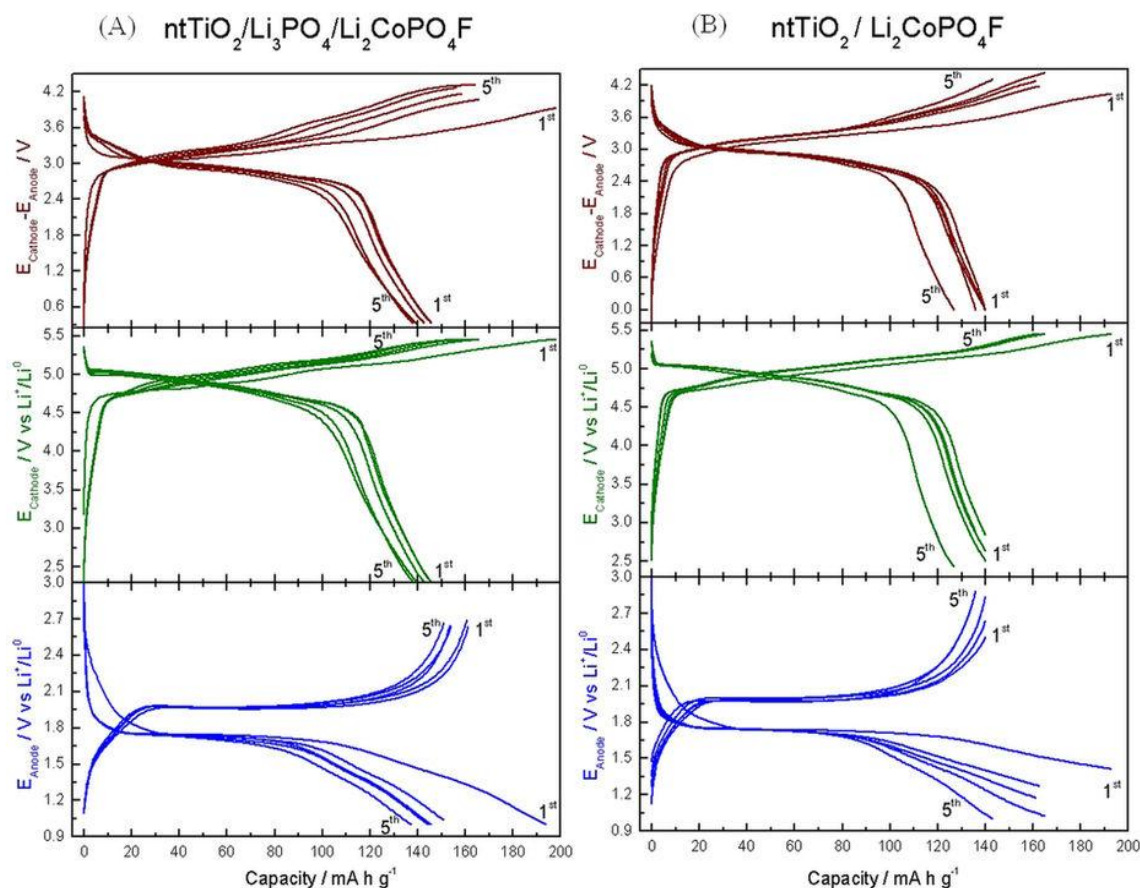


Fig.4. Galvanostatic charge/discharge cycles representing the $E_{\text{Cathode}} - E_{\text{Anode}}$ vs. capacity of (A) $\text{nt-TiO}_2/\gamma\text{-Li}_3\text{PO}_4/\text{Li}_2\text{CoPO}_4\text{F}$, and (B) $\text{nt-TiO}_2/\text{Li}_2\text{CoPO}_4\text{F}$ cells. This figure includes the voltage profiles of the cathode (E_{Cathode} vs. capacity) and the anode (E_{Anode} vs. capacity) in the middle and bottom plots. The capacity of the full cell is calculated using the cathode mass.

$\text{Li}_4\text{Ti}_5\text{O}_{12}$ is a well-known material for LIBs and typically shows a stable plateau at 1.54 V (vs. Li^+/Li) [7,37-39]. However, such a plateau is not visible in the charge/discharge curves (Figure 4A and B bottom plots). Instead, the typical plateau of anatase TiO_2 can be seen. The lithium titanate phase is formed in a minute fraction at the interphase between TiO_2 and Li_3PO_4 , as detected by SAED and HRTEM measurements (Figure 3). However, this phase was not detected by XRD (Figure 2), due to its particularly low proportion. Then, its contribution to battery functionality is expected to be negligible.

The stability of chosen electrode materials is another key factor for battery cycling. Figure 5 compares the cycling stability of $\text{TiO}_2/\text{Li}_3\text{PO}_4/\text{Li}_2\text{CoPO}_4\text{F}$ and $\text{TiO}_2/\text{Li}_2\text{CoPO}_4\text{F}$ measured at 1 C, 2 C and 5 C rates. The battery that utilizes

Li_3PO_4 shows very good cycling behavior as compared to that of the full cell without Li_3PO_4 , operating at 1 C, 2 C and 5 C rates for more than 240 charge-discharge cycles with high coulombic efficiencies of 79, 62 and 73%, respectively. These differences were found significant from a statistical analysis of cycling experiments of five different cells for each composition (Table S1). As expected, capacity decay from 150 mA h g^{-1} at 1 C to 120 mA h g^{-1} is recorded at 2 C, and to 90 mA h g^{-1} at 5 C. This battery, based on $\text{TiO}_2/\text{Li}_3\text{PO}_4/\text{Li}_2\text{CoPO}_4\text{F}$, exhibits much better performance in terms of cyclability and coulombic efficiency than $\text{TiO}_2/\text{Li}_2\text{CoPO}_4\text{F}$ and that previously reported and based on $\text{Li}_4\text{Ti}_5\text{O}_{12}$ as an anode material [11]. The excellent performance of this battery observed in terms of specific capacity, cycling life and rate capability is to the best of our knowledge only seldom reported, and confirms the great potential of $\text{TiO}_2/\text{Li}_3\text{PO}_4$ as an innovative electrode material that can aid the progress of lithium-based energy storage systems.

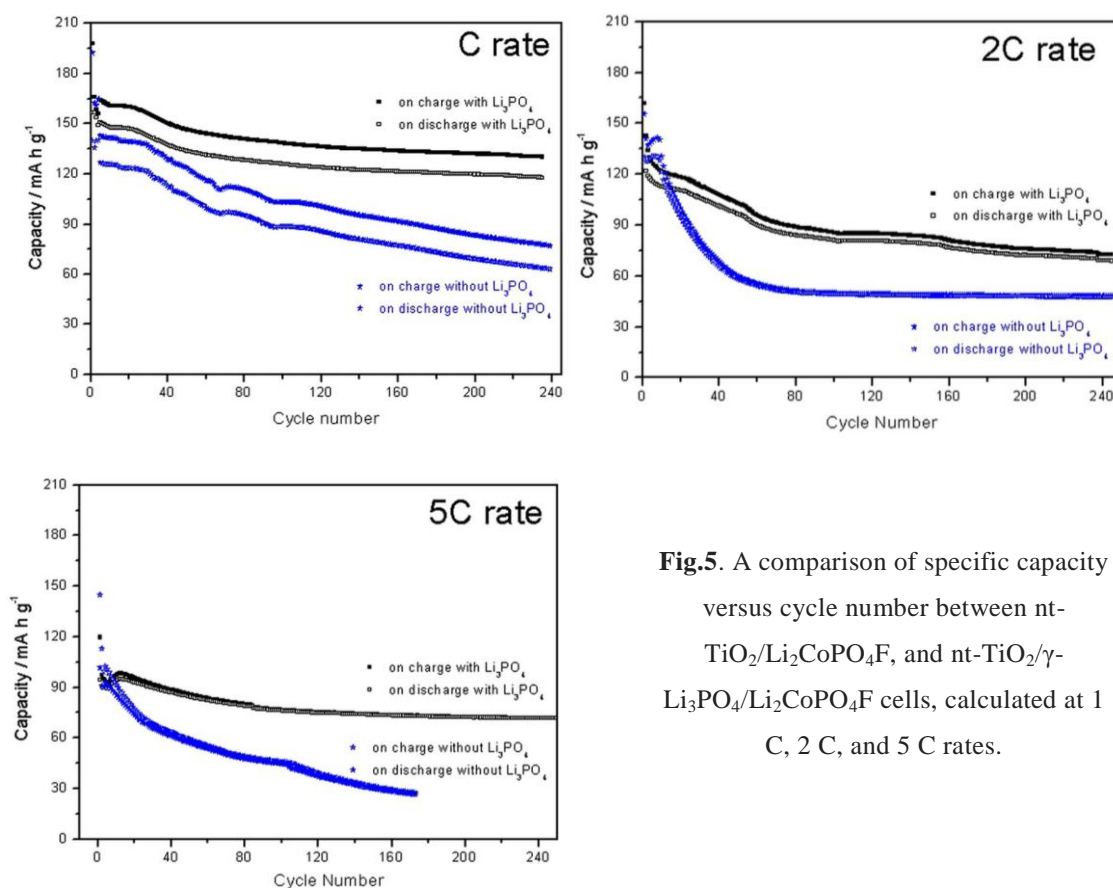


Fig.5. A comparison of specific capacity versus cycle number between nt- $\text{TiO}_2/\text{Li}_2\text{CoPO}_4\text{F}$, and nt- $\text{TiO}_2/\gamma\text{-Li}_3\text{PO}_4/\text{Li}_2\text{CoPO}_4\text{F}$ cells, calculated at 1 C, 2 C, and 5 C rates.

2.3.4 Conclusions

The high working voltage and excellent rate capability observed of the TiO₂/Li₃PO₄/Li₂CoPO₄F full cell makes it a promising high energy density LIB with acceptable rate performance (472 W h kg⁻¹ at a 1 C rate, and 284 W h kg⁻¹ at a 5 C rate), preventing the emergence of safety issues caused by the highly reactive lithiated graphite present in most LIB systems. The existence of Li₃PO₄ and the minute fraction of Li₄Ti₅O₁₂ present between the TiO₂/ Li₃PO₄ interfaces can explain the good cyclability of the full cell as this inactive matrix allows rapid transportation of the lithium ions.

Acknowledgements

The authors are grateful to MEC (MAT2011-22753) and Junta de Andalucía for financial support (FQM-7206 and FQM-288). G.F. Ortiz is indebted to the “Ramón y Cajal” program (RYC-2010-05596) and to MESC for a scholarship at Xiamen University. Y. Yang acknowledges funding from the National Natural Science Foundation of China (Grant No. 21233004).

2.3.5 References

1. K. Amine, H. Tukamoto, H. Yasuda, Y. Fujita, J. Electrochem. Soc. 143 (1996) 1607.
2. M. G. Kim, J. Cho, Adv. Funct. Mater. 19 (2009) 1497.
3. G. T. K. Fey, W. Li, J. R. Dahn, J. Electrochem. Soc. 141 (1994) 2279.
4. A. Kraytsberg, Y. Ein-Eli, Adv. Energy. Mater. 2 (2012) 922.
5. K. Amine, H. Yasuda, M. Yamachi, Electrochem. Solid-State Lett. 3 (2000) 178.
6. S. Okada, M. Ueno, Y. Uebou, J. I. Yamaki, J. Power Sources 146 (2005) 565.
7. T. Ohzuku, A. Ueda, N. Yamamoto, J. Electrochem. Soc. 142 (1995) 1431.

8. E. M. Sorensen, S. J. Barry, H. K. Jung, J. R. Rondinelli, J. T. Vaughey, K. R. Poeppelmeier, *Chem. Mater.* 18 (2006) 482.
9. P. G. Bruce, B. Scrosati, J. M. Tarascon, *Angew. Chem. Int. Edit.* 47 (2008) 2930.
10. G. F. Ortiz, I. Hanzu, T. Djenizian, P. Lavela, J. L. Tirado, P. Knauth, *Chem. Mater.* 21 (2009) 63.
11. X. Wu, Z. Gong, S. Tan, Y. Yang, *J. Power Sources* 220 (2012) 122.
12. P. Reale, S. Panero, B. Scrosati, J. Garche, M. Wohlfahrt-Mehrens, M. A. Wachtler, *J. Electrochem. Soc.* 151 (2004) A2138.
13. M. C. López, G. F. Ortiz, J. R. González, R. Alcántara, J. L. Tirado, *ACS Appl. Mater. Interfaces* 6 (2014) 5669.
14. M. Cabello, G. F. Ortiz, M. C. López, P. Lavela, R. Alcántara, J. L. Tirado, *Electrochem. Commun.* 56 (2015) 61.
15. X. Wu, S. Wang, X. Lin, G. Zhong, Z. Gong, Y. Yang, *J. Mater. Chem. A* 2 (2014) 1006.
16. Q. D. Truong, M. K. Devaraju, Y. Ganbe, T. Tomai, I. Honma, *Electrochim. Acta* 127 (2014) 245.
17. J. Hadermann, A. M. Abakumov, S. Turner, Z. Hafideddine, N. R. Khasanova, E. V. Antipov, G. V. Tendeloo, *Chem. Mater.* 23 (2011) 3540.
18. K. Takada, T. Inada, A. Kajiyama, H. Sasaki, S. Kondo, M. Watanabe, M. Murayama, R. Kanno, *Solid State Ionics* 158 (2003) 269.
19. S. Seki, Y. Kobayashi, H. Miyashiro, Y. Mita, T. Iwahori, *Chem. Mater.* 17 (2005) 2041.
20. Y. A. Du, N. A. W. Holzwarth, *Phys. Rev. B.* 76 (2007) 174302.
21. C. Frayret, C. Masquelier, A. Villesuzanne, M. Morcrette, J. M. Tarascon, *Chem. Mater.* 21 (2009) 1861.

22. J. Zemann, *Acta Crystallogr.* 13 (1960) 863.
23. C. Keffer, A. Mighell, F. Mauer, H. Swanson, S. Block, *Inorg. Chem.* 6 (1967) 119.
24. A. Laumann, H. Boysen, M. Bremholm, K. T. Fehr, M. Hoelzel, M. Holzapfel, *Chem. Mater.* 23 (2011) 2753.
25. M. Rezaee, S. M. M. Khoie, K. H. Liu, *CrystEngComm*, 13 (2011) 5055.
26. O. S. Bondareva, M. A. Simonov, N. V. Belov, *Doklady Akademii Nauk SSSR* 240 (1978) 75.
27. D. Wang, J. Xiao, W. Xu, Z. Nie, C. Wang, G. Graff, J. G. Zhang, *J. Power Sources* 196 (2011) 2241.
28. S. Amaresh, K. Karthikeyan, K. J. Kim, M. C. Kim, K. Y. Chung, B. W. Cho, Y. S. Lee, *J. Power Sources* 244 (2013) 395.
29. S. Amaresh, K. Karthikeyan, K. J. Kim, J. Y. An, S. J. Cho, K. Y. Chung, B. W. Cho, K. W. Nam, Y. S. Lee, *J. Nanosci. Nanotechnol.* 14 (2014) 7545.
30. T. Okumura, M. Shikano, Y. Yamaguchi, H. Kobayashi, *Chem. Mater.* 27 (2015) 2839.
31. H. G. Jung, M. W. Jang, J. Hassoun, Y. K. Sun, B. Scrosati, *Nat. Commun.* 2 (2011) 516.
32. A. Swiderska-Mocek, *Electrochim. Acta* 139 (2014) 337.
33. J. W. Kim, D. H. Kim, D. Y. Oh, H. Lee, J. H. Kim, J. H. Lee, Y. S. Jung, *J. Power Sources* 274 (2015) 1254.
34. P. P. Prosini, C. Cento, A. Pozio, *J. Solid State Electrochem.* 18 (2014) 795.
35. J. Hassoun, F. Bonaccorso, M. Agostini, M. Angelucci, M. G. Betti, R. Cingolani, M. Gemmi, C. Mariani, S. Panero, V. Pellegrini, B. Scrosati, *Nano Lett.* 14 (2014) 4901.

36. R. Verrelli, B. Scrosati, Y. K. Sun, J. Hassoun, ACS Appl. Mater. Interfaces. 6 (2014) 5206.
37. K. Zaghbi, M. Simoneau, M. Armand, M. Gauthier, J. Power Sources 81–82 (1999) 300.
38. F. Ronci, P. Reale, B. Scrosati, V. Rossi Albertini, P. Perfietti, M. Di Michiel, J. M. Merino, J. Phys. Chem. B 106 (2002) 3082.
39. L. Aldon, P. Kubiak, M. Womes, J. C. Jumas, J. Olivier-Fourcade, J. L. Tirado, J. I. Corredor, C. Pérez-Vicente, Chem. Mater. 16 (2004) 5721.

2.3.6 Supplementary information

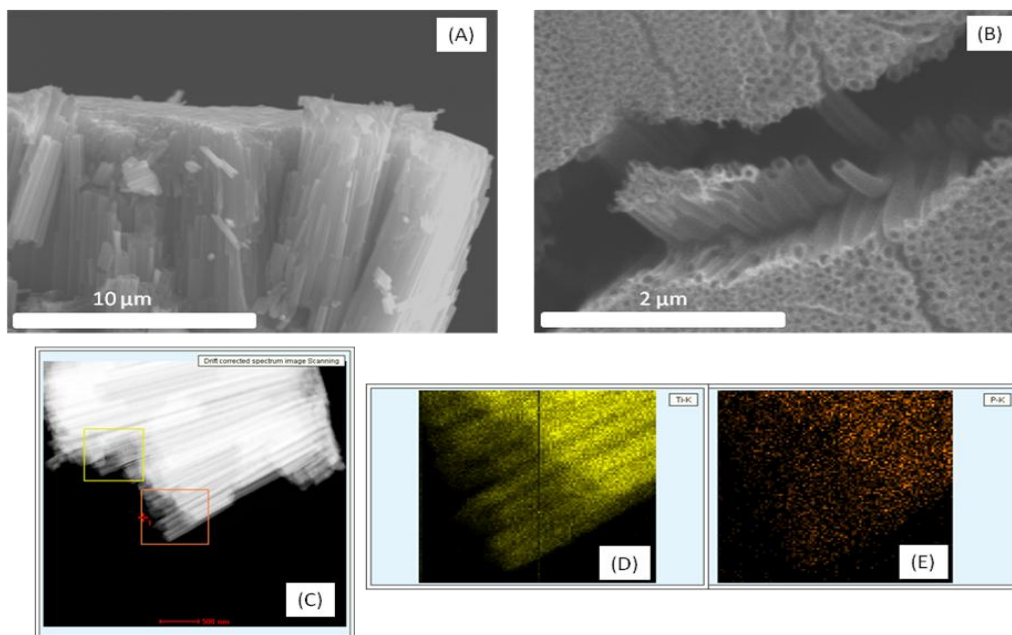


Fig.S1. (A) Cross sectional and (B) top view SEM images of deposited Li_3PO_4 on titania nanotubes after annealing at $500\text{ }^\circ\text{C}$. (C) The corresponding dark-field TEM image and (D) Ti-K and (E) P-K EDAX analyses from previous TEM image.

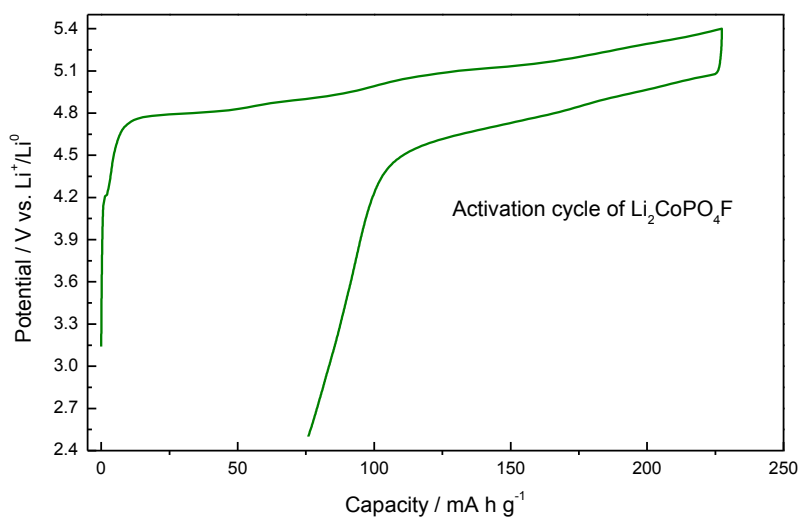


Fig.S2. The first charge/discharge profile of the $\text{Li}_2\text{CoPO}_4\text{F}$ sample at 1C rate using a liquid electrolyte containing 1 M LiPF_6 (EC:DMC).

Table S1. Statistical analysis of the capacity on discharge obtained for the nt-TiO₂/ γ -Li₃PO₄/ Li₂CoPO₄F and nt-TiO₂/ Li₂CoPO₄F cells, cycled at 1 C.

Treatment	Cathode mass (mg)	1 st Reversible Capacity (mA h g ⁻¹)	120 th Reversible Capacity (mA h g ⁻¹)
With Li₃PO₄	1.30	156.7	124.4
	1.17	154.0	123.7
	1.19	151.8	119.6
	1.15	152.5	122.4
	1.05	149.3	121.0
Mean±s		152.9±2.7	122.2±2.0
Without Li₃PO₄	1.30	141.7	85.4
	1.19	139.8	85.8
	1.15	140.2	81.4
	1.1	137.6	83.0
	1.05	134.3	78.7
Mean±s		138.7±2.9	82.9±2.9

CAPÍTULO 3

**Baterías post-litio: ánodos para
baterías de ion sodio**

3.1 Self-organized sodium titanate/titania nanoforest for the negative electrode of sodium-ion microbatteries

Marta Cabello ^a, Gregorio F. Ortiz ^a, María C. López ^a, Ricardo Alcántara ^a, José R. Gonzalez ^a, José L. Tirado ^a, Radostina Stoyanova ^b, Ekaterina Zhecheva ^b.

^aLaboratorio de Química Inorgánica. Universidad de Córdoba. Edificio C3, Campus de Rabanales. Spain

^bInstitute of General and Inorganic Chemistry, Bulgarian Academy of Sciences, Sofia. Bulgaria

Abstract

A nanocomposite of sodium titanate/titania nanotrees self-organized in a parallel fashion to form nanoforests is successfully prepared and used as high-performance anode for Na-ion microbatteries. The first step of the synthesis is the anodic oxidation of Ti foils to form self-organized amorphous TiO₂ nanotubes followed by insertion of sodium in aqueous media at room temperature. Then the composite is thermally dehydrated and crystallized as monoclinic Na₂Ti₆O₁₃/rutile nanotrees. EPR spectra evidence a significant increase in Ti³⁺ content during sodium/proton insertion and a decrease on heating. SEM images reveal that while the height of the nanotubes is similar to the nanoforest (c.a. 8.0 μm) the morphology changes from aligned nanotubes to nanotrees of complex texture. The electrochemical results of sodium test cells in non-aqueous electrolyte using the Na₂Ti₆O₁₃/TiO₂ nanocomposite electrodes show flat profiles of sodium insertion and de-insertion at 0.7 and 0.9 V, respectively. The observed reversible capacity of 130 μA h cm⁻² over 150 cycles is almost threefold the value of titania nanotubes annealed at a same temperature. Both characteristics are of great interest to achieve safe and efficient Na-ion microbatteries.

Keywords

Nanostructured materials; thin films; energy storage materials; nanofabrications; electron paramagnetic resonance; self-organized nanotrees



ELSEVIER



Volume 614

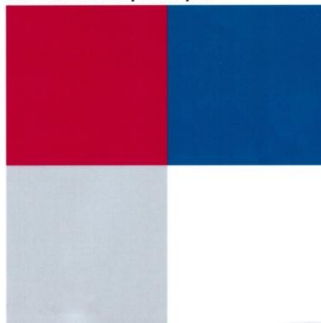
25 November 2014
ISSN 0925-8388

Journal of
**ALLOYS
AND COMPOUNDS**

An Interdisciplinary Journal
of Materials Science and
Solid-State Chemistry and Physics

EDITOR-IN-CHIEF
L. SCHULTZ

EDITORS
K.H.J. BUSCHOW
J. CHAN
L.P. COOK
D.G. ESKIN
H. FAN
J.-M. GRENECHE
V.G. HARRIS
M. HENINI
H. KLEINKE
H.G. PAN
V. PECHARSKY
M. RICHTER
H. SAKAGUCHI



Journal of Alloys and Compounds 646 (2015) 816-826

3.1.1 Introduction

Together with Li-ion batteries and supercapacitors, rechargeable sodium-ion batteries are a very promising alternative for energy storage. The low-price, high-abundance and sustainable sources of sodium are particularly attractive for large-scale battery applications. The use of sodium cells could solve in part the uncertainty related to lithium resources which may become a major problem in the next years. From an industrial point of view such strategy will reduce production costs for stationary grid storage.

Sodium ion technology still needs finding suitable hosts to reversibly intercalate ions in their structure using an optimum operational voltage potential. Indeed, the challenge is to find batteries with improved safety, smaller size, good efficiency on cycling and high energy density [1,2]. The chemistry of sodium presents some similarities as compared to lithium, which a priori could help the search of electrodes with similar chemistries. Nevertheless, because the ionic volume of Na^+ ions almost doubles that of Li^+ ions, some Li^+ ion hosts cannot be used to intercalate Na^+ ions. Certainly, a great variety of phases which are able to accommodate sodium have been used as cathodes [3,4]. In contrast, very few materials have been reported to be useful as anodes for Na-ion cells. Disordered carbons such as hard carbon emerged as capable candidates for anode materials. During several years of research it was possible to get good initial reversible capacities of about 300 - 285 mA h g^{-1} [5,6], but a satisfactory capacity retention has not been reported yet [7].

Recently, there have been several reports in the literature on non-carbon based anodes for Na-ion batteries. An anatase nanotube array with double-wall structure showed improved electrochemical behavior and specific capacity in sodium cells due to pseudocapacitive storage, as a consequence of the alkali ions easily reaching the complete surface of the electrode active material [8]. Also, amorphous titania nanotube arrays with large lengths offered high areal capacities (ca. 1000 $\mu\text{A h cm}^{-2}$), but the capacity to react with sodium is lower than with lithium, probably due to the poor conductivity of $\text{nt-Na}_x\text{TiO}_2$, and voltage varies continuously in the charge-discharge profiles [9,10]. The occurrence of amorphous sodium titanate in the electrode material

after electrochemical reaction of TiO_2 with sodium has been recently suggested by different authors [8,11]. In this regard, several sodium titanates such as $\text{Na}_2\text{Ti}_4\text{O}_9$, $\text{Na}_2\text{Ti}_6\text{O}_{13}$, and $\text{Na}_4\text{Ti}_5\text{O}_{12}$ are well known in the literature for their ability to intercalate lithium-ions into their frameworks [12-16]. On the other hand, $\text{Na}_2\text{Ti}_3\text{O}_7$ intercalates sodium at 0.2 – 0.3 V [17,18] while $\text{Na}_2\text{Ti}_6\text{O}_{13}$ may be considered as a safer anode material since it displays the insertion plateau at 0.8 V. Theoretically, one mole of charge storage for $\text{Na}_2\text{Ti}_6\text{O}_{13}$ corresponds to $\sim 50 \text{ mA h g}^{-1}$ (174 mA h cm^{-3}). The possibility to reach higher capacity was recently examined by Shen et al. [19]. They found that lowering the cutoff voltage from 0.3 to 0.0 V vs. Na^+/Na^0 resulted in a capacity increase from a moderate 50 mA h g^{-1} to a promising 196 mA h g^{-1} ($\text{Na}_{2+4}\text{Ti}_6\text{O}_{13}$). A different way to increase capacity is using longer TiO_2 nanotubes [20].

In the present work, we propose a new approach for tailoring composite materials in the Na–Ti–O system with a nanoforest morphology that is suitable for an intimate contact with the electrolyte, thus improving the electrode performance vs. sodium.

3.1.2 Experimental

Fabrication of the electrodes: A schematic illustration of the fabrication process used to obtain $\text{Na}_2\text{Ti}_6\text{O}_{13}/\text{ntTiO}_2$ electrodes is shown in Figure. 1. First, the self-organized titania nanotubes (ntTiO_2) layer is fabricated by an anodization process at 60 V and 2 h following the procedure already described in the literature [21]. Then, the electrochemical insertion of sodium into ntTiO_2 was carried out using two different electrolytic baths: i) Electrolyte 1: 0.5 M NaNO_3 , and ii) electrolyte 2: 0.5 M NaCl . Additionally we have used a 0.02 M solution of $\text{NH}_4\text{H}_2\text{PO}_4$ as phosphate additive in both electrolytes. The idea is to form a partially reduced titania nanotube $\text{Na}_x\text{H}_y\text{TiO}_2$ ($x, y \ll 1$) and afterwards to promote by thermal annealing the formation of $\text{Na}_2\text{Ti}_6\text{O}_{13}/\text{TiO}_2$ and preserving the thickness of the initial titania nanotube layer. The insertion of sodium was carried out at room temperature using galvanostatic pulse technique (-37.5 mA cm^{-2} from 1 to 20 min) and cyclic voltammetry (CV) experiments. For this purpose, the ntTiO_2 layer on the Ti substrate was directly used as the working electrode (area c.a. 0.64 cm^2) in a three-electrode cell, where the reference

electrode was Ag/AgCl and a wire of Pt was used as counter electrode. For CV experiments the films were charged using current densities of 5, 10, 20, 50 and 100 mV s^{-1} to + 0.2 V and discharged at - 1.5 V vs. Ag/AgCl. Additionally, the as-prepared sodiated specimens were further annealed at 500 – 800 °C during 2 h in air with a heating ramp of 3.3 °C min^{-1} .

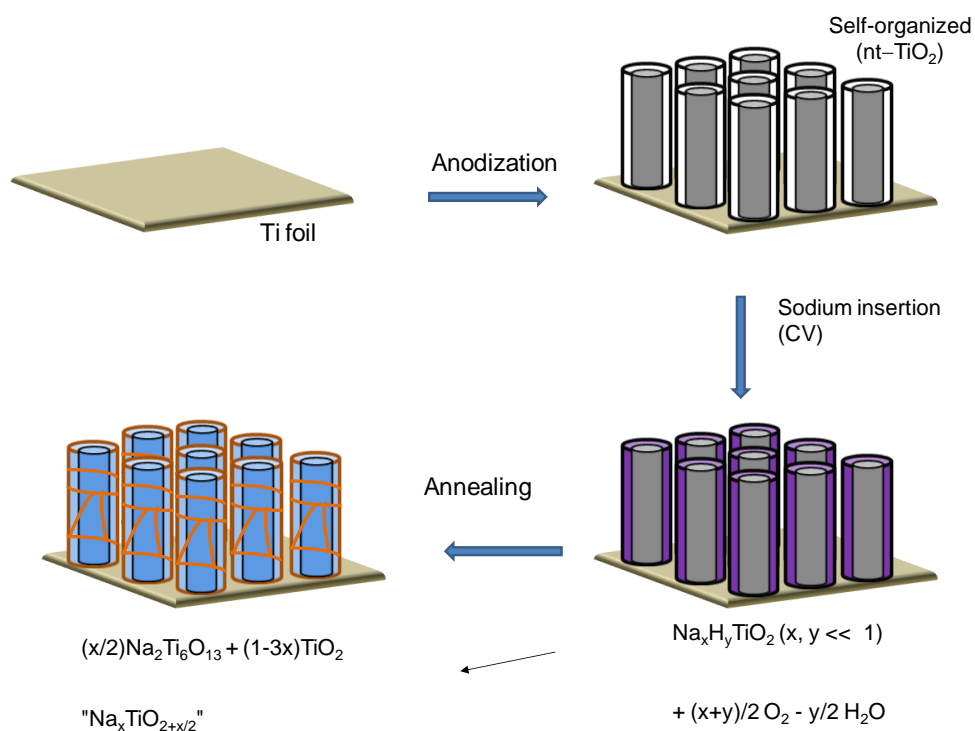


Fig.1. Synthetic illustration of the approach of fabrication of self-organized $\text{Na}_2\text{Ti}_6\text{O}_{13}/\text{TiO}_2$ nanoforests.

The crystal structures of the as-deposited and annealed thin films are analyzed by X-ray diffraction (XRD) in a D5000 Siemens diffractometer ($\text{CuK}\alpha$ radiation). The morphology and composition of the electrode materials is examined in a JEOL SM6300 Scanning Electron Microscope (SEM) equipped with Energy-Dispersive X-ray Spectroscopy (EDS) microanalysis and in a Philips CM10 Transmission Electron Microscope (TEM).

The electron paramagnetic resonance (EPR) spectra were recorded as the first derivative of the absorption signal of an ERS-220/Q spectrometer within the temperature range of 90 – 400 K. The g factors were determined with respect to a

Mn²⁺/ZnS standard. The signal intensity was established by double integration of the experimental EPR spectrum.

The electrochemical behavior of the electrode material was studied in a VMP-type apparatus (Biologic Science Instruments). For this purpose, the electrochemical test cells were assembled in a dry-box filled with Ar. The positive electrode was the sodium titanate/titania composite supported on the Ti-substrate, and was dried under vacuum at 120 °C prior to use. No binder or conductive agents were used in the electrodes. A piece of sodium was used as a negative electrode, and the electrolyte solution was a non aqueous media that consisted in 1 M NaPF₆ in the ethylene carbonate: diethyl carbonate (EC: DEC = 1: 1).

3.1.3 Results and discussion

The synthetic approach to obtain Na₂Ti₆O₁₃/TiO₂ nanoforests is schematically depicted in Figure 1. In a first step, the well-known procedure of obtaining self-organized amorphous TiO₂ nanotubes by Ti foil anodization was applied [21]. Then sodium/hydrogen insertion in the as-prepared nanotubes was carried out from an aqueous electrolyte at room temperature to form a partially reduced product Na_xH_yTiO₂ (x, y << 1). Finally, thermal annealing was used to promote the formation of Na₂Ti₆O₁₃/TiO₂ while preserving the thickness of titania nanotubes. To examine the possibility of electrochemical TiO₂ reduction by sodium ion insertion from aqueous sodium electrolytes, CV experiments were recorded for the two electrolytes described in the experimental section (Figure 2 a and b). During the reduction process (negative current intensity) the color of the ntTiO₂ electrode turned to black, suggesting sodium intercalation and reduction of titanium ions from Ti⁴⁺ to Ti³⁺ as discussed below from EPR data. From Figure 2a, it can be deduced that the amorphous ntTiO₂ electrode exhibits different insertion properties depending on the electrolyte. In order to know the amount of inserted sodium, the anodic charge was quantified for each electrolyte as a function of the scan rate (Figure 3). Thus, the maximum anodic charge measured at 5 mV s⁻¹ for ntTiO₂ samples was 120 and 45 mC cm⁻² for NaCl and NaNO₃ electrolytes, respectively. On increasing the scan rate a progressive decrease in the anodic charge is observed at 10, 20, 50 and 100 mV s⁻¹. For the latter rate, the observed values of anodic

charge were 45 and 20 mC cm^{-2} for NaCl and NaNO_3 electrolytes, respectively. These values are considerably higher than those obtained for Ti foil used as a blank (2 mC cm^{-2}) (Figure 2b). According to the determination of the areal mass of ntTiO_2 (0.67 mg cm^{-2}), the data for NaCl cycled at 5 mV s^{-1} lead to charge storage values of 180 C g^{-1} and average composition of $\text{Na}_{0.15}\text{TiO}_2$. Then, the maximum charge storage was 67 C g^{-1} and average composition of $\text{Na}_{0.06}\text{TiO}_2$ for NaNO_3 .

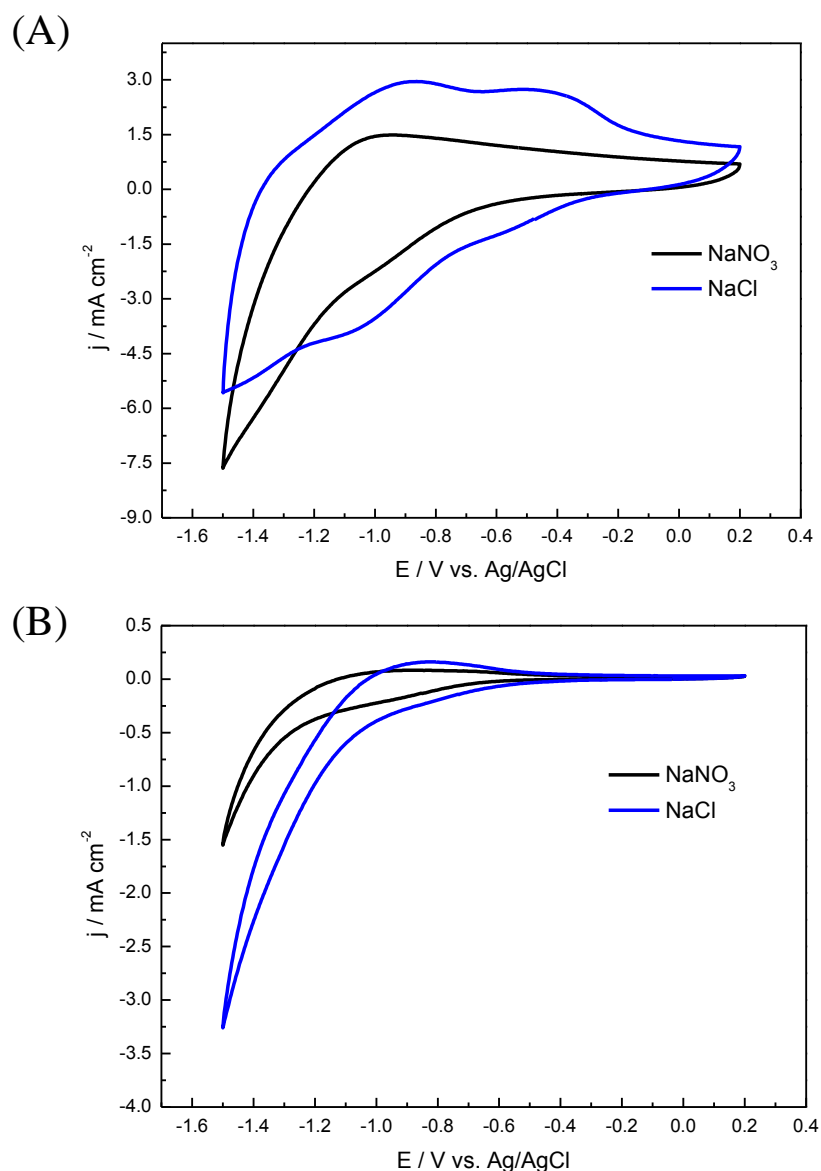


Fig.2. (A) A comparison of cyclic voltammograms of ntTiO_2 films recorded at 50 mV s^{-1} between $+0.2 \text{ V}$ and -1.5 V vs. Ag/AgCl using NaNO_3 and NaCl. (B) A comparison of cyclic voltammograms of Ti foils recorded at 50 mV s^{-1} between $+0.2 \text{ V}$ and -1.5 V vs. Ag/AgCl using NaNO_3 and NaCl electrolytes.

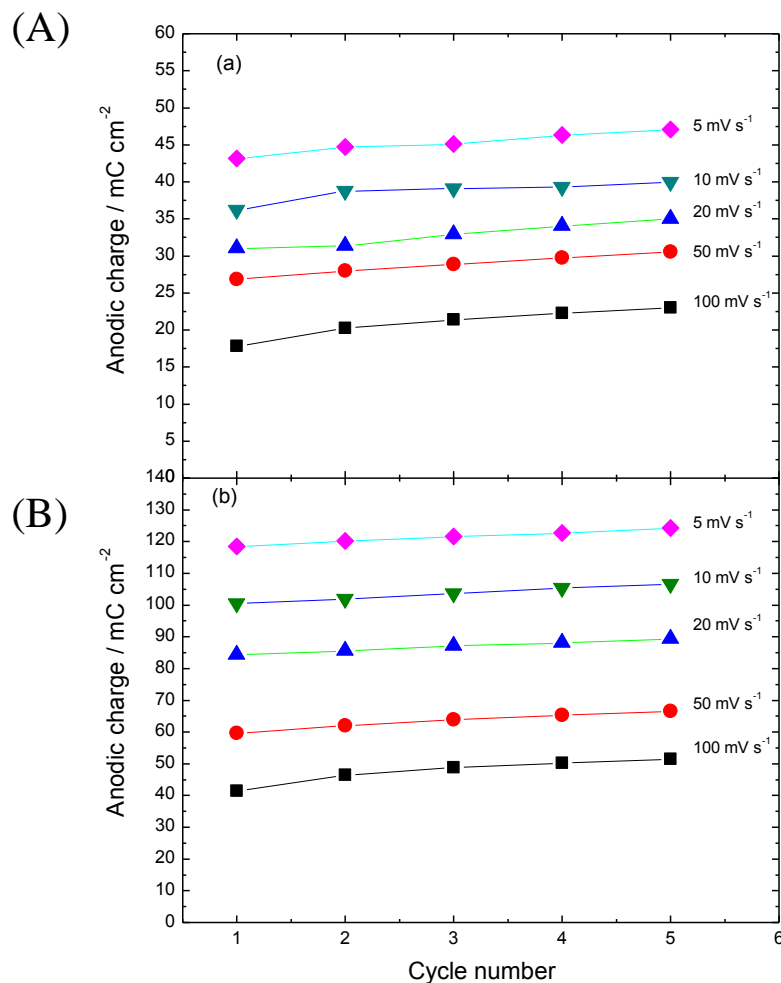


Fig.3. Anodic charge stored in ntTiO_2 film cycled at different scan rates using: (A) NaNO_3 and (B) NaCl electrolyte.

Variable scan rate cyclic voltammetry (Figure 4) was used to deconvolute the charge/potential relation (Figure 5) from mass transport effects. The differences between cathodic (sodium insertion) and anodic (sodium deinsertion) charge branches are ascribable to parasitic reactions of hydrogen evolution, being about 60 and 7 mC cm^{-2} for experiments at currents of 5 and 100 mV s^{-1} , respectively (Figure 5). A linear relationship between the normalized intensity versus the square root of scan rate, deduced from the cyclic voltammograms of amorphous ntTiO_2 films for NaNO_3 and NaCl electrolytes is observed in the insets of Figure 4a and b. The observed linearity is ascribable to diffusion-controlled processes, in contrast to the mostly pseudocapacitive Na-storage in anatase TiO_2 [22].

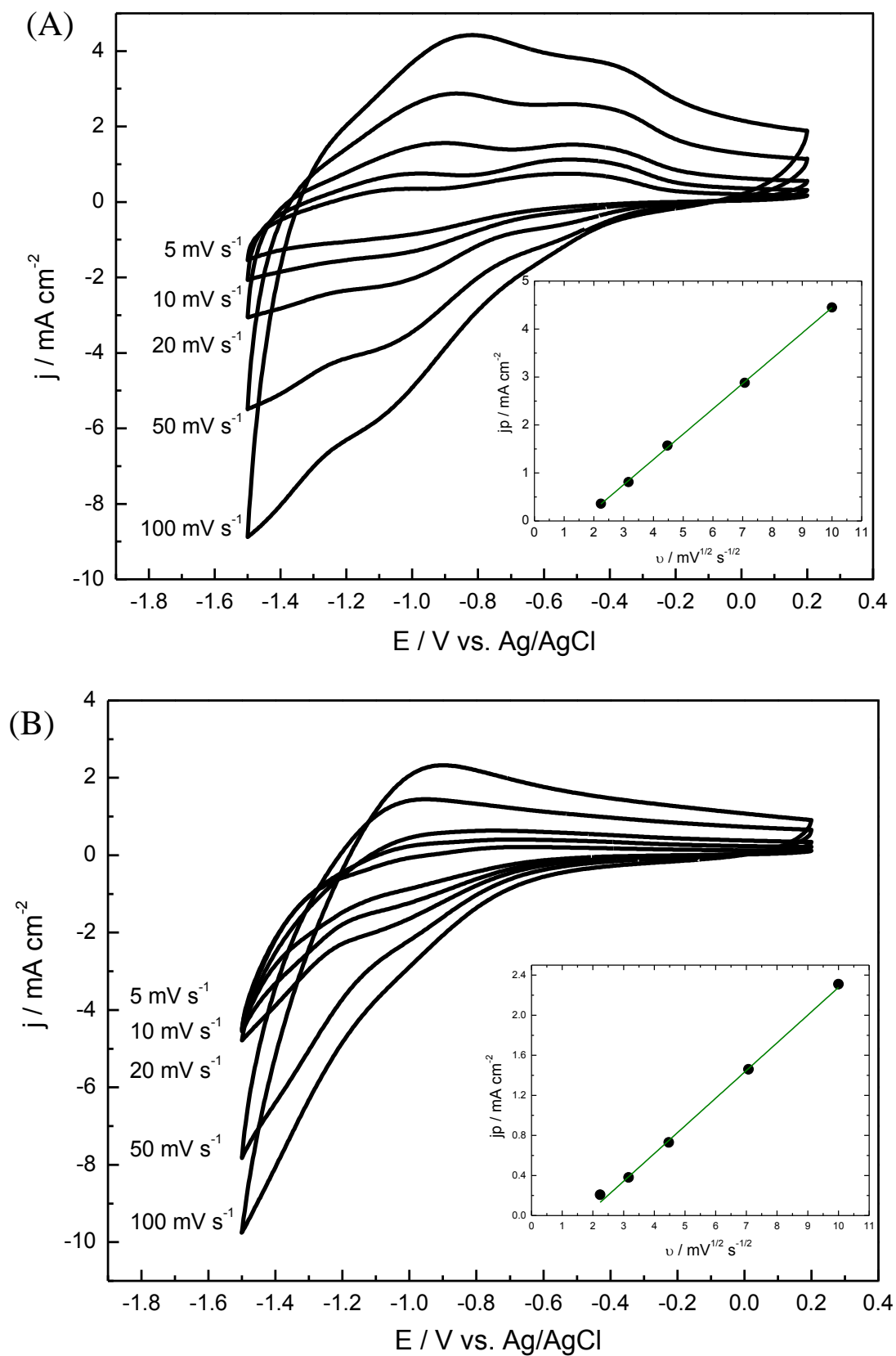


Fig.4. Cyclic voltammograms of ntTiO_2 films at different scan rate and relationship between the anodic peak intensity and square root of the scan rate for: (A) NaNO_3 and (B) NaCl electrolyte.

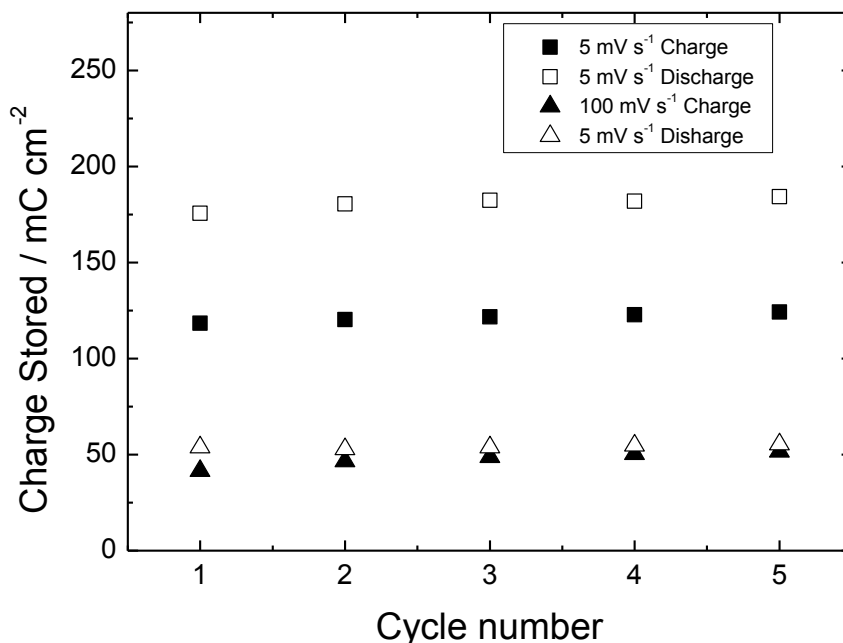


Fig.5. Comparison of the charge storage (during charge and discharge) in nTiO₂ film deduced from cyclic voltammograms at scan rate of 5 and 100 mV s⁻¹.

X-ray diffraction patterns were recorded to confirm the phase composition of the as-prepared samples and after annealing (Figure 6a and b). For the samples obtained at R.T., the reflections of the titanium substrate (PDF file # 05-0682) are visible for the two electrolytes. Between 10 – 33° (2θ), the patterns presented a broad and low intense band which is indicative of low crystallinity or an X-ray amorphous character of the materials. After mild thermal annealing at 500 °C most of the strong reflections located at 25.2°, 37°, 37.6°, 38.9° 47.9° 53.8° 55.1° and 62.2° (2-θ) can be clearly ascribed to anatase TiO₂ (PDF file # 21-1272), and the rest of peaks correspond to the titanium substrate. The broad and low intense band at 10 – 33 ° vanished after this first annealing and this effect is observed for the two electrolytes. Further annealing at 700 – 800 °C caused drastic changes in the X-ray patterns. Thus, by using both electrolytes the Na₂Ti₆O₁₃ phase is detectable (Figure 6b) by new peaks at 11.4°, 14.1°, 24°, 29.5°, 30.1°, 33.4°, 35.2°, 48.2°, 52.7°, which are clearly indexed in the monoclinic Na₂Ti₆O₁₃ phase (PDF file # 37-0951). This sodium titanate phase coexists with rutile TiO₂ (PDF file # 21-1276). The X-ray diffraction pattern for the product obtained in NaCl electrolyte indicated the coexistence of Na₂Ti₆O₁₃ with anatase and rutile not only at 700 but also at

800°C. According to equilibrium phase diagrams, the expected behavior is the conversion of amorphous ntTiO_2 to anatase by annealing at about 500 °C and the conversion to rutile starting at 600 °C, as observed from similar TiO_2 nanotube arrays [23]. The mechanism through which titanate nanotubes are dehydrated and converted into their condensed titanates and/or TiO_2 polymorphs after thermal treatment changes with the sodium content [24]. Depending on the amount of sodium in TiO_2 Morgado et al. [24] observed different situations. The sample with the highest amount contained sodium hexatitanate ($\text{Na}_2\text{Ti}_6\text{O}_{13}$) and sodium trititanate ($\text{Na}_2\text{Ti}_3\text{O}_7$). The middle sample was a mixture of sodium hexatitanate ($\text{Na}_2\text{Ti}_6\text{O}_{13}$), and TiO_2 in both rutile and anatase phases. These two samples were annealed at 800 °C. TiO_2 with very low amount of sodium ions and heated at 550 °C contained anatase and metastable $\beta\text{-TiO}_2$ as final phases. Our results suggest that the formation of sodium titanate on ntTiO_2 surfaces impedes the phase transformation of anatase to rutile at 800 °C (Figure 6b) and may improve the thermal stability of the anatase phase. These results are in agreement with those observed for nanocrystalline $\text{Li}_4\text{Ti}_5\text{O}_{12}$ -coated TiO_2 nanotube arrays [25].

Further insight on the mechanism of formation of sodium titanate from titania nanotubes was obtained from the EPR spectra of the as-prepared ntTiO_2 and after sodium insertion in aqueous media (Figure 7a and b). The as-prepared nanotubes exhibited two Ti^{3+} signals: (i) a narrow signal at ca. 338 mT attributed to the presence of Ti^{3+} in the lattice, and (ii) a very broad signal at ca. 349 mT attributed to the presence of Ti^{3+} on the surface [8]. The EPR signal for the non-calcined $\text{Na}_x\text{H}_y\text{TiO}_2$ films confirmed that the quantity of superficial Ti^{3+} increases whereas the quantity of Ti^{3+} from lattice disappears at high current densities (-37.5 mA cm^{-2}). The overall Ti^{3+} quantity after sodium insertion is higher than before insertion, thus causing the reduction of Ti^{4+} to Ti^{3+} and sodium insertion into amorphous ntTiO_2 . Moreover, the change in color of the nanotubes surface to black could also be attributed to Ti^{4+} reduction. On heating up to 500, 700 and 800 °C, it can be seen that the Ti^{3+} signal disappeared from ntTiO_2 (Figure 7a), but this is not the case for the $\text{Na}_x\text{H}_y\text{TiO}_2$ film. The changes of the EPR signal for the $\text{Na}_x\text{H}_y\text{TiO}_2$ film showed a different tendency: (i) at 500 and 700 °C there is no EPR signal related to the complete oxidation of Ti^{3+} to Ti^{4+} , and (ii) at 800 °C an asymmetric signal appeared, associated with the appearance of defect Ti^{3+} ions when titania transforms from anatase to rutile in NaNO_3 electrolyte or due to the formation of Na_xTiO_2 (Figure 7b). In conclusion, on increasing temperature the promotion from

$\text{Na}_x\text{H}_y\text{TiO}_2$ to form sodium titanate/titania (anatase and/or rutile) composites is possible. In addition, it should be highlighted that this procedure is far away from others commonly used in the synthesis of sodium titanates, which are based on solid state reactions [26,27].

(A)

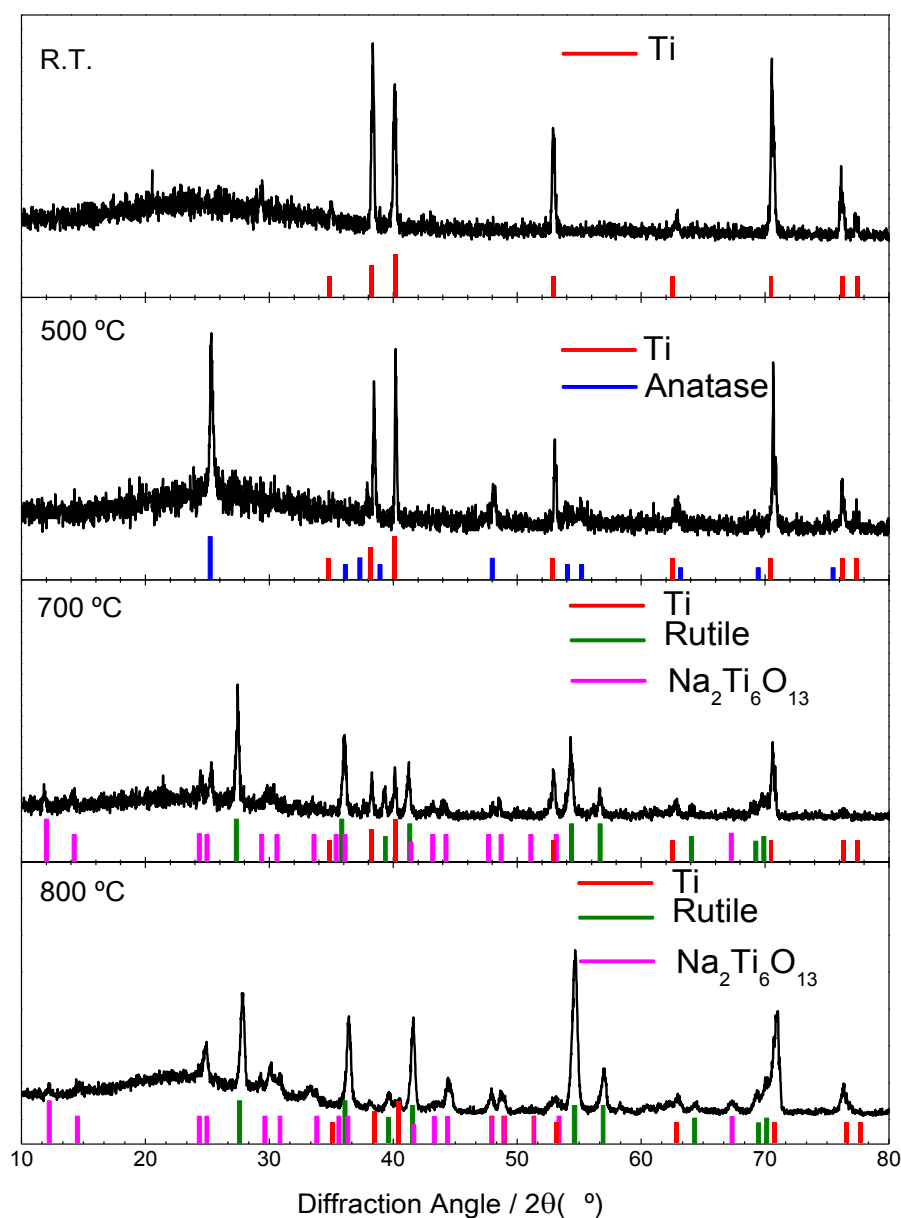


Fig.6A. X-ray patterns of ntTiO_2 specimens after insertion of sodium obtained at R.T., and after calcining in air at 500, 700 and 800 °C using NaNO_3 .

(B)

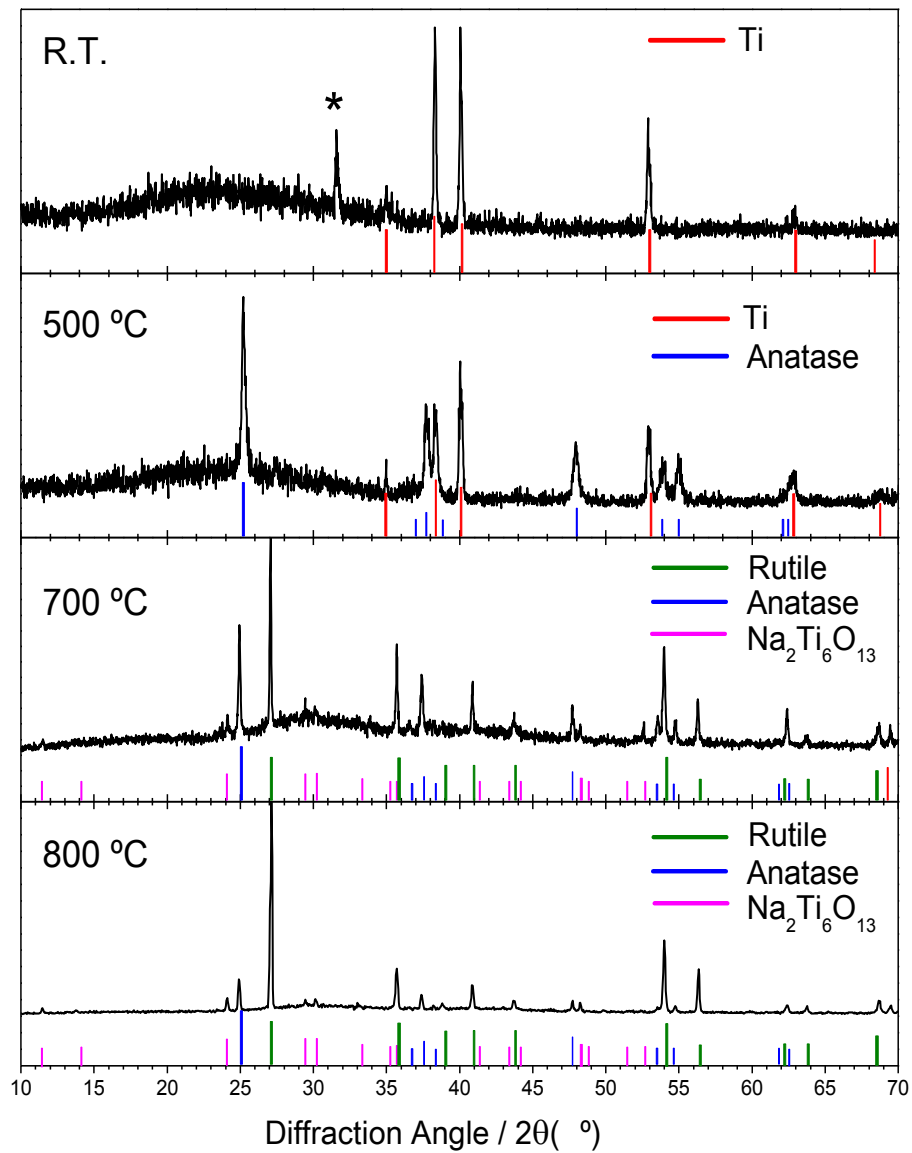


Fig.6B. X-ray patterns of ntTiO_2 specimens after insertion of sodium obtained at R.T., and after calcining in air at 500, 700 and 800 °C using NaCl.

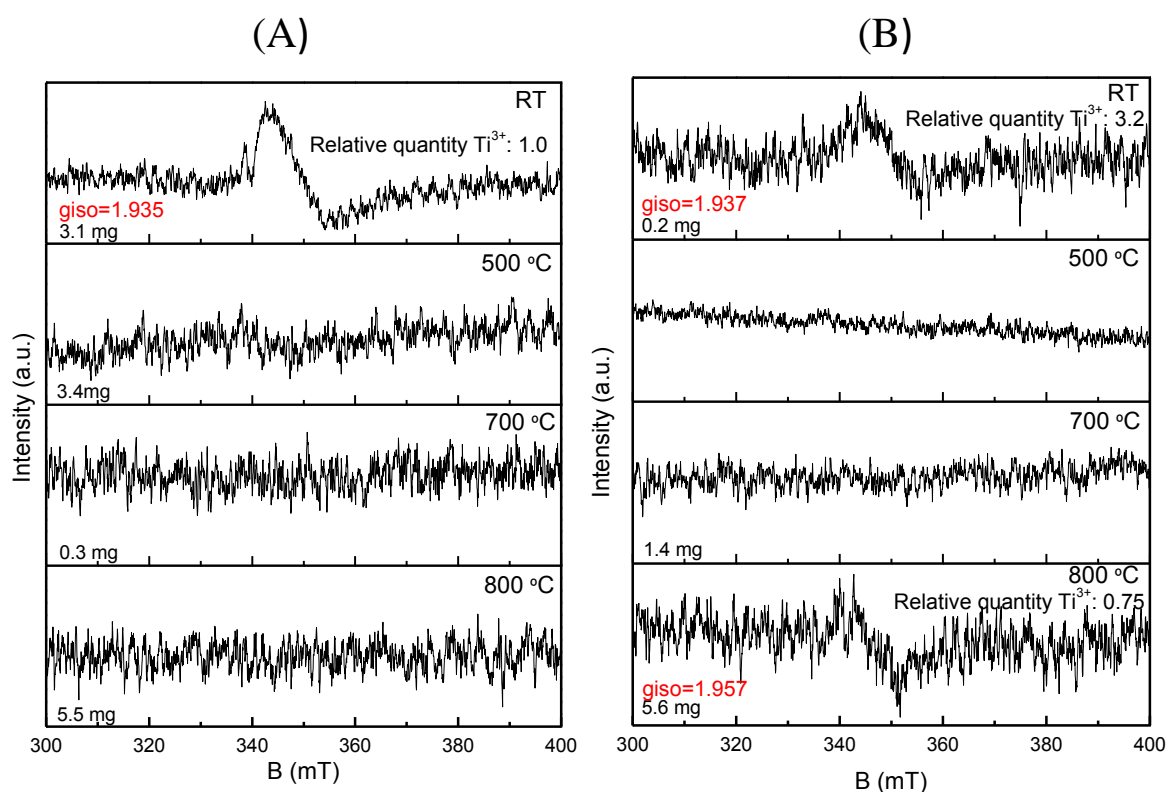


Fig.7. EPR spectra of: (A) ntTiO_2 and (B) $\text{Na}_x\text{H}_y\text{TiO}_2$ specimens obtained at R.T and after thermal annealing at 500, 700 and 800 °C in air.

The thickness, shape and morphology of the samples are studied using SEM and TEM (Figure 8 and 9). For the sake of clarity samples obtained at 500, 700 and 800 °C are presented. It can be seen from the top view and the cross section image (Figure 8a and b) that the thickness of $\text{Na}_x\text{H}_y\text{TiO}_2$ is about 8 μm and no surface deposits can be discerned. It should be highlighted that the thickness of the nanotubular slab grown on Ti foils by anodization at 60 V during 2 h is preserved in the titanate forest [28]. TEM revealed that the inner diameter of $\text{Na}_x\text{H}_y\text{TiO}_2$ of ca. 80 nm is rather uniform, (Figure 9a and b). These features are also observed for samples annealed at 500 °C. However, a drastic change in morphology is observed when annealing at 700 and 800°C. The shape of nanotubes is destroyed and turns into self-organized structures with branched connections, which resemble nanotrees growing parallel to form a nanoforest (Figure 8c and d for 700°C and Figure 8e and f for 800°C). From TEM images we have detected that the rupture of nanotubes is taking place simultaneously to $\text{Na}_2\text{Ti}_6\text{O}_{13}$ crystallization (Figure 9c). The rod-like branches of the nanotrees obtained at 800 °C exhibited ca. 550

nm length and ca. 120 nm external diameter (Figure 9d). Moreover, the empty space between branches could facilitate the access of the electrolyte to the total mass of active electrode material.

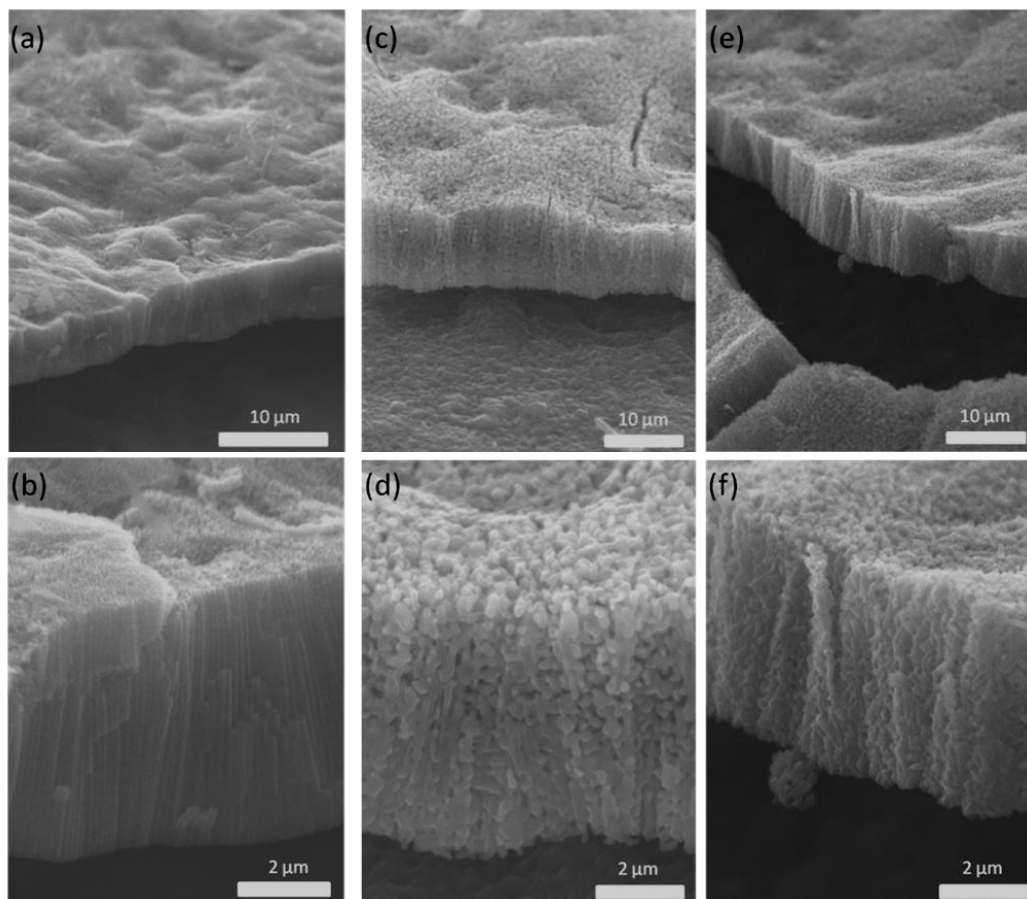


Fig.8. SEM images obtained from different angles for: (a,b) ntTiO_2 , (c,d) $\text{Na}_2\text{Ti}_6\text{O}_{13} / \text{TiO}_2$ at 700 °C and (e,f) $\text{Na}_2\text{Ti}_6\text{O}_{13} / \text{TiO}_2$ at 800 °C.

An electrochemical study of the electrodes prepared in this work in sodium batteries was carried out. For this purpose, the use of binding or conductive additives was not necessary, and the titanium substrate acted as current collector. The galvanostatic charge-discharge curves of as-prepared $\text{Na}_x\text{H}_y\text{TiO}_2$ and the sample annealed at 500 °C showed a constant decay of the potential without clear plateau from 3 – 0.05 V, which is typical behavior of amorphous samples when reacting with sodium (Figure S.1). Their derivative curves (Figure S.1b) recorded on further cycling confirmed the above observation, as no peaks are resolved, and consequently faradic reactions can be discarded at R.T. and 500 °C. Such galvanostatic profile has already

been observed for anatase TiO_2 where the main reaction with sodium is dominated by surface redox processes (pseudocapacitance), not controlled by sodium diffusion [29].

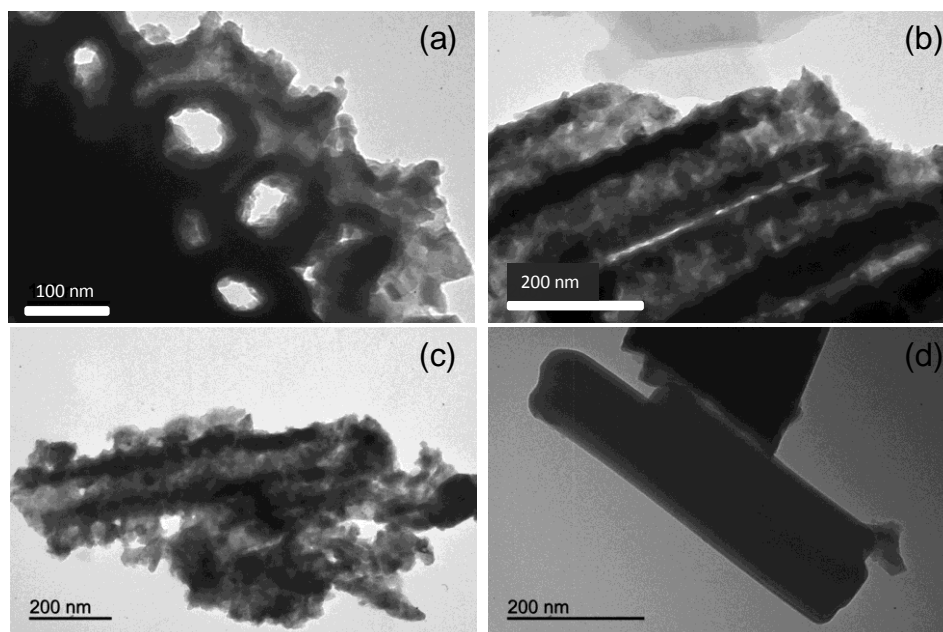


Fig.9. TEM images of sodium titanates on TiO_2 nanotubes at: (a) as-prepared by sodium insertion from aqueous electrolyte, (b) 500, (c) 700 and (d) 800 °C.

To get further insights into the mechanism of reaction, galvanostatic discharge charge curves of X-ray crystalline $\text{Na}_2\text{Ti}_6\text{O}_{13}/\text{TiO}_2$ annealed at 700 and 800 °C are studied in detail in Figure 10. In the first discharge, a large capacity of 250 and 235 $\mu\text{A h cm}^{-2}$ is obtained, which includes reversible and irreversible reactions, respectively. Both exhibited a rapid decay of the potential from open circuit voltage to 0.5 V that can be assigned to irreversible decomposition of the electrolyte with the consequent formation of a solid film at the surface of the electrode [30], while from 0.5 to 0.05 V sodium insertion takes place [31]. The first signal became very weak and disappeared completely on the second cycle indicating an irreversible process. The profile from second to further charge/discharge cycles exhibited typical peaks of Na insertion and de-insertion at 0.72 and 0.92 V (Figure 10), respectively. The potential of sodium insertion reported here is similar to that reported by Rudola et al. [31] for pure $\text{Na}_2\text{Ti}_6\text{O}_{13}$ without additives (0.83 V), with a gravimetric capacity of 65 mA h g^{-1} and

reversibility of around 61 % after 50 cycles using voltage windows of 0.5 – 2.5 V. On cycling between 0.05 – 3 V, the initial coulombic efficiencies in our electrodes were 48 and 54 % for 700 and 800 °C, respectively. Another example previously published in literature indicated that a 47 % of efficiency is obtained in Na/Na₂Ti₆O₁₃ cells from first to second cycle [27]. For instance the as-prepared NaTi₃O₆(OH)·2H₂O (NNT) and dehydrated sodium titanate samples in Na half-cells showed coulombic efficiencies from first to second cycle of about 18 % ($d_1 = 250 \text{ mA h g}^{-1}$ and $d_2 = 45 \text{ mA h g}^{-1}$) and 56 % ($d_1 = 220 \text{ mA h g}^{-1}$ and $d_2 = 125 \text{ mA h g}^{-1}$), respectively [32]. Although we have not used carbon conductive additive, the first cycle efficiency by irreversible reduction of electrolyte to form a solid electrolyte interface (SEI) was not improved. However, the goal of our study is to validate the utility of rutile/anatase-TiO₂ as a carbon-free coating layer to improve the kinetics of Na₂Ti₆O₁₃ toward fast sodium insertion/extraction. Doeff et al. suggested that on subsequent charge/discharge cycles the intercalation limit is $x = 1$ in Na_{2+x}Ti₆O₁₃, corresponding to approximately 50 mA h g⁻¹ which can lead to a composition of Na₃Ti₆O₁₃ for the fully reduced material [27]. However, very recently Shen et al. proposed that by lowering the cutoff voltage from 0.3 to 0 V vs. Na⁰/Na⁺ capacity increases from 50 mA h g⁻¹ (Na₂Ti₆O₁₃) to a promising value of 196 mA h g⁻¹ (Na₂₊₄Ti₆O₁₃) [19]. However, a detailed study by in-situ X-ray diffraction and DFT calculations showed that sodium intercalation in the Na_{2+x}Ti₆O₁₃ host structure is limited to Na₂₊₂Ti₆O₁₃.

Figure 11 shows the capacity values of the Na half-cells on extended cycling, extracted from Figure 10 and Figure. S.1. Capacity and cycling performance differ significantly as a function of temperature and synthesis conditions. The initial discharge capacity of the room-temperature Na_xH_yTiO₂ sample is about 205 and 280 μA h cm⁻² for NaCl and NaNO₃, respectively. The first reversible capacity is about 70 – 80 μA h cm⁻² for both electrolytes (Figure 11). The initial coulombic efficiency is rather low (36%). The capacity increased on cycling to around 82 % of the initial capacity over 50 cycles (175 μA h cm⁻²). This tendency of increasing the capacity upon cycling has been also observed for crystalline anatase TiO₂ with sodium [29,33]. The Na_xH_yTiO₂ prepared using NaNO₃ and NaCl electrolytes and annealed at 500 °C exhibited a first discharge capacity of 300 μA h cm⁻², a first reversible discharge of 125 μA h cm⁻² and an increase in capacity up to 175 μA h cm⁻² on further cycling, thus exhibiting a similar tendency than as-prepared samples before annealing. The initial coulombic efficiency is rather

low (42%), but then significantly increases to around 58% over 100 cycles. These initial capacity fluctuations would require conditioning of the electrode to reach the full performance in potential Na-ion cells.

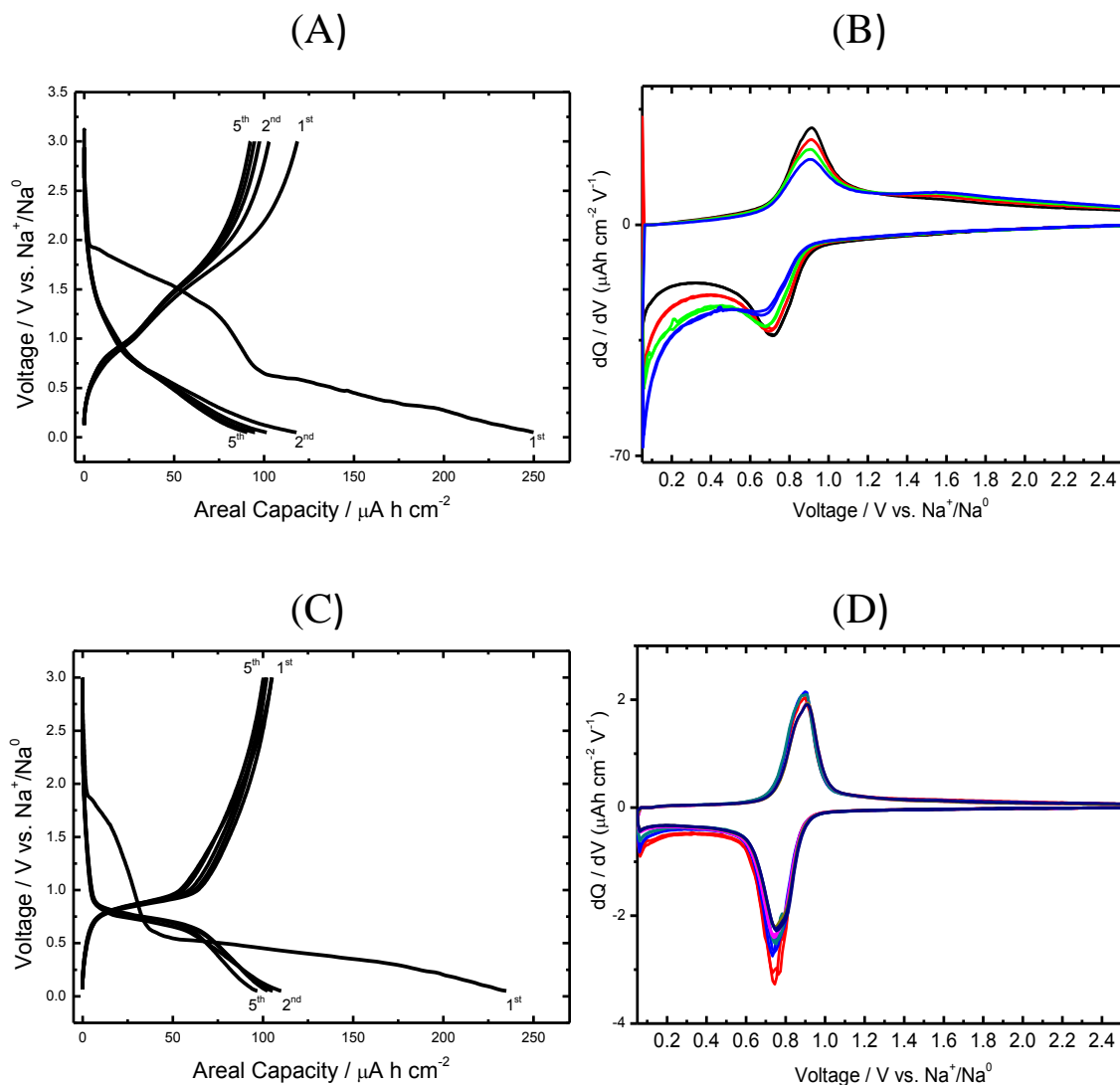


Fig.10. Galvanostatic discharge/charge and derivatives curves of X-ray crystalline $\text{Na}_2\text{Ti}_6\text{O}_{13}/\text{TiO}_2$ prepared with NaCl electrolyte and annealed at 700 (A and B) and 800 °C (C and D), respectively.

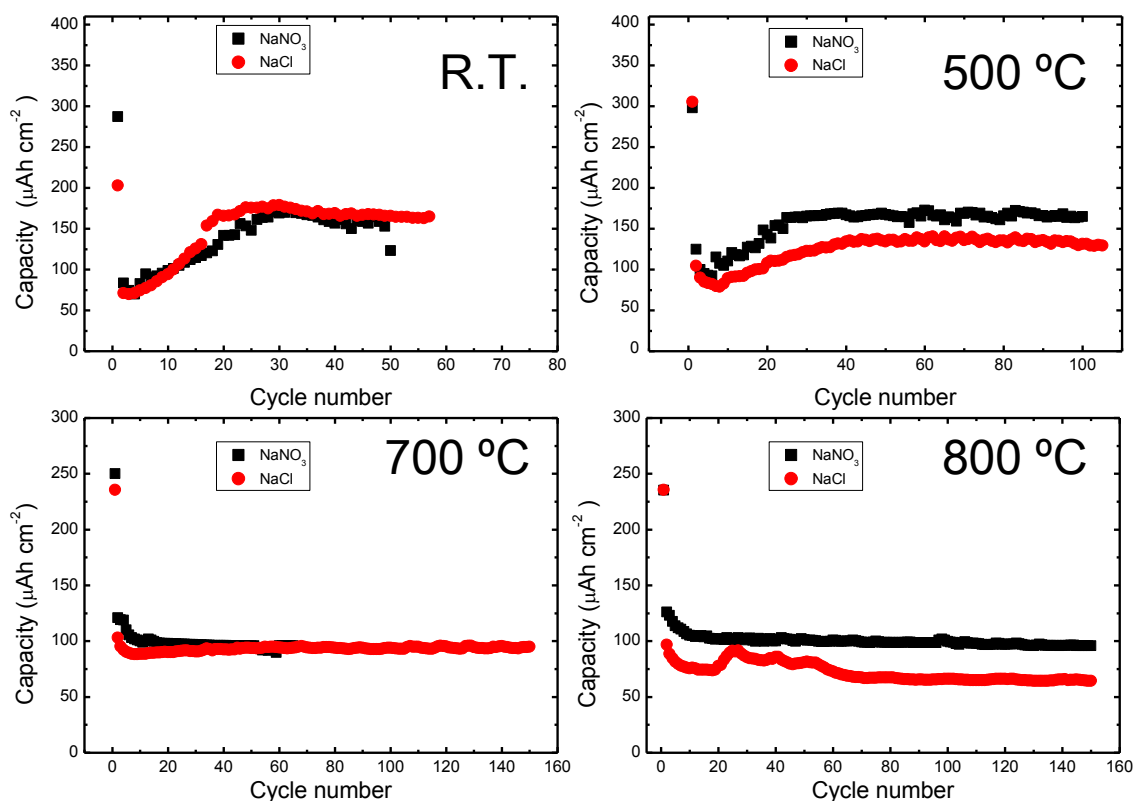


Fig.11. Comparison of the capacity as a function of the cycle number of $\text{Na}_x\text{H}_y\text{TiO}_2$ prepared from two different electrolytes at R.T. and after annealing at 500, 700 and 800 °C.

The electrochemical behavior for samples prepared at 700 and 800 °C changed drastically. Two main improvements have been observed: (i) the capacity does not fluctuate as compared to samples annealed at 500 °C, and (ii) there is no a capacity fading during prolonged cycles even at cycling windows of 3 – 0.05 V which is a typical drawback found in similar compositions [19,25,31]. The electrodes showed capacity retention close to 100 % over 150 cycles as referred from the first reversible cycle (Figure 11). In particular, better electrochemical behavior in terms of capacity retention was found for electrodes annealed at 700 and 800 °C, from $\text{Na}_x\text{H}_y\text{TiO}_2$ prepared in NaNO_3 electrolyte, which exhibited areal capacities of 125 and 130 $\mu\text{A h cm}^{-2}$, respectively. Our nano-architected thin films sodium titanate/titania nanotrees exhibited 130 $\mu\text{Ah cm}^{-2}$ ($15,000 \mu\text{Ah cm}^{-2} \text{ nm}^{-1}$) stabilized capacities over 150 cycles which are almost triple than that of titania nanotubes 36 $\mu\text{A h cm}^{-2}$ ($4,500 \mu\text{Ah cm}^{-2} \text{ nm}^{-1}$) (Figure. S.2). Up to now, most of sodium titanates have been cycled avoiding low

voltage window limits (e.g. < 0.3 V) because a loss of crystallinity may lead to capacity fading. One of the mayor problems of sodium titanate prepared in the form of powder is that the capacity of the sodium cell dropped to negligible values after the first few cycles. For instance, in the case of $\text{NaTi}_3\text{O}_6(\text{OH})\cdot 2\text{H}_2\text{O}$ the capacity decayed below 20 mA h g^{-1} after five cycles [32] and below 40 mA h g^{-1} for $\text{Na}_2\text{Ti}_6\text{O}_{13}$ after six cycles [27]. Rudola et al. demonstrated that by adding carbon black and graphite in $\text{Na}_2\text{Ti}_6\text{O}_{13}$ it is possible to retain the capacity over 40 and 30 mA h g^{-1} after 700 cycles at 5C using voltage window of $0.5 - 2.5$ V, respectively [31]. This behavior is particularly useful to implement robust thin film microbatteries. Recently Lacey et al. proposed fundamental science studies on SEI properties on MoS_2 electrodes by *in-situ* AFM techniques [35]. The goal was to get information regarding how to control the interfacial reactions and improve rechargeable battery performance by designing both electrode and electrolyte materials. The use of nanotree morphologies was recently found particularly useful to harvest light and carry out water splitting [36]. However, little attention has been paid to exploit the advantages on this morphology in battery electrodes. The above results clearly demonstrate the usefulness of nanoforests to facilitate the interfacial contact between active material and electrolyte, thus allowing the use of the complete slab of active material in 3-D microbatteries.

Ex-situ EPR analyses of the electrode after reaction with sodium at 0.05 V was performed. The signals are normalized considering the mass of sample used in each case. Figure S.3 shows that the sample discharged to 0.05V has higher signal intensity than the freshly prepared sample after heating. Between 335 and 338 mT a new weak signal appeared, which may correspond to the appearance of Ti^{3+} in the "lattice" as previously assigned in other samples. Therefore in the sample at 0.05V we would have Ti^{3+} with two different environments: (i) on the surface and (ii) located in the crystal lattice, while in the pristine sample it is only possible to identify the surface Ti^{3+} . This increase in Ti^{3+} in the discharged electrode indicates that the capacity of the electrochemical cell is not due to capacitive processes but also to faradaic or pseudocapacitive processes, in agreement with the electrochemical curves previously described.

3.1.4 Conclusions

The low cost and abundance of titanium oxides and their easy conversion to titanates make them interesting candidates for the anode of Na-ion batteries. In particular the 3D tunnel structures of monoclinic $\text{Na}_2\text{Ti}_6\text{O}_{13}$ results in a potentially attractive host to store Na ions reversibly. XRD and EPR results show that X-ray amorphous $\text{Na}_x\text{H}_y\text{TiO}_2$ films can be obtained at room temperature by titanium reduction (Ti^{4+} to Ti^{3+}) in an aqueous medium. Then the conversion to $\text{Na}_2\text{Ti}_6\text{O}_{13}$ is possible by annealing at 700 °C. Phase composition and morphology of the products was followed by a detailed structural characterization, and controlled by modifying the synthesis conditions. The resulting optimized nanoforest electrode shows three-times larger capacities than the starting TiO_2 , and excellent cycleability. This additive-free electrode configuration could be very useful for future micro-battery designs.

Acknowledgements

The authors are indebted to MEC (MAT2011-22753), “Ramón y Cajal” contract (RYC-2010-05596) and “Junta de Andalucía” (FQM-288 and FQM-7206).

3.1.5 References

1. J. Yan, J. Zhang, M. C. W. Kintner-Meyer, X. Lu, D. Choi, J. P. Lemmon, J. Liu, *Chem. Rev.* 111 (2011) 3577.
2. V. Palomares, P. Serras, I. Villaluenga, K. B. Hueso, J. Carretero-González, T. Rojo, *Energy Environ. Sci.* 5 (2012) 5884.
3. K. Saravanan, C. W. Mason, A. Rudola, K. H. Wong, P. Balaya, *Adv. Energy Mater.* 3 (2013) 444.
4. M. J. Aragón, C. Vidal-Abarca, P. Lavela, J. L. Tirado, *J. Power Sources* 252 (2014) 208.
5. D. A. Stevens, J. R. Dahn, *J. Electrochem. Soc.* 147 (2000) 1271.

6. R. Alcántara, P. Lavela, G. F. Ortiz, J. L. Tirado, *Electrochem. Solid-state Lett.* 8 (2005) A222.
7. S. Komaba, W. Murata, T. Ishikawa, N. Yabuuchi, T. Ozeki, T. Nakayama, A. Ogata, K. Gotoh, K. Fujiwara, *Adv. Funct. Mater.* 21 (2011) 3859.
8. J. R. González, E. Zhecheva, R. Stoyanova, D. Nihtianova, P. Markov, R. Ravelle-Chapuis, R. Alcántara, F. Nacimiento, J. L. Tirado, G. F. Ortiz, *Phys. Chem. Chem. Phys.* 17 (2015) 4687.
9. J. R. González, R. Alcántara, G. F. Ortiz, F. Nacimiento, J. L. Tirado, *J. Electrochem. Soc.* 160 (2013) A1390.
10. J. R. González, R. Alcántara, F. Nacimiento, G. F. Ortiz, J. L. Tirado, *CrystEngComm* 16 (2014) 4602.
11. L. Wu, D. Bresser, D. Buchholz, G. A. Giffin, C. Ramírez-Castro, A. Ochel, S. Passerini, *Adv. Energy Mater* 5 (2015) 1401142.
12. M. Zikalava, M. Kalbac, L. Kavan, I. Exnar, M. Graetzel, *Chem. Mater.* 17 (2005) 1248.
13. R. Dominko, E. Baudrin, P. Umek, D. Arcon, M. Gaberscek, J. Jamnik, *Electrochem. Comm.* 8 (2006) 673.
14. S. Baliteau, A.-L. Sauvet, C. Lopez, P. Fabry, *Solid State Ionics* 178 (2007) 1517.
15. C. Pérez-Flores, A. Kuhn, F. García-Alvarado, *J. Power Sources* 196 (2011) 1378.
16. N. D. Trinh, O. Crosnier, S. B. Schougaard, T. Brousse, *ECS Trans.* 35 (2011) 91.
17. A. Rudola, K. Saravanan, C. W. Masona, P. Balaya, *J. Mater. Chem. A* 1 (2013) 2653.
18. P. Senguttuvan, G. Rousse, V. Seznec, J. M. Tarascon, M. R. Palacín, *Chem. Mater.* 23 (2011) 4109.

19. K. Shen, M. Wagemaker, *Inorg. Chem.* 53 (2014) 8250.
20. J. R. González, R. Alcántara, F. Nacimiento, G. F. Ortiz, J. L. Tirado, E. Zhecheva, R. Stoyanova, *J. Phys. Chem. C* 116 (2012) 20182.
21. L. V. Taveira, J. M. Macak, H. Tsuchiya, L. F. P. Dick, P. Schmuki, *J. Electrochem. Soc.* 152 (2005) B405.
22. J. R. González, R. Alcántara, F. Nacimiento, G.F. Ortiz, J.L. Tirado, *J. Electrochem. Soc.* 162 (2015) A3007.
23. R. Liu, L. S. Qiang, W. D. Yang, H. Y. Liu, *Mater. Res. Bull* 48 (2013) 1458.
24. E. Morgado Jr., M.A.S. de Abreu, O.R.C. Pravia, B. A. Marinkovic, P. M. Jardim, R. C. Rizzo, A. S. Arajo, A. Arajo, *Solid State Sci.* 8 (2006) 888.
25. T. Yiping, T. Xiaoxu, H. Guangya, Z. Guoqu, *Electrochim. Acta* 117 (2014) 172.
26. S. Andersson, A. D. Wadsley, *Acta Cryst.* 15 (1962) 194.
27. M. M. Doeff, J. Cabana, M. Shirpour, *J. Inorg. Organomet. Polym.* 24 (2014) 5.
28. M. C. López, G. F. Ortiz, J. R. González, R. Alcántara, J. L. Tirado, *ACS Appl. Mater. Interfaces* 6 (2014) 5669.
29. J. R. González, R. Alcántara, F. Nacimiento, G. F. Ortiz, J. L. Tirado, *CrystEngComm* 16 (2014) 4602.
30. M. D. Levi, D. Aurbach, *J. Phys. Chem. B.* 101 (1997) 4630.
31. A. Rudola, K. Saravanan, S. Devaraj, H. Gongb, P. Balaya, *Chem. Commun.* 49 (2013) 7451.
32. M. Shirpour, J. Cabana, M. Doeff, *Energy Environ. Sci.* 6 (2013) 2538.
33. L. Wu, D. Buchholz, D. Bresser, L. G. Chagas, S. Passerini, *J. Power Sources.* 251 (2014) 379.
34. C. Pérez-Flores, A. Kuhn, F. García-Alvarado, *The 15th International Meeting on Lithium Batteries – IMLB, 2010*, p280.

- 35.** S. D. Lacey, J. Wan, A. vW. Cresce, S. M. Russell, J. Dai, W. Bao, K. Xu, L. Hu, *Nano letter*, 15 (2015) 1018.
- 36.** K. Sun, Y. Jing, C. Li, X. Zhang, R. Aguinardo, A. Kargar, K. Madsen, K. Banu, Y. Zhou, Y. Bando, Z. Liu, D. Wang, *Nanoscale*, 4 (2012) 1515.

3.1.6 Supplementary information

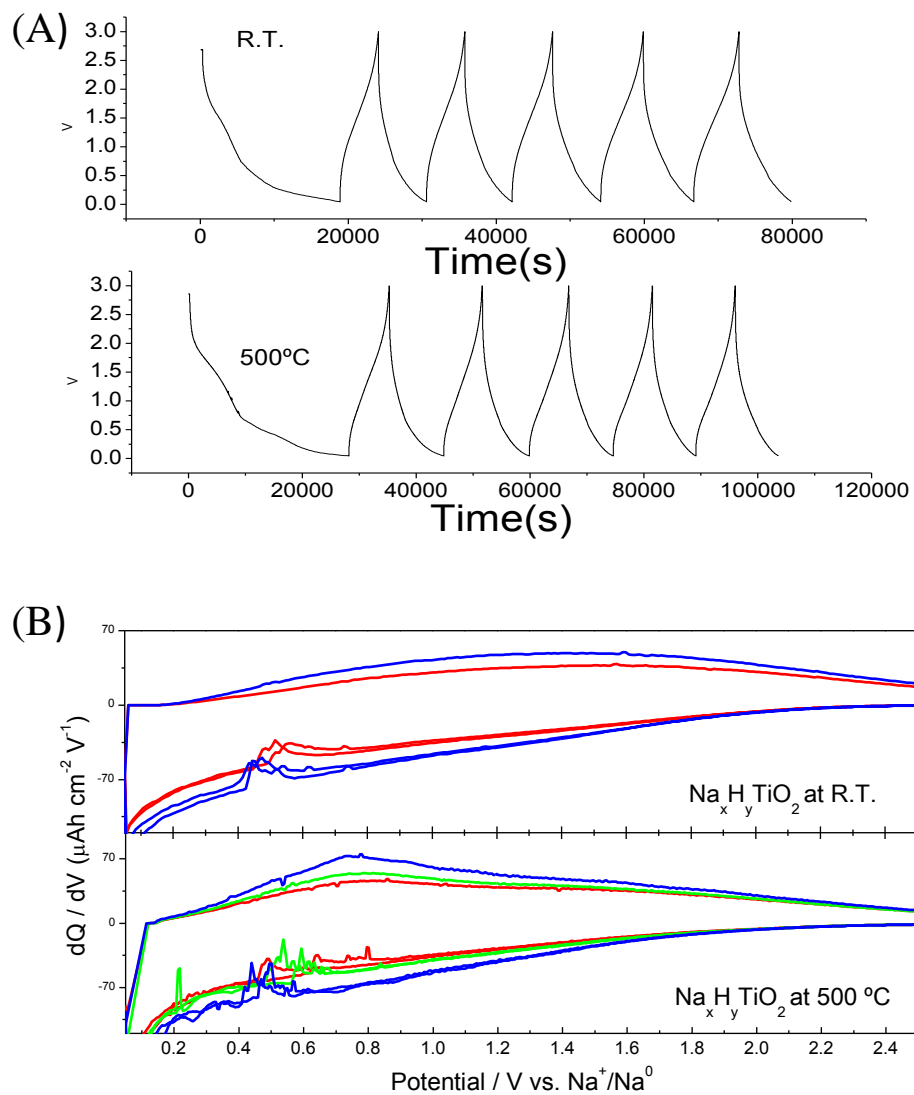


Fig.S1. A typical galvanostatic discharge/charge curves (A) and their corresponding derivative curves (B) for $\text{Na}_x\text{H}_y\text{TiO}_2$ thin films prepared at R.T. and 500 °C for NaNO_3 electrolyte.

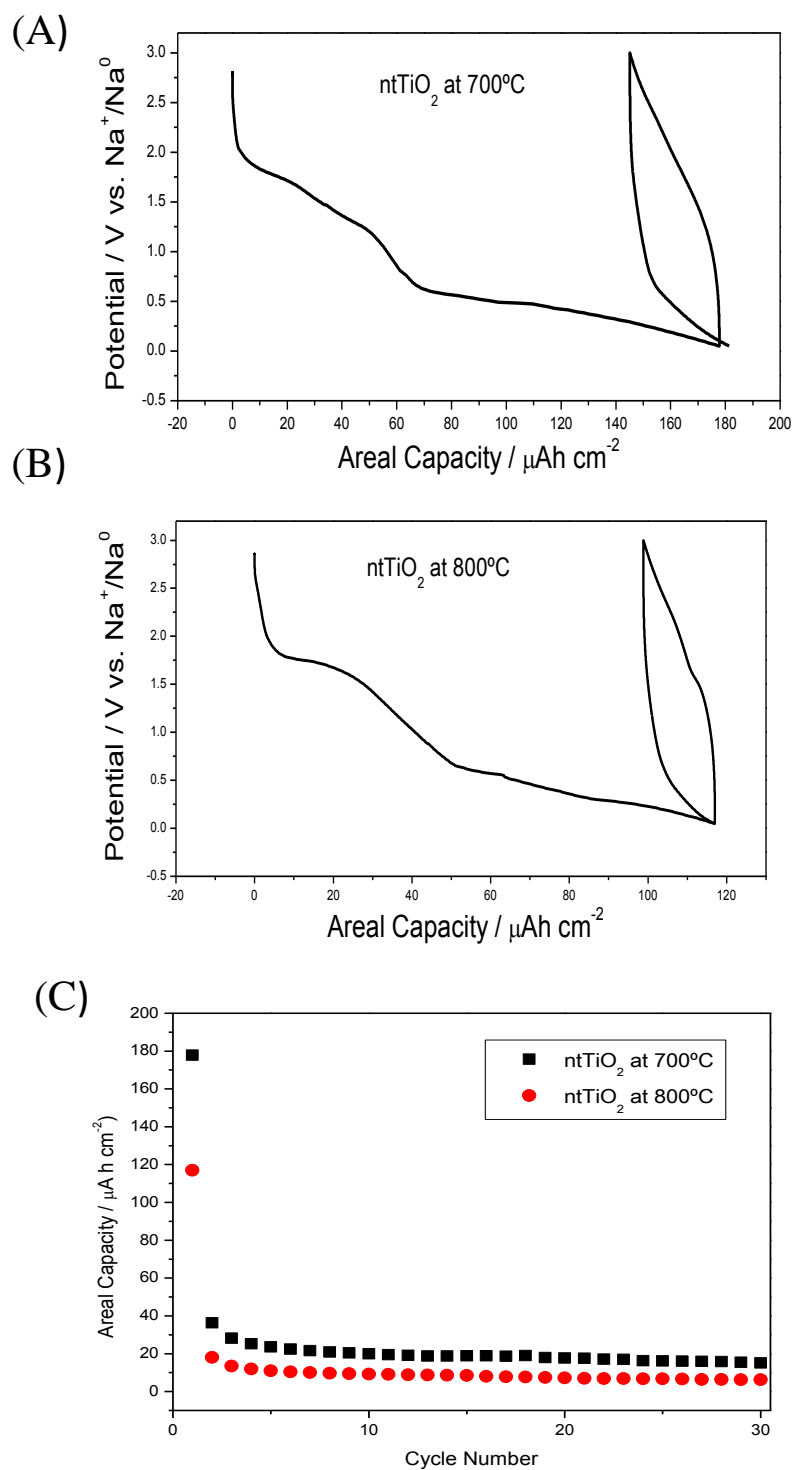


Fig.S2. Galvanostatic discharge/charge curves versus sodium of ntTiO_2 layer annealed at 700°C (A) and 800°C (B), and capacity retention up to 30 cycles (C).

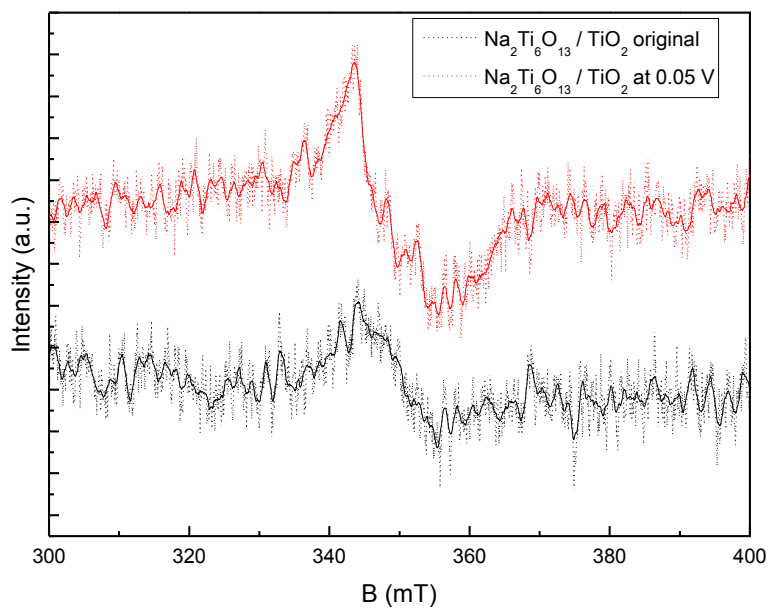


Figure S3. Comparison of EPR signals of Na₂Ti₆O₁₃/TiO₂ at 800 °C before and after discharge at 0.05 V in sodium cell.

3.2 Treasure Na-ion anode from trash coke by adept electrolyte selection

Marta Cabello ^a, Taras Chyrka ^b, Rafael Klee ^a, María J. Aragón ^a, Xue Bai ^a, Pedro Lavela ^a, Gennadiy M. Vasylenko ^b, Ricardo Alcántara ^a, José L. Tirado ^a, Gregorio F. Ortiz ^a.

^aLaboratorio de Química Inorgánica. Universidad de Córdoba. Edificio C3, Campus de Rabanales. Spain

^b Scientific research centre “Resource saving technologies”, National technical university of Ukraine “Kyiv polytechnic institute”, Kyiv, Ukraine.

Abstract

Converting ‘trash’ waste residua to active functional materials ‘treasure’ with high added value is being regarded as a promising way to achieve the sustainable energy demands. Carbonaceous materials cannot insert sodium except when graphite co-intercalates solvents such as diglyme. Here, we show that petroleum coke and shale coke annealed at different temperatures can also insert sodium by reversible intercalation phenomena in a diglyme-based electrolyte. The structural and morphological studies will reveal significant differences justifying their distinct electrochemical behavior. Galvanostatic tests exhibit a flat plateau at about 0.7 V ascribable to the reversible reaction. At the end of the discharge, a Stage-I ternary intercalation compound is detected. Two diglyme molecules are co-intercalated per alkali ion, as evidenced by 1-D Patterson diagrams, FTIR and TGA analyses. The full sodium-ion cell made with P-2500/NaPF₆(diglyme)/Na₃V₂(PO₄)₃ delivered an initial reversible capacity of 75 mA h g⁻¹ at C rate and an average potential of 2.7 V. Thus, the full cell provides an energy density of 202 W h kg⁻¹. This sodium-ion system can be considered a promising power source that encourages the potential use of low-cost energy storage systems.

Keywords

Sodium-ion batteries; shale coke; petroleum coke; diglyme; co-intercalation



ELSEVIER



Journal of Power Sources 347 (2017) 127-135

3.2.1 Introduction

The implementation of Na-ion batteries (NIBs) is a firmly established research field with renewed interest as a mean to overcome some of the economic and geopolitical drawbacks of the lithium equivalent [1–5]. The search for increased performance runs parallel to the interest on sustainability, cost reduction and environmental friendliness of the constituent active materials in NIBs.

The sodium electrode operates at room temperature with a redox potential of -2.71 V (versus standard hydrogen electrode). This value is lower than that of the Li^+/Li couple (0.3 V above that of lithium), thus leading to a decrease in working potential [6,7]. Moreover, NIBs benefit of a similar technology to Li-ion cells, as they can also be composed of insertion materials electronically separated by aprotic polar solvent-based electrolytes. Thus, performance issues can be solved relying on related mechanisms [8–10]. As compared to high-temperature sodium-based batteries such as sodium-sulfur [11] or sodium nickel-chloride [12] systems, their room temperature operational conditions and the absence of metallic sodium lead to safer batteries while ensuring suitable conductivities.

A large number of cathode materials have already demonstrated to yield high capacity and extended cyclability [6–10,13–15]. Nevertheless, a suitable negative electrode has not yet been found, mainly because of the inexistence of sodium intercalated graphite compounds, resulting from the unfavorable structural mismatch between graphite and Na^+ [16,17]. Otherwise, better performances have been achieved in disordered carbons. Thus, non-graphitizable hard carbons show a complex structure mainly composed by micropores distributed between disorderly-stacked carbon layers, which favor the reaction with sodium [18–20]. Otherwise, soft carbon consists of a disordered structure which is readily graphitizable at high temperature. Unfortunately, a large irreversible capacity is detected during the first discharge, which has been explained by the electrolyte decomposition at the carbon surface [21,22]. Both hard and soft carbons have demonstrated to be highly sensitive to the electrolyte composition and the use of additives [23,24]. It has been explained by the rather difficult surface passivation during the electrochemical reaction in sodium cells as compared to lithium [25].

Recently, it has been reported that the limited sodium insertion in graphitized carbons can be circumvented by using cointercalation phenomena in a diglyme-based electrolyte, resulting in a small irreversible loss during the first cycle, and a superior cycle life [26].

Converting ‘trash to treasure’ has been recalled several times as a possible way to achieve the sustainable demands. Thus polymer, algae, prawn shells or coke are trash raw materials that can be easily converted into active carbon material for the negative electrode of a NIB [27–29]. In this work, new trash materials, derived from the petroleum industry, are used to prepare carbons at 1300, 2500 and 3000 °C with different levels of graphitization. For the first time, sodium insertion was achieved in two types of coke (at 2500 and 3000 °C) and this fact compared favorably with other typical industrial carbon materials for electrode. The actual feasibility of the electrodes is demonstrated in a full Na-ion cell, evidencing that irreversible capacity in the first and subsequent cycles can be minimized.

3.2.2 Experimental

3.2.2.1 Sample characterization

Petroleum coke is a carbonization product of high boiling point hydrocarbon fractions obtained by petroleum processing (heavy residues). In our investigation we used calcined petroleum coke and needle petroleum coke. Carbonized coke is a petroleum coke or coal-derived pitch coke obtained by thermal treatment of green coke to about 1300 °C. Calcined coke normally has a hydrogen content of less than 0.1 wt%. Needle petroleum coke has extremely high ability to graphitize, resulting from a strongly preferred parallel orientation of its turbostratic layer structure and particular grain morphology [30]. Shale coke is obtained during carbonization of shale pitch at 420 °C [31]. For our investigation, we used needle shale and coke calcined at 1300 °C. In addition, samples graphitized at 2500 °C and 3000 °C were obtained.

The reason why this temperature levels were used is due to the nature of soft carbon materials and their ability to change their structure from disordered state of amorphous carbon to ordered of graphite. Experimental practice shows that 1300 °C

treatment allows to extract gaseous substances and some impurities from amorphous carbon without modification of the carbon structure [32]. At the same time heating carbon material at 2500 °C and higher temperatures (in our case, up to 3000 °C) leads to structural ordering and graphite formation. Treatment at temperatures between 2500 and 3000 °C is important from the point of view of expediency, as the product of higher temperature treatments is already graphite regardless the material, although with slight differences in crystallite size and interlayer spacing. In addition, for the thermal treatment procedure we used a laboratory high temperature furnace of Tammana™, constructed as graphite tubular furnace. 100 g of raw bulk material was placed in graphite crucible with cover (thus we can assume that environment was inert during heating). Temperature measurement was carried out by optical pyrometer (uncertainty $\pm 1.5\%$). At every temperature level we kept material during time 5 min (based on empirical formula of Kaverov [32], 1 min is enough for graphitization). To be precise regarding the preparation of graphitized petroleum and shale coke at temperature 3000 °C actually we used grounded graphite electrode manufactured at 3000 °C. Electrodes were prepared by mixing 80% of graphitized bulk coke and 20% pitch coke, followed by the thermal treatment in the Tammana furnace.

3.2.2.2 Characterization

X-ray diffraction (XRD) patterns were recorded in a Bruker D8 Advance diffractometer with a LYNXEYE XE - High-Resolution Energy-Dispersive 1-D Detector and Cu K α radiation. The patterns were scanned between 10 and 80° (2-theta degrees) at a 0.02°/s scan rate. To highlight the observation of some characteristic peaks a zoom was carried out. Raman spectra were recorded with a Renishaw Raman instrument (InVia Raman Microscope), equipped with a Leica microscope. Spectra were obtained by excitation with red laser light (785 nm) in the range between 1000 and 2000 cm⁻¹. The fitting of the spectra was carried out with the Peakfit v.4.11 software package. Scanning electron microscopy (SEM) images were recorded in a JEOL-SM6300 microscope.

FTIR data were obtained with a Bruker Tensor 27 FT-MIR spectrophotometer with CsI beam splitters and a DTGS detector. OPUS version 6.5 software was used to collect the transmission spectra. Thermogravimetric analysis (TGA) experiments were

performed under dynamic Ar (20 mL min^{-1}), at $10 \text{ }^\circ\text{C/min}$ of heating rate, using a Shimadzu instrument and aluminum pans.

3.2.2.3 Electrochemical characterization

The electrochemical measurements were carried out on Swagelok™ type cells assembled in an argon-filled glove box (MBraun Lab master 130). For this purpose, carbon-based electrodes were composed by active material (92%) and PVDF (polyvinylidene fluoride) (8%). $\text{Na}_3\text{V}_2(\text{PO}_4)_3$ was prepared by a sol-gel method as described elsewhere [33] and then was mixed with 15% of PVDF and 5% of carbon black. These components were finely dispersed in *N*-methyl-2-pyrrolidone Ultra-Turrax® high-performance disperser, yielding a homogenous paste which is spread onto a 9 mm copper (for anode) and aluminum foils (for cathode). The electrode is vacuum dried at $120 \text{ }^\circ\text{C}$ for at least 2 h. The reference electrode consisted of a 9 mm sodium disk. The electrodes were separated by glass fiber disks (GF/A-Whatman) impregnated in the electrolyte solution. The cells were assembled in an argon filled glove box under controlled O_2 (2 ppm) and H_2O (1 ppm) traces. The sodium half cells were cycled by the galvanostatic method between 0.003 and 3.0 V at C/10 – 1C rates. The full cells were cycled between 0.0 and 4.3 V at a C rate. The experimental mass ratio m^+/m^- was the value derived from the stoichiometric reaction ($0.82 m^- = 1 m^+$). Thus, the utilization of both active materials was optimum, and the specific capacities referred to the mass of each electrode are coincident. All these electrochemical experiments were monitored in a galvanostat/potentiostat VMP system. Several electrolyte solutions were tested: (i) 1 M NaOTf (sodium triflate or NaCF_3SO_3 , 98%, Aldrich) dissolved in DGM (diglyme 99%, Sigma-Aldrich) and (ii) 1 M NaPF_6 (99%, Strem Chemicals) dissolved in DGM. For comparison, standard electrolyte such as NaPF_6 dissolved in EC:DEC (ethylene carbonate and diethyl carbonate 99%, Aldrich) was also used.

3.2.3 Results and discussion

Irrespective of the carbon source (shale or coke), the XRD patterns of the samples carbonized to $1300 \text{ }^\circ\text{C}$ exhibited broad signals at 25.4° , 42.0° and 52° (2θ), which are respectively indexed as the 002, 100 and 004 reflections of

the $P6_3/mmc$ space group of the hexagonal system. The reflections appear highly broadened, which is characteristic of disordered carbons with a marked turbostratic character. On increasing the temperature of the thermal treatment to 2500 °C, new reflections are not observed, but a meaningful narrowing and a slight shifting to higher angles (26.36°, 44.41°, 54.36° (2 θ) of those reflections is clearly detected (Fig. S1). These observations are typical of a graphitization process in which the initially small crystallites composed of buckled carbon layers merge and an ordered layer stacking prevails. It is also consistent with the patterns recorded for samples annealed at 3000 °C. The calculated unit cell parameters are included in Table 1. Irrespective of the precursor, the parameter a slightly increased, while the parameter c significantly decreased from turbostratic to graphitized samples. This is the expected behavior for a graphitization process inducing a progressive parallel stacking of the graphene layers. Assuming the typical stacking of graphene layers in carbon materials, the evaluation of L_c was carried out by two different methods. First, the Scherrer equation was applied to the 002 peak. Second, the integral breadth based volume-weighted column height (L_{Vol}) was obtained. Both values, written in Table 1, were very similar. As expected from the profiles in Fig. S1, the most significant increase is observed from samples annealed at 1300 to 2500 °C, while they barely increased up to 3000 °C.

Table 1. Cell parameters and crystallite sizes (L_c and L_a) calculated for the carbon samples.

	$a / \text{Å}$	$c / \text{Å}$	L_{Vol} / nm	L_c / nm XRD	L_a / nm Raman	I_G/I_{D1}
P-1300	2.430 (2)	6.910 (1)	3.02 (4)	3.9	20.5	0.41
P-2500	2.4637 (3)	6.7673 (2)	22.1 (3)	22.9	53.5	1.07
P-3000	2.4617 (3)	6.7497 (3)	23.2 (6)	26.0	255.5	5.11
S-1300	2.431 (3)	6.949 (1)	3.48 (5)	3.6	20.0	0.40
S-2500	2.4609 (3)	6.7424(2)	28.0 (3)	27.9	144	2.88
S-3000	2.4651 (4)	6.7417(2)	30.3 (3)	29.6	151	3.02

A more detailed information about the level of graphitization of carbon materials can be gathered by recording the Raman spectra in the region between 1000 and 2000 cm^{-1} (Fig. 1). The spectra recorded on samples annealed at 1300 °C is characterized by two broadened and overlapped bands at ca. 1350 and 1597 cm^{-1} , respectively ascribed to the D1 and G modes belonging to sp^2 phases. The former mode is due to the lack of long range translational symmetry in disordered carbons while the G mode is assigned to an ‘in plane’ displacement of the ordered carbons coupled in the hexagonal sheets. The large polarizability of the conjugated π bonds at the sp^2 sites is responsible for the prevalence of these two modes [34]. However, a full decomposition of these spectra reveals two additional Gaussian components. Thus, D3 and D4 modes, respectively located at ca. 1510 ca. 1198 cm^{-1} , are ascribed to amorphous carbon at interstitial defects and C–C and C=C stretching vibrations of polyene-like structures [35].

On increasing the annealing temperature, the profiles change in a way that the D bands, correlated to disordered carbon, decrease their relative contribution as compared to the G band. Bearing in mind this fact, the level of graphitization can be calculated from the I_G/I_{D1} ratio (Table 1). This value increases with the annealing temperature from 1300 to 3000 °C, though a different trend was followed by each carbon precursor. Thus, the I_G/I_{D1} ratio slightly increased for P2500 to 1.07, while an abrupt increase was observed for P3000 (5.11). Contrarily, a higher value was calculated for S2500 (2.88), which was only slightly increased to 3.02 for S3000. The in-plane correlation length (L_a) can be inferred from the I_G/I_{D1} ratio according to the following equation [36]:

$$I_{D1}/I_G=C/L_a \quad (1)$$

where C depends on the Raman laser excitation energy and takes a value of 50 Å for the wavelength here employed ($\lambda = 532 \text{ nm}$). The calculated L_a values are written in Table 1. These data revealed that the graphitized P3000 sample reached the largest in-plane crystallite size, while the growth in this dimension was more restricted for the graphitized sample prepared from an oil-shale precursor.

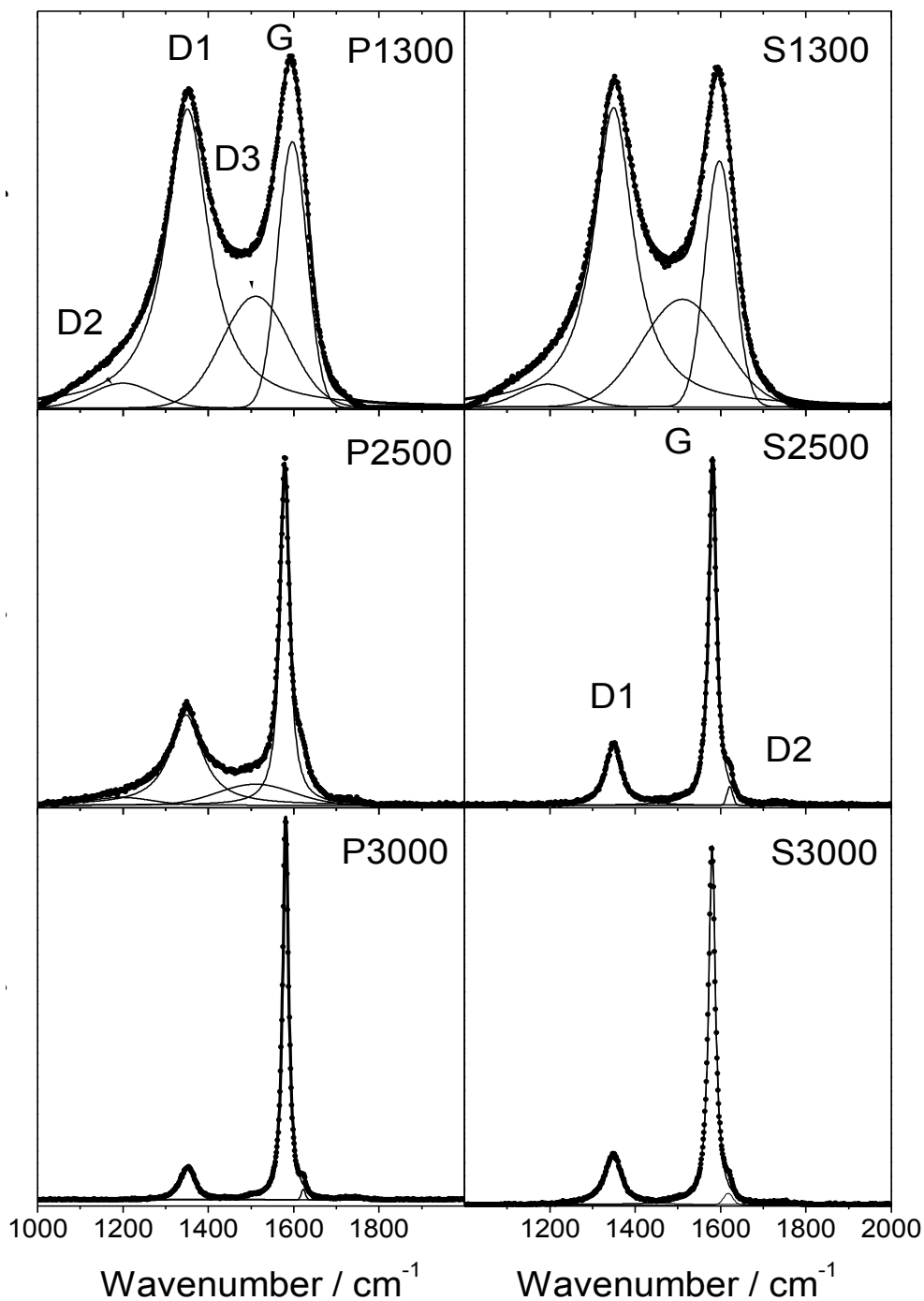


Fig.1. Raman spectra of carbon samples prepared from a petroleum precursor (P samples) and an oil shale precursor (S samples) annealed at 1300, 2500 and 3000 °C.

SEM images of the studied samples are displayed in Fig. 2. The common textural features of carbon materials can be indentified in these pictures. Thus, the above mentioned stacking of graphene layer is clearly observed. However, these layers

appear more buckled for carbons prepared from a petroleum precursor than from oil shale. On increasing the annealing temperature, this differential morphology is preserved. Thus, corrugated tile-like particles are observed for P3000, while more planar graphene layers appear for S3000. It is indubitable that these distinct structural and morphological properties of carbon obtained from either petroleum or oil shale precursor will have a marked influence on the electrochemical properties for sodium insertion.

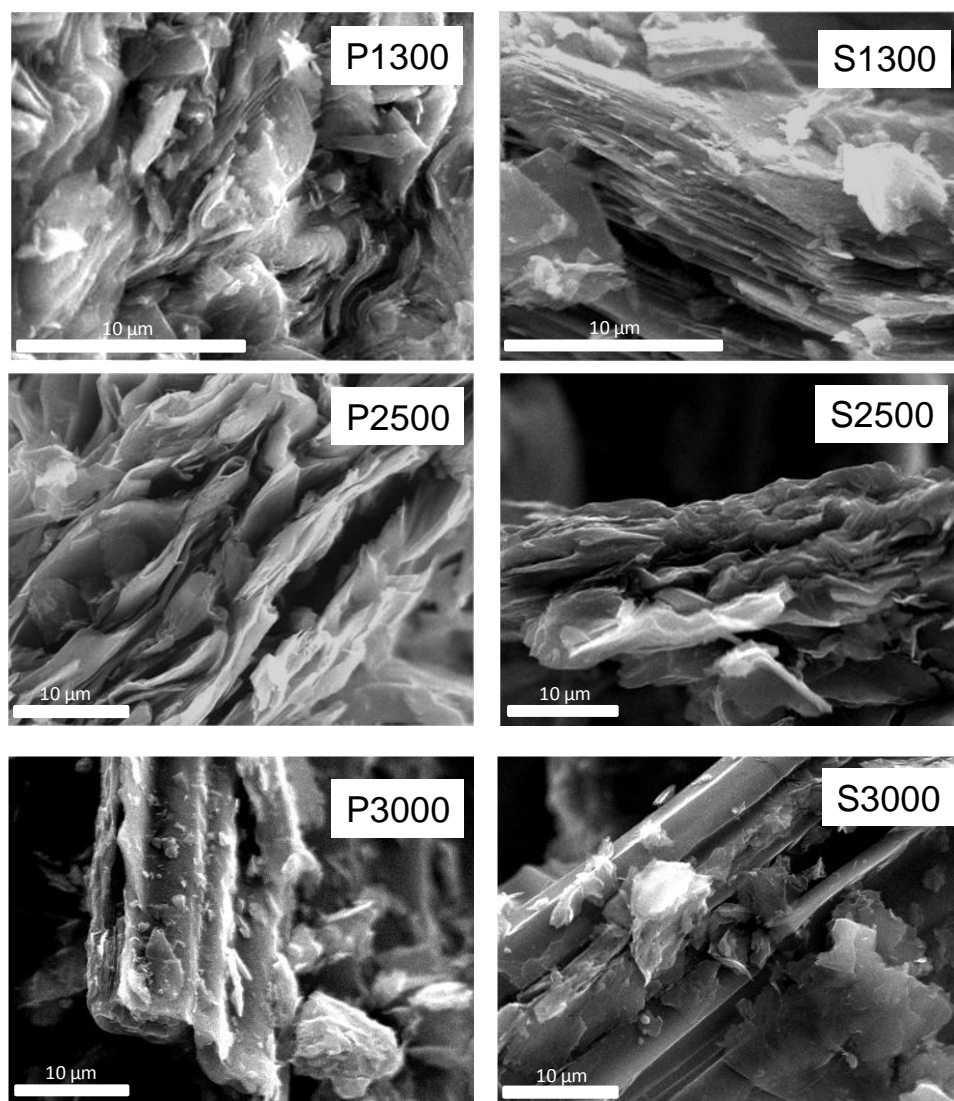


Fig.2. Scanning electron micrographs of P and S samples annealed at 1300, 2500 and 3000 °C.

In samples with graphitic order, the intercalation process is strongly affected by the type of solvent (Fig. 3A). The standard electrolyte used in NIBs is based on a

solution of NaPF_6 in EC/DEC. In this electrolyte, the formation of intercalation compounds is rarely formed, instead accumulation/adsorption of sodium takes place at potentials below 0.5 V with a first discharge capacity of 40 mA h g^{-1} . The achievable reversible capacities are close to 15 mA h g^{-1} . When using a single-solvent electrolyte based on diglyme and sodium triflate (NaCF_3SO_3) or NaPF_6 as conductive salts, the electrochemical behavior is drastically improved (Fig. 3A). In both cases, first discharge capacities and reversible capacities are around 116 and 123 mA h g^{-1} , respectively. The voltage profile during discharge/charge curves exhibits several steps mainly observed between 0.7 and 0.5 V , which are indicative of an ordering phenomenon with different thermodynamic stabilities. The initial irreversible capacity is small (with values around 20 mA h g^{-1}). Fig. 3B shows galvanostatic voltage profiles for selected cycles at 1C in $1 \text{ M NaCF}_3\text{SO}_3/\text{DGM}$ electrolyte. As can be seen, coke and shale annealed at $1300 \text{ }^\circ\text{C}$ show a large variability leading to a continuous loss of hysteresis between charge and discharge. This progressive electrode activation is indicative of an improvement of the sodium diffusion. Thus, an irreversible structural modification is occurring to facilitate ion migration on further cycling. On increasing the carbonization temperature to 2500 and $3000 \text{ }^\circ\text{C}$, a better reproducibility of profiles is observed, except for the typical irreversibility at the first cycle. Likely, the large particles produced at these temperatures are less prone to be modified by the electrochemical reaction.

(A)

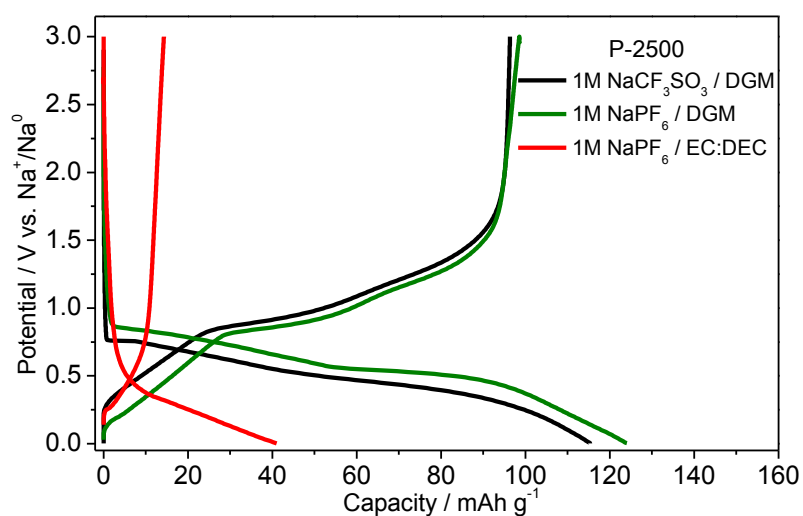


Fig.3A. Charge/discharge profile of coke (P2500) in sodium cells cycled at 1C rate in different electrolytes: a) $1 \text{ M NaCF}_3\text{SO}_3$ in DGM, b) 1 M NaPF_6 in DGM and c) 1 M NaPF_6 in EC:DMC (1:1).

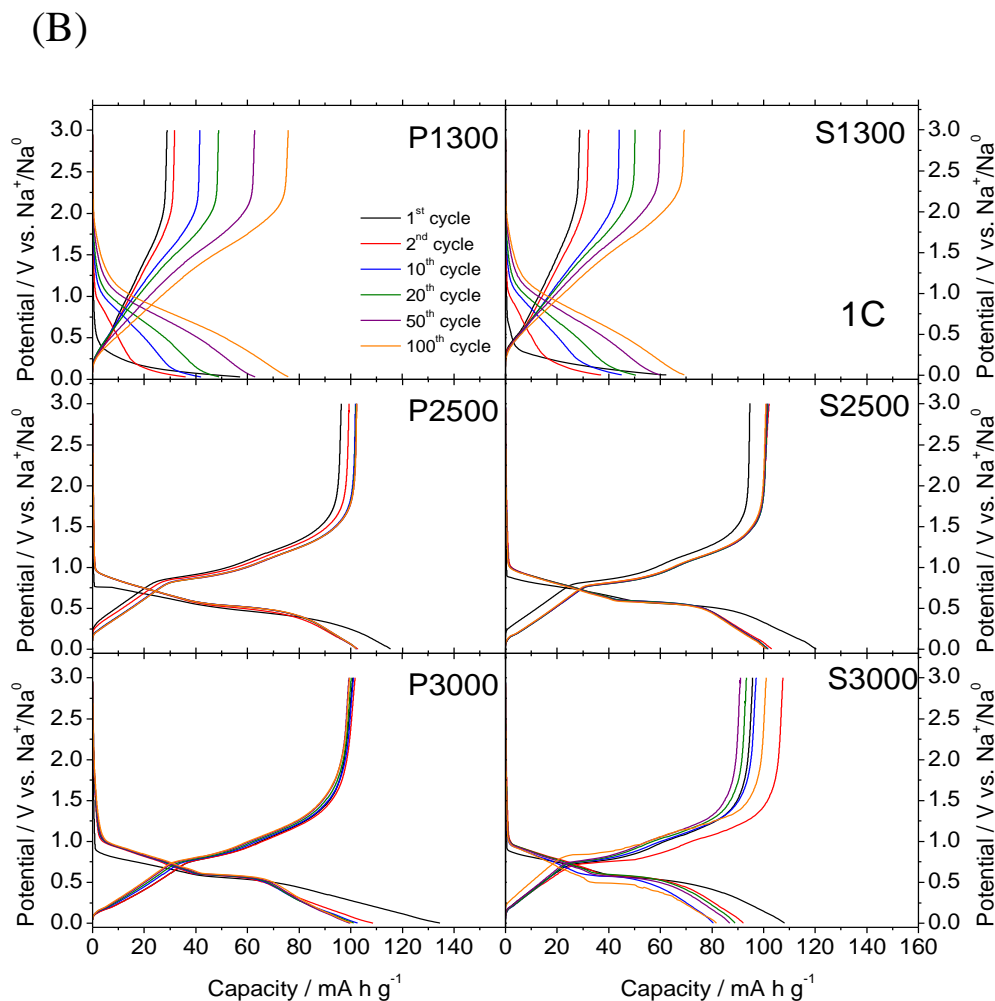


Fig.3B. Galvanostatic charge and discharge curves recorded at the 1st, 2nd, 10th, 20th, 50th and 100th cycle at a 1C rate in 1 M NaCF₃SO₃/DGM electrolyte for shale and coke obtained at 1300, 2500 and 3000 °C.

The capacity retention of half cells cycled at 1C can be observed in Fig. 4A. P1300 and S1300 evidenced that the electrode activation is also reflected in a continuous increase of the reversible capacity from the second cycle. Thus, the low capacity values recorded for the second cycle, close to 40 mA h g⁻¹ progressively increase to 93 and 77 mA h g⁻¹ for P1300 and S1300, respectively. To elucidate this question, the P1300 sample was cycled at a low rate, C/10, revealing a less enhanced decrease of capacity during the first cycles (Fig. 4A). Such response evidences the occurrence of kinetic impediments to sodium diffusion in this highly disordered carbon that prevent a suitable reversible capacity for high rates. The higher capacity of the P1300 coke prepared from a petroleum source could be ascribed to the less organized

morphology, as seen by SEM in Fig. 2. The larger void spaces yielded by the highly buckled graphenic layer may facilitate the sodium diffusion on prolonged cycling. Concerning the electrochemical behavior of samples annealed at 2500 and 3000 °C, a typical irreversible capacity is observed during the first cycle. Then, capacity stabilizes for a large number of cycles. P2500, S2500 and P3000 yielded reversible capacity values close to 100 mA h g⁻¹ after 350 cycles. These values are close to those reported for related graphitized compounds [26]. However, the irreversibility at the first cycle was lower for samples annealed at 2500 °C, as compared to P3000. Contrarily, S3000 delivered lower capacity values of ca. 88 mA h g⁻¹. Because of the good performance of P2500, this sample was selected for more exhaustive study of the rate capability at different kinetics (Fig. 4B). At the lowest rate of C/10, the specific reversible capacity is 110.7 mA h g⁻¹ while at the fastest rate of 1C is around 98–100 mA h g⁻¹. More importantly, a stable capacity retention can be obtained with negligible loss at different rates. The reversibility is demonstrated by the fact that the capacity of 100 mA h g⁻¹ is regained after 65 cycles at 1C rate.

Ex-situ XRD patterns were recorded for the S1300 and P1300 samples (Figs. S2a and S2b). For both samples, the first discharge of the electrodes involved an increase of turbostratic character reflected on the broadening of the 002 reflection. A significant band shifting of the 002 reflection to low angles from 25.4° to 24.9° is a direct proof of the true sodium intercalation between the graphenic layers (Fig. S2). On charge up to 3 V, a similar profile is observed for the pristine sample. This profile remained invariable up to 500th cycles for S1300, indicating that the resulting turbostratic structure is stable and allows a suitable sodium diffusion. Probably, this fact is also responsible for the capacity recovery demonstrated at C rate. In addition, the ex-situ XRD profile recorded on a P1300 electrode discharged at C rate reveals a smaller shifting of the 002 reflection than for the sample discharged at C/10. This behavior may be indicative of the steric impediments to the sodium diffusion when a high C rate is imposed to the cell.

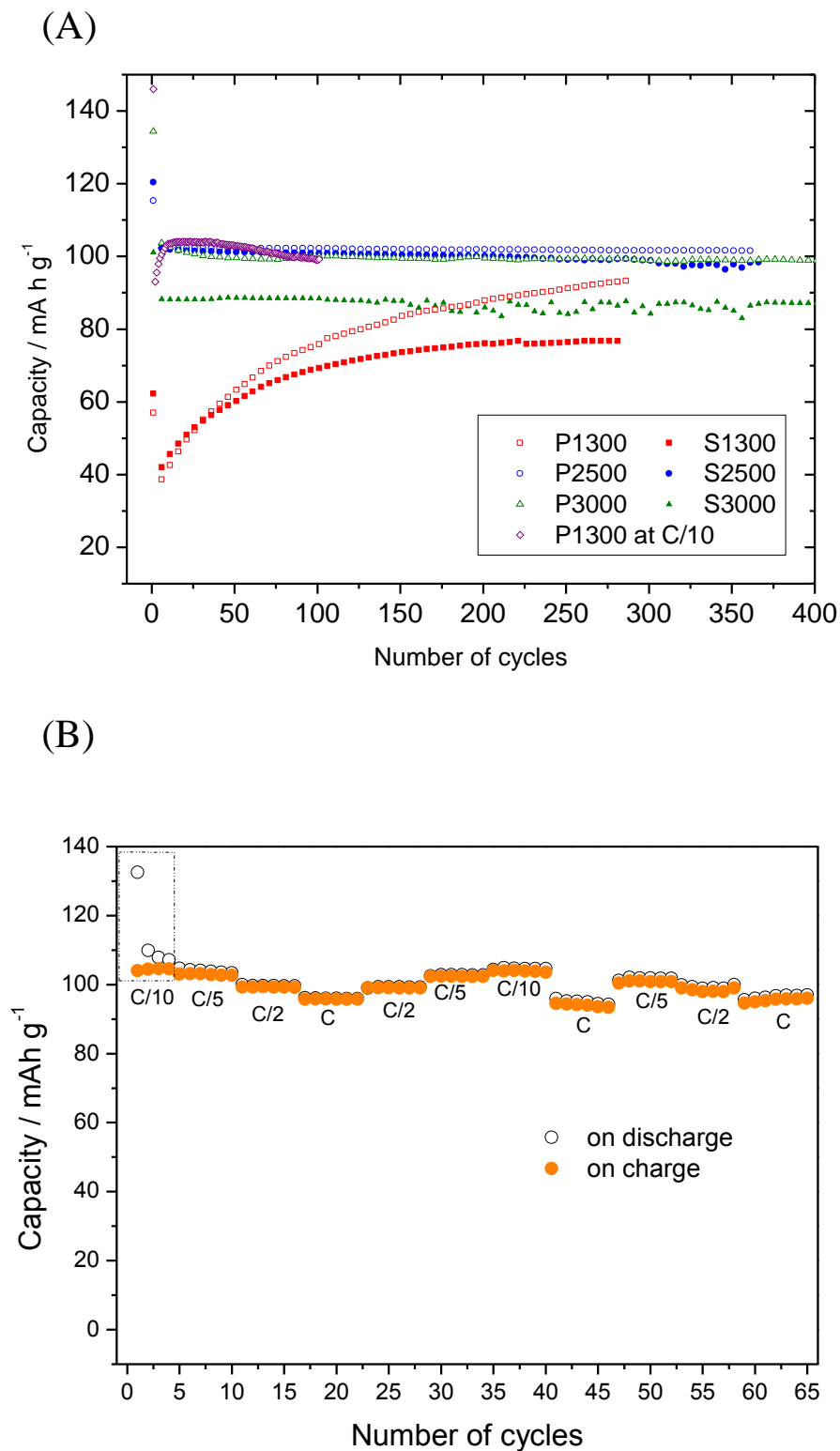


Fig.4. (A) Capacity versus the number of cycles of sodium cells assembled with P and S samples annealed at 1000, 2500 and 3000 °C. Kinetic rate: 1C. (B) Cycling performance of the P-2500 sample at different charge and discharge rates.

Similarly, ex-situ diffraction patterns were recorded for discharge and charge in sodium half-cells assembled with P2500 as working electrode (Fig. 5). After a first discharge, a new set of (00*l*) reflection appeared, which are indexed as belonging to the Stage-1 of the Na_x(DGM)₂C₂₀ compound [26,37]. A small diffraction peak at 23.5° (labeled with an arrow symbol in Fig. 5A) assigned to stage-2 is detected for the electrode discharged at 50 and 75 mA h g⁻¹ [37]. Besides, a narrow peak at ca. 9.05° (labeled with * symbol in Fig. 5A) is attributable to Na(DGM)_xOTf side product. Fig. S3 shows the XRD pattern of NaOTf after exposure to DGM during 50 h. The XRD profile for the charged electrode reveals a broadened 002 reflection, with a position corresponding to the pristine carbon. It evidences the reversibility of the insertion process. The enhanced broadening of this reflection involves a structural modification of the interlayer spacing to allow sodium diffusion.

The effect of cell relaxation on the stability of the sodium inserted phases was evaluated by recording the XRD patterns at different relaxation times after full discharge at C/10 rate (Fig. 5B). For 1 h relaxation, the electrode exhibited diffraction peaks typical of stage-1 as previously described. After 115 h relaxation, sodium diffusion is observed as the peaks coming from stage-1 are sifted to new positions ca. 23.3 and 29.4° belonging to stage-2 [26,37]. Then, for 180 of relax the progressive formation of the 002 peak ascribable to pristine carbon is reached.

In order to model the arrangement of sodium insertion between graphitic layers of P2500, a 1-D Patterson diagram along the c-axis direction was generated from the XRD (00*l*) peak intensities (Fig. 6A). To have comparative results, commercial graphite (KS6 from TIMCAL) was also evaluated (Fig. 6B).

Considering an interlayer distance of 11.7 Å the c-axis, in the unit cell, the Na-C distance is 5.85 Å (Fig. 6A and B). Also, three additional signals are observed at 2.93 Å, 5.27 Å and 8.55 Å for P2500 and at 2.84 Å, 5.59 Å and 8.33 Å for commercial graphite. These maxima are attributed C-C, C-O and O-O bonds coming from the two molecules of diglyme necessary to reach a stable solvation shell in dilute solution. Consequently, the assumption that two diglyme molecules are co-intercalated per alkali ion seems plausible.

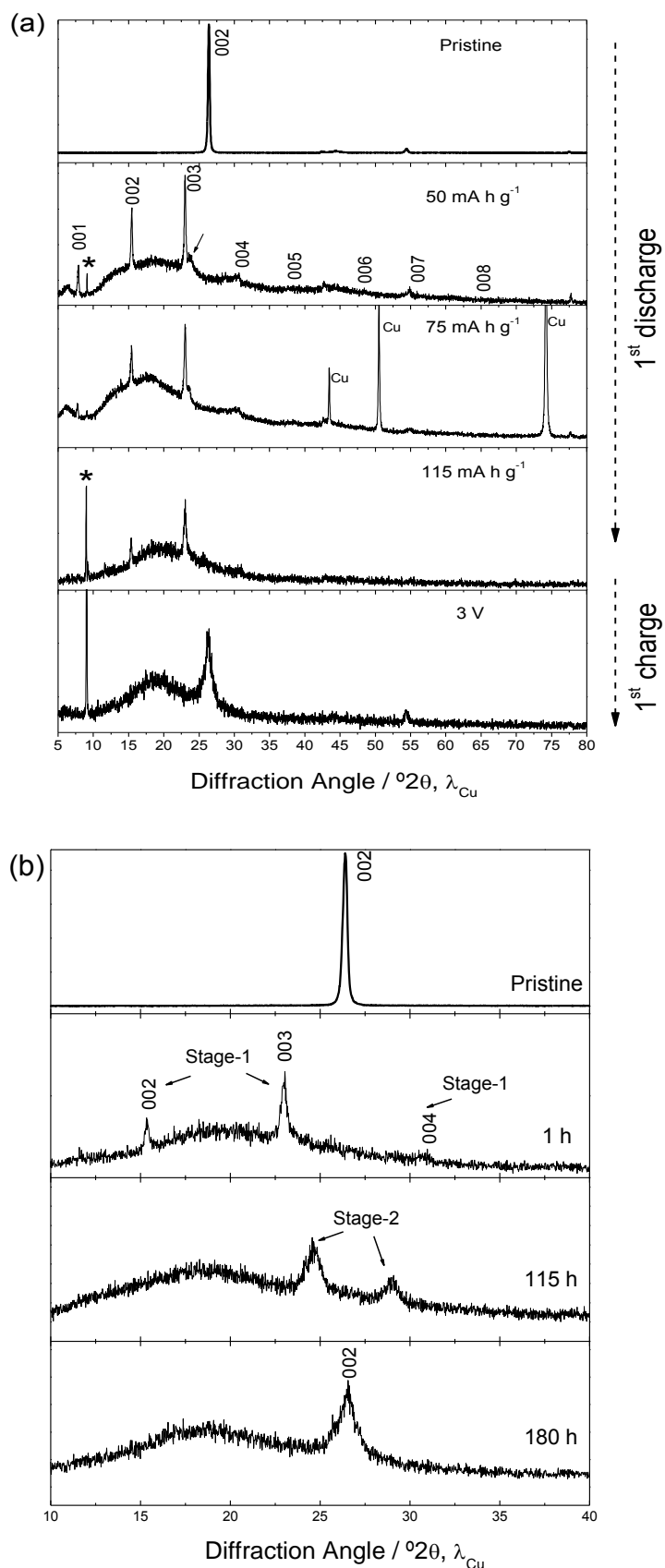


Fig.5. Ex-situ XRD patterns recorded for: (a) P2500 electrodes discharged and charged during the first and second cycles at 1C rate and (b) a comparison of the XRD patterns recorded after different relaxation time after complete first discharge at C/10 rate.

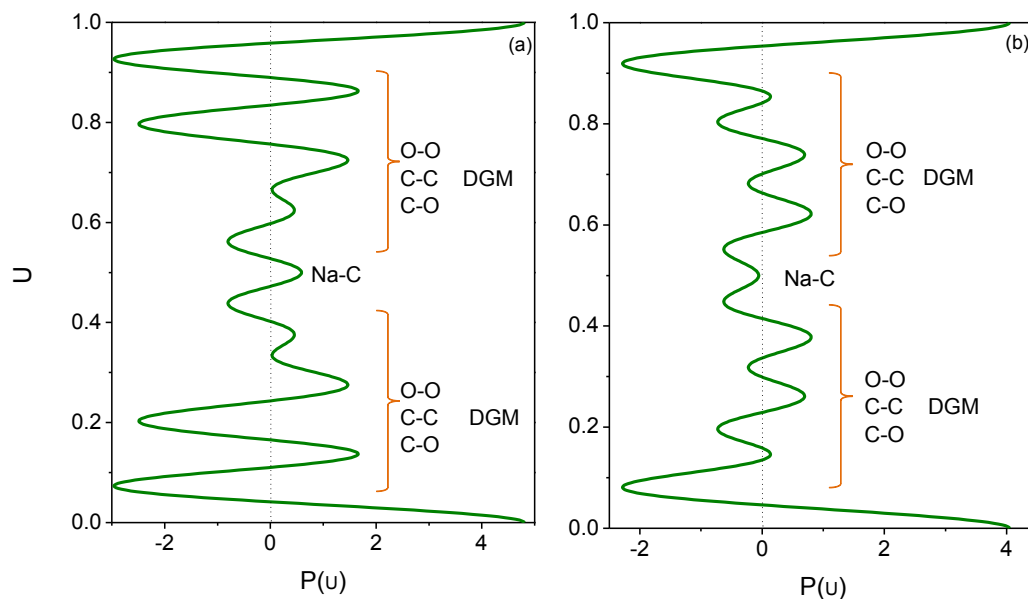


Fig.6. Patterson analysis of electron density after sodium insertion into (a) petroleum coke at 2500 °C and (b) commercial graphite (TIMKAL “KS6” for 135 mA h g⁻¹).

Possible changes in the molecular structure of diglyme upon co-intercalation with sodium have been studied by infrared spectroscopy. Fig. S4 and Fig. 7 show changes in diglyme conformation, which alter the OCCO torsional angles, induced by coordinating metal ions. In order to unveil this effect, we compared the FTIR spectra from 1700 to 800 cm⁻¹ of the electrolyte solution (1 M NaOTf in DGM), a freshly electrolyte soaked P2500 electrode before cell discharge, and a P2500 electrode discharged at 0.003 V. Some common and pronounced peaks related to surface species of DGM and NaOTf are observed. The vibrational bands of the triflate anion appear in the stretching region between 1300 and 1000 cm⁻¹, where the C-F stretching modes at 1273 cm⁻¹ and S-O stretching modes at 1174 and 1040 cm⁻¹ appeared. Also, symmetric bands of C-F and C-S are visible at 1232 cm⁻¹ (Fig. S4) [38]. Distinctive peaks of alkoxy surface species (1450–1350 cm⁻¹, δ CH₂, CH₃ and 1112 cm⁻¹ ν_{CO}) and various C-C stretch vibrations (977, 911 and 850 ν_{C-C}) are due to DGM [39]. For the fully discharged electrode, two new features are observed (Fig. S4 and Fig. 7). Firstly, the CH₂ in-plane bending or “scissors” region (1457 cm⁻¹) and the CH₂ wagging region (1365 cm⁻¹) increased their intensity upon complexation (Fig. S4 from ‘a’ to ‘c’) meaning a change in the molecular conformation. Secondly, the infrared spectrum of the fully discharged electrode revealed a new and strong band at 880 cm⁻¹ (Fig. 7). This

mode can be attributed to two diglyme molecules coordinated by a sodium ion, with a dihedral angle sequence of each diglyme molecule O-C-C-O (conformation about O-C bond and C-O bond is trans, and the conformation about the C-C is gauche) and O-C-C-O (idem as before, but with gauche-minus) as found previously in (diglyme)₂ LiSbF₆ crystal [40]. Previous studies have shown that ethylene oxide units with gauche OCCO torsional angles have bands in the range from 825 to 890 cm⁻¹ [41].

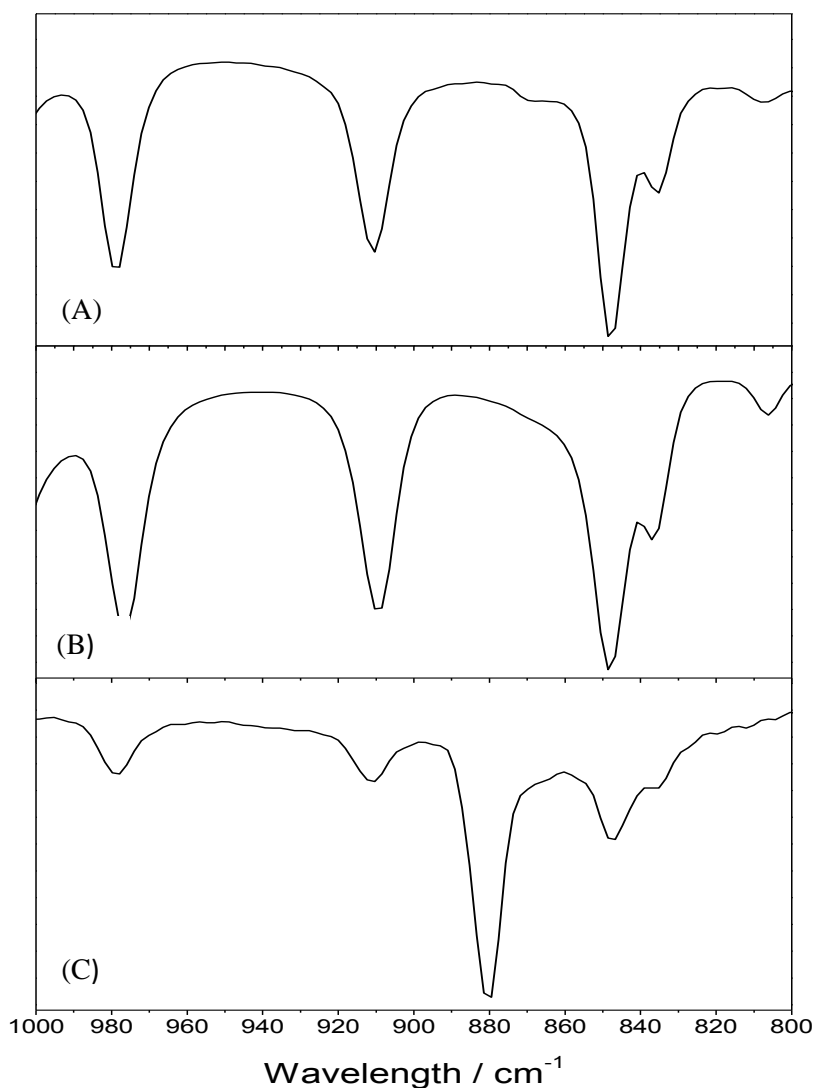


Fig.7. FTIR spectra from 1000 to 800 cm⁻¹ for: (A) the electrolyte (1M NaOTf in DGM), (B) P2500 electrode at 3.0 V before the discharge and (C) P2500 electrode discharged at 0.003V.

On the other hand, the TGA trace of a fully discharged electrode (P2500) was compared with diglyme solvent (Fig. S5e), the electrolyte solution (Fig. S5d) and sodium triflate (Fig. S5b). The decomposition of triflate occurs at ca. 500 °C. The weight loss ascribable to diglyme evaporation appears at similar temperatures when present (ca. 100 °C). The recordings were carried out under dynamic Ar atmosphere (20 mL min⁻¹), which decreases the standard boiling point of the solvent. The intercalated electrode exhibited a weight loss at this temperature of 55%, which is similar to the theoretical value for DGM/C₂₀ (DGM)₂Na.

Prompted by the promising behavior of sample P2500, a full sodium-ion cell was assembled using Na₃V₂(PO₄)₃ as a positive electrode. The latter material was chosen due to its low hysteresis between charge and discharge and excellent capacity retention on extended cycling [33]. Fig. 8 shows the galvanostatic charge and discharge profiles for positive and negative electrode versus a metallic sodium electrode acting as a reference. These curves are fairly coincident to those recorded for the sodium half-cells (Fig. 3A and B) and demonstrate that both electrodes perform low hysteresis between charge and discharge. A suitable match between the active masses of the positive and negative electrodes is also required. For this reason, several m⁺/m-ratios and cut-off voltages were essayed until reaching the maximum deliverable capacity. The full cell delivered an initial capacity of 75 mA h g⁻¹ based on the mass of cathode active material, and an average discharge potential of 2.7 V. These data allow inferring an energy density value of 202 W h kg⁻¹ when cycling at C rate. This extraordinary performance of the petroleum coke promises new avenues for the development of reliable and cost-effective Na ion batteries. Indeed, different sodium full cells have been already reported in the literature. Kim et al. based their cell on graphite as anode and Na_{1.5}VPO_{4.8}F_{0.7} cathode, delivering an energy density of 120 W h kg⁻¹ referred to the total mass of electroactive materials (anode plus cathode) at a current rate of 0.5 A g⁻¹ [42]. Zhu et al. coupled graphite anode with a Na₃V₂(PO₄)₃@C composite cathode showing an average operation voltage of ~2.2 V and a discharge capacity of ~90 mA h g⁻¹ (on the basis of the graphite mass) [37]. The reason of the outstanding electrochemical behavior is due to the fact of having flat plateau in the full cell (Fig. 8), which is a desired feature for designing commercial products.

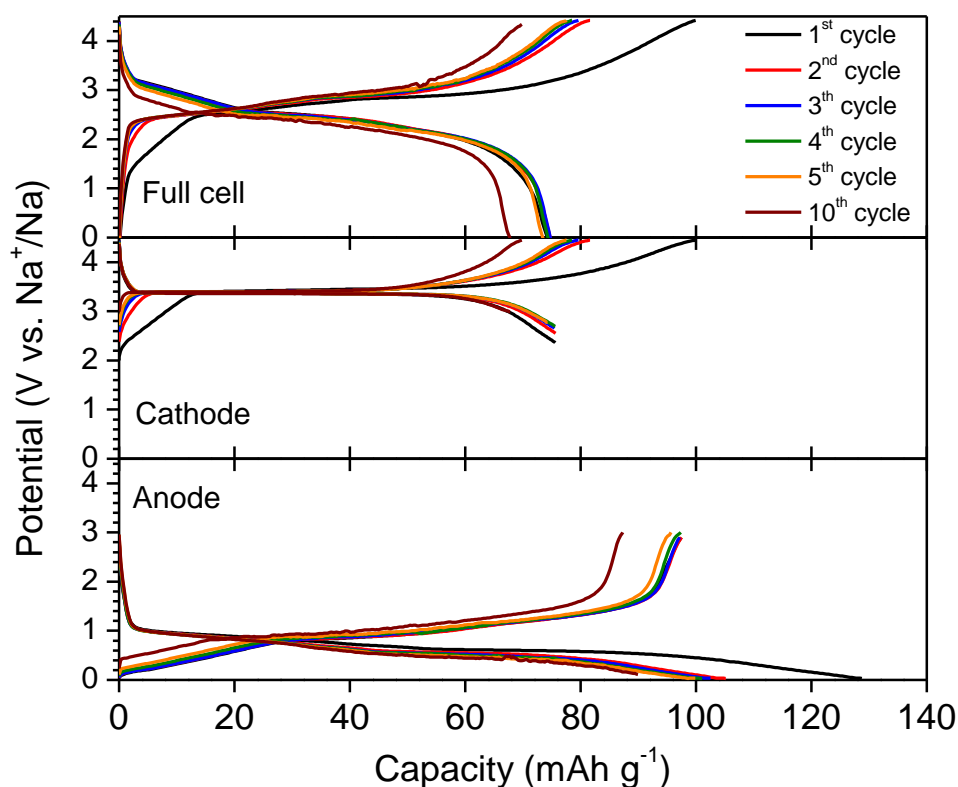


Fig.8. Galvanostatic cycling of a full sodium-ion cell $\text{Na}_3\text{V}_2(\text{PO}_4)_3/\text{C}/\text{P2500}$ recorded at 1C. Charge and discharge curves for $\text{Na}_3\text{V}_2(\text{PO}_4)_3/\text{C}$ versus reference, P2500 versus reference and full cell are plotted separately.

Due to their interesting electrochemical performance, many layered oxides and polyanionic insertion compounds have been proposed in the literature as positive electrodes for Na-ion batteries [43–45 and references therein]. Table 2 displays the reported average voltage and capacity of a selection of these cathodes, as well as the expected operational voltage and energy density of the full cell when combined with the petroleum coke studied in this work. Theoretical values of operating voltage of the full cell as high as 3.9 V and energy densities close to 400 W h kg^{-1} can be expected in some cases, which gives interest to the negative electrode material reported here. Also, the experimental results obtained with the $\text{Na}_3\text{V}_2(\text{PO}_4)_3$ positive electrode selected for the tests described in this work are better than those calculated in Table 2 in some cases.

Cathode	Average voltage of the cathode (V)	Capacity of the cathode (mAhg ⁻¹)	Voltage of the full cell (V)	Energy density of the full cell (W h kg ⁻¹)
Na₃V₂(PO₄)₃^a	3.4	75	2.7	202
Na_{1.5}VPO_{4.8}F_{0.7}Ref. [42]	3.7	120	3.1	372
Na_xCoO₂ Ref. [43]	2.7	45	2.1	95
Na_{2/3}Fe_{1/2}Mn_{1/2}O₂Ref. [43]	2.8	180	2.2	396
Na_{2/3}Mn_{1/2}Co_{1/2}O₂Ref. [43]	2.7	120	1.9	228
NaFeO₂ Ref. [44]	3.3	82	2.7	221
Na_{2+2x}Fe_{2-x}(SO₄)₃Ref. [44]	3.9	100	3.3	330
NaFePO₄Ref. [44,45]	2.8	128	2.2	282
Na₂FePO₄F Ref. [44,45]	3.2	110	2.6	286
Na₄Co₃(PO₄)₂(P₂O₇) Ref. [45]	4.5	97	3.9	378

^a Experimental results reported in this work.

3.2.4 Conclusions

With the aim of finding inexpensive and performance materials for the negative electrode of sodium-ion batteries, several materials derived from waste side products of the petroleum industry and carbonized at different temperatures have been examined. Besides the higher level of graphitization and more buckled layered morphology as compared to carbons obtained from shale-oil, their electrochemical performance was enhanced by the adept selection of electrolytic solution. The use of diglyme based electrolytes (NaOTf in DGM and NaPF₆ in DGM), was crucial to achieve Na (dgm)₂⁺ intercalation, which resulted in higher capacities and excellent retention as compared to standard carbonate based solvents. Regarding the intercalation reaction in the studied materials, FTIR and TGA and XRD techniques have unambiguously shown the progressive and reversible formation of the Na_x(DGM)₂C₂₀ stage 1 with two diglyme molecules co-intercalated per alkali ion, which is contrast with commercial graphite. Eventually, the practical feasibility of petroleum coke in NIB full cells was confirmed by combining with a Na₃V₂(PO₄)₃ cathode, which could deliver an energy of

202 W h kg⁻¹ with an average discharge voltage of 2.7 V under C rate. This suitable electrochemical performance encourages regarding P2500 carbon material for the development of sustainable, reliable and cost-effective Na ion batteries.

Acknowledgements

The authors are grateful to Ministerio de Economía y Competitividad and FEDER funds (MINECO) (MAT2014–56470-R) and Junta de Andalucía for financial support (FQM288 and FQM7206). We also thank SCAI (UCO Central Service for Research Support), the European Research Institute ERI-ALISTORE and Institute of Fine Chemistry and Nanochemistry. Sincere thanks to JSC “Ukrainian graphite” for the carbonaceous samples and a grant from the Erasmus+: Erasmus Mundus Joint Master Degree (EMJMD) “Materials for Energy Storage and Conversion” (MESCE).

3.2.5 References

1. A. Yaksic, J.E. Tilton, *Resour. Policy* 34 (2009) 185.
2. C. Wadia, P. Albertus, V. Srinivasan, *J. Power Sources* 196 (2011) 1593.
3. B. Andersson, I. Råde, *Transp. Res. Part D. Transp. Environ.* 6 (2011) 297.
4. M.C. McManus, *Appl. Energy* 93 (2012) 288.
5. M. D. Gerst, T. E. Graedel, *Environ. Sci. Technol.* 42 (2008) 7038.
6. B. L. Ellis, L. F. Nazar, *Curr. Opin. Solid State Mater. Sci.* 16 (2012) 168.
7. V. Palomares, M. Casas-Cabanas, E. Castillo-Martínez, M. H. Han, T. Rojo, *Energy Environ. Sci.* 6 (2013) 2312.
8. N. Yabuuchi, K. Kubota, M. Dahbi, S. Komaba, *Chem. Rev.* 14 (2014) 11636.
9. M. D. Slater, D. Kim, E. Lee, C. S. Johnson, *Adv. Funct. Mater.* 23 (2013) 947.
10. H. Pan, Y. S. Hu, L. Chen, *Energy Environ. Sci.* 6 (2013) 2338.

11. J. T. Kummer, N. Weber, Battery having a molten alkali metal anode and molten sulfur cathode, U.S. Patent U.S. 3413150, 1968.
12. J. L. Sudworth, *J. Power Sources* 100 (2001) 149.
13. H. Zou, S. Li, X. Wu, M. J. McDonald, Y. Yang, *ECS Electrochem. Lett.* 4 (2015) A53.
14. X. Wu, J. Guo, D. Wang, G. Zhong, M. J. McDonald, Y. Yang, *J. Power Sources* 281 (2015) 18.
15. M. Kalapsazova, G. F. Ortiz, J. L. Tirado, O. Dolotko, E. Zhecheva, D. Nihtianova, L. Mihaylov, R. Stoyanova, *ChemPlusChem* 80 (2015) 1642.
16. M. Doeff, Y. P. Ma, S. J. Visco, L. C. Dejonghe, *J. Electrochem. Soc.* 140 (1993) L169.
17. S. Komaba, T. Itabashi, M. Watanabe, H. Groult, N. Kumagai, *J. Electrochem. Soc.* 154 (2007) A322.
18. D. A. Stevens, J. R. Dahn, *J. Electrochem. Soc.* 147 (2000) 1271.
19. R. Alcántara, J. M. Jiménez-Mateos, P. Lavela, J. L. Tirado, *Electrochem. Commun.* 3 (2001) 639.
20. A. Ponrouch, M. R. Palacín, *Electrochem. Commun.* 54 (2015) 51.
21. R. Alcántara, F. J. Fernández Madrigal, P. Lavela, J. L. Tirado, J. M. Jiménez Mateos, C. Gómez de Salazar, R. Stoyanova, E. Zhecheva, *Carbon* 38 (2000) 1031.
22. R. Alcántara, P. Lavela, G. F. Ortiz, J. L. Tirado, R. Menéndez, R. Santamaría, J. M. Jiménez-Mateos, *Carbon* 41 (2003) 3003.
23. R. Alcántara, P. Lavela, G. F. Ortiz, J. L. Tirado, *Solid-State Lett.* 8 (2005) A222.
24. A. Ponrouch, A. R. Goñi, M. R. Palacín, *Electrochem. Commun.* 27 (2013) 85.

25. M. Dahbi, N. Yabuuchi, K. Kubota, K. Tokiwa, S. Komaba, *Phys. Chem. Chem. Phys.* 16 (2014) 15007.
26. B. Jache, P. Adelhelm, *Angew. Chem. Int. Ed.* 53 (2014) 10169.
27. W. S. Fonseca, X. Meng, D. Deng, *ACS Sust. Chem. Eng.* 3 (2015) 2153.
28. X. Meng, P. E. Savage, D. Deng, *Environ. Sci. Technol.* 49 (2015) 12543.
29. I. Elizabeth, B. P. Singh, S. Trikha, S. Gopukumar, *J. Power Sources* 329 (2016) 412.
30. E. Fitzer, K. H. Kochling, H. P. Boehm, H. Marsh, *Pure Appl. Chem.* 67 (1995) 473.
31. A. Oberlin, *Carbon* 22 (1984) 521.
32. E. M. Baitinger, V.A. Ivanov, V.A. Kul'bachinskii, S.V. Shulepov *Fiz. Tverd. Tela Peterbg.* 32 (1990) 151.
33. R. Klee, P. Lavela, M. J. Aragón, R. Alcántara, J. L. Tirado, *J. Power Sources* 313 (2016) 73.
34. F. Tuinstra, J. I. Koenig, *J. Chem. Phys.* 53 (1970) 1126.
35. A. Sadezky, H. Muckenhuber, H. Grothe, R. Niessner, U. Pöschl, *Carbon* 43 (2005) 1731.
36. A. C. Ferrari, J. Robertson, *Phys. Rev. B* 61 (2000) 14095.
37. Z. Zhu, F. Cheng, Z. Hu, Z. Niu, J. Chen, *J. Power Sources* 293 (2015) 626.
38. D. H. Johnston, D. F. Shiver, *Inorg. Chem.* 32 (1993) 1045.
39. D. Aurbach, E. Granot, *Electrochim. Acta* 42 (1997) 697.
40. V. Seneviratne, R. Frech, J. E. Furneaux, M. Khan, *J. Phys. Chem. B* 108 (2004) 8124.
41. H. Matsuura, K. J. Fukuhara, *Polym. Sci. B Polym. Phys.* 24 (1986) 1383.

42. H. Kim, J. Hong, Y. U. Park, J. Kim, I. Hwang, K. Kang, *Adv. Funct. Mater.* 25 (2015) 534.
43. M. H. Han, E. Gonzalo, G. Singh, T. Rojo, *Energy Environ. Sci.* 8 (2015) 81.
44. P. Barpanda, *Chem. Mater.* 28 (2016) 1006.
45. H. Kim, H. Kim, Z. Ding, M. H. Lee, K. Lim, G. Yoon, K. Kang, *Adv. Energy Mater.* (2016) 1600943.

3.2.6 Supplementary information

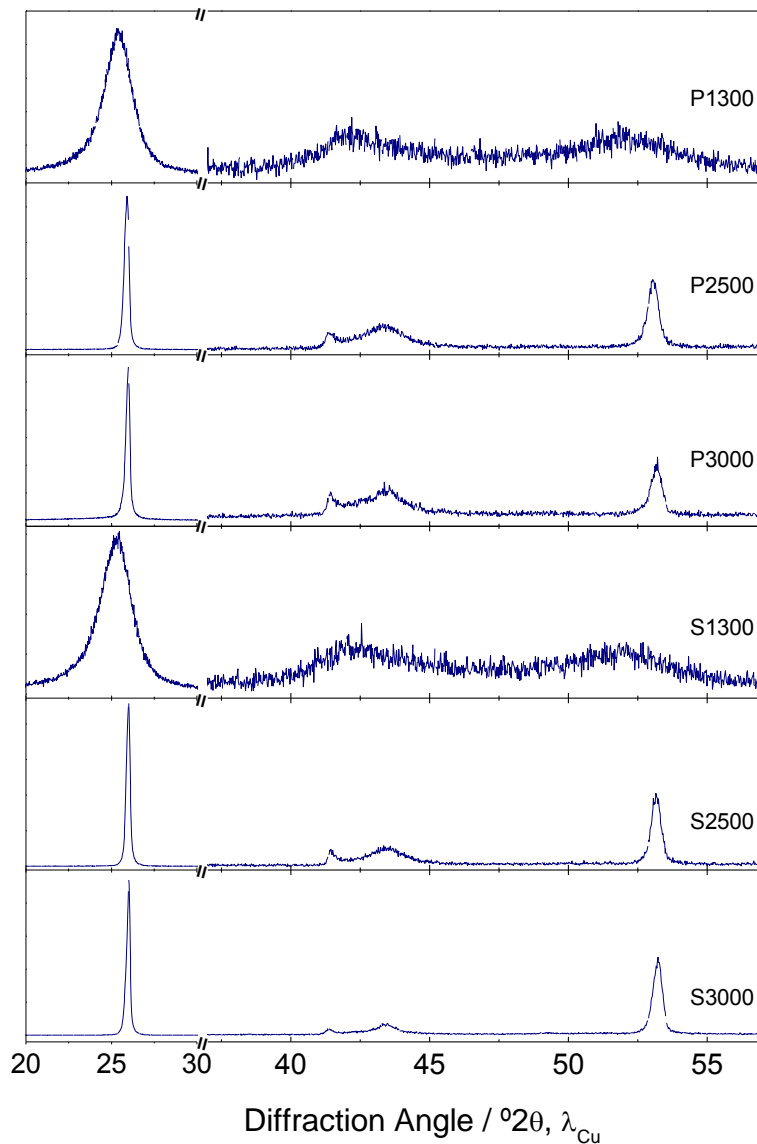


Fig.S1. X ray diffraction patterns of carbon samples prepared from a petroleum precursor (P samples) or an oil shale precursor (S samples) annealed at 1300, 2500 and 3000 °C.

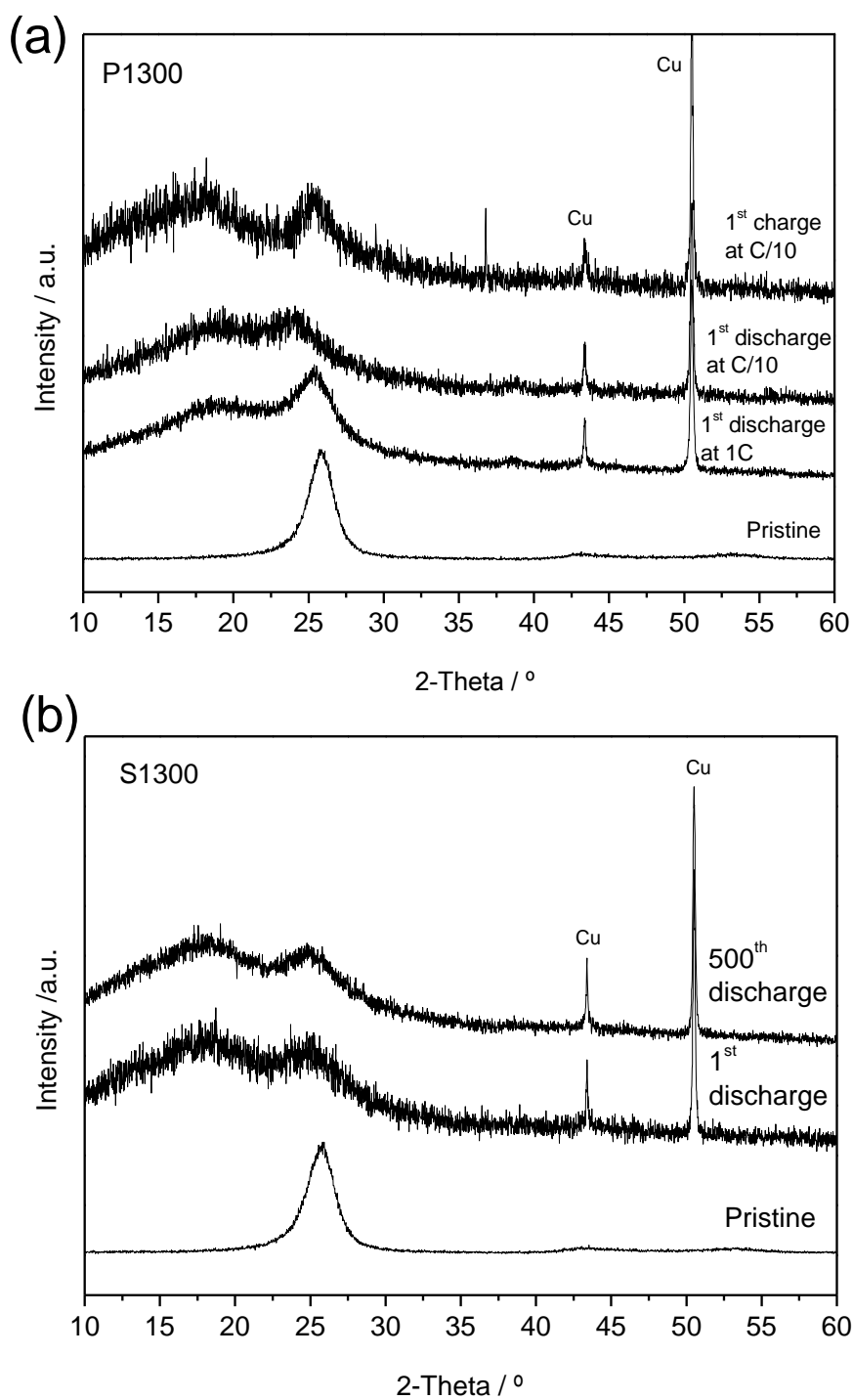


Fig.S2. Ex-situ XRD patterns recorded for cycled electrodes: a) P1300 at C/10 and 1C during the first cycle; b) S1300 discharged after the first and five hundredth discharge at 1C. The appearance of a highly broadened band centered at ca. 17° is due to the kapton tape used for the ex-situ measurements.

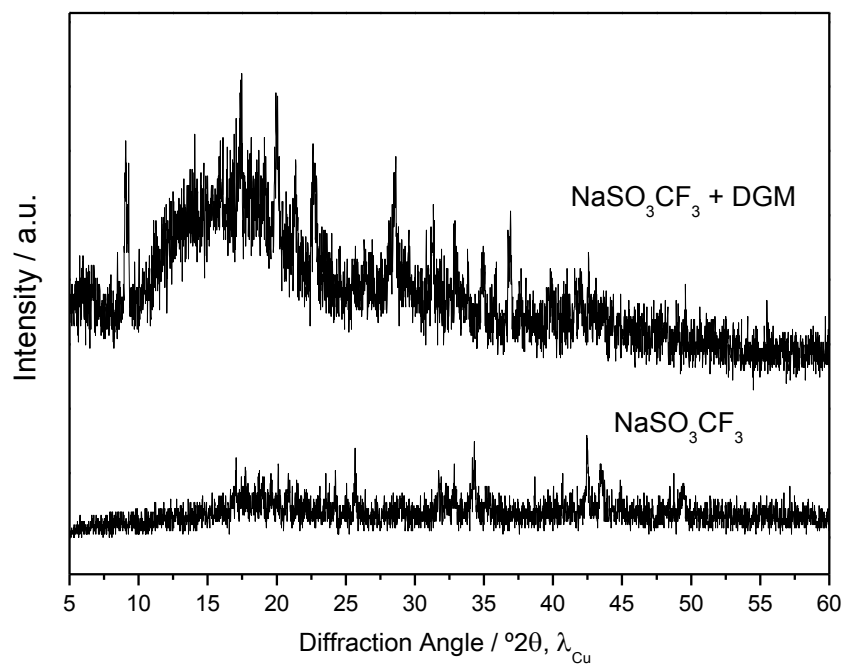


Fig.S3. XRD patterns of sodium triflate (NaOTf, solid electrolyte) before and after exposure to diglyme (DGM) during 50 h.

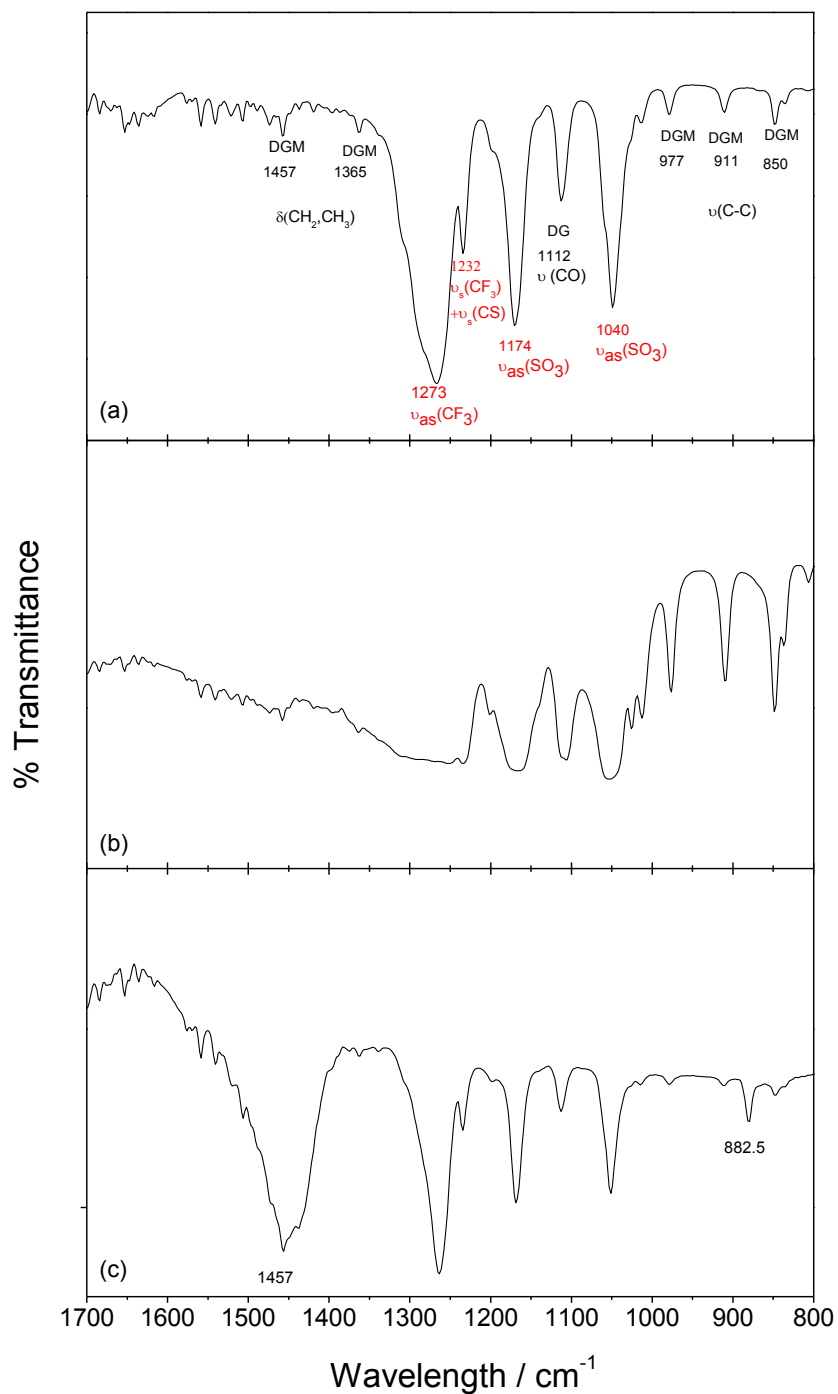


Fig.S4. FTIR spectra from 1700 to 800 cm^{-1} for: (a) the electrolyte (1M NaOTf in DGM), (b) PC2500 electrode at 3.0 V before the discharge and (c) PC2500 electrode discharged at 0.003V.

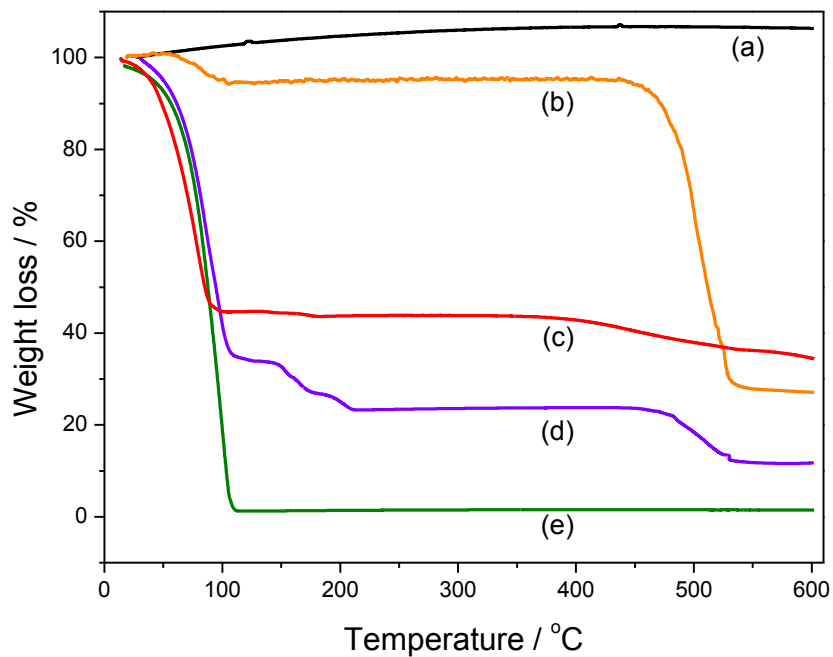


Fig. S5. TGA analyses of: (a) original petroleum coke (P2500), (b) sodium triflate (NaOTf), (c) P2500 discharged at 0.003 V using as electrolyte 1M NaOTf in DGM, (d) 1M NaOTf in DGM, and (e) DGM.

3.3 On the reliability of sodium co-intercalation in expanded graphite prepared by different methods as anodes for sodium-ion batteries

Marta Cabello ^a, Xue Bai ^a, Taras Chyrka ^b, Gregorio F. Ortiz ^a, Pedro Lavela ^a, Ricardo Alcántara ^a, José L. Tirado ^a.

^aLaboratorio de Química Inorgánica. Universidad de Córdoba. Edificio C3, Campus de Rabanales. Spain

^bScientific research centre “Resource saving technologies”, National technical university of Ukraine “Kyiv polytechnic institute”, Kyiv, Ukraine.

Abstract

Recent improvements of sodium ion batteries have been achieved by the use of graphitic carbon as an anode and glyme-based electrolytes. In this work, expanded graphites are prepared by thermal expansion, Broddie and Hummer’s modified methods. Their structural, morphological and electrochemical properties are compared with those of the original natural graphite. XRD patterns, XPS and Raman spectra corroborate the presence of graphite oxide intermediates and reveal different reduced forms of expanded graphite which can affect the sodium insertion properties. The use of sodium triflate in diglyme enhanced the electrochemical performance in terms of delivering a flat plateau at ca. 0.65 and 0.55 V in discharge/charge cycles. The thermally expanded graphite increased the capacity and efficiency from 100 to 115 mA h g⁻¹ and from 93 to 96 % over 100 cycles when cycled at C rate as compared to natural graphite. Ex-situ XRD patterns reveal the presence of new set of reflections ascribable to sodium ordering in different stages as evidenced by the calculated Patterson diagrams. The new results described here would account for development of carbon-based material and their prospects and challenges for sodium ion battery anodes.

Keywords

Thermally expanded graphite; insertion; sodium ion battery; stages



Journal of The Electrochemical Society 164 (14) (2017) A3804-
A3813

3.3.1 Introduction

The sodium intercalation into graphite is still one of the most interesting and unusual in the solid state chemistry of intercalation compounds. Neither ionic nor hard sphere model theory explains why the liquid phase interaction of molten sodium with graphite provides only high-stage compositions [1,2]. This effect contrasts with that for other alkali metals [3], in which first-stage graphite intercalation compounds (GICs) can be easily obtained. Udod suggested that the discrepancy between the size of sodium atoms and the distances between potential minima in the graphite sheet causes the absence of low-stage Na-GICs [4].

Graphite has a long-range-ordered layered structure where Li^+ ion can be easily intercalated between the graphene layers by electrochemical means. The main lithium insertion reaction occurs at a flat plateau around 0.2 V, and the capacity is 372 mA h g^{-1} [6]. Unlike, the graphite anode does not intercalate sodium to any appreciable extent. The galvanostatic curves during the full sodiation/desodiation shows a monotonic voltage curves, which capacity is lower than 35 mA h g^{-1} [7,8]. This normally refers to the standard electrolytes that are based on organic carbonates (EC ethylene carbonate, DMC dimethylcarbonate) and lithium salts (LiPF_6) or sodium salts (NaPF_6).

In the search for alternative secondary batteries that will replace lithium ion batteries (LIBs), sodium ion batteries (SIBs) have received attention due to the following reasons: (i) abundance of sodium sources (it is the 4th most abundant element in the earth crust), (ii) the low cost of sodium compare to lithium, especially for large-scale electric storage applications, and (iii) the similar chemistry of sodium and lithium [9]. So far, several issues have scoffed at the optimal performance of graphite anodes at both lithium ion (LIB) and sodium ion batteries (SIB). For instance: (i) the risk of inserting alkali metals near to 0 V is known to jeopardize the safety in batteries, and (ii) the lack of a flat plateau during sodium insertion hinders the manufacturing of carbon-based commercial sodium-ion batteries. The engineering knowledge developed until lately for successful SIBs can be influenced to ensure rapid progress in this area, although distinct electrolytes and functional carbon materials will be required for dual intercalation systems based on sodium.

Regarding the electrolyte, systems based on poly(ethylene oxide), PEO, with dissolved alkali metal salts have received significant attention as polymer electrolytes [10]. Glymes are glycol dimethoxy ethers with the general formula $\text{CH}_3(\text{OCH}_2\text{CH}_2)_n\text{OCH}_3$, which are PEO analogs with low molecular weight ($n < 6$) [11]. Glymes based electrolytes have been recently proposed as new electrolyte for SIB [12,13]. Indeed, Kim et al. reported unusual Na storage behavior in natural graphite through Na^+ -solvent co-intercalation combined with pseudocapacitive behaviors using ether-based electrolytes [14,15]. Jache et al. demonstrated that graphite may insert sodium by using cointercalation phenomena in a diglyme-based electrolyte [16]. Zhu et al. showed the sodium storage performance of graphite in linear ether-based electrolytes using sodium perchlorate and/or sodium triflate in tetraglyme (TGM), diglyme (DGM), and 1,2-dimethoxyethane (DME) [17]. However, the mechanism of ionic transport is not well already understood. Some results revealed that in polymer electrolytes with bendable backbones, the ionic transport is highly coupled to the relaxation processes of the polymer backbone [18,19]. Also, it is suggested that the anion plays a role in the transport of cations, either through correlated motion of cations and anions or via transport of cation-anion clusters [10,20,21].

Regarding the carbon material, the influence of several factors such as heteroelement contents [8,22], structural differences in soft and hard carbons [8,23-25], morphological properties (nanowires, nanotubes, microbeads reduced graphene oxides or hollow carbon nanoparticles) [26-32], have been investigated as anodes for NIBs using standard electrolytes. Nonetheless, it is needed a further progress in the preparation of C-based materials.

The Na-ion battery system is potentially promising power sources for encouraging the substantial use of low-cost energy storage systems. The design of a full cell with stable energy density requires using suitable materials exhibiting flat plateau. While for the cathode there are many compounds showing flat plateau, in the anode this characteristic has been barely reported.

In this work we report the use of expanded graphite as a Na-ion battery anode. They are obtained from natural graphite (GSM) using three different approaches: i) by means of fast heating of graphite bisulfate precursors, ii) Brodie and iii) Hummer's modified methods. The interlayer spacing of expanded graphite can be tailored by

controlled oxidation and reduction processing. An entire physicochemical and electrochemical characterization of the electrodes is presented. The insertion properties of sodium into different kind of graphite are described by electrochemical means. We have found that using diglyme-based electrolyte (different to standard electrolytes) is possible to achieve flat plateau in a safe voltage windows during cycling.

3.3.2 Experimental

Raw material is natural flake crystalline graphite (GSM). Thermally expanded graphite (TEG) is obtained by fast heating of graphite bisulfate at 1400 °C during less 1 s. The thermal treatment can be described as following (Fig. S1). Using compressed air, the dried oxidized graphite is supplied with speed of 1 m s⁻¹ through the nipple 1 to the mixing chamber 2, where simultaneously primary air is supplied to for combustion. Additionally to the chamber 2, secondary air is going through the nipple 3 composing necessary stoichiometric ratio 1:10 (natural gas-air). Gas is supplied through the nipple 4 to the chamber 2. Obtained mixture is passing to the turbulent chamber 5, where spontaneous combustion occurs that causes temperature rise up to 1400 °C. During short time intercalated compounds (sulfuric acid) decompose converting to the gas products and cause expansion of graphite. Thermally expanded graphite surrounded by combustion products goes out to the burning chamber, where particulate calcination occurs. Then graphite is directed to the calcinating furnace.

Another different procedure to get expanded graphite is based on a two-step oxidation-reduction process. For that purpose, the Brodie [33] and Hummer's [34] modified methods were used to compare the effects on the carbon structure with the previous method. For Brodie's method, natural graphite GSM (1 g), nitric acid 65 % (30 ml) and sodium chlorate (7.5 g) were used. This mixture was magnetically stirred (24, 92, and 144 h) at room temperature and washed in distilled water until reaching a neutral pH. Then, the graphite oxide (GO) was dried at 60 °C overnight. Eventually GO is thermally reduced (500, 1000 and 1300 °C) under Ar atmosphere for 3 h.

For Hummer's method, natural graphite GSM (1g) and 0.5 g of NaNO₃ were added into 23 mL of sulphuric acid (98%) in a round-bottomed flask that was

previously cooled into an ice bath for 20 min ensuring temperature about 5 – 7 °C. Then, three grams of KMnO_4 were slowly added into the mixture while stirring, keeping the temperature at about 5 – 7 °C. This mixture is stirred during 30 min under the ice bath to release gas under continuous stirring. Then, distilled water (46 mL) was added slowly, which produced a rapid increase in the solution temperature. The reaction was held for 30 min to increase the oxidation degree of the GO. Afterwards, 140 mL of distilled water and 20 mL of hydrogen peroxide (H_2O_2 , %) are added to the solution. In order to wash the solid, the resultant product was transferred to a beaker containing 150 mL of water and then it was settle down overnight and water was poured. The last step was repeated until the supernatant water was pH neutral. After that, the GO is dried in air atmosphere at 60 °C overnight. Eventually, oxidized graphites were thermally reduced (500, 1000 and 1300 °C) in Ar atmosphere for 3h. For the sake of clarity, the samples are labeled as GSM-B and GSM-H for the as-prepared oxidized graphite and GSM-BR and GSM-HR for the expanded (reduced) graphite according to Brodie and Hummer's modified method, respectively.

The powders were checked by X-ray powder diffraction (XRD) on a BrukerD8 Discover diffractometer using monochromatic $\text{CuK}\alpha$ radiation equipped with a LYNXEYE XE - High-Resolution Energy-Dispersive 1-D Detector within a 2θ angle range between 5 and 80°. Ex-situ XRD measurements were performed using Kapton tape to prevent air contamination of the samples. Raman spectra were recorded in a Renishaw Raman instrument (InVia Raman Microscope) in the range of 750 – 2000 cm^{-1} using a green laser light excitation source (532 nm) and equipped with a Leica microscope. The profiles were decomposed with a Peakfit v.4.12 software package. X-ray photoelectron spectroscopy (XPS) measurements were performed on a SPECS Phoebos 150MCD instrument using Mg $\text{K}\alpha$ source (1253.6 eV) and a chamber pressure of $4 \cdot 10^{-9}$ mbar. The C1s peak at 284.6 eV of adventitious carbon was used as a reference. The CasaXPS version 2.3.16 PR1.6 was used for the fitting of the spectra. The microstructure was examined by field-emission scanning electron microscope JSM-7800F (FE-SEM).

The electrochemical measurements were performed with SwagelokTM type cells assembled in an argon-filled glove box (MBraun Lab master 130). For this purpose, carbon-based electrodes were composed by active material (92%) and PVDF

(polyvinylidene fluoride) (8%). The electrode is vacuum dried at 120 °C for at least two hours. The sodium half cell consists of metallic sodium as anode (disc of 9 mm), the electrolyte, and the C-based electrode as cathode. The electrodes were separated by glass fiber disks (GF/A-Whatman) impregnated in the electrolyte solution. The cells were assembled in an argon filled glove box under controlled O₂ (2 ppm) and H₂O (1 ppm) traces. The sodium half cells were cycled by the galvanostatic method between 0.003 and 3.0 V at different rates (C/10, C/2, C and 2C). All the electrochemical experiments were monitored in a galvanostat/potentiostat VMP system. Several electrolyte solutions were tested: (i) 1 M NaOTf (NaCF₃SO₃ or sodium triflate, 98%, Aldrich) dissolved in DGM (diglyme 99%, Sigma-Aldrich), (ii) 1 M NaPF₆ (99%, Strem Chemicals) dissolved in DGM, (iii) 1 M NaPF₆ dissolved in EC:DEC (99%, Aldrich) and 1 M NaClO₄ in EC:DEC. The melting and boiling points of the diglyme are – 64 °C (209 K) and 162 °C (435 K), respectively. The electrolyte based on NaClO₄ in PC (propylene carbonate) is not studied in these experiments because the PC solvent can be co-intercalated into graphite causing exfoliation [35].

3.3.3 Results and discussion

Natural graphite (GSM) revealed an intense crystalline (002) peak at 26.55° corresponding to a interlayer distance of $d_{002} = 3.357 \text{ \AA}$ [36,37] and a small shoulder at 26.2° (Fig. 1 and Fig. S2). Due to the oxidation and subsequent partial reduction of graphite, a shifting and broadening of the (002) peak is observed. The thermally expanded graphite (TEG) exhibits an asymmetric reflection at 26.28° and a shoulder at 26.53°. It involves a slight increase of the interlayer distance ($d_{002} = 3.388 \text{ \AA}$) as compared to GSM, while the crystallite size (L_c) decreased from 37.65 nm to 17.86 nm for TEG (Table S1). The calculated unit cell parameters are included in Table S1. When using Hummer's modified method, the oxidized graphite is successfully formed (sample labeled as GSM-H(1h)) as evidenced by the development of the new (001) peak appearing at 10.5° ($d_{001} = 8.418 \text{ \AA}$, in Fig. S2). The large interlayer spacing of the GSM-H(1h) sample can be attributed to the oxygenated functional groups introduced by the harsh oxidation treatment of graphite [37-39]. The full oxidation in GSM-H(1h) sample is not achieved as evidenced by the presence of a (002) peak of graphite with an

asymmetric shape located at 25.84° ($d_{002} = 3.445 \text{ \AA}$, Fig. 1) and crystallite size of 6 nm. In turn, when using the Brodie's method (sample labeled as a GSM-B(24h)), the peak ascribable to graphite oxide ($\sim 10.5^\circ$) is not observed.

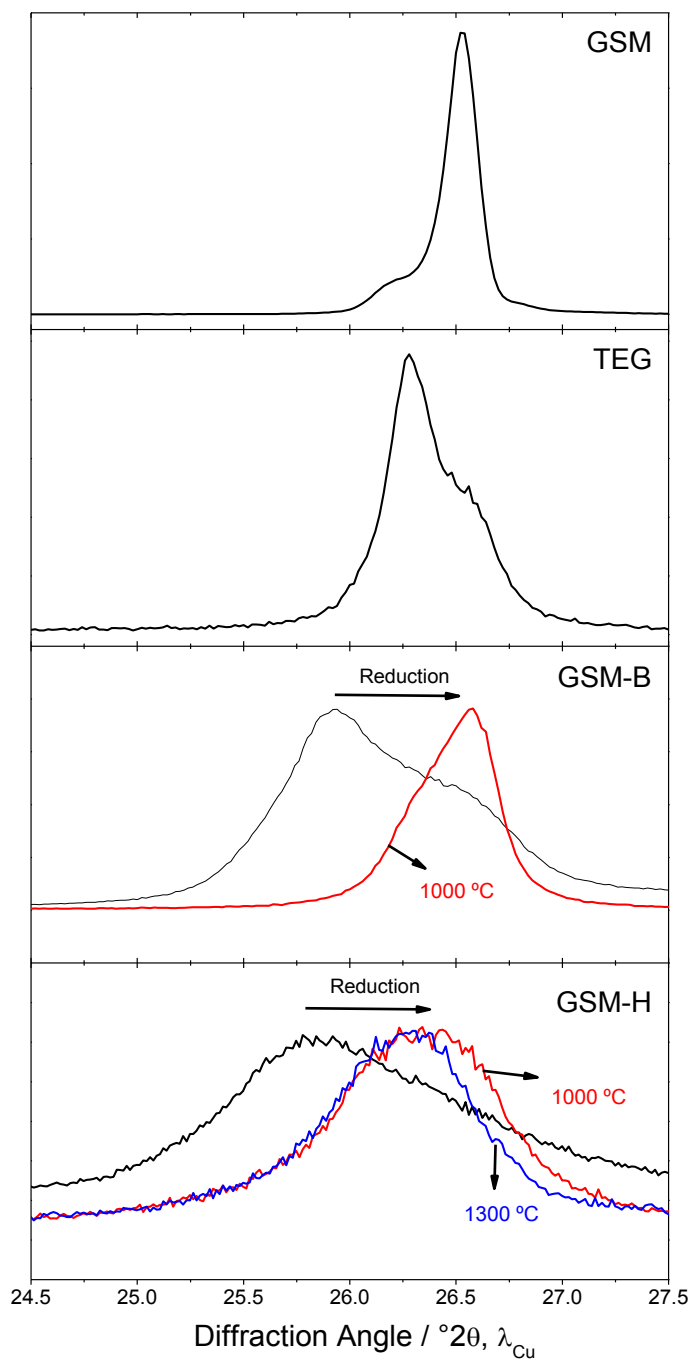


Fig.1. Comparison of the XRD patterns between the natural graphite (GSM), thermally expanded graphite (TEG), and after partial oxidation and reduction prepared by Brodie (GSM-B(24h)) and Hummer's (GSM-H(1h)) modified methods. The XRD patterns of the reduced sample at 1000°C (red lines) and 1300°C (blue line) are represented.

This method leads to a less extensive oxidation degree (Fig. S2). However, after the reduction process a shifting and broadening of the (002) peak with a maximum at 25.93° ($d_{002}= 3.352\text{\AA}$) and a crystallite size of 8.46 nm is observed (Fig. 1). As expected, the patterns recorded for reduced samples (labeled as GSM-HR and GSM-BR in Fig. 1 and Fig. S2) revealed that the diffraction peaks shifts back to $2\theta \sim 26.3^\circ$. These values are still smaller than that of original natural graphite (GSM) that appeared at 26.55° . The crystallite size (L_c) measured after the thermal reduction at 1000°C is 9.66 and 15.84 nm for GSM-HR and GSM-BR samples, respectively (Table S1, Fig. 1). The partial reduction at 1300°C has an enlarged interlayer lattice distance of 3.7\AA . In summary, these chemically treated GSM samples preserved the graphite-like structure with a larger inter-planar distance.

Gathering more detailed information about the level of graphitization of carbon materials will be crucial for understanding the influence of sodium insertion properties. For that, Raman spectra were recorded in the region between 750 and 2000 cm^{-1} (Fig. 2). The spectrum of GSM is mainly characterized by the contribution from the G band which represents the in-plan displacement of the ordered carbons couples in the hexagonal sheets [40]. The fitting for the GSM sample is composed by two peaks. The main peak at ca. 1580 cm^{-1} corresponds to an ideal graphitic lattice vibration mode with E_{2g} symmetry and was fitted with Lorentz Amp Function. The small D1 bands at ca. 1350 cm^{-1} corresponds to the lack of long-range translation symmetry in the disordered carbon and was fitted with Gauss Amp Function. Although TEG sample showed a similar profile, the graphitization index (I_G/I_{D1}) is higher for TEG as compared to GSM (Table 1), which could be indicative of a full reduction of graphene layers observed by Raman. In addition, the in-plane correlation length (L_a) has been calculated from the following equation:

$$I_{D1}/I_G = C/L_a \quad (1)$$

where C depends on the Raman laser excitation energy ($C=50$ for $\lambda = 532\text{ nm}$). The spectra of GSM-B and GSM-H exhibit a relative enhancement of the D1 and consequently a decrease of the graphitization index (Table 2). Moreover, new contributions ascribable to disordered local environments, named as D2, D3 and D4, are observed. Note that D2 is observed as a shoulder on the part of G band and it shares the same E_{2g} symmetry vibration mode with G band. D2 corresponds to a disordered

graphitic lattice mode and the disorder comes from the surface graphene layers. The D3 band appears between D1 and G bands and represents the amorphous carbon at interstitial defects (such as organic molecules fragments or functional groups). Besides that, the peak from D1 exhibits another shoulder at around 1200 cm^{-1} , which is found as D4 with disordered graphitic lattice (A_{1g} symmetry) normally attributed to sp^2 - sp^3 bonds or C-C and C=C stretching vibrations of polyene-like structures [41]. Finally, a recovery of the graphitic order is observed after the reduction by heat treatment, leading to graphitization indexes of 35.4 and 23.9 for GSM-BR and GSM-HR, respectively (Fig. 2). These results showed higher level of graphitization as compared to XRD. Most probably, by Raman is possible to detect graphite with different orientation levels, depending on their origin, and that could be the source of their different I_G/I_D values [42]. This observation is influenced by the fact that we have introduced oxygenated functional groups by the harsh oxidation treatment of graphite. Then, the thermal treatment would reduce the graphite in different ways.

Table 1. Graphitization index, position of D and G bands and *in-plane* crystallite size (La) calculated from Raman.

Sample	I_G/I_D	$W_D/\text{cm-1}$	$W_G/\text{cm-1}$	La /nm
GSM	17.8	1350	1582	89.3
TEG	59.6	1352	1582	294.1
GSM-H	1.0	1349	1583	4.9
GSM-HR	23.9	1350	1582	119.0
GSM-B	1.8	1350	1582	9.1
GSM-BR	35.4	1351	1583	178.6

Table 2. Type and amount of functional groups determined by XPS.

	XPS									
	C/O	O%	C%	Si%	S%	C(sp ²)%	C-OH-%	C-O-C%	CO(OH)%	π - π^* %
GSM	24.9	3.8	95.4	0.8	-	55.9	33.6	-	1.4	9.1
TEG	18.4	5.1	93.8	1.1	-	55.8	35.1	-	1.5	7.6
GSM-H	2.8	25.84	71.45	0.54	2.2	17.1	0.6	49.7	26.5	6.1
GSM-HR	6.8	12.5	85.5	1.3	0.7	42.1	45.9	-	9	3
GSM-B	11.4	8.00	91.55	0.44	-	48.9	38	2.2	3.3	7.6
GSM-BR	14.2	6.5	92.5	1.0	-	46	40.3	-	5	8.7

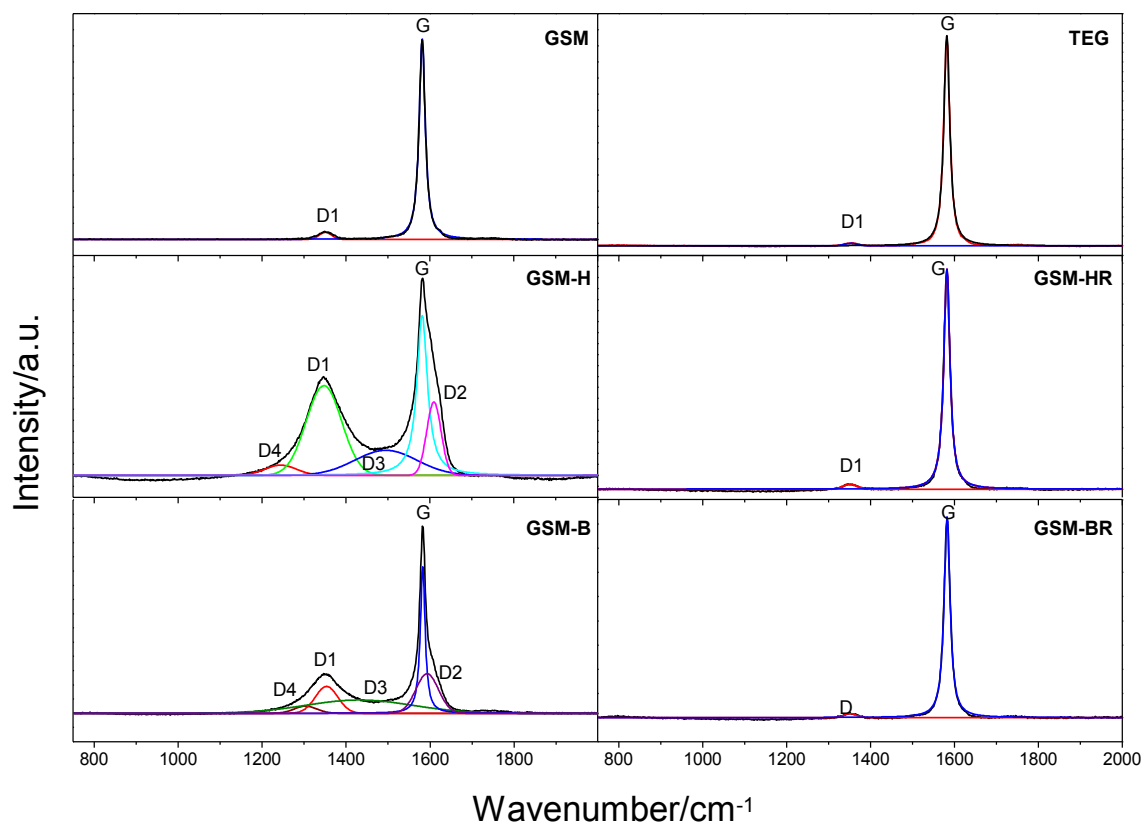


Fig.2. Raman spectra of GSM, TEG, GSM-H, GSM-B, GSM-HR and GSM-BR samples.

FE-SEM images reveal a common lamellar morphology, though with different sizes and stacking of layers (Fig. 3 a-f). It seems that the thermally expanded treatment (TEG) could strongly alter the lamellar morphology of GSM. Thus, the compacted stacking observed in GSM is replaced by buckled layers creating void spaces between layers [43]. A close inspection of TEG sample allowed inferring an average distance between layers of 50 nm (inset in Fig. 3b). The lamellar morphology of GSM-H and GSM-B also evidences an interlayer expansion as compared to GSM. After reduction, the images reveal randomly aggregated, thin, crumpled sheets closely associated with each other. However, some isolated graphitic layers have been detected for GSM-HR and GSM-BR, exhibiting an apparent thickness of about 36 and 92 nm, respectively (Fig. 3).

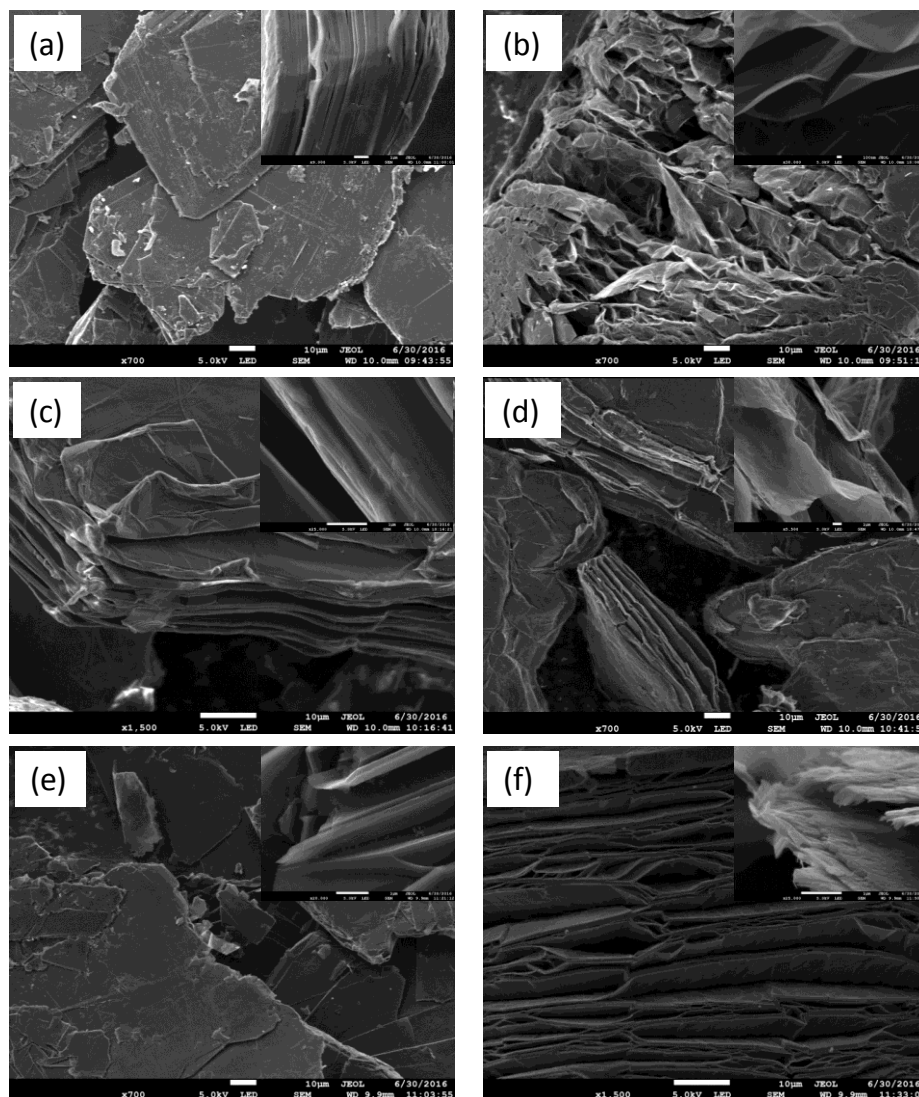


Fig.3. SEM images of: (a) GSM, (b) TEG, (c) GSM-H, (d) GSM-HR, (e) GSM-B, and (f) GSM-BR. The insets show a detailed magnification of each sample.

The occurrence of functional groups at the carbon surface is unveiled by XPS spectroscopy. The C1s core level spectra are depicted in Fig. 4. The spectra were fitted using Gaussian-Lorentzian components. In Table 2 are listed the quantitative analyses of all the components in the samples and the percentage of each signal in the C 1s spectra. Thus, GSM sample exhibits a peak at 284.6 eV which is assigned to graphitic carbon (sp^2) as the main phase, while sp^3 C-C bonding appear at 285.3 eV which probably overlap with the C-OH normally observed at 285.6 eV [44,45]. Two additional components can be resolved at the long tail existing at high binding energies centered at

288.9 eV and 290.8 eV. These signals are attributed to O=C-OH in carboxylic groups, and the shake-up satellite peaks due to π - π^* transitions in aromatic rings, respectively [44-48]. The thermally expanded graphite (TEG) shows a similar profile than GSM sample, both have about 1 % at. conc. of Si, but the main difference is observed in the carbon to oxygen ratio (C/O= 24.9 for GSM and C/O=18.4 for TEG) meaning that some oxygenated functional groups still remain in the TEG sample after thermal treatment. When the natural graphite is oxidized, a new peak contribution at 286.7 eV due to C-O-C bonds is observed for GSM-H (49.7 %) and GSM-B (2.2 %) samples. This result evidence the formation of more oxygenated functional groups with Hummer than with Brodie's modified method. The C/O ratios determined by XPS are 2.8 and 11.4, respectively. Also, in the case of GSM-H sample a small amount of sulfur is observed (2.2 % at. conc.) as a result of the treatment with sulphuric acid. When the oxidized samples are reduced by thermal treatment the C/O ratio increased up to 6.8 for GSM-HR and to 14.2 for GSM-BR which is indicative that some oxygenated groups are removed from graphene layers, but this C/O ratio is still lower as compared to GSM and TEG samples. When heating, the oxygen functional groups between adjacent graphene sheets will decompose in form of CO and CO₂.

It could be expected that the structural and morphological changes in the modified graphite samples and the use of diglyme-based electrolytes may alter the electrochemical sodium insertion properties. Figure 5 evidences the enhanced electrochemical performances for GSM and TEG electrodes when using diglyme-based electrolytes, while a very limited reversible capacity is delivered by cells assembled with NaClO₄ or NaPF₆ in carbonate based solvents (EC:DEC). This enhanced performance is good from the point of view of the observation of flat plateau in a safe voltage window, which is desirable for the anode side. Therefore, 1 M NaCF₃SO₃ in DGM electrolyte was chosen as the best electrolyte for further electrochemical experiments (Fig. 6 and Fig. 7). The galvanostatic profile of GSM exhibits a drop of potential from the open circuit potential until 0.9V, and from 0.9-0.6 V is observed a plateau accounting with 48 mA h g⁻¹. Then, capacity values around 44 and 30.4 mA h g⁻¹ are delivered by a flat plateau at 0.57 V and the 0.5-0.01 V region, respectively (Fig. 6a). At the end of the first discharge the overall capacity is 131.7 mA h g⁻¹. During the subsequent charge, a reversible reaction is observed, with a coulombic efficiency of 83%. Further charge/discharge yields a similar profile with a slight shifting of 0.15 V.

In order to check the rate capability of GSM sample, several experiments were recorded at different rate. Interestingly, the first reversible capacity is 94, 108.4, 102.8 and 101.7 mA h g⁻¹ for 2C, C, C/2 and C/10 rate, respectively. For slow kinetic, like at C/10, the cell tends to present a continuous capacity fade, but at fast rate the capacity is well preserved. Over 100 cycles, an outstanding capacity retention is observed at C rate which delivered 100 mA h g⁻¹, resulting a 93 % of efficiency. The plateau observed in galvanostatic curves for GSM sample is very similar to that observed for a flexible polyimide graphite films reported by Han et al. but they used NaPF₆ in diglyme as electrolyte [49]. However, Zhu et al. [17] reported the electrochemical behavior of natural graphite in NaCF₃SO₃/tetraglyme electrolyte exhibiting a shifting of the potential plateau of ca. 0.2 V as compared with our GSM sample. In turn, this shifting was only 0.1 V when using NaCF₃SO₃ in diglyme [13,14].

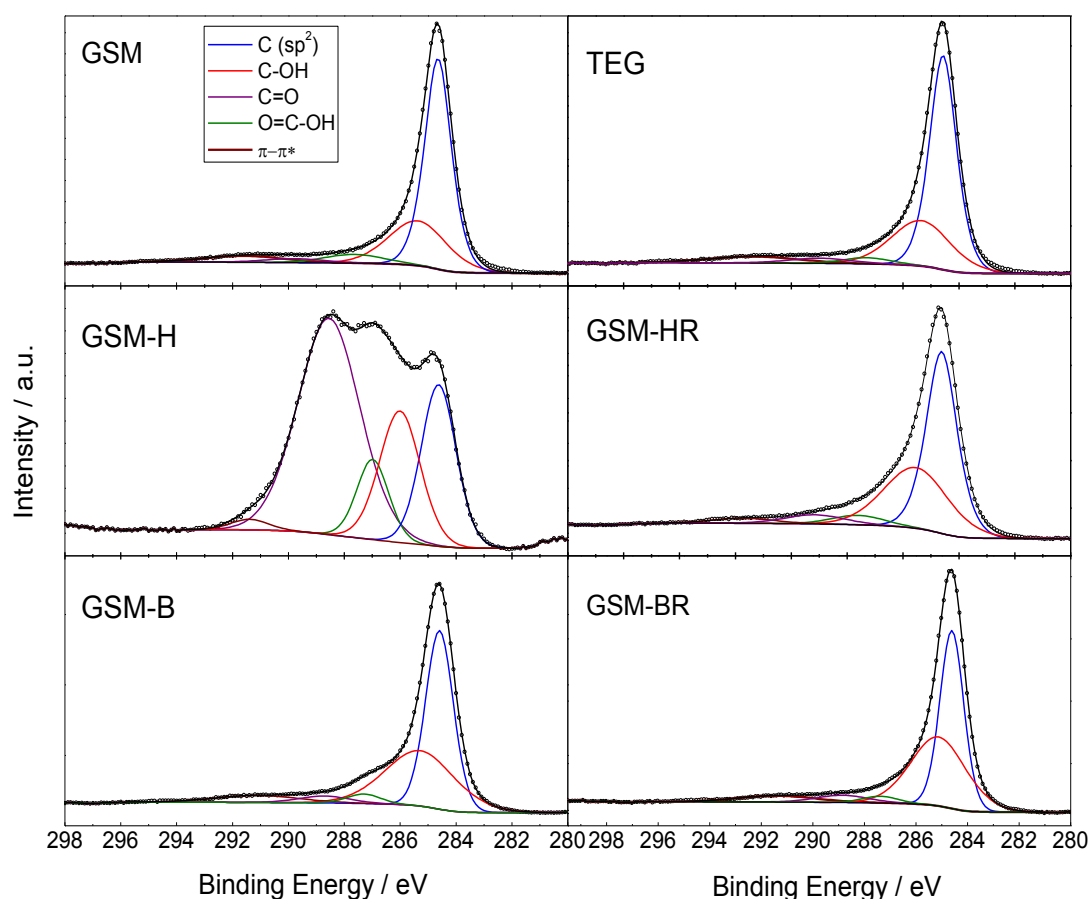


Fig.4. XPS of GSM, TEG, GSM-H,GSM-HR, GSM-B and GSMBR samples.

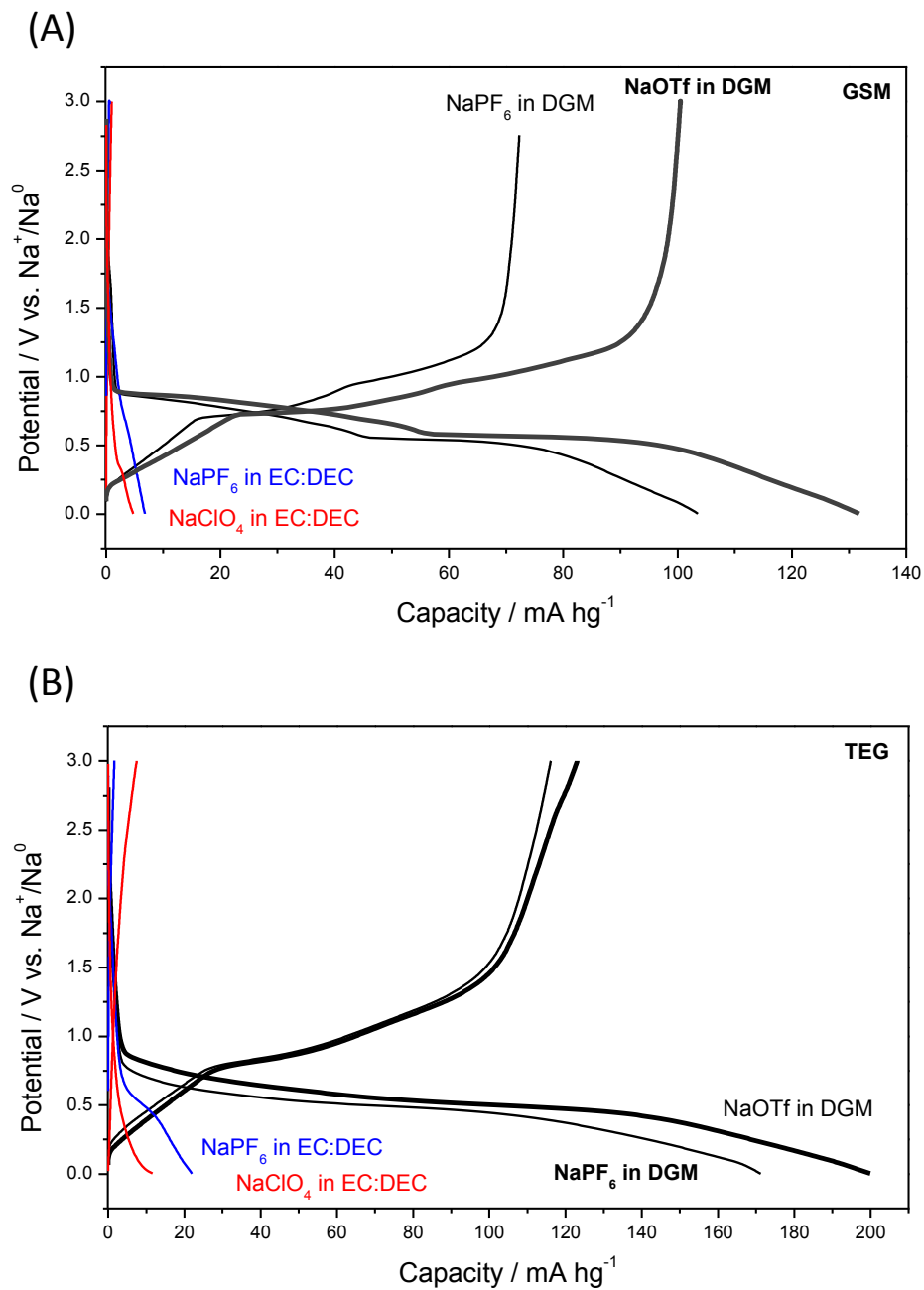


Fig.5. Charge/discharge profile of (A) GSM and (B) TEG in sodium cells in different electrolytes: i) 1 M NaCF_3SO_3 in DGM, ii) 1 M NaPF_6 in DGM and iii) 1 M NaPF_6 in EC:DEC (1:1) and iv) NaClO_4 in EC:DEC. Rate: 1C

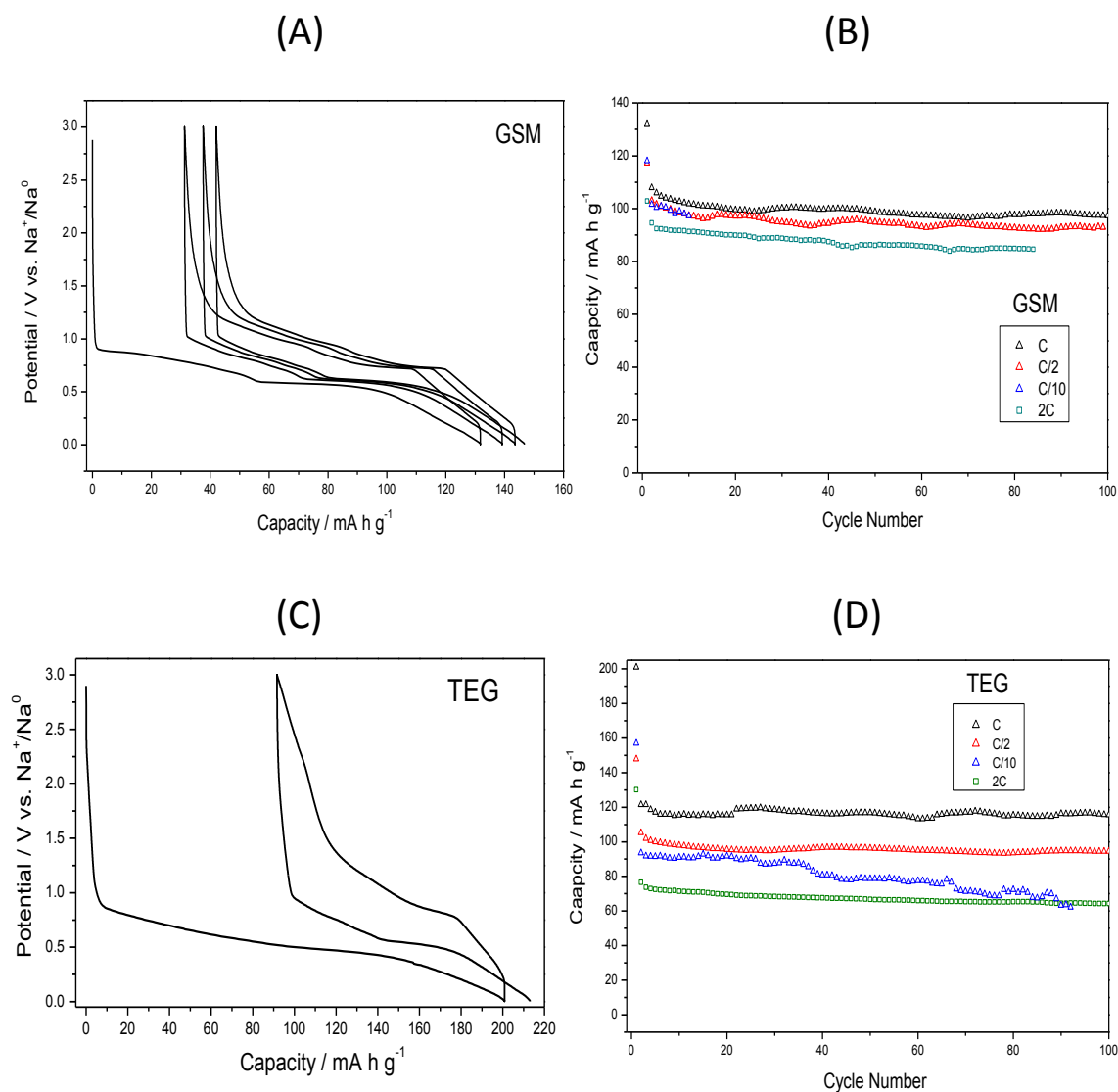


Fig.6. (A) Typical galvanostatic discharge/charge profiles of GSM sample at C rate using 1.0 M $\text{NaCF}_3\text{SO}_3/\text{DGM}$ electrolyte. (B) Sodium storage performance versus cycle number at 2C, C, C/2 and C/10. (C) Typical galvanostatic discharge/charge profiles of TEG sample at C rate using 1.0 M $\text{NaCF}_3\text{SO}_3/\text{DGM}$ electrolyte. (D) Sodium storage performance versus cycle number at 2C, C, C/2 and C/10.

The galvanostatic profile of TEG sample exhibits a flat plateau during discharge between 0.65 – 0.55 V and the total first discharge is 200 mA h g^{-1} . This first discharge capacity is higher than for GSM sample. However, the coulombic efficiency in first cycle is 66 %. The large interlayer distance allowed more Na^+ insertion. The initial irreversible capacity is commonly ascribed to the partial reductive decomposition of the electrolyte, the formation of a solid-electrolyte interphase (SEI) layer, sodium

irreversible trapping and remaining oxygen-containing groups in the interlayer of TEG. Thus, the reversible capacity for TEG is 120 mA h g^{-1} which is still higher than for GSM. The cycling experiments at several rates for TEG electrode yields 78.2, 120, 105.2 and 94.5 mA h g^{-1} for 2C, C, C/2 and C/10 rates, respectively. The best performance is recorded at C rate, being able to deliver 115 mA h g^{-1} after 100 cycles, exhibiting an efficiency of 96%. The capacity and efficiency for TEG is higher than that of original GSM over 100 cycles at C rate. The amount of remaining oxygen-containing groups in the interlayer of TEG should in principle be optimized to maintain the sufficient interlayer distance and maximize possible positions for Na-ion storage. From Raman spectra, the TEG sample exhibited higher graphitization index (59.6) and in-plane correlation length ($L_a = 294$) over all the samples. Due to this fact the higher capacity in Na-cells is observed.

The effect of partial oxidation-reduction performed by Hummer and Brodie's modified method on the electrochemistry is shown in Fig 7. For the sake of clarity, Fig. 7 shows the galvanostatic discharge measured at the 2nd cycle for all the treated samples. The reversible capacity for the expanded graphite obtained by these two methods is lower than 60 mA h g^{-1} . For instance, after thermal treatment at 500 and 1000 °C the capacity is 55 and 38 mA h g^{-1} . When an alternative reduction treatment such as with the glucose under sonication [50] or with Fe and HCl [51] is performed, it is not possible to get an optimum expanded interlayer distance (Fig. S3 and S4) and consequently sodium insertion cannot be improved.

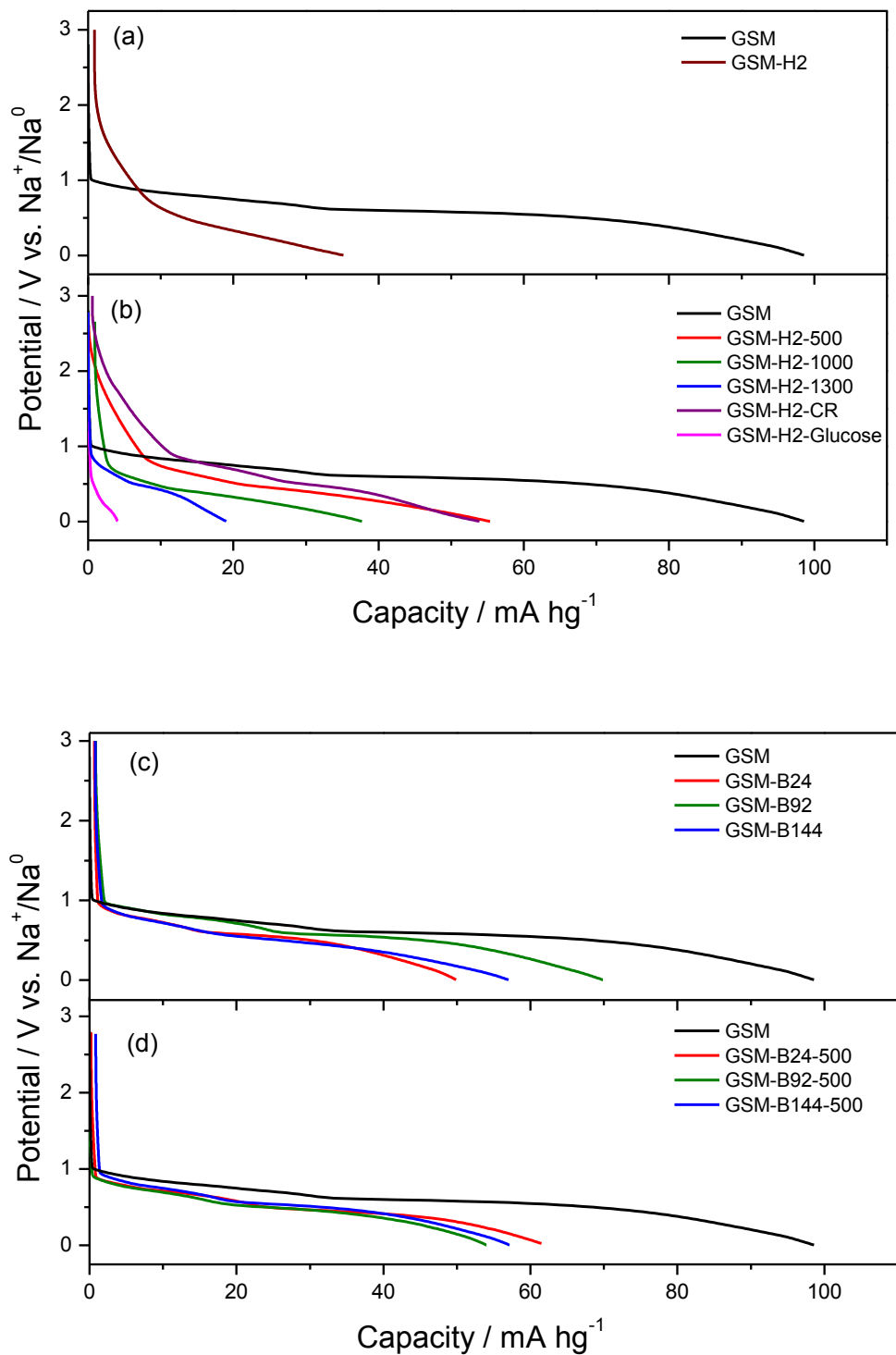


Fig.7. (a) Effects of the oxidation induced by Hummer's method on the electrochemical performance of GSM sample. (b) The same than (a) but after reduction. (c) Effects of the oxidation induced by Brodie's method on the electrochemical performance of GSM sample. (d) The same than (c) but after reduction. A number of oxidized samples were obtained. They were labeled as GSM-HXT and GSM-BXT (where 'X' indicates the number of hours exposed to Hummer or Brodie's method and 'T' the sintering temperature).

The structural changes induced by the electrochemical sodium intercalation were studied in GSM and TEG samples by recording ex situ XRD patterns. An expansion of the graphitic interlayer distance is observed during the intercalation of sodium into GSM and TEG (Fig. 8 and 9). At the beginning of the intercalation, several high stage graphite intercalation compounds will be formed ($n > 2$). For instance, a splitting of the (002) diffraction line to lower and higher angles occurs to values of 25.4° and 27.9° at 0.88 V and then to 24.9° and 28.6° at 0.78 V. As the intercalation proceeds, stage-2 is originated at 0.7 V (Fig. 8e). Then, a transition from stage-2 to stage-1 is observed at 0.55 V (Fig. 8f). In that way, at the end of the discharge, at 0.01 V, several diffraction lines at different angles emerges which correspond to the formation of stage-1. These results are in agreement to those previously reported [16-18]. So far, the intercalation mechanism has not been studied for thermally expanded graphites (TEG) yet. Irrespective of achieving higher capacity (ca. $15 - 20 \text{ mA h g}^{-1}$) for TEG than for GSM, similarities in the ex-situ XRD patterns are observed (Fig. 9). Upon a first discharge, a new set of (001) reflections appeared for TEG, which are indexed as belonging to the stage-1 of the $\text{Na}_x(\text{DGM})_2\text{C}_{20}$ compound [15,16]. Then, upon charging the initial position of the (002) reflection is retrieved, evidencing the reversibility of the insertion process. Its enhanced broadening involves a structural modification of the interlayer spacing to allow sodium diffusion. Recently, Cohn et al. [51] showed stable capacity of ca. 150 mA h g^{-1} , suggesting a stoichiometry of $\text{Na}(\text{Diglyme})_x\text{C}_{15}$, that is in agreement with previous reports on chemically derived stage 1 Na^+ ternary graphite intercalation compounds (GICs).

Figure 10 shows a 1D Patterson diagram along the c-axis calculated from the XRD (001) peak intensities. The vertical axis indicates the electron density of atoms, while the horizontal one shows the distance between atoms. Assuming an interlayer distance of 11.7 \AA , it can be concluded that the Na-C distance is 5.85 \AA . Also, the additional signals at intermediate values can be ascribed to the O-O, C-C and C-O bonds of the two molecules of diglyme that are co-intercalated per alkali ion [52]. Therefore, we confirm that solvated sodium ions intercalate into thermally expanded graphite via a stage evolution process, forming a set of ternary graphite intercalation compounds (Fig. 11) [52].

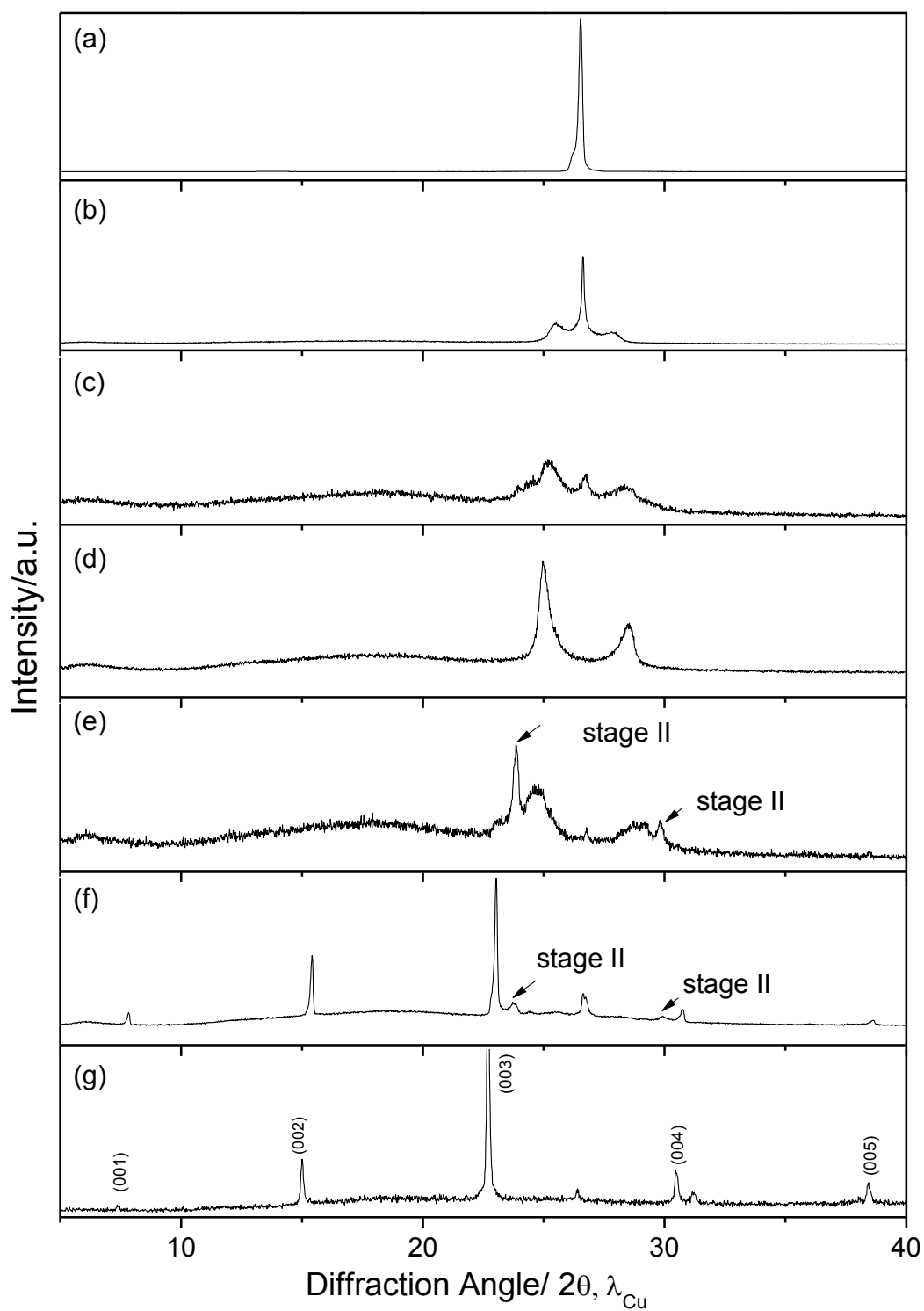


Fig.8. Ex-situ XRD patterns of GSM in sodium cell with 1M sodium triflate in diglyme recorded at different potentials: (a) pristine electrode at 3.0 V, (b) 0.88 V, (c) 0.82 V, (d) 0.78 V and relaxed all weekend, (e) 0.7 V, (f) 0.55 V and (g) at 0.01 V.

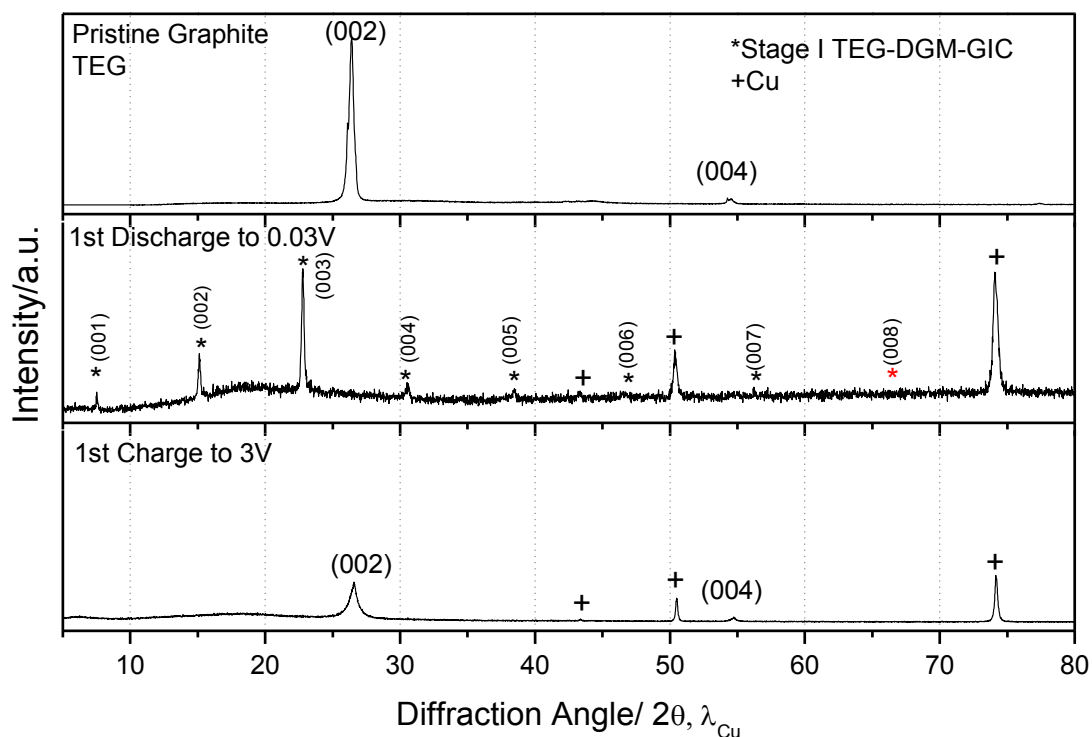


Fig.9. Ex-situ XRD patterns of TEG in sodium cell with 1M sodium triflate in diglyme recorded at different potentials: (a) pristine electrode, (b) at 0.01 V and (c) 3.0 V in first charge.

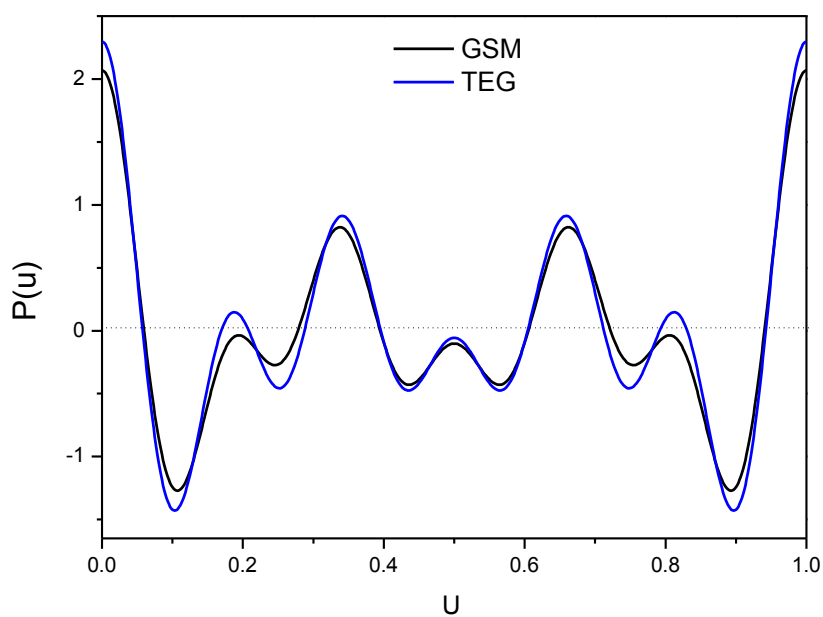


Fig.10. 1D Patterson diagram recorded along c-axis of the TEG and GSM electrodes with the stage-1.

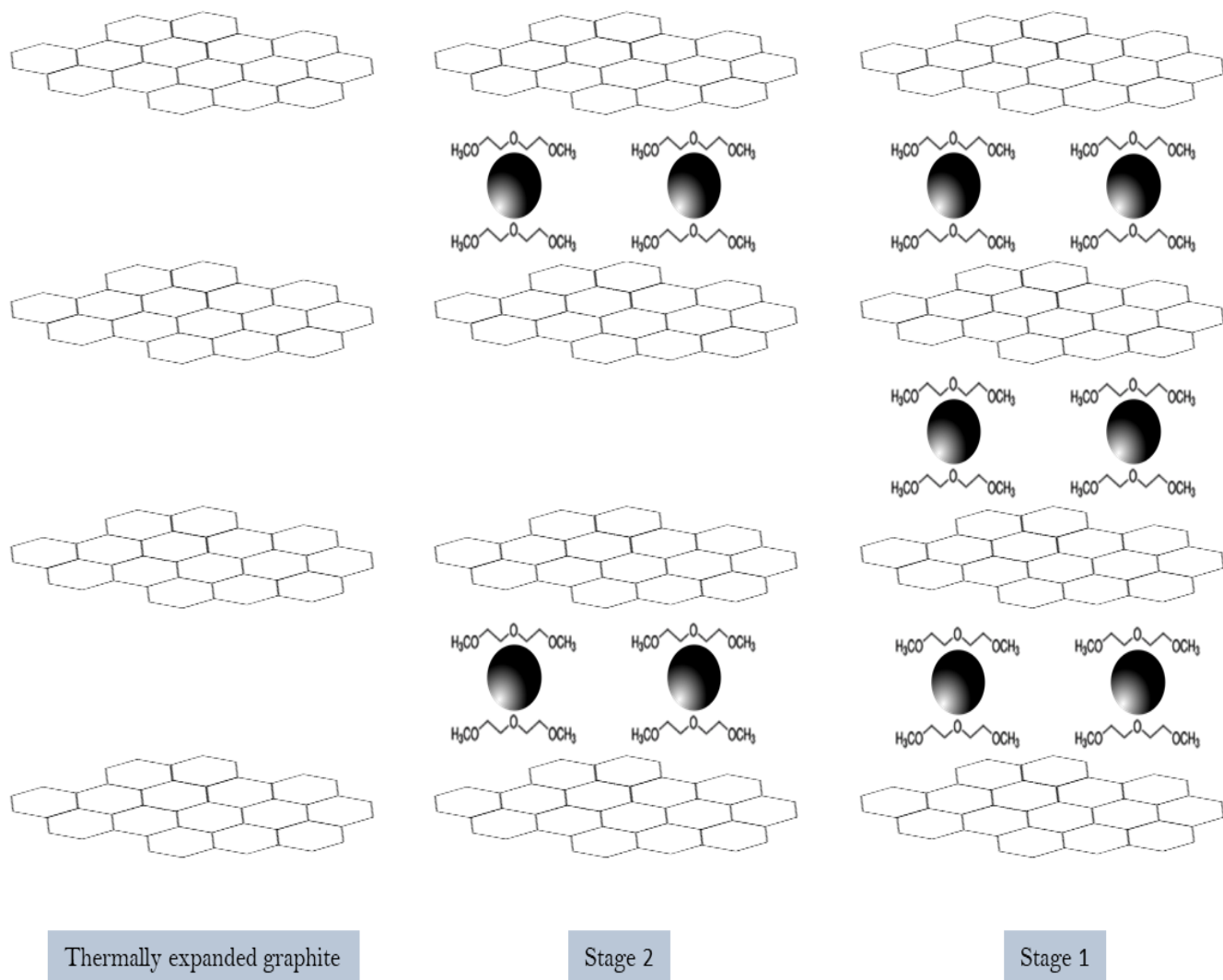


Fig.11. Schematic representation of sodium storage mechanism into thermally expanded graphite electrode showing stage 2 and stage 1.

3.3.4 Conclusions

Among all the expanded graphites evaluated in this work, the thermally expanded graphite exhibits an improved electrochemical performance as compared to its natural graphite. The reduction of graphite oxide obtained by Brodie and Hummer's modified methods has not provided an optimal interlayer distance to co-intercalate sodium. The thermally expanded graphite obtained by means of fast heating of graphite bisulfate at 1400°C reached an optimal interlayer distance of 3.388 Å. This value is slightly higher than for natural graphite and would provide efficient space to co-intercalate sodium. Thus, the use of glyme-based electrolytes (sodium triflate in diglyme), which allow $\text{Na}(\text{dgm})_2^+$ intercalation, resulted in higher capacities for TEG and GSM samples than using standard electrolytes. Excellent capacity retention over 100 cycles is observed for TEG and GSM which retained about 96 and 93% of the capacity, respectively. Also, the use of sodium triflate as a salt minimized the voltage polarization to 0.15 V which compared very favorable with previous studies (~ 0.2 V). The ex-situ XRD patterns of TEG and GSM cycled electrodes showed the progressive and reversible formation of the $\text{Na}_x(\text{DGM})_2\text{C}_{20}$ stage 1.

Acknowledgements

The authors are grateful to “Ministerio de Economía y Competitividad” (MINECO) (MAT2014–56470-R), Junta de Andalucía for financial support (FQM288 and FQM7206) and “Ramón y Cajal” Program. Sincere thanks to JSC “Ukrainian graphite” for the carbonaceous samples and a grant from the Erasmus⁺: Erasmus Mundus Joint Master Degree (EMJMD) “Materials for Energy Storage and Conversion” (MESC). We also thank SCAI (UCO Central Service for Research Support) and Institut of Fine Chemistry and Nanochemistry.

3.3.5 References

1. MS. Dresselhaus, G. Dresselhaus, *Adv. Phys.* 30 (1981) 139.
2. I. A. Udod, *Synthetic Metals* 88 (1997) 127.

3. R. C. Asher, S. A. Wilson, *Nature*, 181 (1958) 409.
4. I. A. Udod, Ext. Abstr., Proc. 20th Biennial Conf. Carbon, Santa Barbara, CA, 1991, p. 688.
5. R. Alcántara, P. Lavela, G. F. Ortiz, J. L. Tirado, R. Menéndez, R. Santamaría, J. M. Jiménez-Mateos, *Carbon*, 41 (2003) 3003.
6. S. Flandrois, B. Simon, *Carbon*, 37 (1999) 165.
7. P. Ge, M. Foulletier, *Solid State Ionics* 28–30 (1988) 1172.
8. D. A. Stevens, J. R. Dahn, *J. Electrochem. Soc.* 148 (2001) A803.
9. M. D. Slater, D. Kim, E. Lee, C. S. Johnson, *Adv. Funct. Mater.* 23, (2013) 947.
10. P. G. Bruce, C. A. Vincent, *J. Chem. Soc. Faraday Trans.* 89 (1993) 3187.
11. C. P. Rhodes, M. Khan, R. Frech, *J. Phys. Chem. B* 106 (2002) 10330.
12. Y. Zhu, L. Suo, T. Gao, X. Fan, F. Han, C. Wang, *Electrochem. Commun.* 54 (2015) 18.
13. I. Hasa, X. Dou, D. Buchholz, Y. S. Horn, J. Hassoun, S. Passerini, B. Scrosati, *J. Power Sources* 310 (2016) 26.
14. H. Kim, J. Hong, Y. U. Park, J. Kim, I. Hwang, K. Kang, *Adv. Funct. Mater.* 25 (2015) 534.
15. H. Kim, J. Hong, G. Yoon, H. Kim, K. Y. Park, M. S. Park, W. S. Yoon, K. Kang, *Energy Environ. Sci.* 8 (2015) 2963.
16. B. Jache, P. Adelhelm, *Angew. Chem. Int. Ed.* 53 (2014) 10169.
17. Z. Zhu, F. Cheng, Z. Hu, Z. Niu and J. Chen, *J. Power Sources* 293 (2015) 626.
18. M. A. Ratner, A. Nitzan, *Faraday Discuss.* 88 (1989) 19.
19. M. A. Ratner, *Aspects of the Theoretical Treatment of Polymer Solid Electrolytes: Transport Theory and Models*, Elsevier, 1987.

20. S. Bhattacharja, S. W. Smoot, D. H. Whitmore, *Solid State Ionics* 18-19 (1986) 306.
21. S. Arumugam, J. Shi, D. P Tunstall, C. A. Vincent, *J. Phys. Condens. Matter.* 5 (1993) 153.
22. D. Yoon, D. H. Kim, K. Y. Chung, W. Chang, S. M. Kim and J. Kim, *Carbon* 98 (2016) 213.
23. J. Zhao, L. W. Zhao, K. Chihara, S. Okada, J. Yamaki, S. Matsumoto, S. Kuze, K. Nakane, *J. Power Sources* 244 (2013) 752.
24. S. Komaba, W. Murata, T. Ishikawa, N. Yabuuchi, T. Ozeki, T. Nakayama, A. Ogata, K. Gotoh, K. Fujiwara, *Adv. Funct. Mater.* 21 (2011) 3859.
25. A. Ponrouch, E. Marchante, M. Courty, J. M Tarascon, M. R. Palacin, *Energy Environ. Sci.* 5 (2012) 8572.
26. Y. Cao, L. F. Xiao, M. L. Sushko, W. Wang, B. Schwenzer, J. Xiao, Z. M. Nie, L. V. Saraf, Z. G. Yang, J. Liu, *Nano Lett.* 12 (2012) 3783.
27. R. Alcántara, G. F. Ortiz, P. Lavela, J. L. Tirado, R. Stoyanova, E. Zhecheva, *Chem. Mater.* 18 (2006) 2293.
28. Y.-X. Wang, S.-L. Chou, H.-K. Liu, X. X. Dou, *Carbon* 57 (2013) 202.
29. Y. Wen, K. He, Y. Zhu, F. Han, Y. Xu, I. Matsuda, Y. Ishii, J. Cumings, C. Wang, *Nat. Commun.* 5 (2014) 4033.
30. K. Tang, L. J. Fu, R. J. White, L. H. Yu, M. M. Titirici, M. Antonietti, J. Maier *Adv. Energy Mater.* 2 (2012) 873.
31. M. S. Balogun, Y. Luo, W. Qiu, P. Liu, Y. Tong, *Carbon* 98 (2016) 162.
32. R. Alcántara, P. Lavela, G. F. Ortiz, J. L. Tirado, *Electrochem. Solid State Lett.* 8 (2005) A222.
33. B. C. Brodie, *Ann. Chim. Phys.* 59 (1860) 466.
34. W. S. Hummers, R. E Offeman, *J. Am. Chem. Soc.* 80 (1958) 1339.

35. G. C. Chung, H. J. Kim, S. I. Yu, S. H. Jun, J. W. Choi, M. H. Kim, J. Electrochem. Soc. 147 (2010) 4391.
36. T. Yagi, W. Utsumi, M. Yamakata, T. Kikegawa, O. Shimomura, Phys. Rev. B 46 (1992) 6031.
37. D. Aurbach, Y. Ein-Eli, J. Electrochem. Soc. 142 (1995) 1746.
38. H. K. Jeong, Y. P. Lee, Rob J. W. E. Lahaye, M. H. Park, K. H. An, I. J. Kim, C. W. Yang, C. Y. Park, R. S. Ruoff, Y. H. Lee, J. Am. Chem. Soc. 130 (2008) 1362.
39. J. Chen, B. Yao, C. Li, G. Shi, Carbon 64 (2013) 225.
40. F. Tuinstra, J. I. Koenig, J. Chem. Phys. 53 (1970) 1126.
41. A. Sadezky, H. Muckenhuber, H. Grothe, R. Niessner, U. Pöschl, Carbon 43 (2005) 1731.
42. M. R. Baldan, E. C. Almeida, A. F. Azevedo, E. S. Gonçalves, M. C. Rezende, N. G. Ferreira, Appl. Surf. Sci. 254 (2007) 600.
43. E. V. Strativnov, Nanoscale Res. Lett. 10 (2015) 245.
44. C. Botas, P. Álvarez, P. Blanco, M. Granda, C. Blanco, R. Santamaría, L. J. Romasanta, R. Verdejo, M. A. López-Manchado, R. Menéndez, Carbon 65 (2013) 156.
45. M. C. Zafra, P. Lavela, G. Rasines, C. Macías, J. L. Tirado, J Solid State Electrochem. 18 (2014) 2847.
46. D. Yoon, D. H. Kim, K. Y. Chung, W. Chang, S. M. Kim, J. Kim, Carbon 98 (2016) 2013.
47. E. R. Edwards, E. F. Antunes, E. C. Botelho, M. R. Baldan, E. J. Corat, Appl Surf. Sci. 258 (2011) 641.
48. S. Biniak, G. Szymanski, J. Siedlewski, A. Swiatkowski, Carbon 35 (1997) 1799.

49. P. X. Han, X. Q. Han, J. H. Yao, Z. H. Liu, X. Y. Cao, G. L. Cui, *Electrochem. Commun.* 61 (2015) 84.
50. C. Zhu, S. Guo, Y. Fang, S. Dong, *ACS Nano* 4 (2010) 2429.
51. A. P. Cohn, K. Share, R. Carter, L. Oakes, C. L. Pint, *Nano Lett.* 16 (2016) 543.
52. M. Cabello, T. Chyrka, R. Klee, M. J. Aragón, X. Bai, P. Lavela, G. Vasylychenko, R. Alcántara, J. L. Tirado, G. F. Ortiz. *J. Power Sources* 347 (2017) 127.

3.3.6 Supplementary information

Table S1. Cell parameters and crystallite sizes (L_c) calculated for the carbon samples from XRD measurements of the (002) reflection.

Sample	a/Å	c/ Å	Lc/nm	Lc/nm
			TOPAS	SHERRER
GSM	2.35	6.73	36.76	37.65
TEG	2.54	6.75	15.18	17.86
GSM-H	2.46	6.85	4.33	6.00
GSM-B	2.37	6.83	7.81	8.46
GSM-BR	2.47	6.74	13.72	15.84
GSM-HR	2.47	6.81	7.91	9.66

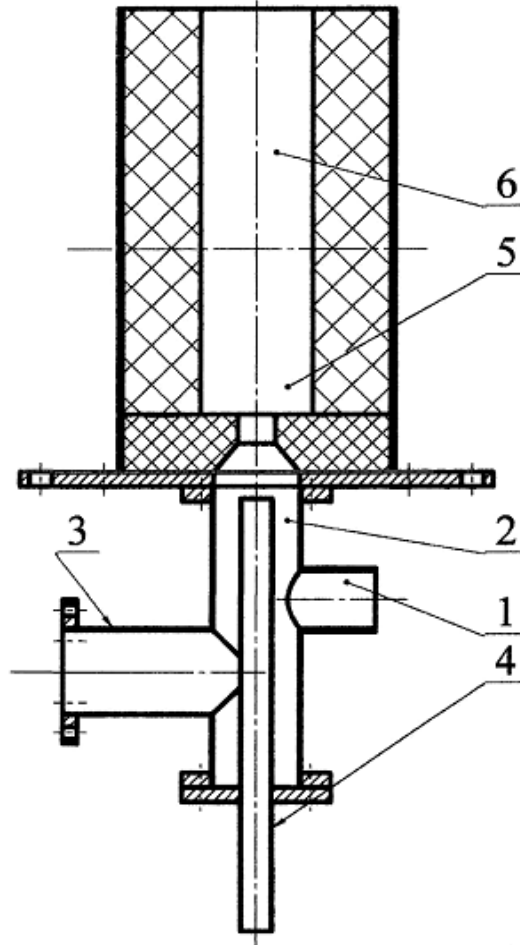


Fig.S1. Schematic diagram of the process of thermal treatment carried out to get the thermally expanded graphite (TEG). Thermally expanded graphite (TEG) is obtained by fast heating of graphite bisulfate at 1400 °C during less 1 s.

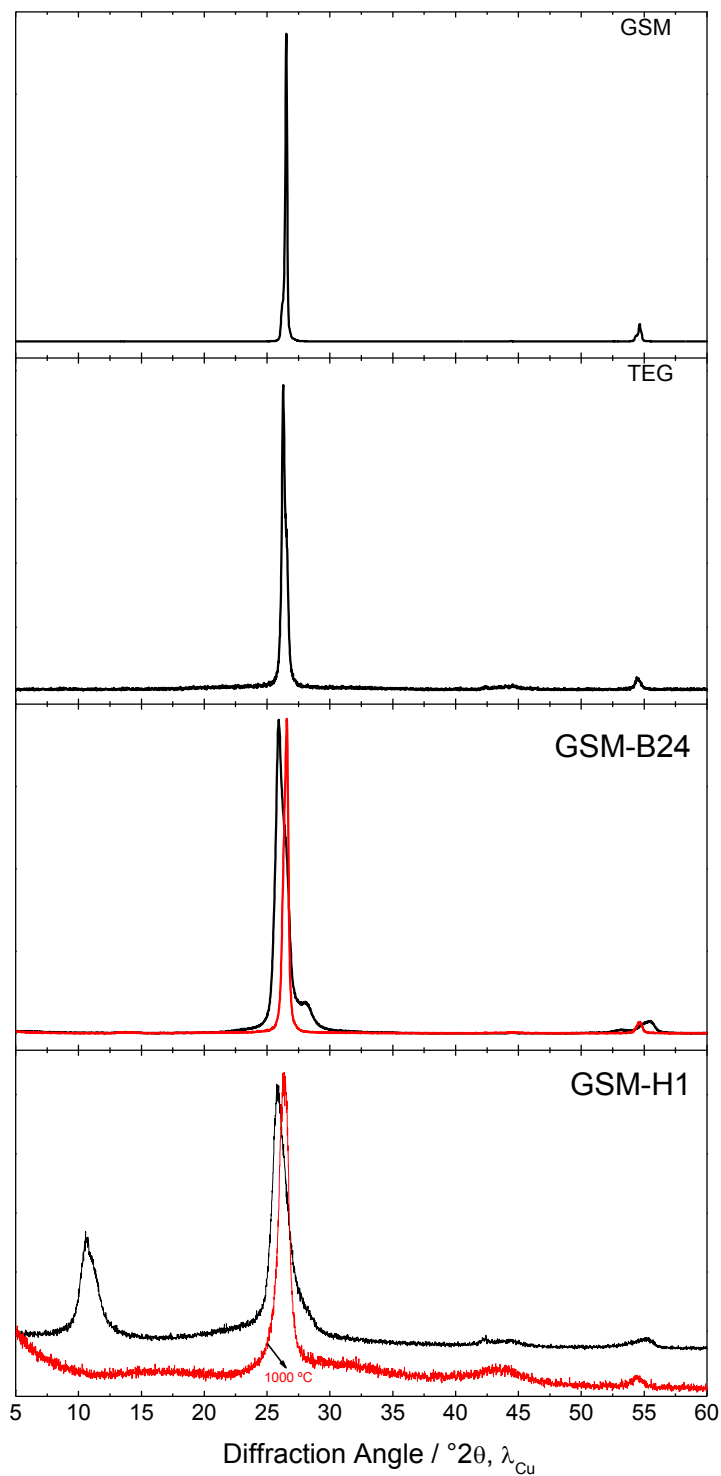


Fig.S2. XRD patterns of GSM, and after thermal expansion TEG, GSM-B(24h) and GSM-H(1h). The red lines correspond to XRD patterns after reduction by thermal treatment at 1000°C (samples labeled as GSM-HR and GSM-BR).

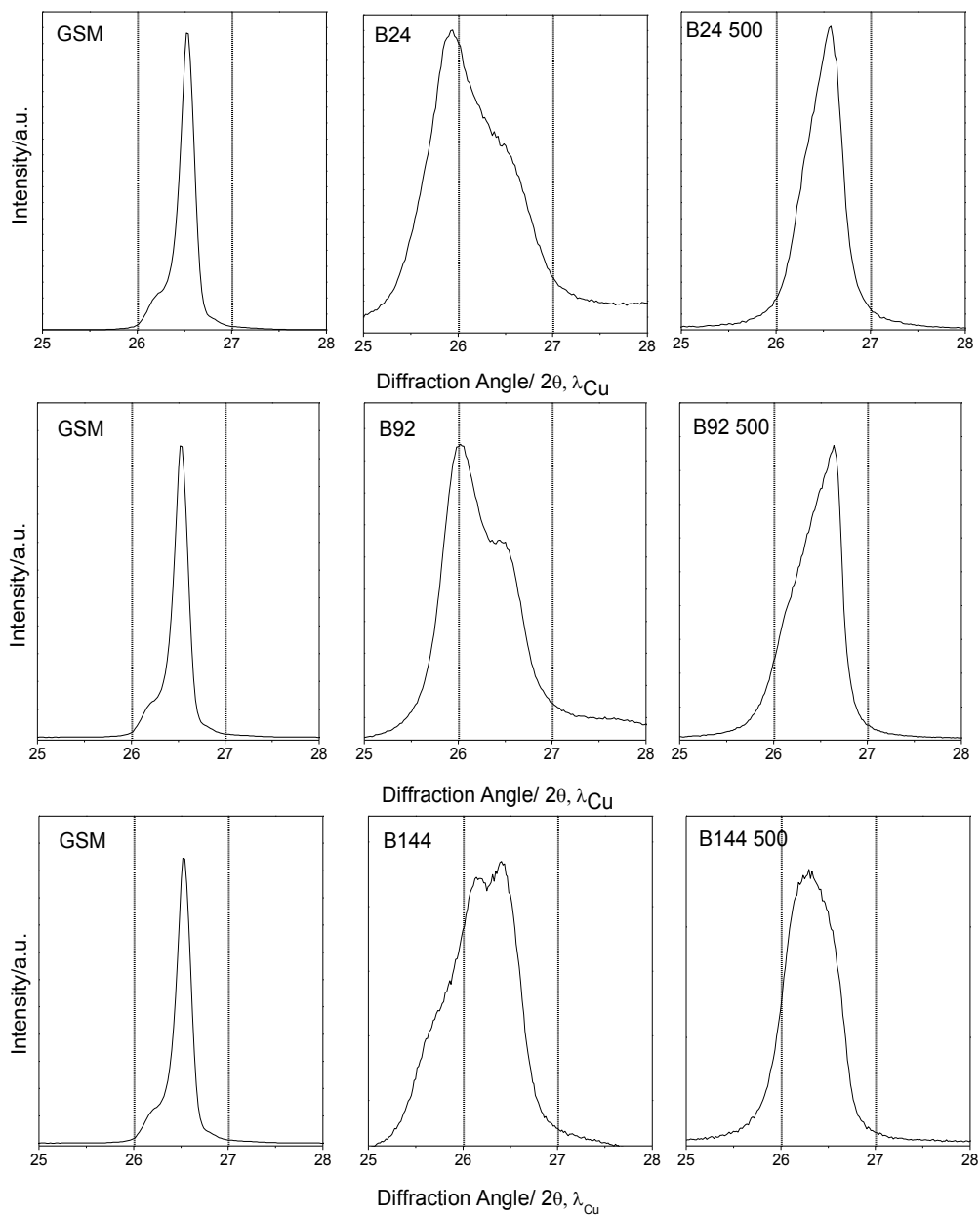


Fig.S3. Comparison of the XRD patterns between the natural graphite (GSM) and GSM treated by Brodie's for 24hrs (GSM B24), 92hrs (GSM B92) and 144hrs (GSM B144) and followed by thermal reduction in Ar at 500 for 3hrs (GSM B24 500, GSM B92 500, GSM B144 500).

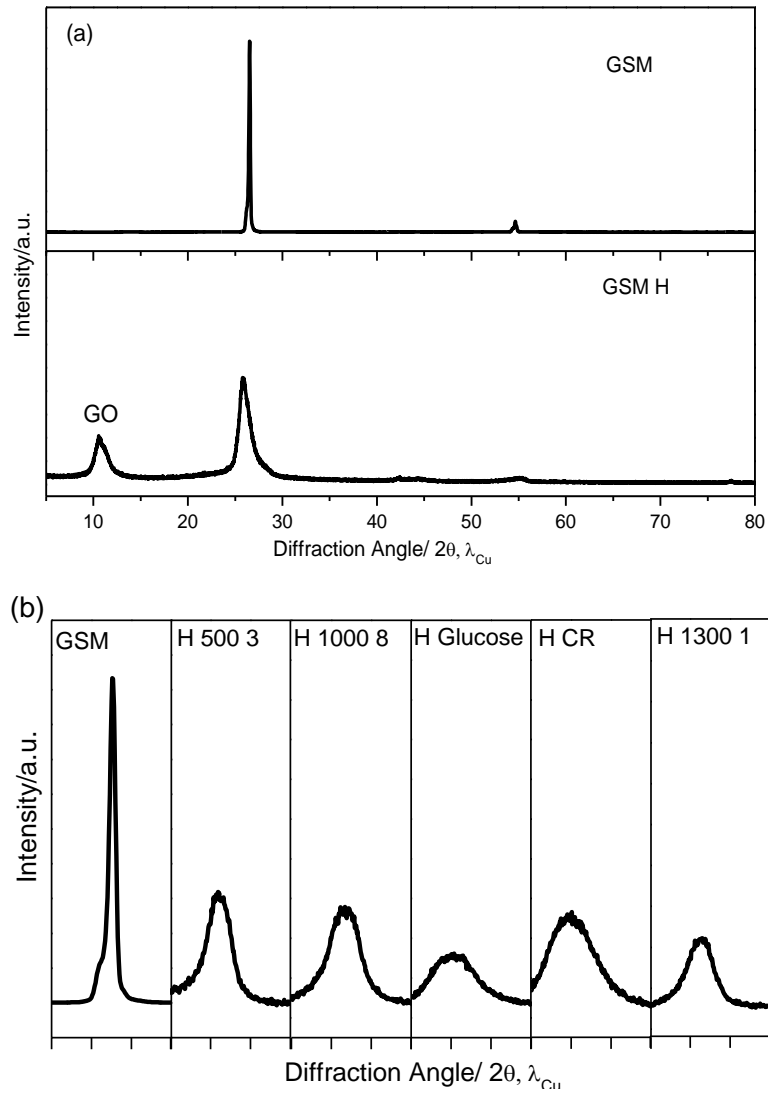


Fig.S4. Comparison of XRD of (a)GSM, and GSM after Hummer Method(GSM H), (b) GSM, GSM H 500, GSM H 1000, GSM H G, GSM H CR and GSM H 1300 from 25 to 28° in 2θ.

CAPÍTULO 4

**Baterías post-litio: materiales para
baterías de iones multivalentes**

4.1 Electrochemical and chemical insertion/deinsertion of magnesium in spinel-type MgMn_2O_4 and $\lambda\text{-MnO}_2$ for both aqueous and non-aqueous magnesium-ion batteries

Marta Cabello, Ricardo Alcántara, Francisco Nacimiento, Gregorio Ortiz, Pedro Lavela, José Luis Tirado.

Laboratorio de Química Inorgánica. Universidad de Córdoba. Edificio C3, Campus de Rabanales. Spain

Abstract

By using both chemical and electrochemical methods, magnesium has been reversibly removed from MgMn_2O_4 (s.g. I41/amd) with appropriate texture to form single-phase and nanocrystalline $\lambda\text{-MnO}_2$ (s.g. Fd-3m). Cubic $\lambda\text{-MnO}_2$ is not stable after annealing in both air and Ar atmospheres. The oxidation of Mn(III) to Mn(IV) eliminates the tetragonal distortion of the spinel-type lattice, but $\lambda\text{-MnO}_2$ is more effectively obtained when powdered MgMn_2O_4 has a large specific surface area and a small particle size. In an aqueous solution of a magnesium salt, $\lambda\text{-MnO}_2$ is formed by galvanostatic charge of MgMn_2O_4 and continuous Ar-flowing for removing oxygen from the solution. Starting from $\lambda\text{-MnO}_2$, the tetragonal structure of MgMn_2O_4 and the cubic structure of LiMn_2O_4 are generated by electrochemical cycling in aqueous solutions containing salts of magnesium and lithium, respectively. In an aqueous solution cell, this material exhibits a reversible capacity of about 150 mA h g^{-1} and can be used in magnesium-ion batteries demonstrating it to be competitive against their lithium counterparts. In the absence of metallic Mg, the use of carbonate-based solvents can be a good choice for veritable non-aqueous magnesium-ion batteries, for example using positive electrode materials like MgMn_2O_4 (magnesium-ion source) and negative electrode materials like V_2O_5 . In non-aqueous solvents (ethylene carbonate–diethyl carbonate mixture), the cubic phase $\lambda\text{-MnO}_2$ is not formed, the tetragonal structure of $\text{Mg}_x\text{Mn}_2\text{O}_4$ is preserved and its lattice cell is contracted.



CrystEngComm 17 (2015) 8728-8735

4.1.1 Introduction

The insertion of polyvalent cations (Mg^{2+} , Ca^{2+} , Al^{3+} and others) offers the advantage of charging two (or three) electrons per ion to the host material, and this fact may drive the development of high-energy batteries which would be competitive against lithium-ion batteries and other systems that use monovalent ions [1]. Thus, several compounds have been proposed for reversible accommodation of magnesium in their frameworks, such as MnO_2 , Mo_6S_8 and V_2O_5 [2]. However, the polyvalent ions used are strongly bonded to the host solid and the extraction process is slow. Although it is generally believed that the diffusion of magnesium ions in host materials is slow, however, based on calculations, Ling and Mizuno reported that the mobility of Mg^{2+} in compounds such as MgMn_2O_4 can be comparable to that of Li^+ in a typical Li-ion battery [3].

Several phases of MnO_2 such as hollandite, todorokite, birnessite and spinel-type λ - MnO_2 can intercalate magnesium ions, but the retention of the capacity upon charge/discharge cycling is usually poor. Recently, Zhang et al. proposed that the magnesiumation process of α - MnO_2 proceeds through a conversion-type reaction on the surface of the MnO_2 particles rather than an intercalation reaction [4]. Besides the intrinsic properties of MnO_2 , it may be that some parts of the irreversibility and capacity fade observed for MnO_2 batteries could be produced by the incompatibility between the metallic Mg electrode and the electrolyte solution.

A key aspect for developing batteries is to select a suitable electrolyte, and both aqueous and non-aqueous electrolytes have been studied for magnesium batteries [5]. Metallic magnesium cannot be used in the presence of carbonate solvents, such as propylene carbonate (PC), ethylene carbonate (EC) and diethyl carbonate (DEC), because the electrodeposition of Mg is impossible in these solvents. Acetonitrile (AN) is more compatible than carbonates, but the cycling behaviour is still poor. PhMgCl-AlCl_3 (a Grignard-type compound) in tetrahydrofuran (THF) solution forms acidic species that dissolve surface films and reversible dissolution/electrodeposition of magnesium can be achieved, but this solution can corrode the stainless steel used like a current collector in the battery. In solutions of THF containing PhMgCl and AlCl_3 , Yagi et al. observed pitting corrosion on the surfaces of Cu, Ni, stainless steel, Ti, and Al electrodes after the

first anodic polarization from 0 to 4 V [6]. It would be preferred to use Pt, glassy carbon and graphite as current collector, the substrate of the electrode active material and battery case, respectively, but this solution seems unfeasible for commercial batteries.

In this work, we have explored and optimized the experimental conditions to reversibly remove magnesium from MgMn_2O_4 . For this purpose, firstly MgMn_2O_4 was prepared at several temperatures. The obtained samples have different microstructure and texture properties that influence the possibility of achieving demagnesiumation to form $\lambda\text{-MnO}_2$. Finally, we have studied the electrochemical behaviour of this material as an electrode for magnesium-ion batteries in both aqueous and non-aqueous batteries, and we have found that it can be competitive against lithium.

4.1.2 Experimental

4.1.2.1 Preparation of MgMn_2O_4

MgMn_2O_4 was prepared following the method of Pechini. Citric acid and ethylene glycol were added to an aqueous solution of 0.5 M $\text{Mg}(\text{NO}_3)_2 \cdot 6\text{H}_2\text{O}$ and 0.25 M $\text{Mn}(\text{NO}_3)_2 \cdot 4\text{H}_2\text{O}$ to yield the molar ratio magnesium : manganese : citric acid : ethylene glycol = 0.5 : 1.0 : 3.0 : 9.0. The solution was heated to about 70°C to remove water while mechanical stirring was applied. The resulting rubbery polymer was transferred to a high-form crucible of alumina and heated to 200°C overnight. The obtained powder was ground in an agate mortar and then heated to 400, 550 or 800°C for ten hours.

4.1.2.2 Chemical conversion of MgMn_2O_4 to $\lambda\text{-MnO}_2$

To obtain $\lambda\text{-MnO}_2$, 0.4 g of MgMn_2O_4 was placed in a beaker with about 140 mL of nitric acid solution at pH 2, under continuous stirring for 50 minutes. The solution pH was monitored and stabilized at ca. 2.0. After the acid treatment, the solid was separated by centrifugation, washed with deionized water and dried under vacuum at 90°C.

4.1.2.3 Characterization methods

XRD measurements were carried out in a Bruker D8-Advance instrument with CuK α 1 radiation. In the case of the XRD patterns of electrodes supported on a Ti substrate, the Bragg reflections of Ti were used for calibration. The in situ XRD patterns of λ -MnO₂ were collected at several temperatures in a Bruker D8-Advance instrument equipped with an Anton Paar HTK1200N furnace.

The FTIR spectra were obtained in transmission mode in a FT-MIR Bruker Tensor 27 spectrophotometer. The spectra were recorded on pellets prepared by diluting the samples with KBr.

The nitrogen adsorption isotherms were recorded in a Quantachrome instrument at the temperature of liquid nitrogen. The samples were previously outgassed under dynamic vacuum. The isotherms were used to calculate the specific surface area using the Brunauer–Emmett–Teller theory (BET), while the pore size distribution, the average pore size and the total pore volume were calculated by applying the Barrett–Joyner–Halenda (BJH) formalism to the desorption branch.

To study the microstructure of the particles, a JEM1400 Transmission Electron Microscope (TEM) was used.

Differential scanning calorimetry (DSC) measurements were recorded in a Calisto Labsys Evo instrument at a heating rate of 10°C min⁻¹ using alumina pans.

4.1.2.4 Electrochemical experiments

The electrochemical experiments were performed in a multichannel VMP instrument. Electrochemical tests in aqueous solution were carried out in a beaker cell, with Pt as the counter electrode and Ag/AgCl as the reference electrode. The working electrode was a mixture of active material: carbon black: binder = 80: 10: 10 supported on a Ti substrate. The carbon black sample was supplied by SAFT. The electrode mass charge was 2.1–3.7 mg cm⁻². The electrolyte solution was 100 mL of 3 M Mg(NO₃)₂.

The electrolyte aqueous solution was degassed by flowing Ar at a rate of 70 ml min⁻¹. For the non-aqueous batteries, Swagelok-type cells were mounted in an M-Braun glove-box filled with Ar. The positive electrode was a mixture of the active material

(MgMn_2O_4 , 80%), carbon black (10%) and binder (PVDF, 10%) on a Pt substrate. The electrolyte solution was 0.5 M $\text{Mg}(\text{ClO}_4)_2$ in EC : DEC (50 : 50). Pt was used as the reference electrode. The negative electrode was a mixture of the active material (V_2O_5 , 80%), carbon black (10%) and binder (10%).

4.1.3 Results and discussion

4.1.3.1 Microstructure and texture analyses

The only phase observed in the samples obtained after annealing the precursor at 400 and 550 °C is nanocrystalline MgMn_2O_4 , and the corresponding XRD patterns can be indexed in the space group $I4_1/amd$ (Fig. 1). The average grain size values of this phase obtained from the Scherrer equation for 400, 550 and 800°C are 17.2, 24.3 and 93.6 nm, respectively. At 800°C, the occurrence of the minor phase Mg_6MnO_8 is also detected. In the TEM micrographs, it is observed that the particle size tends to increase with the annealing temperature.

From 400 to 550°C, there is a substantial change in the texture, surface area and porosity (Fig. 2 and Table 1). The adsorption isotherm of the sample prepared at 400°C exhibits a hysteresis loop of type H4 which can be associated with a complex material containing both micropores and mesopores. For the sample annealed at 550°C, the observed inverse type H2 hysteresis loop can be associated with the occurrence of pore blocking, and this hysteresis type was previously observed in materials where the pore size distribution of the main pores is narrower than the pore size distribution of the entrance (neck) diameters and where the entrances to the pores had been widened by calcinations [7]. According to the pore size distribution plot, those pores with width smaller than ca. 10 nm disappear after annealing at 550°C, meanwhile pores with a diameter larger than ca. 20 nm are created, resulting in an increase of the average pore width from 7.3 to 23.5 nm. It can be regarded as Ostwald ripening of the pores. The specific surface area of the sample annealed at 800°C is smaller than $1 \text{ m}^2 \text{ g}^{-1}$. The textural properties are crucial for the demagnesiumation process as discussed below.

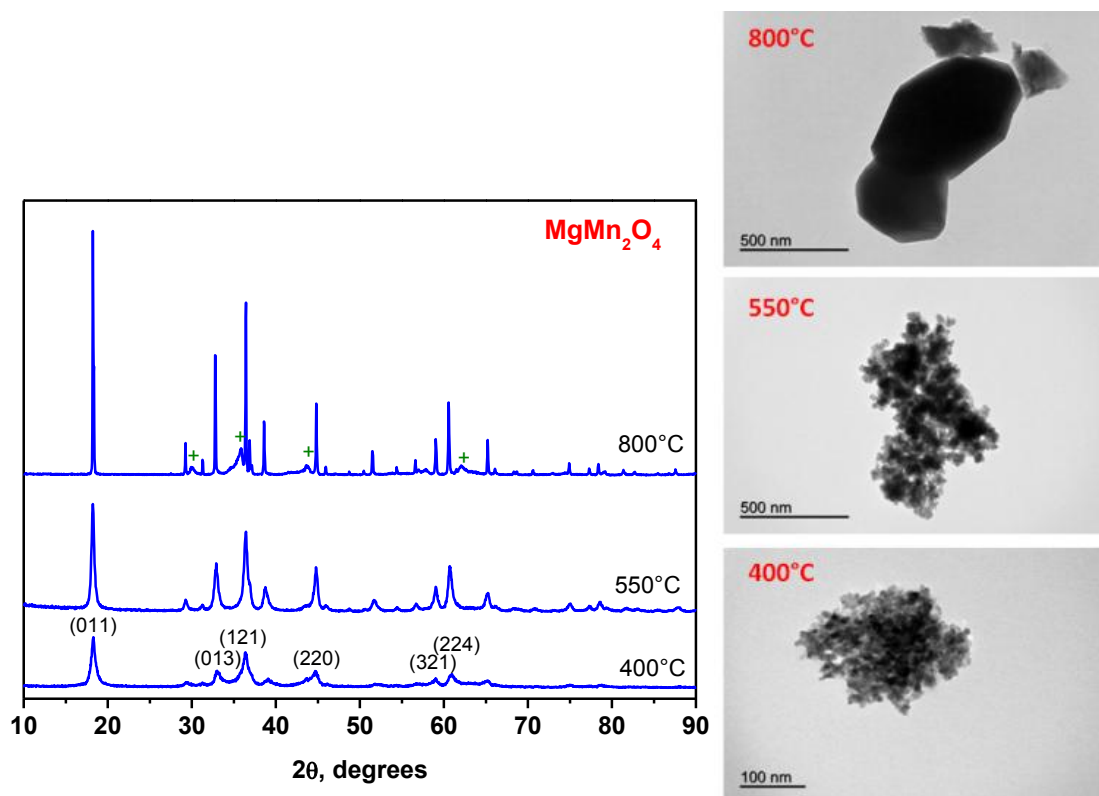


Fig. 1. XRD patterns and TEM micrographs for MgMn_2O_4 (JCPDS:23-0392) prepared at 400, 550 and 800°C. The Miller indexes are given (s.g. $I4_1/amd$). The Bragg peaks of the impurity MgMn_6O_8 (JCPDS:11-0031) are marked with a green cross (+).

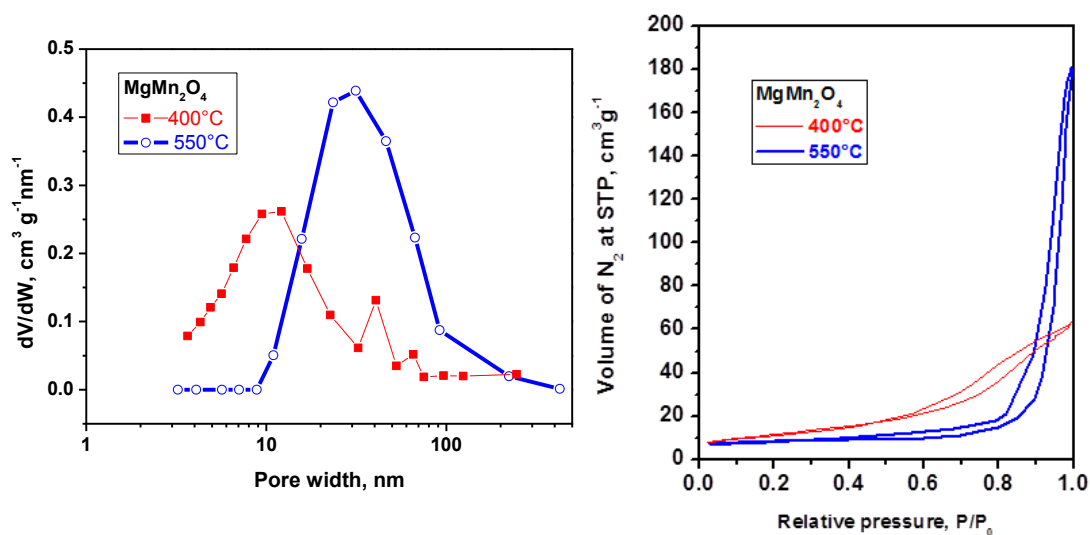


Fig. 2. Isotherms and pore size distribution for MgMn_2O_4 prepared at 400 and 550°C.

4.1.3.2 Chemical demagnesiumation

Magnesium can be removed from MgMn_2O_4 of appropriate texture by chemical methods. The acid treatment of the tetragonal spinel MgMn_2O_4 (s.g. $I4_1/amd$) yields the transformation to cubic $\lambda\text{-MnO}_2$ (s.g. $Fd-3m$, JCPDS: 44-0992) where the tetragonal distortion of the lattice due to the Jahn–Teller effect in the Mn(III) ions is suppressed (Fig. 3). The change in symmetry is confirmed by XRD and infrared spectroscopy. The magnesium ions are removed from the tetrahedral sites of MgMn_2O_4 while the manganese ions remain in the octahedral sites, and thus $\lambda\text{-MnO}_2$ has a structure with open tunnels. Besides magnesium, the manganese ions are also dissolved, and the reaction can be written as:



According to ICP analysis, the resulting solid sample contains traces of magnesium (2.2% wt). The lattice parameter of the resulting $\lambda\text{-MnO}_2$ is $a = 8.07(3)$ Å. The unit cell of $\lambda\text{-MnO}_2$ with empty tetrahedral sites and Mn^{4+} ions is smaller than the cell of the spinel-type LiMn_2O_4 ($a = 8.24$ Å) in which the tetrahedral sites are occupied by lithium ions and larger manganese (III) ions are present.

Table 1. Results for the analysis of the isotherms corresponding to MgMn_2O_4 prepared at 400 and 550°C and $\lambda\text{-MnO}_2$ obtained by chemical demagnesiumation from MgMn_2O_4 -400°C. D_{pore} = average pore diameter. V_{pore} =total pore volume. SBET= specific surface area measured by BET method.

	MgMn_2O_4 (550°C)	MgMn_2O_4 (400°C)	$\lambda\text{-MnO}_2$
$S_{\text{BET}}, \text{m}^2\text{g}^{-1}$	25.8	85.6	196.9
$V_{\text{pore}}, \text{cm}^3\text{g}^{-1}$	0.29	0.20	0.38
$D_{\text{pore}}, \text{nm}$	23.5	7.3	7.3

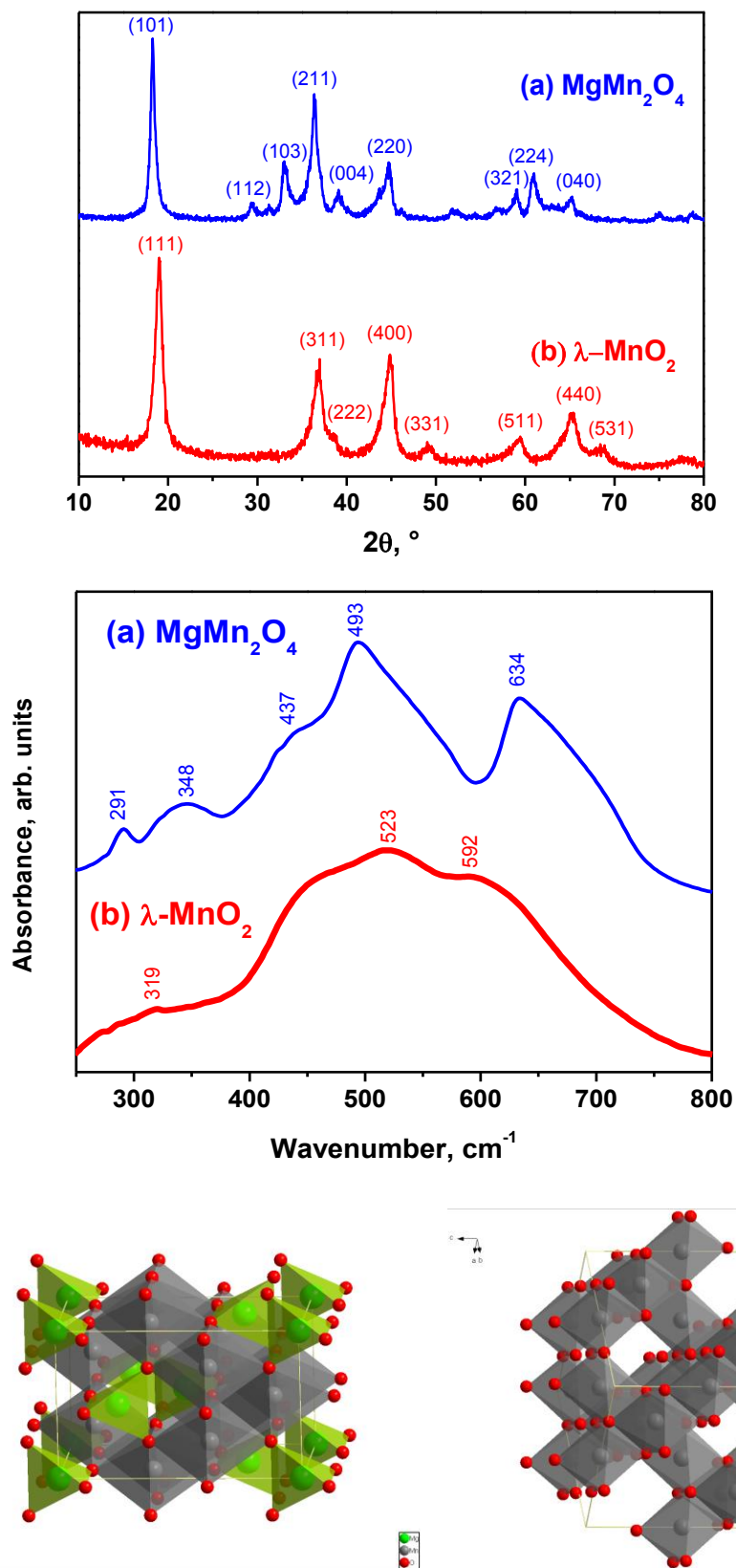


Fig. 3. X-ray diffraction patterns and FTIR spectra of (a) MgMn_2O_4 and (b) $\lambda\text{-MnO}_2$, where $\lambda\text{-MnO}_2$ was obtained through chemical demagnesiumation of MgMn_2O_4 with nitric acid solution. The perspective view of MgMn_2O_4 and $\lambda\text{-MnO}_2$ are also shown. Mg, Mn and O atoms are shown as green, grey and red, respectively. The empty tunnels of $\lambda\text{-MnO}_2$ after the removal of Mg ions are visible.

In the FTIR spectra, at least five bands are observed in the range between 250 and 800 cm^{-1} for tetragonal MgMn_2O_4 . These bands are shifted to higher frequencies in comparison with the hausmannite (Mn_3O_4) normal tetragonal spinel, and this fact is consistent with the lighter mass of Mg^{2+} and the shorter distance of the magnesium–oxygen bond. The removal of magnesium involves changes in the FTIR spectra. The high local symmetry of the cubic $\lambda\text{-MnO}_2$ and the vacancies in the tetrahedral sites are reflected in the observation of fewer bands. The spectrum of $\lambda\text{-MnO}_2$ is consistent with the literature and the predicted three infrared-active vibrations (${}^3\text{F}_{1u}$) [8].

On the other hand, the acid treatment of MgMn_2O_4 annealed at 400 °C yields $\lambda\text{-MnO}_2$ where more mesopores with width between ca. 4 and 30 nm are formed, the total pore volume increases and the average pore radius remains unchanged (Fig. 4 and Table 1). The resulting $\lambda\text{-MnO}_2$ sample possesses a higher specific surface area ($\text{SBET} = 196.9 \text{ m}^2 \text{ g}^{-1}$) than pristine MgMn_2O_4 ($\text{SBET} = 85.6 \text{ m}^2 \text{ g}^{-1}$).

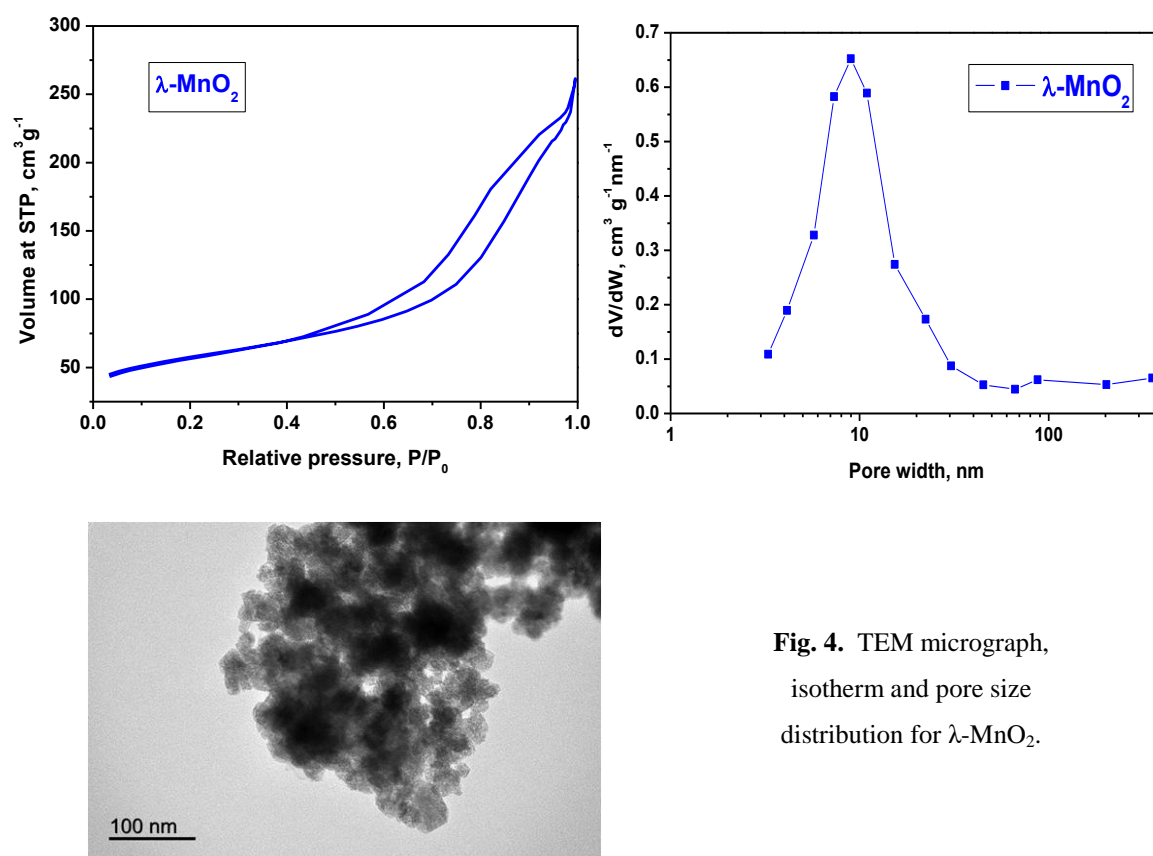


Fig. 4. TEM micrograph, isotherm and pore size distribution for $\lambda\text{-MnO}_2$.

In contrast to MgMn_2O_4 obtained at 400 °C, the sample annealed at 550 °C and treated with acid solution under the same experimental conditions does not yield single-phase $\lambda\text{-MnO}_2$, the pristine tetragonal structure is preserved and only a small amount of cubic $\lambda\text{-MnO}_2$ is obtained (Fig. S1). This fact reveals that the surface and porosity of the particles that are in contact with the acid solution are key parameters to achieve the chemical demagnesian. For the sample prepared at 550 °C, the surface of the particles in contact with the acid solution is smaller and the diffusion path of ions in the particles is longer.

4.1.3.3 Effect of thermal annealing on $\lambda\text{-MnO}_2$

Another adequate method to characterize manganese dioxide is by using thermal analysis. In addition, the electrode materials used in batteries often are thermally treated to obtain dry and high-crystallinity powders. The DSC and XRD (Fig. 5) results reveal that the as-prepared $\lambda\text{-MnO}_2$ is not stable with respect to thermal annealing. This shows that $\lambda\text{-MnO}_2$ with high crystallinity and a large crystallite size could not be prepared by thermal treatment, because it is a metastable form of MnO_2 . And this fact may limit its potential use in nonaqueous batteries. In the DSC curve, there is an endothermic and broadened peak at about 60–250°C. The XRD patterns only show progressive loss of crystallinity in the $\lambda\text{-MnO}_2$ phase up to 300°C. An exothermic peak is observed at about 340°C, while the occurrence of the Mn_5O_8 ($\text{Mn}_2^{2+}\text{Mn}_3^{4+}\text{O}_8$) phase is detected at 400°C ($C2/m$, $a = 10.36(5)$ Å, $b = 5.72(1)$ Å, $c = 5.69(3)$ Å, $\beta = 110.53^\circ$, JCPDS: 39-1218) and the reflections of $\lambda\text{-MnO}_2$ disappear.

After annealing at 600–800°C, the observed reflections are ascribed to cubic bixbyite $\alpha\text{-Mn}_2\text{O}_3$ ($P2_13$, $a = 9.42(2)$ Å, JCPDS: 41-1442) and tetragonal $\gamma\text{-Mn}_2\text{O}_3$ ($I4_1/amd$, $a = 5.74(1)$ Å, $c = 9.403(4)$ Å). Although Mn_3O_4 and MgMn_2O_4 also crystallize in the same space group as $\gamma\text{-Mn}_2\text{O}_3$, the positions of the Bragg reflections and the calculated lattice parameters agree better with the latter phase. The endothermic peak placed at ca. 614°C is ascribed to the formation of bixbyite $\alpha\text{-Mn}_2\text{O}_3$ [9]. This last endothermic peak was not observed in the DSC experiment recorded under Ar-flow, and the XRD pattern of the sample retrieved from the DSC experiment did not exhibit reflections of orthorhombic $\gamma\text{-Mn}_2\text{O}_3$; only the tetragonal phase was detected (Fig. S2).

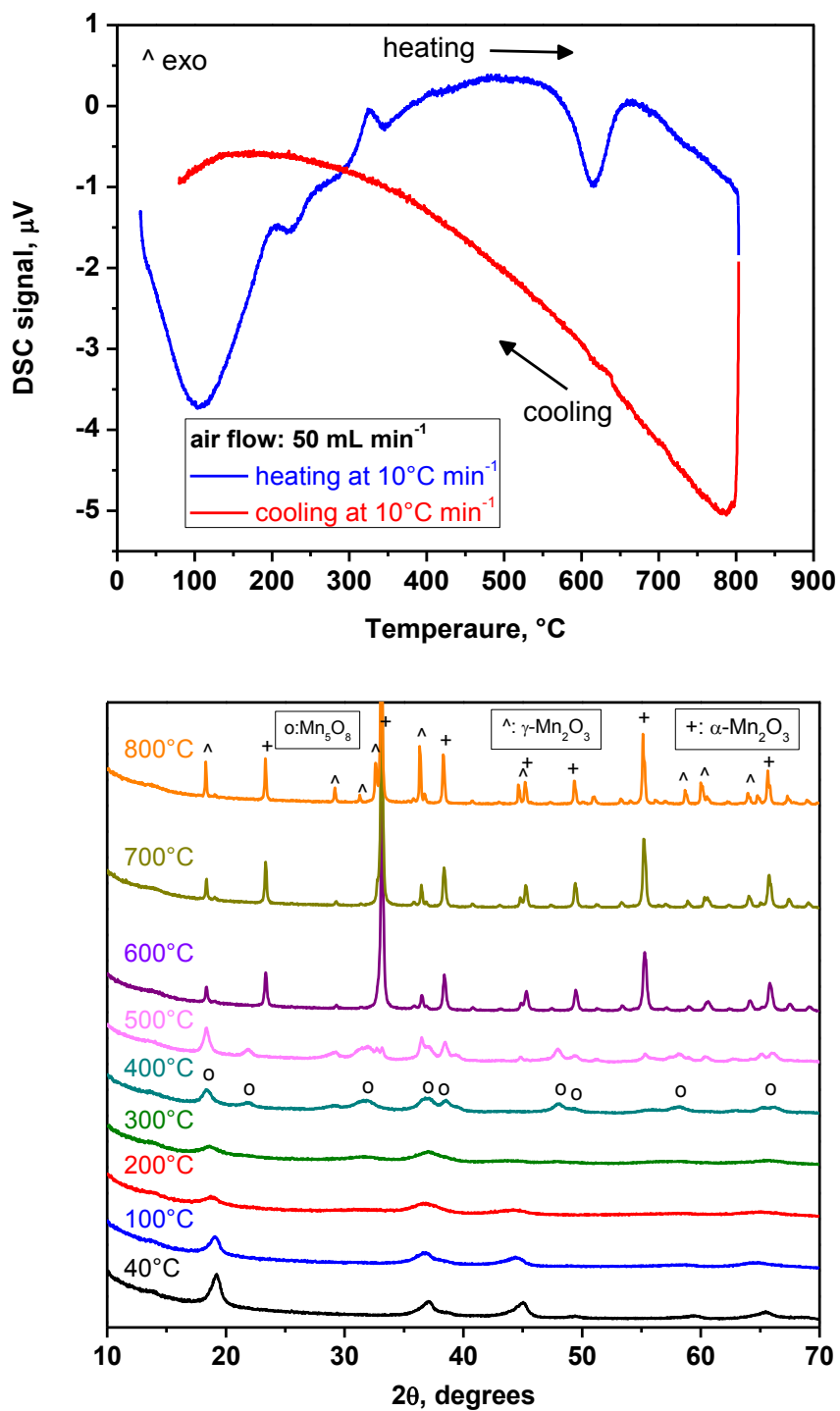


Fig. 5. DSC curves for heating and cooling of $\lambda\text{-MnO}_2$ under air-flow, and *in-situ* recorded XRD patterns for the annealing of $\lambda\text{-MnO}_2$ in air atmosphere. Endothermal is downward and exothermal is upward.

4.1.3.4 Electrochemical demagnesiumation and cycling of MgMn_2O_4 in aqueous solution

In an attempt to remove magnesium from MgMn_2O_4 , prepared at 400°C (LT) and 800°C (HT), by electrochemical methods, an aqueous solution of magnesium nitrate was used as the electrolyte (Fig. 6). During the first sweep, the voltage was increased from the open circuit voltage (OCV) to 3.0 V vs. Ag/AgCl, then the cell was relaxed for one minute, and finally a second anodic sweep was imposed from OCV to 3.0 V at the same scan rate. Decomposition of the electrolyte solution and gas evolution also took place at these anodization voltages in competition against the oxidation of MgMn_2O_4 , thus decreasing the coulombic efficiency. Two anodic peaks are observed between 1.0 and 2.5 V which are ascribed to the oxidation of Mn(III) to Mn(IV) (similar to the deinsertion of lithium from LiMn_2O_4), and at a higher voltage, oxygen evolution is observed. The capacity of the first charge process is 112.6 mA h g⁻¹ for HT and 296 mA h g⁻¹ for LT. The peaks between 1.4 and 2.1 V are not observed during the second anodic sweep and the capacity of this second charge process is 59 mA h g⁻¹ for HT and 45 mA h g⁻¹ for LT. The ex situ XRD patterns of both HT and LT MgMn_2O_4 electrochemically oxidized electrodes show that the pristine structure of MgMn_2O_4 is preserved and the unit cell is only slightly contracted ($a = b = 5.715(5)$ Å, $c = 9.3154(9)$ Å, vol. = 304.23 Å³). The cubic spinel λ - MnO_2 is not formed. The oxidation of manganese(III) under these experimental conditions apparently does not involve the significant extraction of magnesium from the inner part of the particle, and the electrochemical reaction mainly takes place at the particle surface, similarly to an electrochemical capacitor.

It is important to find suitable conditions for the demagnesiumation process. The upper voltage limit of the working electrode and the parasitic reactions need to be controlled.

In contrast to the voltammetry results, the oxidation of LT- MgMn_2O_4 under constant current (galvanostatic method) and continuously flowing Ar through the aqueous solution yields the whole extraction of magnesium and the formation of λ - MnO_2 (Fig. 7):



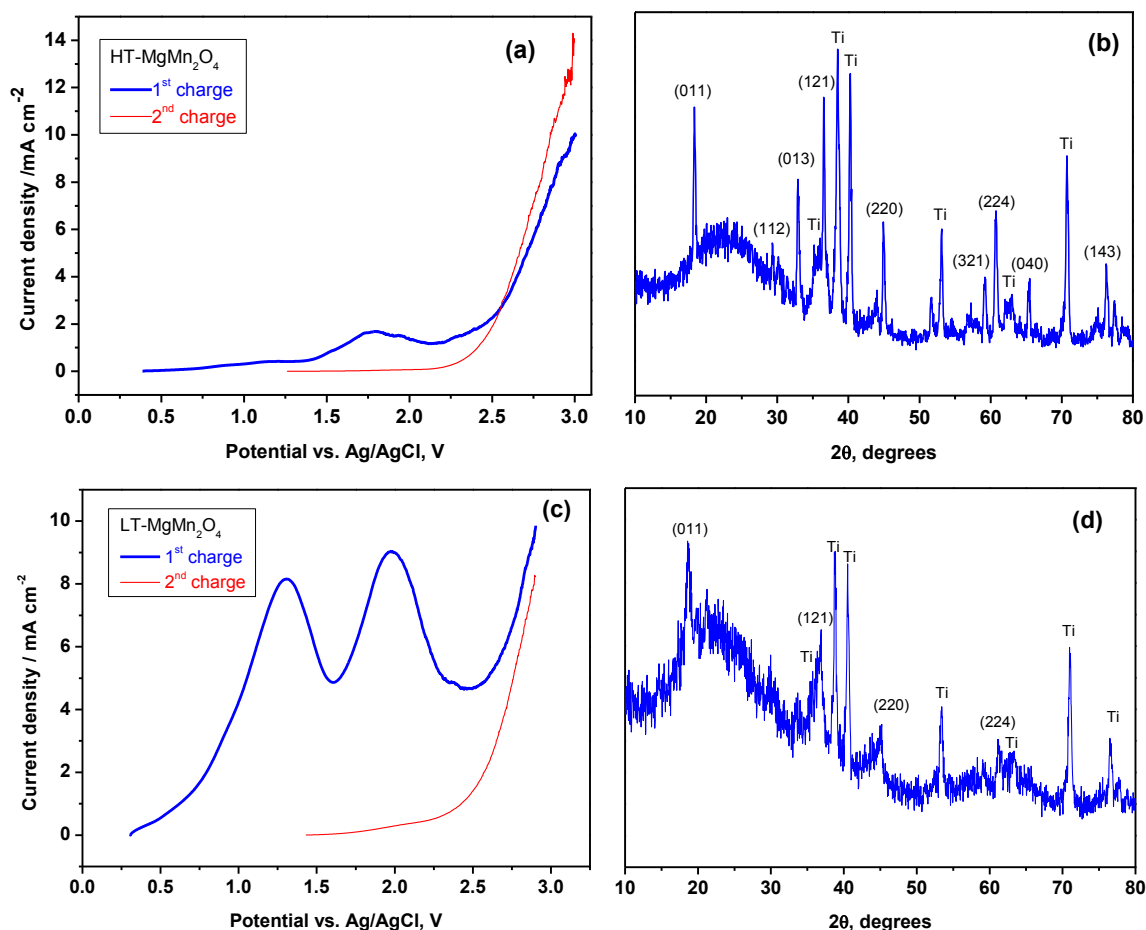


Fig. 6. Voltammetry results (two consecutive anodization processes) for trying to remove magnesium from MgMn_2O_4 prepared at 400 (LT) and 800°C (HT). (a) Intensity-voltage plot for HT. (b) Resulting XRD for HT. (c) Intensity-voltage plot for LT. (d) Resulting XRD for LT. Scan rate: 5 mV/s. The reflections of the Ti substrate are marked, and the hump at 15-30°/2 θ is also due to the Ti substrate.

A plateau is observed at ca. 1.4 V which involves demagnesiumation from MgMn_2O_4 and finally formation of $\lambda\text{-MnO}_2$ (Fig. 7). The limited contribution of the irreversible decomposition of the electrolyte solution to this plateau cannot be discarded. If one compares Fig. 6 and 7, it is deduced that besides the imposed voltage limit, Ar-flow and oxygen removal from the electrolyte solution can also contribute to the improvement of the stability of the electrode material in an aqueous cell and to the decrease in the cell polarization, like other authors previously found in other aqueous batteries [10]. We can speculate that the continuous Ar-flow avoids some parasitic reactions and self-discharge which are related to the presence of O_2 dissolved in the solution. Thus, if an oxidation is being performed at the positive electrode (MgMn_2O_4)

in the aqueous solution, the dissolved O_2 can be electrochemically reduced at the negative electrode (Pt) or, alternatively, H_2 can be formed at the Pt electrode. It may be that the oxygen reduction produces compounds (e.g. H_2O_2) which chemically react at the working electrode and also reduce the activity of the Pt electrode. In contrast, the Ar-flow suppresses these irreversible reactions and improves the overall electrochemical performance.

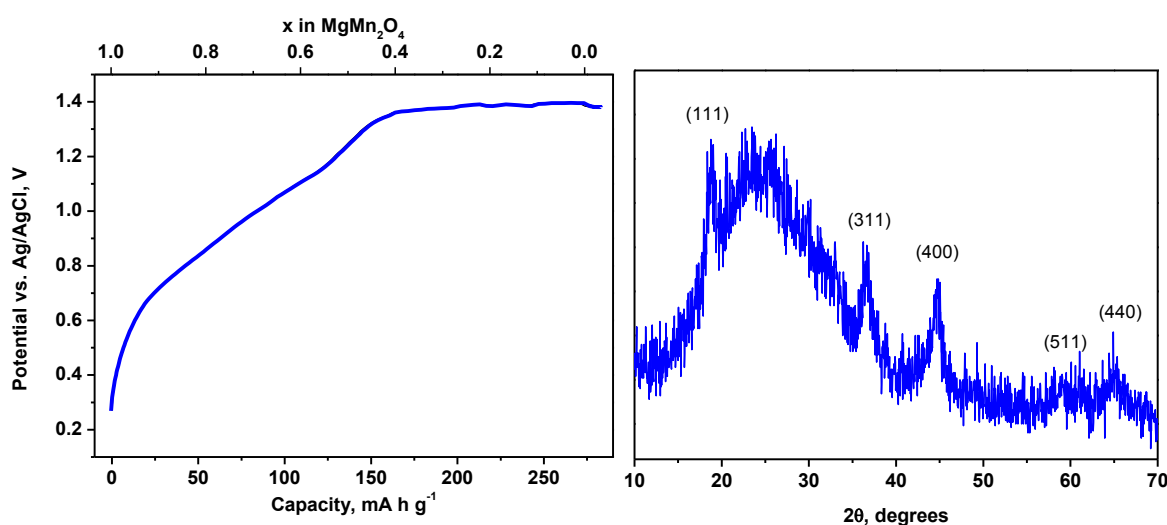


Fig. 7. Galvanostatic charge of LT- $MgMn_2O_4$ in aqueous battery and *ex-situ* XRD of the charged electrode. The Miller indexes of the cubic λ - MnO_2 phase are shown.

In addition, we observed that after cycling voltammetry of λ - MnO_2 in an aqueous solution of magnesium nitrate, the cubic structure of λ - MnO_2 is transformed into the tetragonal structure of $MgMn_2O_4$ (Fig. 8). On the other hand, the lithiation of λ - MnO_2 by cyclic voltammetry in an aqueous solution containing lithium nitrate drives the expansion of the cubic cell ($a = 8.3(2) \text{ \AA}$) nearly up to the value corresponding to $LiMn_2O_4$ (Fig. 8).

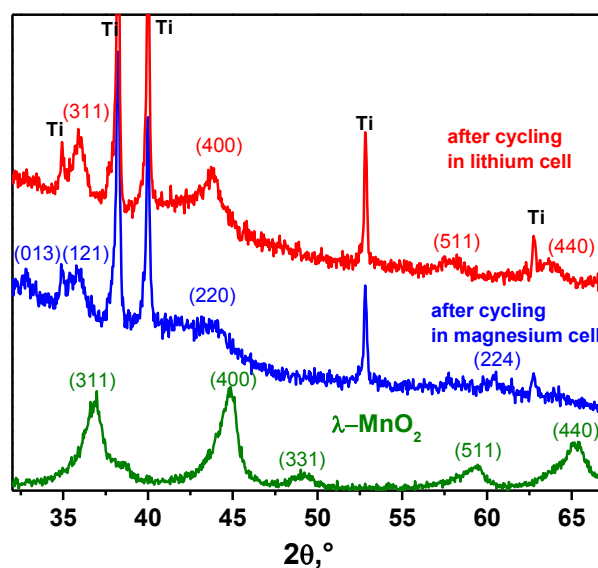


Fig. 8. Ex-situ XRD patterns for the cycled electrodes of λ - MnO_2 in aqueous electrolyte containing lithium and magnesium salts. The Miller indexes of the cubic and tetragonal phases are shown.

The reversible lithiation/delithiation of the cubic $\text{Li}_x\text{Mn}_2\text{O}_4$ is well-known in the literature. However, the reversible magnesiation/demagnesiation process starting from tetragonal MgMn_2O_4 is less known, and this is the first time that single-phase λ - MnO_2 has been prepared by chemical and electrochemical demagnesiation and then reinserted by electrochemical methods. These findings suggest that the manganese oxides may be effectively used in magnesium-ion batteries. Moreover, all these results show evidence that the magnesiation/demagnesiation is a reversible process for the spinel-type $\text{Mg}_x\text{Mn}_2\text{O}_4$ in spite of the tetragonal distortion in the lattice. The divalent charge of the $\text{Mg}(\text{II})$ ion theoretically can double the coulombic capacity in comparison with systems based on lithium-ion.

For galvanostatic cycling in an aqueous cell, the initial reversible capacity of MgMn_2O_4 is ca. 150 mA h g^{-1} , and this value is higher than those reported for LiMn_2O_4 in aqueous lithium electrolyte which are typically below 130 mA h g^{-1} (Fig. 9) [11]. Probably, the electrostatic interactions between the Mg^{2+} ions and the water molecules enhance the reversible electrochemical activity of the manganese oxides [12]. However, electrolyte decomposition and the deterioration of the lattice structure, mostly due to the Jahn–Teller distortion, may contribute to the capacity fade upon cycling. Further improvement of the electrochemical system would be needed before commercial application.

Aqueous magnesium-ion batteries may be superior to aqueous lithium-ion batteries in terms of specific capacity, economic cost, sustainability and environmental issues.

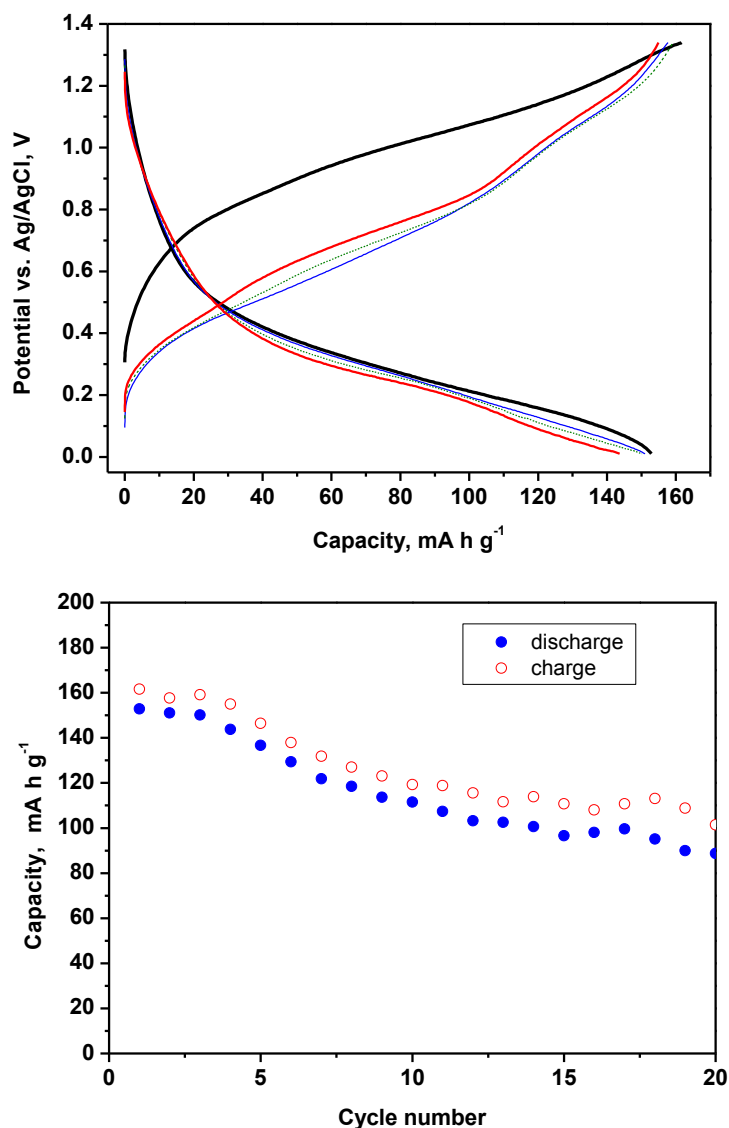


Fig. 9. Results of the galvanostatic cycling for LT-MgMn₂O₄ in aqueous cell. Current intensity: 60 μ A.

4.1.3.5 Electrochemical cycling of MgMn₂O₄ in a non-aqueous solution

Another strategy concerns the use of non-aqueous electrolytes which may deliver higher voltages, higher capacities and prolonged cycling. Non-aqueous electrolyte solutions made of magnesium salts such as Mg(ClO₄)₂ and carbonate

solvents such as PC, EC and DEC do not allow the reversible dissolution/deposition of magnesium from/on a metallic Mg electrode. Mg in AN solution is passivated by spontaneous formation of surface films and, although magnesium dissolution may occur by breakdown of this surface film, these types of electrolyte solutions do not allow reversible release of magnesium ions from the Mg metal electrode. It is due to the reactivity of AN, where its reduction forms a surface film that covers the Mg electrode leading to the rise of the cell impedance [5]. Solutions of Grignard compounds in THF exhibit better reversibility for magnesium deposition, but corrosion of the current collectors and battery case used to happen with these solutions.

We have made and tested non-aqueous magnesium-ion batteries with MgMn_2O_4 as the positive electrode versus V_2O_5 as the negative electrode and using a non-aqueous and noncorrosive electrolyte solution (Fig. 10). The reversible capacity referred to the mass of MgMn_2O_4 is about 120 mA h g^{-1} . The results show that the magnesium ions are reversibly inserted/deinserted in both the positive and the negative electrodes and the concept of a veritable magnesium-ion battery can be viable. Since the operation voltage of the battery shown in Fig. 10 is not satisfactory, then a problem to overcome is to use positive electrode materials of higher voltage and negative electrode materials of lower voltage for achieving a higher voltage in the whole battery.

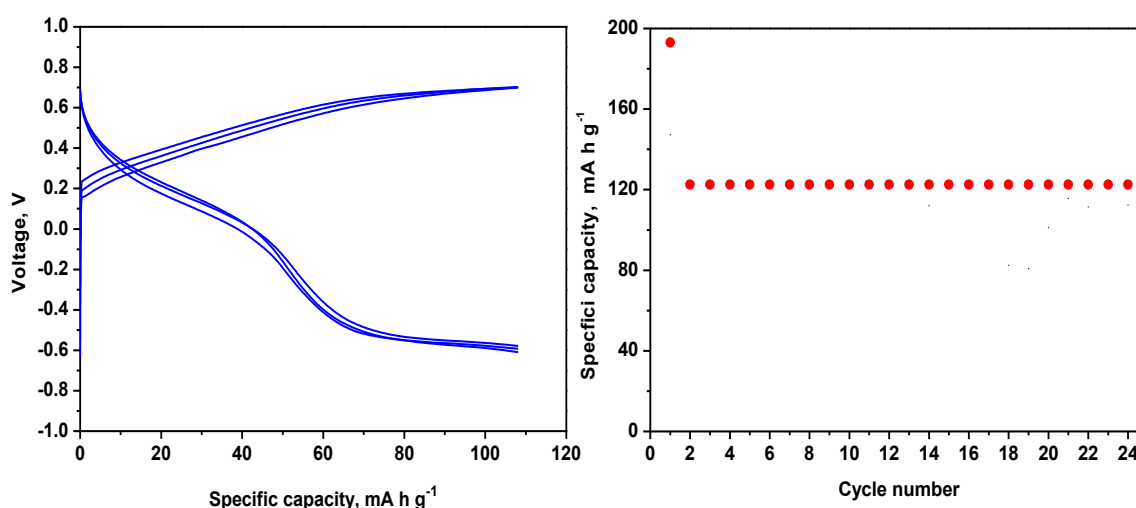


Fig. 10. Typical voltage-capacity curves and capacity vs. cycle number plots for a magnesium-ion battery in a non-aqueous and non-corrosive electrolyte solution. Positive electrode: MgMn_2O_4 -400°C. Negative electrode: commercial V_2O_5 (used in excess, $m_+/m_-=0.53$). Electrolyte solution: 0.5 M $\text{Mg}(\text{ClO}_4)_2$ in EC:DEC. Current intensity: $10 \mu\text{A}$.

The ex situ XRD patterns recorded at selected states of the first charge process of MgMn_2O_4 obtained at 800 °C show that the structure of MgMn_2O_4 is preserved during the extraction of magnesium (Fig. S5). Cubic λ - MnO_2 is not formed, and there is no clear explanation of this fact. There is a contraction of the lattice in the direction of the c-axis and the tetragonal lattice is slightly contracted. One may think that the crystallinity of MgMn_2O_4 -800 °C hinders the formation of λ - MnO_2 . However, we have checked that, the tetragonal structure of MgMn_2O_4 -400 °C is also preserved at the end of the first electrochemical charge (280 mA h g^{-1}) in the non-aqueous cell (Fig. S6), and also a contraction of the cell is observed ($a = 5.72(3)$ Å, $c = 9.21(3)$ Å, vol. =301.26 Å³). These results indicate that the cubic phase of manganese dioxide is only stabilized in aqueous solution and not in EC–DEC solvents. Probably, water molecules are incorporated into the framework of λ - MnO_2 during its electrochemical cycling in aqueous solution. On the other hand, in the case of a non-aqueous solvent, probably, the lack of water in the oxide improves the cycling stability of the tetragonal phase.

The effective use of MgMn_2O_4 as an active material for the positive electrode in a magnesium-ion battery, in turn, requires appropriate materials that can be used like a negative electrode. These negative electrode materials should have high specific capacity and operate within a certain voltage window. V_2O_5 and MnO_2 operate in a voltage which is too high. Alloys and compounds containing magnesium-alloying elements should be explored.

4.1.4 Conclusions

We have observed that magnesium can be reversibly removed from MgMn_2O_4 by chemical and electrochemical methods and by using aqueous and non-aqueous media. Even the cubic phase λ - MnO_2 can be obtained in aqueous solution, but the textural properties and the experimental conditions have to be carefully selected. The chemical demagnesiumation is easier for particles prepared at low temperature, with a small particle size and having many mesopores with a diameter smaller than ca. 20 nm. This mechanism of ion extraction is different from $\text{Li}_x\text{Mn}_2\text{O}_4$, where the spinel-type structure is always cubic for $0 < x < 1$. The results show that it may be possible to develop a veritable magnesium-ion battery based on non-corrosive electrolyte solutions.

Although the use of deoxygenated aqueous solutions is also promising, the electrochemical cycling of MgMn_2O_4 seems to be more stable in a non-aqueous electrolyte based on carbonate solvents. In a non-aqueous electrolyte, the charge process (demagnesiation) of MgMn_2O_4 leads to a contraction of the tetragonal lattice in the direction of the c-axis, and the $\lambda\text{-MnO}_2$ phase is not formed.

Acknowledgements

The authors would like to greatly acknowledge the Ministerio de Economía y Competitividad (MINECO) (MAT2014–56470-R) and FEDER cofinancing. We are also indebted to the Junta de Andalucía for financial support to the FQM-288 research group and project FQM-7206. We also thank SCAI (UCO Central Service for Research Support), the European Research Institute ALISTORE-ERI and Institute of Fine Chemistry & Nanochemistry.

4.1.5 References

1. A. Luntz, *J. Phys. Chem. Lett.* 6 (2015) 300; M. Armand, J. M. Tarascon, *Nature* 451 (2008) 652; P. Novák, R. Imhof, O. Haas, *Electrochim. Acta* 45 (1999) 351; P. G. Bruce, F. Krok, V. C. Gibson, K. Tavakkoli, *J. Mater. Chem.* 1 (1991) 705.
2. M. M. Huie, D. C. Bock, E. S. Takeuchi, A. C. Marschilok, K. J. Takeuchi, *Coord. Chem. Rev.* 287 (2015) 15; C. Kim, P. J. Phillips, B. Key, T. Yi, D. Nordlund, Y. S. Yu, R. D. Bayliss, S. D. Han, M. He, Z. Zhang, A. K. Burrell, R. F. Klie, J. Cabana, *Adv. Mater.* 27 (2015) 3377; J. S. Kim, W. S. Chang, R. H. Kim, D. Y. Kim, D. W. Han, K. H. Lee, S. S. Lee, S. G. Doo, *J. Power Sources* 273 (2015) 210; J. Muldoon, C. B. Bucur, T. Gregory, *Chem. Rev.* 114 (2014) 11683; P. Saha, M. K. Datta, O. I. Velikokhatnyi, A. Manivannan, D. Alman, P. N. Kumta, *Prog. Mater. Sci.* 66 (2014) 1.
3. C. Ling, F. Mizuno, *Chem. Mater.* 25 (2013) 3062.

4. R. Zhang, T. S. Arthur, C. Ling, F. Mizuno, J. Power Sources 282 (2015) 630.
5. R. Mohtadi, F. Mizuno, Beilstein J. Nanotechnol. 5 (2014) 1291; O. Mizrahi, N. Amir, E. Pollak, O. Chusid, V. Marks, H. Gottlieb, L. Larush, E. Zinigrad, D. Aurbach, J. Electrochem. Soc. 155 (2008) A103; Z. Lu, A. Schechter, M. Moshkovich, D. Aurbach, J. Electroanal. Chem. 466 (1999) 203.
6. S. Yagi, A. Tanaka, Y. Ichikawa, T. Ichitsubo, E. Matsubara, J. Electrochem. Soc. 160 (2013) C83.
7. M. Kruk, E. B. Celer, J. Matos, S. Pikus, M. Jaroniec, J. Phys. Chem. B 109 (2005) 3838; M. Thommes, Chem-Ing-Tech. 82 (2010) 1059.
8. C.M. Julien, M. Massot, C. Poinignon, Spectrochim Acta A 60 (2004) 689.
9. C. Hunter, J. Solid State Chemistry 39 (1981) 142; N. Wang, X. Cao, L. He, W. Zhang, L. Guo, C. Chen, R. Wang, S. Yang, J. Phys. Chem. C 112 (2008) 365; C. Wang, Y. Zhai, X. Wang, M. Zeng, Front. Chem. Sci. Eng. 8 (2014) 471.
10. J. Y. Luo, W. J. Cui, P. He and Y. Y. Xia, Nat Chem. 2 (2010) 760; P. He, J. L. Liu, W. J. Cui, J. Y. Luo, and Y. Y. Xia, Electrochim. Acta 56 (2011) 2351; M. Zhao, B. Zhang, G. Huang, H. Zhang, X. Song, J. Power Sources 232 (2013) 181.
11. Y. Wang, L. Chen, Y. Wang, Y. Xia, Electrochim. Acta 173 (2015) 178; S. Liu, S. H. Ye, C. Z. Li, G. L. Pan and X. P. Gao, J. Electrochem. Soc. 158 (2011) A1490; L. Liu, F. Tian, M. Zhou, H. Guo, X. Wang, Electrochim. Acta 70 (2012) 360; W. Li, J. R. Dahn, D. S. Wainwright, Science 264 (1994) 1115; H. Manjunatha, G. S. Suresh, T. V. Venkatesha, J. Solid State Electrochem. 15 (2011) 431; G. X. Wang, S. Zhong, D. H. Bradhurst, S. X. Dou, H. K. Liu, J. Power Sources 74 (1998) 198.
12. K. W. Nam, S. Kim, S. Lee, M. Salama, I. Shterenberg, Y. Gofer, J. S. Kim, E. Yng, C. S. Park, J. S. Kim, S. S. Lee, W. S. Chang, S. G. Doo, Y. N. Jo, Y. Jung, D. Aurbach, J.W. Choi, Nano Lett. 15 (2015) 4071.

4.1.6 Supplementary information

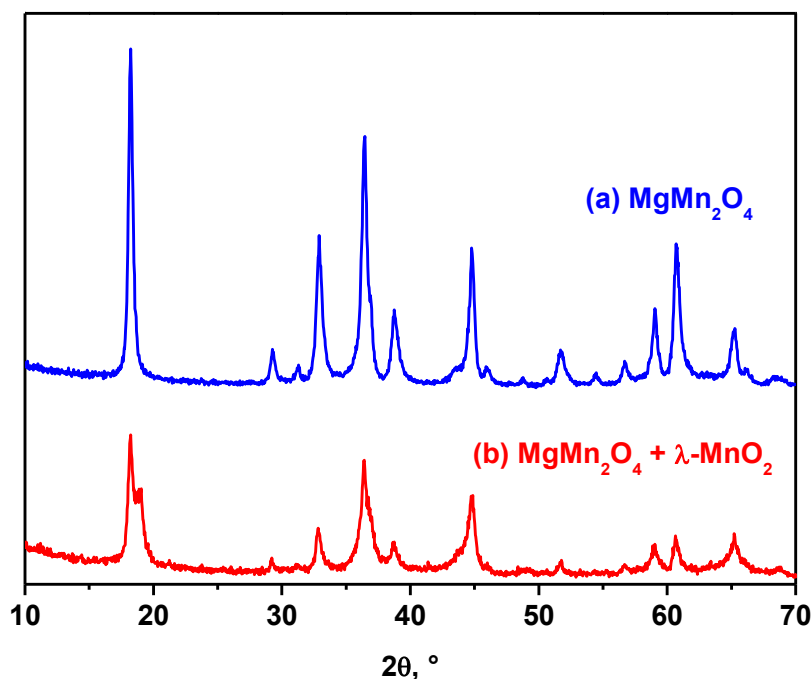


Fig. S1. X-ray diffraction patterns for tetragonal MgMn_2O_4 prepared at 550°C before (a) and after treatment with nitric acid at pH 2 during 50 minutes. The transformation into cubic manganese dioxide ($\lambda\text{-MnO}_2$) is only partial and the two phases coexist in (b). For the pristine sample in (a), the parameters of the tetragonal cell are: $a=b=5.716(3)$ Å and $c=9.2867(5)$ Å. The cell parameters obtained from (b) are the following: for the tetragonal phase $a=b=5.719(5)$ Å and $c=9.297(2)$ Å, and for the cubic phase $a=8.1(1)$ Å.

This figure can be used to see comparatively how the acid treatment more easily transforms MgMn_2O_4 prepared at 400°C into $\lambda\text{-MnO}_2$. After acid treatment, the extraction of magnesium does not reduce the tetragonal distortion of the cell in the remaining MgMn_2O_4 phase. The most probably is that the texture of $\text{MgMn}_2\text{O}_4\text{-}550^\circ\text{C}$ with blocked pores hinder the acid attack and the demagnesiumation is limited.

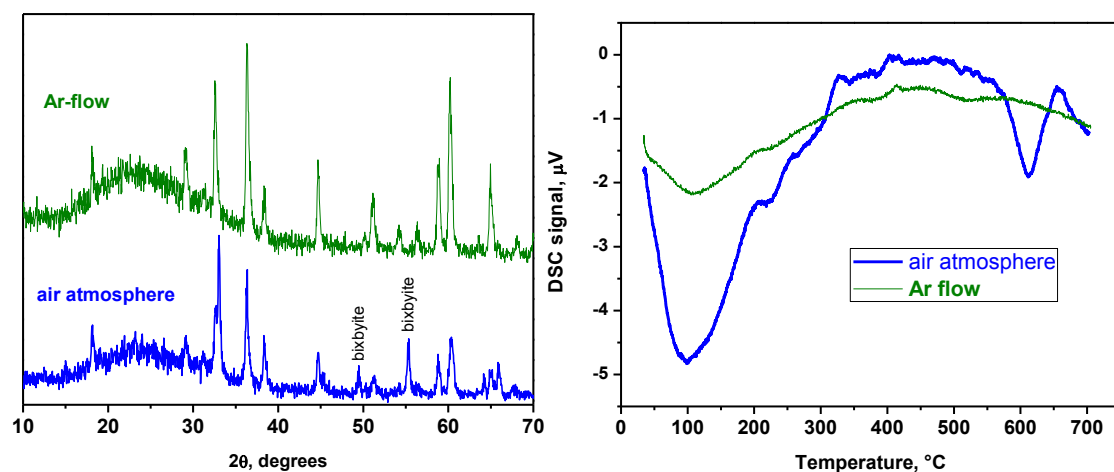


Fig. S2. XRD patterns of samples recuperated from DSC experiments (up to 700°C) that were carried out in air atmosphere and under Ar-flow starting from λ - MnO_2 .

Under Ar flow the endothermic peak at 614°C is not observed and bixbyite α - Mn_2O_3 (JCPDS:41-1442) is not formed. Two Bragg reflections of the bixbyite phase are marked.

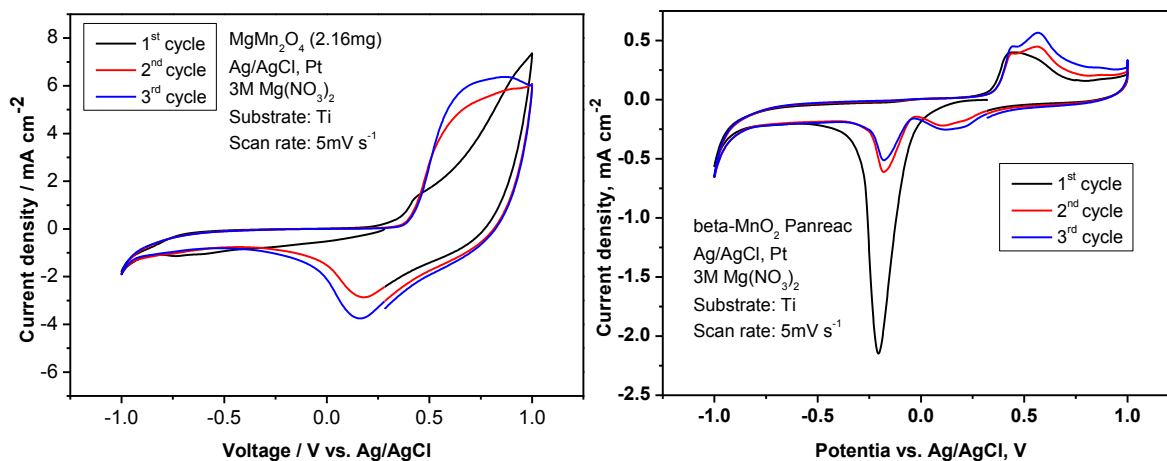


Fig. S3. Cyclic voltammety results for 400°C- MgMn_2O_4 in aqueous solution. For the sake of comparison the voltammogram of pyrolusite β - MnO_2 (commercial from Panreac) is also shown. Reference electrode: Ag/AgCl. Counter electrode: Pt. Electrolyte: 3M $\text{Mg}(\text{NO}_3)_2$. Scan rate: 5mV s^{-1} .

A reversible anodic/cathodic peak is observed, which is ascribed to the faradic reaction involving $\text{Mn}^{3+}/\text{Mn}^{4+}$. Pyrolusite phase exhibits more irreversibility and more polarization between charge and discharge.

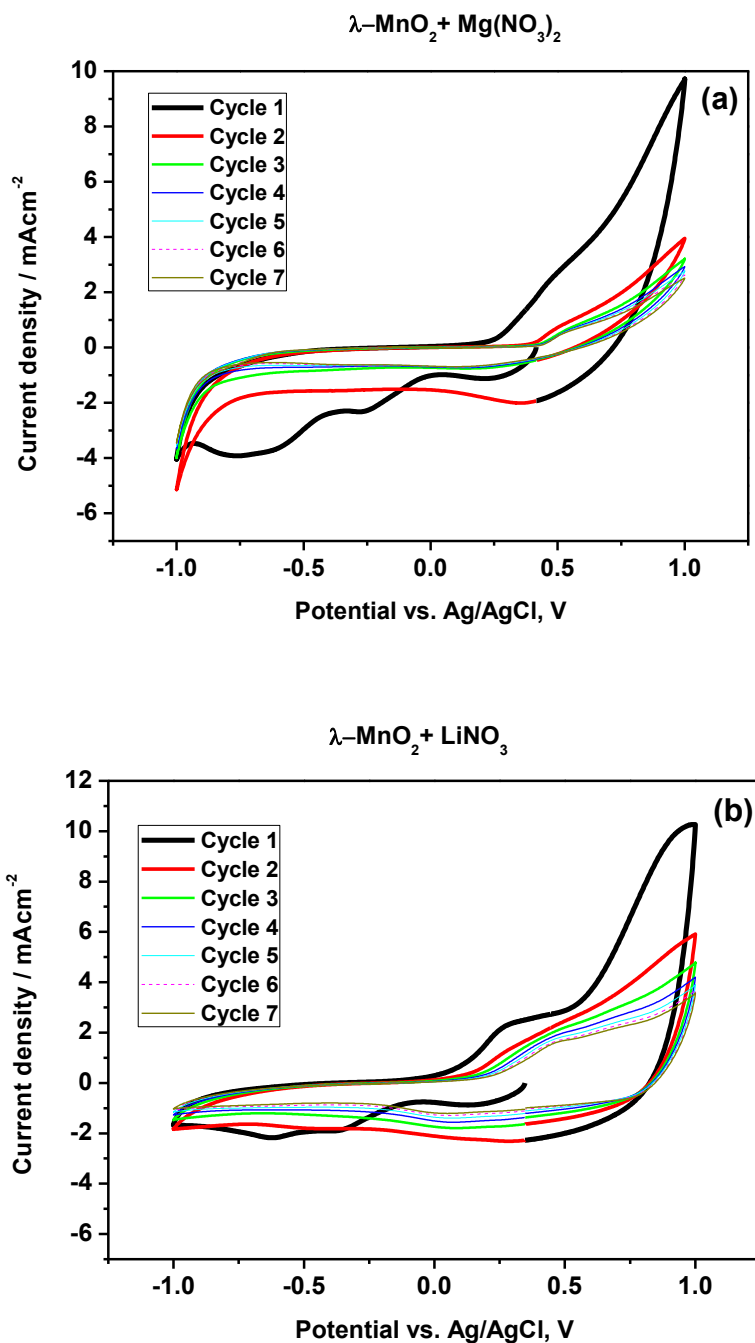


Fig. S4. Voltammetry results for $\lambda\text{-MnO}_2$ (prepared from MgMn_2O_4) in magnesium (a) and lithium (b) nitrate aqueous electrolyte. The corresponding XRD patterns of the cycled electrodes are shown in Fig. 8.

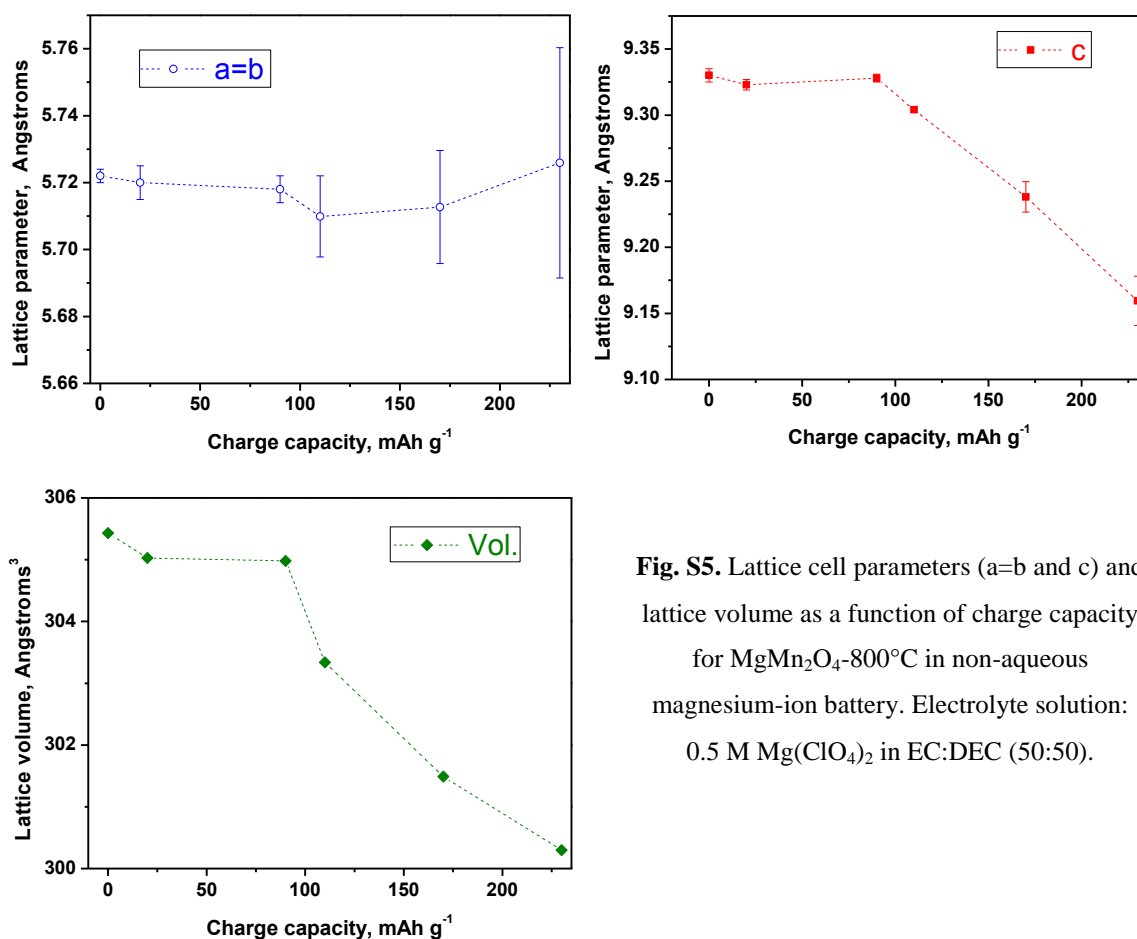


Fig. S5. Lattice cell parameters (*a=b* and *c*) and lattice volume as a function of charge capacity for MgMn₂O₄-800°C in non-aqueous magnesium-ion battery. Electrolyte solution: 0.5 M Mg(ClO₄)₂ in EC:DEC (50:50).

The tetragonal structure is preserved. The lattice parameters were obtained from the ex-situ XRD of MgMn₂O₄ (positive) electrode recuperated from magnesium-ion batteries. The negative electrode was commercial V₂O₅. The electrodes recuperated from the electrochemical cells in the dry box and its reaction with air atmosphere during XRD recording was avoided by covering the sample with a protective plastic film.

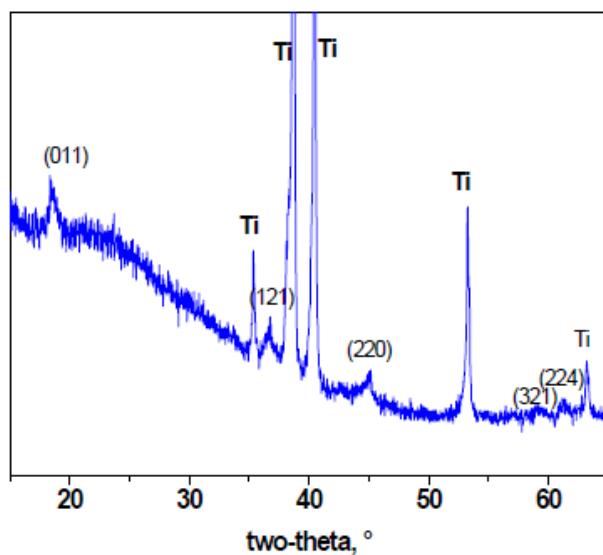


Fig. S6. Ex-situ XRD for MgMn_2O_4 -400°C electrode recuperated from the first charge in non-aqueous magnesium-ion battery. Electrolyte solution: 0.5 M $\text{Mg}(\text{ClO}_4)_2$ in EC:DEC (50:50).

It is observed that the tetragonal structure (s.g. $I4_1/amd$) is preserved. The reflections of Ti substrate are marked.

4.2 Nanobelts of beta-sodium vanadate as electrode for magnesium and dual magnesium-sodium batteries

Marta Cabello, Francisco Nacimiento, Ricardo Alcántara, Pedro Lavela, Gregorio Ortiz,
José L. Tirado.

Laboratorio de Química Inorgánica. Universidad de Córdoba. Edificio C3, Campus de Rabanales. Spain

Abstract

Nanoparticles of sodium vanadate (composition approximately $\text{NaV}_6\text{O}_{15}$) with nanobelt morphology and monoclinic structure (β -phase) were prepared by using the hydrothermal method, α - V_2O_5 as vanadium source and sodium dodecyl sulfate as both surfactant and source of sodium. This material can reversibly accommodate lithium, sodium and magnesium in its framework. Sodium vanadate nanobelts exhibit lower capacity than V_2O_5 in lithium and sodium cell. In sodium cell, the electrochemical performance with NaOTf-diglyme electrolyte solution was much better than with NaClO_4 -propylene carbonate solution. In the case of dual sodium-magnesium electrolyte, the presence of sodium in β - $\text{NaV}_6\text{O}_{15}$ and the small particle size improve the electrochemical behavior and increase the capacity (125 mAh g^{-1}) in comparison with α - V_2O_5 (10 mAh g^{-1}). The electrolyte solution based on $\text{Mg}(\text{BH}_4)_2$ and NaBH_4 dissolved in diglyme is compatible with Mg metal and yields to better electrochemical performance than magnesium perchlorate dissolved in acetonitrile. Both sodium and magnesium are reversibly intercalated at the positive electrode and electrodeposited at the negative electrode and, consequently, it can be described as a dual battery. On the other hand, a veritable magnesium-ion battery was made using MgMn_2O_4 as positive electrode and $\text{NaV}_6\text{O}_{15}$ as negative electrode, although the resulting operation voltage is low.



Journal of The Electrochemical Society 163 (13) (2016) A2781-
A2790

4.2.1 Introduction

Irrespective of the successful commercialization of lithium ion batteries since 1990's, it is necessary to develop new batteries based on other elements such as sodium and magnesium. Taking into account its significance to clean energy and its supply risk, it results that nowadays lithium is a near-critical mineral resource. In addition, Mg would be a better negative electrode for reasons such as its natural abundance, high volumetric capacity and no formation of dendrites upon electrochemical cycling [1-3]. This alkaline-earth element can be particularly useful for stationary applications batteries. However, the effective use of Mg still needs for further improvement of the electrolyte solution. On the other hand, the diffusion of magnesium into host materials is slow, and the intercalation reactions of magnesium are not well understood.

Some of the most relevant electrode materials for the forthcoming post-lithium era are vanadium oxides [4]. Vanadium oxides are of special interest as electrode materials for batteries, mainly because of their open structures with interlayer spaces and tunnels that allow ions diffusion and because of the high voltage provided by the redox pair of V^{5+}/V^{4+} . The orthorhombic polymorph α - V_2O_5 has a layered-type structure consisting of VO_5 -square pyramids [5]. Vanadium pentoxide gels and xerogels ($V_2O_5 \cdot nH_2O$) are layered-structure materials with water or protonated water (H_3O^+) in the interlayer space that have ion-exchange and ion-intercalation capabilities. Alkaline and alkaline-earth vanadium oxide xerogel with M^{n+} can be prepared ($M_xV_2O_5 \cdot nH_2O$) for example by ionic exchange reactions [6]. The intercalated cations M^{n+} are placed in the interlayer space and neutralize the negative charge of the vanadium oxide sheets. The compounds with formula $M_xV_2O_5 \cdot nH_2O$ are members of the hewettite family, being hewettite the naturally found mineral $CaV_6O_{16} \cdot 9H_2O$. The thermal annealing at about 250-600°C of $M_xV_2O_5 \cdot nH_2O$ xerogels drives to the formation of anhydrous vanadium bronzes ($M_xV_2O_5$) in which vanadium ions are presents in +5 and +4 oxidation states [6,7]. These monovalent (M^+) and divalent (M^{2+}) bronzes can possess different structures, including tunnel-type structure.

Besides the chemical composition and the lattice structure, the particle size and morphology can affect to the electrochemical behavior and, thus, materials with very small particle size can be better electrodes in terms of intercalation capacity [3,8].

Intercalation of magnesium into large particles of V_2O_5 is a slow process, but decreasing the particle size can improve the capacity [9,10]. Aurbach's group reported V_2O_5 thin-film electrodes that can be cycled over a potential range of 2.2–3.0 V vs. Mg with a specific capacity of 150 mAh g^{-1} [11]. Sa et al., using bilayered $V_2O_5 \cdot nH_2O$ xerogel obtained a reversible capacity of about 50 mAh g^{-1} in the voltage region between ca. 0.1 and 3.0 V vs. Mg, and they found that Mg insertion is accompanied by cointercalation of solvent molecules (diglyme) [10]. On the other hand, the hydrothermal synthesis can be a more successful approach to prepare nanomaterials in comparison with the ceramic method [12]. Yu et al. reported the synthesis of single-crystals nanobelts of $Na_2V_6O_{16} \cdot 3H_2O$ (s.g. $P2_1/m$) using V_2O_5 , NaF and hydrothermal conditions [13]. Zhou et al. used V_2O_5 powder, sodium sulfate and hydrothermal conditions to obtain NaV_6O_{15} nanowires with several tens of micrometers in length [14]. Shi et al. used V_2O_5 powder, sodium dodecylsulfate (SDS) surfactant and hydrothermal conditions to prepare layered-structure V_2O_5 nanobelts [15]. Besides the particle size, another critical aspect is water content [16,17]. The presence of water in the electrolyte can facilitate the magnesium intercalation/deintercalation in V_2O_5 by solvation of magnesium ions, protons can participate in the intercalation process, and the increase of the water content in the electrolyte increases the intercalation voltage [16]. Unfortunately, water can react with metallic Mg at the negative electrode and cause its passivation and battery failure.

The faradic insertion of lithium and sodium into anhydrous NaV_6O_{15} (tunnel structure) prepared both by sol-gel and solid state reaction was studied by Pereira-Ramos and others [18]. Later, the intercalation of lithium and sodium was studied using the hydrate form of sodium vanadium oxide (lamellar structure), and it was found that the presence of water does not hinder lithium accommodation and, in fact, the initial reversible capacity even can be higher in the presence of water [19].

Electrochemical insertion of Mg^{2+} into vanadium bronzes was firstly reported by Novák et al. [20]. It has been found that water molecules can stabilize Mg^{2+} ion in insertion compounds of V_2O_5 and vanadium bronzes and, consequently, water content in electrolyte solution is a critical aspect [9,6,20].

The optimization of the electrolyte solution is a key aspect of the batteries, particularly magnesium batteries. The main difficulty is that the electrolytes supporting the reversible electrodeposition of Mg usually are not stable at the high voltage

exhibited by the positive electrode. On the other hand, the greater charge-to-size ratio of Mg^{2+} in comparison with Li^+ and Na^+ claims for a better electrostatic shielding of Mg^{2+} in the electrolyte solution and in the intercalated electrode. Cointercalation of water or other solvents can influence on the electrochemical intercalation of magnesium [16], and the presence of water in the electrolyte changes the phase behavior of the Mg-xerogel- V_2O_5 . Recent computational calculations found that Mg^{2+} can interact strongly with the carbonyl (C=O) oxygen atom of the carbonates (e.g. ethylene carbonate) in the primary solvation sphere [21]. Unfortunately, the electrode of Mg seems to be incompatible with many solvents, such as water and carbonates which can passivate the surface of Mg. Thus, another choice can be the use of dual salt electrolyte and hybrid batteries [22,23].

In this work we study the capacity of sodium vanadate in the form of nanobelts to intercalate magnesium. Besides magnesium-electrolyte, we have tested lithium, sodium and sodium-magnesium electrolytes. Having in mind the goal of evaluating $\text{NaV}_6\text{O}_{15}$ nanobelts as positive electrode vs. Mg metal as negative electrode, we have also used an anhydrous electrolyte based on dual sodium-magnesium borohydride and diglyme as a solvent. For the sake of comparison with magnesium one, electrochemical cells of lithium and sodium are also studied. To further proof the reversible intercalation of magnesium, we have built a full magnesium-ion battery with two intercalation compounds, MgMn_2O_4 and $\text{NaV}_6\text{O}_{15}$, and with an electrolyte solution based on carbonate solvents and containing water molecules.

4.2.2 Experimental

4.2.2.1 Synthesis

A surfactant-assisted hydrothermal method was used to obtain high-aspect-ratio sodium vanadate nanobelts. A solution consisting of 1.8 mmol of SDS, 0.6 mmol of V_2O_5 (Sigma-Aldrich) and 60 mL of deionized water were loaded into a Teflon-lined stainless steel autoclave filled up to 60% of its volume. The autoclave containing the reactant solution was sealed and placed into an oven at 150 °C for 48 h, and then it was naturally cooled to room temperature. The resulting precipitate was collected and

washed with deionized water and absolute ethanol several times, and finally dried at 50 °C for 8 h in a vacuum oven. SDS acts both as a source of sodium ions and as a surfactant.

MgMn₂O₄ was prepared by thermal decomposition of oxalates at 400°C as described in elsewhere [24], and this spinel-type material was used as a positive electrode of the full magnesium-ion battery.

4.2.2.2 Structure, composition and microstructure

To study the structure, X-ray diffraction (XRD) measurements were performed in a BrukerD8 Discover A25 diffractometer equipped with Cu-K_α radiation source and a graphite monochromator.

The microstructure was examined by using scanning electron microscopy (SEM) and Transmission Electron Microscopy (TEM). Field-emission scanning electron microscopy (FE-SEM) micrographs were obtained using a JSM-7800F Prime apparatus. The TEM micrographs were acquired with a JEOL 1400 microscope.

X-ray photoelectron spectra (XPS) furnished with a MgK source and a chamber pressure able to reach 4×10^{-9} mbar (SPECS Phoebios150 MCD) allowed to analyse the chemical state of the samples. In the case of electrodes recuperated from the electrochemical cell, the electrodes were rinsed with diglyme before recording the spectra.

4.2.2.3 Electrolyte preparation

The preparation of the non-aqueous electrolyte solutions was conducted in an argon-filled glove box using dry solvents. The electrolyte for metal Mg cell was 1 M anhydrous magnesium perchlorate in acetonitrile.

The dual electrolyte solution used was composed of 0.09 M Mg(BH₄)₂ (Aldrich, 95%) and 0.25 M NaBH₄ (Panreac, 98%) in diglyme (DGM). NaBH₄ was previously dried at 70 °C overnight using a Büchi oven. In a typical preparation 22 mL of DGM were added to NaBH₄ which is left stirring for 30 min, and then Mg(BH₄)₂ is carefully added to obtain a clear solution. The dual salt electrolyte was stirred overnight at room temperature prior to use.

The electrolyte solution for the full magnesium-ion battery was 1 M $\text{Mg}(\text{ClO}_4)_2 \cdot 4\text{H}_2\text{O}$ in ethylene carbonate (EC) and diethyl carbonate (DEC) solvents mixture with EC:DEC=1:1.

4.2.2.4 Electrochemical measurements

Before preparing the electrodes, we checked by thermal analysis that the active materials did not contain water. The positive electrodes were prepared by mixing 80 wt% of active material with 10 wt% carbon black and 10 wt% polyvinylidene fluoride (PVDF) as a binder in *n*-methyl-2-pyrrolidone (NMP). The slurry was coated over a carbon foil (Goodfellow) used as electrode substrate, and subsequently dried under vacuum at 100°C for 12 h. Electrochemical measurements were conducted using Swagelok cells with vanadium oxide as positive electrode, Mg (or Na or Li) foil as negative electrode, and Whatman glass fiber sheets impregnated with the electrolyte solution as separator. The assembly of the electrochemical cells was conducted in an argon filled MBRAUN glove box. All the electrochemical experiments were performed using a Biologic VMP instrument. Blank (reference) experiments were conducted to make sure that no side reactions were contributing to the assumed intercalation reaction.

4.2.3 Results and discussion

4.2.3.1 Structure and microstructure

The vanadium pentoxide sample used as reactant shows an XRD-pattern (Fig. 1a) that is ascribed to orthorhombic vanadium pentoxide ($\alpha\text{-V}_2\text{O}_5$) with space group Pmmn (JCPDS 41-1426). The average crystallite size obtained from application of the Scherrer equation to the broadening of the Bragg peaks is $L=45.8$ nm.

The as-prepared sample of sodium vanadate was of greenish color, indicating the partial reduction of vanadium ion from the initial reactant (brownish/yellowish V_2O_5). Taking into account the JCPDS files 49-0998, 24-1155 and 28-1172 and the literature, the XRD pattern of the as-prepared sample (Fig. 1b) can be ascribed to anhydrous sodium vanadium bronze, β -phase, with composition approximately $\text{Na}_{0.33}\text{V}_2\text{O}_5$ (or $\text{NaV}_6\text{O}_{15}$) and with monoclinic space group C2/m [14,19,25]. Reflections of raw V_2O_5

or other impurities are not observed. The intensity of the reflections is in good agreement with the preferential growth in a one-dimensional-like structure. The average crystallite size obtained from the broadening of the Bragg reflections and applying the Scherrer equation is $L=34.6$ nm. The resulting lattice cell parameters are: $a=15.43(2)$ Å, $b=3.580(3)$ Å, $c=10.08(1)$ Å, $\alpha=90^\circ$, $\beta=109.41(9)^\circ$ and $\gamma=90^\circ$. It is worth to note that the structure of the bronze obtained here $\text{NaV}_6\text{O}_{15}$ differs from the bronzes of multivalent ions $\text{M}_x\text{V}_2\text{O}_5$ (with $M=\text{Ba}^{2+}$, Ni^{2+} , Al^{3+} , Fe^{3+}) which have orthorhombic α -phase and space group Pmmn [6]. The $\text{NaV}_6\text{O}_{15}$ is a bronze with bannermanite-type structure [25-27] (Figure 1). In this structure, the V_6O_{15} layers are linked to each other by one oxygen atom per unit cell and only one kind of tunnels with two interstitial M^+ - sites exist. The vanadium atoms occupy three crystallographically independent sites, two of them with octahedral coordination and another site with square pyramidal coordination. The Na^+ ions occupy the seven-coordinated sites within the tunnel. This crystal structure is highly anisotropic and $\beta\text{-Na}_{0.33}\text{V}_2\text{O}_5$ displays quasi-1D conductivity [28]. On the other hand, Pereira-Ramos and co-workers reported up to ca. $\text{NaLi}_{4.8}\text{V}_6\text{O}_{15}$ by using electrochemical lithium insertion into $\text{NaV}_6\text{O}_{15}$ [18,19], being this composition nearby the total occupancy of the sites ($\text{M}_6\text{V}_6\text{O}_{15}$ for M being monovalent ion and vanadium in oxidation state +4).

In the method of synthesis that we have employed, sodium vanadium bronze is directly obtained in a single step thanks to the hydrothermal synthesis conditions. In several pioneer works, the authors firstly intercalated sodium into $\alpha\text{-V}_2\text{O}_5$ and secondly heated the resulting product at ca. 550°C to yield the monoclinic phase $\beta\text{-NaV}_6\text{O}_{15}$ [6,7]. Concerning the hydrothermal method, other authors used Na_2SO_4 like source of sodium instead of the hydrothermal method [14], but in our case the surfactant (SDS) is the source of sodium.

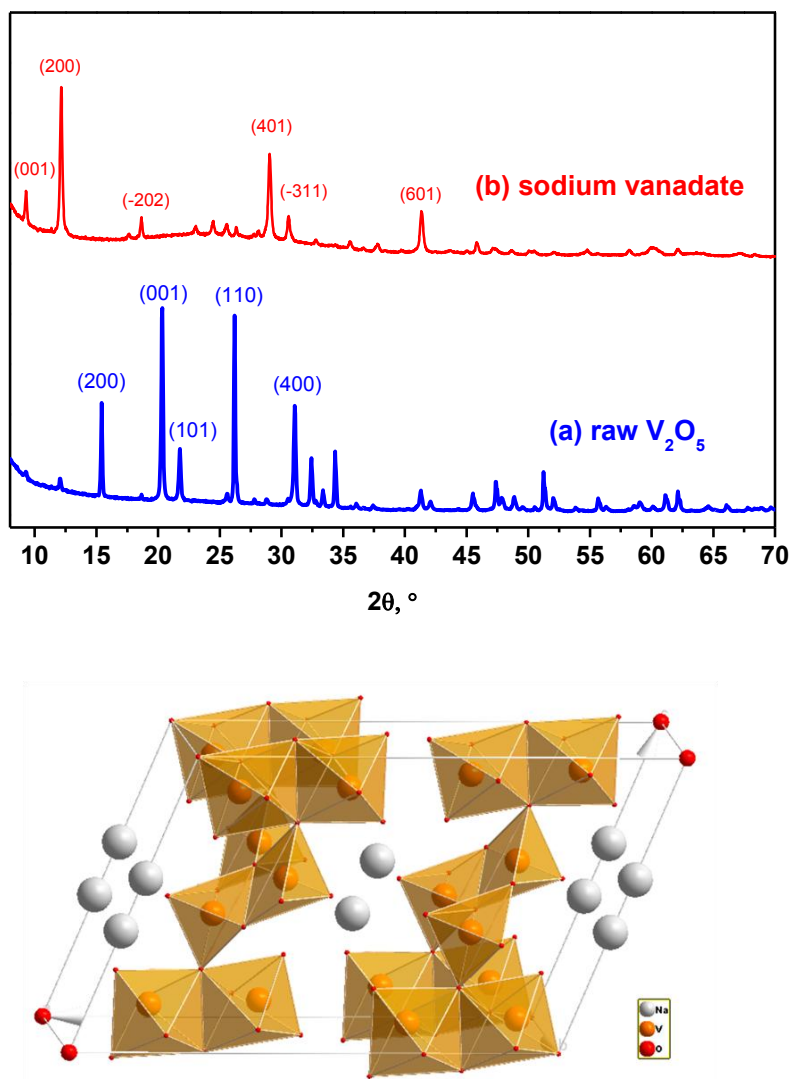


Fig.1. XRD patterns of (a) α - V_2O_5 raw material with space group Pmmn, and (b) as-prepared sodium vanadate nanobelts with space group C2/m. The main Miller indexes are given. Unit cell of β - $Na_xV_6O_{15}$ with bannermanite-type structure showing the two different coordination polyhedra of vanadium ions and interstitial Na^+ sites.

4.2.3.2 Composition and oxidation state

SEM images reveal that the obtained particles have the morphology of straight nanobelts (Fig. 2). These nanobelts are up to several tens of micrometers in length, ca. 60-90 nm in diameter and ca. 20 nm in thickness. Each single nanobelt has uniform diameter.

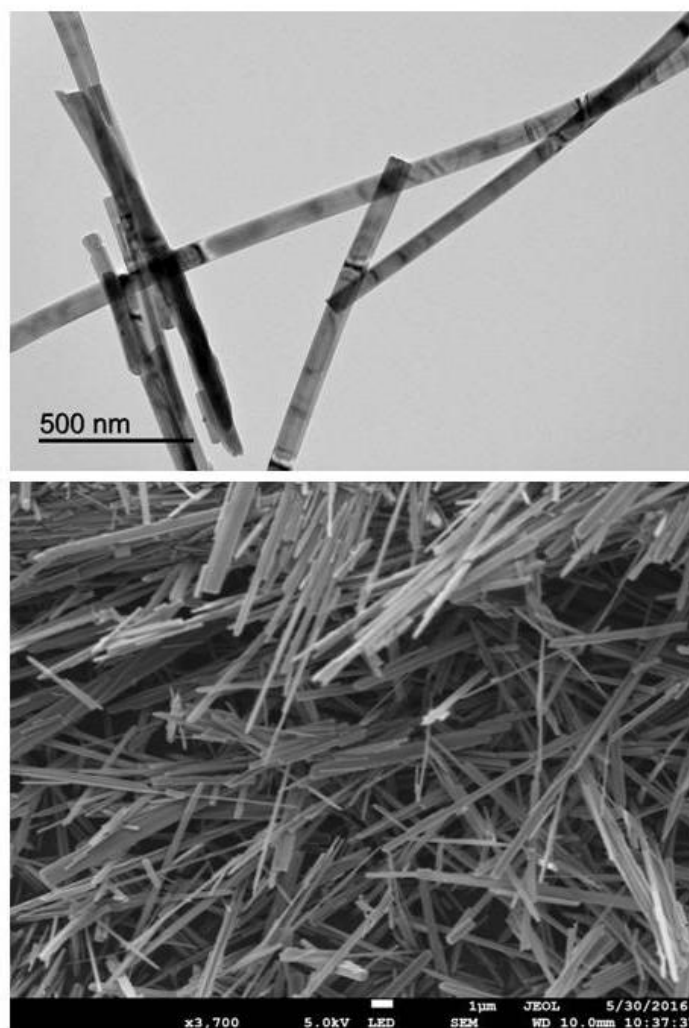


Fig.2. Selected FE-SEM and TEM images of as-prepared sodium vanadate nanobelts.

According to the microanalysis coupled to SEM with EDS-type detector, the approximate chemical composition of the obtained sample is $\text{Na}_{0.8}\text{V}_6\text{O}_{14.9}$. The chemical composition and oxidation state was further studied by XPS (Fig. 3). The XP spectra confirm that sodium vanadium bronze was obtained from raw V_2O_5 . For the raw V_2O_5 sample, the binding energies of O 1s and V 2p_{3/2} lines are 530.2 and 517.3 eV, respectively. The binding energy splitting between V 2p_{3/2} and V 2p_{1/2} is 7.7 eV. These values agree very well with the reported data for V_2O_5 [29-31]. There is an additional O 1s component at ca. 533 eV that is ascribed to more covalently bonded oxygen in defects or contamination on the surface of V_2O_5 [31,32]. For the sodiated bronze, the lines of intercalated sodium are observed and the V 2p lines become broader and shifted to lower binding energy because of the occurrence of a new signal attributed to V^{4+} . The

fitting of the V 2p shows that the V^{4+}/V^{5+} atomic ratio is 0.38. The O 1s line also becomes broadened and is slightly shifted to lower binding energies (from 530.2 to 329.9 eV) and the component of defects at ca. 533 eV becomes more intense. These results mean that the intercalation of sodium involves the reduction of vanadium ions and the shift of the Fermi level of the host. If one takes into account the oxygen line only centered at 530.2 eV, the resulting composition would be $Na_{0.7}V_6O_{14.5}$. This chemical composition would involve that the average oxidation state of vanadium is +4.7.

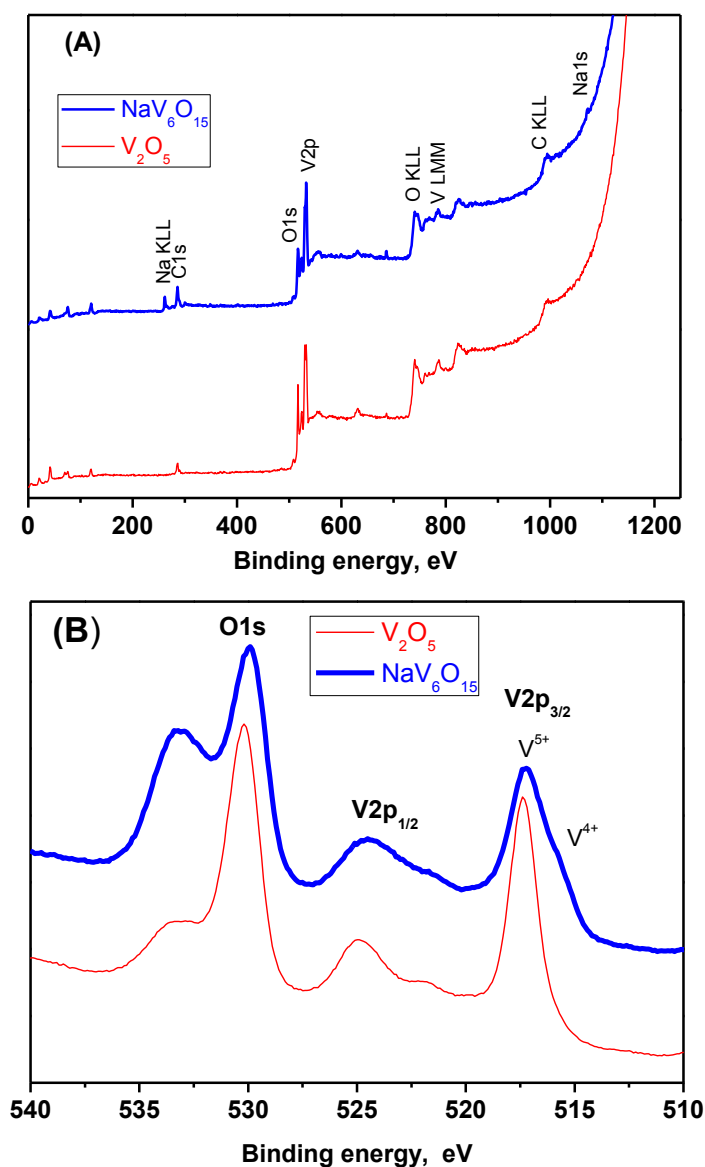


Fig.3. X-ray photoelectron spectra of NaV_6O_{15} nanobelts and raw V_2O_5 . (A) Survey spectra. (B) Spectra in the O 1s and V 2p core levels.

4.2.3.3 Electrochemistry in metal sodium cell

The main goal of this work is to study the electrochemical behavior in Mg cell. However, for the sake of comparison Li (Fig. S1) and Na (Fig. 4) cells were also tested. The specific capacity measured in the first discharge of sodium vanadate is lower than the capacity of V_2O_5 in sodium cell (Fig. 4). A great amount of sodium is irreversibly trapped in V_2O_5 after the first discharge and the structure is irreversibly modified through two successive pseudoplateaus (Fig. 4A) [33]. For sodium vanadate the first two cycles are more reversible, and extended plateaus are not observed in Fig. 4B. The intercalation voltage is lower for Na cell than for Li one, as expected. The structural composition limit of the β -phase is $Na_2V_6O_{15}$ [33]. The full reduction of V^{5+} to V^{4+} would correspond to the composition $Na_6V_6O_{15}$ (total occupancy of the sites in the tunnels). More than 4 Na per formula are inserted, while a maximum of ca. 2.7 Na per formula (ca. 140 mAh g^{-1}) can be deintercalated within the voltage range of 1.0-4.0 V vs. Na/Na⁺ (Fig. 4B). Apparently, sodium ions are more strongly trapped than lithium ions. Pereira-Ramos and co-workers reported an initial reversible capacity of 85 mAh g^{-1} for NaV_6O_{15} in sodium cell [18]. More probably, the nanometric size of our sample and the electrolyte solution allow achieving a higher capacity value. Similarly to our results, other authors recently reported capacities of around 75-142 mAh g^{-1} for nanorods of monoclinic NaV_6O_{15} [34, 35], although these authors used carbonate-based solvents. For the sake of comparison, and having in mind the use of DGM in Mg battery, we also used DGM in Na cell. For both α - V_2O_5 and β - $Na_6V_6O_{15}$, the resulting specific capacity values are higher in NaOTf-DGM electrolyte solution than in $NaClO_4$ -PC (Fig. 4C). Apparently, the electrolyte solution $NaClO_4$ -PC is not very compatible with metal Na, and the electrolyte solution NaOTf-DGM is much better (Fig. 4C). In addition, other authors found that sodium-DGM can be cointercalated into graphite below ca. 1.0 V vs. Na⁺/Na using 1 M NaOTf in DGM as electrolyte solution [36], and we cannot discard that DGM molecules can be co-intercalated into these vanadium oxides.

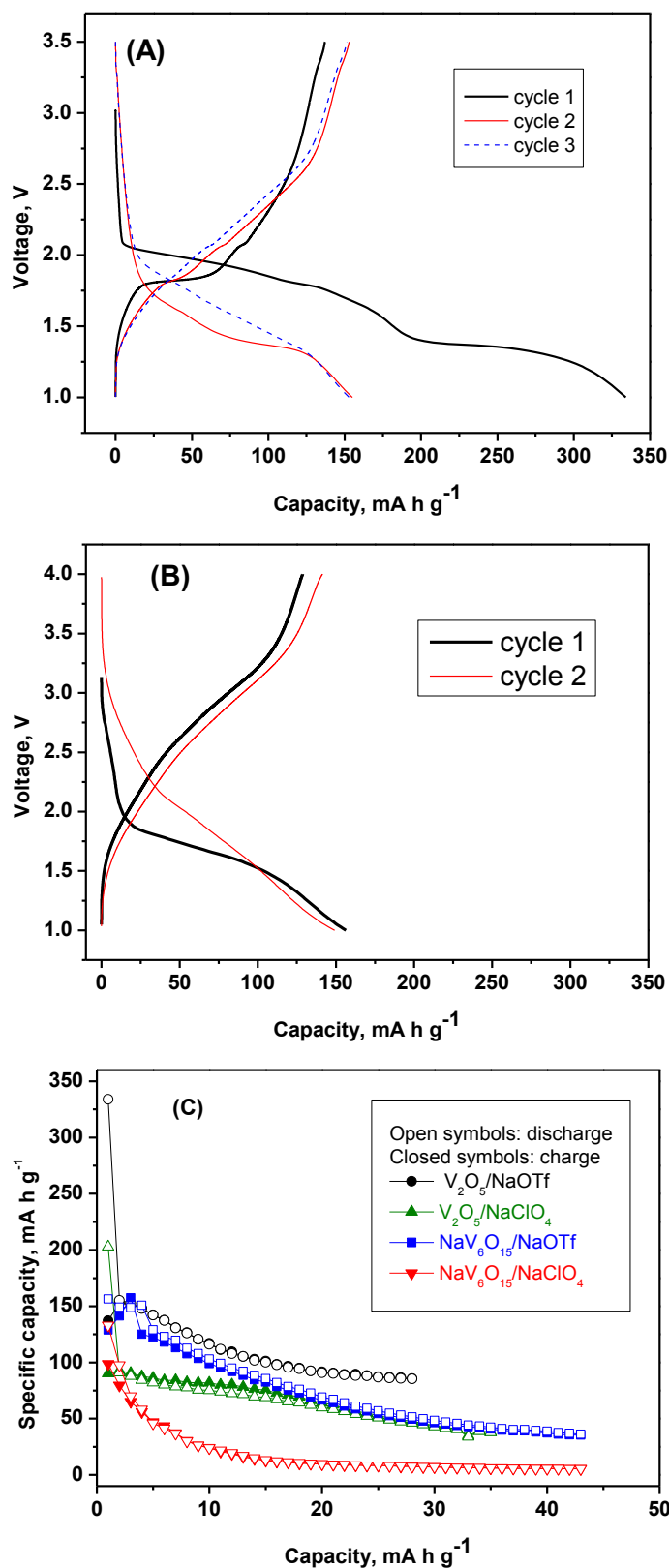


Fig.4. Electrochemical experiments in sodium cell using 1 M NaOTf-DGM as electrolyte solution. Galvanostatic discharge-charge curves for (A) V_2O_5 and (B) NaV_6O_{15} . (C) Capacity vs. cycle number. Current: 30 μ A.

4.2.3.4 Electrochemistry in metal magnesium battery

The electrochemical behavior of sodium vanadate was tested in Mg cell using magnesium perchlorate in dry acetonitrile as electrolyte solution electrode (Fig. 5). For comparison, the results with V_2O_5 are shown in the supplementary information (Fig. S2) and agree well with previous reports [10]. For both V_2O_5 and $Na_6V_6O_{15}$ the average voltage is ca. 1.1 V vs. Mg/Mg^{2+} , but the specific capacity values can be higher for nanobelts $Na_6V_6O_{15}$. In two-electrode configuration, the resulting electrochemical behavior is very poor (Fig. 5A,B), probably because the electrolyte solution can react irreversibly with metal Mg electrode. During the electrochemical cycling, the cell polarization increases, and the capacity rapidly decreases from 90 mAh g^{-1} in the first discharge to almost 0 mAh g^{-1} after ca. 20 cycles (Fig. 5B). The observed capacity values are higher in the charge than in the discharge and this fact can be related due to irreversible processes at the negative electrode. The three-electrode configuration provides a more adequate measurement of the voltage and also the electrochemical cycling is improved (Fig. 5C and D). During the first five cycles the discharge capacity tends to increase, probably due to electrodes activation. After that, the discharge capacity tends to decrease whereas the charge capacity increases, suggesting that the charge process (Mg plating at the negative electrode) involves irreversible electrolyte decomposition. The metal Mg at the negative electrode is not compatible with this electrolyte solution, because Mg becomes electrochemically inactive due to the formation of a blocking layer on the electrode surface [9]. After 50 cycles the capacity is only 45 mAh g^{-1} . In the control experiment of Fig. 5E, the cyclic voltammetry results show that Mg is plated on carbon below 0.0 V and over ca. 2.5 V the electrolyte solution is decomposed. These results illustrate the difficulty of finding a magnesium electrolyte solution adequate for both the negative and positive electrode. Besides, the apparent potential values can be affected by surface film formation at the electrode/electrolyte solution interface.

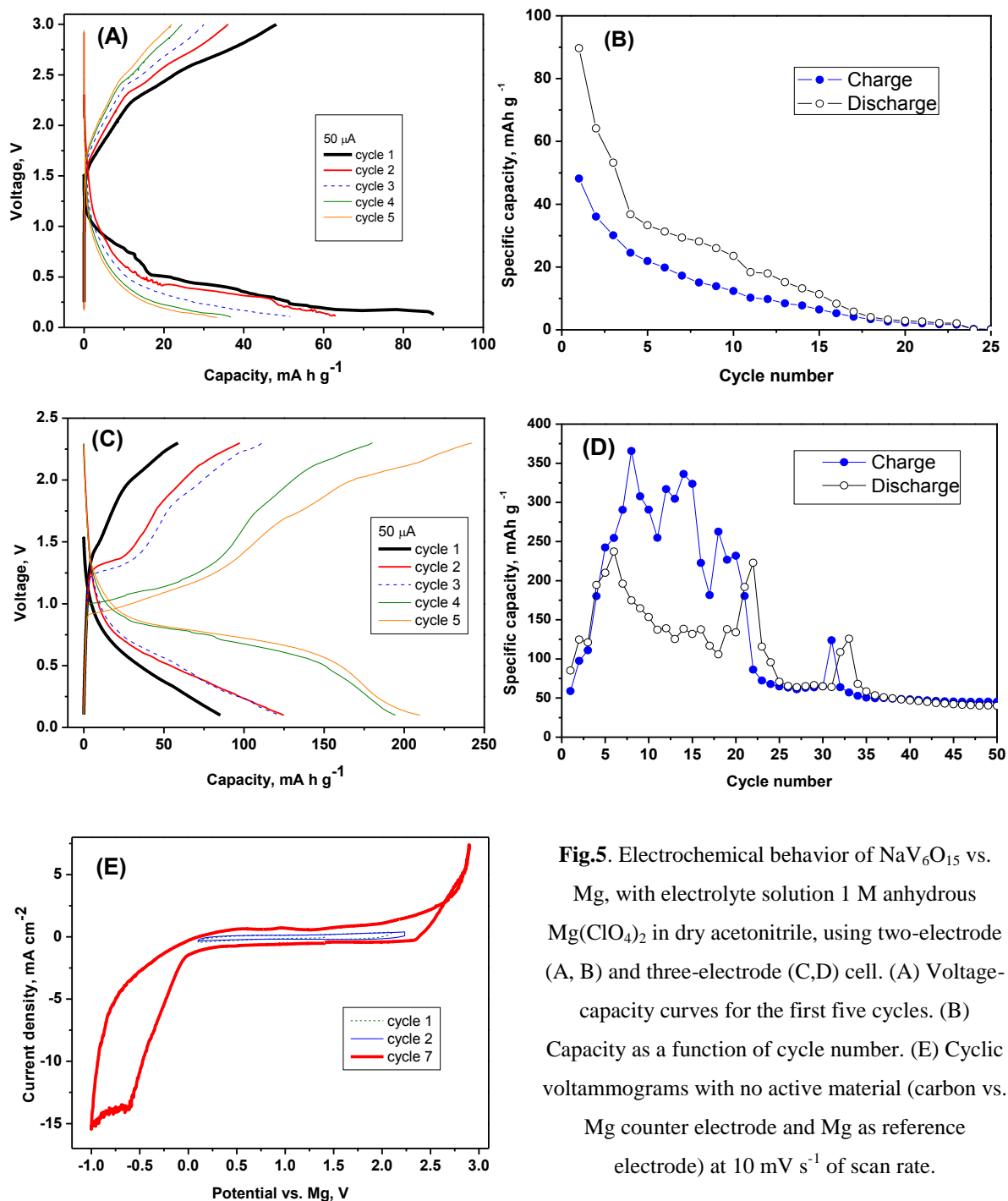


Fig.5. Electrochemical behavior of $\text{NaV}_6\text{O}_{15}$ vs. Mg, with electrolyte solution 1 M anhydrous $\text{Mg}(\text{ClO}_4)_2$ in dry acetonitrile, using two-electrode (A, B) and three-electrode (C,D) cell. (A) Voltage-capacity curves for the first five cycles. (B) Capacity as a function of cycle number. (E) Cyclic voltammograms with no active material (carbon vs. Mg counter electrode and Mg as reference electrode) at 10 mV s^{-1} of scan rate.

Taking into account the electrochemical behavior using magnesium perchlorate-acetonitrile, other electrolyte solutions were tested (Figs. 6-11). The range of electrochemical stability of the dual electrolyte solution $\text{NaBH}_4\text{-Mg}(\text{BH}_4)_2$ in DGM was studied by cyclic voltammetry and galvanostatic cycling in reference experiments (Fig. 6). The dual electrolyte solution is stable in the voltage range between 0.0 and 2.8 V vs.

Mg/Mg^{2+} (Fig. 6A). Below 0.0 V, Mg is reversibly electrodeposited on the positive electrode. The anodic peak at ca. 2 V vs. Mg is ascribed to stripping of magnesium previously electroplated. Over ca. 2.8 V the electrolyte solution is irreversibly decomposed. The plating/stripping of Mg metal is indicative of that the electrolyte is properly dry, because water is not compatible with that. Redox activity in the voltage range between ca. 0.1 and 2.2 V is not observed for the graphite (carbon paper) used as substrate of the active material (Fig. 6B), as expected. If one compares Fig. 6A with Fig. 5E, it is concluded that the plating/stripping process is more reversible when using the dual electrolyte, strongly suggesting synergy effects in this dual electrolyte.

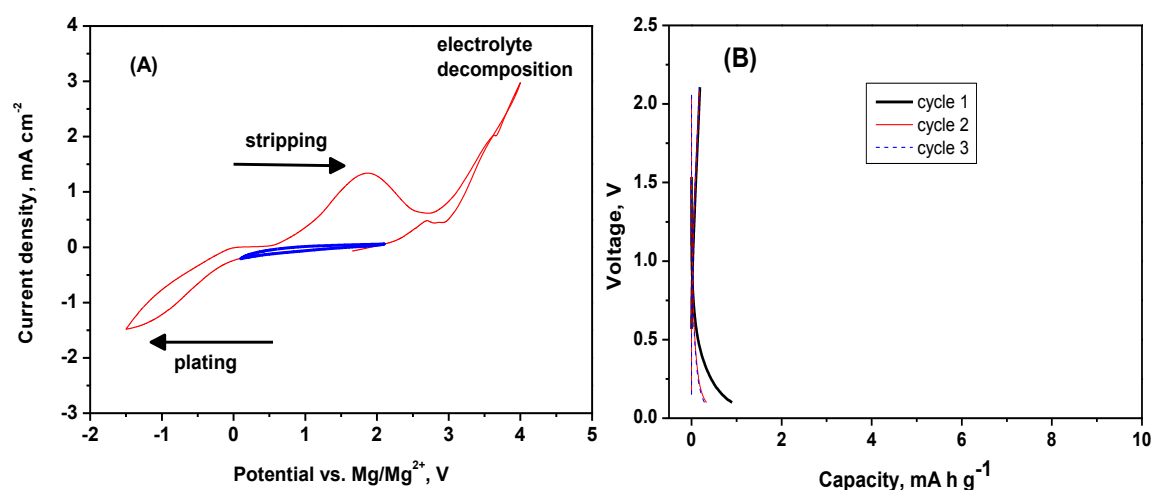


Fig. 6. Control experiments with no active material for the dual electrolyte solution based on $\text{Mg}(\text{BH}_4)_2$ and NaBH_4 in DGM. (A) Cyclic voltammetry and (B) galvanostatic cycling. Negative electrode: Mg. Positive electrode: carbon paper. In (A) the scan rate is 10 mV s^{-1} , the blue and thicker line represents the first scan of a CV between 0.1 and 2.1 V, and the red and thinner line represents the first scan of a CV between -1.5 and +4.0 V. The current in (B) is $50 \mu\text{A}$.

It is observed that sodium vanadate can be efficiently cycled vs. metal Mg using an electrolyte solution based on $\text{Mg}(\text{BH}_4)_2$ and NaBH_4 dissolved in DGM (Figs. 7,8). Since the redox potential of Na^+/Na (-2.71 V vs. SHE) is more negative than the redox potential of Mg^{2+}/Mg (-2.38 V vs. SHE) it would be expected that Mg be electrodeposited at the negative electrode and reversibly intercalated at the positive one. On the other hand, we cannot discard that DGM cointercalation can contribute to improve the insertion reaction [36]. The reversible capacity with (Na-free) Mg-DGM

electrolyte is negligible (Fig. S3), because the presence of NaBH_4 ion in the electrolyte solution modifies the interactions between magnesium and solvent molecules, weakening the interaction between Mg^{2+} and BH_4^- , and increasing the kinetics of Mg electrodeposition [23]. In Fig. 7E,F, the reversible capacity of sodium vanadate at slow rate is about 125 mAh g^{-1} , while at higher rates (Fig. 7A-D) the observed capacity values are around $70\text{-}100 \text{ mAh g}^{-1}$. The irreversible pseudoplateau observed in the first discharge at low rate (Fig. 7C,E) suggests structural changes or electrolyte decomposition (passivating layer). At higher current (Fig. 7A) the cell polarization affects to the voltage-capacity curve and the discharge plateau is not observed. In the charge process, the pseudoplateau, which is located at ca. 1.8 V tends to increase its voltage when the current increases, suggesting that the demagnesiumation is a slow process. In addition, the voltage of this pseudoplateau tends to decrease when the cycle number increases suggesting an activation process. This pseudoplateau is not observed in the discharge process, and we think that, besides oxidation of the working electrode, it is affected by the electroplating at the negative electrode. By comparing V_2O_5 (Fig. 9) and $\text{NaV}_6\text{O}_{15}$ (Figs. 7,8), it is observed that nanobelts sodium vanadate has much more capacity and better cycling stability, although the reason for this fact is not completely elucidated. In turn, we believe that magnesium-DGM is more easily (co)intercalated into $\text{NaV}_6\text{O}_{15}$ nanobelts. After activation during 70 cycles, the reversible insertion (faradic process) into sodium vanadate is observed in the intensity-voltage curves recorded at slow rate as a reduction peak at 0.4 V and an oxidation peak at 0.7 V (Fig. 8A). The discharge capacity is ca. 54 mAh g^{-1} at 1 mV s^{-1} of scan rate (Fig. 8B), 40 mAh g^{-1} at 2 mV s^{-1} (Fig. S4) and 86 mAh g^{-1} at 0.1 mV s^{-1} (Fig. S5). The charge process is more irreversible at slow rate than at rapid rate, probably due to electrolyte decomposition above ca. 2.0 V .

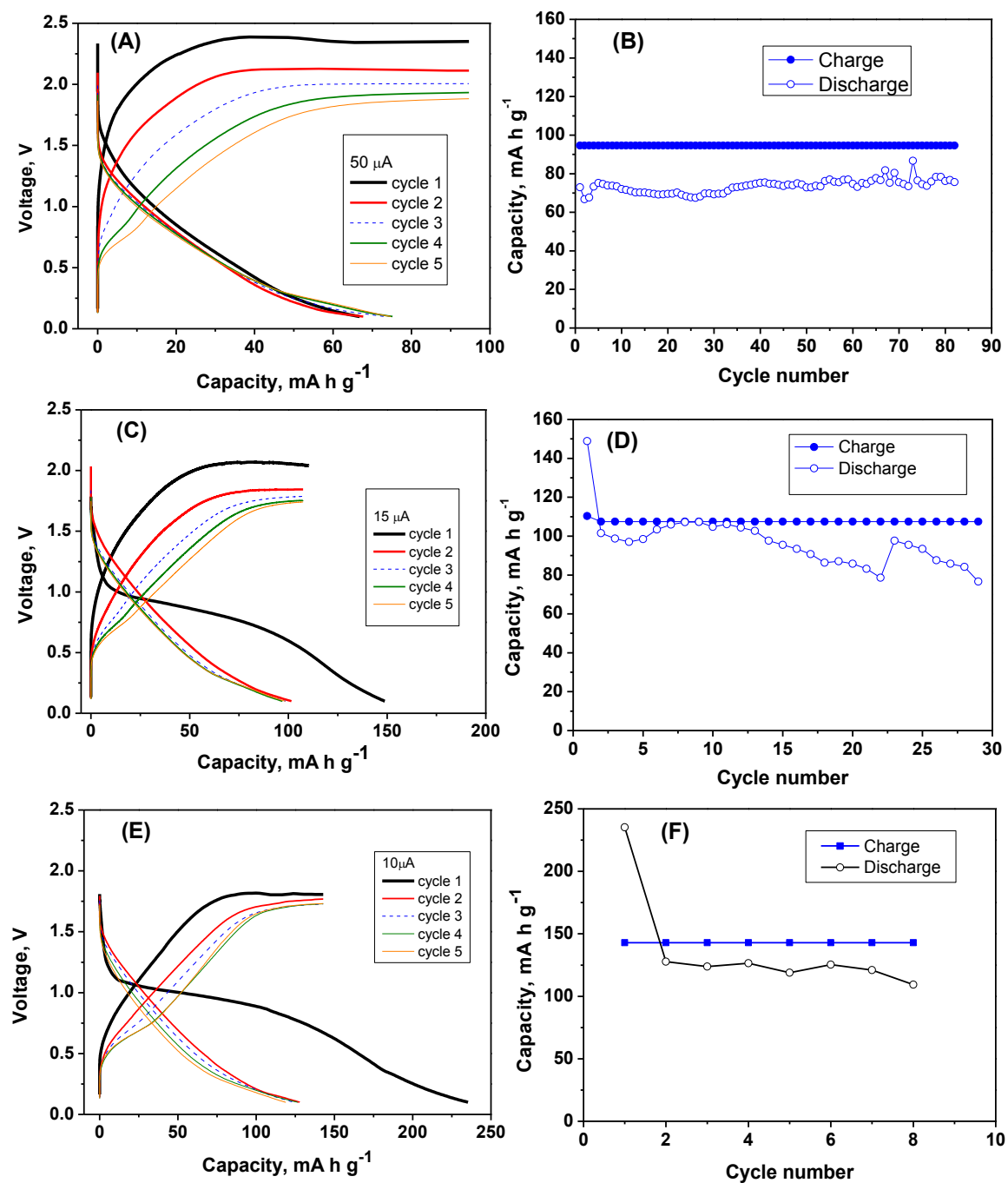


Fig.7. Electrochemical behavior of $\text{NaV}_6\text{O}_{15}$ vs. Mg with dual electrolyte solution ($\text{Mg}(\text{BH}_4)_2$ and NaBH_4 in DGM) using different current intensities. A, C and E show the galvanostatic curves, and B, D and F show the respective capacity-cycle number plots.

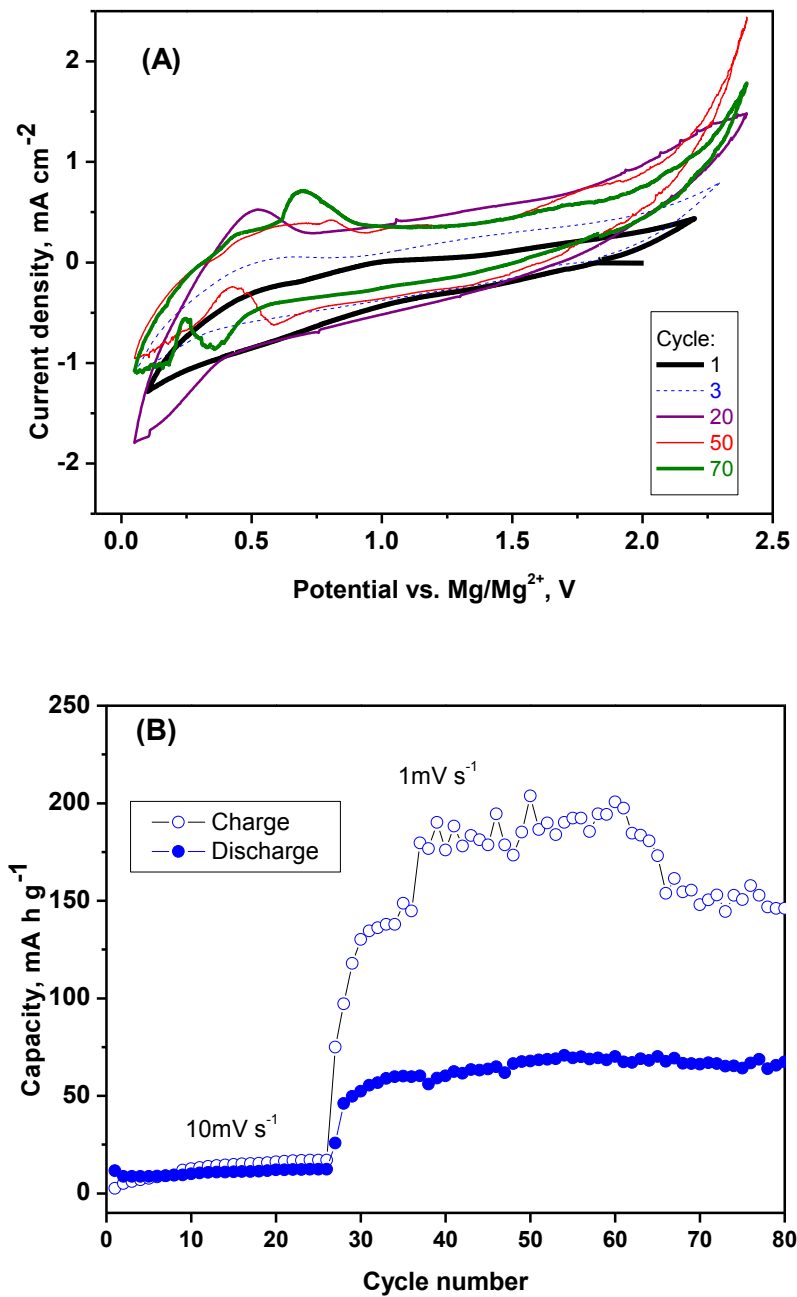


Fig.8. CV results for sodium vanadate vs. Mg with dual magnesium-sodium electrolyte. (A) Intensity-voltage curves. (B) Capacity as a function of cycle number. The scan rate is 10 mV s⁻¹ for the first 26 cycles, and then 1 mV s⁻¹.

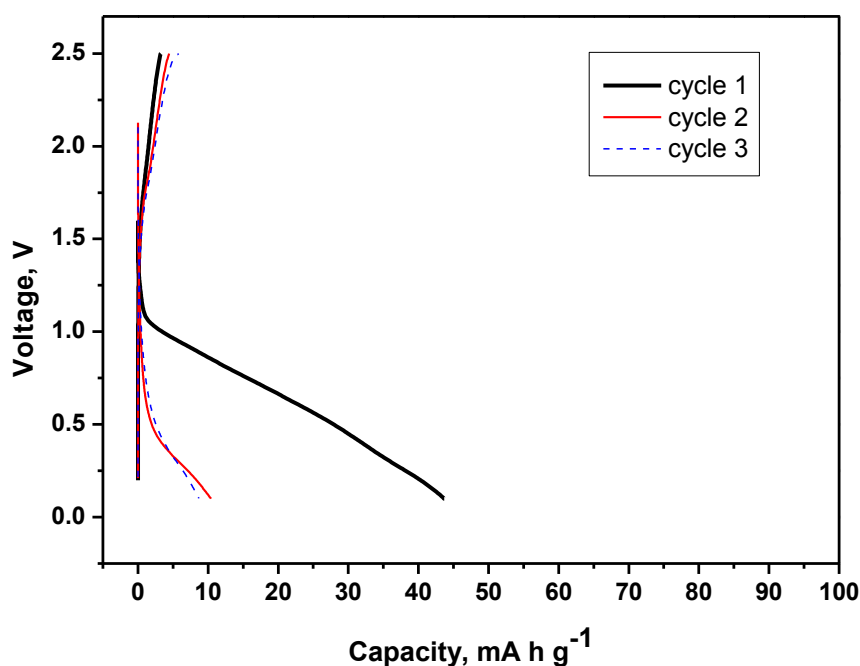


Fig.9. Electrochemical behavior of V_2O_5 vs. Mg with dual electrolyte. Current: $50 \mu A$.

In a try to deintercalate the sodium atoms and to unveil its role in the dual electrolyte, the electrochemical behavior of sodium vanadate with the electrochemical cycling starting by charge (oxidation of the working electrode) is shown in Fig. 10. In this case, the voltage rapidly increases up to 2.85 V vs. Mg and a pseudoplateau is observed at this voltage (Fig. 10). This voltage value corresponds in the control experiments to the region of decomposition of the electrolyte solution, and very probably the irreversible side-reactions create films on the electrode surface and deteriorate the electrochemical performance. After the first discharge process, the voltage-capacity curve is modified and it becomes equivalent to the results shown in Fig. 7, but the observed reversible capacity is only about 20-40 mAh g⁻¹. These results strongly suggest that sodium atoms in pristine NaV_6O_{15} are not properly deintercalated. Nevertheless, we cannot completely discard that during the discharge process the co-intercalation of sodium, magnesium and DGM may stabilizes the structure of the vanadate and then the sodium ions may be deintercalated after further cycling.

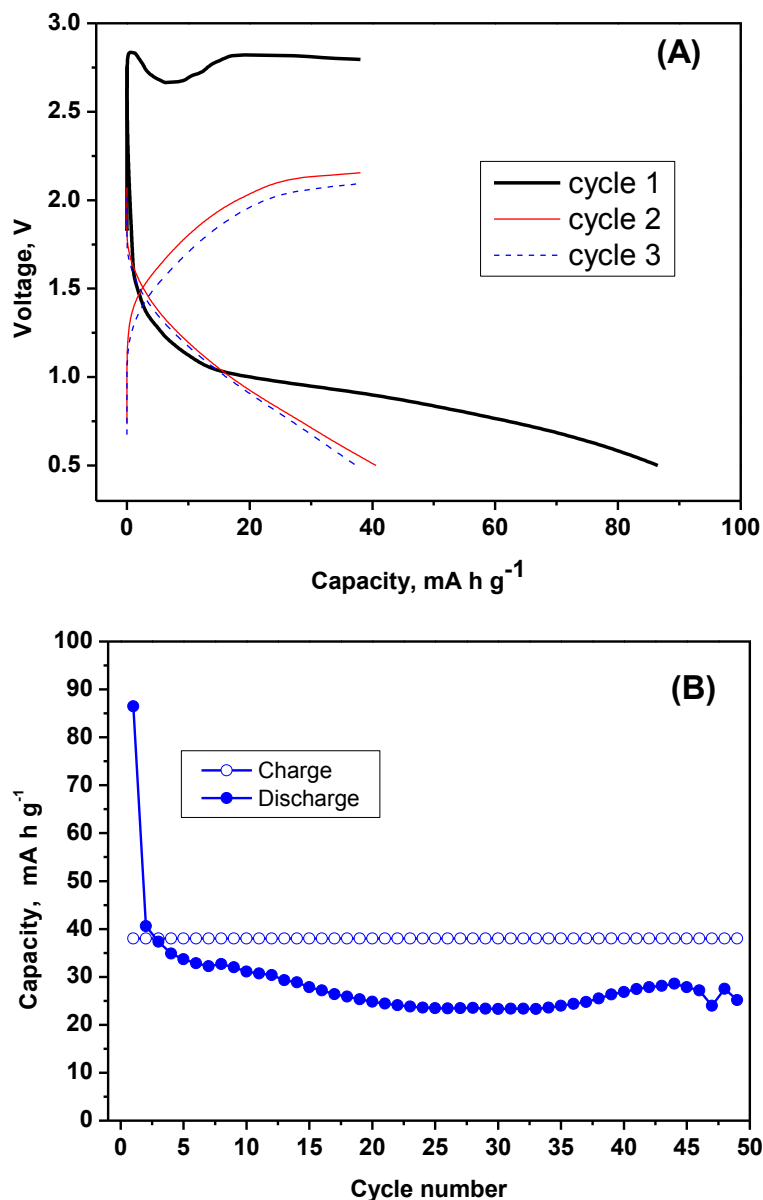


Fig.10. Electrochemical behavior of sodium vanadate in dual-electrolyte cell starting from charge process. (A) Galvanostatic curves. (B) Capacity as a function of cycle number. Current: 50 μ A.

4.2.3.5 EDX spectra

The chemical microanalysis coupled to SEM (EDX spectra) was used to determine the chemical composition of the cycled Mg electrode. Electrodes were recuperated after the first discharge and also in the charge state after 38 cycles, and then washed with DGM-solvent. Sodium is not detected after the first discharge (Fig. 11A). In contrast, sodium is detected at the negative electrode (metal Mg) in the charged state and after 38 cycles (Fig. 11B), indicating that sodium can be electrodeposited on Mg

electrode. The surface of the negative electrode becomes more crumpled as a result of metal electrodeposition. This result is in very good agreement with the behavior of a veritable dual battery.

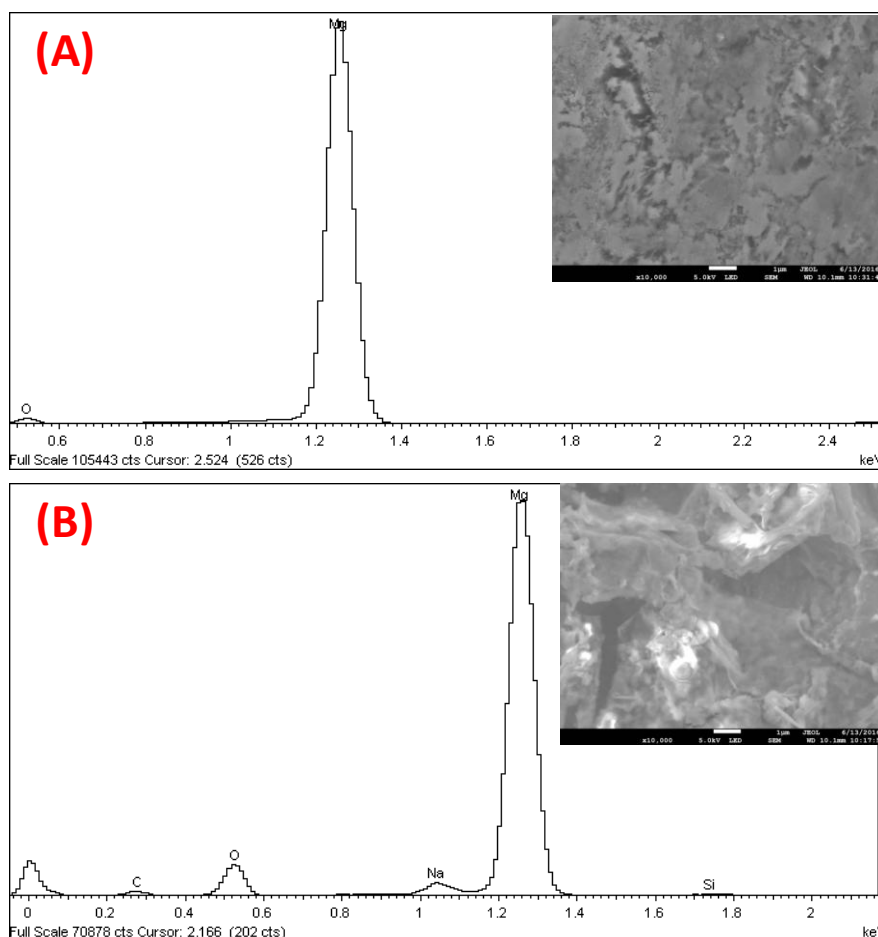


Fig.11. SEM micrographs and EDX spectra for the negative electrode (metal Mg) after the first discharge (A) and after 38 cycles (B) in magnesium-sodium dual cell.

4.2.3.6 Ex-situ XP spectra

In order to analyze the chemical composition and oxidation state in the surface, electrodes of $\text{NaV}_6\text{O}_{15}$ were retrieved from dual-electrolyte Mg batteries and XP spectra were recorded (Fig.12). The discharged electrode shows a shift of the V 2p peak to lower binding energies that allow us to conclude that vanadium is reduced and more V(IV) is formed. After the first discharge-charge cycle, the center of the broadened peak

of V 2p is slightly shifted to higher binding energy in comparison with the discharged electrode, strongly suggesting re-oxidation of vanadium ions (Fig. 12A). These results are equivalent to the XP results reported by other authors on the intercalation of Mg into orthorhombic V_2O_5 [11]

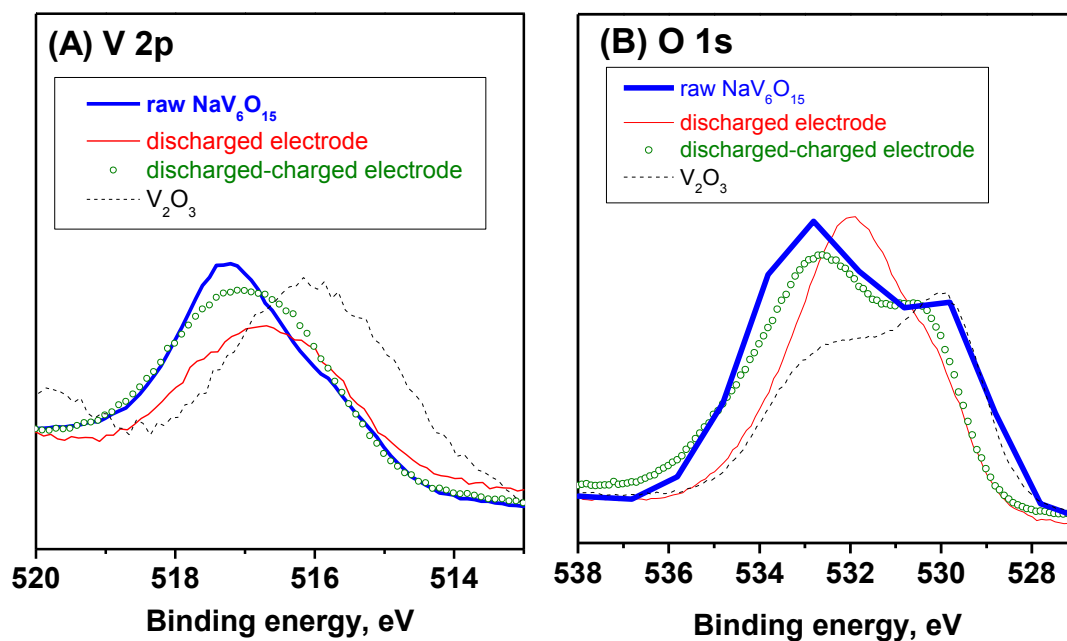


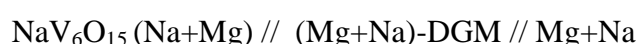
Fig.12. XP spectra of electrode materials in the (A) vanadium 2p and (B) oxygen 1s regions. The spectrum of V_2O_3 is shown as a reference.

In the region of O 1s (Fig. 12B), a reversible behavior is also observed. The reduced electrode has a XP spectrum less broadened in this O 1s region. This fact would suggest that oxide ions also can participate in the redox process, unless in the surface of the particles. However, the formation of a passivating layer and traces of electrolyte solution can affect to this result.

The chemical compositions of the electrodes obtained by XPS are $Na_{5.3}Mg_{12.2}V_6O_{15.4}$ and $Na_3Mg_{6.6}V_6O_{15.8}$ in the discharged and charged state, respectively. These results must be regarded carefully because XPS is a method of surface analysis. The results also showed the presence of boron due to traces of electrolyte and/or formation of a passivating layer. The quantification of elements with a low photoelectron cross-section, such as boron, is particularly susceptible to errors.

Irrespectively of the presence of electrolyte traces, the results reveal that the atomic ratio $(\text{Na}+\text{Mg})/\text{V}$ is 1.8 times higher in the discharge than in the charge one, corroborating the reversible intercalation process. In the discharged and charged states, the atomic ratio Mg/Na is nearly the same (2.2-2.3). Thus, the XPS results are in very good agreement with reversible intercalation of both magnesium and sodium (dual battery).

In conclusion, with the dual-salt electrolyte the resulting dual battery can be represented by:



The concept of this dual battery is schematically drawn in Fig. 13.

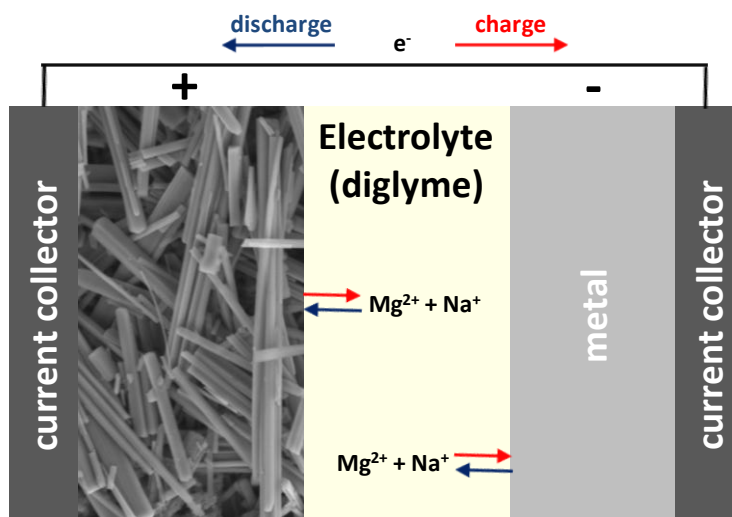


Fig.13. Schematic representation of dual battery based on vanadate as positive electrode, Mg as negative electrode and sodium and magnesium borohydride in diglyme as electrolyte solution.

4.2.3.7 Ex-situ XRD

Fig. 14 shows the XRD patterns of $\text{NaV}_6\text{O}_{15}$ electrodes which were discharged and discharged-charged in dual magnesium-sodium cell. The raw structure is preserved in all the electrodes, although only a few Bragg peaks can be observed due to the small intensity of the reflections in comparison with graphite peaks and plastic (kapton tape) signal. During the discharge process the Bragg peaks tend to be shifted to higher angles, and this fact suggests a contraction of the unit cell. Probably, the positive charge of the

intercalated Mg^{2+} shields the repulsive interactions between the negative charges of the oxide ions and exerts a strong attractive interaction that counteracts the framework expansion exclusively due to the size of the guest ion. For the nominal composition $\text{Mg}_{0.3}\text{Na}_{0.8}\text{V}_6\text{O}_{15}$, the resulting cell parameters are $a=15.36(2)$ Å, $b=3.60(2)$ Å, $c=9.99(4)$ Å, involving a contraction in the direction of the a-axis. Similarly, Sa et al. observed a contraction of the lattice when magnesium was intercalated into V_2O_5 with monoclinic C2/m structure [10].

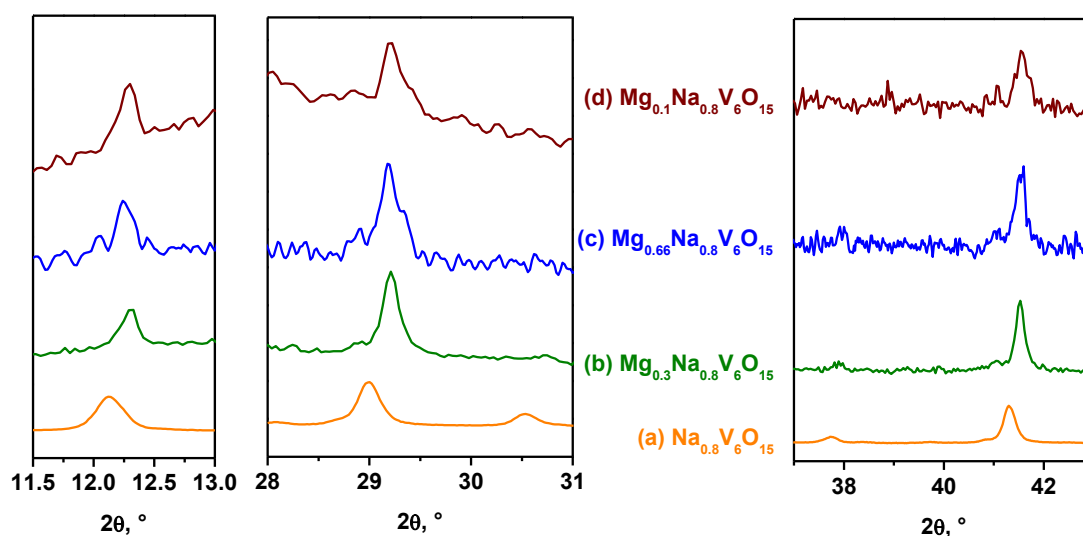


Fig.14. Magnified view of ex-situ XRD data for (a) raw $\text{NaV}_6\text{O}_{15}$ and electrodes retrieved at selected states of the first discharge (b, c) and charge (d) in magnesium cell with dual electrolyte solution.

4.2.3.8 Electrochemistry in full Mg-ion battery

As it was shown above, magnesium perchlorate in acetonitrile apparently does not sustain reversible Mg electrodeposition. In addition, carbonate-based solvents can form an insulating surface film on Mg metal which does not allow diffusion of magnesium-ion throughout it. Besides, water molecules can react with Mg metal. Probably, the weak point of the borohydrides-DGM and other electrolytes is their anodic stability at high voltage. On the other hand, perhaps the intercalation of magnesium might be doubtful when a dual electrolyte is used. However, if one uses a full magnesium-ion cell with two Mg-intercalation compounds as electrode materials and metallic Mg is not employed in the electrochemical cell, then the electrolyte solution can be based on carbonate-type solvents and $\text{Mg}(\text{ClO}_4)_2$ which are highly stable

[3,24]. Also the presence of water molecules might help to the intercalation of magnesium. Having all this in mind, we have used tetrahydrate magnesium perchlorate dissolved in EC:DEC as electrolyte solution in a full magnesium-ion battery. The electrochemical behavior of sodium vanadate (negative electrode) in a veritable magnesium-ion battery is shown in Fig. 15. The selected positive electrode is MgMn_2O_4 [24, 37]. Although in a commercial battery the voltage of the positive electrode must be always higher than the voltage of the negative electrode, however, the voltage of $\text{NaV}_6\text{O}_{15}$ would be only slightly lower in comparison with MgMn_2O_4 (between ca. 2.84 and 1.68 V vs. Mg/Mg^{2+}) [37], and consequently the observed voltage of the full magnesium-ion cell becomes negative during the discharge process (Fig. 15). Nevertheless, the experimental results further confirm that both sodium vanadate and MgMn_2O_4 can intercalate magnesium reversibly. In this case, using an excess of the negative electrode, the reversible capacity referred to the mass of the negative electrode is ca. 50-80 mAh g^{-1} .

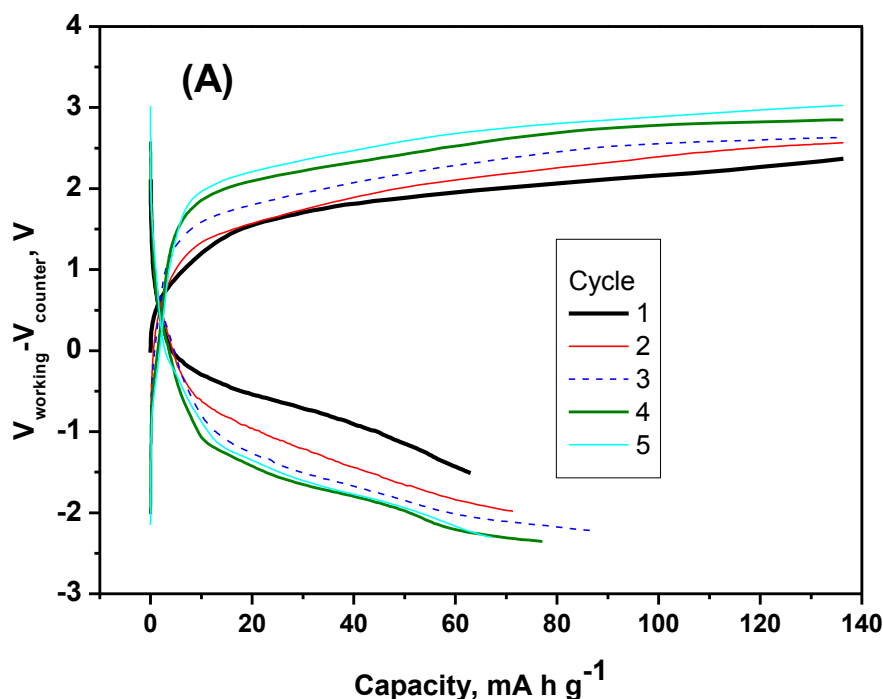


Fig.15. Electrochemical behavior of a full magnesium-ion battery made of MgMn_2O_4 as positive electrode and $\text{NaV}_6\text{O}_{15}$ as negative electrode. (A) Typical voltage-capacity plot with mass ratio $m_+/m_- = 0.88$.

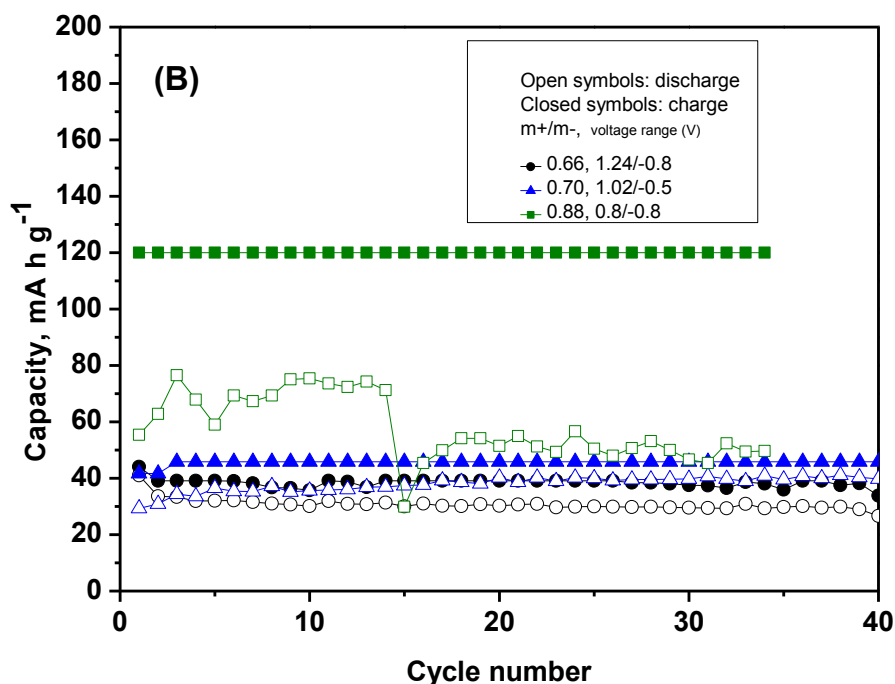


Fig.15. Electrochemical behavior of a full magnesium-ion battery made of MgMn_2O_4 as positive electrode and $\text{NaV}_6\text{O}_{15}$ as negative electrode. (B) Capacity as a function of cycle number for different experiments in which the cycling is controlled by the cut-off voltage of the positive electrode measured vs. Pt as a reference electrode and by capacity. Current: $20 \mu\text{A}$.

4.2.4 Conclusions

Nanobelts of sodium vanadate ($\beta\text{-NaV}_6\text{O}_{15}$) have been prepared by a hydrothermal one-step route. The electrochemical behavior has been tested in cells of lithium, sodium, magnesium and dual sodium-magnesium. The results have been compared with those of V_2O_5 . Besides lithium and sodium, reversible magnesium and dual magnesium-sodium intercalation in $\beta\text{-NaV}_6\text{O}_{15}$ are feasible. The efficiency of the first discharge/charge cycle is higher for sodium vanadate in comparison with that of vanadium pentoxide. When $\text{NaV}_6\text{O}_{15}$ is discharged down to 1.7 V vs. Li^+/Li , the voltage plateaus do not disappear and there is not irreversible phase transformation, in contrast to V_2O_5 , suggesting that the structure of sodium vanadate is more stable. In sodium cell, the efficiency of the discharge/charge cycle is much better with NaOTf-DGM electrolyte solution than with $\text{NaClO}_4\text{-PC}$. The reversible reduction/oxidation of $\beta\text{-}$

NaV₆O₁₅ in magnesium cell has been observed by XPS. The XPS, EDX, XRD and electrochemical results all together strongly suggest that both sodium and magnesium are intercalated in NaV₆O₁₅ when the dual magnesium-sodium electrolyte is used. This dual sodium-magnesium battery is advantageous because it allows using efficiently Mg metal as negative electrode, although sodium is also (co)deposited on the counter electrode. A veritable full magnesium-ion battery has also been tested using two Mg-intercalation compounds for the positive and negative electrode.

Acknowledgments

The authors are grateful to MINECO (grant number MAT2014-56470-R), FEDER funds, and Junta de Andalucía (research group FQM288) for financial support. SCAI-UCO (XPS, SEM and TEM), Institute of Fine Chemistry and Nanochemistry (XRD) are also thanked for instruments and facilities.

4.2.5 References

1. D. Aurbach, Z. Lu, A. Schechter, Y. Gofer, H. Gizbar, R. Turgeman, Y. Cohen, M. Moshkovich, E. Levi, *Nature* 407 (2000) 724.
2. Z. Zhao-Karger, X. Y. Zhao, D. Wang, D. Thomas, R. J. Behm, M. Fichtner, *Adv. Energy Mater.* 5 (2015) 1401155.
3. J. Song, E. Sahadeo, M. Noked, S. B. Lee, *J. Phys. Chem. Lett.* 7 (2016) 1736.
4. N. Sa, H. Wang, D. L. Proffit, A. L. Lipson, B. Key, M. Liu, Z. Feng, T. T. Fister, Y. Ren, C. J. Sun, J. T. Vauhey, P. A. Fenter, K. A. Persson, A. K. Burrell, *J. Power Sources* 323 (2016) 44.
5. J. M. Gallardo-Amores, N. Biskup, U. Amador, K. Persson, G. Ceder, E. Morán, M. E. Arroyo y de Dompablo, *Chem. Mater.* 19 (2007) 5262.
6. N. Baffier, L. Znaidi, M. Huber, *Mat. Res. Bull.* 25 (1990) 705.

7. M. Millet, J. Farcy, J. P. Pereira-Ramos, E. M. Sabbar, M. E. De Roy, J. P. Besse, *Solid State Ionics* 112 (1998) 319.
8. D. B. Le, S. Passerini, F. Coustier, J. Guo, T. Soderstrom, B. B. Owens, W. H. Smyrl, *Chem. Mater.* 10 (1998) 682.
9. M. M. Huei, D. C. Bock, E. S. Takeuchi, A. C. Marschilok, K. J. Takeuchi, *Coord. Chem. Rev.* 287 (2015) 15.
10. N. Sa, T. L. Kinnibrugh, H. Wang, G. S. Gautam, K. W. Chapman, J. T. Vaughey, B. Key, T. T. Fister, J. W. Freeland, D. L. Proffit, P. J. Chupas, G. Ceder, J. G. Barenó, I. D. Bloom, A. K. Burrell, *Chem. Mater.* 28 (2016) 2962.
11. G. Gershinsky, H. D. Yoo, Y. Gofer, D. Aurbach, *Langmuir* 29 (2013) 10964.
12. T. Chirayil, P. Y. Zavalij, M. S. Whittingham, *Chem. Mater.* 10 (1998) 2629.
13. J. G. Yu, J. C. Yu, W. K. Ho, L. Wu, X. Wang, *J. Am. Chem. Soc.* 126 (2004) 3422.
14. G. T. Zhou, X. Wang, J. C. Yu, *Cryst. Growth Des.* 5 (2005) 3.
15. S. Shi, M. Cao, X. Fle, H. Xie, *Cryst. Growth Des.* 7 (2007) 1893.
16. G. S. Gautam, P. Canepa, W. D. Richards, R. Malik, G. Ceder, *Nano Lett.* 16 (2016) 2426.
17. N. Sa, H. Wang, D. L. Proffit, A. L. Lipson, B. Key, M. Liu, Z. Feng, T. T. Fister, Y. Ren, C. J. Sun, J. T. Vaughey, P. Feneter, K. A. Persson, A. K. Burrell, *J. Power Sources* 323 (2016) 44.
18. J. P. Pereira-Ramos, R. Messina, S. Bach, N. Baffier, *Solid State Ionics* 40-41 (1990) 970.
19. M. Millet, J. Farcy, J. P. Pereira-Ramos, E. M. Sabbar, M. E. De Roy, J. P. Besse, *Solid State Ionics* 112 (1998) 319.
20. P. Novák, W. Scheifele, F. Joho, O. Haas, *J. Electrochem. Soc.* 142 (1995) 2544.

21. M. Shakourian-Fard, G. Kamath, S. K. R. S. Sankaranarayanan, *ChemPhysChem* 16 (2015) 3607.
22. M. Walter, K. V. Kravchyk, M. Ibañez, M. V. Kovalenko, *Chem.Mater.* 27 (2015) 7452.
23. Y. Guo, H. Yao, Y. You, Y. Yin, L. Wan, *Phys. Chem. Chem. Phys.* 18 (2016) 9326.
24. M. Cabello, R. Alcántara, F. Nacimiento, G. Ortiz, P. Lavela, J. L. Tirado, *CrystEngCommun* 17 (2015) 8728.
25. M. Najdoski, V. Koleva, S. Demiri, *Mater. Res. Bull.* 47 (2012) 737.
26. A. D. Wadsley, *Acta Crystallogr.* 8 (1955) 695.
27. J. M. Hughes, L. W. Finger, *Am. Mineral.* 68 (1983) 634.
28. B. Chen, J. Laverock, D. Newby, T. Y. Su, K. E. Smith, W. Wu, L. H. Doerrer, N. F. Quackenbush, S. Sallis, L. F. J. Piper, D. A. Fischer, J. C. Woicik, *J. Phys. Chem. C* 118 (2014) 1081.
29. Q. H. Wu, A. Thißen, W. Jaegermann, *Appl. Surf. Sci.* 252 (2005) 1801.
30. G. Silversmit, D. Depla, H. Poelman, G. B. Marin, R. De Gryse, *Surf. Sci.* 600 (2006) 3512.
31. A. Benayad, H. Martinez, A. Gies, B. Pecquenard, A. Levasseur, D. Gonbeau, *J. Electron Spectrosc.* 150 (2006) 1.
32. A. Thissen, D. Ensling, F. J. Fernández-Madrigal, W. Jaegermann, R. Alcántara, P. Lavela, J. L. Tirado, *Chem. Mater.* 17 (2005) 5202.
33. K. West, B. Zachau-Christiansen, T. Jacobsen, *Solid State Ionics* 28-30 (1988) 1128.
34. H. Liu, H. Zhou, L. Chen, Z. Tang and W. Yang, *J. Power Sources* 196 (2011) 814.

35. Y. Cai , J. Zhou, G. Fang, G. Cai, A. Pan, S. Liang, *J. Power Sources*, 328 (2016) 241.
36. B. Jache, P. Adelhelm, *Angew. Chem. Int. Ed.* 53 (2014) 10169.
37. C. Ling, F. Mizuno, *Chem. Mater.* 25 (2013) 3062.

4.2.6 Supplementary information

4.2.6.1 Electrochemistry in metal lithium cell

Although the main goal of this work is to study sodium vanadate in magnesium cell, for the sake of comparison lithium cells were also tested, and V_2O_5 is also used for comparative purposes.

For lithium cell, the electrolyte supplied by Merck was 1 M $LiPF_6$ in ethylene carbonate:diethyl carbonate (EC:DEC=1:1) solvents mixture. The electrolyte used for sodium batteries was 1 M sodium triflate ($NaOTf$, Aldrich, 98%) $NaCF_3SO_3$ in diglyme (DGM, Aldrich, 99.5%) or, alternatively, 1 M $NaClO_4$ in propylene carbonate (PC).

The electrochemical behavior of raw V_2O_5 and NaV_6O_{15} in lithium cell is summarized in Fig. S1. Raw V_2O_5 shows the typical voltage-capacity curves which are described in the literature (Fig. S1A) [C. Delmas, H. Cognacauradou, J. Cocciantelli, M. Menetrier, J.P. Doumerc, *Solid State Ionics* 69 (1994) 257] [B.Y. Liaw, I.D. Raistrick, R.A. Huggins, *Solid State Ionics* 45 (1991) 323] [I.D. Raistrick, *Solid State Ionics* 9-10 (1983) 425] [S. Afyon, F. Krumeich, C. Mensing, A. Borgschulte, R. Nesper, *Sci. Rep.* 4 (2014) 7113]. The insertion of lithium into orthorhombic α - V_2O_5 with less than ca. 1 Li per formula can be considered as a solid solution of lithium in the α - V_2O_5 phase. Through the lithiation of α - V_2O_5 there are successive formations of β - $Li_{0.3}V_2O_5$, ϵ - $Li_{0.5}V_2O_5$, γ - LiV_2O_5 and δ - $Li_2V_2O_5$ (equivalent to 294 mAh g^{-1}). Even more lithium can be inserted below 1.9 V, theoretically up to ω - $Li_3V_2O_5$ (equivalent to 441 mAh g^{-1}) with rock-salt type structure, but it drives to irreversibility and capacity loss upon cycling. In Fig. S1A, the second discharge of V_2O_5 down to 1.7 V drives to the formation of ω - $Li_3V_2O_5$, and the plateaus are irreversibly lost as it can be seen in the cycle number 3.

In the case of sodium vanadate, the starting structure is different from that of α - V_2O_5 , and also there are sites occupied by both sodium and lithium ions in the discharged electrode. Starting from β - NaV_6O_{15} in lithium cell (Fig. S1B), $Li_3NaV_6O_{15}$ (equivalent to ca. 147 mAh g^{-1}) is formed at ca. 2.4 V in the first discharge, and $Li_4NaV_6O_{15}$ at 1.8 V. The nominal composition is $Li_5NaV_6O_{15}$ at ca. 1.7 V in the second and third discharge. The voltage-capacity curve shows three successive plateaus or pseudoplateaus at ca. 3.3, 2.9 and 2.5 V vs. Li^+/Li , and these features involve structural

modifications which still are not well known. The discharge capacity is lower for β - $\text{NaV}_6\text{O}_{15}$ than for α - V_2O_5 . The voltage pseudoplateau at ca. 3.3 V is longer in the first charge than in the first discharge, and the total capacity of the first charge (230 mAh g^{-1}) is higher than the total capacity of the first discharge. This fact involves that both lithium and sodium ions are deintercalated. However, the alkali ions are not completely removed from $\text{M}_x\text{V}_6\text{O}_{15}$ (with $\text{M}=\text{Li}$ and Na) even after the first charge at 4.0 V, in contrast to α - V_2O_5 , and $x=0.2$ atoms of M per formula remain trapped in $\text{M}_x\text{V}_6\text{O}_{15}$. It seems that the collapse of the tunnel structure is prevented by the alkali ions that remain in the bronze (approximately $\text{M}_{0.5}\text{V}_6\text{O}_{15}$). In contrast to V_2O_5 , the low-voltage plateau at ca. 1.8 V does not disappear in the successive cycle when $\text{NaV}_6\text{O}_{15}$ is discharged down to 1.7 V, and hence there is not an irreversible phase transformation, as it can be seen in the cycle number 2-4 in Fig. S1B. The sodium vanadate sample has lower specific capacity than V_2O_5 (Fig. S1C). The reasons can be the mass of the alkali ions and the presence of V^{4+} in $\text{NaV}_6\text{O}_{15}$, and also because less alkali atoms are electrochemically intercalated. This fact prevents from irreversible structural transformation at low voltage.

In the case of using sodium vanadium bronze obtained in a two step procedure (firstly intercalation of sodium into α - V_2O_5 and secondly heated the resulting product at ca. 550°C to obtain the monoclinic phase β - $\text{NaV}_6\text{O}_{15}$, Pereira-Ramos and co-workers found that up to 4.8 Li per formula could be inserted into anhydrous $\text{NaV}_6\text{O}_{15}$ in lithium cell, but only about 2.4 Li were reversibly inserted and poor capacity retention 3 was observed [M. Millet, J. Farcy, J.P. Pereira-Ramos, E.M. Sabbar, M.E. De Roy, J.P. Besse, *Solid State Ionics* 112 (1998) 319] [J.P. Pereira-Ramos, R. Messina, S. Bach, N. Baffier, *Solid State Ionics* 40/41 (1990) 970] [J.P. Pereira-Ramos, R. Messina, L. Znaidi N. Baffier *Solid State Ionics* 28-30 (1988) 886] [M.E. Spahr, P. Novák, W. Scheifele, O. Haas, R. Nesper, *J. Electrochem. Soc.* 145 (1998) 421]. Whereas, higher reversible capacity (up to ca. 4.8 Li) and better capacity retention were found for the hydrate form $\text{NaV}_6\text{O}_{15.9}9.9\text{H}_2\text{O}$ [M. Millet, J. Farcy, J.P. Pereira-Ramos, E.M. Sabbar, M.E. De Roy, J.P. Besse, *Solid State Ionics* 112 (1998) 319]. Compare to these results on sodium vanadate, our nanobelts of $\text{NaV}_6\text{O}_{15}$ exhibit better electrochemical cycling probably due the particle morphology. Recent studies on micro-rod β $\text{NaV}_6\text{O}_{15}$ showed capacities more similar to our results [I. Seo, G.C. Hwang, J.K. Kim, Y. Kim, *Electrochim. Acta* 193 (2016) 160].

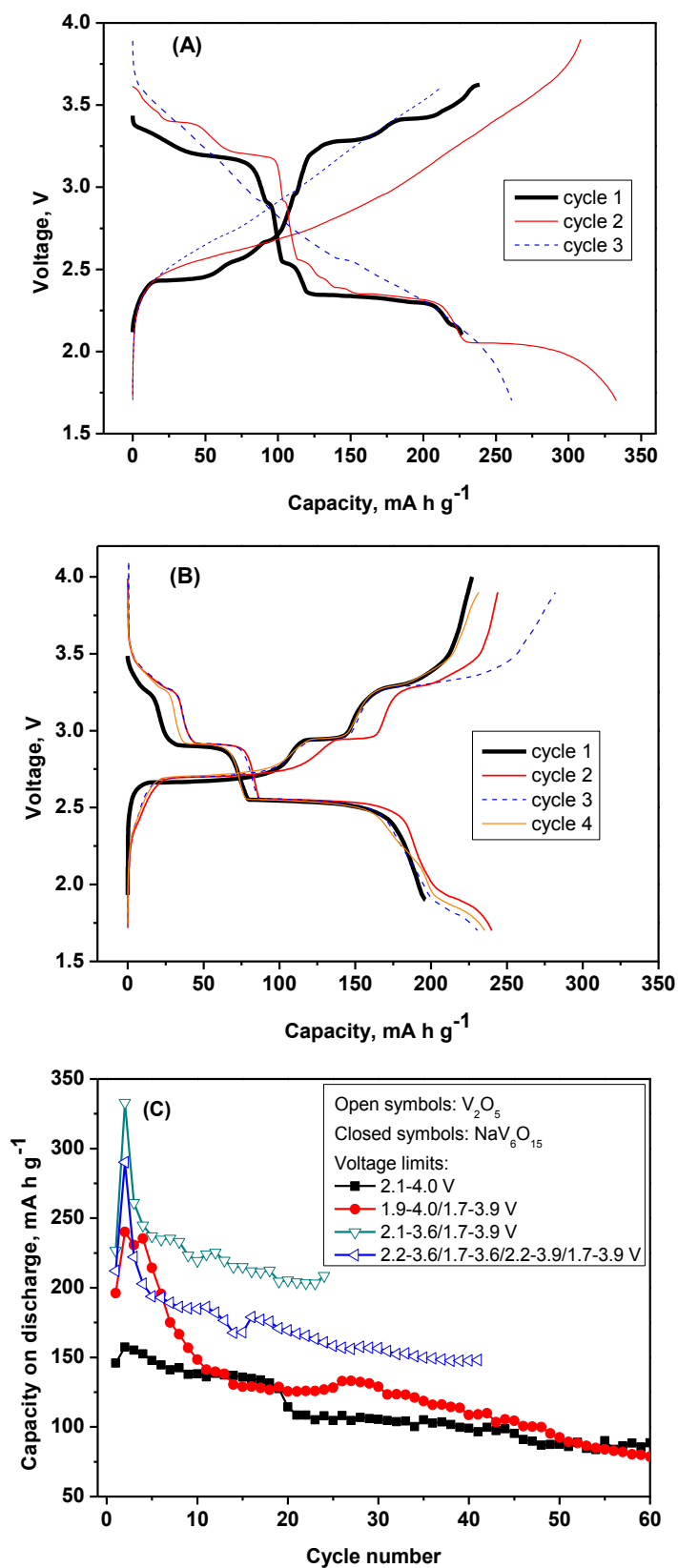


Fig.S1. Galvanostatic experiments in lithium cell. Discharge-charge curves for (A) V_2O_5 and (B) NaV_6O_{15} . (C) Specific capacity as a function of cycle number. The voltage limits of the successive cycles are given in the inset.

4.2.6.2 Electrochemistry in sodium-free metal magnesium cell

The results of V₂O₅ in Mg cell (Fig. S2) are equivalent to the results reported by other authors [P. Novák, W. Scheifele, F. Joho, O. Haas, J. Electrochem. Soc. 142 (1995) 2544] [L. Jiao, H. Yuan, Y. Wang, J. Cao, Y. Wang, Electrochem. Commun. 7 (2005) 431] [N. Sa, T.L. Kinnibrugh, H. Wang, G.S. Gautam, K.W. Chapman, J.T. Vaughey, B. Key, T.T. Fister, J.W. Freeland, D.L. Proffit, P.J. Chupas, G. Ceder, J.G. Barenó, I.D. Bloom, A.K. Burrell, Chem. Mater 28 (2016) 2962] [J. Yin, C.J. Pelliccione, S.H. Lee, E.S. Takeuchi, K.J. Takeuchi, Z.C. Marschilok, J. Electrochem. Soc. 163 (2016) A1941] [Y. Cheng, Y. Shao, V. Raju, X. Ji, B.L. Mehdi, K.S. Han, M.H. Engelhard, G. Li, N.D. Browning, K.T. Mueller, J. Liu, Adv. Funct. Mater. 26 (2016) 3446]. Dry solvent is used, and water cointercalation cannot be significant.

After, looking at Fig. S3 (Mg(BH₄)₂ in DGM and in THF), it is clear the reason of moving to sodium-magnesium dual electrolyte. It is known that the electrochemical behavior of dual electrolyte (A+B) can be completely different in comparison with single electrolyte (A or B), due to synergy effect, although the role may be not completely elucidated. Aurbach et al. reported that adding LiCl to the solution of magnesium organo-halo-aluminates in ethers considerably improves solution ionic conductivity, the kinetics of Mg deposition/dissolution process, and the intercalation behavior of Mg_xMo₆S₈ Chevrel cathodes [Y. Gofer, O. Chusid, H. Gizbar, Y. Viestfrid, H. E. Gottlieb, V. Marks and D. Aurbach, Electrochemical and solid-state letters 9 (2006) A257]. Hwang et al. proposed using LiBH₄ as an additive in DME solution because the addition of lithium can weaken the interaction between Mg²⁺ and BH₄⁻ [R. Mohtadi, M. Matsui, T. S. Arthur and S. J. Hwang, Angewandte Chemie International Edition 51 (2012) 9780]. Kovalenko et al. reported dual ion mixed electrolyte (magnesium+sodium) with cathode FeS₂ nanocrystals and Mg anode [M. Walter, K. V. Kravchyk, M. Ibáñez and M. V. Kovalenko, Chemistry of Materials 27 (2015) 7452], and these authors showed that the capacity of the same material is negligible when using sodium-free 0.2M Mg(BH₄)₂ in diglyme as the electrolyte solution. These last results are equivalent to our results on nanobelts of sodium vanadate.

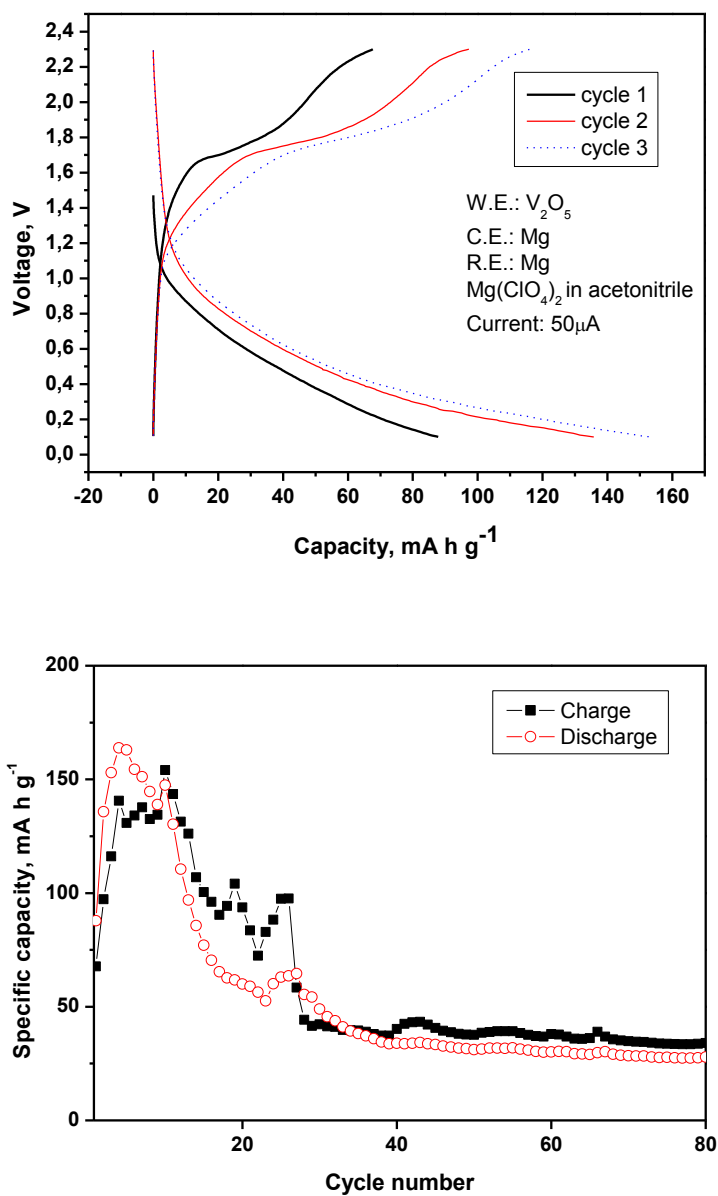


Fig.S2. Galvanostatic experiments of V₂O₅ in sodium-free magnesium cells. Positive electrode: V₂O₅. Negative electrode: Mg. Electrolyte solutions: 1 M Mg(ClO₄)₂ in acetonitrile.

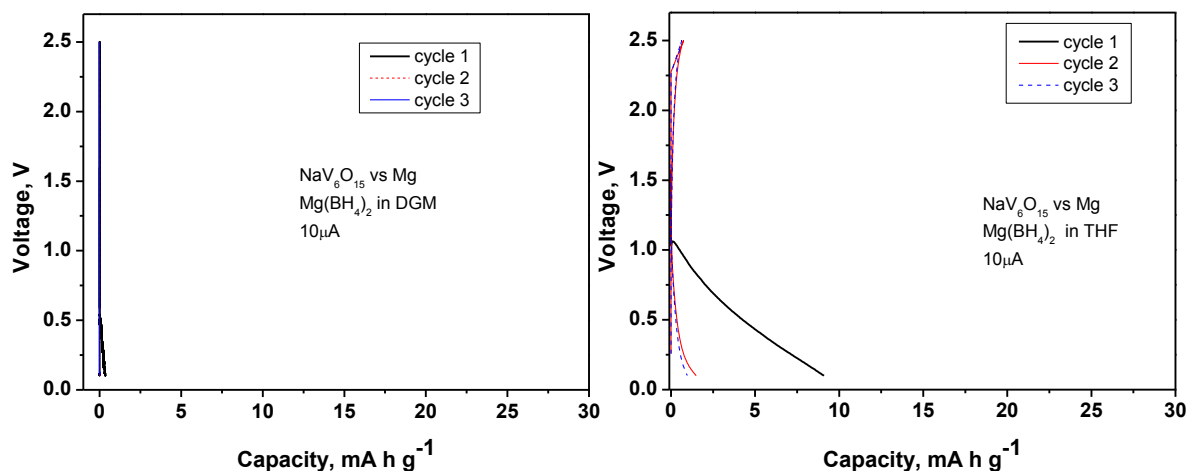


Fig.S3. Galvanostatic experiments of $\text{NaV}_6\text{O}_{15}$ in (sodium-free) magnesium cells. Positive electrode: sodium vanadate. Negative electrode: Mg. Electrolyte solutions: $\text{Mg}(\text{BH}_4)_2$ in diglyme (top) and $\text{Mg}(\text{BH}_4)_2$ in tetrahydrofuran (bottom). The resulting capacity is negligible in both cases, in contrast to the dual electrolyte (sodium+magnesium).

4.2.6.3 Further electrochemical results in dual sodium-magnesium cell

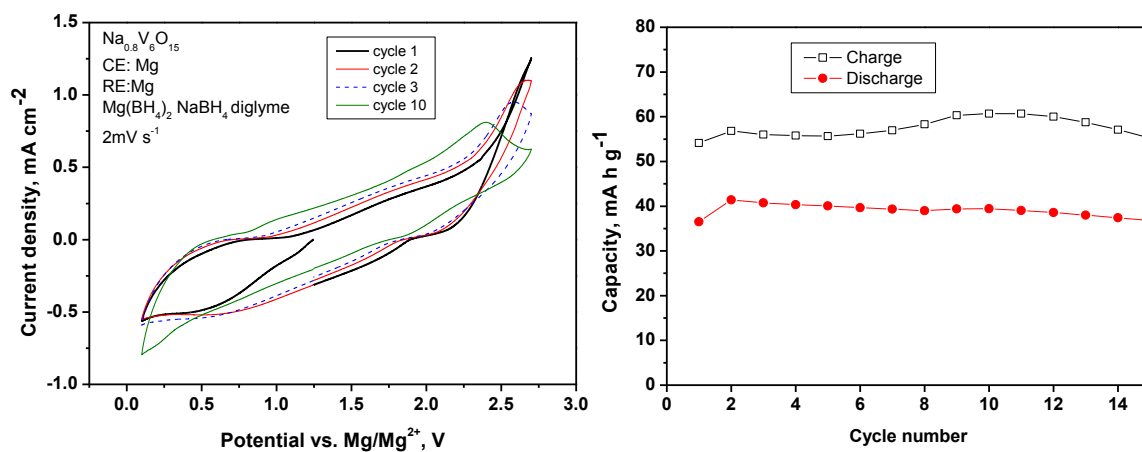


Fig.S4. CV results for sodium vanadate vs. Mg with dual magnesium-sodium electrolyte at scan rate of 2 mV s^{-1} .

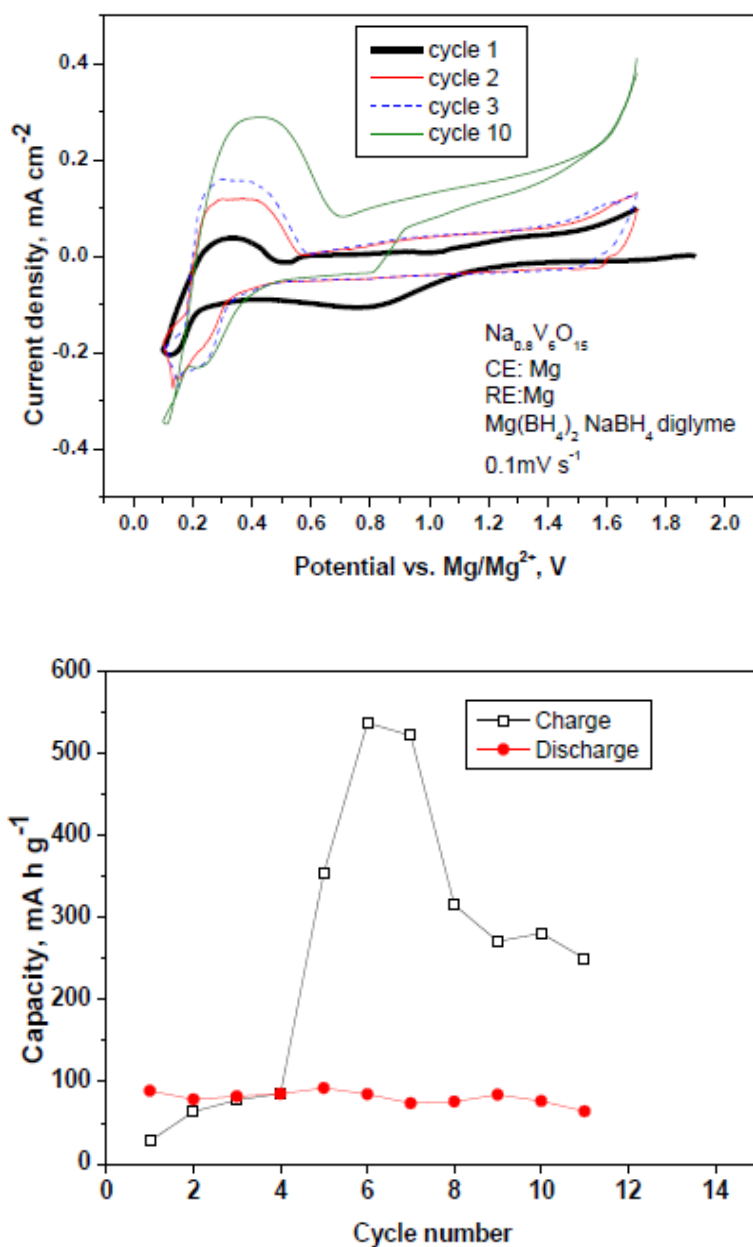


Fig.S5. CV results for sodium vanadate vs. Mg with dual magnesium-sodium electrolyte at scan rate of 0.1 mV s⁻¹.

4.3 $\text{Na}_3\text{V}_2(\text{PO}_4)_3$ as electrode material for rechargeable magnesium batteries: a case of sodium-magnesium hybrid battery

Marta Cabello, Ricardo Alcántara, Francisco Nacimiento, Pedro Lavela, María J.

Aragón, José L. Tirado.

Laboratorio de Química Inorgánica. Universidad de Córdoba. Edificio C3, Campus de Rabanales. Spain

Abstract

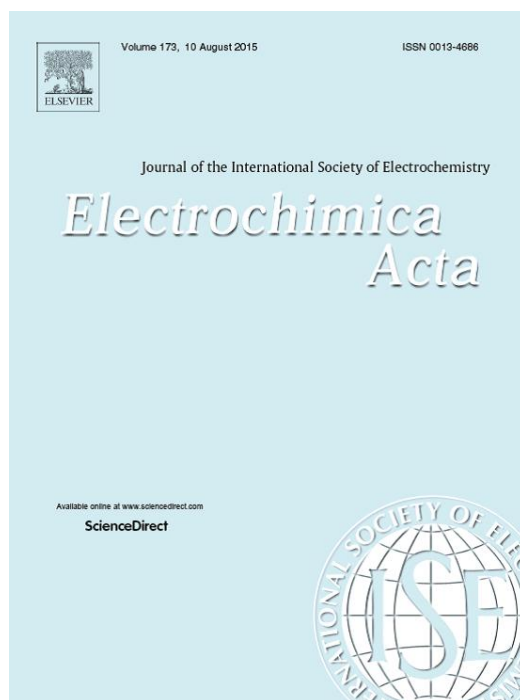
The use of Mg in rechargeable batteries can be competitive with Li in terms of economy, safety, environment and capacity. In contrast to lithium and sodium, the compounds with NASICON-type structure have received little attention as hosts for reversible magnesium insertion. The selection of the electrolyte solution and voltage window seems to be crucial for controlling sodium/magnesium (de)insertion. Here, $\text{Na}_3\text{V}_2(\text{PO}_4)_3$ (NVP) has been tested as a positive electrode vs. Mg metal with 0.5 M magnesium bis(trifluoromethanesulfonimide) in 1,2-dimethoxyethane as electrolyte solution, and the mechanism of the charge/discharge process has been studied. In magnesium cell, firstly sodium is partially deinserted from the framework of NVP up to ca. $\text{Na}_{1.3}\text{V}_2(\text{PO}_4)_3$ through a single voltage-plateau at 1.7 V, the cell of the crystal lattice is contracted, and a magnesium-sodium hybrid electrolyte is formed *in situ*. Secondly, sodium and magnesium are inserted through two consecutive voltage-plateaus at 1.6 and 1.2 V, respectively, while the main framework is preserved and the lattice is expanded. With further charge-discharge cycling, only one discharge plateau is observed at 1.2 V due to insertion of magnesium. If sodium ions are removed from the electrolyte solution after the first charge, only magnesium is inserted in the NASICON-type framework during the discharge. The electrochemical behavior of this material as electrode in magnesium battery is very promising, providing a reversible capacity of ca. 60 mAh g^{-1} after 100 cycles.

Keywords

Magnesium batteries; NASICON; sodium batteries; hybrid electrolyte



ELSEVIER



Electrochimica Acta 246 (2017) 908-913

4.3.1 Introduction

It is envisaged that the implementation of electric vehicles will require development of new and more sustainable battery chemistry beyond lithium [1, 2]. The main drawbacks of using lithium for batteries are limited mineral resources, high-cost, limited capacity and safety issues such as dendrites-formation upon electrochemical cycling. Lithium-ion batteries do not use Li metal as negative electrode and, consequently, the dendrite problem is overcome, but the resulting specific capacity and energy density are lower, and the safety problems are not completely resolved. Natural resources of sodium and magnesium are much more abundant than for lithium, although sodium is even more prone to dendrite growth than lithium. Magnesium is very competitive in terms of low-cost and safety (dendrites-free). In addition, the multivalent character of magnesium and its high density increase its volumetric capacity up to 3833 mAh cm⁻³ compared to lithium (2062 mAh cm⁻³) and sodium (1128 mAh cm⁻³). Consequently, the use of Mg as the negative electrode of rechargeable batteries is very promising [3]. For the efficient use of Mg batteries, the positive electrode material and the electrolyte solution must be urgently optimized, and for achieving this purpose the chemical and electrochemical processes governing these systems should be known much better [4-7]. Another way to implement Mg as negative electrode may be using hybrid electrolytes containing Mg²⁺ and Li⁺ or Na⁺ [8-10], although the chemistry behind these systems seems to be even more complex.

M_xV₂(PO₄)₃ (with M=Li, Na, and 1<x<7) compounds are considered as candidates for being used as positive electrode materials for lithium [11] [12], sodium [13-16] and hybrid lithium-sodium batteries [17-19]. Usually, the electrochemical cycling is started by charging (oxidation of M_xV₂(PO₄)₃) and deinsertion vs. M metal (negative electrode), although the electrochemical cycling also could be initiated with a reduction process. In fact, M₃V₂(PO₄)₃ can be regarded as a redox amphoteric material. Alternatively, these materials may be used as negative electrode in lithium and sodium ion batteries [20,21].

Na₃V₂(PO₄)₃ (hereafter referred to as NVP) has a rhombohedral NASICON-type structure (s.g. R-3c) and it is a super-ionic conductor, with Na placed at 18e and 6b sites, with eight-coordination and six-coordination respectively. Although this structure

exhibits an open framework which allows rapid ions diffusion through the interstitial sites, however, for achieving a good electrochemical cycling it is needed to enhance the electronic conductivity by intimately mixing the particles with carbon [13,14,16]. The electrochemical desodiation (V^{3+}/V^{4+}) of $Na_3V_2(PO_4)_3$ takes place at ca. 3.4 V vs. Na, although part of the Na atoms remains in the lattice [22]. The sodiation process of $Na_3V_2(PO_4)_3$ to form $Na_4V_2(PO_4)_3$ (V^{3+}/V^{2+}) occurs at ca. 1.6 V vs. Na^+/Na , further sodium can be inserted up to $Na_5V_2(PO_4)_3$ at 0.3 V (V^{2+}/V^+), and the maximum reversible capacity is 170 mAh g^{-1} between 3.0 and 0.01 V (corresponding to three sodium) [20,23]. On the other hand, Dong et al proposed using of solid solutions $Li_{3-x}Na_xV_2(PO_4)_3$ ($0 < x < 3$) for reversible sodium storage [24], and Du et al found that sodium atoms in $Na_3V_2(PO_4)_3$ can be exchanged for lithium in a hybrid cell [19].

In contrast to lithium and sodium, the NASICON-type structure has received little attention as a host for magnesium ion. Huan et al. [25] obtained monoclinic $V_2(PO_4)_3$ by electrochemical delithiation of monoclinic LVP (s.g. $P2_1/c$) at 55°C and then used the resulting vanadium phosphate ($V_2(PO_4)_3$) as host for magnesium insertion. Although only five discharge/charge cycles were reported by these authors, the reversible insertion of magnesium in monoclinic VP was probed. Li et al. inserted divalent ions (Zn^{2+} and Mg^{2+}) into NASICON-type NVP using aqueous solutions [26]. These authors found that the insertion of Zn into $NaV_2(PO_4)_3$ preserves the framework of the NASICON-type structure. Makino et al. in a pioneering work used NASICON-type $Mg_{0.5}Ti_2(PO_4)_3$ as electrode material for magnesium insertion in non-aqueous cell [27], but deinsertion was not studied. It is worth to note that the initial oxidation state of titanium (Ti^{4+}) in this compound does not allow starting the electrochemical cycling with an oxidation process.

In this work we study the reversible insertion of magnesium into partially desodiated NVP. Galvanostatic and voltammetry experiments with three-electrode cell in non-aqueous solvent are used. The mechanisms of the deinsertion/insertion processes, structural transformations and replacement of sodium by magnesium are followed by using XRD and composition analysis.

4.3.2 Experimental

In order to improve the electrical conductivity and the electrochemical behavior, NVP containing 7.3 wt% of amorphous carbon was prepared by using the wet-ball-milling method as is described in elsewhere [14].

The structure was studied by x-ray diffraction (XRD) in a Bruker D8 instrument with $\text{CuK}\alpha$ radiation. Rietveld refinement was performed with Topas program. To record XRD patterns of electrodes recuperated from the electrochemical cell, special care was taken to avoid reaction with the air atmosphere. The electrochemical cells were disassembled in the glove-box under inert atmosphere and covered with kapton tape. The chemical composition of the electrodes was analyzed by Electron Probe Microanalysis (EPMA) with Energy Dispersive Spectrometer (EDS) detector coupled to FE-SEM using a JSM-7800F Prime instrument. Prior to their analysis, the electrodes were washed with 1,2-dimethoxyethane (DME) solvent to remove the electrolyte.

All the electrochemical experiments were performed in a Biologic instrument, and the electrochemical cells were assembled in a glove-box filled with Ar atmosphere. The working electrode was prepared by mixing the active material (80 wt%), carbon black (10 wt%) as conductive agent and PTFE (10 wt%) as binder, and the mixture was pasted on a Ti disc. The electrochemical tests were performed in three-electrode cells of Swagelok-type, using NVP as active material of the working electrode, a disc of Mg as counter electrode and another Mg disc as reference electrode. The electrolyte solution was 0.5 M magnesium bis(trifluoromethanesulfonimide) ($\text{Mg}(\text{TFSI})_2$) in DME. Whatman discs of glass microfiber impregnated with electrolyte solution were used as separators.

4.3.3 Results and discussion

The electrochemical behavior of NVP was studied in magnesium cells using cyclic voltammetry (CV) and galvanostatic experiments. In the CV results (Fig.1), an intense anodic peak is observed in the charge at ca. 1.8 V vs. Mg, which is ascribed to partial oxidation from V^{3+} to V^{4+} and deinsertion of sodium located at the sites 18e in the NASICON-type structure, similarly to the electrochemical behavior in sodium cell [14, 23]. From the first to the third scan, the anodic peak becomes slightly more

broadened towards lower voltages. Two cathodic peaks are observed in the discharge at 1.5 and 0.9 V, respectively, which are ascribed to reduction of vanadium ions and insertion of sodium and/or magnesium, as discussed below. In the discharge process, the intensity of the peak at ca. 1.5 V decreases when the cycle number increases, while the intensity of the peak at ca. 0.9 V increases. These results suggest structural and/or compositional changes during the electrochemical cycling.

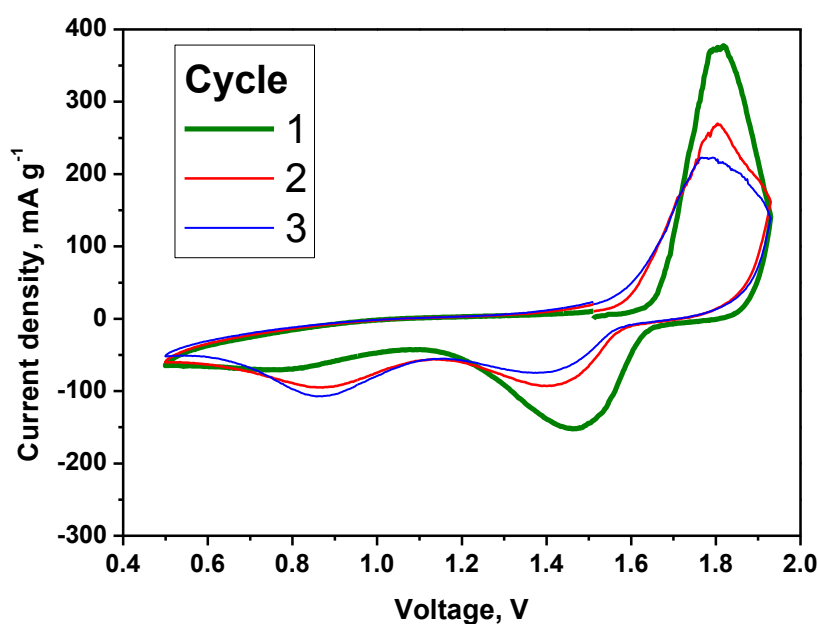


Fig.1. CV curves for NVP in magnesium cell. Scan rate: 0.2 mV s^{-1} .

In the galvanostatic experiment (Fig. 2A), a voltage plateau is observed at 1.8 V during the first charge which can be ascribed to partial desodiation and vanadium oxidation through a biphasic mechanism. The experimental charge capacity is nearly the same than the capacity previously reported in sodium cell (around $100\text{-}110 \text{ mAh g}^{-1}$) [13, 14, 23], although the voltage measured vs. Mg is lower than vs. Na as expected. During the discharge process, two plateaus (or pseudoplateaus) are observed at ca. 1.6 and ca. 1.2 V, respectively, which cannot be exclusively ascribed to the reversible insertion of the same amount of sodium atoms that was previously deinserted during the previous charge. In contrast to these results in Mg cell, one plateau is observed in the discharge in Na cell according to the literature only. In turn, Huang et al. also found two

discharge-pseudoplateaus for Mg (and Li)-insertion into monoclinic VP previously obtained by delithiation of monoclinic LVP [25], and they proposed that the observed transformation of these two plateaus into a sloping profile after electrochemical cycling was due to decreasing contribution of lithium insertion and increasing contribution of magnesium insertion. Similarly, we are prompted to ascribe the discharge plateaus to the subsequent intercalation of sodium and magnesium. During the second charge, we can distinguish two regions which are different from the first charge. Firstly, there is a sloping (solid solution mechanism) and shorter region at around 1.45-1.65 V and, secondly, another and longer region with a plateau (biphasic mechanism) at ca. 1.7 V. On further cycling, the discharge plateau at 1.6 V tends to become shorter and the discharge plateau at 1.2 V tends to become longer. In addition, with electrochemical cycling the charge plateau at ca. ca. 1.7 V tends to become shorter and the region near 1.4-1.6 V tends to become larger. We tested that when the lower cut-off voltage is limited to 1.0 V, the discharge plateau at ca. 1.6 V was also progressively replaced by the plateau at 1.2 V (not shown). These results suggest that sodium in NVP is being progressively replaced by magnesium as is discussed below. The observed cycling behavior is good (Fig. 2B), with a stable capacity of ca. 60 mAh g⁻¹ between the cycle number 60 and 140, and the structural stability of the NASICON-type framework undoubtedly contributes to this behavior.

In addition, we tested the electrochemical cycling behavior by using lower cut-off voltage (0.1 V vs. Mg), and it was observed that although the initial capacity was increased, the capacity fade was rapid (not shown). Thus, it seems that the reduction of vanadium to V²⁺ or V⁺ at very low voltages should be avoided to achieve good electrochemical performance in this system, although electrolyte decomposition also could take place near 0 V. On the other hand, in the case that the electrochemical cycling was initiated by a reduction (discharge) process the resulting discharge capacity was only ca. 11 mAh g⁻¹, indicating that firstly sodium must be deinserted and vanadium oxidized to activate the electrode material. Very probably, part of the 18e sites must be free of sodium for magnesium diffusion.

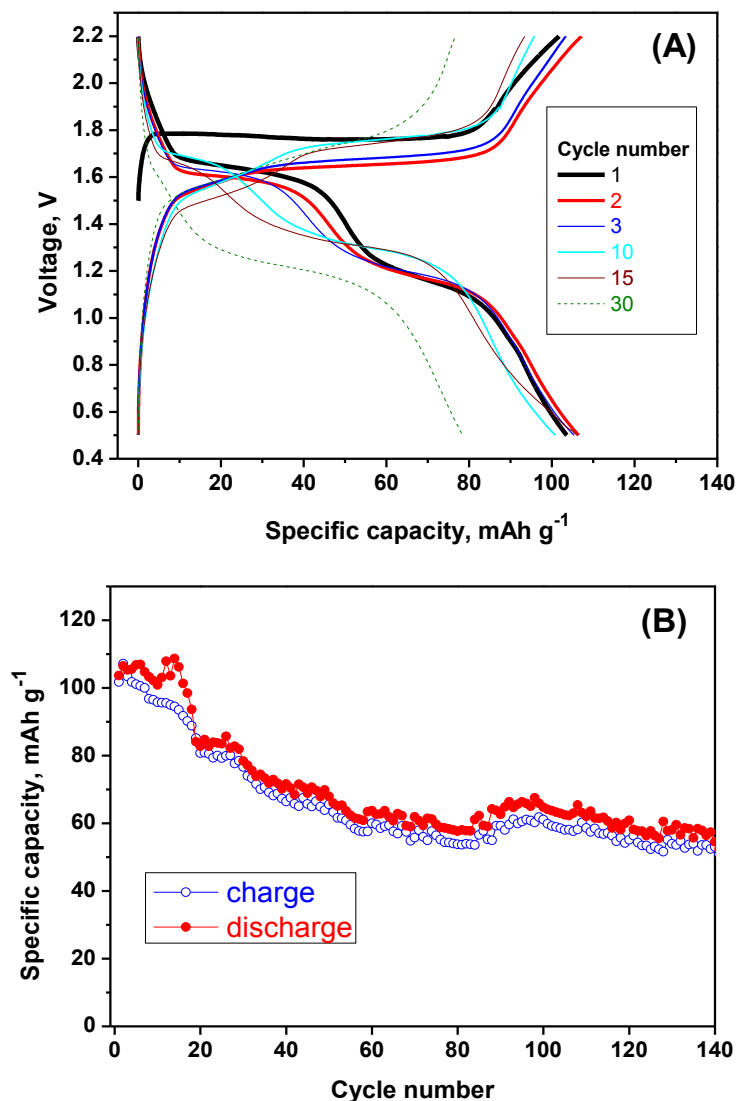


Fig.2. Galvanostatic cycling results for NVP in magnesium cell. (A) Voltage-capacity plot. (B) Capacity vs. cycle number. Current density: 10 mA g⁻¹.

According to the electrochemical experiments and to the chemical analysis by EPMA of electrodes retrieved from electrochemical cells after the first charge (Table 1), it can be concluded that around 1.7-1.8 Na per formula can be electrochemically deinserted, under the experimental conditions used in this work. Thus, the reaction of the first charge can be written as:

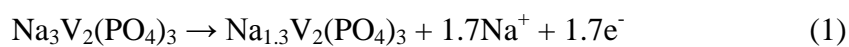
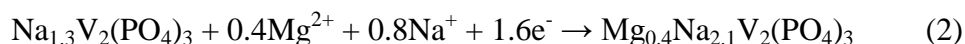


Table 1. Compositions of NVP electrode materials. The given theoretical compositions were calculated assuming that all the electrons that flow through the electrochemical cell are employed to the assumed (de)insertion reaction (coulometric measurement). The experimental compositions were obtained by using electron probe microanalysis (EPMA).

NVP electrode	Theoretical composition	Experimental composition
Pristine NVP	$\text{Na}_3\text{V}_2(\text{PO}_4)_3$	$\text{Na}_{2.8}\text{V}_2(\text{PO}_4)_{3.5}$
Charge 2.2 V	$\text{Na}_{1.3}\text{V}_2(\text{PO}_4)_3$	$\text{Mg}_{0.15}\text{Na}_{1.2}\text{V}_2(\text{PO}_4)_{2.9}$
Charge 2.2 V + discharge 1.4 V	$\text{Na}_{1.9}\text{V}_2(\text{PO}_4)_3$	$\text{Mg}_{0.35}\text{Na}_{2.07}\text{V}_2(\text{PO}_4)_{2.6}$
Charge 2.2 V + discharge 0.5 V	$\text{Mg}_{0.5}\text{Na}_{1.9}\text{V}_2(\text{PO}_4)_3$	$\text{Mg}_{0.6}\text{Na}_{2.25}\text{V}_2(\text{PO}_4)_{2.7}$
Charge 2.2 V + washing + discharge 0.5 V	$\text{Mg}_{0.8}\text{Na}_{1.3}\text{V}_2(\text{PO}_4)_3$	$\text{Mg}_{2.8}\text{Na}_{1.2}\text{V}_2(\text{PO}_4)_{2.7}$
140 cycles + discharge 0.5 V		$\text{Mg}_2\text{NaV}_2(\text{PO}_4)_3$

Consequently, sodium ions are introduced in the electrolyte solution forming *in situ* a hybrid sodium-magnesium electrolyte. The estimated concentration of sodium liberated from the NVP electrode in this electrolyte solution is around 0.01-0.03 M, depending on the electrode mass and volume of the electrolyte solution, which cannot be neglected. Otherwise, sodium could be removed from the electrolyte and deposited at the negative electrode upon electrochemical cycling.

According to the electrochemical experiments and to the chemical analysis of the electrodes retrieved from the electrochemical cells after the first charge-discharge cycle, the overall reaction of the first discharge down to 0.5 V can be approximately written as:



From 1.4 V to 0.5 V, the experimental atomic ratio Mg/Na found in the working electrode changes from 0.17 to 0.27 (Table 1). The content of magnesium due to traces of electrolyte is ca. 0.11 Mg per formula of NVP, as determined from a blank experiment with an electrode retrieved from a non-cycled cell. During the first discharge process, firstly sodium ions are inserted through the plateau near 1.6 V into

the 18e sites, and the concentration of sodium in the electrolyte solution is severely depleted. Secondly, and before the complete filling of the 18e sites by sodium, magnesium ions are inserted in the sites 18e or 6a by giving rise to the second pseudoplateau at ca. 1.2 V. The repulsive effect between the cations in the 18e sites may drive to the occupancy of the 6a sites.

We further investigated the mechanism of electrochemical insertion of magnesium into NVP by using a sodium-free electrolyte. For this purpose, the cell was first charged up to 2.2 V vs. Mg (reaction 1) to remove 1.7Na from NVP. Then, the oxidized working electrode was retrieved and washed with DME. Finally, a magnesium cell was freshly assembled with oxidized NVP. The resulting discharge curve (Fig. 3) reveals that the discharge plateau at ca. 1.6 V disappears, while the plateau at 1.2 V is longer. The experimental Na/Mg atomic ratio is 0.36. This result confirms that magnesium is inserted throughout the 1.2 V-plateau, and that the 1.6 V-plateau (in the hybrid sodium-magnesium electrolyte) is due to sodium insertion. On the basis of the electrochemical results, the reduction reaction in the sodium-free electrolyte can be written as:

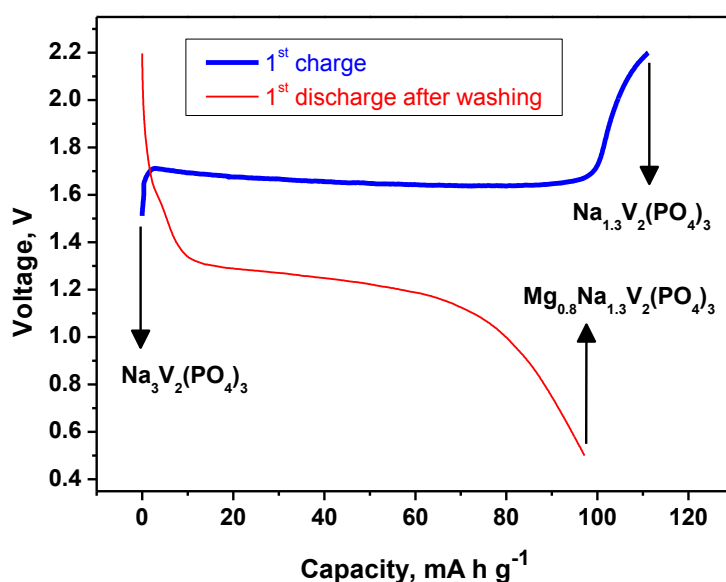
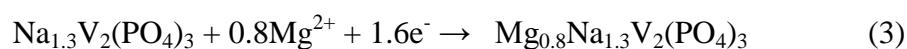


Fig.3. Voltage-capacity plot for the galvanostatic experiment obtained firstly charging (desodiation) in magnesium cell, then washing with DME the charged electrode and assembling a new cell with fresh magnesium electrolyte, and finally discharging in a new magnesium cell with sodium-free electrolyte solution. Current density: 10 mA g⁻¹.

It is worthy to note here that very recently Li et al. found that, using a hybrid electrolyte based on $[\text{Mg}_2\text{Cl}_2][\text{AlCl}_4]_2$ -DME, NVP as working electrode and Mg as counter electrode, sodium was reversibly (de)inserted [28]. In the paper of Li et al. the cut-off voltage was 1.6 V, and the second plateau and capacity that we observe at ca. 1.2 V could not be seen in that case. Although we used three-electrode cell, the measured voltage can be influenced by the electrolyte, making more difficult a direct comparison of the redox voltages in different papers. Furthermore, for achieving magnesium intercalation, we found more convenient using magnesium bis(trifluoromethanesulfonimide) in DME solvent as (chloride-free) electrolyte solution. Thus, following the work of Li et al., it may be more difficult for magnesium (MgCl^+) to lose Cl^- and then to intercalate into NVP. We tested the electrochemical behavior of NVP vs. Mg using another hybrid sodium-magnesium electrolyte ($\text{Mg}(\text{BH}_4)_2$ and NaBH_4 in diglyme, and these results agree well with sodium intercalation through a plateau (data not shown), in good agreement with the results of Yifei Li et al. We feel that the work of Li et al. [28] and our own work can be complementary to illustrate how the electrolyte solution can change the electrochemical intercalation, particularly for batteries of multivalent ions.

In order to study the structural changes induced in NVP during the electrochemical cycling, we recorded *ex situ* XRD patterns of working electrodes retrieved from magnesium cells (Fig. 4). The XRD pattern of the as-prepared NVP sample can be indexed in the R-3c space group (Fig. 4Aa), and can be ascribed to a NASICON-type structure. The lattice parameters obtained using the positions of the Bragg peaks and using hexagonal axis are $a=8.727(2)$ Å, $c=21.798(1)$ Å and $vol.=1437.7$ Å³. At the end of the first charge up to the nominal composition $\text{Na}_{1.3}\text{V}_2(\text{PO}_4)_3$, the XRD pattern (Fig. 4Ab) can be indexed using the same space group (R-3c), and a shrinkage of the unit cell is observed in both the a and c axis ($a=8.445(3)$ Å, $c=21.531(3)$ Å, $vol.=1329.7$ Å³). The coexistence of two phases, with compositions approximately $\text{Na}_3\text{V}_2(\text{PO}_4)_3$ and $\text{NaV}_2(\text{PO}_4)_3$, is responsible for the first charge plateau at ca. 1.8 V. The unit cell volume decreases due to both sodium deinsertion and vanadium oxidation. When $\text{Na}_3\text{V}_2(\text{PO}_4)_3$ is oxidized, sodium is partially removed from the 18e sites, and theoretically only 6b sites would be occupied in the resulting $\text{NaV}_2(\text{PO}_4)_3$ phase. However, it has been reported that some sodium atoms may migrate from 18e to 6b [22]. During the first discharge (Fig. 4Ac-e), we can estimate the

nominal compositions of the electrodes assuming that all the electrons consumed in the 1.6 V-plateau are used for sodium insertion, and that in the 1.2 V-plateau all the electrons are used for magnesium insertion. When ions are reductively inserted into $\text{Na}_x\text{V}_2(\text{PO}_4)_3$ (with $1 < x < 3$), there are sites 18e (C.N.=8) and 6a (C.N.=6) available for being occupied. According to Jian et al., sodium accommodation is energetically more favorable at 6b sites. Thus, sodium at 6b sites would be immobile, whereas sodium at 18e sites is mobile and can be reversibly deinserted in sodium cell [22]. As compared to the larger sodium, it would be expected that smaller magnesium ions have greater tendency to be inserted in 6-fold sites (6b and 6a). However, 6a sites could be occupied only at very low voltage [23]. The XRD pattern of the electrode material with nominal composition $\text{Na}_{1.8}\text{V}_2(\text{PO}_4)_3$, obtained in the first discharge plateau at 1.2 V, exhibits reflections of two NASICON-type phases with different lattice parameters (Fig. 4Ac). The main reflections are ascribed to a unit cell with the same size than the charged electrode and composition close to $\text{Na}_{1.3}\text{V}_2(\text{PO}_4)_3$, while minor reflections correspond to a unit cell with larger volume, with tentative composition $\text{Na}_3\text{V}_2(\text{PO}_4)_3$. Further discharge down to the second plateau at ca. 1.2 V, the electrode with nominal composition $\text{Mg}_{0.3}\text{Na}_{1.9}\text{V}_2(\text{PO}_4)_3$ exhibits reflections that also can be ascribed to two different NASICON-type phases with different cell volumes (Fig. 4Ad). In this case the relative contribution of the phase with the largest cell volume is the highest. After a whole charge-discharge cycle, the resulting XRD pattern (Fig. 4Ae) of the electrode material with nominal composition $\text{Mg}_{0.5}\text{Na}_{1.9}\text{V}_2(\text{PO}_4)_3$ corresponds to a single phase with lattice parameters $a=8.729(4)$ Å, $c=21.806(3)$ Å and $\text{vol.}=1438.9$ Å³. These lattice parameters are very like those of $\text{Na}_3\text{V}_2(\text{PO}_4)_3$, suggesting that magnesium insertion (together with sodium) is highly topotactic. The little contrast between sodium and magnesium ions does not allow unambiguously ascribing the distribution of the atoms in the crystal. Nevertheless, the Rietveld refinements confirm a slight contraction of the unit cell due to magnesium insertion and suggest that magnesium atoms could be placed rather at 18e sites.

In addition, the recorded XRD pattern corresponding to the electrode retrieved after charging, then washing to remove sodium from the electrolyte, and then discharging using sodium-free magnesium electrolyte (see reaction 3 and Fig. 3) is shown in Fig. 5a. An apparent loss of crystallinity is observed, perhaps due to the coexistence of crystallites with different composition (Na/Mg ratio) and spacing. The

low-intensity reflections observed at 32.3 and 24.2 °2θ can be ascribed to the reflections (116) and (113) of the NASICON framework. These reflections are shifted to higher angles as compared to raw NVP, indicating that the unit cell of $\text{Mg}_{0.8}\text{Na}_{1.3}\text{V}_2(\text{PO}_4)_3$ is smaller as compared to $\text{Na}_3\text{V}_2(\text{PO}_4)_3$. The XRD patterns obtained in the discharge state at 0.5 V, after 30 (Fig. 5b) and 100 (Fig. 5c) cycles in the normal (hybrid) cell (Fig. 5b), can be ascribed to a NASICON-type structure, but the reflections are clearly shifted to higher angles than in raw $\text{Na}_3\text{V}_2(\text{PO}_4)_3$ and $\text{Mg}_{0.8}\text{Na}_{1.3}\text{V}_2(\text{PO}_4)_3$. Consequently, the calculated lattice parameters ($a=8.51(1)$ Å, $b=21.07(3)$ Å and $\text{vol.}=1323$ Å³) unveil a contraction of the unit cell, in good agreement with a large amount of small and polarizing magnesium ions inserted in the host framework. Nevertheless, the compositional analyses suggest that nearly one Na per formula remains immobile in NVP, and sodium is never completely deinserted upon electrochemical cycling. This immobile sodium can contribute to the structural stability.

In conclusion, sodium can be deinserted from NVP and partially replaced by magnesium during the electrochemical cycling, although magnesium/sodium insertion is strongly influenced by the composition of the electrolyte solution and the imposed voltage window. The discharge plateau at ca. 1.6 V tends to disappear on cycling, because the relative amount of the phase with composition ca. $\text{NaV}_2(\text{PO}_4)_3$ decreases on cycling and is replaced by a magnesiated phase with smaller unit cell. In the charge process, more probably the sloping region at around 1.45-1.6 V is due to magnesium deinsertion, and the plateau at ca. 1.7 V is due to sodium deinsertion, and during cycling the plateau becomes shorter and the sloping region is progressively longer. The strong magnesium-oxygen bond could weaken the sodium-oxygen bonds, making easier the progressive replacement of sodium by magnesium upon electrochemical cycling.

To deepen in the study of the insertion mechanism, we tried to prepare the same materials that are formed in the electrochemical cells, with general formula $\text{Mg}_x\text{Na}_{3-2x}\text{V}_2(\text{PO}_4)_3$, by using an experimental procedure equivalent to that used one for magnesium-free $\text{Na}_3\text{V}_2(\text{PO}_4)_3$. However, a mixture of NASICON-type phase and other compounds was obtained (not shown). It is worthy to note here that several authors doped NVP with magnesium, replacing a very small amount of vanadium by magnesium, and then used this material in sodium battery [29,30]. In our case we aimed to replace sodium by magnesium. However, the substitution of sodium by magnesium

seems to be more efficiently achieved by electrochemical cycling. These finds are an example of the powerful capability of the soft chemistry to prepare new materials even at room temperature. Diffusion of magnesium in NASICON-type host also could open the possibility of using ionic conductors for future all-solid state magnesium batteries.

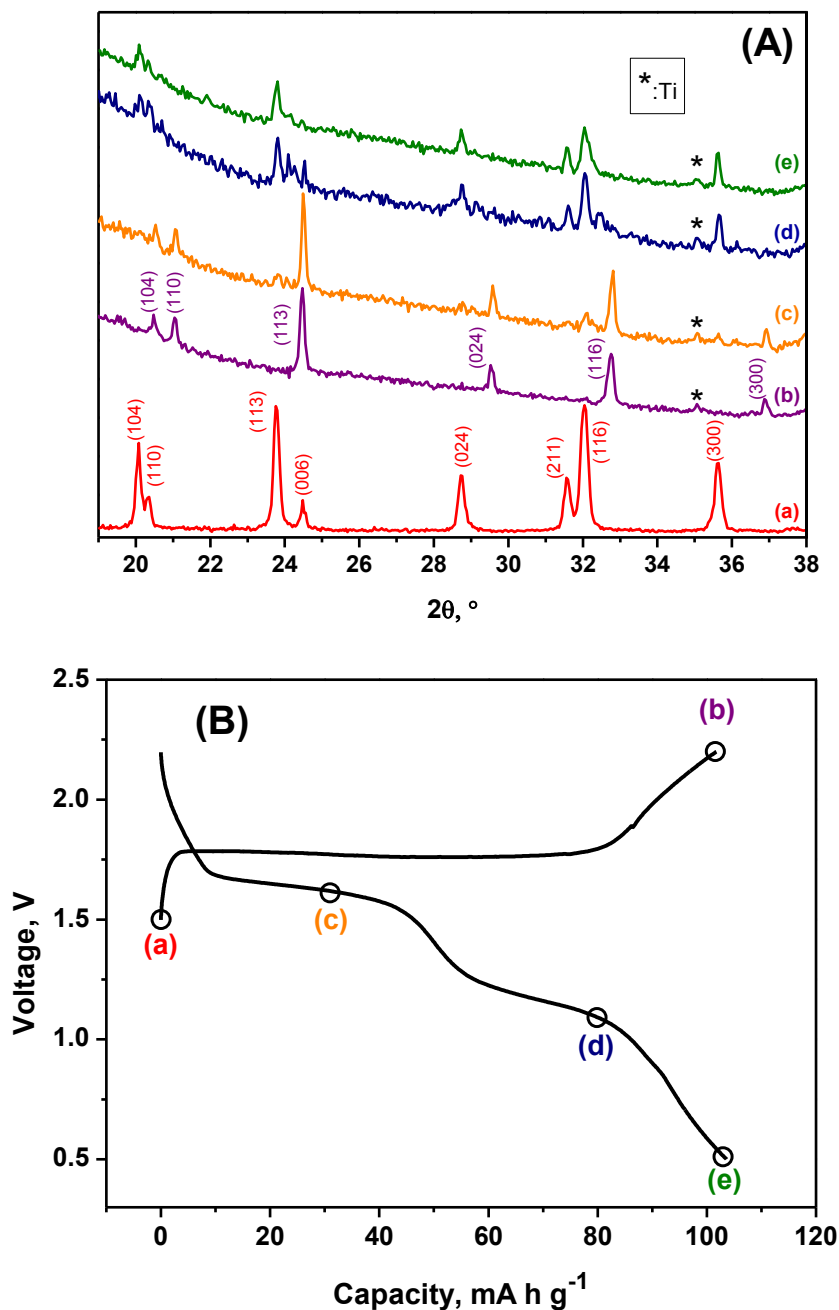


Fig.4. (A) XRD patterns for (a) raw NVP and electrodes at selected states of the first charge (b) and first discharge (c-e) in magnesium cell. (B) Voltage-capacity curve showing the points in which the electrochemical experiment was interrupted to record XRD patterns. Reflections from Ti current collector are marked.

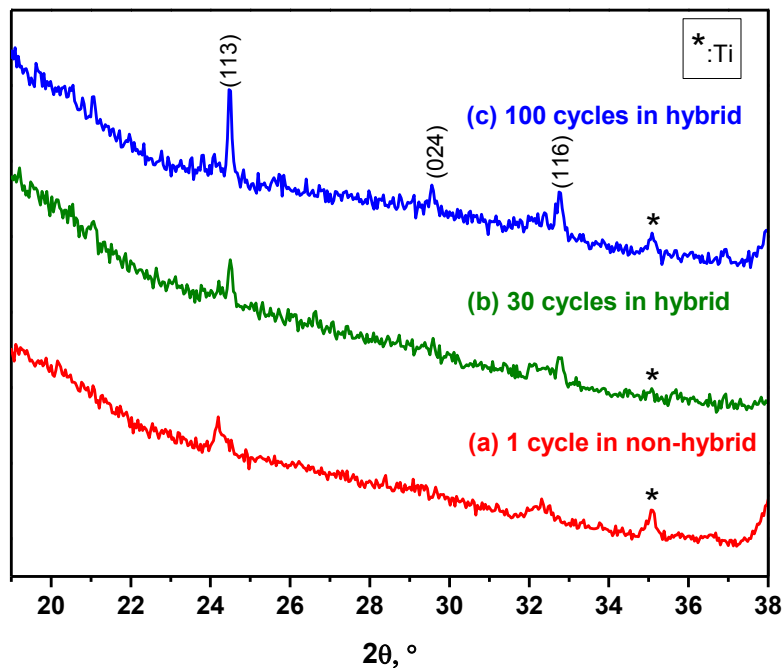


Fig.5. *Ex situ* XRD patterns of NVP electrodes retrieved from magnesium cells. (a) After one charge-discharge, with washing of the electrode after the first charge (equivalent to $\text{Mg}_{0.8}\text{Na}_{1.3}\text{V}_2(\text{PO}_4)_3$ at 0.5 V in Fig. 3). (b) After 30 cycles. (c) After 100 cycles (equivalent to 0.5 V in Fig. 2). Reflections from Ti current collector are marked.

4.3.4 Conclusions

For the $\text{Na}_3\text{V}_2(\text{PO}_4)_3$ phase with NASICON-type structure (s.g. R-3c) in magnesium cell, a voltage plateau is observed through the first charge ($\text{V}^{3+}/\text{V}^{4+}$) which corresponds to the coexistence of $\text{Na}_3\text{V}_2(\text{PO}_4)_3$ phase and partially desodiated phase, similarly to the behavior in sodium cell. Then, during the discharge process firstly sodium and secondly magnesium are inserted, and phases with general formula $\text{Mg}_x\text{Na}_y\text{V}_2(\text{PO}_4)_3$ are formed. After further electrochemical cycling, a NASICON-type structure with a unit cell slightly smaller than the cell of raw $\text{Na}_3\text{V}_2(\text{PO}_4)_3$ is formed, in good agreement with incorporation of magnesium in the framework. The observed partial replacement of sodium by magnesium by using electrochemical charge/discharge at room temperature is a nice example of soft chemistry. The NASICON structure is a rigid framework valid as a host for accommodation of not only lithium and sodium, but also magnesium. The drawbacks of this system could be the slow kinetics of magnesium insertion and the deterioration of the crystalline structure due to the strains generated by insertion of large amounts of magnesium. However, the immobile sodium atoms and the

rigid framework contribute to stabilize the structure for reversible magnesium insertion. These finds should be considered together with those of Li et al. [28] to develop rechargeable magnesium batteries.

Acknowledgements

The authors are grateful to MINECO (grant number MAT2014-56470-R), ERDF funds and Junta de Andalucía (research group FQM288) for financial support. SCAI-UCO and Institute of Fine Chemistry and Nanochemistry are also thanked for facilitating the use of several instruments.

4.3.5 References

1. A. Luntz, *J. Phys. Chem. Lett.* 6 (2015) 300.
2. C. P. Grey, J. M. Tarascon, *Nat. Mat.* 16 (2017) 45.
3. J. Muldoon, C. B. Bucur, T. Gregory, *Chem. Rev.* 114 (2014) 11683.
4. M. M. Huie, D. C. Bock, E. S. Takeuchi, A. C. Marschilok, K. J. Takeuchi, *Coordin. Chem. Rev.* 287 (2015) 15.
5. R. Chen, R. Luo, Y. Huang, F. Wu, L. Li, *Adv. Sci.* 3 (2016) 1600051.
6. J.W. Choi, D. Aurbach, *Nat. Rev. Mat.* 1 (2016) 16013.
7. A. J. Crowe, B. M. Bartlett, *J. Solid State Chemistry* 242 (2016) 102.
8. H. R. Yao, Y. You, Y. X. Yin, L. J. Wan, Y. G. Guo, *Phys. Chem. Chem. Phys.* 18 (2016) 9326.
9. M. Cabello, F. Nacimiento, R. Alcántara, P. Lavela, G. Ortiz, J. L. Tirado, *J. Electrochem. Soc.* 163 (2016) A2781.
10. M. Walter, K. V. Kravchyk, M. Ibáñez, M. V. Kovalenko, *Chem. Mater.* 27 (2015) 7452.

11. C. X. Huang, D. D. Chen, Y. Y. Huang, Y. L. Guo, *Electrochim. Acta* 100 (2013) 1.
12. R. von Hagen, A. Lepcha, X. Song, W. Tyrre, S. Mathur, *Nano Energy* 2 (2013) 304.
13. Z. Jian, L. Zhao, H. Pan, Y. S. Hu, H. Li, W. Chen, L. Chen, *Electrochem. Commun.* 14 (2012) 86.
14. R. Klee, M. J. Aragón, R. Alcántara, J. L. Tirado, P. Lavela, *Eur. J. Inorg. Chem.* 2016 (19) (2016) 3212.
15. C. Masquelier, L. Croguennec, *Chem. Rev.* 113 (2013) 6552.
16. R. Klee, P. Lavela, M. J. Aragón, R. Alcántara, J. L. Tirado, *J. Power Sources* 313 (2016) 73.
17. N. V. Kosova, D. O. Rezepova, S. A. Petrov, A. B. Slobodyuk, *J. Electrochem. Soc.* 164 (2017) A6192.
18. W. X. Song, X. B. Ji, C. C. Pan, Y. R. Zhu, Q. Y. Chen, C. E. Banks, *Phys. Chem. Chem. Phys.* 15 (2013) 14357.
19. K. Du, H. W. Guo, G. R. Hu, Z. D. Peng, Y. B. Cao, *J. Power Sources* 223 (2013) 284.
20. D. Wang, N. Chen, M. Li, C. Wang, H. Ehrenberg, X. Bie, Y. Wei, G. Chen, F. Du, *J. Mater. Chem. A* 3 (2015) 8636.
21. L. S. Plashnitsa, E. Kobayashi, Y. Noguchi, S. Okada, J. I. Yamaki, *J. Electrochem. Soc.* 157 (2010) A536.
22. Z. Jian, C. Yuan, W. Han, X. Lu, L. Gu, X. Xi, Y. S. Hu, H. Li, W. Chen, D. Chen, Y. Ikuhara, L. Chen, *Adv. Funct. Mater.* 24 (2014) 4265.
23. Z. Jian, Y. Sun, X. Ji, *Chem. Comm.* 25 (2015) 6381.
24. Y. Dong, S. Qian, L. Shao, H. Yu, L. Yan, P. Li, X. Lin, N. Long, M. Shui, J. Shu, *Ceram. Int.* 42 (2016) 10943.

25. Z. D. Huang, T. Masese, Y. Orikasa, T. Mori, K. Yamamoto, RSC Adv. 5 (2015) 8598.
26. G. Li, Z. Yang, Y. Jiang, C. Jin, W. Huang, X. Ding, Y. Huang, Nano Energy 25 (2016) 211.
27. K. Makino, Y. Katayama, T. Miura, T. Kishi, J. Power Sources 99 (2001) 66.
28. Y. Li, Q. An, Y. Cheng, Y. Liang, Y. Ren, C. J. Sun, H. Dong, Z. Tang, G. Li, Y. Yao, Nano Energy 34 (2017) 188.
29. H. Li, X. Yu, Y. Bai, F. Wu, C. Wu, L.Y. Liu, X.Q. Yang, J. Mater. Chem. A 3 (2015) 9578.
30. G. Xu, G. Sun, Ceram. Int. 42 (2016) 14774.

4.4 Advancing towards a veritable calcium-ion battery: CaCo_2O_4 positive electrode material

Marta Cabello, Francisco Nacimiento, José R. González, Gregorio Ortiz, Ricardo Alcántara, Pedro Lavela, Carlos Pérez-Vicente, José L. Tirado.

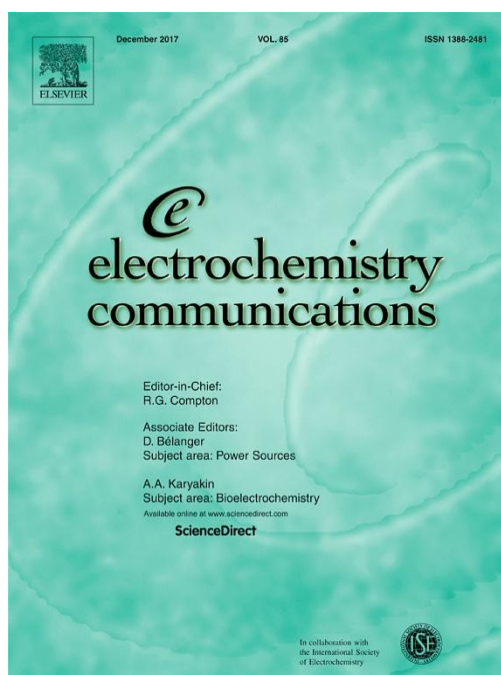
Laboratorio de Química Inorgánica. Universidad de Córdoba. Edificio C3, Campus de Rabanales. Spain

Abstract

A veritable calcium-ion battery using CaCo_2O_4 (s.g. P2/m) as a positive electrode, V_2O_5 (s.g. Pmmn) as a negative electrode and calcium perchlorate in acetonitrile as electrolyte solution has been evaluated for the first time. The electrochemical tests, XRD results and X-ray photoelectron spectra confirm that the calcium ion can be firstly removed from CaCo_2O_4 and then reintercalated, and this material can be an interesting candidate for developing non-aqueous calcium-ion batteries.

Keywords

Post-lithium batteries; calcium; CaCo_2O_4 ; V_2O_5 ; intercalation



Electrochemistry Communications 67 (2016) 59-64

4.4.1 Introduction

New electrochemical systems are being investigated within the context of a forthcoming post lithium-ion era, in which sodium-ion, aluminium-ion and magnesium-ion batteries are considered as the most promising systems [1-4]. Actually, aluminium-ion and magnesium-ion batteries have serious issues to find suitable electrolytes. For instance, ionic liquids have been proposed, though these are expensive and corrosive substances. However, batteries based on calcium ions have attracted little attention, probably due to the slow diffusion of Ca(II) into the host materials [5-10]. Despite this fact, it has been found that Ca(II) can be indeed inserted into materials such as V₂O₅ [5,6,9], K₂BaFe(CN)₆ [7] and very recently MnFe(CN)₆ [11, 12]. Regarding the electrolyte solution, it was found that the metallic Ca electrode is only stable in acetonitrile-based solutions while it is corroded in carbonate-based solutions [6]. It was believed that, as due to electrolyte decomposition, the back deposition of calcium on the counter electrode during the electrochemical reduction does not happen when organic solvents, such as acetonitrile, dimethylformamide or propylene carbonate are used. However, the feasibility of calcium plating at moderate temperatures using conventional organic electrolytes has been very recently proposed [13].

We believe that metallic calcium can be replaced by a calcium containing oxide, although this type electrode material has not been still reported. In this work we study a veritable calcium-ion battery based on intercalation compounds in both the positive and negative electrode, for first the time. Plating and stripping of calcium is avoided by using two electrode materials which intercalate calcium ions. For this purpose, we have explored the novel use of CaCo₂O₄ as a positive electrode. Vanadium pentoxide, which has been previously described in the literature like a calcium-intercalating material, has been selected as a negative electrode in this approach. The results confirm that calcium cobaltate can reversibly intercalate Ca²⁺ ion.

4.4.2 Experimental

4.4.2.1 Synthesis

CaCo_2O_4 was prepared by following the method of Pechini [14]. Firstly 50 ml of 1 M $\text{Ca}(\text{NO}_3)_2 \cdot 4\text{H}_2\text{O}$ and 100 ml of 1 M $\text{Co}(\text{NO}_3)_2 \cdot 6\text{H}_2\text{O}$ were mixed in a glass beaker. Then, citric acid and ethylene glycol were added to the solution. The molar ratio was calcium: cobalt: citric acid: ethylene glycol=1:2:3:6. The solution was continuously stirred and heated to 70°C until water evaporates and polymerization happens. The resulting slurry was transferred to a high crucible made of alumina and heated to 300°C. The resulting solid residue was ground with an agate mortar, and then further annealed at 600°C for 72 h.

4.4.2.2 Characterization

X-Ray Diffraction (XRD) experiments were carried out in a Bruker Advance instrument with $\text{CuK}\alpha$ radiation. Rietveld and Le Bail refinements were performed using the program Topas. The oxidation state of cobalt was analyzed by X-ray Photoelectron Spectroscopy (XPS) measurements in a SPECS Phobios 150 MCD using $\text{MgK}\alpha$.

4.4.2.3 Electrochemistry

All the electrochemical experiments were carried out in a VMP instrument. The two-electrode Swagelok-type cells were mounted in a glove-box under Ar atmosphere, using Whatman separators soaked with 0.5 M anhydrous calcium perchlorate in acetonitrile (AN). The working electrode was a mixture of active material (CaCo_2O_4 , 80%), carbon black (10%) and PVDF as binder (10%) pasted on titanium current collector. Commercial vanadium pentoxide (Aldrich) with layered structure (orthorhombic phase) was used as the negative electrode (active material: carbon black:PVDF=80:10:10).

Cyclic voltammetry (CV) was carried out in three-electrode cells made of glass (Gamry-type), using both aqueous (1 M CaCl_2 in distilled water) and non-aqueous (1 M $\text{Ca}(\text{ClO}_4)_2 \cdot 4\text{H}_2\text{O}$ in AN) electrolytes and Ag/AgCl like reference electrode. Ar gas was passed through the solution before and during performing the experiment to remove O_2 .

4.4.3 Results and discussion

The structure of the as-prepared calcium cobaltate was examined by XRD (Fig. 1 and Table 1). The XRD pattern of layered CaCo_2O_4 was refined according to the previously described structure $\text{P}'3\text{-Ca}_{0.5}\text{CoO}_2$ [15], using the atomic positions and coordinates published for the analogous $\text{P}'3\text{-Na}_{0.62}\text{CoO}_2$, s.g. C2/m [16]. The unit cell parameters agree well with those previously reported [15]. The monoclinic distortion can be evaluated by computing $D = \frac{a}{b\sqrt{3}}$. For a non-distorted hexagonal unit cell, $D = 1$. In this case, $D = 1.0003$, indicating that the monoclinic distortion of the axis can be neglected. The XRD pattern shows some additional weak lines that cannot be assigned to that unit cell (see, for example, at 24.1° , 32.8° 2θ). These reflections can be indexed assuming a superlattice with s.g. P2/m , with $a_s=a$, $b_s=2b$, and $c_s=2c$. Such a superlattice has also been previously observed by other authors [14]. Of course, the new computed D value (corrected for the superlattice) is the same.

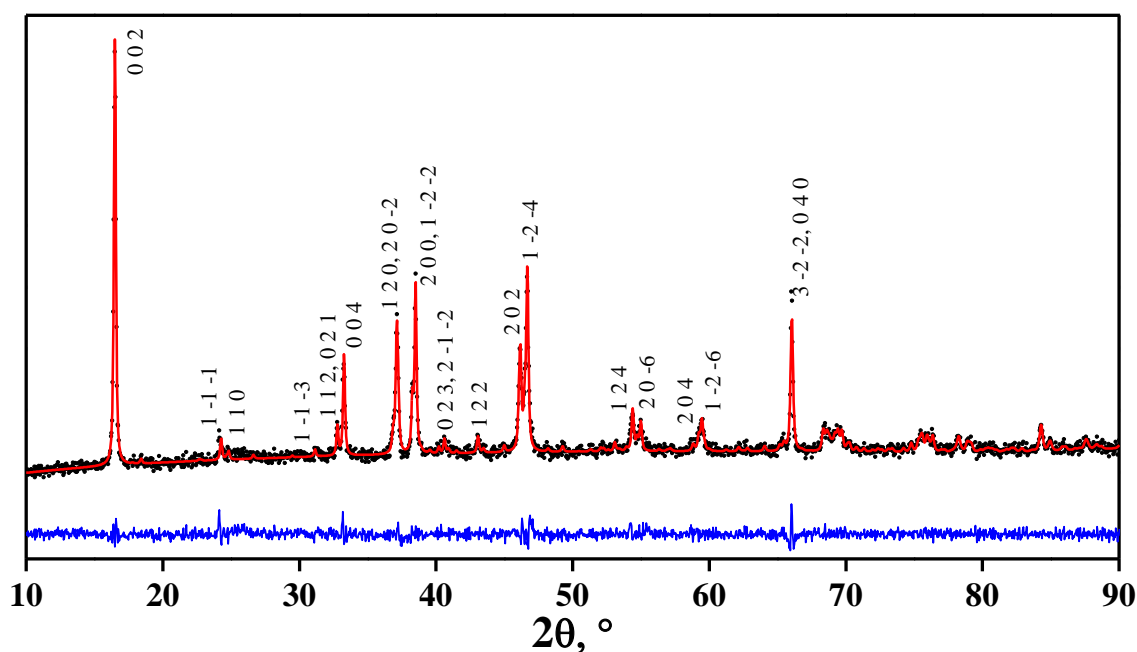


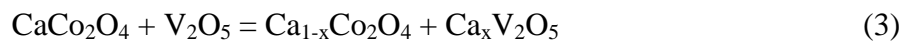
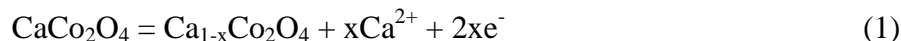
Fig. 1. XRD pattern of layered-like CaCo_2O_4 and Le Bail refinement using space group P2/m . The main Miller indexes are shown. The [100] projection of the structure of CaCo_2O_4 is shown below, with the unit cell C2/m plotted in black line and the unit cell P2/m plotted in dotted red line. Atoms color code:

oxygen=green, cobalt=red and calcium=light blue.

Table 1. Summary of XRD results and Rietveld refinement for CaCo_2O_4 .

Space group	a, Å	b, Å	c, Å	β , °
C2/m	4.9064(5)	2.8319(2)	5.6221(7)	106.115(8)
P2/m	4.9034(4)	5.6600(4)	11.236(1)	106.126(6)

In the electrochemical experiments of CaCo_2O_4 (working electrode) vs. metallic Ca (counter electrode) we observed poor electrochemical behavior and great irreversibility (not shown), probably due to the fact that metallic Ca is not stable in acetonitrile solution and under the selected experimental conditions, in good agreement with the literature [6]. Perhaps, the electrolyte composition and temperature may be selected to achieve good electrochemical performance using metallic Ca [13], but this is not the goal of our work. Thus, we use V_2O_5 or Pt as counter electrode. The galvanostatic (Fig. 2) and cyclic voltammetry (Fig. 3) results are in good agreement with reversible faradic reactions and calcium intercalation/deintercalation into/from CaCo_2O_4 . Taking into account that the material has low surface area ($S_{\text{BET}}=8.9 \text{ m}^2 \text{ g}^{-1}$) and that it is a non-porous material, contribution of the surface (pseudocapacitance) to the electrochemical behavior is not expected. Electrolyte decomposition (containing a small amount of water) starts at ca. -1.0 V in the discharge process (Fig. 3B). In the impedance spectrum (Fig. 3C), the semicircle is ascribed to the charge transfer resistance of the intercalation/deintercalation of calcium into CaCo_2O_4 . The observed operating voltage of CaCo_2O_4 is in the range between ca. -0.3 and ca. +1.6 V versus Ag/AgCl reference electrode and, consequently, non-aqueous electrolyte should be used to avoid water splitting. This operation voltage is higher than others previously reported in the literature for materials such as V_2O_5 [5,6,9]. We found an operation voltage for V_2O_5 in the range between ca. +1.0 and -0.7 V vs. Ag/AgCl. Thus, we have used V_2O_5 (orthorhombic type-structure, s.g. Pmmn) as the negative electrode to avoid the use of metallic Ca and the associated parasitic reactions (electrolyte decomposition by metallic Ca). The results confirm that CaCo_2O_4 can be used as a positive electrode in a full calcium-ion battery in which the electrochemical cycling starts with a charge process where Ca^{2+} is reversibly removed from CaCo_2O_4 and intercalated into V_2O_5 , according to the following half-reactions (1, 2) and overall reaction (3):



In the voltage-capacity curves of Fig. 2A, the plotted voltage is the difference of voltage between the positive and negative electrode of a full calcium-ion battery. Looking at the operation voltage one can conclude that the material of the negative electrode (V_2O_5) should be further optimized by using a redox potential below that of vanadium. Lower than expected working voltages have also been reported in recent studies on calcium-ion batteries [11]. The reversible capacity referred to the mass of calcium cobaltate is between ca. 30 and ca. 100 mAh g^{-1} , depending on the experimental conditions (Fig. 2B). Up to $x=0.35$ can be reversibly deintercalated from $\text{Ca}_{1-x}\text{Co}_2\text{O}_4$. Better cycling stability is observed for smaller ratio between the mass of the positive and negative electrode (excess of V_2O_5). In addition, a less negative value of the low cut-off voltage favored a better cycling performance. At higher current (100 μA), the electrochemical cycling is poor, probably due to slow calcium diffusion. In aqueous electrolyte (Fig. 2C), the charge process of CaCo_2O_4 can overlap with water decomposition and, consequently, the presence of water should be avoided.

The XPS Co2p core level spectra recorded on the pristine CaCo_2O_4 and charged electrodes are shown in Fig. 4. The spectrum of CaCo_2O_4 (Fig. 4A) reveals large and asymmetric signals and two satellites for both Co2p3/2 and Co2p1/2 regions. The fitting of the Co2p3/2 region in Gaussian-Lorentzian components allowed ascribing the components at 779.5 and 781.5 eV to Co^{3+} and Co^{4+} , respectively. The presence of minor amounts of the tetravalent state is supported by the satellite at 785.4 eV [17]. On charging (Fig. 4B,C), the intensity of the Co^{4+} signal increases, evidencing the electroactivity of cobalt in the positive electrode. To fit the spectra of the charged electrodes it is necessary to introduce a third component at higher binding energy which is assigned to cobalt ions in a slightly more electronegative environment than for the Co^{4+} ions [17]. These results are equivalent to those found for LiCoO_2 [17].

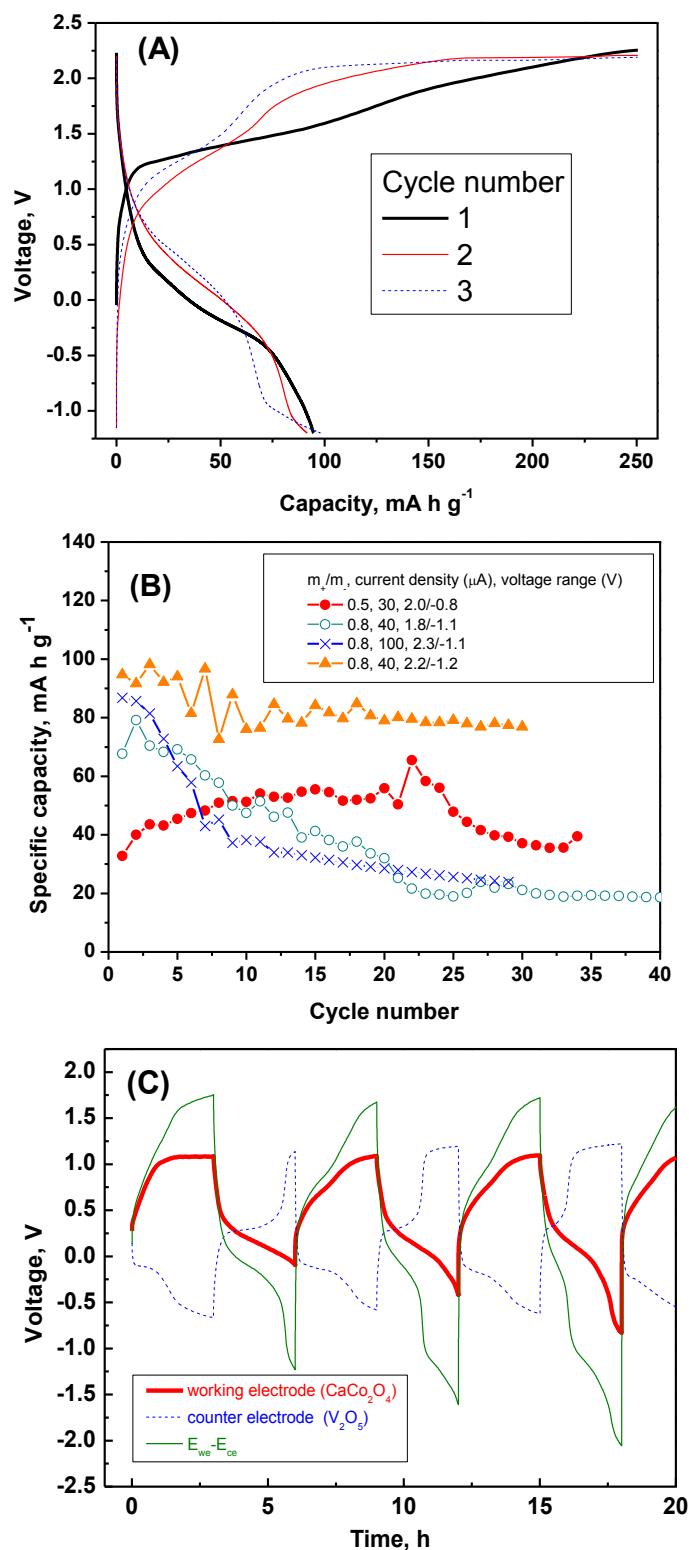


Fig. 2. Selected galvanostatic results for full calcium-ion battery based on CaCo_2O_4 (positive electrode) and V_2O_5 (negative electrode). (A) Typical voltage-capacity curves in non-aqueous electrolyte and mass ratio: $m_+/m_-=0.8$. (B) Specific capacity as a function of cycle number using different experimental conditions (mass ratio, current density and voltage range) in non-aqueous electrolyte. (C) Voltage-time curve for galvanostatic cycling in aqueous electrolyte, with $m_+/m_-=1.3$, reference electrode: Ag/AgCl and current: $50 \mu\text{A}$.

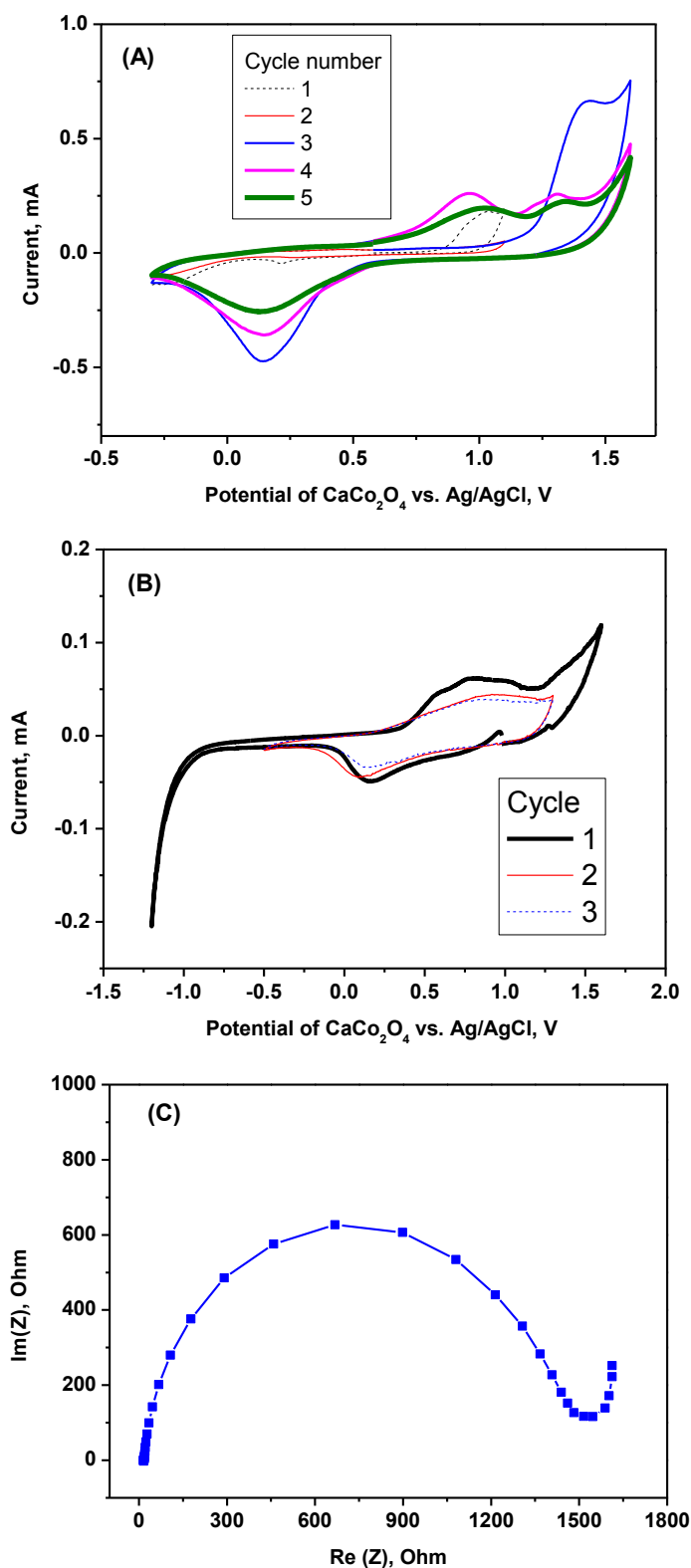


Fig. 3. Selected cyclic voltammetry results. (A) Full calcium-ion battery $\text{CaCo}_2\text{O}_4/\text{V}_2\text{O}_5$ (mass ratio: $m_+/m_-=0.55$) and scan rate: 0.5mV s^{-1} . (B) Half-cell with CaCo_2O_4 (working electrode), Pt as counter electrode and Ag/AgCl as reference electrode, and scan rate of 0.1 mV s^{-1} . (C) Impedance spectrum of CaCo_2O_4 obtained from (B) after three cycles.

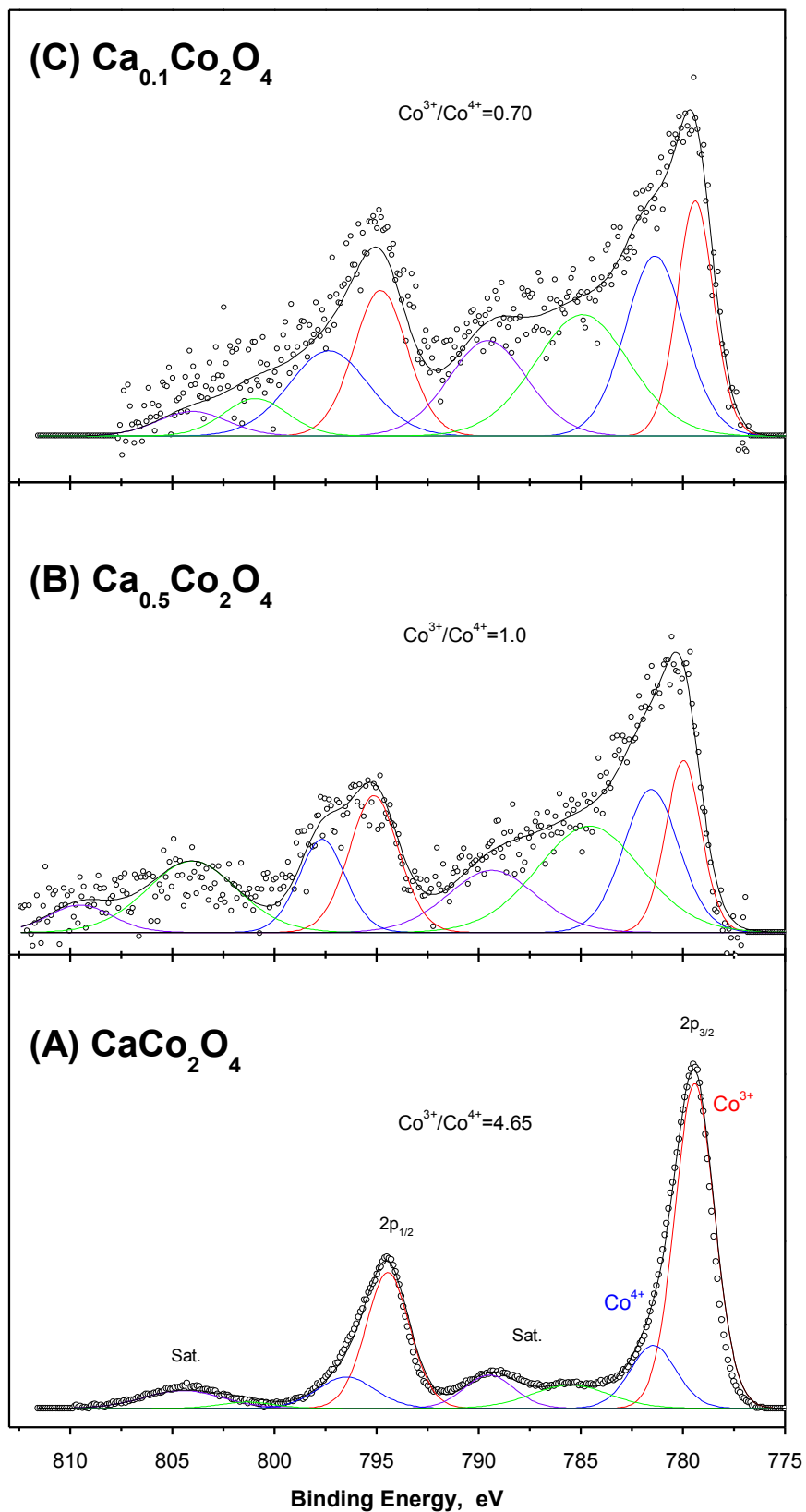


Fig. 4. X-ray photoelectron spectra at the Co_{2p} level for (A) pristine CaCo_2O_4 and after the electrochemical charge of the electrode up to (B) $\text{Ca}_{0.5}\text{Co}_2\text{O}_4$ and (C) $\text{Ca}_{0.1}\text{Co}_2\text{O}_4$.

According to the (002) Bragg reflection in the *ex-situ* XRD patterns (Fig. 5A), the removal of calcium from monoclinic CaCo_2O_4 up to $\text{Ca}_{0.6}\text{Co}_2\text{O}_4$ results in little changes in the basal spacing, which remains close to 5.4 Å. This result is similar to the description in reference [15] for samples obtained by cation exchange up to $\text{Ca}_{0.52}\text{Co}_2\text{O}_4$, and the explanation by the fact that the electrostatic interaction provided by Ca^{2+} is enough to overcome the repulsive forces between the negatively charged layers is also coherent with the electrochemical extraction. However, from $\text{Ca}_{0.55}\text{Co}_2\text{O}_4$ new reflections appear (Fig. 5A). If the same indexing is used, the basal spacing would be shifted to ca. 6.6 Å. The extraction of lithium from LiCoO_2 and NaCoO_2 also involves expansion of the unit cell although it is limited to ca. 0.4 Å [18, 19]. Two explanations of the new reflections can be proposed. First, the solvent cointercalation, as found in layered Na_xMnO_2 [20], but this is not commonly found for A_xCoO_2 . Second, the formation of a new superstructure due to the removal of most of the trigonal prismatic coordinated Ca^{2+} that could allow a change to O3 or even O6, as found in Na_xMnO_2 [21, 22], and the resulting basal spacing is basically preserved. The formation of the new superstructure is irreversible for CaCo_2O_4 .

Calcium is also intercalated into V_2O_5 and new reflections of $\text{Ca}_x\text{V}_2\text{O}_5$ appear in Fig. 5B [6, 23], found an increase of only 3% of the unit cell volume of vanadium pentoxide and the occurrence of a new orthorhombic phase ($\text{Ca}_x\text{V}_2\text{O}_5$). It seems that the reflections of the “new phase” that we observe are placed at nearly the same angles than those observed by Hayashi. However, we cannot confirm that these reflections are due to an orthorhombic unit cell.

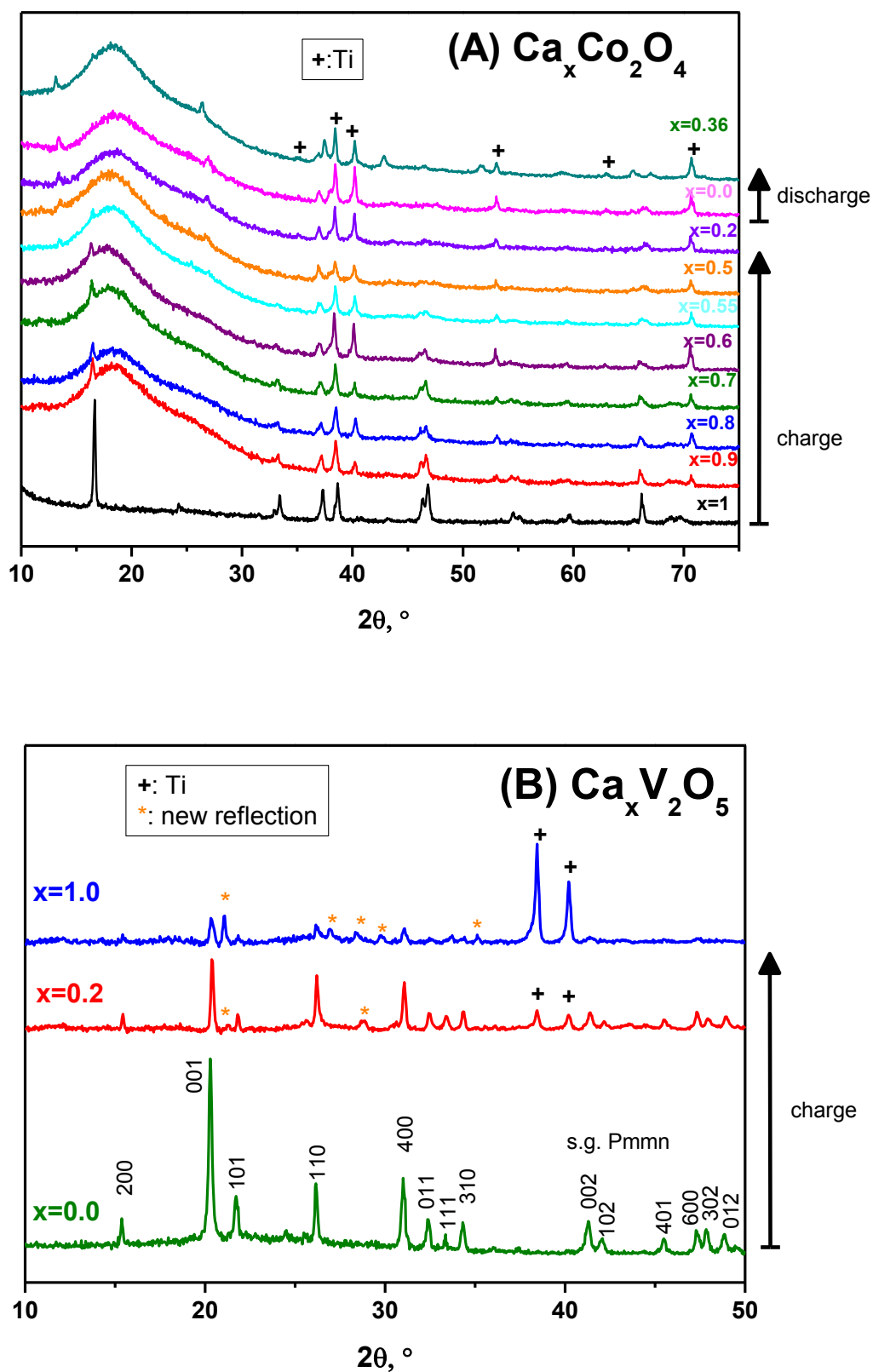


Fig. 5. *Ex-situ* XRD results for electrochemical calcium-extraction (charge) and reinsertion (discharge) in (A) $\text{Ca}_x\text{Co}_2\text{O}_4$ and (B) $\text{Ca}_x\text{V}_2\text{O}_5$.

4.4.4 Conclusions

CaCo_2O_4 has been efficiently used as a positive electrode material in a calcium-ion battery, equivalently to LiCoO_2 in lithium-ion batteries. Even if the use of V_2O_5 as a negative electrode results in low average voltages for the full cell, we have demonstrated that the concept of a Ca-ion cell is affordable.

Acknowledgements

The authors are grateful to MINECO, FEDER (MAT2014–56470-R), Junta de Andalucía (FQM288), SCAI-UCO, Institute of Fine Chemistry and Nanochemistry and European Research Institute ERI-ALISTORE

4.4.5 References

1. H. Zhou, *Energy Environ. Sci.* 6 (2013) 2256.
2. D. Datta, J. Li, V. B. Shenoy, *ACS Appl. Mater. Interfaces* 6 (2014) 1788.
3. R. van Noorden, *Nature* 507 (2014) 26.
4. P. Novák, R. Imhof, O. Haas, *Electrochim. Acta* 45 (1999) 351.
5. G. G. Amatucci, F. Badway, A. Singhal, B. Beaudoin, G. Skandan, T. Bowmer, I. Plitz, N. Pereira, T. Chapman, R. Jaworski, *J. Electrochem. Soc.* 148 (2001) A940.
6. M. Hayashi, H. Arai, H. Ohtsuka, Y. Sakurai, *J. Power Sources* 119–121 (2003) 617.
7. P. Padigi, G. Goncher, D. Evans, R. Solanki, *J. Power Sources* 273 (2015) 460.
8. R. Y. Wang, C. D. Wessells, R. A. Huggins, Y. Cui, *Nano Lett.* 13 (2013) 5748.
9. M. Bervas, L. C. Klein, G. G. Amatucci, *Solid State Ionics* 176 (2005) 2735.
10. J. Muldoon, C. B. Bucur, T. Gregory, *Chem. Rev.* 114 (2014) 11683.

11. A. L. Lipson, B. Pan, S. H. Lapidus, C. Liao, J. T. Vaughey, B J. Ingram, *Chem. Mater.* 27 (2015) 8442.
12. T. Shiga, H. Kondo, Y. Kato, M. Inoue, *J. Phys. Chem. C* 119 (2015) 27946.
13. A. Ponrouch, C. Frontera, F. Bardé, M. R. Palacín, *Nature Materials* 15 (2016) 169.
14. H. Tran, T. Mehta, M. Zeller, R. H. Jarman, *Mat. Res. Bull.* 48 (2013) 2450.
15. B. L. Cushing, J. B. Wiley, *J. Solid State Chem.* 141 (1998) 385.
16. M. Blangero. Ph.D. thesis. Cobaltites lamellaires d'alcalins : cristallographie et thermoelectricite. Material chemistry. Universite Sciences et Technologies – Bordeaux I, 2008.
17. J. C. Dupin, D. Gonbeau, H. Benqlilou-Moudden, Ph. Vinatier, A. Levasseur, *Thin Solid Films* 384 (2001) 23.
18. B. L. Cushing, J. B. Wiley. *J. Solid State Chem.* 141 (1998) 385.
19. J. N. Reimers, J. R. Dahn, *J. Electrochem. Soc.* 139 (1992) 2091.
20. G. G. Amatucci, J. M. Tarascon, C. Klein, *J. Electrochem. Soc.* 143 (1996) 1114.
21. S. Komaba, N. Yabuuchi, T. Nakayama, A. Ogata, T. Ishikawa, I. Nakai, *Inorg. Chem.* 51 (2012) 6211.
22. M. Kalapsazova, G. F. Ortiz, J. L. Tirado, O. Dolotko, E. Zhecheva, D. Nihtianova,, J Lyuben Mihaylov, R. Stoyanova, *ChemPlusChem* 80 (2015) 1642.
23. Y. Hinuma, Y. S. Meng, K. S. Kang, G. Ceder, *Chem. Mater.* 19 (2007) 1790.

4.5 Reversible intercalation of aluminium into vanadium pentoxide xerogel for aqueous rechargeable batteries

José R. González, Francisco Nacimiento, Marta Cabello, Ricardo Alcántara, Pedro Lavela, José L. Tirado.

Laboratorio de Química Inorgánica. Universidad de Córdoba. Edificio C3, Campus de Rabanales. Spain

Abstract

Rechargeable batteries based on the intercalation of aluminium ions may be competitive against lithium-ion batteries, but their development and comprehension are full of difficulties. The charge/discharge processes are particularly complex in aqueous electrolyte solutions. The electrochemical behaviour of orthorhombic V_2O_5 , obtained from xerogel, in aluminium cell is studied here by using electrochemical cycling, impedance spectroscopy, XRD and XPS results. After electrochemical intercalation of aluminium, the resulting $(Al^{3+})_{x/3}[(V^{4+})_x,(V^{5+})_{2-x}]O_5 \cdot nH_2O$ is XRD-amorphous at approximately $x=1.5$. The reversible capacity is ca. 120 mAh g^{-1} (equivalent to $Al_{0.27}V_2O_5$). The loss of crystallinity induced by the electrochemical intercalation enhances the chemical exchange between the electrode material and the electrolyte solution. In the presence of acidic water solution, besides the faradic electrochemical process driven by the electrical current, aluminium, proton and water also can be intercalated into V_2O_5 by chemical reactions or ion exchange.



RSC Advances



RSC Advances 6 (2016) 62157-62164

4.5.1 Introduction

Lithium-ion batteries have been successfully commercialized since the 1990s. At present, batteries based on aluminium may be advantageous against lithium battery in terms of economy, sustainability and energy density [1]. Although, lithium and sodium intercalation reactions have been extensively studied during decades, the study of the insertion of multivalent cations has deserved less attention and it is still in its infancy. Several of the most promising materials proposed for reversible intercalation of aluminium ion are titanium dioxides [2-4] and vanadium oxides [5-8].

Orthorhombic vanadium pentoxide (V_2O_5) possesses a layered structure built up from VO_5 square pyramids sharing edges and corners, with V_2O_5 layers held together via weak vanadium-oxygen interaction [9]. The layered character of V_2O_5 and the high redox potential of V^{5+} make it an interesting and versatile host material for many guest species and for batteries based on intercalation of ions such as lithium, sodium, magnesium and aluminium. It is worth to note that xero- V_2O_5 adsorbs water at the oxide-air interface and that, according to the layer structure of V_2O_5 , water absorption may be described as an intercalation process [10]. The xerogel (xero- V_2O_5) consists of V_2O_5 bilayers with water between them and it is a Brønsted acid. Thus, the intercalated water can play an important role in the electrochemistry of V_2O_5 [11-13]. In addition, vanadium pentoxide gels are very sensitive to some reduction of vanadium ions (weak mixed V^{5+} - V^{4+} character) and its content in V^{4+} is related to the water content (dehydration leads to some reduction of vanadium). In non-aqueous lithium cell, vanadium pentoxide exchanges its residual water with the organic solvent and probably the discrepancies in the electrochemical behaviour reported by different authors may be due to different water content in their samples [10-15]. According to the literature [14,15], the xerogel of V_2O_5 can contain protonated water (H_3O^+) in the interlayer space and the layers of vanadium oxide are negatively charged ($V_2O_5^{m-}$) with about 0.2 charge per vanadium atom. This fact is due to the acidity of V^{5+} which drives to hydrolysis. Thus, the xero- V_2O_5 is a protonic conductor and presents ionic exchange properties between the H_3O^+ cations and various charged species (M^{n+}), such as Al^{3+} [14]. By immersion of amorphous or poorly crystallized xero- V_2O_5 in an aqueous solution of cations, the negative charge of the $V_2O_5^{m-}$ layer remains fixed while the H_3O^+ ions in the interlayer space are exchanged with the outer cations of the solution. By thermal

annealing of the M-intercalated xero- V_2O_5 materials (M_x^{n+} , $(V_2O_5)^{m-}$, yH_2O), vanadium bronzes are formed ($M_xV_2O_5$) in which the initial vanadium is partially reduced (about 600°C for M=Al) [15].

Surprisingly, in contrast to lithium and magnesium batteries, the role of water molecules in the aluminium intercalation into V_2O_5 has received little attention. Within the field of post-lithium batteries, the intercalation of aluminium into TiO_2 for batteries using aqueous electrolyte solutions has been explored [2,3]. However, to the best of our knowledge, the intercalation of aluminium into vanadium pentoxide for batteries using aqueous electrolyte has not been reported yet; irrespectively of the reports using electrolytes based on ionic liquids [16-18].

4.5.2 Experimental

4.5.2.1 Synthesis of V_2O_5

The V_2O_5 sample was prepared by using the ion exchange method. A 0.5 M solution of sodium metavanadate in water was eluted through a proton exchange resin (Downing). The resulting hydrogel was aged and dried in an air atmosphere for two weeks. Amorphous xerogel of vanadium pentoxide is obtained at this stage. Then, the xerogel (xero- V_2O_5) is manually milled, further dried at 120°C and crystallized at 300°C for three hours in air atmosphere.

4.5.2.2 Characterization of materials

X-ray diffraction (XRD) patterns were recorded in a Bruker D8 instrument with $CuK\alpha$ radiation and reflection geometry. For recording XRD of the recuperated electrodes, the samples were protected against reaction with air by covering with kapton tape.

For the images of electron microscopy, TEM (JEM 1400) and FE-SEM (JSM 7800F) were used.

Thermogravimetric analysis (TGA) was carried out in Shimadzu instrument at 10°C/min of heating rate in air atmosphere.

The chemical state and composition were analyzed by X-ray photoelectron (XP) spectra that were recorded using a SPECS Phobios 150MCD and Mg K α source. Before recording the XPS of the electrode recuperated from the electrochemical cell, the electrode material was washed with water to remove the remaining electrolyte solution and then dried under vacuum.

4.5.2.3 Electrochemical tests

All the electrochemical experiments were performed in a VMP Biologic instrument. The electrochemical cells were of Swagelok-type in T-configuration and, in order to prevent corrosion, the use of metals as current collectors was avoided. The active material (xero- V₂O₅ annealed at 300°C, 80%) was mixed with polytetrafluorethylene (PTFE, 10%) binder and carbon black (conductive additive, 10%), and the resulting mixture was spread on carbon paper (graphite, Goodfellow). The electrolyte solution was 1 M AlCl₃ in deionized water which was previously outgassed by flowing Ar. Several discs of Whatman glass fiber filter were used like separator. The counterelectrode was glassy carbon. Mercury/mercurous sulfate electrode Hg/Hg₂SO₄, K₂SO₄(sat'd) was used as reference electrode (MSE).

4.5.3 Results and discussion

4.5.3.1 Microstructure

The V₂O₅ xerogel dried at 120°C is XRD-amorphous (Fig. 1a). After annealing at 300°C it shows a XRD-pattern (Fig. 1b) that is ascribed to orthorhombic vanadium pentoxide (layered structure), with space group Pmmn. The resulting lattice parameters are a=11.521(2) Å, b=3.563(1) Å and c=4.3719(6) Å. The relative intensity of the reflection (001) is in good agreement with the layered character and with preferred orientation of the particles. The average crystallite size obtained by applying the Scherrer equation ($L = \lambda \beta^{-1} \cos\theta^{-1}$) to the broadening (β) of the Bragg reflections is L=45(4) nm.

The morphology of the particles was examined by SEM and TEM (Fig. 2). In the SEM results the particles of the sample dried at 120°C have the appearance of

crumpled layers, and after annealing at 300°C the layered particles become less crumpled and more flat. In the TEM micrographs (Fig. 2 E, F), the particles show layered character, with around 30-250 nm of diameter.

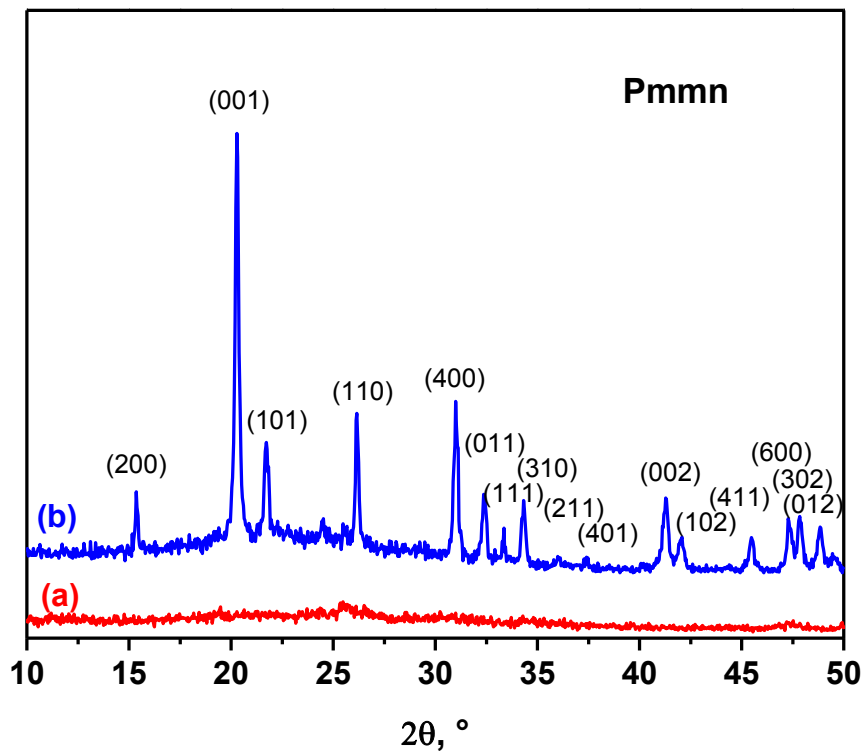


Fig. 1 XRD pattern of xero- V_2O_5 dried at 120 (a) and 300°C (b). The Miller indexes are given.

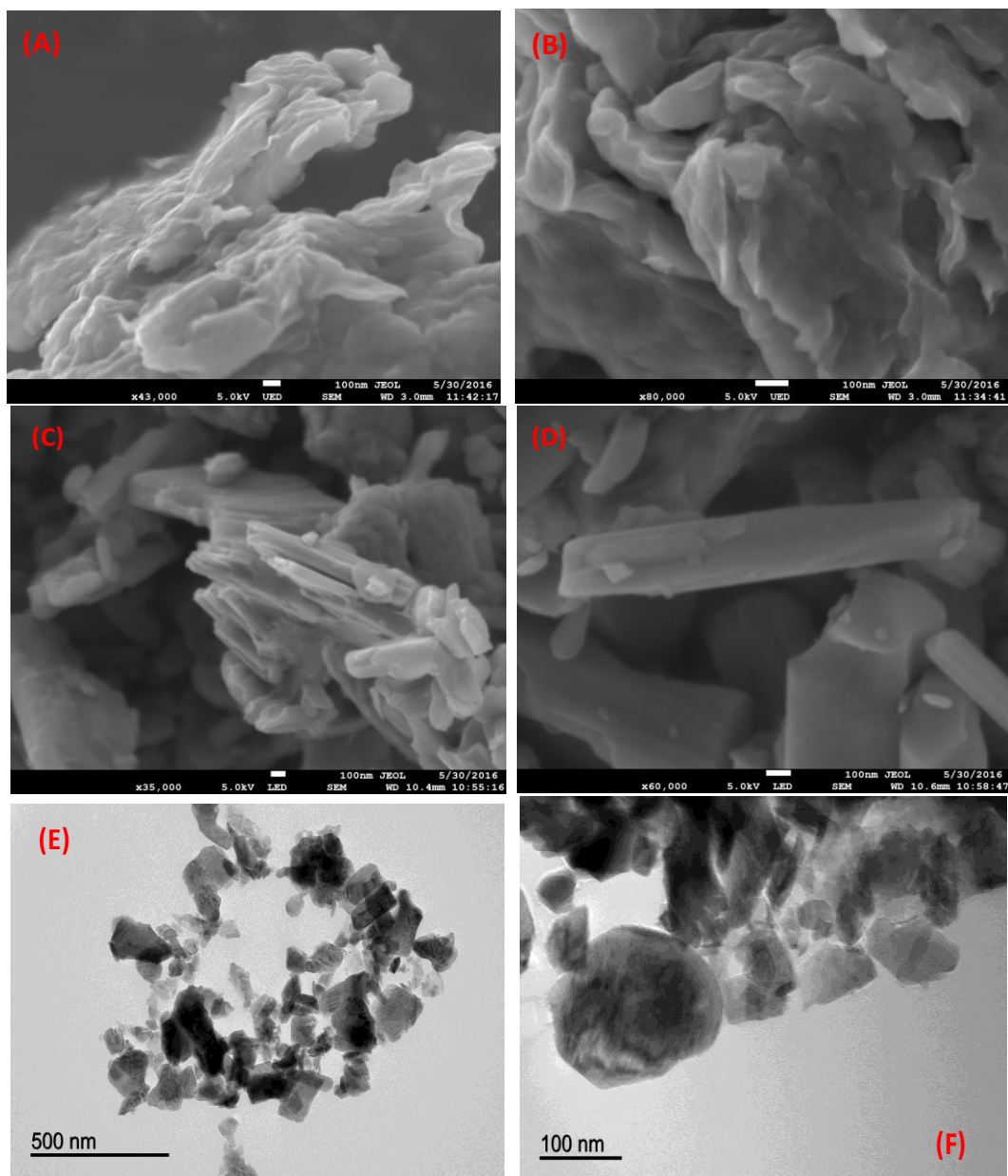


Fig.2. SEM (A-D) and TEM (E, F) micrographs of xero-V₂O₅ heated to 120 (A,B) and 300°C (C-F).

4.5.3.2 Thermogravimetric analysis

The water content of V₂O₅ can greatly influence on its electrochemical cycling and capacity in batteries [11,12]. Water may be detrimental for non-aqueous batteries, but a small amount of water can help to the intercalation of the cation into vanadium oxide. It is possible to obtain the anhydrous form of V₂O₅ whether the sample is heated for enough time at 250°C or higher temperature, although the water can be reabsorbed.

Figure 3 shows to the TGA results of a xero- V_2O_5 sample annealed at 300°C and stored in air atmosphere for two months. The xero- V_2O_5 sample contains a small amount of water ($V_2O_5 \cdot nH_2O$). Firstly, weakly bonded or adsorbed water is released at ca. 100°C . Then, more strongly water is lost at $250\text{-}300^\circ\text{C}$. If one takes into account all the water content found in the TGA up in all the range of temperature from 30 to 300°C , then it results that $n=0.29$ in $V_2O_5 \cdot nH_2O$. If the water loss at lower temperature is considered to be free or weakly adsorbed water, the content of more strongly bonded water is $n=0.16$ (from 100 to 300°C). According to the resulting spacing of the basal plane obtained from the XRD pattern and the literature [19], the water molecules are not placed in the interlayer spacing. Even after annealing at 600°C , the XRD pattern of vanadium oxide remains nearly unchanged (not shown), confirming that there was not a significant amount of water in the interlayer space. These results show that xero- V_2O_5 has tendency to adsorb limited amounts of water from the atmosphere.

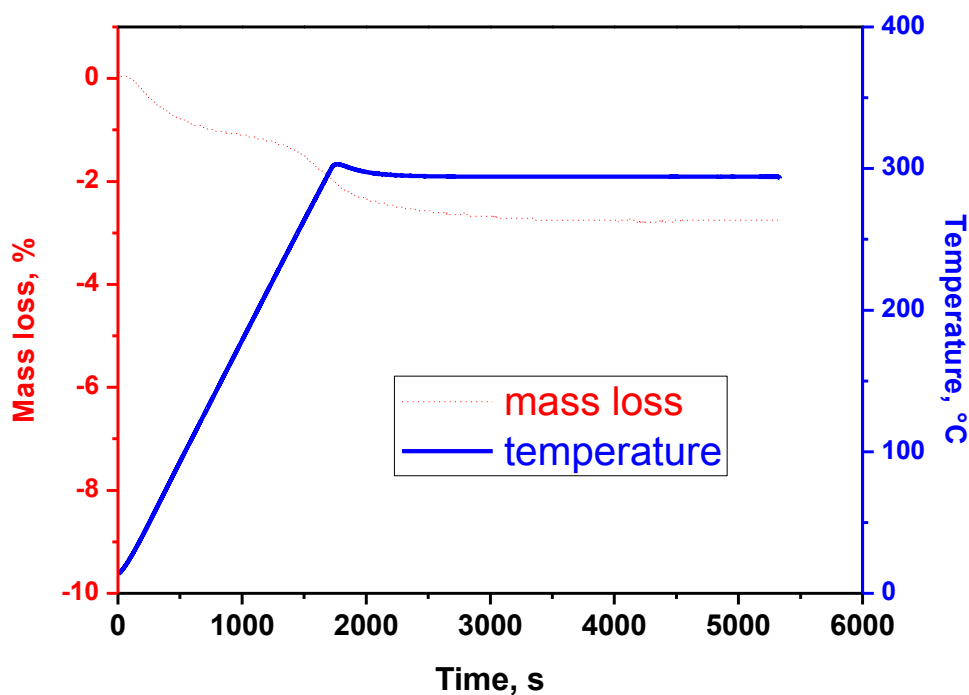


Fig.3. TGA curve of xero- V_2O_5 (heated to 300°C two months before recording the TGA experiment). Firstly, the sample was heated at a rate of $10^\circ\text{C min}^{-1}$ up to 300°C , and then the temperature was hold at 300°C for one hour.

4.5.3.3 Electrochemical performance

The electrochemical behavior of the as-prepared V_2O_5 sample was examined using cyclic voltammetry (Fig. 4) and galvanostatic cycling (Fig. 5). In the cyclic voltammogram (CV) of V_2O_5 in aluminium cell a pair of redox peaks can be observed at -0.30 and -0.03 V (vs. MSE) in the cathodic and anodic sweep, respectively (Fig. 4A). These peaks agree well with a reversible faradic process. Corrosion and electrolyte decomposition are not taking place in the voltage range in which V_2O_5 is employed.

As a blank test, the CV obtained in the absence of active material (the working electrode is a carbon foil) shows no redox activity in the voltage range between -1.3 and +0.5 V. In comparison with anatase,² the voltage of V_2O_5 is higher, and this fact can involve higher energy density and that H_2 is not evolved during the reduction process. For the sake of comparison, aqueous solutions of $AlCl_3$ and HCl were used as electrolytes.

If one looks at the cyclic voltammetry results of V_2O_5 in hydrochloric solution (Fig. 4A), it is evident that the protons can play an important role. In solution of aluminium-free hydrochloric acid at pH 1.3 the current becomes more intense than at pH 2.3, strongly suggesting that more protons are inserted at more acidic pH.

The electrochemical intercalation in aqueous solution of protons yielding $H_xV_2O_5$ ($0 < x < 0.5$) and the insertion of lithium to form $Li_xV_2O_5$ ($0 < x < 1.0$) were previously reported by other authors [20]. The same authors reported that larger cations are not intercalated into V_2O_5 . Taking into account that the crystal ionic radius of Al^{3+} (0.68 Å) is smaller than Li^+ (0.90 Å), it seems reasonable to believe that aluminium can be intercalated. In this sense, other authors found minimum activation energy for aluminium insertion (by exchange in water solution) into xero- V_2O_5 [21]. Thus, in Fig. 4A, for a pH value of 2.3, the CV curve is modified in the presence of aluminium ions in comparison with aluminium-free solution at the same pH, indicating that aluminium insertion is preferential to proton insertion. The redox peaks in 1 M $AlCl_3$ (aq.) are resulted from aluminium insertion. In Fig. 4B, it is observed that the capacity is higher at lower scan rates, and the capacity retention is good. In the CV at low rate the peak intensity is smaller (Fig. 4C), as expected for a diffusion-controlled process.

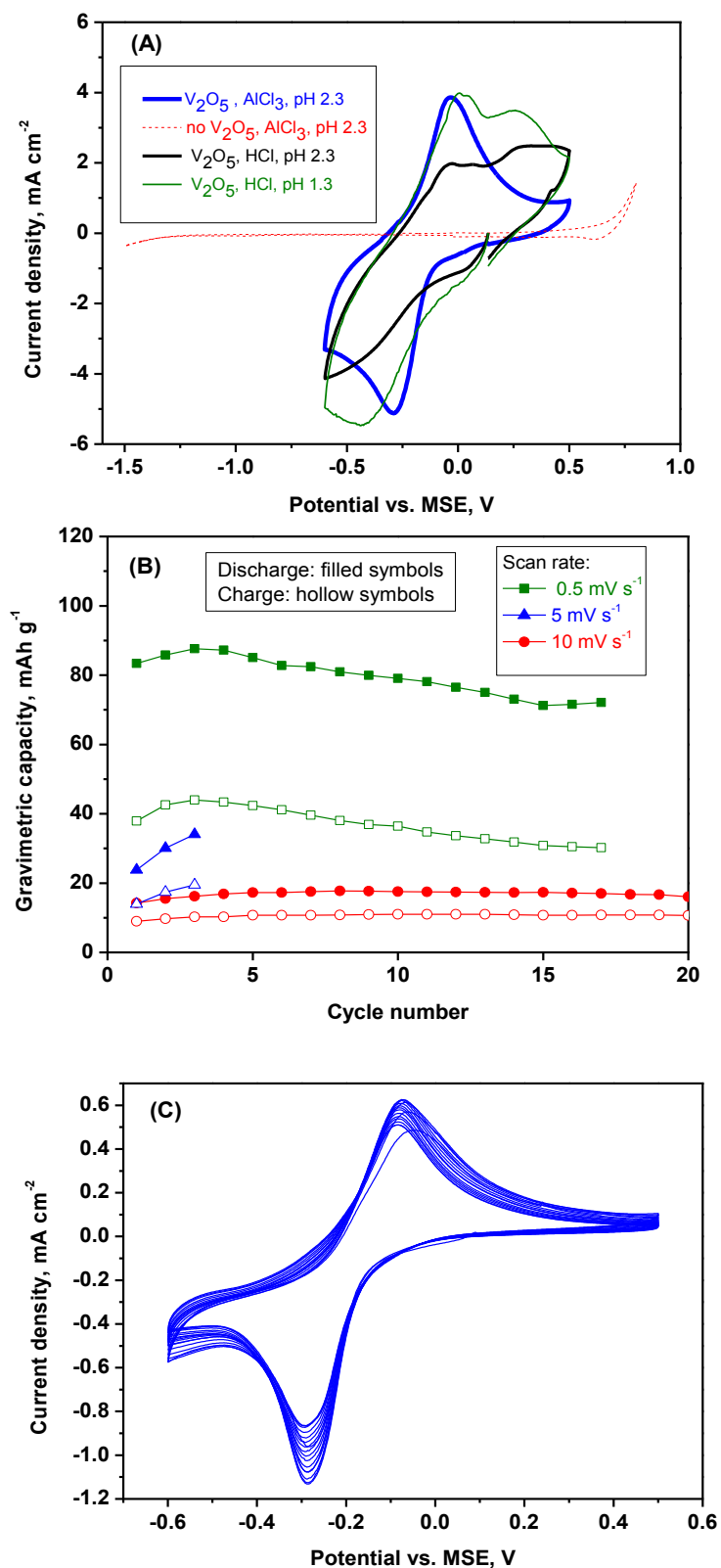
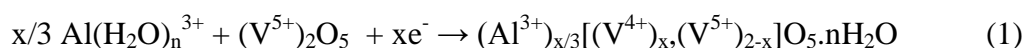


Fig.4. Cyclic voltammetry results. (A) Comparison of cyclic voltammograms (CV) of V_2O_5 (working electrode) and blank experiment (no V_2O_5) using different solutions and at scanning rate of 10 mV s^{-1} . (B) Capacity as a function of cycle number at different scan rates in $1 \text{ M AlCl}_3(\text{aq.})$ solution (pH 2.3). (C) CV of V_2O_5 in $1 \text{ M AlCl}_3(\text{aq.})$ at 0.5 mV s^{-1} .

In the galvanostatic experiment, the voltage-capacity curve shows a reversible pseudoplateau at ca. -0.15 V in the discharge process and at ca. 0.0 V in the charge process (Fig. 5A). The origin of this pseudoplateau can be the intercalation process of hydrated aluminium and the coexistence of crystalline and amorphous phase as it is further discussed below in the light of XRD and XPS results. The reversible capacity is substantially lower at higher rates (ca. 20 mAh g⁻¹ at 200 mA g⁻¹ of current density) than at low rate (in the order of 120 mAh g⁻¹ at 60 mA g⁻¹) (Fig. 5B), suggesting that the reaction is controlled by diffusion.

Hydrated aluminium ions are intercalated into the interlayer space of V₂O₅ and V⁵⁺ ions are reduced to V⁴⁺ according to the next reaction:



Water molecules can shield the charge of the aluminium ion facilitating its insertion/deinsertion into vanadium oxide. Thus, it is expected that water molecules are co-intercalated simultaneously to aluminium-intercalation. On the other hand, it is known that in the interlayer space of V₂O₅ in contact with water, protonated water (H₃O⁺) and Al³⁺ can be chemically exchanged [22]. In the same sense, other authors found that V₂O₅ can be doped with aluminium ions (Al_xV₂O₅·nH₂O) using soft chemistry [15,23]. Thus, chemical exchange can overlap with the electrochemical process that is driven by the flow of electrons through the external electrical circuit during the discharge/charge. There is a competition between chemical exchange and electrochemical insertion/deinsertion of aluminium ions and water molecules (or H₃O⁺). Most probably, some protons are also intercalated during the discharge process. Then, aluminium ions are also chemically inserted into V₂O₅ by cationic exchange with protons in competition to the electrochemical deinsertion during the charge process, though the ion exchange process is slower than the faradic reaction. It involves that the aluminium content in Al_xV₂O₅, determined from charge passed through the cell, would be overestimated. Therefore, the apparent discharge capacity could be slightly lower than the charge capacity, particularly at low kinetics (60 mA g⁻¹ in Fig. 5B).

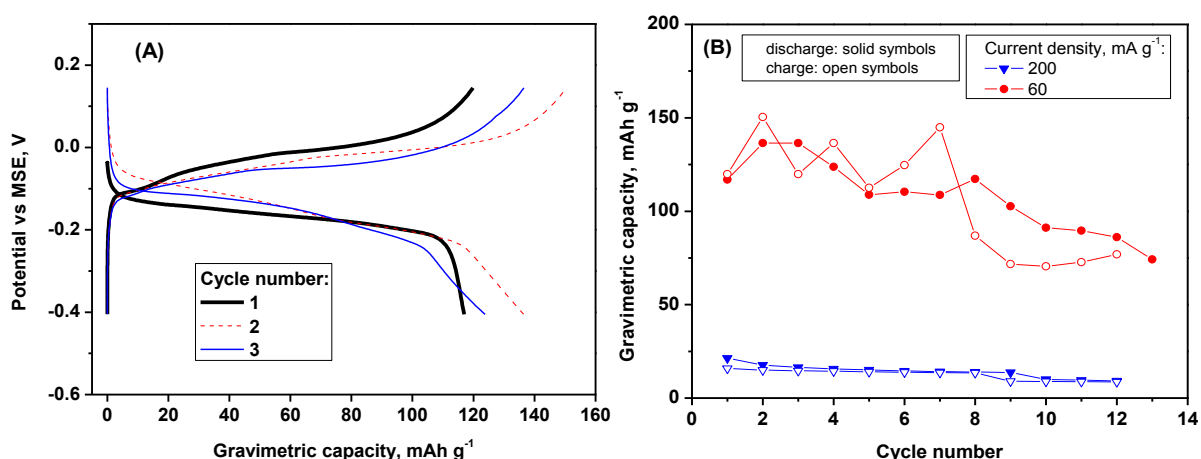


Fig. 5. Galvanostatic experiments. (A) A typical voltage-capacity curve of V_2O_5 in aluminium aqueous cell at 60 mA g^{-1} of current density. (B) Specific capacity as a function of cycle number at different current densities.

For the sake of comparison, the electrochemical intercalation of lithium into V_2O_5 was explored. The results agree well with the literature and hence the capacity fade upon cycling in Figs. 5 and 6 is due to the dissolution of vanadium compounds [24-26]. A discharge capacity around $130\text{-}250 \text{ mA h g}^{-1}$ and a charge capacity of only ca. 70 mA h g^{-1} is observed in (Fig. 6). The operating voltage is lower in the lithium electrolyte than in aluminium one. In contrast to aluminium, lithium is intercalated in non-hydrated form [20], only a fraction of lithium can be deintercalated and the charge capacity is substantially smaller than the discharge capacity (Fig. 6). Some amount of lithium is irreversibly trapped in the framework of V_2O_5 , and the charge of Li^+ helps to shield the repulsions between the oxygens in the framework of V_2O_5 . It is worth to note that, in comparison with other ions, such as Li^+ and Na^+ , Al^{3+} is a smaller ion with a higher hydration number. It is expected that the chemical exchange between the solution and intercalated vanadium oxide is enhanced for aluminium, and that water (or protonated water) helps to shield the repulsions between the oxygens in the framework of $Al_xV_2O_5$.

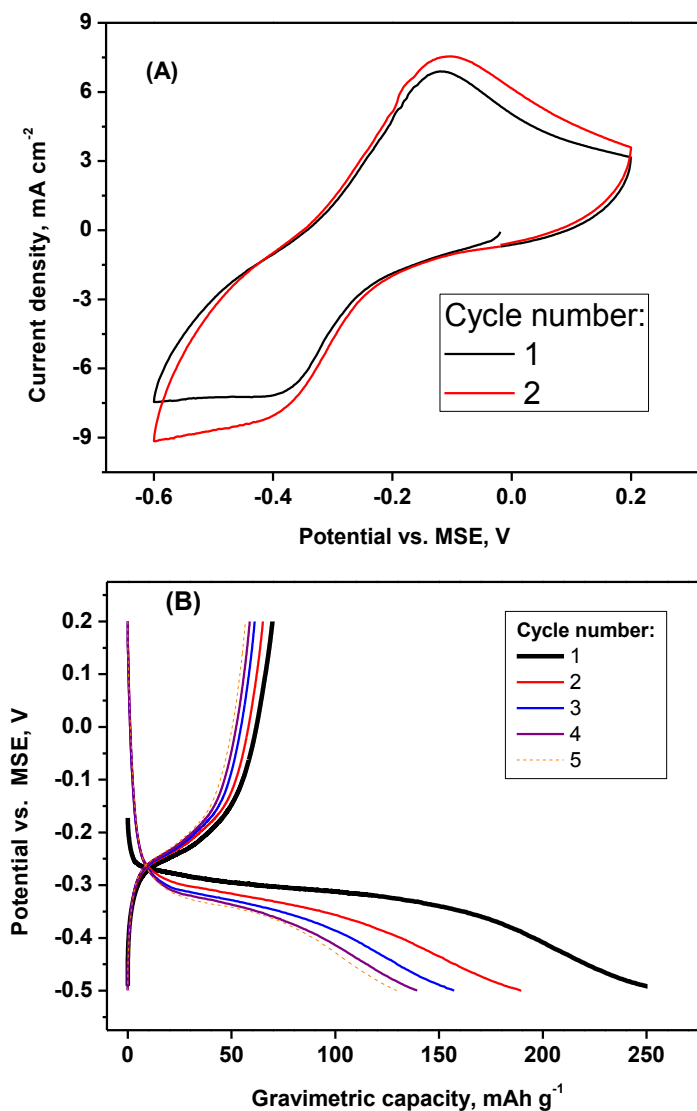


Fig.6. Electrochemistry of V_2O_5 in lithium cell: (A) CV at 10 mV s^{-1} of scan rate and (B) galvanostatic cycling at 20 mA g^{-1} of current density. Electrolyte: 1 M LiCl in water.

4.5.3.4 Ex-situ XRD

According to the ex-situ XRD patterns (Fig. 7) of the electrodes recorded at different states of discharge, the structure of V_2O_5 is initially preserved during the beginning of the discharge process, the position of the Bragg peaks remain nearly unchanged and become more broadened. New Bragg peaks are not observed. It is worth to note that the interlayer spacing in V_2O_5 is much larger than the ionic size of Al^{3+} . With further discharge depth, the oxide irreversibly becomes XRD-amorphous at the nominal composition $Al_{0.5}V_2O_5$ (equivalent to 221 mAh g^{-1}). The amorphous state of

Al-intercalated vanadium oxide is strongly indicative of the hydration of the interlayer spacing [10]. In other words, aluminium and water molecules are co-intercalated and the resulting hydrated vanadium oxide $(Al^{3+})_{x/3}[(V^{4+})_x,(V^{5+})_{2-x}]O_5 \cdot nH_2O$ is XRD-amorphous. Another possible explanation would be that the chemical exchange between intercalated aluminium and protons from the solution in the form of H_3O^+ provokes the amorphization of the vanadium oxide electrode, but it could not explain alone the high capacity of the charge process. In contrast to the insertion of hydrated aluminium, according to the literature the insertions of lithium and protons preserve the crystalline character of V_2O_5 [20].

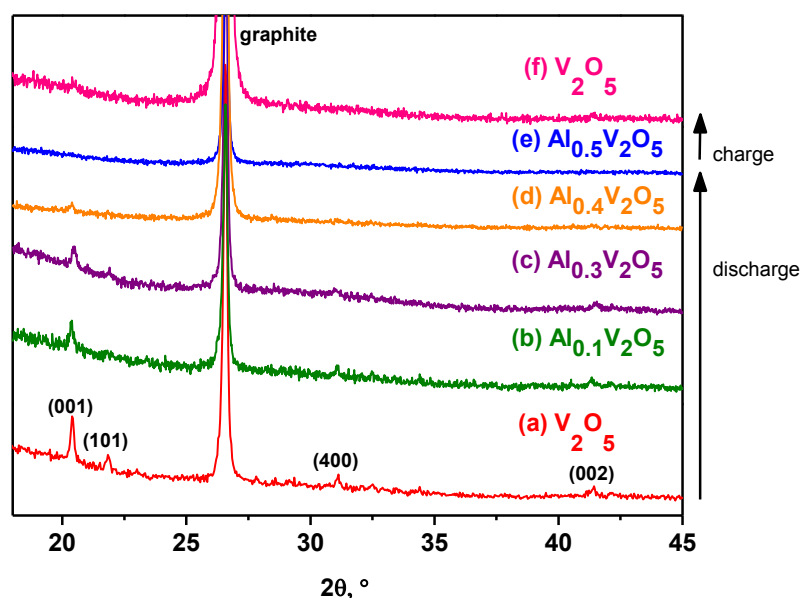


Fig.7. Ex-situ XRD patterns of (a) raw V_2O_5 and electrodes recuperated from aluminium cells at selected states of discharge (b-e) and charge (f) at slow current density. The (002) reflection of hexagonal graphite (substrate of the electrode active material) is also observed at ca. 26.4° .

4.5.3.5 Chemical and electrochemical intercalation

The redox potential of V^{5+} is quite high ($E^\circ(VO_2^+/VO^{2+}) = +1.0$ V vs. SHE), but this potential in principle would not be enough to decompose water ($E^\circ(O_2/H_2O) = +1.229$ V vs. SHE). In contrast to crystalline V_2O_5 , it is known that amorphous or poorly crystallized xero- V_2O_5 immersed into an aqueous solution containing certain cations can intercalate these cations by easy exchange with the H_3O^+ ion [15]. We tested the stability of crystalline V_2O_5 in aqueous solution containing Al^{3+} ions. After

immersion of V_2O_5 in 1 M $AlCl_3$ (aq.) solution during two hours, a slight decrease of the pH value (ca. 0.15 units) and formation of tiny bubbles (more probably oxygen) were observed. In addition, the crystalline structure of vanadium oxide is preserved (Fig. S1 and S2) and no relevant change of the unit cell parameters was observed. The solution remained colourless. These results suggest that, although V_2O_5 is not soluble, it may spontaneously suffers a very limited intercalation, proton/aluminium exchange and redox reaction in which vanadium oxide would be slightly reduced and O_2 is released:



The positive charge of the chemically intercalated aluminium ion balances the negative charge left in $V_2O_5^{3x-}$ by the electrons released by oxygen.

In the electrochemical cell, the loss of crystallinity that is induced by the electrochemical intercalation of aluminium (reaction (1)) can enhance the extent of the chemical exchange in XRD-amorphous $(Al^{3+})_{x/3}[(V^{4+})_x, (V^{5+})_{2-x}]O_5 \cdot nH_2O$ (reaction (2)). The reaction (2) also can explain the apparently higher charge capacity observed in some cycles of the galvanostatic experiments. In the same sense, the reduction of V^{5+} and formation of O_2 was reported by Znaidi et al. [14]. In addition, Schöllhorn et al. reported the proton-exchange reaction in vanadium bronzes [22].

4.5.3.6 X-ray photoelectron spectroscopy

To further understand the mechanism of aluminium intercalation into V_2O_5 , the X-ray photoelectron spectra of the samples are shown in Fig. 8. For the raw V_2O_5 sample the main XP lines of O 1s (Fig. 8Aa) and V $2p_{3/2}$ (Fig. 8Ba) are placed at the binding energies lines of 530.5 (O^{2-}) and 517.5 eV (V^{5+}), respectively. These values agree very well with the reported data for V_2O_5 [27]. A minor component at 516.1 eV is ascribed to traces of V^{4+} . These V^{4+} ions can increase the electronic conductivity. There are two additional O 1s components with very low intensity and placed at ca. 532 and 534 eV that are ascribed to more covalently bonded oxygen in defects and contamination on the surface of V_2O_5 [27,28].

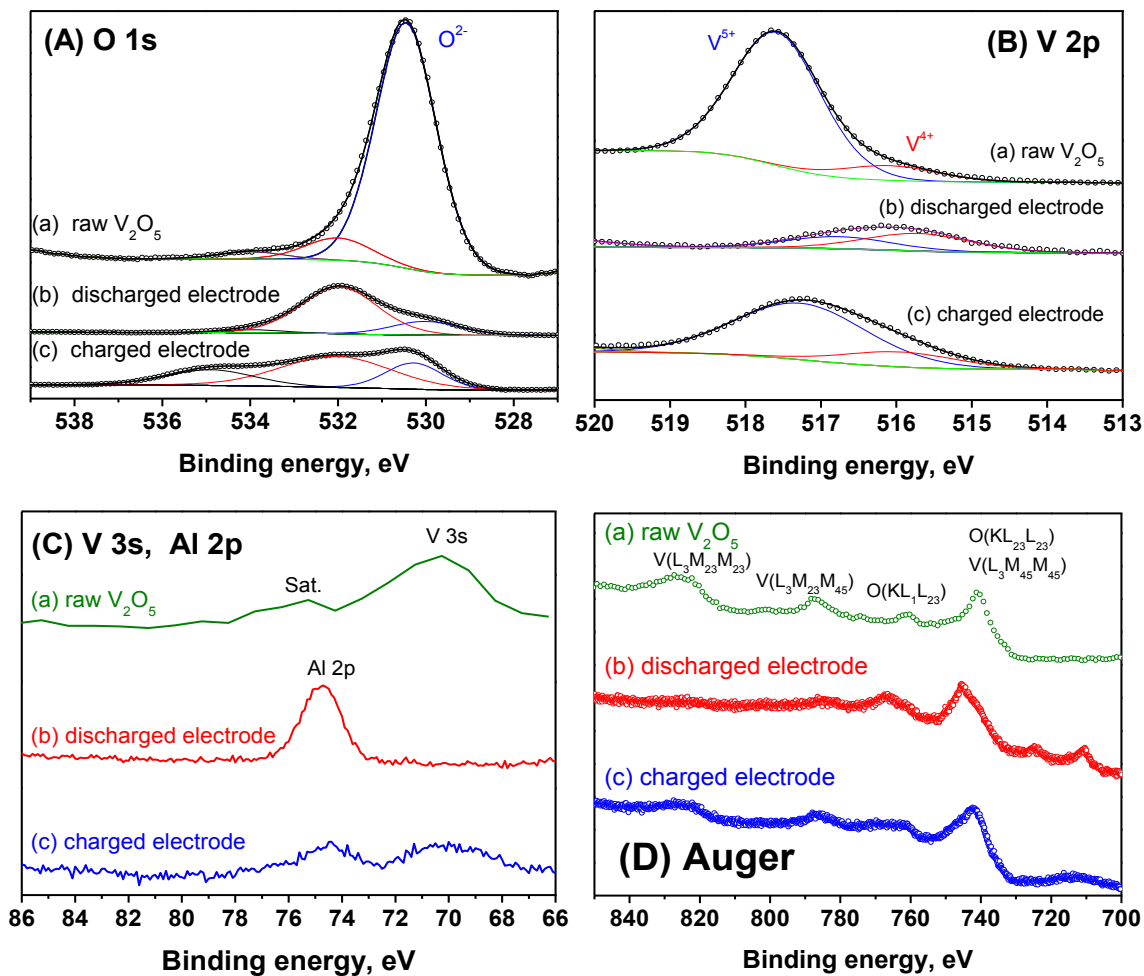


Fig.8. X-ray photoelectron spectra of (A) O 1s core level and (B) V 2p_{3/2}, (C) Al 2p and V 3s core levels for (a) as prepared V_2O_5 , (b) discharged electrode (end of the first discharge at -0.3 V vs. MSE) and (c) electrode after the first discharge-charge cycle (+0.15 V vs. MSE).

After reaction with aluminium, the V 2p line is shifted to lower binding energy as due to the reduction of V^{5+} to V^{4+} (Fig. 8Bb), and the O 1s line is shifted to higher energy (Fig. 8Ab). The charge process leads to the re-oxidation of vanadium (Fig. 8Bb). The broadening of XPS in the region of O 1s core peak in the charged electrode (Fig. 8Ac) is in good agreement with a more disordered structure.

In the discharged electrode, the Al 2p line is observed at 74.6 eV (Fig. 8C). The V 3s core hole lines have a binding energy of ca. 70.3 eV and a small satellite at ca. 4-8 eV higher binding energy (Fig. 8C). It has been suggested that the satellite structure of V 3s is caused by core hole screening [29]. The satellite observed in raw V_2O_5 (Fig.

8Ca) is in good agreement with the presence of traces of V^{4+} . According to the literature, in vanadium oxides there is exchange coupling of the 3s electrons and the valence shell (3d electrons), but this exchange does not directly reflect the 3d occupancy [29]. In the discharged electrode (Fig. 8Cb), more probably the V 3s signal is too small to be observed.

The Auger transitions are significant to reveal the reversible change of the oxidation state of vanadium (Fig. 8D). The $V(L_3M_{4,5}M_{4,5})$ transition is mixed with the $O(KL_{2,3}L_{2,3})$ transition, making this Auger peak more intense [27]. The $V(L_3M_{4,5}M_{4,5})$ transition is shifted to higher energies for the discharged electrode that contains V^{4+} ($3d^1$). The peak of the $V(L_3M_{2,3}M_{4,5})$ Auger transition is due not only to the vanadium transition, but also to interatomic transitions between vanadium and oxygen, and such peak has lower intensity for the discharged electrode (Fig. 8Db) as expected according to the literature [27]. In V_2O_5 (V^{5+} , $3d^0$), the greater covalency leads to a higher density of electrons (coming from oxide ion) around vanadium ions as compared with $Al_xV_2O_5$.

From the quantitative analysis of the XP spectra, the chemical compositions of the discharged and charged electrodes would be $Al_5V_2O_5 \cdot 5.6H_2O$ and $Al_{0.52}V_2O_5$, respectively. These formulas must be regarded with a lot of caution because XPS is a surface technique and the electrode surface can be contaminated with traces of electrolyte, but the results strongly suggest that hydrated aluminium is reversibly intercalated into vanadium pentoxide in good agreement with reaction (1).

4.5.3.7 Impedance spectra

The electrochemical impedance spectra (Fig. 9) are in good agreement with the diffusion of aluminium ions into the framework of V_2O_5 . The spectrum recorded on the freshly assembled cell, at -0.05 V of open circuit voltage (OCV), shows a linear behaviour with an angle of ca. 45° . It is characteristic of a system under diffusion control since the kinetics of the charge transfer at the electrode-electrolyte interface is faster than the diffusion of the Al^{3+} ions in V_2O_5 . After the first discharge at -0.2 V, the resulting spectrum still shows a linear behaviour. After 10 cycles, a depressed semicircle is observed at high-medium frequencies, which is ascribed to charge transfer resistance and double-layer capacitance. The detailed view of the high-medium frequencies region is shown in Fig. 9B. The linear part at medium-low frequencies is

ascribed to Warburg impedance associated with diffusion of aluminium in V_2O_5 . The small size of the semicircle shows that the charge transfer resistance is low, and according to the fitting using the equivalent circuit shown as an inset in Fig. 9B, the resistance values is $R_2=18\ \Omega$.

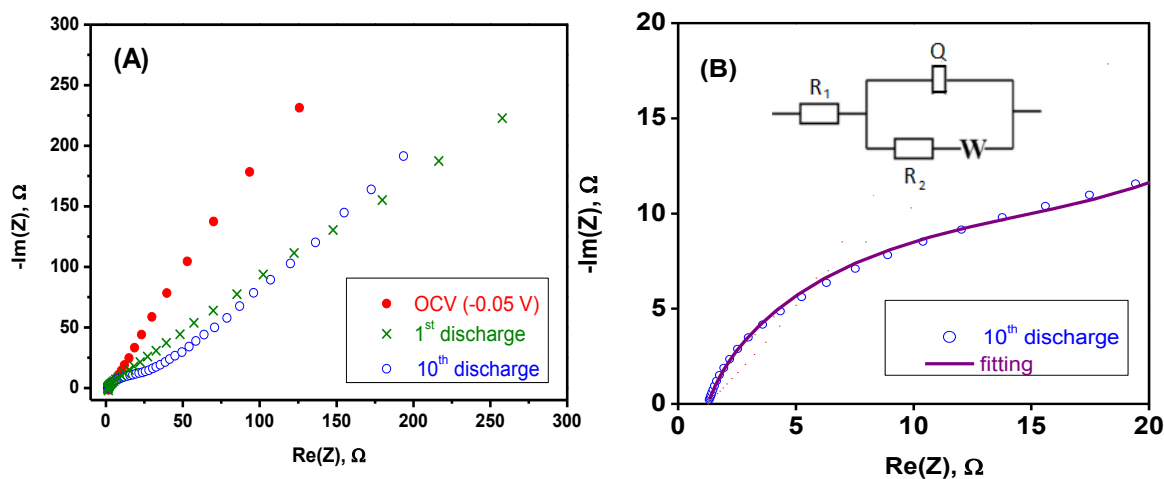


Fig.9. (A) Impedance spectra (Nyquist plots) of V_2O_5 electrode measured at OCV and at the end of the first discharge (-0.3 V vs. MSE) and after ten cycles. (B) A detailed view of the high-medium frequencies region after ten cycles and equivalent circuit. W=Warburg impedance. R=resistance. Q=constant phase element.

4.5.4 Conclusions

Vanadium pentoxide has been used as an active electrode material in rechargeable aluminium battery based on aqueous electrolyte. These batteries can be environmentally friendly and more sustainable in comparison with lithium batteries. The intercalation/deintercalation process of aluminium is complex. During the discharge process, vanadium is reduced and the resulting product becomes XRD-amorphous at $Al_{0.5}V_2O_5$, in good agreement with bulk intercalation. As due to the high charge-to-size ratio of Al^{3+} and the chemical exchange properties, the electrochemical (faradic) intercalation of aluminium into V_2O_5 is parallel to water intercalation, and some protons also can be intercalated. During the charge (oxidation) process the chemical intercalation and exchange of protons and aluminium can compete against the faradic deintercalation process. These features should be taken into account for the future

development of batteries based on intercalation of multivalent ions. Perhaps, further optimization of the electrolyte composition, the selection of another binder and the formation of composite materials may improve the coulombic efficiency and cycling stability.

Acknowledgements

The authors would like to greatly acknowledge MINECO, FEDER (MAT2014–56470-R). The instruments for XPS, SEM and TEM were provided by SCAI (UCO Central Service for Research Support). We also thank Institute of Fine Chemistry and Nanochemistry and European Research Institute ERI-ALISTORE.

4.5.5 References

1. M. C. Lin, M. Gong, B. Lu, Y. Wu, D. Y. Wang, M. Guan, M. Angel, C. Chen, J. Yang, B. J. Hwang, H. Dai, *Nature* 520 (2015) 324; V. Rani, V. Kanakaiah, T. Dadmal, M. S. Rao, S. Bhavanarushi, *J. Electrochem. Soc.* 160 (2013) A1781; R. Mori, *RSC Adv.* 3 (2013) 11547; R. Mori, *RSC Adv.* 4 (2014) 1982.
2. S. Liu, J. J. Hu, N. F. Yan, G. L. Pan, G. R. Li and X. P. Gao, *Energy Environ. Sci.* 5 (2012) 9743.
3. Y. J. He, J. F. Peng, W. Chu, Y. Z. Li, D. G. Tong, *J. Mater. Chem. A* 2 (2014) 1721.
4. S. Sang, Y. Liu, W. Zhong, K. Liu, H. Liu, Q. Wu, *Electrochim. Acta* 187 (2016) 92.
5. H. Wang, Y. Bai, S. Chen, X. Luo, C. Wu, F. Wu, J. Lu, K. Amine, *ACS Appl. Mater. Interfaces* 7 (2015) 80.
6. N. Jayaprakash, S. K. Das and L. A. Archer, *Chem. Comm.* 47 (2011) 12610.

7. W. Wang, B. Jiang, W. Xiong, H. Sun, Z. Lin, L. Hu, J. Tu, J. Hou, H. Zhu, S. Jiao, *Sci. Rep.* 3 (2013) 3383.
8. D. B. Le, S. Passerini, F. Coustier, J. Guo, T. Soderstrom, B. B. Owens, W. H. Smyrl, *Chem. Mater.* 10 (1998) 682.
9. R. Enjalbert, J. Galy, *Acta Cryst.* C42 (1986) 1467.
10. J. Livage, *Chem. Mater.* 3 (1991) 578; H. H. Kristoffersen, H. Metiu, J. *Phys. Chem. C* 120 (2016) 3986.
11. J. Wang, C. J. Curtis, D. L. Schulz, J. G. Zhang, *J. Electrochem. Soc.* 151 (2004) A1.
12. Y. Wang, H. Shang, T. Chou, G. Cao, *J. Phys. Chem. B* 109 (2005) 11361.
13. M. Vujković, I. Pašti, I. Stojković Simatovića, B. Šljukić, M. Milenković, S. Mentus, *Solid State Ion.* 176 (2015) 130.
14. L. Znaidi, N. Baffier, M. Huber, *Mat. Res. Bull.* 24 (1989) 1501.
15. N. Baffier, L. Znaidi, M. Huber, *Mat. Res. Bull.* 25 (1990) 705.
16. N. Jayaprakash, S. K. Das, L. A. Archer, *Chem. Comm.* 47 (2011) 12610.
17. L. D. Reed, E. Menke, *J. Electrochem. Soc.* 160 (2013) A915.
18. M. Chiku, H. Takeda, S. Matsumura, E. Higuchi, H. Inoue, *ACS Appl. Mater. Interfaces* 7 (2015) 24385.
19. P. Aldebert, N. Baffier, N. Gharbi, J. Livage, *Mat. Res. Bull.* 16 (1981) 669.
20. P. G. Dickens, A. M. Chippindale, S. J. Hibble, *Solid State Ion.* 34 (1989) 79.
21. J. C. Badot, N. Baffier, *J. Mater. Chem.* 2 (1992) 1167.
22. R. Schöllhorn, F. Klein-Reesink, R. Reimold, J. C. S. *Chem. Comm.* 9 (1979) 398.

23. K. Zhu, H. Qiu, Y. Zhang, D. Zhang, G. Chen, Y. Wei, *ChemSusChem* 8 (2015) 1017.
24. I. Stojkovic, N. Cvjeticanin, I. Pašti, M. Mitric, S. Mentus, *Electrochem. Commun.* 11 (2009) 1512.
25. M. Vujković, I. Pašti, I. Stojković Simatović, B. Šljukić, M. Milenković, S. Mentus, *Electrochim. Acta* 176 (2015) 130.
26. H. Wang, Y. Zeng, K. Huang, S. Liu, L. Chen, *Electrochim. Acta* 52 (2007) 5102.
27. Q. H. Wu, A. Thißen and W. Jaegermann, *Appl. Surf. Sci.* 252 (2005) 1801; G. Silversmit, D. Depla, H. Poelman, G. B. Marin, R. De Gryse, *Surf. Sci.* 600 (2006) 3512; A. Benayad, H. Martinez, A. Gies, B. Pecquenard, A. Levasseur, D. Gonbeau, *J. Electron. Spectrosc. Relat. Phenom.* 150 (2006) 1; A. Meisel, K. H. Hallmeier, R. Szargan, J. Muller, W. Schneider, *Phys. Scr.* 41 (1990) 513; J. Kasperkiewicz, J. A. Kovacich, D. Lichtman, *J. Electron. Spectrosc. Relat. Phenom.* 32 (1983) 123; P. Mezentzeff, Y. Lifshitz, J. W. Rabalais, *Nucl. Instrum. Methods Phys. Res. Sect. B* 44 (1990) 296.
28. A. Thissen, D. Enslin, F. J. Fernández-Madrigal, W. Jaegermann, R. Alcántara, P. Lavela, J. L. Tirado, *Chem. Mater.* 17 (2005) 5202.
29. P. Krüger, M. Taguchi, J. C. Parlebas, A. Kotani, *Phys. Rev. B* 55 (1997) 16466; R Zimmermann, R Claessen, F Reinert, P Steiner, S Hüfner, *J. Phys. Condens. Matter.* 10 (1998) 5697.

4.5.6 Supplementary information

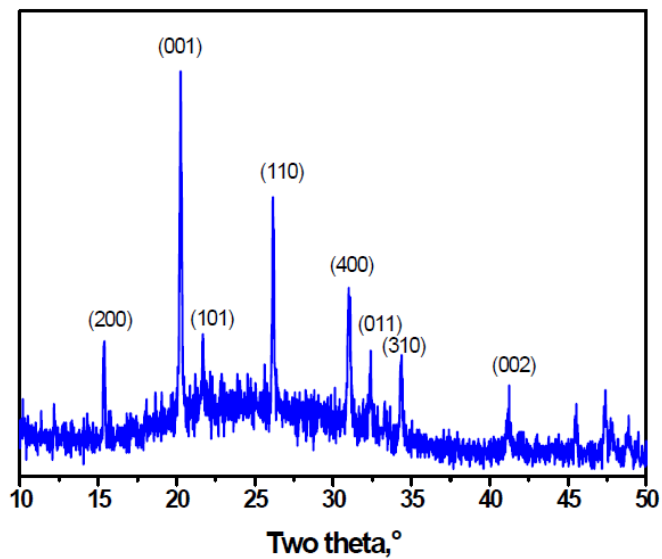


Fig.S1. XRD patterns of the vanadium pentoxide sample heated to 600°C.

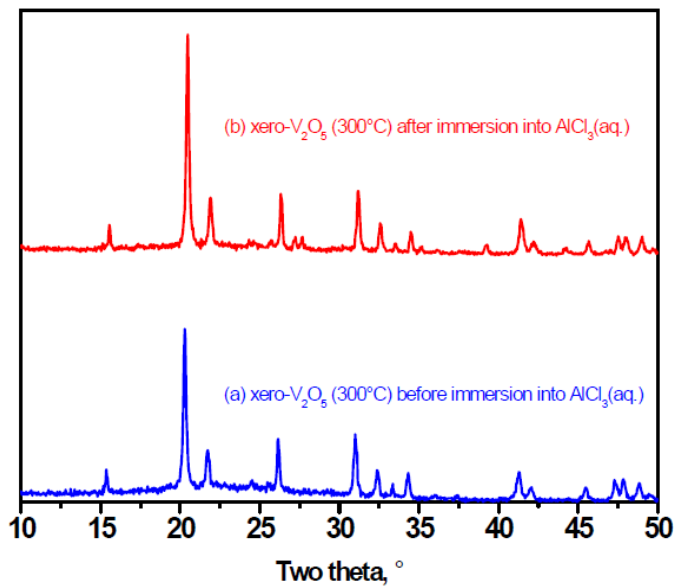


Fig.S2. XRD patterns of V₂O₅ before (a) and after (b) its immersion into 1 M AlCl₃ aqueous solution during two hours. The positions of the Bragg peaks remain unchanged after the treatment.

4.6 NASICON-type $\text{Na}_3\text{V}_2(\text{PO}_4)_3$ as a new positive electrode material for rechargeable aluminium battery

Francisco Nacimiento, Marta Cabello, Ricardo Alcántara, Pedro Lavela, José L. Tirado.

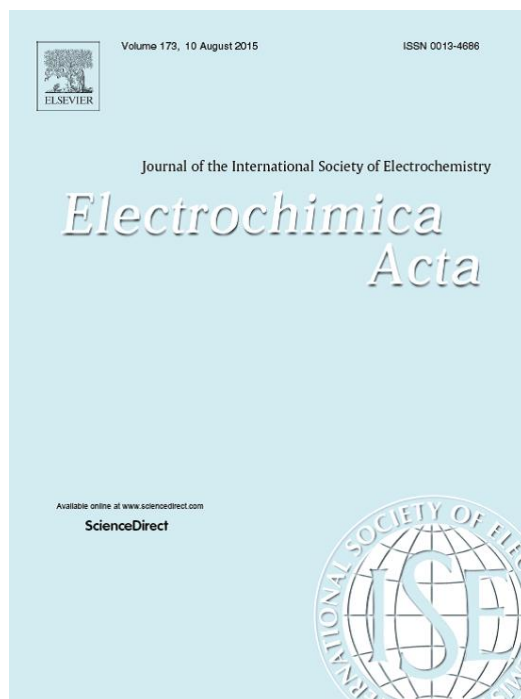
Laboratorio de Química Inorgánica. Universidad de Córdoba. Edificio C3, Campus de Rabanales. Spain

Abstract

Although rechargeable aluminium-ion batteries could be very promising, there are only a few materials described in the literature that can insert aluminium. NASICON-type $\text{Na}_3\text{V}_2(\text{PO}_4)_3$ (NVP) is here investigated as a new positive electrode, using aluminium chloride dissolved in O_2 -free water as electrolyte solution. The reversible capacity is around 60-100 mAh g^{-1} , depending on the cycling conditions. The electrochemical, analytical, NMR, XPS and XRD results all together corroborate that sodium is deinserted during first charge and then aluminium is inserted during the discharge. Both bulk insertion and surface capacitance can contribute to the specific capacity. This is the first report about true insertion of a trivalent cation into a NASICON-type structure. In addition, this material is also electrochemically active vs. Al metal in non-aqueous cell, using ionic liquid as electrolyte solution, with a reversible capacity about 60-70 mAh g^{-1} at ca. 1.25 V vs. Al. However, in the case of using ionic liquid, sodium (and not aluminium) is reversibly (de)inserted [23]. The results demonstrate that NVP is promising as electrode for rechargeable aluminium batteries, and that the electrolyte solution strongly influence on the electrochemical reaction.

Keywords

Aluminium batteries; NASICON; aqueous batteries; ionic liquid



Electrochimica Acta 260 (2018) 798-804

4.6.1 Introduction

Lithium rechargeable battery has been commercialized since the 1990s and is one of the most successful technologies for energy storage, though a post-lithium era is being envisaged. Thus, multivalent metals as aluminium can deliver higher volumetric capacity than Li and are advantageous for large-scale energy storage [1-7]. The high natural abundance, low cost and high volumetric capacity (8040 mAh cm^{-3}) are the main advantages of aluminium. However, to find suitable electrode materials and electrolyte solutions is a great challenge, and the rechargeable aluminium battery is still in its infancy. The main electrode materials proposed in the literature for rechargeable aluminium batteries are vanadium oxides [3,8-11] titanium dioxide [12] sulphides [13], organic polymers [14], Prussian blue analogues [15] and graphite [16-18].

The NASICON-type structure is very useful for providing a stable and open framework that can serve as a host for the insertion of cations. Thus, $A_3V_2(PO_4)_3$ (with $A=Li, Na$) have been extensively tested as electrode materials for diverse types of rechargeable batteries, particularly lithium, sodium and zinc batteries [19-22]. Very recently, a hybrid Na-Al cell using an ionic liquid containing $NaAlCl_4$ as electrolyte was reported, in which sodium (not aluminium) was reversibly (de)inserted in $Na_3V_2(PO_4)_3$ (NVP) [23]. Nevertheless, the choice of the electrolyte solution can have a strong influence on the (de)insertion process and electrochemical behaviour.

Aqueous ion batteries can be safe, low-cost and environment-friendly [24]. In addition, aqueous electrolytes can exhibit high ionic conductivity and, consequently, deliver high-charge/discharge rates. Nevertheless, the stability of the electrode active material in water limits their development. Besides, aqueous cells can serve as a proof of ion insertion in the meantime that other non-aqueous electrolyte compatible with Al are developed [12]. Sodium vanadium phosphates have been widely investigated as positive electrode in aqueous sodium-ion batteries [25-29], although it has been suggested that NVP degrades upon cycling in aqueous batteries. In comparison with lithium and potassium, it seems that the insertion of sodium in NVP is easier [25]. The use of NVP/C nanocomposites

improves the cycling stability because the carbon phase enhances the electrical conductivity and slows down the dissolution of NVP [26]. Zhou et al. suggested that, on the contrary to Li-Mn-O spinels, NVP cannot support physical adsorption of water through its channels and water cannot interfere with sodium insertion/deintercalation during electrochemical cycling [26]. An aqueous rechargeable battery based on NVP vs. Zn has also been reported [27,30-33].

In this work, the electrochemical insertion of aluminium ions into NVP from aqueous solution is studied, and the mechanism is explored by using XRD, SEM-EDS, XPS and NMR. In addition, the electrochemical behaviour in non aqueous batteries is also studied using ionic liquid as electrolyte solution.

4.6.2 Experimental

NVP containing carbon to improve the conductivity was prepared by using a wet ball-milling method, as described elsewhere [34]. For this purpose, firstly ammonium metavanadate (Panreac, 98 %; 1.2 g), sodium dihydrogen phosphate (Aldrich, 98–102 %, 2.1 g), and citric acid (Aldrich, 99 %; 2.9 g) at Na:V:P=2:3:3 molar ratios were added to an agate vessel. Then, 10 mL of ethanol were added to the mixture and the resulting slurry was ball-milled at 300 rpm for 24 h in air. After drying the slurry in an oven at 70°C overnight, a solid precursor was obtained. The final product was prepared by annealing the precursor at 800 °C for 8 h in an argon atmosphere. The presence of the carbon residue (7.3 % wt.) was determined precisely with an Elemental CHNS Eurovector EA 3000 analyzer.

The crystal structure was studied by X-ray diffraction (XRD) using a Bruker D8 instrument with Cu K α radiation. Rietveld refinement was performed with the TOPAS 4.2 program. The crystal structures were drawn with the VESTA 3.4.0 program [35].

FE-SEM images were obtained using a JSM-7800F Prime instrument. The chemical composition of the electrodes was analyzed by Electron Probe Microanalysis (EPMA) with Energy Dispersive Spectrometer (EDS) detector coupled to FE-SEM.

²⁷Al MAS NMR spectra were acquired at room temperature in a Bruker Avance III HD 400 WB instrument at 12 kHz of spin rate. The chemical shifts were referenced to 1 M aluminium chloride solution (0 ppm). The chemical state of the surface was studied by X-ray Photoelectron Spectroscopy (XPS) in a SPECS Phobios 150 MCD provided with Mg $\kappa\alpha$ source.

All the electrochemical tests were performed in three-electrode cell and using a VMP Biologic instrument. For aqueous batteries, flooded beaker cells were used. The electrolyte solution was 0.1 M AlCl₃ in deionized water, the reference electrode was Ag/AgCl and the counterelectrode was Pt. For control experiments, aqueous solutions of HCl and 0.1 M NaCl/HCl at the same pH value (3.0). The working electrode was prepared by mixing the active material (80 %) with carbon black (10 %) and PVDF (10 %) as binder. The aqueous solution was outgassed to remove dissolved oxygen by flowing Ar before carrying out, and during, the electrochemical experiment.

For non-aqueous cell, chloroaluminate ionic liquid was used as electrolyte. This ionic liquid was prepared in the dry box under Ar atmosphere by dissolving anhydrous AlCl₃ (99.999% purity, Sigma Aldrich) in 1-ethyl-3-methylimidazolium chloride (EMIC) in molar ratio AlCl₃: EMIC=1.1:1.0. The Swagelok-type electrochemical cells comprise three glassy carbon rods (Goodfellow) as current-collectors, a disc of high-purity Al (Aldrich) as reference electrode, another piece of Al as counterelectrode and a working electrode. To prepare the working electrode, the active material (NVP) was mixed with PFTE (binder) and carbon black, and the mixture was pasted on a Pt disc. The use of metals and steel corrodible in ionic liquid was avoided. Whatman glass fiber filter papers were used as separators. The cells were assembled in an M-Braun glove-box filled with Ar.

4.6.3 Results and discussion

4.6.3.1 Electrochemistry in aqueous cell

The cyclic voltammograms (CV) performed at 1 mV/s are displayed in Fig. 1a. The cut-off voltage was imposed to study the main redox reaction, to achieve approximately the same charge/discharge capacity in all the experiments and to avoid

side-reactions, and so it was not fixed. The operating voltage is within the stability window of water. A redox peak is observed at ca. +0.6 for the anodic scan and at ca. +0.2 V for the cathodic scan, although the exact position changes with the cycle number and other experimental conditions. This peak is ascribed to the V^{3+}/V^{4+} redox couple and reversible insertion. In contrast with the observed faradic peak, a pure capacitor behaviour would exhibit intensity-voltage curves with typical rectangular shape, as was found for example in the case of V_2O_5 in KCl aqueous solution [36]. Song et al. proposed that the surface capacitance plays a key role for NVP in aqueous sodium-ion batteries and that the electrochemical reaction is diffusion-controlled [25]. On the other hand, larger size ions as K^+ are preferentially adsorbed on the surface of NVP, rather than inserted into the lattice. Figure 1b shows the CV profiles using 0.1 M NaCl/HCl or HCl as electrolyte solutions at pH 3.0. By comparison, it can be concluded that the CV in $AlCl_3$ solution cannot be ascribed exclusively to sodium and/or protons (de)insertion. In fact, the faradic electrochemical behaviour is better in $AlCl_3$ solution. We can conclude that aluminium is playing a main role in the electrochemistry of NVP.

The separation between the anodic and cathodic peaks is larger at higher rates and the peak current becomes smaller when the scan rate decreases (Fig. 1c). The dependence of the CV with the scan rates (Fig. 1c,d) can be understood on the basis of diffusion and/or capacitive processes. According to the Randles-Sevcik equation, a linear relationship between the intensity of the peak current and the square root of the scan rate is followed when the redox reaction is controlled by diffusion [25,37]. In contrast, a capacitive behaviour normally follows a linear dependence between the current and the scan rate. Thus, in general, the relationship between the peak current (i) and the scan rate (v) is given by the power law [31,37]:

$$i = av^b \quad (1)$$

where a and b are adjustable parameters. The value of b can be obtained from the slope of the linear fitting of the experimental results on a log-log scale (Figure 1d), and one can expect the current to be dominated by capacitive behaviour at $b=1.0$, while the current would be dominated by diffusion at $b=0.5$. This procedure must be taken with caution because capacitive currents can arise from the unavoidable reorganization of the Helmholtz layer at the electrode surface when the potential is swept linearly [37]. Thus, the result is valid within the range of scan rate that is taken (between 5 and 0.3 $mV s^{-1}$ in

Figure 1d). The value calculated from the slope of the plot obtained from the oxidation process of the first sweep is $b=0.67$, and in the reduction process of the first sweep $b=0.70$. These b -values are intermediate between a purely capacitive behaviour and a diffusion-controlled process. This result implies that at high rate the particle surface would be used for charge storage rather than insertion/deinsertion into the bulk. At high rate, the slow diffusion of the ions limits the insertion/deinsertion process to the outer surface of the NVP particles. Li et al found a value of $b=0.58$ for zinc in NVP, indicating a diffusion-dominated process (not pseudocapacitive) [31]. These results compared to the literature suggest that aluminium diffusion in NVP is slower than that of zinc [32]. It is worth to note here that He et al. found that both bulk insertion (slower process) and surface storage (faster process) contribute to aluminium storage in black anatase TiO_2 , although the b -value was not reported in that case [12]. In fact, the coexistence of the two mechanisms (bulk insertion and surface capacitance) in the same electrode material can be beneficial for its electrochemical performance.

In the galvanostatic experiment (Fig. 2) the results agree well with the CV. The profile and capacity of the first charge are different compared with the second and successive charges, in good agreement with irreversible sodium deinsertion. The reversible capacity values in aluminium-ion aqueous batteries are around 60-100 mAh g^{-1} , depending on the cycling conditions. These capacity values are comparable with the results reported for NVP in non-aqueous sodium-ion batteries [20], and better than the results reported for aqueous sodium-ion batteries (typically around 50-80 mAh g^{-1}) [26,29]. The capacity fade upon further cycling, particularly at slow kinetics, can be due to partial cathode dissolution in the acidic electrolyte as was found in other aqueous batteries, or to structure degradation due to the electrochemical insertion. Perhaps, in future works the resistance of NVP against corrosion could be improved for example by using additives.

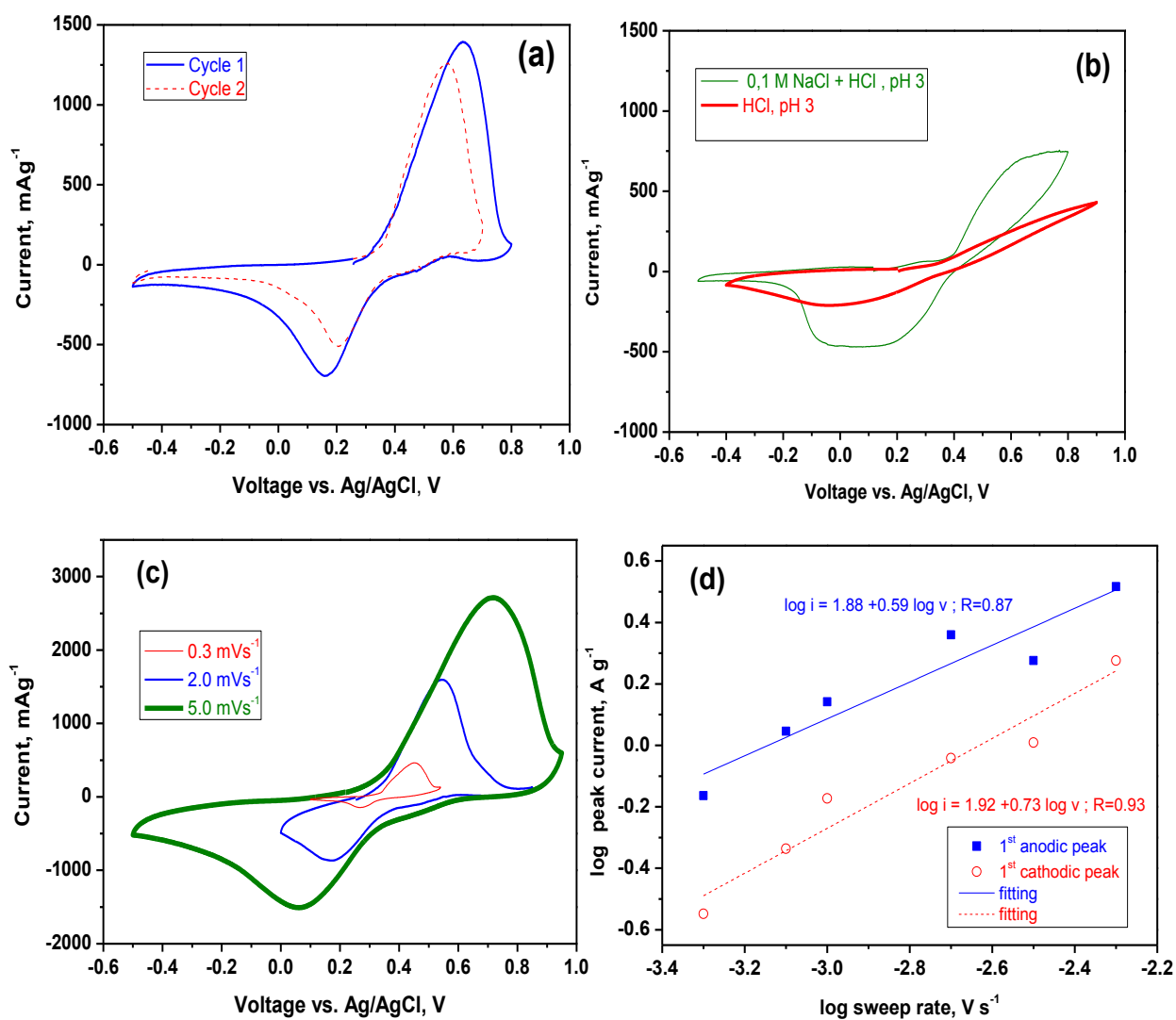


Fig. 1. Selected CV results for NVP. (a) First and second scan in $\text{AlCl}_3(\text{aq})$ at 1.0 mV s^{-1} . (b) First scan in NaCl/HCl and HCl solutions at 1 mV s^{-1} (c) Second scan at several scan rates in $\text{AlCl}_3(\text{aq})$. (d) Peak intensity as a function of sweep rate in $\text{AlCl}_3(\text{aq})$.

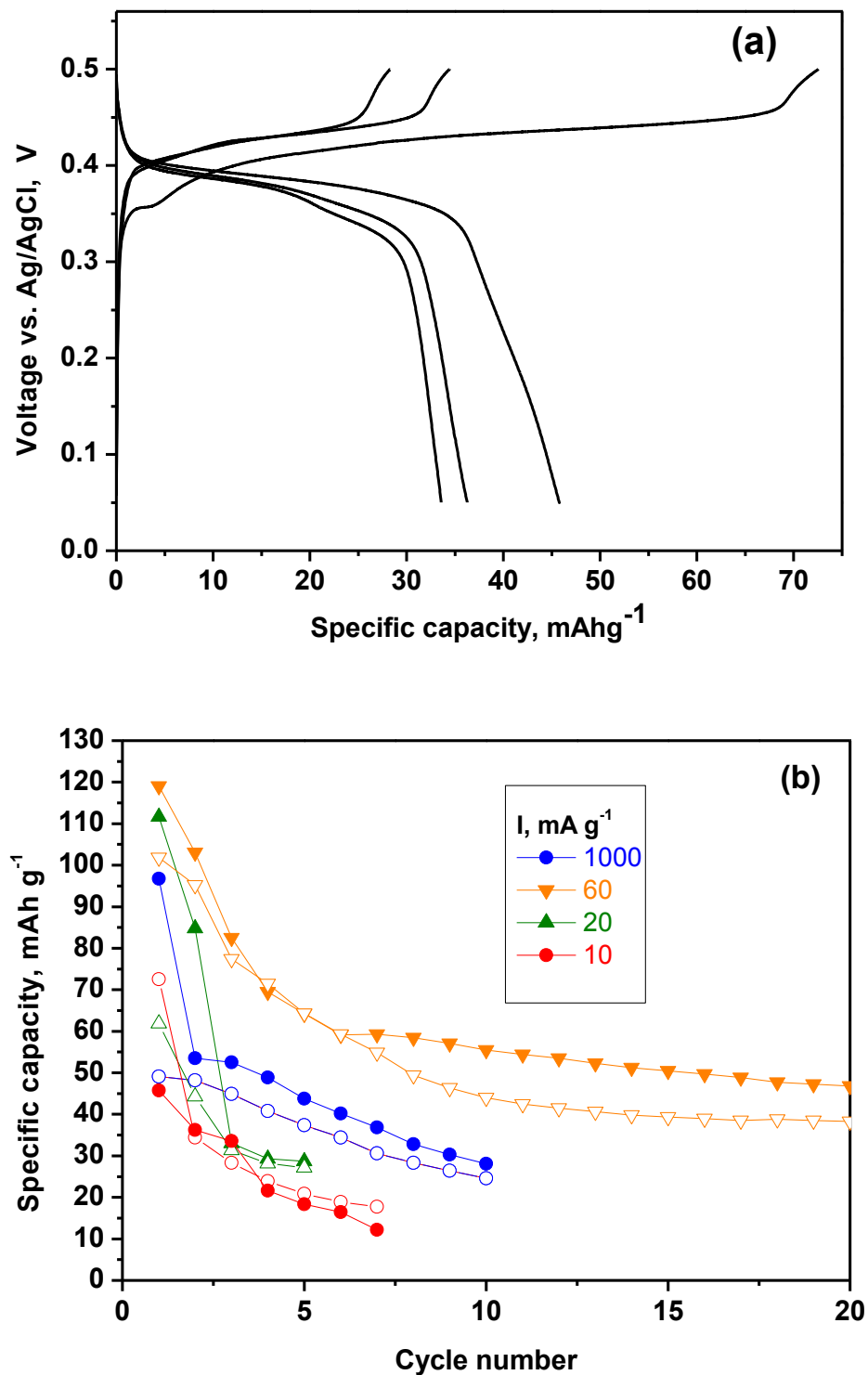
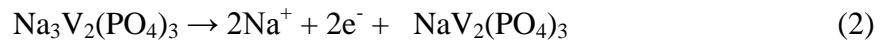


Fig. 2. Galvanostatic cycling of NVP in AlCl₃ (aq). (a) Typical voltage-capacity curves at 10 mA g⁻¹ of current density. (b) Capacity-cycle number at several rates (charge: open symbols, discharge: closed symbols).

4.6.3.2 Reaction mechanism and insertion

During the first charge, sodium is removed from NVP. Consequently, some sodium ions are incorporated to the electrolyte solution and a sodium-aluminium hybrid electrolyte is *in-situ* formed, though the relative amount of aluminium ions must be much higher than for sodium ions taking into account the large volume of the flooded cell. The removal of 2 Na per formula is equivalent to 117 mAh g⁻¹, which is the theoretical maximum charge capacity that can be reported in non-aqueous sodium cell and it corresponds to the following reaction:



According to previous studies in non-aqueous sodium cell, it is expected that one sodium ion of NaV₂(PO₄)₃ remains immobilized at the 6b site and two sodium ions at the 18e site could be extracted [38]. Other authors suggested that sodium can be removed from both sites [39]. The sodium that remains inactive serves as structure Stabilizer. Other reports remarked that water decomposition and O₂ evolution can take place when up to two sodium ions per NVP formula are utilized in aqueous electrolyte [32]. Consequently, we limited the maximum charge capacity up to the nominal composition Na_{1.1}V₂(PO₄)₃, irrespectively of the voltage limit. The experimental results of the semiquantitative microanalysis (EPMA-type) coupled to SEM agree quite well with this theoretical composition (Table 1), although traces of electrolyte are detected at the electrode surface.

During the subsequent reduction process, aluminium ions are inserted into partially desodiated NVP, and an aluminated (ANVP) material is formed according to the following reversible reaction:



According to the microanalysis results, the composition of ANVP electrode retrieved from the cell after the first charge-discharge cycle, and washing the electrode with deionized water, is Al_{0.25}Na_{0.81}V₂(PO₄)_{2.6} (Table 1). Taking into account the theoretical composition (Al_{0.3}Na_{1.1}V₂(PO₄)₃) obtained by assuming that all the electrons that flow through the circuit in the reduction process are used for aluminium insertion, the experimental result is in good agreement with aluminium insertion (or surface

accommodation). The intrinsic error in the technique (typically higher than 5%), side reactions and traces of electrolyte can contribute to the slight difference between the theoretical and experimental compositions. Besides, the mapping of composition shows that the distribution of aluminium in NVP is homogeneous (Fig. 3). Nevertheless, we cannot completely discard some protons cointercalation together aluminium.

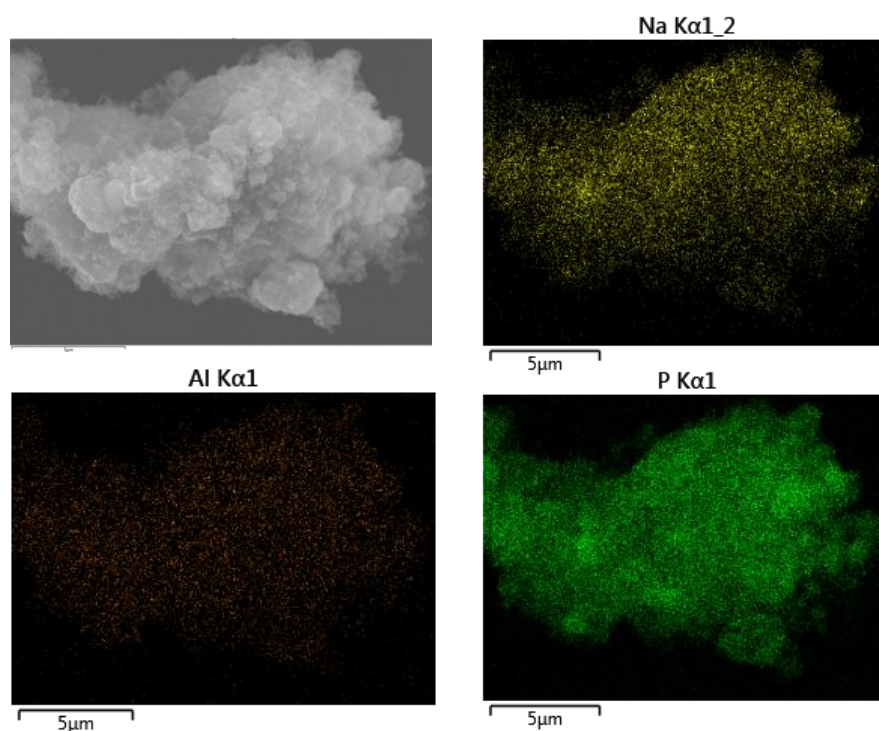


Fig. 3. SEM micrograph of ANVP electrode and mapping of composition for Na, Al and P, obtained after the first charge-discharge cycle of NVP and washing with deionized water.

The ^{27}Al NMR spectrum of the electrode after one charge-discharge cycle (Fig. 4a) is in excellent agreement with both insertion and surface accommodation of aluminium. It is worth recalling here that Zhou et al. pointed out that the cross section of the channel in NVP is smaller than the diameter of the water molecule, and inserted aluminium must not be hydrated, and we agree with that find [26]. The spectrum of $\text{Al}_{0.3}\text{Na}_{1.2}\text{V}_2(\text{PO}_4)_3$ was fitted with two Gaussian/Lorentzian peaks centered at +37 and -7 ppm, respectively. The broadening of the peaks can be due to the low mobility of aluminium. The peak at -7 ppm (44% contribution) can be due to aluminium near the surface of NVP particles, while the peak shift due to +37 ppm (56% contribution) can

be ascribed to aluminium inserted into the NASICON-type framework. He et al. found smaller shifts for aluminium inserted into anatase, irrespectively of their finding of aluminium accommodation near the surface of anatase particles [12]. For the sake of comparison in a reference measurement, the spectrum of a non-cycled electrode NVP which was simply impregnated overnight with the electrolyte solution (Fig. 4b) only shows an asymmetric peak at -1.4 ppm and the corresponding spinning side bands. This shift to +37 ppm of the electrode with nominal composition $\text{Al}_{0.3}\text{Na}_{1.2}\text{V}_2(\text{PO}_4)_3$ must be due to the effect of the vanadium 3d electrons (Fig. 4a). Thus, this result is a very strong proof of veritable insertion of aluminium ion (peak at + 37 ppm), together with aluminium placed near the particle surface (peak at -7 ppm). Similarly, other authors also used ^{27}Al NMR results as a main proof of aluminium intercalation in other materials [12,18].

Table 1. Compositions and lattice cell parameters of NVP and ANVP electrode materials. The given theoretical compositions were calculated by assuming that all the electrons that flow through the electrochemical cell are employed to the assumed (de)insertion reaction (coulometric measurement). The experimental compositions were obtained by EPMA.

NVP electrode	Theoretical composition	Experimental composition	Lattice cell parameters, Å
raw	$\text{Na}_3\text{V}_2(\text{PO}_4)_3$	$\text{Na}_{2.8}\text{V}_2(\text{PO}_4)_{3.5}$	a=8.735(5) c=21.82(1)
after first charge	$\text{Na}_{1.1}\text{V}_2(\text{PO}_4)_3$	$\text{Al}_{0.06}\text{Na}_{0.94}\text{V}_2(\text{PO}_4)_{2.6}$	a=8.401(1) c=21.444(4)
after charge+discharge	$\text{Al}_{0.3}\text{Na}_{1.1}\text{V}_2(\text{PO}_4)_3$	$\text{Al}_{0.25}\text{Na}_{0.81}\text{V}_2(\text{PO}_4)_{2.2}$	a=8.51(1) c=21.81(3)

Although XPS only delivers information about the surface of the particles, it can be useful to follow the electrochemical reactions. The V 2p spectra of raw NVP show two bands at 523.2 and 516.9 eV, which can be attributed to the V 2p_{3/2} and V 2p_{1/2} transitions, respectively (Fig. 5). These binding energy values are ascribed to V³⁺ [40]. The minor contribution at ca. 520.5 eV corresponds to the O 1s satellite peak. After the

charge, the shift of the V 2p bands to higher energies unambiguously demonstrates the partial oxidation of vanadium. During subsequent discharge, the bands are shifted back to values close to those of raw NVP. Irrespectively of the fact that the surface of the charged electrode unavoidably can contain traces of aluminium from the electrolyte, it is evident that in the discharged electrode the relative intensity of the Al 2p band at ca. 75 eV grows, in good agreement with aluminium insertion into NVP. From the relative intensity of the Na 1s band in the spectra, it is deduced that part of sodium is irreversibly removed from NVP. The broadening of the Na 1s band could be due to the presence of sodium in sites with different ionic character and/or near defects. In addition, the ionic character of the sodium-oxygen bond could be affected by the intercalation of aluminium. Thus, the stronger bond aluminium-oxygen can weaken the sodium-oxygen bond.

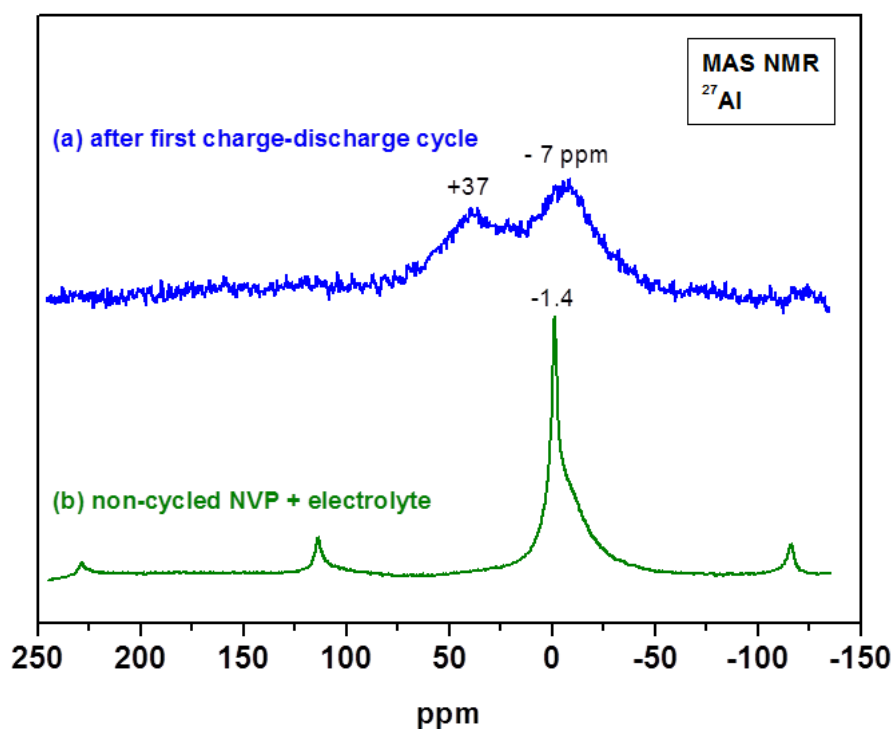


Fig.4. ^{27}Al MAS NMR spectra for: (a) NVP after the first charge-discharge cycle (nominal composition $\text{Al}_{0.3}\text{Na}_{1.2}\text{V}_2(\text{PO}_4)_3$) and after washing to remove electrolyte, and (b) NVP electrode impregnated with electrolyte solution (no cycling, no washing).

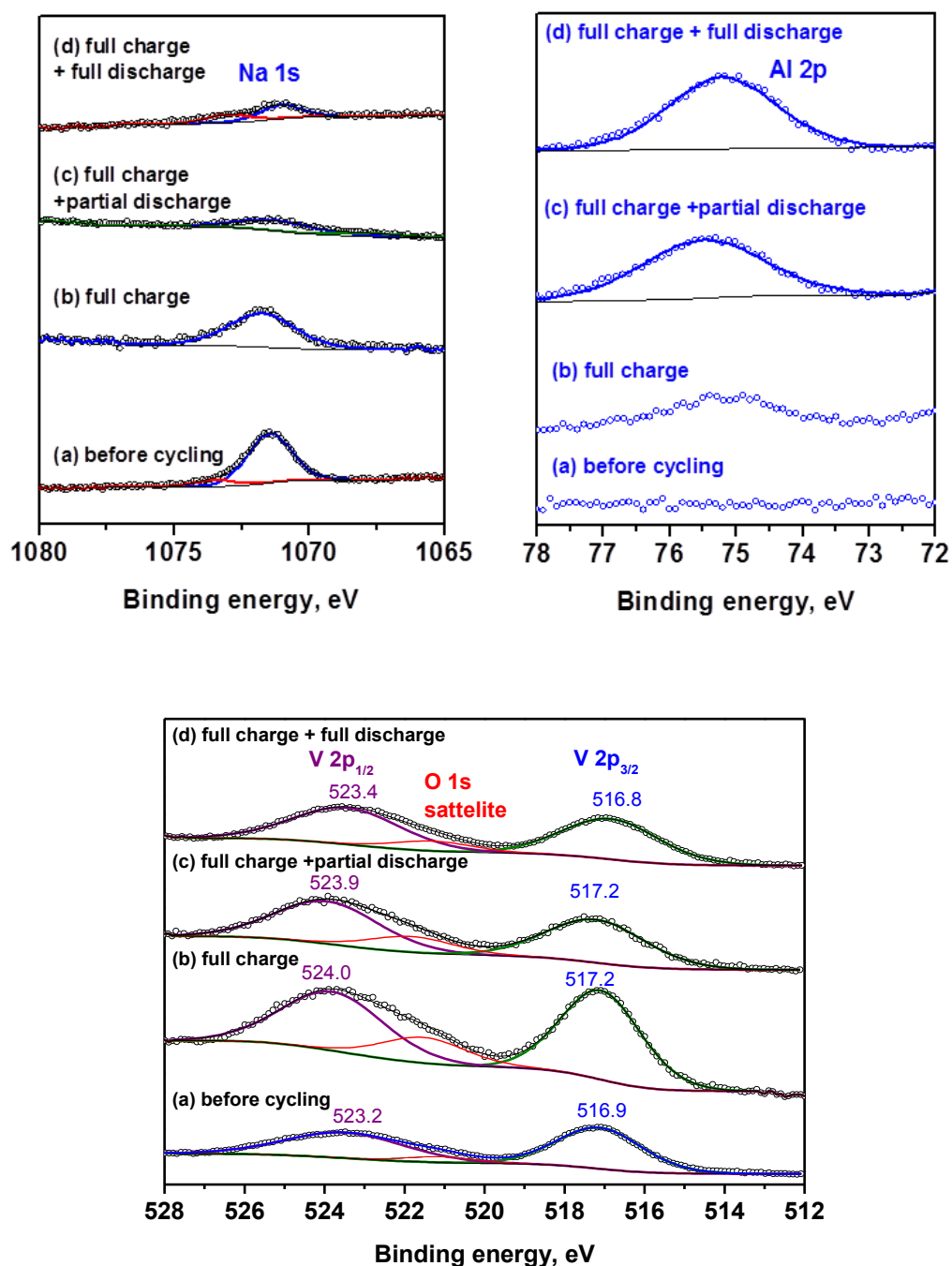


Fig.5. XPS spectra for pristine NVP and electrodes retrieved from the cells.

To study the structural changes occurring in the electrode material during the charge/discharge reaction, we carried out *ex-situ* XRD experiments of NVP in aqueous aluminium cells (Fig. 6). The XRD pattern of the as-prepared NVP sample (Fig. 6) can be indexed on the space group R-3c group. From Rietveld refinement, the resulting lattice parameters are: $a=8.735(5)$ Å, $c=21.82(1)$ Å and $V=1442(2)$ Å³. It is worth to remember that partial deintercalation of sodium from NVP does not drive to any drastic

change of its structure, and that there is little contrast between sodium and aluminium. Nevertheless, if one takes into account the results of electrochemistry, XPS, microanalysis and NMR, it seems reasonable to deal the XRD results considering aluminium intercalation. After the first partial charge in aqueous solution up to the nominal composition $\text{Na}_{1.4}\text{V}_2(\text{PO}_4)_3$ the observed reflections can be also indexed in the same space group. At the end of the first charge up to the nominal composition $\text{Na}_{1.1}\text{V}_2(\text{PO}_4)_3$, the XRD pattern can be indexed using the same space group, but the shrinkage of the unit cell is more significant ($a=8.401(1)$ Å, $c=21.444(7)$ Å, $\text{vol.}=1310.8(6)$ Å³), as expected after regarding the shift of the reflections to higher angles. Also, the splitting of the (104)/(110) peak is observed. Thus, the coexistence of two phases with compositions $\text{Na}_3\text{V}_2(\text{PO}_4)_3$ and ca. $\text{Na}_{1.1}\text{V}_2(\text{PO}_4)_3$ can be the reason the charge plateau, in good agreement with the literature on sodium batteries. When $\text{Na}_3\text{V}_2(\text{PO}_4)_3$ is oxidized, sodium is partially removed from the 18e sites, and then only 6b sites would be occupied in the phase $\text{NaV}_2(\text{PO}_4)_3$, although some sodium atoms initially placed at 18e sites may migrate to 6b sites. According to our Rietveld refinement results, most of sodium is placed at 6b sites while only a small amount of sodium remains at 18e sites. After the first charge (up to $\text{NaV}_2(\text{PO}_4)_3$) and then full discharge down to -0.5 V, the reflections tend to become more broadened due to the lattice strain, and the cell is slightly expanded in the a-axis ($a=8.51(1)$ Å, $c=21.81(3)$ Å, $\text{vol.}=1368(4)$ Å³) as compared to the charged material. In comparison with pristine NVP before electrochemical cycling, the unit cell after the first charge-discharge cycle is contracted particularly in the a-b plane, in good agreement with the replacement of sodium by smaller and more polarizing aluminium. Due to the large charge/radius ratio of Al^{3+} and to the attraction between aluminium and oxygen, the diameter of the channel is decreased from 2.723 to 2.676 Å (oxygen-oxygen distance measured in the a-direction). To compensate this contraction, the distance Na1-O2 in the 6b site is expanded from 2.51 to 2.67 Å. This implies that the formation of Al-O bonds weakens the Na-O bonds. The strain of the NASICON-type structure can be the reason of capacity loss upon electrochemical cycling. The Rietveld refinement, in which the occupancy factor of sodium and aluminium sites was independently liberated, is in good agreement with the occupancy of the 18e sites by both sodium and aluminium atoms (Table 2). The resulting site occupancy would involve an average oxidation state $\text{V}^{+1.98}$.

It has been reported that the sodiation capacity of NVP can be up to $\text{Na}_5\text{V}_2(\text{PO}_4)_3$ [41]. The crystallographic structure of ANVP is drawn in Fig.7.

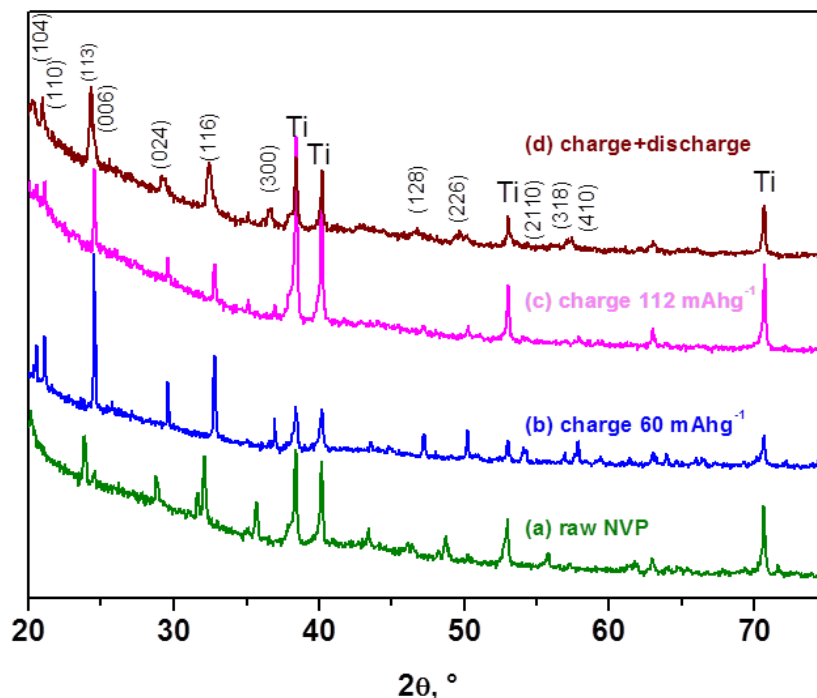


Fig.6. Ex situ XRD of NVP electrodes at selected states of charge in aqueous aluminium cell. The Miller indexes of the main reflections are given. The reflections from Ti current collector are marked.

Table 2. Crystallographic data for the ANVP electrode after-charge discharge of NVP in aluminum cell, obtained from Rietveld refinement. Space group: R-3c.

atom	Wyckoff site	x	y	z	occupancy
Na1	6b	0.0000	0.0000	0.0000	0.9753
Na2	18e	0.7745	0.0000	0.2500	0.2432
Al	18e	0.7522	0.0000	0.2500	0.4042
V	12c	0.0000	0.0000	0.1439	1.0000
P	18e	0.3068	0.0000	0.2500	1.0000
O1	36f	0.1700	-0.0074	0.2000	1.0000
O2	36f	0.1953	0.1637	0.1006	1.0000

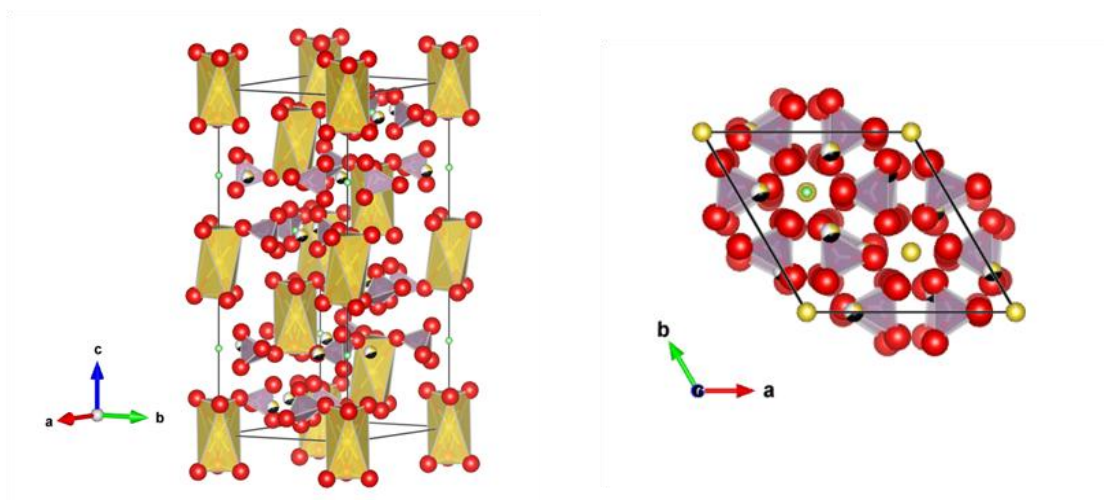


Fig. 7. Structural views of ANVP.

In contrast to the preservation of the NASICON-type structure, Wu et al. found very recently that the intercalation of Al^{3+} into V_2O_5 nanowires leads to the irreversible formation of an amorphous layer on the edge of nanowires and formation of a new crystalline phase [42]. Compared to V_2O_5 and other non-carbonaceous host materials [1,3,8-12,42], it seems that the structure of NVP is more stable and suitable for aluminium insertion, although it is a slow process and the electrolyte solution should be optimized.

4.6.3.3 Electrochemistry in non- aqueous cell

The selected electrochemical result using NVP in Al cell with ionic liquid as electrolyte solution (Fig.8) shows a flat and reversible plateau at ca. 1.25 V vs. Al, and the reversible capacity is about 60-70 mAh g^{-1} . This plateau could be particularly suitable for developing Al batteries with a stable output voltage. These electrochemical results are very similar to those reported by Sun et al. [23], who proposed using NaAlCl_4 dissolved in EMIC. The mechanism of (de)intercalation could involve Al^{3+} , AlCl_4^- and/or Na^+ . In our case, the solution initially is sodium-free, but it is expected that after the first charge, a hybrid aluminium-sodium electrolyte be *in-situ* formed. Taking into account the size of the channels in NVP [26] and the size of AlCl_4^- [17],

intercalation of chloroaluminate ion is not expected. Our results agree well with those of Sun et al. [23], and sodium would be reversibly inserted in the case of using EMIC ionic liquid. However, having in mind our results using aqueous electrolyte, it could be possible to develop electrolytes compatible with both Al metal and aluminium ion insertion. An advantage could be a more rapid diffusion of smaller Al^{3+} compared to larger ions, such as sodium and lithium. Similarly, we have recently shown that the electrolyte also influences on the (de)insertion of magnesium in NVP [34].

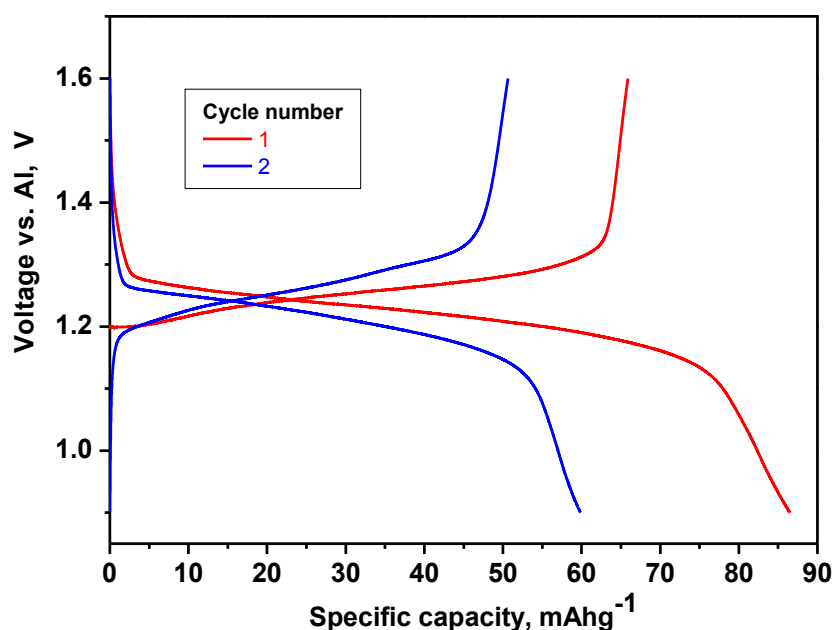


Fig.8. Galvanostatic results for NVP in non-aqueous cell. Current density: 3 mA g^{-1} .

4.6.4 Conclusions

Although Al-ion batteries are not yet competitive against lithium batteries, new possibilities have been studied here. We have proposed $\text{Na}_3\text{V}_2(\text{PO}_4)_3$ with NASICON-type structure as a new material for rechargeable aluminium batteries. Looking at the whole of all the results, it can be concluded that aluminium ions are effectively inserted in the framework of NVP using aqueous electrolyte,

although some contribution of proton insertion cannot be completely excluded. A drawback would be the slow kinetics of the true insertion process, and at high charge/discharge rate the reaction is rather a pseudocapacitive process in the surface of NVP. Further efforts should be made to improve the cycling stability of this system. These finds suggest that after improving non-aqueous electrolyte that be compatible with both Al and NVP, new rechargeable batteries could be developed. This electrode material also can be used in non-aqueous cell vs. Al metal, with ionic liquid as electrolyte solution, in good agreement with the results of Sun et al. [23].

Acknowledgements

The authors are grateful to MINECO (grant number MAT2014-56470-R), FEDER funds and Junta de Andalucía (research group FQM288) for financial support. SCAI-UCO and Institute of Fine Chemistry and Nanochemistry are also thanked for facilitating the use of several instruments. The authors thank the help of M.J. Aragón with the synthesis.

4.6.5 References

1. Z. Rong, R. Malik, P. Canepa, G.S. Gautam, M. Liu, A. Jain, K. Persson, G. Ceder, *Chem. Mater.* 27 (2015) 6016.
2. G.A. Elia, K. Marquardt, K. Hoeppe, S. Fantini, R. Lin, E. Knipping, W. Peters, J.F. Drillet, S. Passerini, *Adv. Mater.* 28 (2016) 7564.
3. J. R. González, F. Nacimiento, M. Cabello, R. Alcántara, P. Lavela, J. L. Tirado, *RSC Adv.* 6 (2016) 62157.
4. S. Liu, J. J. Hu, N. F. Yan, G. L. Pan, G. R. Li, X. P. Gao, *Energy Environ. Sci.* 5 (2012) 9743.
5. R. Chen, R. Luo, Y. Huang, F. Wu, L. Li, *Adv. Sci.* 3 (2016) 1600051.

6. Z.A. Zafar, S. Imtiaz, R. Razaq, S. Ji, T. Huan, Z. Zhang, Y. Huang, J.A. Anderson, *Energy Environ. Sci.* 5 (2017) 5646.
7. Q. Li, N.J. Bjerrum, *J. Power Sources* 110 (2002) 1.
8. M. Chiku, H. Takeda, S. Matsumura, E. Higuchi, H. Inoue, *ACS Appl. Mater. Interfaces* 7 (2015) 24385.
9. W. Wang, B. Jiang, W. Xiong, H. Sun, Z. Lin, L. Hu, J. Tu, J. Hou, H. Zhu, S. Jiao, *Scientific Reports* 3 (2013) 3383.
10. N. Jayaprakash, S. K. Das, L. A. Archer, *Chem. Commun.* 47 (2011) 12610.
11. S. Gu, H. Wang, C. Wu, Y. Bai, H. Li, F. Wu, *Energy Storage Materials* 6 (2017) 9.
12. Y. J. He, J. F. Peng, W. Chu, Y. Z. Li, D. G. Tong, *J. Mater. Chem. A* 2 (2014) 1721.
13. B. Lee, H. R. Lee, T. Yim, J. H. Kim, J. G. Lee, K. Y. Chung, B. W. Cho, S. H. Oh, *J. Electrochem. Soc.* 163 (2016) A1071.
14. N.S. Hudak, *J. Phys. Chem. C* 118 (2014) 5203.
15. S. Liu, G. L. Pan, G. R. Li, X. P. Gao, *J. Mater. Chem. A* 3 (2015) 959.
16. M. C. Lin, M. Gong, B. Lu, Y. Wu, D. Y. Wang, M. Guan, M. Angell, C. Chen, J. Yang, B. J. Hwang, H. Dai, *Nature* 520 (2015) 324.
17. S. C. Jung, Y. J. Kang, Y. K. Han, *Electrochim. Acta* 223 (2017) 135.
18. K. V. Kravchyk, S. Wang, L. Piveteau, M. V. Kovalenko, *Chem. Mater.* 29 (2017) 4484.
19. C. Masquelier, L. Crogenec, *Chem Rev.* 113 (2013) 6552.
20. R. Klee, M. Wiatrowski, M. J. Aragón, P. Lavela, G. F. Ortiz, R. Alcántara, J.L. Tirado, *ACS Appl. Mater. Interfaces* 9 (2017) 1471.
21. G. Li, Z. Yang, Y. Jiang, C. Jin, W. Huang, X. Ding, Y. Huang, *Nano Energy* 25 (2016) 211.

22. V. Palomares, P. Serras, I. Villaluenga, K.B. Hueso, J. Carretero-González, T. Rojo, *Energy Environ. Sci.* 5 (2012) 5884.
23. X. Sun, Z. Zhang, H. Guan, C. A. Bridges, Y. Fang, Y. Hu, G. M. Veith, S. Dai, *J. Mater. Chem. A* 5 (2017).
24. J. Y. Luo, W. J. Cui, P. He, Y. Y. Xia, *Nat. Chem.* 2 (2010) 760.
25. W. X Song, X. B. Ji, Y. R Zhu, H. J Zhu, F. Q Li, J. Chen, F. Lu, Y. P Yao, C. E. Banks, *ChemElectroChem* 1 (2014) 871.
26. H. Zhou, Z. R. Tian, S. S. Ang, *Mater Renew Sustain Energy* 5: 3 (2016).
27. C. W. Mason, F. Lange, *ECS Electrochem. Lett.* 4 (2015) A79.
28. L. Zhang, T. Huang, A. Yu, *J. Alloy Compd.* 646 (2015) 522.
29. Q. Zhang, C. Liao, T. Zhai, H. Li, *Electrochim. Acta* 196 (2016) 470.
30. G. Li, Z. Yang, Y. Jiang, W. Zhang, Y. Huang, *J. Power Sources* 308 (2016) 52.
31. G. Li, Z. Yang, Y. Jiang, C. Jin, W. Huang, X. Ding, Y. Huang, *Nano Energy* 25 (2016) 211.
32. P. R. Kumar, Y. H. Jung, C. H. Lim, D. K. Kim, *J. Mater. Chem. A* 3 (2015) 6271.
33. H. B. Zhao, C. J. Hu, H. W. Cheng, J. H. Fang, Y. P. Xie, W. Y. Fang, T. N. L. Doan, T. K. A. Hoang, J. Q. Xu, P. Chen, *Scientific Reports* 6 (2016) 25809.
34. M. Cabello, R. Alcántara, F. Nacimiento, P. Lavela, M. J. Aragón, J. L. Tirado, *Electrochim. Acta* 246 (2017) 908.
35. K. Momma, F. Izumi, *J. Appl. Crystallogr.* 44 (2011) 1272.
36. R.N. Reddy, R.G. Reddy, *J. Power Sources* 156 (2006) 700.
37. H. Lindström, S. Söldergrén, A. Solbrand, H. Rensmo, J. Hjelm, A. Hagfeldt, S.E. Lindquist, *J. Phys. Chem. B* 101 (1997) 7717.

38. Z. Jian, C. Yuan, W. Han, X. Lu, L. Gu, X. Xi, Y. S. Hu, H. Li, W. Chen, D. Chen, Y. Ikuhara, L. Chen, *Adv. Funct. Mater.* 24 (2014) 4265.
39. W. X. Song, X. Y. Cao, Z. P. Wu, J. Chen, *Phys. Chem. Chem. Phys.* 16 (2014) 6845.
40. M. J. Aragón, J. Gutiérrez, R. Klee, P. Lavela, R. Alcántara, J. L. Tirado, J. *Electroanal. Chem.* 47 (2017) 47.
41. Z. Jian, Y. Sun, X. Ji, *Chem. Commun.* 51 (2015) 6381.
42. S. Gu, H. Wang, C. Wu, Y. Bai, H. Li, F. Wu, *Energy Storage Mater.* 6 (2017) 9

CAPÍTULO 5

Resumen y conclusiones finales
Summary and final conclusions

5.1 Resumen

En esta tesis doctoral se han sintetizado y caracterizado micro- y nano-materiales para usarlos como electrodo positivo o negativo en baterías de ion litio y baterías post litio. Teniendo en cuenta el gran número de muestras y de celdas electroquímicas estudiadas, y para conseguir una exposición ordenada de los resultados obtenidos, este resumen ha sido dividido en tres partes:

1- Materiales nanoestructurados para baterías de ion litio

2- Ánodos para baterías de ion sodio

3- Materiales para baterías de iones multivalentes

1- Materiales nanoestructurados para baterías de ion litio

Siguiendo un proceso de anodización-deposición se pueden obtener **composites autoorganizados**. La primera etapa es la anodización de una lámina de Ti a 60 V durante 2 horas, dando lugar a la formación sobre el Ti de una capa fina de nanotubos de dióxido de titanio (nt-TiO₂) autoorganizados. La segunda etapa del proceso conduce a la formación de una capa finísima de la fase beta-Li₃PO₄, que ha sido depositada electrolíticamente sobre los nanotubos de dióxido de titanio sin afectar prácticamente al espesor total de la película delgada.

Mediante calentamiento del *composite* anterior a 700°C durante 2 horas, se logra su transformación en un **nano-bosque de Li₄Ti₅O₁₂/TiO₂/Li₃PO₄** (LTL). Los difractogramas de rayos-X de LTL mostraron reflexiones de la fase gamma-Li₃PO₄, rutilo y de la espinela Li₄Ti₅O₁₂. La respuesta electroquímica de este electrodo de capa fina implica inserción de litio a 1,55 V, que corresponde a la transición de Li₄Ti₅O₁₂ a Li₇Ti₅O₁₂, y la desinserción de litio a 1,57 V, lo cual evidencia la baja polarización de la celda. Los voltamogramas confirmaron que sólo la fase Li₄Ti₅O₁₂ es activa electroquímicamente en el LTL en el voltaje usado. Por primera vez, los efectos del fosfato de litio en el titanato de litio han sido explorados. Así, rutilo y Li₃PO₄ inducen una mejora de la estabilidad del ciclado y de la difusión de Li⁺. Para la celda completa de ion litio, se empleó como cátodo un electrodo de LiFePO₄. La transferencia de litio desde el LiFePO₄ hasta el LTL ocurrió a un potencial de 1,9 V, y la reacción inversa a

1,8 V. Además, ciclando entre 2,7 y 0,75 V la celda completa LTL/LiPF₆-EC:DEC/LiFePO₄ proporcionó valores de capacidad de 145 mA h g⁻¹ y una densidad energética de 260 W h Kg⁻¹ a una cinética de C/2.

Se empleó un enfoque diferente para sintetizar TiO₂/Li₃PO₄ autoorganizado, combinando procesos de anodización-deposición y calentamiento a 500°C. Modificando la temperatura de calcinación se puede obtener γ -Li₃PO₄ o β -Li₃PO₄. Por otra parte, se obtuvieron nanohilos de LiNi_{0,5}Mn_{1,5}O₄ (LNMO) con estructura espinela a través de un proceso sin electricidad, empleando un molde de alúmina y calentando a 800°C. Cuando se usa como ánodo nt-TiO₂, el deterioro de los nanotubos conlleva una retención pobre de la capacidad con el ciclado electroquímico prolongado. Esto puede solucionarse usando nt-TiO₂/ γ -Li₃PO₄ (preparado por deposición-calcinación), o nt-TiO₂/ β -Li₃PO₄ (preparado por calcinación-deposición). A través de la microscopía electrónica de transmisión de alta resolución se detectó la presencia de la fase Li₄Ti₅O₁₂ en la interfase entre TiO₂ y Li₃PO₄. Con respecto al material catódico LNMO, se pueden observar dos platós (o mesetas de potencial) cerca de 5 V vs. Li, atribuidas al par redox Ni²⁺/Ni⁴⁺. La combinación de estos electrodos da lugar a la batería **nt-TiO₂/Li₃PO₄/LiPF₆-EC:DEC/LiNi_{0,5}Mn_{1,5}O₄** que opera entre 2,6 y 3,0 V. A cinéticas más rápidas (5C), se puede observar una mejora de la capacidad (110 mA h g⁻¹ durante 100 ciclos) al usar nt-TiO₂/Li₃PO₄ como electrodo negativo, en comparación con el uso de nt-TiO₂ (la capacidad cayó por debajo de 90 mA h g⁻¹ tras 60 ciclos). La celda completa presenta una capacidad de 125 mA h g⁻¹ y la densidad energética lograda fue de 325 W h Kg⁻¹.

Otro ejemplo de batería de alto voltaje es la siguiente: **nt-TiO₂/Li₃PO₄/LiPF₆-EC:DEC/Li₂CoPO₄F-C**. El *composite* nt-TiO₂ (anatasa)/ γ -Li₃PO₄ se preparó a 500°C y se usó como ánodo, y Li₂CoPO₄F-C se usó como cátodo. El nanomaterial Li₂CoPO₄F-C se sintetizó por vía sol-gel. Una vez más, se encontraron trazas de Li₄Ti₅O₁₂ en la interfase entre TiO₂ y Li₃PO₄. El perfil de carga de Li₂CoPO₄F-C frente a litio muestra un plató a 5,0 V, revelando su importancia como cátodo de alto voltaje, y puede encajar con el plató del ánodo de anatasa (1,8-1,9 V). En las semiceldas de litio, el electrodo Li₂CoPO₄F-C mostró una alta ineficiencia desde el primer ciclo hasta el segundo. Por tanto, se hace necesaria una activación del cátodo previa a su empleo en la celda completa. Su combinación con nt-TiO₂/Li₃PO₄ da lugar a una batería que opera en el rango de potencial 3,1-3,2 V. La capacidad reversible es cerca de 150 mA h g⁻¹

(alcanzando casi el 99% del máximo de capacidad reversible) y la densidad de energía es 472 W h Kg^{-1} a cinética C.

2- Ánodos para baterías de ion sodio

La tecnología de ion sodio todavía necesita encontrar sólidos anfitriones apropiados para intercalar reversiblemente iones en su estructura en una ventana de potencial óptima. Un ánodo no carbonoso para baterías de ion sodio es el **nanocomposite** $\text{Na}_2\text{T}_{16}\text{O}_{13}/\text{TiO}_2$, el cual se preparó exitosamente con una morfología de nanobosque. Para obtener las películas finas de $\text{Na}_x\text{H}_y\text{TiO}_2$ se siguieron procesos de anodización-deposición. Es necesario un calentamiento entre 500 y 800°C para obtener el **nanocomposite** $\text{Na}_2\text{T}_{16}\text{O}_{13}/\text{TiO}_2$. Los difractogramas de rayos-X mostraron reflexiones de titanato de sodio en combinación con las de rutilo. Los espectros de resonancia paramagnética electrónica (siglas en inglés EPR) evidenciaron un aumento significativo en el contenido de Ti^{3+} durante la inserción de sodio/protones, y una disminución después de calentar. Para el estudio electroquímico usando como electrolito NaPF_6 disuelto en la mezcla de disolventes EC:DEC, el perfil galvanostático es diferente para muestras obtenidas a temperatura ambiente y para muestras calentadas a 500°C . Las muestras no calentadas mostraron una caída constante del potencial sin un plató claro, siendo este comportamiento típico de muestras amorfas cuando reaccionan con sodio. Por el contrario, se observaron platós en la inserción y desinserción a $0,7$ y $0,9 \text{ V}$, respectivamente para muestras calentadas a 700°C y 800°C . La estructura túnel 3D de $\text{Na}_2\text{T}_{16}\text{O}_{13}$ es potencialmente atractiva para acomodar iones Na^+ . El electrodo de nanobosque optimizado exhibió una capacidad por área de $130 \mu\text{A h cm}^{-2}$ durante 150 ciclos, la cual es casi el triple de la proporcionada por los nanotubos de dióxido de titanio ($36 \mu\text{Ah cm}^{-2}$).

Con respecto a los materiales carbonosos no grafiticos, se usaron como material de electrodo coque de petróleo y coque de esquistos bituminosos calentados a 1300°C . Además, se prepararon muestras calentadas a 2500°C y 3000°C para dar lugar a la ordenación estructural y a la formación de grafito. Los difractogramas de rayos-X de las muestras obtenidas a 1300°C eran característicos de un material turbostrático. Al incrementar la temperatura de tratamiento, las reflexiones se desplazan ligeramente a ángulos altos, lo que sugiere un proceso de grafitización y la consecuente indexación en el grupo espacial $P6_3/mmc$. El grafito no puede insertar sodio electroquímicamente

excepto cuando co-intercala moléculas de un disolvente como la diglima. El coque de petróleo y el coque de esquistos bituminosos calentados a diferentes temperaturas también pueden insertar sodio de forma reversible en un electrolito basado en diglima como disolvente. Cuando se usa triflato de sodio (NaCF_3SO_3) o NaPF_6 en diglima, el comportamiento electroquímico del coque de petróleo y el del coque de esquistos bituminosos mejoran considerablemente con respecto al uso de la mezcla EC:DEC como disolvente. Así, se obtuvieron capacidades en la descarga de 116 y 123 mA h g^{-1} para NaCF_3SO_3 y NaPF_6 , respectivamente. Además, el perfil de voltaje en celdas de sodio durante la descarga mostró platós principalmente entre 0,5 V y 0,7 V. Al final de la descarga, se detectó un compuesto ternario de intercalación en *stage-1*. Dos moléculas de diglima son co-intercaladas por ion alcalino, y este hecho se evidenció en los diagramas 1-D de Patterson, en los espectros de infrarrojo por transformada de Fourier (siglas en inglés FTIR) y mediante análisis termogravimétricos (ATG). El mejor comportamiento electroquímico se atribuyó al coque de petróleo calcinado a 2500°C (muestra P2500). Este ánodo se utilizó en la celda completa, con un cátodo de $\text{Na}_3\text{V}_2(\text{PO}_4)_3$ y usando NaPF_6 -diglima como electrolito. La celda proporcionó una densidad de energía de 202 W h kg^{-1} a cinética C y a un potencial medio de 2,7 V.

Más investigaciones sobre co-intercalación de sodio se llevaron a cabo para grafito y grafito expandido térmicamente (siglas en inglés TEG). Se obtuvieron diferentes muestras de grafitos expandidos a través de la expansión térmica del grafito natural y de los métodos de Broddie y Hummer modificados. Las diferentes estructuras y morfologías de las muestras afectaron a las propiedades de inserción de sodio. El grafito expandido térmicamente, el cual mostró el mejor comportamiento electroquímico en términos de reversibilidad y capacidad, se obtuvo a través de un calentamiento muy rápido de bisulfato de grafito a 1400°C durante menos de 1 segundo. Los difractogramas de rayos-X y espectros de espectroscopia fotoelectrónica de rayos-X (siglas en inglés XPS) y de Raman corroboraron la presencia de compuestos intermedios de óxido de grafito y formas reducidas de grafito expandido. La muestra TEG mostró un incremento de la distancia interlamina (50 nm según las imágenes de microscopía electrónica de barrido de emisión de campo, siglas en inglés FE-SEM) y una disminución del tamaño de cristalito (desde 37,65 nm hasta 17,86 nm). Los espectros de Raman confirmaron que la muestra TEG exhibía el índice de grafitización más alto (59,6%) en comparación con el resto de los grafitos expandidos preparados. El

perfil galvanostático de la muestra TEG en celda de sodio usando NaCF_3SO_3 en DGM como electrolito, exhibió un plató durante la descarga entre 0,65 y 0,55 V a cinética C, proporcionando una capacidad de 115 mA h g^{-1} después de 100 ciclos, la cual corresponde a una eficiencia del 96%. Durante la primera descarga, se observó por difracción de rayos-X *ex-situ* una expansión en la distancia entre las láminas de grafito y, también, un conjunto de reflexiones pertenecientes al **stage-I** de $\text{Na}_x(\text{DGM})_2\text{C}_{20}$.

3- Materiales para baterías de iones multivalentes

La inserción de cationes multivalentes ofrece la ventaja de cargar dos o tres electrones por ion en el material anfitrión, y este hecho puede conducir al desarrollo de baterías de alta energía. Así, magnesio, calcio y aluminio pueden ser muy útiles.

El magnesio ha sido extraído reversiblemente del compuesto MgMn_2O_4 usando métodos químicos y electroquímicos. En primer lugar, la fase MgMn_2O_4 con grupo espacial $I4_1/amd$ se sintetizó usando el método de Pechini y a diferentes temperaturas (400, 550 y 800°C). Las micrografías de microscopía electrónica de transmisión (siglas en inglés TEM) revelaron que el tamaño de partícula aumentaba con la temperatura de calentamiento. La desmagnesiación química por tratamiento ácido de la espinela tetragonal MgMn_2O_4 da lugar a su transformación en la fase cúbica $\lambda\text{-MnO}_2$ (grupo espacial $Fd3m$). Cabe destacar que el ion Mn^{3+} es un ion de efecto *Jahn-Teller*, y este efecto local puede distorsionar la estructura de la celda unidad de cúbica a tetragonal. La fase cúbica se obtiene más efectivamente cuando la espinela MgMn_2O_4 tiene una mayor área superficial específica y un tamaño de partícula pequeño. En el caso de la desmagnesiación electroquímica de la muestra MgMn_2O_4 preparada a 400°C (LT- MgMn_2O_4), y en disolución acuosa, se obtuvo $\lambda\text{-MnO}_2$. A través de voltametría cíclica de $\lambda\text{-MnO}_2$ con electrolito acuoso, la estructura cúbica se transforma en $\text{Mg}_x\text{Mn}_2\text{O}_4$ tetragonal. Por tanto, este proceso de (des)magnesiación es reversible en disolución acuosa. El ciclado galvanostático en la celda acuosa proporcionó capacidades reversibles de 150 mA h g^{-1} . Además, se exploró una **batería de ion-magnesio** empleando LT- MgMn_2O_4 como electrodo positivo y un electrolito basado en $\text{Mg}(\text{ClO}_4)_2$ en EC:DEC. Los disolventes carbonatados no permiten una deposición/disolución reversible y eficiente del magnesio, por tanto, como electrodo negativo se utilizó V_2O_5 frente al LT- MgMn_2O_4 . Esta batería mostró valores de capacidad reversible de 120 mA h g^{-1} referidos a la masa del electrodo positivo. Según los resultados electroquímicos y

de difracción de rayos-X, los iones magnesio son insertados/desinsertados reversiblemente en la batería no acuosa, dando lugar a una contracción de la red tetragonal de MgMn_2O_4 , aunque la fase cúbica $\lambda\text{-MnO}_2$ no se formó, probablemente debido a la incompleta desmagnesiación y a la ausencia de moléculas de agua.

Se emplearon **nanocintas de beta- $\text{NaV}_6\text{O}_{15}$** como electrodo positivo en baterías de magnesio, sodio e híbridas magnesio/sodio. Las nanocintas se sintetizaron en un solo paso por vía hidrotermal. Este material, el cual posee una estructura monoclinica con grupo espacial $C2/m$, puede acomodar reversiblemente en su estructura iones litio, iones sodio e iones magnesio. Su comportamiento electroquímico se evaluó en una celda de magnesio empleando como electrolito $\text{Mg}(\text{ClO}_4)_2$ en acetonitrilo y Mg como contraelectrodo, aunque el magnesio se vuelve inactivo electroquímicamente después de unos pocos ciclos debido a la formación de una capa aislante, dando lugar a capacidades de 45 mA h g^{-1} después de 50 ciclos. Este vanadato puede ciclarse más eficientemente frente a Mg metal usando como electrolito $\text{Mg}(\text{BH}_4)_2$ y NaBH_4 en diglima, mostrando capacidades reversibles de 125 mA h g^{-1} a cinéticas lentas. Los espectros de XPS *ex-situ* mostraron un desplazamiento de la señal de V2p hacia valores de energía de enlace más bajos (516.8 eV) y más altos (517.2 eV), lo que sugiere que el vanadio es reducido y re-oxidado durante la descarga y la carga, respectivamente. Los resultados de XPS, XRD y microanálisis por EDS (Energy Dispersive X-Ray Spectroscopy en inglés), sugirieron que tanto el sodio como el magnesio son intercalados en el electrodo positivo y electrodepositados en el electrodo negativo y, en consecuencia, puede describirse como una **batería híbrida**. Además, se probó una celda de ion magnesio completa usando $\text{NaV}_6\text{O}_{15}$ como electrodo negativo, MgMn_2O_4 como electrodo positivo y $\text{Mg}(\text{ClO}_4)_2$ EC:DEC como electrolito. Esta batería proporciona capacidades reversibles (referidas a la masa del electrodo negativo) de 50-80 mA h g^{-1} .

Otro candidato a electrodo positivo en una batería de magnesio es **$\text{Na}_3\text{V}_2(\text{PO}_4)_3$ con estructura tipo NASICON** (grupo espacial $R-3c$). La estructura NASICON es un entramado rígido y abierto que puede ser válido para acomodar iones magnesio. Así, se ha probado $\text{Na}_3\text{V}_2(\text{PO}_4)_3$ como electrodo positivo frente a Mg metal, usando como electrolito 0,5 M bis(trifluorometanosulfonimida) de magnesio ($\text{Mg}(\text{TFSI})_2$) en 1,2-dimetoxietano (DME). En los resultados de voltametría cíclica se observó un pico anódico intenso a 1,8 V, adscrito a la oxidación parcial de V^{3+} a V^{4+} . Se encontraron dos picos catódicos en la descarga a 1,5 y 0,9 V, asignados a la reducción de los iones

vanadio y a la inserción de sodio y/o magnesio. En los experimentos galvanostáticos, se detectó un plató durante la carga a 1,8 V, correspondiente a la desinserción parcial de iones sodio. Según los experimentos galvanostáticos y los resultados de EDS de los electrodos recuperados de las celdas, se puede concluir que cerca de $1,7^+$ Na por fórmula pueden ser desinsertados electroquímicamente (de $\text{Na}_3\text{V}_2(\text{PO}_4)_3$ hasta $\text{Na}_{1.3}\text{V}_2(\text{PO}_4)_3$), la celda de la red cristalina se contrae y estos iones sodio son introducidos en el electrolito formando *in-situ* un electrolito híbrido sodio-magnesio. En el proceso de descarga, tanto sodio como magnesio se insertaron a través de dos platós consecutivos a 1,6 y 1,2 V, respectivamente. Así, se formaron fases con fórmula general $\text{Mg}_x\text{Na}_y\text{V}_2(\text{PO}_4)_3$. Esta batería híbrida sodio-magnesio proporcionó capacidades reversibles de 60 mA h g^{-1} durante 100 ciclos a una densidad de corriente de 10 mA g^{-1} .

La próxima era post-litio también contempla **baterías de ion calcio**. Teniendo esto en mente, se preparó CaCo_2O_4 con grupo espacial $P2/m$ por modificación del método de Pechini, y se estudió como electrodo positivo en baterías de calcio. Para evitar el uso de Ca metal como electrodo y sus reacciones parásitas asociadas, se empleó CaCo_2O_4 como fuente de calcio y como electrodo positivo, y V_2O_5 comercial (grupo espacial $Pmmn$) como electrodo negativo. La disolución no acuosa que se empleó como electrolito fue $\text{Ca}(\text{ClO}_4)_2$ en acetonitrilo. En esta batería, el ciclado electroquímico comenzó con un proceso de carga en el cual 0.35 iones Ca^{2+} pueden ser extraídos reversiblemente de CaCo_2O_4 e intercalados en V_2O_5 . Los difractogramas de rayos-X y los espectros de XPS confirmaron este hecho, aunque la transformación de la estructura no pudo ser resuelta completamente. La capacidad reversible que proporcionó esta batería de ion calcio fue de hasta 100 mA h g^{-1} .

Los metales multivalentes como el aluminio pueden proporcionar capacidades volumétricas más altas que el litio y, probablemente, puede ser más conveniente el empleo de este metal para aplicaciones de almacenamiento de energía a gran escala y estacionarias. Sin embargo, las **baterías recargables de aluminio** aún están en etapas incipientes por lo que su desarrollo y comprensión están llenos de dificultades. En este contexto, se estudió el comportamiento electroquímico de V_2O_5 ortorrómbico en disolución acuosa. Se sintetizó pentóxido de vanadio laminar usando el método de intercambio iónico, obteniendo primero un xerogel amorfo que cristalizó calentándolo a 300°C. La celda electroquímica se preparó usando carbono vítreo como electrodo negativo, un electrodo de mercurio/sulfato mercurioso como referencia y empleando

como electrolito AlCl_3 1 M en agua desionizada. Los voltamogramas mostraron un par de picos redox a -0,3 V y -0,03 V en los barridos catódicos y anódicos, respectivamente. En el experimento galvanostático se obtuvieron capacidades reversibles de 120 mA h g^{-1} y apareció un pseudoplató reversible a -0,15 V durante la descarga y a 0,0 V durante la carga. Este pseudoplató puede ser atribuido al proceso de intercalación de aluminio hidratado. Por otra parte, cuando el espaciado interlaminar de V_2O_5 entra en contacto con el agua, se pueden intercambiar químicamente agua protonada (H_3O^+ , ion hidronio u oxonio) y Al^{3+} . Más probablemente, algunos protones también son intercalados durante el proceso de descarga. Después de la intercalación electroquímica de aluminio, el compuesto resultante $(\text{Al}^{3+})_{x/3}[(\text{V}^{4+})_x, (\text{V}^{5+})_{2-x}]\text{O}_5 \cdot n\text{H}_2\text{O}$ es amorfo según los difractogramas de rayos-X a una composición aproximada de $x=0,5$, y esta pérdida de cristalinidad mejora el intercambio químico entre el electrodo y el electrolito.

Se demostró la inserción verdadera de este catión trivalente en $\text{Na}_3\text{V}_2(\text{PO}_4)_3$ (NVP) tipo NASICON. Se montó una celda de tres electrodos usando NVP como electrodo positivo, Pt como electrodo negativo, una referencia de Ag/AgCl y AlCl_3 disuelto en agua desionizada como electrolito. Los voltamogramas mostraron un pico redox a 0,6 V en carga y a 0,2 V en descarga, adscrito al par redox $\text{V}^{3+}/\text{V}^{4+}$ y a la (des)inserción. Además, los experimentos galvanostáticos, que concordaron bien con los resultados de voltametría cíclica, exhibieron valores de capacidad reversible de entre 60 y 100 mA h g^{-1} según las condiciones del ciclado. Durante la primera carga, el sodio es extraído del NVP y, en consecuencia, los iones sodio son incorporados al electrolito, por lo que se formó *in-situ* un **electrolito híbrido sodio-aluminio**. Durante la descarga, los iones aluminio son insertados (aunque no puede descartarse por completo una contribución asociada a la inserción de protones) formándose un material aluminato con una composición teórica de $\text{Al}_{0,3}\text{Na}_{1,1}\text{V}_2(\text{PO}_4)_3$. El espectro de resonancia magnética nuclear (siglas en inglés RMN) de ^{27}Al demostró la inserción de aluminio y su acomodación en la superficie. Por otra parte, el material NVP se usó en una celda de aluminio no acuosa empleando un disco de Al metal como contraelectrodo y otro como electrodo de referencia, y líquido iónico de cloroaluminato como electrolito. Teniendo en cuenta el tamaño de los canales en el NVP y el tamaño de AlCl_4^- , no se esperaba la intercalación de los iones cloroaluminato y sólo los iones sodio fueron (des)insertados de forma reversible.

Un avance principal de este trabajo es estudiar los mecanismos de (des)intercalación de cationes multivalentes en distintos tipos de redes estructurales. En comparación con el litio, estos mecanismos parecen ser mucho más complejos, y el tamaño de partícula podría ser más crítico. Los resultados nos llevan a dirigir nuestras investigaciones futuras hacia las baterías híbridas.

5.2 Summary

In this doctoral thesis micro- and nano-materials have been synthesized and characterized for using either as positive or negative electrode in lithium ion batteries and post-lithium batteries. Taking into account the large number of samples and electrochemical cells studied here, and in order to achieve an orderly exposure of the results obtained, this summary has been divided into three parts.

1- Nanoarchitected materials for lithium ion batteries

2- Anodes for sodium ion batteries

3- Materials for multivalent ion batteries

1- Nanoarchitected materials for lithium ion batteries

Following an anodization-deposition process, **self organized composites** can be obtained. The first step is the anodization of a Ti foil at 60 V for 2 h which leads to the formation of self organized titania nanotubes (nt-TiO₂) while the second step leads to the formation of a beta-phase Li₃PO₄ layer which has been electrolytically deposited onto titania nanotubes without affecting the overall thickness of the thin film.

Further annealing at 700°C during 2 hours is necessary in order to achieve the **Li₄Ti₅O₁₂/TiO₂/Li₃PO₄ (LTL) composite nanoforest layer**. X-ray diffraction patterns showed reflections of gamma-phase Li₃PO₄, rutile and the spinel-type Li₄Ti₅O₁₂. The electrochemical response of this thin film electrode exhibited lithium insertion at 1.55 V corresponding to the transition from Li₄Ti₅O₁₂ to Li₇Ti₅O₁₂ and de-insertion at 1.57 V, evidencing the low polarization of the cell. Cyclic voltammograms confirmed that only Li₄Ti₅O₁₂ is electrochemically active. The effects of lithium phosphate on lithium

titanate are explored for the first time. Thus, rutile and Li_3PO_4 exert an improvement of the cycling stability and Li^+ diffusion. For the lithium ion full cell, LiFePO_4 electrode was employed as a cathode. The lithium transfer from LiFePO_4 to LTL occurred at 1.9 V and the reverse reaction at 1.8 V. Therefore, by cycling between 2.7 and 0.75 V the full cell LTL/ $\text{LiPF}_6\text{-EC:DEC/LiFePO}_4$ delivered 145 mAh g^{-1} of capacity and leading to an energy density of 260 W h Kg^{-1} at C/2 rate.

A different approach used to synthesize self-organized $\text{TiO}_2/\text{Li}_3\text{PO}_4$ was performed by combining anodization-deposition and heating to 500°C. Selecting the calcination temperature, $\gamma\text{-Li}_3\text{PO}_4$ or $\beta\text{-Li}_3\text{PO}_4$ can be obtained. On the other hand, $\text{LiNi}_{0.5}\text{Mn}_{1.5}\text{O}_4$ (LNMO) nanowires with spinel structure were obtained through an electroless method employing alumina template and heating to 800°C. When using nt- TiO_2 as anode, surface deterioration at the tips of the nanotubes leads to poor capacity retention on prolonged cycling. This fact can be solved either using nt- $\text{TiO}_2/\gamma\text{-Li}_3\text{PO}_4$ (by deposition-calcination process) or nt- $\text{TiO}_2/\beta\text{-Li}_3\text{PO}_4$ (by calcination-deposition process). By HRTEM the phase $\text{Li}_4\text{Ti}_5\text{O}_{12}$ was detected in the interphase between TiO_2 and Li_3PO_4 . Regarding LNMO cathode material, we can observe two high-voltage plateaus near 5 V vs. Li, attributed to the $\text{Ni}^{2+}/\text{Ni}^{4+}$ redox couple. The combination of these electrodes gives rise to a battery **nt- $\text{TiO}_2/\text{Li}_3\text{PO}_4/\text{LiPF}_6\text{-EC:DEC/LiNi}_{0.5}\text{Mn}_{1.5}\text{O}_4$** operating in the voltage range between 2.6 and 3.0 V. At fast rates (5C), an improved capability when using nt- $\text{TiO}_2/\text{Li}_3\text{PO}_4$ as negative electrode (110 mA h g^{-1} over 100 cycles) can be observed as compared to single nt- TiO_2 (capacity fell below 90 mA h g^{-1} after 60 cycles). The full cell has a capacity of 125 mA h g^{-1} and the energy density value achieved was 325 W h Kg^{-1} .

Another example of a high-voltage full battery is the following: **nt- $\text{TiO}_2/\text{Li}_3\text{PO}_4/\text{LiPF}_6\text{-EC:DEC/Li}_2\text{CoPO}_4\text{F-C}$** . The nt- TiO_2 (anatase)/ $\gamma\text{-Li}_3\text{PO}_4$ composite was prepared at 500°C and used as anode and $\text{Li}_2\text{CoPO}_4\text{F-C}$ as cathode. The nano- $\text{Li}_2\text{CoPO}_4\text{F-C}$ material was prepared via sol-gel. Once again, small traces of $\text{Li}_4\text{Ti}_5\text{O}_{12}$ were found forming a minute fraction at the interphase between TiO_2 and Li_3PO_4 . The charge profile of $\text{Li}_2\text{CoPO}_4\text{F-C}$ versus lithium shows a plateau at 5.0 V, revealing its importance as potentially high-voltage cathode and could perfectly fit with the plateau of anatase anode (1.8-1.9 V). The behavior of $\text{Li}_2\text{CoPO}_4\text{F-C}$ in lithium half-cell showed a high inefficiency from the first to the second cycle. Therefore, an activation of the cathode before using in the full lithium-ion cell is needed. Its combination with nt-

TiO₂/Li₃PO₄ leads to a battery operating in the 3.1-3.2 V voltage range. The reversible capacity is about 150 mAh g⁻¹ (reaching about 99% of the maximum reversible capacity) and the energy density is 472 W h Kg⁻¹ at C rate.

2- Anodes for sodium ion batteries

Sodium ion technology still needs finding suitable hosts in order to reversibly intercalate ions in their structure in an optimum voltage window. A non-carbonaceous based anode for Na-ion batteries is **Na₂Ti₆O₁₃/TiO₂ nanocomposite**, which is successfully prepared with nanoforest morphology. Anodization-deposition processes are followed so as to obtain Na_xH_yTiO₂ films. Annealing at 500°C-800°C is needed for obtaining the Na₂Ti₆O₁₃/TiO₂ nanocomposite. X-ray diffraction patterns showed reflections of sodium titanate in combination with rutile. EPR spectra evidenced a significant increase in Ti³⁺ content during sodium/proton insertion and a decrease on heating. For the electrochemical study using NaPF₆ in EC:DEC as electrolyte, the galvanostatic profile is different for the samples obtained at room temperature and the samples thermally annealed at 500°C. Non-annealed samples showed a constant decay of the potential without clear plateau, being this behavior typical of amorphous samples when reacting with sodium. On the contrary, flat plateaus of sodium insertion and deinsertion were observed at 0.7 and 0.9 V, respectively, for samples thermal annealed at 700°C and 800°C. The 3D tunnel structure of Na₂Ti₆O₁₃ results in a potentially attractive host to store Na⁺ ions reversibly. The resulting optimized nanoforest electrode exhibited 130 μA h cm⁻² of areal capacity over 150 cycles which is almost triple than that of titania nanotubes (36 μA h cm⁻²).

Regarding non-graphitic carbon-based materials, **petroleum coke** and **shale coke** annealed at 1300°C were used as electrode material. In addition, samples further heated to 2500°C and 3000°C were prepared in order to lead to structural ordering and graphite formation. The XRD patterns of the samples obtained at 1300°C were characteristic of a turbostratic material. On increasing the temperature, the reflections are slightly shifted to higher angles, suggesting a graphitization process and possible indexing in the space group *P6₃/mmc*. Graphite cannot insert sodium, except when graphite co-intercalates solvent molecules such as diglyme. Petroleum coke and shale coke samples annealed at different temperatures can also insert sodium reversibly in a diglyme-based electrolyte. When using sodium triflate (NaCF₃SO₃) or NaPF₆ in

diglyme, the electrochemical behavior of petroleum coke and shale coke is considerably improved than when using EC:DEC mixture as a solvent in the electrolyte. Therefore, discharge capacities of 116 and 123 mA h g⁻¹ were obtained for NaCF₃SO₃ and NaPF₆, respectively. In addition, the voltage profile during discharge in sodium cells exhibited flat plateaus mainly between 0.5 V and 0.7 V. At the end of the discharge, a stage-I ternary intercalation compound is detected. Two diglyme molecules are co-intercalated per alkali ion and this fact was evidenced by 1-D Patterson diagrams, FTIR spectra and TGA analyses. The best electrochemical performance was attributed to the petroleum coke sample calcined at 2500°C (sample P2500). A full cell with this anode, and Na₃V₂(PO₄)₃ as positive electrode in NaPF₆-diglyme solution was assembled, providing an energy density of 202 W h kg⁻¹ under C-rate and an average potential of 2.7 V.

Further research on sodium co-intercalation was conducted for graphite and **thermally expanded graphite** (TEG). Different expanded graphite samples were obtained from natural graphite by thermal expansion, Broddie and Hummer's modified methods. The differences in structure and morphologies between them affected the sodium insertion properties. TEG, that exhibited the best performance in terms of reversibility and capacity, was obtained by fast heating of graphite bisulfate at 1400°C during less than 1 s. X-ray diffraction patterns, XPS and Raman spectra corroborated the presence of graphite oxide intermediates and reduced forms of expanded graphite. TEG showed an increase of the interlayer distance (50 nm revealed by FE-SEM images) and a decrease of the crystallite size (from 37.65 nm to 17.86 nm). The Raman spectra confirmed that the TEG sample exhibited the highest graphitization index (59.6%) compared to the rest of the prepared expanded graphites. The galvanostatic profile of TEG in sodium cell using NaCF₃SO₃ in DGM electrolyte exhibited a flat plateau during discharge between 0.65 and 0.55 V at C-rate, delivering a capacity of 115 mA h g⁻¹ after 100 cycles which corresponds to an efficiency of 96 %. During the first discharge an expansion of the graphitic interlayer distance was observed by ex-situ XRD and also a set of reflections belonging to the **stage-I Na_x(DGM)₂C₂₀**.

3- Materials for multivalent ion batteries

The insertion of multivalent cations offers the advantage of charging two or three electrons per ion to the host material, and this fact may drive the development of high-energy batteries. Thus, magnesium, calcium and aluminium could be very useful.

Magnesium has been reversibly removed from **MgMn₂O₄** by using chemical and electrochemical methods. Firstly, the phase MgMn₂O₄ with space group *I4₁/amd* was prepared by Pechini's method at several temperatures (400, 550 and 800°C). TEM micrographs revealed that the particle size increased with the annealing temperature. The chemical demagnesiumation by acid treatment of the tetragonal spinel-type MgMn₂O₄ yields to its transformation into cubic λ -MnO₂ (space group *Fd3m*). It is worth to remember here that Mn³⁺ is a *Jahn-Teller* effect ion, and this local effect can distort the structure of the unit cell from cubic to tetragonal. This cubic phase is more effectively obtained when the MgMn₂O₄ spinel has a large specific surface area and a small particle size. In the case of electrochemical demagnesiumation in an aqueous solution of MgMn₂O₄ prepared at 400°C (LT- MgMn₂O₄), λ -MnO₂ was obtained. Throughout electrochemical cycling of λ -MnO₂ by cyclic voltammetry and using aqueous electrolyte, the cubic structure is transformed into tetragonal Mg_xMn₂O₄. Consequently, this process of (de)magnesiumation is reversible in aqueous solution. The galvanostatic cycling in the aqueous cell provided reversible capacities of 150 mA h g⁻¹. In addition, a **magnesium-ion battery** was explored by using LT-MgMn₂O₄ as positive electrode in a Mg(ClO₄)₂ EC:DEC based electrolyte solution. The carbonate-based solvents do not allow the reversible and efficient deposition/dissolution of magnesium and, therefore, V₂O₅ was tentatively used as negative electrode vs. MgMn₂O₄. This battery showed reversible capacity values of ca. 120 mA h g⁻¹ referred to the mass of the positive electrode. According to the electrochemical and XRD results, magnesium ions are reversibly inserted/deinserted in the non-aqueous battery leading to a contraction of the tetragonal lattice of MgMn₂O₄ but the cubic phase λ -MnO₂ is not formed, probably due to the incomplete demagnesiumation and the absence of water molecules.

Nanobelts of beta-NaV₆O₁₅ were employed as positive electrode in magnesium, sodium and hybrid magnesium/sodium batteries. The nanobelts were synthesized by a hydrothermal one-step route. This material, which possesses a monoclinic structure with space group *C2/m*, can reversibly accommodate lithium, sodium and magnesium ions in its framework. Its electrochemical behavior was tested in magnesium cell using Mg(ClO₄)₂ in acetonitrile as electrolyte and Mg as counter electrode, although Mg becomes electrochemically inactive after a few cycles due to the formation of a blocking layer, leading to a capacity of 45 mA h g⁻¹ after 50 cycles. This vanadate could be more efficiently cycled vs. metallic Mg using an electrolyte solution based on

Mg(BH₄)₂ and NaBH₄ dissolved in diglyme, showing reversible capacities of 125 mA h g⁻¹ at slow rates. Ex-situ XP spectra showed a shifting of V2p signal to lower (516.8 eV) binding energies and higher (517.2 eV) binding energies, suggesting that vanadium is reduced and reoxidized during the discharge and charge, respectively. Not only XPS, but also XRD and microanalysis by EDS, strongly suggested that both sodium and magnesium are intercalated at the positive electrode and electrodeposited at the negative one and, consequently, it can be described as a **hybrid battery**. In addition, a full magnesium ion cell was tested using NaV₆O₁₅ as negative electrode, MgMn₂O₄ as positive electrode and Mg(ClO₄)₂ EC:DEC as electrolyte solution. This battery provides reversible capacities (referred to the mass of the negative electrode) of about 50-80 mA h g⁻¹.

Another candidate proposed here as positive electrode in a magnesium battery is **Na₃V₂(PO₄)₃ with NASICON-type structure** (space group *R-3c*). The NASICON structure is a rigid and open framework that could be valid as a host for accommodation of magnesium ion. Thus, Na₃V₂(PO₄)₃ has been tested as a positive electrode vs. Mg metal with 0.5 M magnesium bis(trifluoromethanesulfonimide) (Mg(TFSI)₂) in 1,2-dimethoxyethane (DME) as electrolyte solution. From cyclic voltammetry results, an intense anodic peak ascribed to partial oxidation from V³⁺ to V⁴⁺ was observed at 1.8 V. Two cathodic peaks were found in the discharge at 1.5 and 0.9 V and they were assigned to reduction of vanadium ions and insertion of sodium and/or magnesium. In the galvanostatic experiments, a plateau was detected during charge at 1.8 V, corresponding to the partially deinsertion of sodium ions. According to the electrochemical experiments and to the EDS results of the electrodes retrieved from the cells, it can be concluded that around 1.7 Na⁺ per formula can be electrochemically deinserted from the framework of Na₃V₂(PO₄)₃ up to Na_{1.3}V₂(PO₄)₃, the cell of the crystal lattice is contracted and these sodium ions are introduced in the electrolyte forming in-situ a **hybrid sodium-magnesium electrolyte**. In the consequent discharge process, both sodium and magnesium were inserted through two consecutive plateaus at 1.6 and 1.2 V, respectively. Therefore, phases with general formula Mg_xNa_yV₂(PO₄)₃ were formed. This sodium-magnesium hybrid battery delivered reversible capacities of 60 mA h g⁻¹ during 100 cycles at a current density of 10 mA g⁻¹.

The forthcoming post lithium-ion era also contemplates **calcium-ion batteries**. Having this in mind, CaCo₂O₄ with space group *P2/m* was prepared by a modification

of the Pechini method, and then it has been tested as positive electrode in calcium batteries. In order to avoid the use of metallic Ca as electrode and the associated parasitic reactions, CaCo_2O_4 was used as calcium source and positive electrode, and commercial V_2O_5 (space group *Pmmn*) as negative electrode. The non-aqueous electrolyte solution employed was $\text{Ca}(\text{ClO}_4)_2$ in acetonitrile. In this battery, the electrochemical cycling started with a charge process where up to 0.35 Ca^{2+} ions could be reversibly removed from CaCo_2O_4 and intercalated into V_2O_5 . This fact was corroborated by X-ray diffraction patterns and XP spectra, although the structure transformation could not be completely resolved. The reversible capacity provided by this calcium ion cell was up to 100 mA h g^{-1} .

Multivalent metals as aluminium can deliver higher volumetric capacity than lithium and could be probably more advantageous for large-scale energy storage and stationary applications. However, **rechargeable aluminium batteries** are still in its infancy and their development and comprehension are full of difficulties. Within this context, the electrochemical behavior of orthorhombic V_2O_5 was studied in aqueous solution. Layered-type vanadium pentoxide was synthesized by using the ion exchange method, firstly obtaining an amorphous xerogel that is then crystallized by annealing at 300°C . The electrochemical cell was assembled using glassy carbon as negative electrode, mercury/mercurous sulfate electrode as reference and 1M AlCl_3 in deionized water as electrolyte solution. The cyclic voltammograms showed a pair of redox peaks at -0.3 V and -0.03 V in the cathodic and anodic sweep, respectively. In the galvanostatic experiment, reversible capacities of 120 mA h g^{-1} were obtained and a reversible pseudoplateau appeared at -0.15 V during discharge and at 0.0 V during charge. This pseudoplateau can be attributed to the intercalation process of hydrated aluminium. On the other hand, protonated water (H_3O^+ , hydronium or oxonium ion) and Al^{3+} can be chemically exchanged when the interlayer space of V_2O_5 is in contact with water. Most probably, some protons are also intercalated during the discharge process. After the electrochemical intercalation of aluminium, the resulting $(\text{Al}^{3+})_{x/3}[(\text{V}^{4+})_x, (\text{V}^{5+})_{2-x}]\text{O}_5 \cdot n\text{H}_2\text{O}$ is XRD-amorphous at approximately $x=0.5$ and this loss of crystallinity enhances the chemical exchange between the electrode and the electrolyte solution.

True insertion of this trivalent cation into a NASICON-type $\text{Na}_3\text{V}_2(\text{PO}_4)_3$ (NVP) was demonstrated. A three-electrode cell was assembled using NVP as positive

electrode, Pt as negative electrode, Ag/AgCl as reference electrode and AlCl₃ dissolved in deionized water as electrolyte solution. The cyclic voltammograms showed a redox peak at 0.6 V in charge and at 0.2 V in discharge ascribed to the V³⁺/V⁴⁺ redox couple and (de)insertion. In addition, the galvanostatic experiments agreed well with the cyclic voltammetry results and exhibited reversible capacity values between 60-100 mA h g⁻¹ depending on the cycling conditions. During the first charge, sodium is removed from NVP and, consequently, sodium ions are incorporated to the electrolyte solution and a **sodium-aluminium hybrid electrolyte** is in-situ formed. During the discharge process, aluminium ions are inserted (although some contribution of proton insertion cannot be completely excluded) and an aluminated material is formed with a theoretical composition of Al_{0.3}Na_{1.1}V₂(PO₄)₃. The ²⁷Al NMR spectrum evidenced the aluminium insertion and surface accommodation. On the other hand, the NVP material was used in non-aqueous aluminium cell using a piece of Al metal as counter and another piece as reference electrode and chloroaluminate ionic liquid as electrolyte solution. Taking into account the size of the channels in NVP and the size of AlCl₄⁻, intercalation of chloroaluminate ions were not expected and only sodium ions were reversibly (de)inserted.

A main advancement of this work is to study the mechanisms of (de)intercalation of multivalent cations in different types of frameworks. Compared to lithium, these mechanisms seem to be even much more complex, and the particle size could be more critical. The results lead us to drive our future investigations towards hybrid batteries.

5.3 Conclusiones finales

1. El bajo coste y la abundancia de los óxidos de titanio, y su fácil conversión a titanatos, los hacen candidatos interesantes como ánodos. Se ha conseguido la síntesis de nuevos materiales anódicos nanoarquitecturados para baterías de ion litio como son Li₄Ti₅O₁₂/TiO₂/Li₃PO₄ con morfología de nanobosque y nanotubos de TiO₂/Li₃PO₄, a través de una ruta de fabricación basada en procedimientos electroquímicos. Estos electrodos negativos nanoarquitecturados tienen una configuración que les permite estar libres de aditivos aglomerantes.

La morfología de nanobosque es muy útil para facilitar el contacto entre caras del material activo y del electrolito.

2. Las películas electrolíticas de Li_3PO_4 se electrodepositaron con éxito sobre la matriz de nanotubos de TiO_2 . Se consiguió a través de un procedimiento electroquímico basado en una reducción de protones, con el consecuente aumento del pH, la disociación de hidrogeno fosfato y la deposición de Li_3PO_4 en la superficie del cátodo. Según los difractogramas de rayos-X, los parámetros de electrodeposición (como el tiempo o la densidad de corriente) pueden permitir controlar los polimorfos de Li_3PO_4 (γ o β) electrodepositados. El análisis morfológico evidenció la formación de una nanoestructura 3D que consiste en el recubrimiento con Li_3PO_4 de la matriz de nanotubos de TiO_2 .
3. Se consiguió un máximo de densidad energética de 260 W h kg^{-1} a cinética C/2 cuando se combinó el *composite* $\text{Li}_4\text{Ti}_5\text{O}_{12}/\text{TiO}_2/\text{Li}_3\text{PO}_4$ con LiFePO_4 . El valor de densidad de energía para la celda $\text{TiO}_2/\text{Li}_3\text{PO}_4/\text{LiNi}_{0.5}\text{Mn}_{1.5}\text{O}_4$ fue de 325 W h kg^{-1} a cinética 5C. La densidad de energía se mejoró con la batería de alto voltaje $\text{TiO}_2/\text{Li}_3\text{PO}_4/\text{Li}_2\text{CoPO}_4\text{F}$, proporcionando 472 W h kg^{-1} a cinética C.
4. La película de fosfato de litio se mantiene a lo largo del ciclado electroquímico. Esta película ejerce un efecto de estabilización en la interfase ánodo/electrolito. Además, desempeña un papel importante al mejorar la conductividad y permitir una rápida movilidad de los iones litio.
5. La estructura de túnel 3D de $\text{Na}_2\text{Ti}_6\text{O}_{13}$ lo convierte en un anfitrión potencialmente atractivo para almacenar iones sodio de forma reversible. El electrodo de nanobosque optimizado presenta capacidades tres veces mayores que las de nt- TiO_2 , y un ciclado excelente.

Las conclusiones 1-5 se deducen de los artículos 2.1, 2.2, 2.3 y 3.1.

6. Varios materiales carbonosos derivados de productos de desecho de la industria del petróleo se han preparado a diferentes temperaturas, y luego se han caracterizado. Estos materiales no son caros y son potenciales candidatos para ánodos en baterías de ion sodio.

7. Para conseguir la intercalación de sodio en materiales gráfiticos, es crucial el empleo de electrolitos basados en diglima. Se encontró que dos moléculas de diglima son co-intercaladas por ion alcalino. La formación progresiva y reversible del *stage-1* de $\text{Na}_x(\text{DGM})_2\text{C}_{20}$ se ha demostrado por los diagramas de Patterson, difracción de rayos-X y análisis termogravimétricos.
8. Se confirmó la viabilidad del coque de petróleo como ánodo en baterías de ion sodio combinándolo con un cátodo de $\text{Na}_3\text{V}_2(\text{PO}_4)_3$, que suministra 202 W h kg^{-1} a cinética C con un voltaje medio de 2.7 V.
9. El grafito expandido térmicamente (TEG) exhibió una mejora del comportamiento electroquímico en comparación con la muestra prístina del grafito natural. El proceso de expansión térmica proporciona una distancia interlaminar óptima para co-intercalar sodio-DGM. El uso del electrolito NaCF_3SO_3 en DGM en la celda de sodio resultó en capacidades más altas (115 mA h g^{-1}) en comparación con el uso de electrolitos estándar como NaClO_4 en PC. Se logró una eficiencia del 96% a cinética C después de 100 ciclos.

Las conclusiones 6-9 han sido deducidas de los artículos 3.2 y 3.3.

10. El magnesio ha sido extraído de forma reversible de la muestra MgMn_2O_4 tetragonal empleando métodos químicos y electroquímicos, y en electrolitos acuosos y no acuosos. En disolución acuosa, MgMn_2O_4 puede transformarse en $\lambda\text{-MnO}_2$ cúbico. En disolventes no acuosos, se detectó la formación de $\text{Mg}_x\text{Mn}_2\text{O}_4$, pero no $\lambda\text{-MnO}_2$.
11. Se prepararon con éxito nanocintas de $\text{NaV}_6\text{O}_{15}$ en un solo paso por vía hidrotermal. Este material actuando como electrodo positivo puede intercalar reversiblemente iones litio, iones sodio e iones magnesio, dependiendo de las condiciones experimentales. También puede usarse en baterías duales utilizando Mg metal como electrodo negativo y con un electrolito de sodio-magnesio.
12. Teniendo en cuenta que los disolventes carbonatados pueden emplearse de forma eficiente como electrolitos en baterías de magnesio sólo cuando se usan compuestos de intercalación y no Mg metal, se probaron las baterías de ion magnesio $\text{MgMn}_2\text{O}_4/\text{Mg}(\text{ClO}_4)_2\text{-EC:DEC/V}_2\text{O}_5$ y $\text{MgMn}_2\text{O}_4/\text{Mg}(\text{ClO}_4)_2\text{-$

EC:DEC/NaV₆O₁₅. Estas celdas electroquímicas permiten verificar la viabilidad de los materiales activos de electrodo para baterías de magnesio reversibles.

13. Na₃V₂(PO₄)₃ con estructura tipo NASICON puede ser parcialmente desodiado, y tanto los iones sodio como los iones magnesio pueden insertarse en su estructura reversiblemente, formando fases con fórmula general Mg_xNa_yV₂(PO₄)₃. A través de difracción de rayos-X se observó la expansión-contracción de la celda. En esta batería, el electrodo negativo puede ser Mg metal, y el electrolito no acuoso puede ser Mg(TFSI)₂ en DME. Sin embargo, el electrolito debería mejorarse aún más.

Las conclusiones 10-13 han sido deducidas de los artículos 4.1, 4.2 y 4.3.

14. Los electrolitos no acuosos conocidos no son muy adecuados para su empleo con Ca metal, por lo que se montó una batería asequible de CaCo₂O₄/Ca(ClO₄)₂-AN/V₂O₅. Este dispositivo electroquímico nos permitió probar por primera vez la (des)intercalación de iones calcio en el cobaltato de calcio, evitando el uso de Ca metal. Se concluyó que hasta 0.35 Ca²⁺ por fórmula son desintercalados del cobaltato e intercalados en V₂O₅. Según los resultados de difracción de rayos-X, la estructura se modifica cuando el calcio es (des)intercalado.
15. Se ha demostrado la intercalación reversible de aluminio en xerogel de pentóxido de vanadio en una batería recargable acuosa. Durante el proceso de intercalación electroquímica, el vanadio es reducido y el producto resultante (Al_xV₂O₅) se vuelve amorfo según los difractogramas de rayos-X a una composición de x=0.5. La intercalación electroquímica de Al³⁺ es paralela a la intercalación de agua y protones. Además de la intercalación electroquímica, también puede tener lugar el intercambio iónico entre el electrodo y el electrolito.
16. Los iones aluminio son insertados de forma eficaz en el entramado de Na₃V₂(PO₄)₃ usando electrolitos acuosos, aunque no puede descartarse por completo algunas contribuciones de la inserción de protones. La capacitancia superficial también puede contribuir a la capacidad aparente. Cuando se emplea líquido iónico como electrolito no acuoso, parece que sólo los iones sodio son (des)intercalados reversiblemente y no el aluminio. Este hallazgo implica que

puede ser factible desarrollar una batería híbrida con Al metal como electrodo negativo y NVP como electrodo positivo de inserción de sodio. La dificultad principal radica en la compatibilidad del electrolito con los materiales de electrodo.

Las conclusiones 14-16 se deducen de los artículos 4.4, 4.5 y 4.6.

Las baterías post-litio pueden ser competitivas frente a las de litio, pero antes de su comercialización se necesitan muchas mejoras, particularmente para el desarrollo de nuevos electrolitos. Otra posibilidad es usar electrolitos híbridos y/o baterías híbridas.

5.4 Final conclusions

1. The low cost and abundance of titanium oxides, and their easy conversion to titanates make them interesting candidates for anodes. The synthesis of new nanoarchitected anode materials for lithium ion batteries, like $\text{Li}_4\text{Ti}_5\text{O}_{12}/\text{TiO}_2/\text{Li}_3\text{PO}_4$ nanoforest and $\text{TiO}_2/\text{Li}_3\text{PO}_4$ nanotubes, has been achieved by a fabrication route based on electrochemical procedures. These nanoarchitected negative electrodes have a binder-free configuration. The nanoforest morphology is usefulness to facilitate the interfacial contact between the active material and the electrolyte.
2. The electrolytic Li_3PO_4 films were successfully deposited onto the TiO_2 nanotube array by an electrochemical procedure consisting in proton reduction with subsequent increase in pH, hydrogen phosphate dissociation and Li_3PO_4 deposition on the surface of the cathode. The Li_3PO_4 polymorphs (γ or β) in the deposit could be tailored by modifying the electrodeposition parameters, such as time or current density, as determined by XRD patterns. The morphological analysis evidenced the formation of a 3D nanostructure consisting of Li_3PO_4 coating the TiO_2 nanotube array.
3. A maximum energy density of about 260 W h kg^{-1} at C/2 rate was reached when combining $\text{Li}_4\text{Ti}_5\text{O}_{12}/\text{TiO}_2/\text{Li}_3\text{PO}_4$ composite with LiFePO_4 . The energy density value for the full cell $\text{TiO}_2/\text{Li}_3\text{PO}_4/\text{LiNi}_{0.5}\text{Mn}_{1.5}\text{O}_4$ was 325 W h kg^{-1} at 5C rate.

The energy density was enhanced with the high-voltage battery $\text{TiO}_2/\text{Li}_3\text{PO}_4/\text{Li}_2\text{CoPO}_4\text{F}$, providing 472 W h kg^{-1} at C rate.

4. Lithium phosphate film is preserved upon electrochemical cycling. This phosphate film exerts a stabilization effect at the anode/electrolyte interface. In addition, it plays an important role by enhancing the conductivity and allowing fast lithium ion mobility.
5. The 3D tunnel structure of $\text{Na}_2\text{Ti}_6\text{O}_{13}$ results in a potentially attractive host to store Na ions reversibly. The resulting optimized nanoforest electrode shows three-times larger capacities than nt- TiO_2 and excellent cyclability.

Conclusions 1 to 5 are deduced from articles 2.1, 2.2, 2.3 and 3.1.

6. Several carbonaceous materials derived from waste products of the petroleum industry have been prepared at different temperatures and then characterized. These materials are inexpensive and potential candidates for anodes in sodium-ion batteries.
7. In order to achieve sodium intercalation in graphitic materials, the use of diglyme-based electrolytes was crucial. It was found that two diglyme molecules per alkali ion are co-intercalated. The progressive and reversible formation of the $\text{Na}_x(\text{DGM})_2\text{C}_{20}$ stage-I is demonstrated by Patterson diagrams, XRD and TGA analyses.
8. The feasibility of the petroleum coke as anode in sodium-ion batteries was confirmed by combining with a $\text{Na}_3\text{V}_2(\text{PO}_4)_3$ cathode, which could deliver 202 W h kg^{-1} at C rate with an average voltage of 2.7 V.
9. The thermally expanded graphite (TEG) exhibited an improved electrochemical performance as compared to the pristine sample of natural graphite. The thermal expansion process provides an optimal interlayer distance to co-intercalate sodium-DGM. The use of NaCF_3SO_3 in DGM as electrolyte in sodium cell resulted in higher capacities (115 mA h g^{-1}) compared to using standard electrolytes such as NaClO_4 in PC. An efficiency of 96 % at C rate was achieved after 100 cycles.

Conclusions 6 to 9 are deduced from articles 3.2 and 3.3.

10. Magnesium has been reversibly removed from tetragonal MgMn_2O_4 by using chemical and electrochemical methods, and aqueous and non-aqueous electrolytes. In aqueous solution, MgMn_2O_4 can be transformed into cubic λ - MnO_2 . In non-aqueous solvent $\text{Mg}_x\text{Mn}_2\text{O}_4$ is detected, but not λ - MnO_2 .
11. Nanobelts of $\text{NaV}_6\text{O}_{15}$ have been successfully prepared by a hydrothermal one-step route. This material acting as positive electrode can reversibly intercalates lithium, sodium and magnesium, depending on the experimental conditions. It also can be used in dual batteries vs. Mg metal as negative electrode and with sodium-magnesium electrolyte solution.
12. Having in mind that carbonate-based solvents can be employed efficiently as electrolytes in magnesium batteries only when using intercalation compounds, but not metallic Mg, veritable magnesium ion batteries like $\text{MgMn}_2\text{O}_4/\text{Mg}(\text{ClO}_4)_2\text{-EC:DEC}/\text{V}_2\text{O}_5$ and $\text{MgMn}_2\text{O}_4/\text{Mg}(\text{ClO}_4)_2\text{-EC:DEC}/\text{NaV}_6\text{O}_{15}$ were tested. These electrochemical cells allow checking the feasibility of the electrode active materials for reversible magnesium batteries.
13. $\text{Na}_3\text{V}_2(\text{PO}_4)_3$ with a NASICON-type structure can be partially desodiated, and both sodium and magnesium ions can be reversibly inserted in its structure, forming phases with general formula $\text{Mg}_x\text{Na}_y\text{V}_2(\text{PO}_4)_3$. The expansion-contraction of the lattice was followed by XRD. In this battery metallic magnesium can be the negative electrode, and the non-aqueous electrolyte solution can be $\text{Mg}(\text{TFSI})_2$ in DME. Nevertheless, the electrolyte solution should be further improved.

Conclusions 10 to 13 are deduced from articles 4.1, 4.2 and 4.3.

14. The known non-aqueous electrolyte solutions are not very suitable for using with Ca metal, therefore an affordable $\text{CaCo}_2\text{O}_4/\text{Ca}(\text{ClO}_4)_2\text{-AN}/\text{V}_2\text{O}_5$ battery was mounted. This electrochemical device allowed us to test by first time the (de)intercalation of calcium ion in calcium cobaltate, while avoiding the use of Ca metal. It was concluded that up to 0.35 Ca^{2+} per formula were reversible deintercalated from the cobaltate and intercalated into V_2O_5 . According to the XRD results, the structure is modified when calcium is (de)intercalated.

15. Reversible intercalation of aluminium into vanadium pentoxide xerogel in an aqueous rechargeable battery has been demonstrated. During the electrochemical intercalation process, vanadium is reduced and the resulting product ($\text{Al}_x\text{V}_2\text{O}_5$) becomes XRD-amorphous at $x=0.5$. The electrochemical intercalation of Al^{3+} is parallel to water and protons intercalation. Besides electrochemical intercalation, chemical exchange of ions between the electrode and the electrolyte solution can also take place.
16. Aluminium ions are effectively inserted in the framework of $\text{Na}_3\text{V}_2(\text{PO}_4)_3$ using aqueous electrolyte although some contribution of proton insertion cannot be completely excluded. The surface capacitance can also contribute to the apparent capacity. In the case of using ionic liquid as non-aqueous electrolyte, it seems that only sodium ions are reversibly (de)intercalated, and not aluminium. This find involves being feasible to develop a hybrid battery with Al metal as negative electrode and NVP as sodium-insertion positive electrode. The main difficulty is the compatibility of the electrolyte solution with the materials of the electrodes.

Conclusions 14 to 16 are deduced from articles 4.4, 4.5 and 4.6.

Post-lithium batteries could be competitive against lithium ones, but many improvements are still needed before their commercialization, particularly for developing new electrolyte solutions. Another possibility is using hybrid electrolytes and/or hybrid batteries.

ANEXO I

Otras aportaciones científicas

Ordered mesoporous titanium oxide for thin film microbatteries with enhanced lithium storage

Gregorio F. Ortiz ^a, Ángel Berenguer-Murcia ^b, Marta Cabello ^a, Diego Cazorla-Amorós ^b, José L. Tirado ^a.

^aLaboratorio de Química Inorgánica. Universidad de Córdoba. Edificio C3, Campus de Rabanales. Spain

^bInstituto Universitario de Materiales. Departamento de Química Inorgánica. Universidad de Alicante. Spain.

Abstract

A 3D mesoporous TiO₂ material with well-developed mesostructure is prepared in the form of a binder-free thin (100 nm) film and studied as potential candidate for the negative electrode in lithium microbatteries. By appropriate thermal treatments, the selected crystal structure (anatase, rutile, or amorphous), and micro-/mesostructure of the materials was obtained. The effects of voltage window and prelithiation treatment improved first cycle reversibility up to 86% and capacity retention of 90% over 100 cycles. After a prolonged intercalation of lithium ions in ordered mesoporous TiO₂ appeared small particles assigned to Li₂Ti₂O₄ with cubic structure as observed from ex-situ TEM micrographs. This study highlights the flexibility of the potential window to which the electrode can operate. Maximum capacity values over 100 cycles of 470 $\mu\text{A h cm}^{-2} \mu\text{m}^{-1}$ and 177 $\mu\text{A h cm}^{-2} \mu\text{m}^{-1}$ are obtained for voltage ranges of 0.1–2.6 V and 1.0–2.6 V, respectively. The observed values are between 6 and 2 times higher than those obtained for films with 600 nm (80 $\mu\text{A h cm}^{-2} \mu\text{m}^{-1}$) and 900 nm (92 $\mu\text{A h cm}^{-2} \mu\text{m}^{-1}$) lengths. This indicates that 100 nm thin TiO₂ films with high accessibility show finite-length type diffusion which is interesting for this particular application.

Electrochimica Acta 166 (2015) 293-301

On the Mechanism of Magnesium Storage in Micro and Nano-Particulate Tin Battery Electrodes

Francisco Nacimiento, Marta Cabello, Carlos Pérez-Vicente, Ricardo Alcántara, Pedro Lavela, Gregorio F. Ortiz, José L. Tirado.

Laboratorio de Química Inorgánica. Universidad de Córdoba. Edificio C3, Campus de Rabanales. Spain

Abstract

This study reports on the electrochemical alloying-dealloying properties of Mg_2Sn intermetallic compounds. ^{119}Sn Mössbauer spectra of $\beta\text{-Sn}$ powder, thermally alloyed cubic- Mg_2Sn , and an intermediate MgSn nominal composition are used as references. The discharge of a Mg/micro-Sn half-cell led to significant changes in the spectra line shape, which is explained by a multiphase mechanism involving the coexistence of c- Mg_2Sn , distorted $\text{Mg}_{2-\delta}\text{Sn}$, and Mg-doped $\beta\text{-Sn}$. Capacities and capacity retention were improved by using nanoparticulate tin electrodes. This material reduces significantly the diffusion lengths for magnesium and contains surface SnO and SnO_2 , which are partially electroactive. The half-cell potentials were suitable to be combined versus the MgMn_2O_4 cathodes. Energy density and cycling properties of the resulting full Mg-ion cells are also scrutinized.

Nanomaterials 8 (7) (2018) 501-510

On the applicability of molybdate as electrode in calcium battery: a structural study of layer-type Ca_xMoO_3

Marta Cabello, Francisco Nacimiento, Ricardo Alcántara, Pedro Lavela, Carlos Pérez-Vicente, José L. Tirado.

Laboratorio de Química Inorgánica. Universidad de Córdoba. Edificio C3, Campus de Rabanales. Spain

Abstract

Calcium batteries could be an alternative to lithium analogues, but this technology is still in its infancy. It is previously known that layered-type molybdate ($\alpha\text{-MoO}_3$) can intercalate hydrated calcium ions in aqueous electrolyte, and this intercalation process increases the interlayer spacing. In this work, we have found that $\alpha\text{-MoO}_3$ is electrochemically active in calcium cell with non-aqueous electrolyte. The mechanism of intercalation has been explored by using XRD, Raman and XPS. The layered structure of $\alpha\text{-MoO}_3$ is preserved upon electrochemical intercalation of unsolvated calcium, and the perovskite-type structure of CaMoO_3 is not formed. The experimental length of the lattice parameter perpendicular to the slab increases from 13.85 Å to 14.07 Å in the first stages of intercalation. This limited increase can be optimum for achieving good electrochemical cycling. The model for calcium intercalation in the interlayer space was optimized by theoretical calculations based on the density functional theory. The resulting experimental reversible capacity is about 80-100 mA h g⁻¹, and the average voltage is ca. 1.3 V vs. Ca. Further improvement of the electrolyte composition and particle size and morphology could render molybdate as a suitable electrode for rechargeable calcium batteries. The slow diffusion of calcium ion, the side-reactions and the competing conversion reaction could be drawbacks, particularly at deep discharge and low voltages.

Enviado el 17 de Marzo de 2018 la revista *Chemistry of Materials*. (Pendiente de aceptación).

ANEXO II

Técnicas

A.II.1. Difracción de rayos-X

La difracción de rayos-X es una técnica no destructiva empleada para dilucidar estructuras cristalinas. La técnica consiste en hacer incidir un haz de rayos-X en la muestra que quiere estudiarse. Este haz se separa en varias direcciones y, por difracción, da lugar a un patrón de intensidades que se interpretarán en base a la ubicación de los átomos en el cristal.

El fenómeno de la difracción puede describirse con la Ley de Bragg, formulada como:

$$n \lambda = 2 d \sin \theta \quad (1)$$

donde n es un número entero que representa el orden de reflexión, λ es la longitud de onda de los rayos-X, d es la distancia interplanar del cristal y θ es el ángulo de Bragg.

En la figura 1 puede verse un esquema de cómo un haz es difractado por los planos de red hkl .

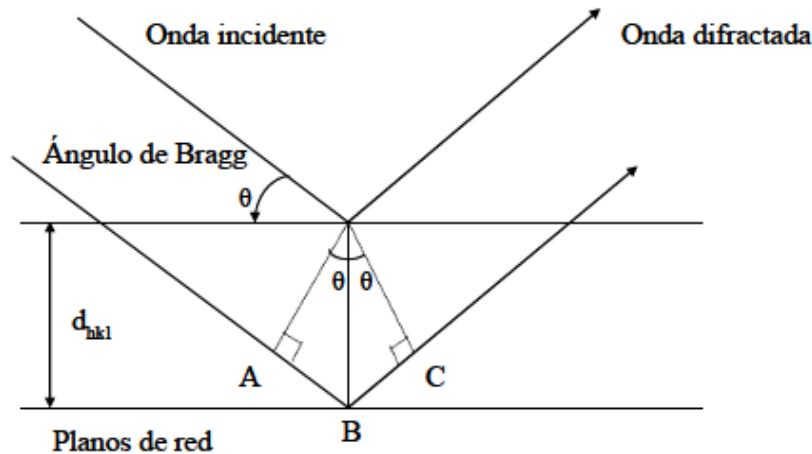


Figura 1. Esquema de difracción de rayos-X.

Los rayos-X del haz incidente son difractados por dos planos sucesivos hkl con espaciado interlaminar d_{hkl} . La difracción se produce cuando la diferencia de caminos recorridos por dos rayos es n veces la longitud de la onda incidente, generando así una interferencia constructiva.

El difractómetro consta de un tubo emisor de rayos-X, un soporte en el cual se coloca la muestra y un detector de rayos-X. Cuando incide un haz de electrones sobre una placa de cobre metálico, se genera el haz. El haz incide sobre la muestra y se difracta, recogiendo esta difracción por el detector. La geometría más empleada en un equipo de difracción es la geometría Bragg-Brentano. En ella, el detector se desplaza a velocidad angular constante. La muestra también gira a una velocidad (la mitad que la del detector) de forma que el ángulo que se forma entre el detector y el plano de la muestra es el mismo que el formado entre ésta y la fuente de radiación. Por otra parte, la geometría de ángulo rasante es aquella en la cual sólo se desplaza el detector, y el ángulo que forma el haz con la muestra permanece fijo durante el análisis. Este tipo de geometría suele emplearse cuando las muestras a analizar son películas delgadas en las que se busca que la profundidad de penetración de los rayos-X no sea mayor al espesor de la película.

La intensidad del rayo difractado depende del número de átomos que hay por unidad de superficie en cada uno de los planos, y del poder de dispersión de las especies que constituyen dicho plano, que es directamente proporcional al número de electrones que hay en sus orbitales.

Las anchuras de las señales de difracción están influenciadas por el tamaño de los dominios de difracción (o cristalitos) y por las microdeformaciones. Así, el tamaño medio de cristalito (L) se puede calcular usando la ecuación de Scherrer:

$$L = \frac{K\lambda}{\beta \cos \theta} \quad (2)$$

donde β es la anchura de una señal de difracción centrada a un cierto valor de ángulo θ , λ es la longitud de onda de la radiación ($\text{CuK}\alpha$), y K depende de la forma de las partículas y direcciones cristalográficas

Para estudiar los difractogramas se puede usar el método de Rietveld, basado en el método matemático de mínimos cuadrados, que se emplea para determinar los parámetros estructurales de la muestra a partir de la creación de un modelo teórico que se ajusta al patrón de difracción experimental. Este modelo teórico incluye factores como son los estructurales, la concentración de fases presentes, el tamaño de cristal y

las microdeformaciones. También contempla el efecto de la óptica del difractor sobre la medición. Los refinamientos de mínimos cuadrados se llevan a cabo hasta que se obtiene el mejor ajuste entre los difractogramas experimental y calculado.

Los difractogramas de rayos-X de esta tesis se han registrado en los difractómetros *Siemens D5000* y *Bruker D8 Discover A25* pertenecientes al Instituto de Química Fina y Nanoquímica de la Universidad de Córdoba, equipados con un monocromador de grafito y una radiación de $\text{CuK}\alpha$.

A.II.2. Microscopía electrónica de barrido

La microscopía electrónica de barrido (siglas en inglés SEM) es una técnica basada en la interacción electrón-materia que se emplea para estudiar la morfología y la textura de la superficie de los sólidos.

El microscopio electrónico de barrido emplea un haz fino de electrones, con energía aproximada de 5 a 50 keV, que se proyecta sobre una pequeña región de la muestra a estudiar y la barre en series de trazos paralelos, desplazándose a lo largo de toda la superficie. Así, la muestra emitirá electrones, secundarios y retrodispersados, que son detectados y transformados en una imagen que puede tener aspecto tridimensional.

Podemos diferenciar tres tipos principales de detección para obtener información en SEM:

- Detección de electrones secundarios. Son los electrones más frecuentemente usados para construir las imágenes. Son electrones de baja energía que se producen cuando el haz incidente provoca que uno o varios de los electrones de los átomos de la muestra pueda abandonarla. Esta interacción proporciona una imagen con contraste topográfico.
- Detección de electrones retrodispersados. Son electrones de alta energía, prácticamente igual a la del haz incidente, que se generan cuando se produce un choque frontal y elástico entre el haz incidente y la muestra. Con ellos se pueden obtener fotografías con contraste tanto topográfico como de composición.

- Detección de rayos-X. El detector de este tipo más usado suele ser de energía dispersiva de rayos-X. Se basa en que los electrones del haz incidente pueden excitar a los átomos de la muestra, arrancar electrones e inducir tránsitos de los electrones entre orbitales de los átomos que hay en la muestra que dan lugar a emisión de fotones con energías características. Se usa para análisis cualitativo y semicuantitativo de los elementos que constituyen la muestra.

Este tipo de microscopios electrónicos puede ampliar la imagen de un objeto hasta más de 200000 veces.

Las imágenes de SEM se han obtenido con los microscopios electrónicos *JEOL SM 6300* y *JEOL SM 7800F*, pertenecientes a los Servicios Centrales de Apoyo a la Investigación (SCAI) de la Universidad de Córdoba.

A.II.3. Microscopía electrónica de transmisión

La técnica de microscopía electrónica de transmisión (siglas en inglés TEM) se emplea para estudiar la estructura interna de partículas muy pequeñas.

El microscopio electrónico de transmisión emplea un haz de electrones de entre 80 y 200 keV de energía, aproximadamente. Este haz es dirigido al objeto que se desea aumentar. Parte de los electrones rebotan o son absorbidos por el objeto y otros lo atraviesan, pasan a través de lentes electromagnéticas y forman una imagen aumentada. Para el registro de la imagen se coloca una pantalla debajo del objeto.

Los electrones habitualmente son generados por efecto termoiónico en un filamento (actúa como cátodo) que puede ser de wolframio o de hexaboruro de lantano. Los electrones son acelerados en un sistema a vacío seleccionando un potencial fijo. El vacío evita la dispersión de dichos electrones, asegurando el principio de la técnica. La formación de la imagen se sucede en dos etapas. En la primera, el haz de electrones que incide sobre la muestra se dispersa en varios haces. En la segunda, estos haces divergentes vuelven a converger y así se forma la imagen ampliada.

Este tipo de microscopios electrónicos puede ampliar la imagen de un objeto hasta un millón de veces.

Las imágenes de TEM se han obtenido con los microscopios electrónicos *JEOL EM 1400* y *JEOL EM 2010*, pertenecientes a los Servicios Centrales de Apoyo a la Investigación (SCAI) de la Universidad de Córdoba.

A.II.4. Espectroscopia fotoelectrónica de rayos-X

La espectroscopia fotoelectrónica de rayos-X (siglas en inglés XPS) nos proporciona información acerca de la composición química de la superficie de la muestra objeto de estudio.

El efecto fotoeléctrico (Figura 2) consiste en la expulsión de electrones de un átomo en un sólido debido a la radiación electromagnética que incide sobre él. Si la radiación electromagnética incidente está en el rango de los rayos-X, como es la radiación $MgK\alpha$ (1253.6 eV), se pueden expulsar electrones tanto desde orbitales de niveles internos, como también desde orbitales de valencia; y mediante la espectroscopia de fotoelectrones de rayos-X se determina la energía e intensidad de los fotoelectrones generados. Esto permite estudiar los elementos presentes en la superficie de la muestra y sus estados de oxidación.

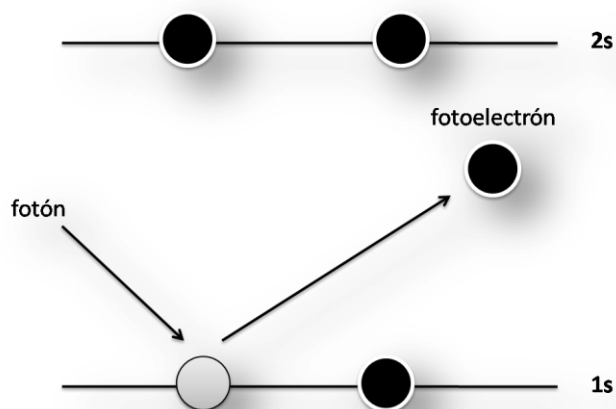


Figura 2. Un fotón incidente causa la expulsión de un fotoelectrón.

En XPS, la superficie a analizar se irradia con fotones de rayos-X blandos. Las fuentes de rayos-X más comunes son Al K (1486.6 eV) y Mg K. Sólo los electrones expulsados en unas decenas de Å de la superficie pueden dejar el sólido sin sufrir pérdida de energía. Estos electrones son detectados de acuerdo a su energía cinética por un espectrómetro de electrones, así se producen los picos útiles en los espectros.

Cuando un fotón de energía $h\nu$ interacciona con un electrón en un nivel con una energía de enlace E_E , la energía del fotón es transferida al electrón. El resultado es la emisión de un fotoelectrón con una energía cinética (E_c) que puede expresarse como:

$$E_c = h\nu - E_E - \phi \quad (3)$$

Donde ϕ es la denominada función de trabajo del espectrómetro.

Cada elemento tiene un espectro característico de XPS. Los únicos elementos que no pueden analizarse con esta técnica son el hidrógeno y el helio.

Cuando se produce la excitación de un nivel de energía interno (*core level*) el pico principal en el espectro corresponde a un proceso en el cual el ión que queda se encuentra en su estado fundamental. Sin embargo, junto al pico principal puede aparecer un pico de menor intensidad y de energía algo diferente (pico satélite).

Los espectros se registraron en un espectrofotómetro *SPECS Phoibos 150MCD*, de la unidad de XPS del área de Determinación Estructural y Análisis del SCAI de la Universidad de Córdoba. Los espectros se ajustaron con el programa SPECS, y el carbono adventicio se usó para calibrar.

A.II.5. Resonancia paramagnética electrónica

La resonancia paramagnética electrónica (siglas en inglés EPR) es una técnica que permite estudiar especies químicas que tienen electrones desapareados. Se pueden medir muestras en estado sólido, líquido o gaseoso. La sensibilidad de la técnica también permite estudiar sistemas que tienen una concentración de centros activos muy baja, por ejemplo disoluciones con radicales libres o materiales con defectos en su

estructura, cuya contribución paramagnética es indetectable en técnicas del magnetismo clásico.

Como puede verse en la Figura 3, en presencia de un campo magnético externo, hay dos estados de espín electrónico posibles: $m_s = +1/2$ y $m_s = -1/2$. La absorción de energía (ΔE) de una cierta frecuencia (en la región de las microondas) sucede cuando la intensidad del campo magnético B es la adecuada.

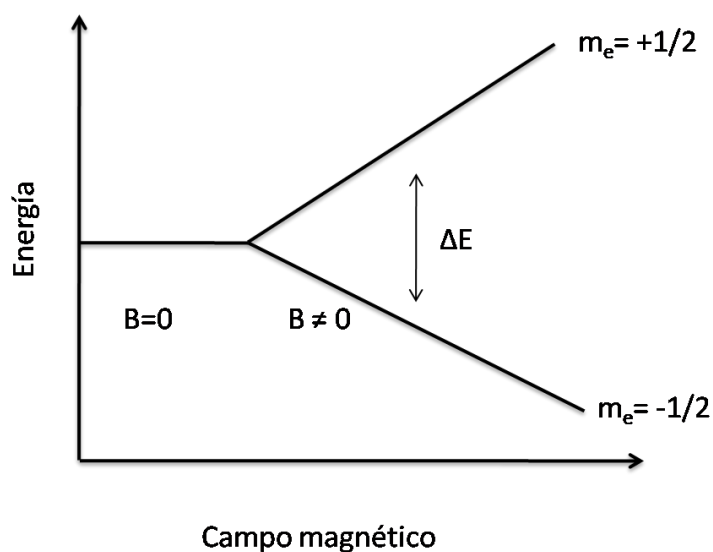


Figura 3. Desdoblamiento de los niveles de energía en electrones desapareados.

La aplicación de un campo magnético permite la promoción de electrones por absorción de energía hacia el nivel de mayor energía, mientras que la relajación de los espines excitados (caídas al nivel energético inferior) puede ocurrir por emisión de radiación o por la pérdida de energía al cedérsela al entorno. La radiación de microondas empleada penetra fácilmente en la mayoría de sólidos no metálicos. En la práctica, se puede proceder de dos formas: variando el campo magnético aplicado o variando la frecuencia. Lo habitual es fijar la frecuencia y variar el valor del campo aplicado, ya que la manipulación de frecuencias dentro del rango de las microondas presenta varios inconvenientes técnicos. La diferencia de energía (ΔE) entre los dos estados de espín electrónico viene dada por la siguiente ecuación:

$$\Delta E = h\nu = g \mu_B B \quad (4)$$

donde h es la constante de Planck, ν es la frecuencia de resonancia, μ_B es la constante del magnetón de Bohr ($\mu_B = eh/4\pi m_e$) y g es el factor de desdoblamiento espectroscópico o factor de Landé. El valor de g teórico viene dado por:

$$g = 1 + \frac{J(J+1) + S(S+1) - L(L+1)}{2J(J+1)} \quad (5)$$

Para un electrón libre el valor de g es 2,0023. En gases y líquidos, g es isotrópica, independiente de la orientación de la muestra respecto del campo magnético aplicado. Para sólidos, g puede ser anisotrópica. Cada sustancia tiene un valor de g característico. Éste se obtiene del punto central en el que la derivada de la curva de absorción queda anulada. La magnitud de la radiación absorbida es proporcional a la diferencia de población entre los dos estados energéticos. Además del valor de g , otros parámetros importantes a tener en cuenta en el espectro de EPR son la anchura y la intensidad de la señal. Los ensanchamientos pueden originarse por la anisotropía del valor de g y/o por la presencia de acoplamientos entre núcleos. Además, la señal observada también puede sufrir distorsiones debido a la interacción dipolo-dipolo entre momentos de espín vecinos y/o la presencia de impurezas paramagnéticas.

Dentro de las interacciones de los electrones con los núcleos podemos destacar:

1. Interacciones hiperfinas: interacción entre un electrón desapareado de un átomo con el espín nuclear ($I \neq 0$) de su propio átomo.
2. Interacciones superhiperfinas: interacción entre el electrón y núcleos distintos al de las especies que contienen el electrón.

Los espectros de EPR de esta tesis se han obtenido en el Instituto de Química General e Inorgánica de la Academia Búlgara de las Ciencias, en Sofía (Bulgaria), usando un espectrómetro *ERS 220/Q* que trabaja a 9,23 GHz.

A.II.6. Resonancia magnética nuclear

La resonancia magnética nuclear (siglas en inglés NMR) es una técnica espectroscópica que se emplea principalmente para el estudio de la estructura molecular.

Ésta se basa en someter a los núcleos (con número cuántico de espín nuclear $I \neq 0$) a un campo magnético que provoca desdoblamiento de los niveles energéticos del espín nuclear y permite absorción de radiación electromagnética en la región de las radiofrecuencias. Al aplicar el campo magnético, los espines de los núcleos, que estaban orientados al azar, se disponen en dos sentidos posibles: paralelo al vector de magnetización el campo (de baja energía), o antiparalelo (de alta energía). La diferencia de energía entre los dos tipos de orientación en el rango de las radiofrecuencias se describe como:

$$\Delta E = \frac{h \omega}{2\pi} = h \omega \quad (6)$$

Teniendo en cuenta que $\omega = 2\pi\nu_0 = \gamma H$, denominado como frecuencia de Larmor se llega a que:

$$\nu = \frac{\gamma H}{2\pi} \quad (7)$$

siendo γ la constante giromagnética y H el campo magnético.

Si se suministra energía de radiofrecuencia, es posible cambiar los momentos magnéticos nucleares desde la orientación de baja energía a la de alta energía siempre que dicha energía sea igual a ΔE , entonces se produce el fenómeno de NMR. La energía emitida es la de la relajación de los espines.

La posición exacta de la señal depende del parámetro de apantallamiento, es decir, los electrones de enlace próximos al núcleo lo “apantallan” del campo magnético externo. Cada núcleo posee un parámetro de apantallamiento distinto, por tanto entrarán en resonancia según el tipo de átomo o grupo al que esté unido nuestro núcleo. Este fenómeno se denomina desplazamiento químico.

El desplazamiento químico se expresa en ppm. Puede expresarse como:

$$\delta = (\nu - \nu_{\text{ref}}) / \nu_{\text{ref}} \quad (8)$$

El origen de la señal en RMN es resultado de la diferencia de energía entre estados. Esta energía es absorbida por los espines, pasando del nivel de menor energía al de mayor energía. La relajación es la transición de estos espines del nivel mayor de

energía al nivel menor, dando lugar a una emisión de energía. La intensidad de la señal es proporcional a la diferencia de población entre ambos estados. La espectroscopia de RMN es una técnica bastante sensible, ya que puede detectar variaciones muy pequeñas de población.

Las muestras líquidas proporcionan espectros bien resueltos mientras que las muestras sólidas producen señales muy anchas, dificultando la interpretación de los mismos. Por tanto, para la obtención de espectros de alta resolución en sólidos, se aplican técnicas especiales como MAS NMR (siglas en inglés). Si una muestra se gira suficientemente rápido alrededor de un eje que forma un ángulo de $54,7^\circ$ con la dirección principal del campo magnético externo, denominado ángulo mágico, el ensanchamiento dipolar se promedia y se pueden obtener espectros de alta resolución. Cuando $\theta = 54.74^\circ$, el término angular $3\cos^2\theta - 1$ tiende a cero, por lo que las interacciones que dependan de esta expresión quedarían anuladas. Esto permite reducir el ensanchamiento de las señales del espectro, mejorando la resolución del mismo.

Los espectros de MAS RMN se registraron en un espectrómetro *Bruker Avance-400*, perteneciente a los Servicios Centrales de Apoyo a la Investigación (SCAI) de la Universidad de Córdoba.

A.II.7. Espectroscopia vibracional Raman

La espectroscopia de Raman se fundamenta en los fenómenos de dispersión de la luz monocromática, generalmente de un láser en el rango visible, infrarrojo cercano o ultravioleta cercano. Cuando un fotón incide sobre una molécula se produce una interacción con la nube electrónica de sus enlaces, excitando a esta molécula a un estado de energía virtual. La mayor parte de la luz que es dispersada tendrá la misma frecuencia que el haz incidente (dispersión de Rayleigh), mientras que otra tendrá energía diferente (dispersión Raman). El desplazamiento Raman es igual al nivel vibratorio que está implicado, por tanto, la intensidad de dispersión Raman vendrá determinada por el cambio de polarizabilidad, y el patrón de frecuencias será determinado por los estados rotacionales y vibracionales característicos de la muestra a estudiar.

Cabe destacar dos tipos de líneas espectrales: Raman Stokes y Raman anti-Stokes. Las primeras son líneas espectrales satélites generadas por una dispersión que ocurre por debajo de la frecuencia incidente. Las segundas, corresponden a líneas débiles que se generan al producirse la dispersión a frecuencias superiores a la frecuencia incidente.

Se empleó un espectrómetro *Raman Renishaw* equipado con microscopía Leica. Este equipo pertenece al Departamento de Química Orgánica de la Universidad de Córdoba.

A.II.8. Espectroscopia vibracional infrarroja

La espectroscopia infrarroja se basa en la interacción entre las moléculas y la radiación infrarroja (longitud de onda > 800 nm). Cuando se produce la absorción de esta radiación por parte de una molécula, se producen vibraciones atómicas, provocando el salto de esta molécula a un estado excitado.

Para una molécula diatómica AB, su frecuencia de vibración fundamental (ν_0) puede expresarse como:

$$\nu_0 = \frac{1}{2\pi} \left(\frac{k}{\mu} \right)^{1/2} \quad (9)$$

donde μ es la masa reducida de la molécula y k es la constante de fuerza del enlace químico. Por tanto, ν_0 es proporcional a k e inversamente proporcional a μ .

La interacción más importante entre radiación IR y moléculas consiste en la absorción de un fotón con frecuencia ν_0 para excitar el correspondiente modo normal de vibración desde el estado fundamental hasta el primer estado excitado. Para que se produzca esta absorción, el campo eléctrico de la radiación del fotón debe interactuar con el campo eléctrico de la molécula vibrante. Esto se refleja en que existen modos normales de vibración que no son activos, invisibles a la radiación IR. Para que un modo normal absorba radiación IR debe inducir un cambio del momento bipolar total instantáneo de la molécula.

En un espectrofotómetro de IR con transformada de Fourier, se produce un haz IR policromático que se separa en dos haces cuando llega a un separador. Uno de los haces se refleja en un espejo inmóvil, y el otro en uno móvil, recorriendo así una distancia extra. Después, los haces se superponen e inciden sobre la muestra, que absorbe parte de la radiación. Mediante la transformada de Fourier, la curva intensidad frente a tiempo es transformada en el espectro.

Las gráficas de espectros IR representan en ordenadas el % de transmitancia T en función del número de onda ν , en unidades de cm^{-1} . La transmitancia indica la fracción de intensidad de radiación de la correspondiente longitud de onda (I_λ) que se transmite a través de la muestra con respecto al haz de referencia ($I_{\lambda,0}$). Normalmente, se expresa en forma de %:

$$\%T = \frac{I_\lambda}{I_{\lambda,0}} 100 \quad (10)$$

Los espectros se han obtenido en un equipo *FT-MIR Bruker Tensor 27*, perteneciente a los Servicios Centrales de Apoyo a la Investigación (SCAI) de la Universidad de Córdoba.

A.II.9. Análisis térmico

Cuando un material se calienta o se enfría, su estructura cristalina y su composición química sufren cambios: fusión, solidificación, amorfización, expansión o compresión de volumen, etc. En el análisis térmico se mide una propiedad de la muestra a una determinada atmósfera en función del tiempo o de la temperatura, cuando dicha muestra se somete a un programa de temperatura controlado. Podemos distinguir tres tipos principales de medidas en análisis térmico.

- Análisis Termogravimétrico (en inglés TGA): mide la variación de la masa de la muestra cuando ésta es sometida a una temperatura controlada (frecuentemente calentamiento a velocidad constante). El registro de esta variación proporciona información sobre si la muestra se descompone o reacciona con otros

componentes. La muestra se coloca en una microbalanza y se calienta en un pequeño horno.

- Análisis Termodiferencial (en inglés DTA): se basa en calentar o enfriar la muestra a estudiar y medir la diferencia de temperatura respecto a una referencia. La referencia no debe sufrir ningún cambio. Generalmente se usa para medir un termopar diferencial que da una señal en unidades de microvoltios, la cual se puede transformar en temperatura o en energía mediante calibrado.
- Calorimetría Diferencial de Barrido (en inglés DSC): mide la diferencia entre la energía suministrada a la muestra y a la referencia que es necesaria para mantener ambas a la misma temperatura durante un proceso de calentamiento. Permite determinar los cambios de entalpía de una forma más cuantitativa y directa que el DTA, y también los valores de capacidad calórica.

Los resultados de TGA y DTA se obtuvieron en un instrumento *Shimadzu DTG-60*. Las curvas de calorimetría se obtuvieron en un instrumento *Calisto Labsys Evo*.

A.II.10. Medidas de la superficie

La superficie de un material controla muchas propiedades, por lo que es pertinente el estudio de las isothermas de adsorción de gases, los poros y la superficie específica.

Según la clasificación de la IUPAC, según su diámetro los poros pueden ser macroporos (>50 nm), mesoporos (entre 50 y 2 nm) o microporos (< 2nm).

Para determinar la superficie específica, el método BET fue desarrollado por los científicos Stephen Brunauer, Paul Emmett y Edward Teller. Con este método, se puede determinar la cantidad de gas necesaria para formar una monocapa sobre la superficie de la muestra a estudiar. Si esta cantidad se expresa en número de moléculas y puede estimarse el área que ocupa cada una, puede determinarse el área superficial del sólido.

Las mediciones de la superficie de las muestras se realizan previa desgasificación, y para ello se lleva a vacío la muestra objeto de estudio y luego se calienta. Posteriormente, ésta se enfría en un baño de nitrógeno líquido (77 K) al cual se admite la entrada de cantidades conocidas de nitrógeno en su forma gaseosa. Si se mide la presión del gas y los cambios de presión que va sufriendo, se puede obtener la isoterma de adsorción/desorción y determinar el punto en el que se forma la monocapa, la superficie específica y la distribución del tamaño de poro.

Según la clasificación de la IUPAC, podemos encontrar seis tipos de isotermas de adsorción, tal y como puede verse en la figura 4.

La isoterma tipo I es característica de procesos de quimisorción, o de llenado de microporos en superficies muy homogéneas, siguiendo la ecuación de Langmuir.

La isoterma tipo II corresponde a adsorción en mono-multicapas, en sólidos no porosos o macroporosos, con marcada superficie heterogénea. En esta isoterma la adsorción-desorción es totalmente reversible.

La isoterma tipo III normalmente aparece asociada a procesos de adsorción en sólidos macroporosos o no porosos con interacciones adsorbato-adsorbente débiles e interacciones adsorbato-adsorbato fuertes.

La isoterma tipo IV es típica de sólidos mesoporosos y se caracteriza por presentar ciclos de histéresis debido a condensación capilar en los mesoporos.

La isoterma tipo V (forma convexa) es poco común, equivalente a la tipo III pero con condensación capilar.

La isoterma tipo VI, es característica de procesos de adsorción en multicapas. Por ejemplo, gases nobles (Kr) sobre superficies altamente homogéneas (grafito).

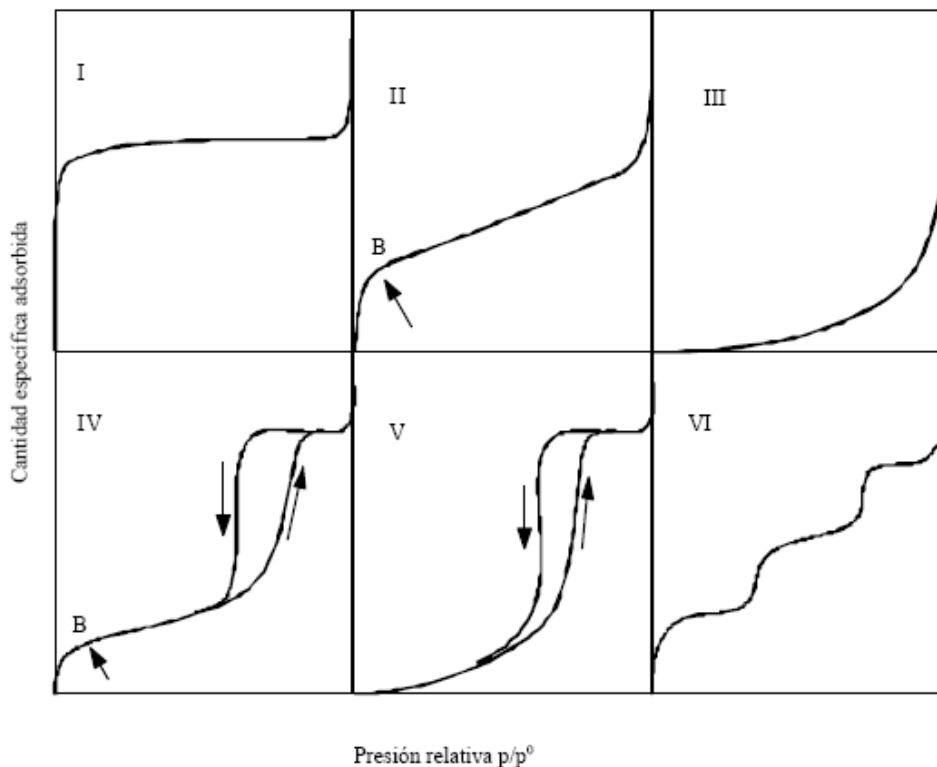


Figura 4. Tipos de isothermas según la clasificación de la IUPAC.

Las medidas de superficie específica y poros de las muestras se realizaron en un equipo *Nova 1200e* (Quantachrome instruments), mediante adsorción física de nitrógeno, y previa desgasificación de las muestras.

A.II.11. Técnicas electroquímicas

Celda electroquímica

En el caso de usar electrolitos no acuosos, las celdas electroquímicas se ensamblan dentro de una caja de guantes *MbraunLabMaster 130* con atmósfera de argón. Las trazas de O_2 y H_2O están controladas mediante sensores. Para el montaje de las baterías se emplean celdas tipo *Swagelok®* de dos y tres electrodos (Figuras 5 y 6). En ellas se introduce el electrodo de trabajo, el contraelectrodo y el electrodo de

referencia, si lo hubiera. Separando los distintos electrodos se encuentran dos hojas de fibra de vidrio *Whatman* empapadas del electrolito que se vaya a utilizar.



Figura 5. *Swagelok*® de dos electrodos.



Figura 6. *Swagelok*® de tres electrodos.

Técnica galvanostática

Consiste en la aplicación de una intensidad de corriente conocida y constante a través de la celda, midiéndose la variación de voltaje que se produce entre los electrodos. Esta técnica permite controlar de forma directa y precisa la cantidad de producto obtenido, siempre y cuando no se produzcan reacciones paralelas.

La diferencia de potencial en una celda electroquímica, viene expresado como la diferencia de potenciales de los dos electrodos en equilibrio:

$$\Delta E = E_{\text{cátodo}} - E_{\text{ánodo}} \quad (11)$$

El potencial de una celda electroquímica en equilibrio (ΔE) está a su vez relacionado con la energía libre de Gibbs:

$$\Delta G = -n F \Delta E \quad (12)$$

Este potencial se modifica en función de la cantidad de metal alcalino intercalado o insertado, al desplazarse la energía de Fermi debido a la donación electrónica del huésped hacia el sólido anfitrión. Además, las interacciones entre las especies huéspedes y los cambios estructurales del anfitrión también influyen en el potencial.

La cantidad de energía liberada por una batería puede expresarse en función de la cantidad del material activo, y la intensidad aplicada debe ser equivalente a dicha cantidad. Según la ley de Faraday puede expresarse la intensidad como:

$$i = \frac{F * m * C}{3600 * M * t} \quad (13)$$

donde i es la intensidad de corriente (mA), F es la constante de Faraday (96500 C), m es la masa del material activo (mg), M es el peso atómico o molecular del material activo (g/mol) y C hace referencia a la cinética que se impone al experimento. Consideramos como cinética la inserción o extracción de un mol del ion en el que se basa la batería por cada mol de compuesto activo cada t horas.

Técnica potencioestática

Se aplica un potencial constante a la celda durante un tiempo determinado. Los valores de relajación de la intensidad quedan registrados, de manera que si se representa la intensidad al final de cada paso de potencial frente al voltaje de la celda, se pueden resolver los distintos procesos de reducción y oxidación que tienen lugar durante el ciclado de la batería. De esta manera, llamamos picos de reducción a las señales que se obtienen en este tipo de representación durante la descarga de la batería, mientras que los picos de oxidación son aquellos que se obtienen durante la carga.

Con estos datos se puede calcular la carga electrónica que ha atravesado la celda. Para ello se realiza la integración de la curva de intensidad frente al tiempo. De nuevo, con las leyes de Faraday, podemos calcular el número de moles de producto que se ha obtenido suponiendo que no hay reacciones paralelas.

Por otra parte, la carga total almacenada en la batería puede separarse en contribución faradaica y no faradaica, que proviene del efecto de la doble capa. El área bajo las curvas de voltametría cíclica (en inglés CV) representa la cantidad total de carga almacenada que proviene de procesos faradaicos y capacitivos. Ambas contribuciones pueden separarse por el análisis de CV a diferentes velocidades de barrido. De acuerdo con la siguiente ecuación:

$$i = av^b \quad (14)$$

donde i es la corriente medida a un valor de potencial específico y v es la velocidad de barrido. Tanto a como b son parámetros ajustables, los valores de b son determinados por la pendiente de la curva de $\log i$ vs $\log v$. Hay dos valores limitantes, $b = 0.5$ y $b = 1.0$. Para el primero, la corriente es proporcional a los procesos de difusión controlada, y es indicativo de un proceso faradaico. En el segundo caso, se trata de una respuesta capacitiva limitante.

Espectroscopia de impedancia compleja (EIS)

En esta técnica se aplica un potencial (en forma de voltaje sinusoidal) a un electrodo y se mide su respuesta en corriente a diferentes frecuencias. La impedancia puede definirse como el cociente entre el potencial aplicado y la intensidad medida a la salida. Alternativamente, también se puede aplicar una corriente sinusoidal.

La corriente resultante tiene la misma frecuencia que el potencial aplicado pero posee diferente magnitud y fase:

$$Z = \frac{E_0}{I_0} = \frac{E_0 \operatorname{sen}(\omega t)}{I_0 \operatorname{sen}(\omega t + \phi)} = Z_0 \frac{\operatorname{sen}(\omega t)}{\operatorname{sen}(\omega t + \phi)} \quad (15)$$

donde E_0 es el potencial, I_0 es la intensidad, ω es la frecuencia y ϕ es el desfase.

La admitancia es la inversa de la impedancia y se define como una función de transferencia del sistema cuando la perturbación sinusoidal se superpone al potencial aplicado en modo potencioestático. En el caso de la impedancia, representa la función de transferencia del sistema en modo galvanostático, es decir, cuando la perturbación sinusoidal se superpone a la intensidad aplicada.

Los espectros de impedancia se representan a través del diagrama de Nyquist, donde la componente real (Z') se representan en el eje de abscisas, mientras que en ordenadas encontramos los valores de la componente imaginaria multiplicada por menos uno ($-Z''$). Cada punto en el diagrama de Nyquist representa la impedancia a una frecuencia determinada.

Lo ideal cuando se realizan medidas de impedancia es que el sistema esté en equilibrio (o pseudoequilibrio) antes de medir. Esto resulta complicado a veces, puesto que el estado de equilibrio puede verse afectado por cambios de temperatura, absorción de impurezas del disolvente, etc.

Para interpretar el espectro de impedancias, hay que seleccionar un modelo eléctrico apropiado que se ajuste a los datos experimentales. A través del modelo se puede obtener información acerca de la resistencia de la disolución, la resistencia de polarización y la capacitancia de la doble capa (debido a interacciones que ocurren en la interfase electrodo/electrolito). La resistencia de la disolución se obtiene a altas frecuencias. A bajas frecuencias, se obtienen datos sobre la cinética e la reacción.

Se pueden emplear para el ajuste circuitos equivalentes sencillos o complejos. En el caso de los circuitos sencillos sólo se tiene en cuenta la transferencia de carga. La función de transferencia teórica $Z(\omega)$ puede expresarse como:

$$Z(\omega) = R_s + \frac{1}{1/R_p + i\omega + C_p} \quad (16)$$

donde R_s es la resistencia del electrolito, R_p es la resistencia a la transferencia de carga, i es la unidad imaginaria, ω es la frecuencia (rad/s) y C_p es la capacitancia de la doble capa.

En el caso de circuitos complejos, se introduce el elemento de fase constante (siglas en inglés CPE) para tener en cuenta el desfase entre el potencial y la respuesta en corriente.

El CPE se expresa como:

$$Z(\omega) = Z_0 (i \omega)^{-n} \quad (17)$$

donde Z_0 es el CPE y n es el coeficiente de idealidad. Según los valores que tome n , el CPE representará:

- resistencia, $n=0$
- capacitancia, $n=1$
- inductancia, $n=-1$
- impedancia de Warburg, $n=0.5$